



# Journal of Mechanics of Materials and Structures

Special issue

Eleventh Pan-American Congress  
of Applied Mechanics (PACAM XI)

Volume 6, No. 7-8

September–October 2011



mathematical sciences publishers

# JOURNAL OF MECHANICS OF MATERIALS AND STRUCTURES

jomms.org

Founded by Charles R. Steele and Marie-Louise Steele

## EDITORS

CHARLES R. STEELE	Stanford University, USA
DAVIDE BIGONI	University of Trento, Italy
IWONA JASIUK	University of Illinois at Urbana-Champaign, USA
YASUHIDE SHINDO	Tohoku University, Japan

## EDITORIAL BOARD

H. D. BUI	École Polytechnique, France
J. P. CARTER	University of Sydney, Australia
R. M. CHRISTENSEN	Stanford University, USA
G. M. L. GLADWELL	University of Waterloo, Canada
D. H. HODGES	Georgia Institute of Technology, USA
J. HUTCHINSON	Harvard University, USA
C. HWU	National Cheng Kung University, Taiwan
B. L. KARIHALOO	University of Wales, UK
Y. Y. KIM	Seoul National University, Republic of Korea
Z. MROZ	Academy of Science, Poland
D. PAMPLONA	Universidade Católica do Rio de Janeiro, Brazil
M. B. RUBIN	Technion, Haifa, Israel
A. N. SHUPIKOV	Ukrainian Academy of Sciences, Ukraine
T. TARNAI	University Budapest, Hungary
F. Y. M. WAN	University of California, Irvine, USA
P. WRIGGERS	Universität Hannover, Germany
W. YANG	Tsinghua University, China
F. ZIEGLER	Technische Universität Wien, Austria

**PRODUCTION** contact@msp.org

SILVIO LEVY Scientific Editor

Cover design: Alex Scorpan

Cover photo: Mando Gomez, [www.mandolux.com](http://www.mandolux.com)

See <http://jomms.org> for submission guidelines.

JoMMS (ISSN 1559-3959) is published in 10 issues a year. The subscription price for 2011 is US \$520/year for the electronic version, and \$690/year (+\$60 shipping outside the US) for print and electronic. Subscriptions, requests for back issues, and changes of address should be sent to Mathematical Sciences Publishers, Department of Mathematics, University of California, Berkeley, CA 94720-3840.

JoMMS peer-review and production is managed by EditFLOW® from Mathematical Sciences Publishers.

PUBLISHED BY  
 mathematical sciences publishers

<http://msp.org/>

A NON-PROFIT CORPORATION

Typeset in LATEX

Copyright ©2011 by Mathematical Sciences Publishers

## PREFACE

The Eleventh Pan-American Congress of Applied Mechanics (PACAM XI) was held in Foz do Iguaçu, Paraná, Brazil, from January 4 to 8, 2010. The aim of the congress series, set forth by the American Academy of Mechanics (AAM), is to promote progress in the broad field of mechanics by exposing engineers, scientists, and advanced graduate students to new research developments, methods, and problems in mechanics, and by providing broad opportunities for personal interactions through formal presentations and informal conversations.

The PACAM series is held every two years, always in a Latin American venue, at a time when few other conferences are scheduled. Previous congresses had been held in Rio de Janeiro, Brazil (1989), Valparaiso, Chile (1991), São Paulo, Brazil (1993), Buenos Aires, Argentina (1995), San Juan, Puerto Rico (1997), Rio de Janeiro, Brazil (1999), Temuco, Chile (2002), Havana, Cuba (2004), Mérida, Mexico (2006), and Cancún, Mexico (2008).

PACAM XI was a cross-disciplinary congress that attracted 230 researchers from thirty countries of the three Americas, Europe, Africa, and Asia. They have presented 202 regular papers and 14 invited lectures in the areas of solid mechanics, fluid mechanics, dynamics, controls, computational mechanics, composite materials, biomechanics, structural reliability and stochastic mechanics, nonlinear phenomena in mechanics, non-Newtonian fluid mechanics, fatigue and fracture mechanics, and other areas of general interest. Also, the Society for Natural Philosophy (SNP) held its 48th meeting during the event. The online version of the Proceedings of PACAM XI can be downloaded from the congress web site at <http://www.set.eesc.usp.br/pacam2010>.

PACAM XI was promoted by AAM, SNP, the Brazilian Society of Mechanical Sciences and Engineering (ABCM), and the Brazilian Society for Applied and Computational Mathematics (SBMAC). A sincere acknowledgment is extended to all the sponsors, which include the Itaipu Technological Park, Itaipu Binacional, ENGEMASA, Brazilian Ministry of Science and Technology, Coordination for the Improvement of Higher Education Personnel (CAPES), The National Council for Scientific and Technological Development (CNPq), and several sectors from the University of São Paulo (USP).

Following a PACAM tradition, authors of selected talks were invited to submit full-length papers related to their presentation at the conference. The selected papers were then subjected to the normal, peer-review process, and the best papers were included in this special issue of the *Journal of Mechanics of Materials and Structures*. I thank the Editors-in-Chief for the opportunity to organize the special issue; the individual authors for their excellent contributions; and the reviewers who not only helped in the selection of the best papers but also used skillful judgment to find merit and to make corrections for the betterment of the selected papers.

A total of 14 papers were selected from a wide range of topics in theoretical, computational, and experimental mechanics, and represent well the areas and mini-symposia of PACAM XI:

In solid mechanics, Nogueira de Codes and Benallal present experimental results about the effects of specimen geometry in the characteristics of Portevin–le Châtelier effect due to dynamic strain aging of an aluminum alloy. Otero and coauthors present analytical results about the dispersion relations for SH waves on a magnetoelectroelastic heterostructure with imperfect interfaces.

In fluid mechanics, Huang and Houchens present a numerical linear stability analysis of a thermocapillary driven liquid bridge with magnetic stabilization. In particular, they present numerical issues that commonly arise when using spectral collocation methods and linear stability analyses in the solution of the associated partial differential equations. Cruz and coauthors conduct a numerical investigation of director orientation and flow of nematic liquid crystals.

In dynamics, Lenci and Marcheggiani investigate the problem of lateral vibrations of footbridges due to the synchronization of the pedestrian's motion with that of the supporting structure by means of a three-dimensional discrete time model. Zhang and Yu use a finite element method combined with the floating frame formulation to investigate vibration of a simulation nuclear fuel bundle structure confined in a circular tube. Orlando and coauthors analyze the influence of geometric imperfections on the nonlinear behavior and stability of Augusti's model under static and dynamic loads. Finally, Mazzilli and Sanches use a nonlinear normal mode approach for the active control of vortex-induced vibrations in offshore catenary risers, which are used in deepwater oil and gas exploitation.

In composites, Shindo and coauthors examine theoretically and experimentally the nonlinear electromechanical response of piezoelectric macrofiber composite. In computational mechanics, Larrosa and coauthors present a three-dimensional implementation of the energy domain integral (EDI) for the analysis of interface cracks in transversely isotropic bimaterials.

In biomechanics, Ehret and coauthors present a technique to prepare thin samples of planar or bulky soft tissue with very accurate geometry and apply it to porcine dermal tissues. They obtain experimental results that are well represented by a constitutive model that accounts for the elastic and dissipative behavior of soft tissues.

In stochastic mechanics, Sampaio and Bellizzi explore the main properties of the smooth Karhunen–Loëve decomposition for nonstationary random processes. At the interface of computational and stochastic mechanics, Lepage and coauthors study the influence on the macroscopic (homogenized) elastic properties of polycrystalline materials induced by uncertainties on the material texture and microstructure geometry. To perform this analysis, the perturbation stochastic finite element method is coupled to the mathematical theory of homogenization that leads to a second-order perturbation-based homogenization method. Also, Evangelatos and Spanos present a collocation approach for spatial discretization of stochastic peridynamics modeling of fracture.

Finally, I would like to express my deep gratitude to all colleagues and staff at USP who helped me in the several stages of the PACAM XI organization. I am also indebted to my wife Rogéria, my son Tiago, and my daughter Helena, who not only helped in the organization, but also were very patient and understanding. To them, all my love and appreciation.

April 2011

ADAIR R. AGUIAR: [aguiarar@sc.usp.br](mailto:aguiarar@sc.usp.br)

*Department of Structural Engineering, São Carlos School of Engineering, University of São Paulo,  
Av. Trabalhador são-carlense, 400, Caixa Postal 359, 13566-590 São Carlos, SP, Brazil*

## **INFLUENCE OF SPECIMEN GEOMETRY ON THE PORTEVIN-LE CHÂTELIER EFFECT DUE TO DYNAMIC STRAIN AGING FOR THE AA5083-H116 ALUMINUM ALLOY**

RODRIGO NOGUEIRA DE CODES AND AHMED BENALLAL

Digital image correlation and digital infrared thermography are employed to capture and characterize the spatiotemporal aspects of the Portevin–Le Châtelier phenomenon due to dynamic strain aging in various types of specimens. Deformation bands are visualized and the effects of the specimen shape on the morphology of the bands are underlined. Further, while the deformation bands are usually seen to propagate along the whole gauge length of smooth specimens, they are observed here to be generally trapped around stress concentrators.

### **1. Introduction**

The mechanical behavior of AA5083-H116 aluminum alloy exhibits irregular plastic flow in a given range of strain rates and temperatures [Clausen et al. 2004; Benallal et al. 2008a; 2008b]. In a uniaxial tension test for instance, this irregular flow results in inhomogeneous deformation with different types of localization bands. These bands can be static, hopping, or even propagating along the specimen when the strain rate is increased or the temperature decreased. It is also observed in the presence of this irregular flow that the material often fails by a shear localization mode prior to any significant diffuse necking.

It is widely accepted that this irregular flow is the consequence of negative strain-rate sensitivity due to dynamic strain aging, that is, the solute-dislocation interaction at the microscopic level, although a firm mechanism for the diffusion process is not established for aluminum alloys. Indeed, while Cottrell's theory on immobilization of dislocations by solute atmospheres is agreed to be involved in a way or another, various mechanisms for the diffusion and segregation of solute atoms to dislocations have been proposed and criticized [Nabarro 1948; Cottrell 1953a; 1953b; Sleeswyk 1958; Mulford and Kocks 1979; van den Beukel 1980; McCormick 1988]. The debate over the mechanisms is still going on in recent proposals [Picu 2004; Curtin et al. 2006].

The results of dynamic strain aging are higher flow stress and greater strain hardening rates at lower strain rates than at higher ones. The phenomenon also referred to as the Portevin–Le Châtelier (PLC) effect is observed in a number of dilute solid solutions (with BCC and FCC, but also HCP, crystal structures). A number of reviews on the phenomenon are available in the literature; see [Kubin and Estrin 1985; Robinson and Shaw 1994; Neuhäuser et al. 2004; Rizzi and Hähner 2004].

The PLC effect is a technologically important problem because it adversely affects the formability of the material. Inhomogeneous plastic straining increases geometrical perturbations in a component and thus reduces the strain to necking. Further, the propagating deformation bands give rise to undesired markings on the surface of the shaped material. Hopperstad et al. [2007] showed in a numerical

---

*Keywords:* Portevin–Le Châtelier effect, AA5083-H116 aluminum alloy, specimen geometry, dynamic strain aging.

study, taking into account dynamic strain aging and negative strain-rate sensitivity through the model of [McCormick 1988], that PLC effects can lead to significant reduction in the strain to necking both under uniaxial and biaxial tension, rendering this type of information vital in metal forming, for instance.

An extensive experimental program has been designed by the authors and their coworkers to understand the features of the PLC effect on AA5083-H116 aluminum alloy, where this effect is pronounced and almost unstudied in the literature. Thus the effects of strain rate and temperature on the appearance of this phenomenon were studied in [Clausen et al. 2004; Benallal et al. 2008a; 2008b]. Various tension tests were carried out on smooth specimens in order to exhibit the PLC domain and further characterize the various observed deformation bands. Strain rates ranging from  $10^{-7} \text{ s}^{-1}$  to  $103 \text{ s}^{-1}$  and temperatures going from  $-75^\circ \text{ C}$  to  $500^\circ \text{ C}$  were considered on flat and round smooth specimens.

The objective of this paper is to extend the former observations by analyzing the effects of specimen geometry and specimen dimensions on the features of the PLC effect. Various types of specimens are thus considered and subjected to tension loadings. Digital image correlation (DIC) and digital infrared thermography (DIT) are used to capture and characterize the spatiotemporal aspects of the PLC effect. Inhomogeneous deformation with different localization bands is observed on the different specimens. Also, deformation bands are visualized showing their formation, evolution, and propagation. This visualization also allows the morphology of the bands to be studied and their characteristics to be measured.

## 2. Material and experimental program

The material studied in this investigation is the aluminum alloy AA5083-H116. The main alloying elements are magnesium with 4.4 weight percent, manganese with 0.7 weight percent, and chromium with 0.15 weight percent. AA5083 may also contain minor quantities of elements such as iron, copper, and zinc. It is important to notice that the amount of magnesium is higher than 3 weight percent, which is the maximum to be retained in solid solution at room temperature. This gives a potential instability leading to precipitation along grain boundaries or slip planes. Stress corrosion is thus a likely consequence in corrosive media. Special precautions have to be made during rolling in order to avoid this problem, and the temper H116 was therefore developed.

The AA5xxx series is well suited for rolling, and plates are thus an important product. The traditional use of such plates is in naval structures such as ship hulls and offshore topsides, and the good corrosion resistance of the AA5xxx series gives further reason for these marine applications.

Smooth flat, prismatic, and round specimens are used in this investigation. The smooth round specimens all have a 6 mm diameter, and the prismatic specimens have cross sections  $5 \times 5 \text{ mm}^2$  and  $5 \times 6 \text{ mm}^2$ . Finally, the flat smooth specimens have a width of 15 mm; their thickness were varied with the following values considered:  $e = 1, 2, 3, 4, 5, 7$ , and 9 mm. The study is completed with U-notched and V-notched flat specimens. The U-notches have radii of 0.4, 0.8, and 2 mm while the V-notches have angles of 0, 30, 45, and  $60^\circ$ . Note that only one notch was used for the  $0^\circ$  V-notch (cracked specimen). However, the crack was not initiated prior to the loading process.

All the specimens were cut from 5 mm and 10 mm thick rolled plates and their axial directions were aligned with the rolling direction. All the tests considered in the paper were carried out at room temperature in a servohydraulic material-testing machine (MTS model 810) with a 10 kN capacity load cell.

Two different techniques were used to observe and eventually characterize the PLC bands spatially and temporally, namely, DIC and DIT. Zones on the gauge length of all the flat specimens were imaged with a fast CCD camera (model Ultima APX-RS) on one side and with an infrared camera (model JADE 570M) on the other side. Prior to the tests, one side of the specimen was decorated with finely sprayed black and white paints to enhance the image contrast and the other was painted with a fully black paint in order to enhance its emissivity. Only DIT was used for round specimens.

For DIC the recorded digital images had a  $256 \times 336$  pixel size. Images were recorded at a shutter speed of 125 frames per second.

The principle of DIC is based on the fact that the distribution of grayscale values of a rectangular area in the initial image corresponds to the distribution of grayscale values of the same area in the destination image. A cumulative strain map can be obtained by comparing each current deformation image with the initial image while an incremental strain map can be computed by comparing the image at the current load step with the image recorded just before the current load increment. These maps are computed from the recorded data by the software Correli Hild and Roux [2006].

The image size and acquisition speed for the DIT were  $31 \times 65$  pixels and 150 frames per second, respectively. The imaged zones for the DIT are sketched in Figure 1 for all the specimens. The imaged zone for the U-notched specimen ( $R = 2$  mm) is shown in detail in Figure 1a and zoomed in Figures 1b and 1c, where one can respectively see the locations of different points and three vertical lines ( $x = 0.65$ ,  $x = 4.84$ , and  $x = 9.68$ ) where some of the experimental results are presented in the next sections.

The tests were carried out at room temperature in a servohydraulic material-testing system (MTS model 810) with a 10 kN load cell (uniaxial tension test).

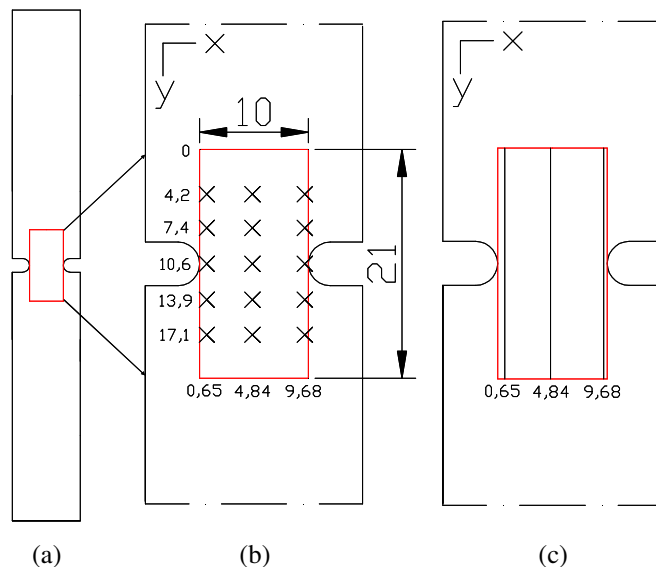


**Figure 1.** (a) Flat U-notched specimen with a 2 mm radius notch (T3) used in the investigation showing the imaged zone area for digital infrared thermography (DIT); (b, c) zooms of the imaged area indicating the locations used for presenting some of the experimental results in Section 3.2.

The acquired thermal information was processed in the following manner: at each acquisition time  $t$ , the acquired data was a matrix  $T(x, y, t)$  representing the chart of temperatures as measured by the infrared camera, with  $x$  representing lines (in the transverse direction) and  $y$  columns (in the longitudinal direction corresponding to the tension axis), and  $(x, y)$  a pixel from the imaged zone in the specimen. To minimize noise in the visualization of the bands, the average temperature change over a time increment  $\delta t$  was considered and expressed mathematically as

$$\Delta T(x, y, t) = \frac{1}{m} \sum_{j=0}^{j=m-1} [T(x, y, t + m\delta t) - T(x, y, t + j\delta t)], \quad (1)$$

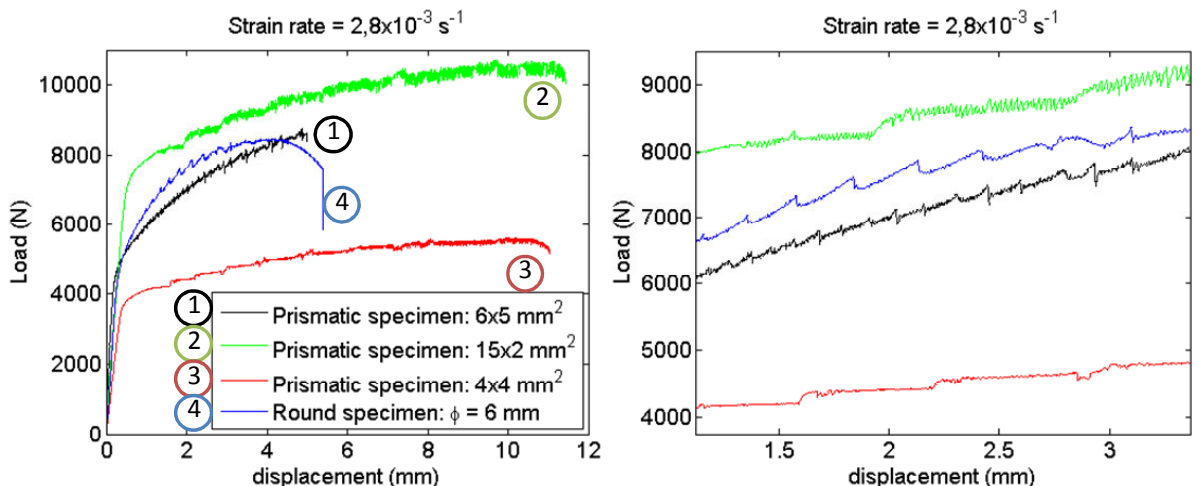
with  $\delta t$  the acquisition shutter speed (in frames per second). The choice of the parameter  $m$  depended on the cross-head velocity and acquisition speed during the test. For the tests carried out in this work,  $m = 1$  and  $m = 10$  were used.

### 3. Results

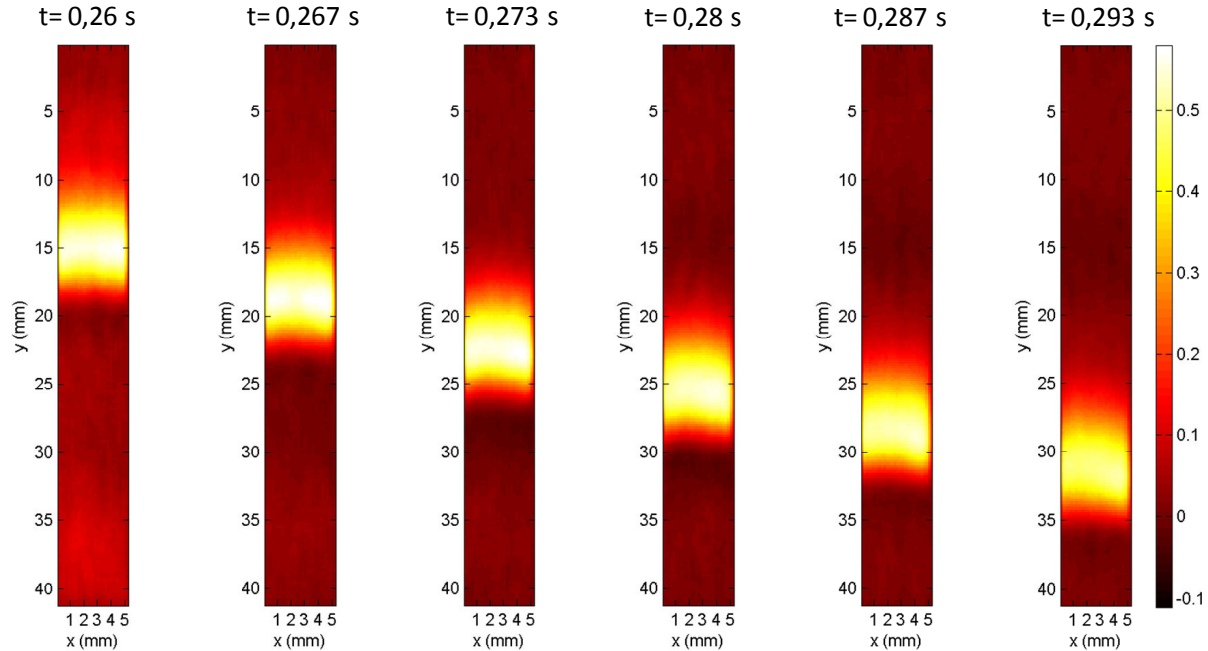
**3.1. Portevin–Le Châtelier effect in uniaxial tension.** We give in this section, for completeness, some results on experimental observations made during uniaxial tension on smooth specimens. More results and details can be found in [Benallal et al. 2008a; 2008b].

Figure 2 shows the load-displacement curves obtained for different uniaxial tests on different smooth specimens. These curves all show the serrated behavior and it is important to emphasize here the different nature of the serrations observed for each type of specimen.

Figure 3 is a sequence of six images taken at different instants displaying the propagation of a PLC deformation band during a tension test on a round specimen, for a nominal strain-rate of  $10^{-1}$  s $^{-1}$ . The pictures represent the change  $\Delta T(x, y, t)$  given by relation (1) over the imaged zone of the specimen. The temperature change is about 0.5° C. These pictures show the band all over the specimen and depicts



**Figure 2.** Load-displacement curves for different smooth specimens (left) and zoom of the curves displaying the serrations (right).



**Figure 3.** Sequence of six DIT images showing the propagation of a PLC deformation band during a tension test in a round specimen ( $\phi = 6$  mm) with nominal strain rate  $10^{-1}$  s $^{-1}$ . The figure displays only the imaged zone of the specimen. The temperature increment  $\Delta T$  given by (1) is displayed here.

therefore its morphology. The band is inclined at an angle of 52° C with respect to the loading access and has a thickness of about 5 mm.

Figure 4 shows again the PLC deformation bands observed during tension tests on round specimens, during almost the whole tests, for different strain rates ranging from  $10^{-5}$  s $^{-1}$  to  $10^{-1}$  s $^{-1}$ . For clarity, the final phase of the tests, namely rupture of the specimens, has been removed, since the significant temperature rise due to fracture would have masked the deformation bands. Figures 4b–4e display spatiotemporal representations of the temperature change  $\Delta T(0, y, t)$  along the vertical centerline of the imaged zone (shown in Figure 4a) as a function of time. For a better interpretation, the load-time curve is also superposed on the figures showing the serrations and associated deformation bands. It is interesting to notice here that at the beginnings of all the tests, the different deformation bands are traveling along the gauge length of the specimens in the same direction, while after a given time or strain, they start traveling back and forth until fracture.

Figure 5 depicts the same spatiotemporal representations for tension tests carried out on different smooth specimen geometries, at the same strain rate of  $2.8 \times 10^{-3}$  s $^{-1}$ . The deformation band patterns look at a first sight different, but they all consist of type A bands. (A type A band is usually defined as a PLC band that nucleates somewhere in the gauge length of the specimen and continuously propagates along this gauge length.)

Figure 6 shows again the same spatiotemporal representations for tension tests carried out at the same strain-rate of  $10^{-2}$  s $^{-1}$  on different smooth flat specimens having the same width but different thicknesses

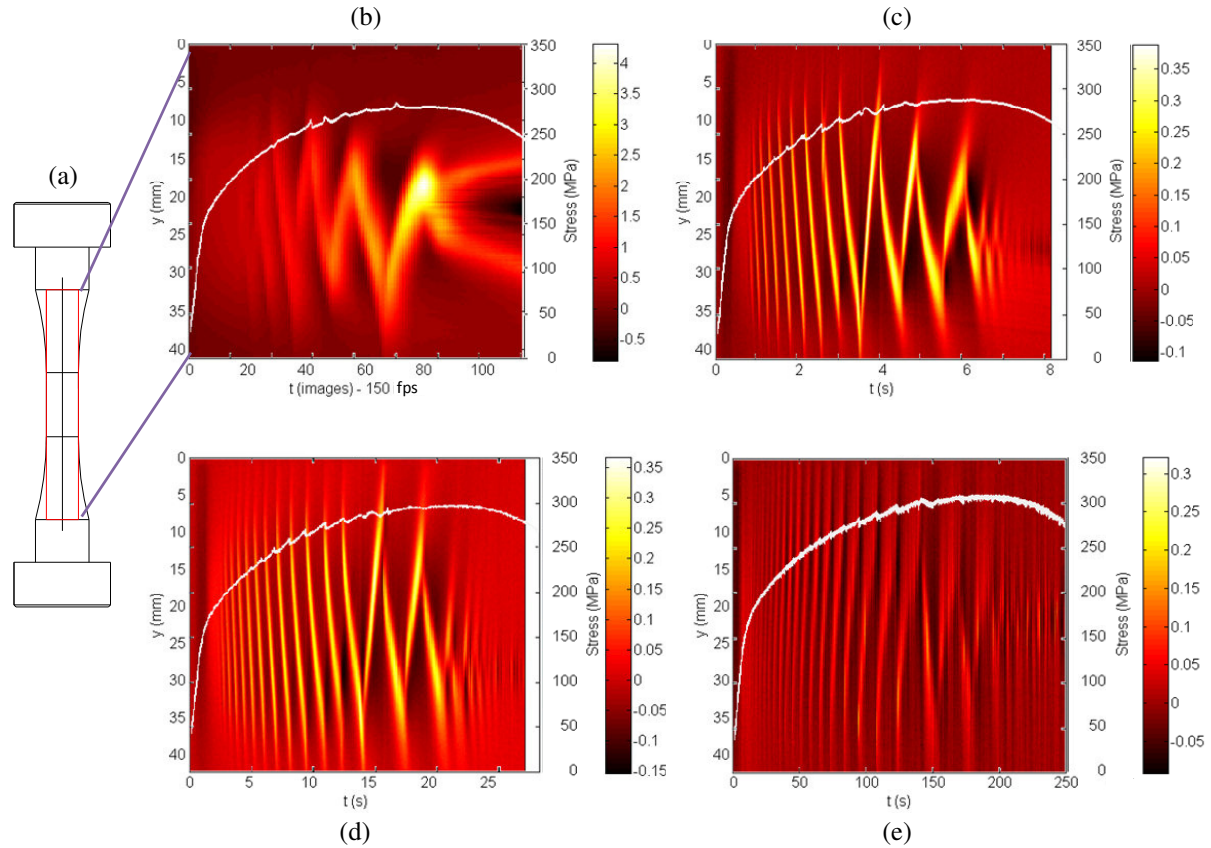


**Figure 4.** Temperature change  $\Delta T$  given by (1) versus time as measured by thermography along the vertical center line of the specimens. For completeness, the stress-time curve is superposed. (a) Round specimen ( $\phi = 6 \text{ mm}$ ) with the imaged zone indicated; (b)  $\dot{\varepsilon} = 10^{-1} \text{ s}^{-1}$ ; (c)  $\dot{\varepsilon} = 10^{-2} \text{ s}^{-1}$ ; (d)  $\dot{\varepsilon} = 2.8 \times 10^{-3} \text{ s}^{-1}$ ; (e)  $\dot{\varepsilon} = 3.33 \times 10^{-4} \text{ s}^{-1}$ .

ranging from 1 mm to 9 mm. For the same tests, Figure 7 displays the orientations of the observed bands as a function of the nominal strain. This orientation is measured by the inclination of the band with respect to the tension axis. While this orientation seems to be well defined around  $60^\circ$  for small thicknesses, it varies somewhat between  $60^\circ$  and  $90^\circ$  when this thickness is increased.

**3.2. Portevin–Le Châtelier effect on notched specimens.** Seven tests, called T1, T2, T3, T4, T5, T6, and T7 in the sequel, were carried out on the flat U-notched and V-notched specimen geometries described in Section 2 (see Table 1) in order to determine the effects of the specimen geometry on the characteristics of the deformation bands and their propagation. All tests were carried out in displacement control with a fixed clamp velocity. Table 1 presents a brief summary of the tests.

Before moving to a detailed analysis of the PLC deformation bands on notched specimens, let us first compare the morphology of these bands for all types of specimens used in this investigation. Figure 8 shows the imaged zones in thermography for all the studied specimens, as well as the associated morphology of the observed deformation bands at given instants of the loading process.

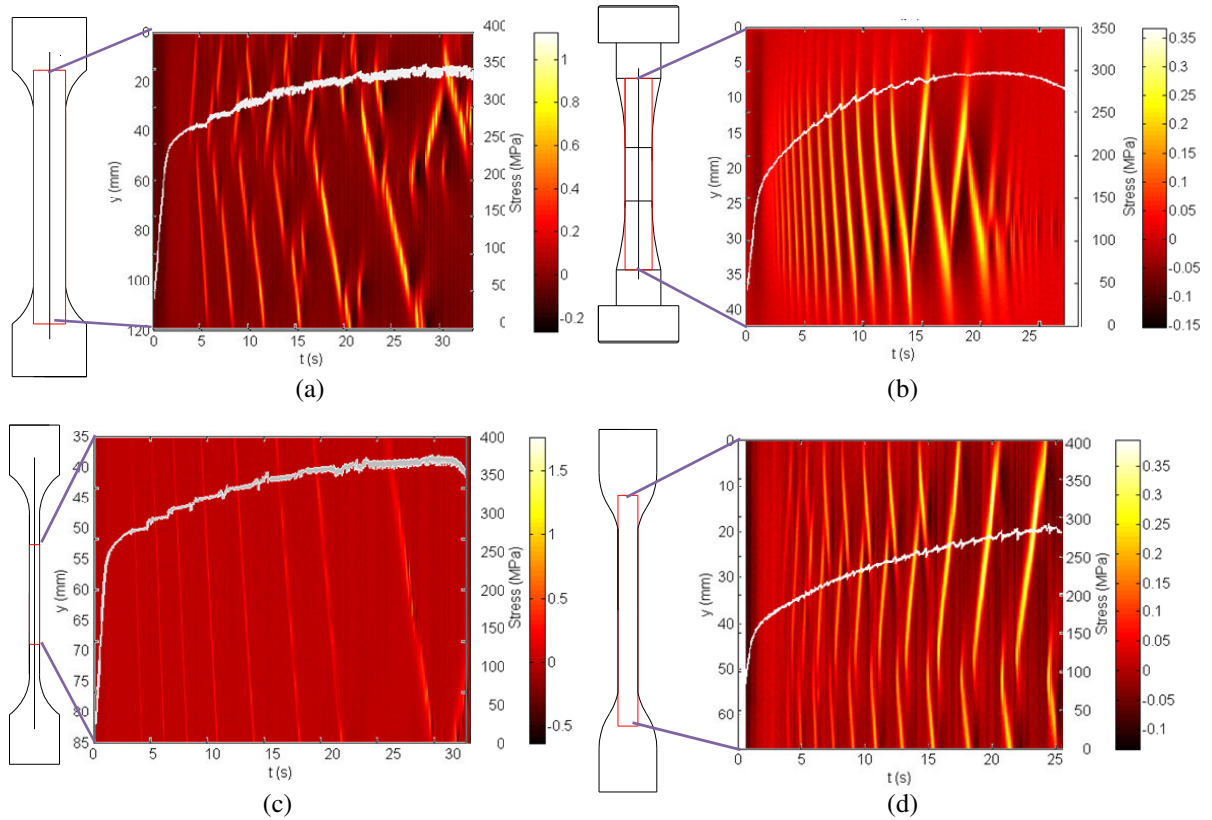


**Figure 5.** Temperature change  $\Delta T$  given by (1) versus time as measured by thermography along the vertical center line for tension tests on different specimens at the same strain-rate of  $2.8 \times 10^{-3} \text{ s}^{-1}$ . For completeness, the stress-time curve is also superposed. (a) Smooth flat specimen ( $15 \times 2 \text{ mm}^2$ ); (b) round specimen ( $\phi = 6 \text{ mm}$ ); (c) smooth flat specimen ( $4 \times 4 \text{ mm}^2$ ); (d) smooth flat specimen ( $6 \times 5 \text{ mm}^2$ ).

Figures 9a and 9b show the force-displacement response for tests T1, T2, T3, and T4 up to failure. Figures 9c and 9d are zooms of the ends of these tests, showing more clearly the serrations observed

Test	Cross head velocity ( $\text{mm s}^{-1}$ )	Notch
T1	0.955	U-notched specimen – $R = 0.4$
T2	0.955	U-notched specimen – $R = 0.8$
T3	0.955	U-notched specimen – $R = 2.0$
T4	0.955	Cracked specimen – (One $0^\circ$ V-notch)
T5	0.0975	V-notched specimen – $30^\circ$
T6	0.0975	V-notched specimen – $45^\circ$
T7	0.0975	V-notched specimen – $60^\circ$

**Table 1.** Summary of all the tests carried out in the present study.

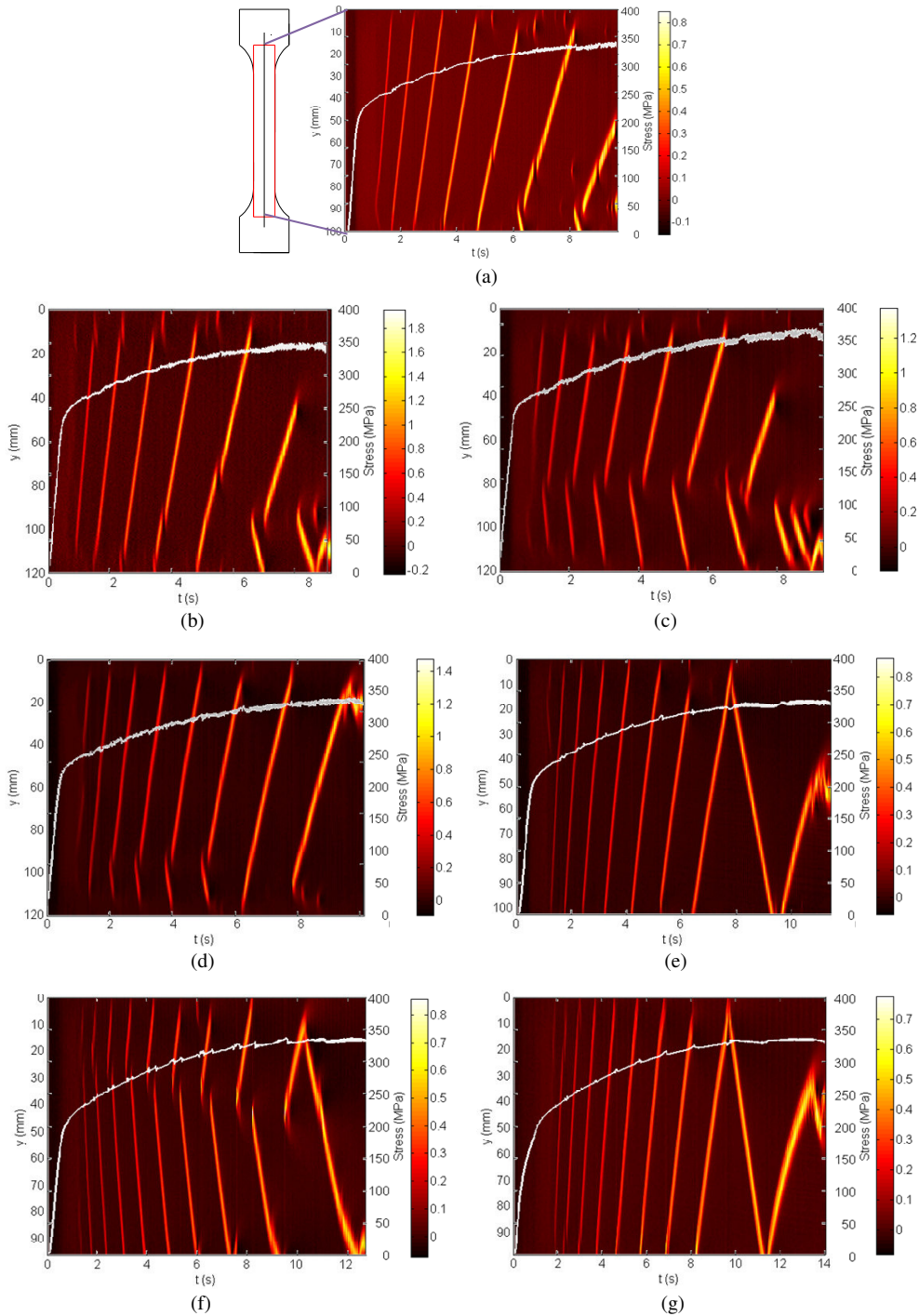


**Figure 6.** Temperature change versus time as measured by thermography along vertical center line of specimens, with stress-time curve superposed. Nominal strain rate is  $10^{-2} \text{ s}^{-1}$  and geometry is a smooth flat specimen with 15 mm width. The thickness  $e$  is (a) 1 mm, (b) 2 mm, (c) 3 mm, (d) 4 mm, (e) 5 mm, (f) 7 mm, and (g) 9 mm.

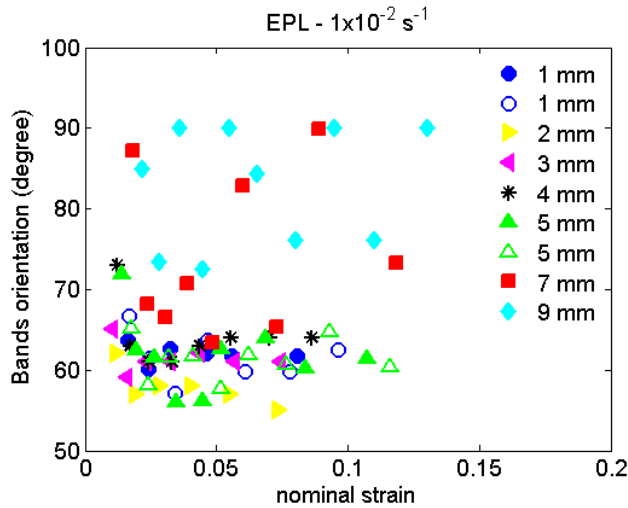


**Figure 7.** Band orientation versus nominal strain obtained during tension tests on different smooth flat specimens with the same 15 mm width but different thicknesses (1, 2, 3, 4, 5, 7, and 9 mm), at a nominal strain-rate of  $10^{-2} \text{ s}^{-1}$ .

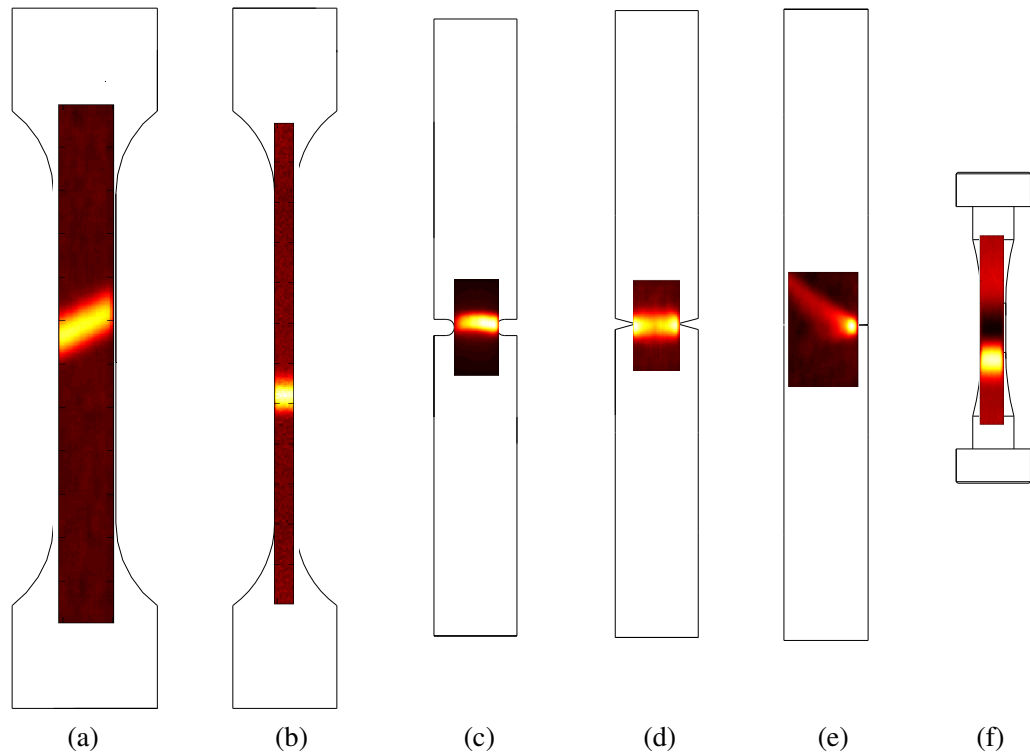


**Figure 8.** Two-dimensional view of PLC bands for different specimen geometries measured by thermography during tensile tests: (a) flat specimen, (b) prismatic specimen, (c) U-notched specimen, (d) V-notched specimen, (e) cracked specimen, and (f) round specimen. The temperature change  $\Delta T$  given by (1) is displayed here.

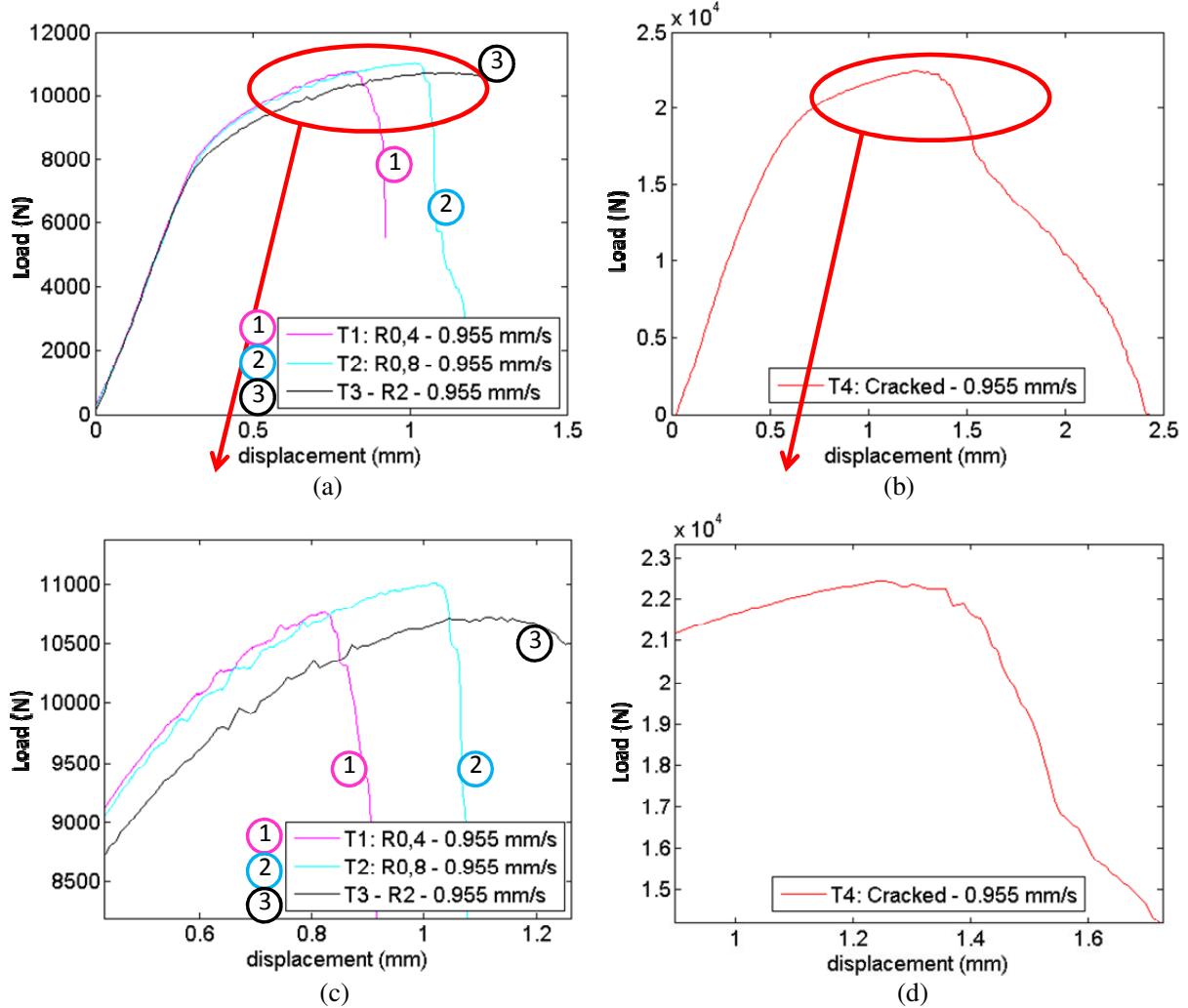


**Figure 9.** Force versus displacement for all tests: (a) T1, T2, and T3; (b) T4; (c) zoom of (a); (d) zoom of (b).

during the tests, signaling the presence of the deformation bands. These serrations only occur after a certain time of plastic strain. The observed final failure mode is a shear failure through the thickness of the specimen. As an illustration, the broken specimen from T3 is shown in Figure 10.



**Figure 10.** Broken specimen from all tests illustrating the observed shear modes for T3.

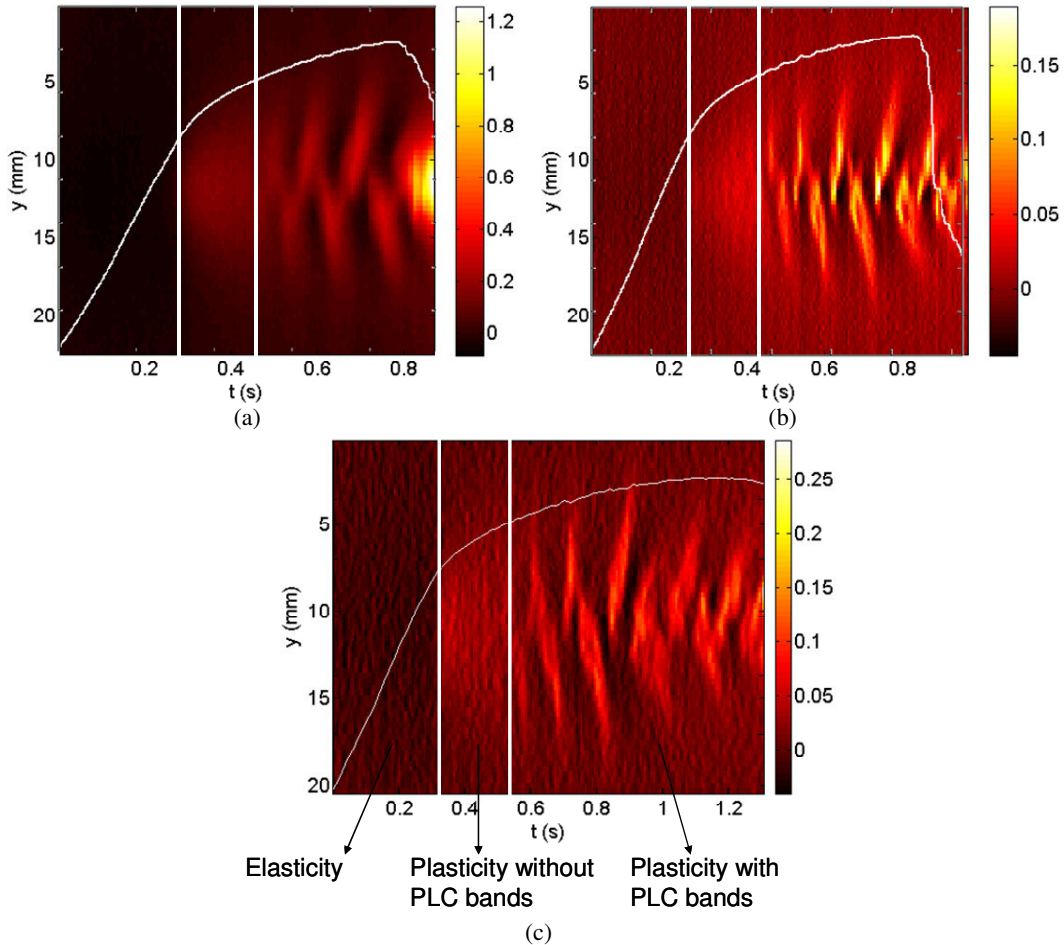


**Figure 11.** Temperature change  $\Delta T(4.84, y, t)$  measured along the vertical line  $x = 4.84$ , in comparison with the response force-time of the test. Note clearly the elasticity, the plasticity without PLC bands, and the plasticity with PLC bands for the three tests: (a) T1, (b) T2, and (c) T3.

Figure 11 shows a summary of tests T1, T2, and T3 carried out at average strain rates of  $7.16 \times 10^{-1} \text{ s}^{-1}$ ,  $7.16 \times 10^{-2} \text{ s}^{-1}$ , and  $7.16 \times 10^{-3} \text{ s}^{-1}$ , respectively, and displays the load-time response (thin white line) superposed on the time evolution of the temperature change observed in the specimen along the vertical line (and longitudinal axis of the specimen)  $x = 4.84 \text{ mm}$ .

The thermal information of Figure 11 clearly shows three regions separated by thick vertical lines and representing respectively the elastic response of the specimen (the rather dark area), the plastic response prior to the development of the PLC (where the temperature slightly increases due to plastic dissipation), and finally the plastic response with the PLC and associated deformations bands. In this last area, one can observe, through the spatiotemporal distribution of temperature changes along the vertical axis of the specimen, the nucleation and propagation of the deformation bands. Similar responses are observed in the three tests T1, T2, and T3.

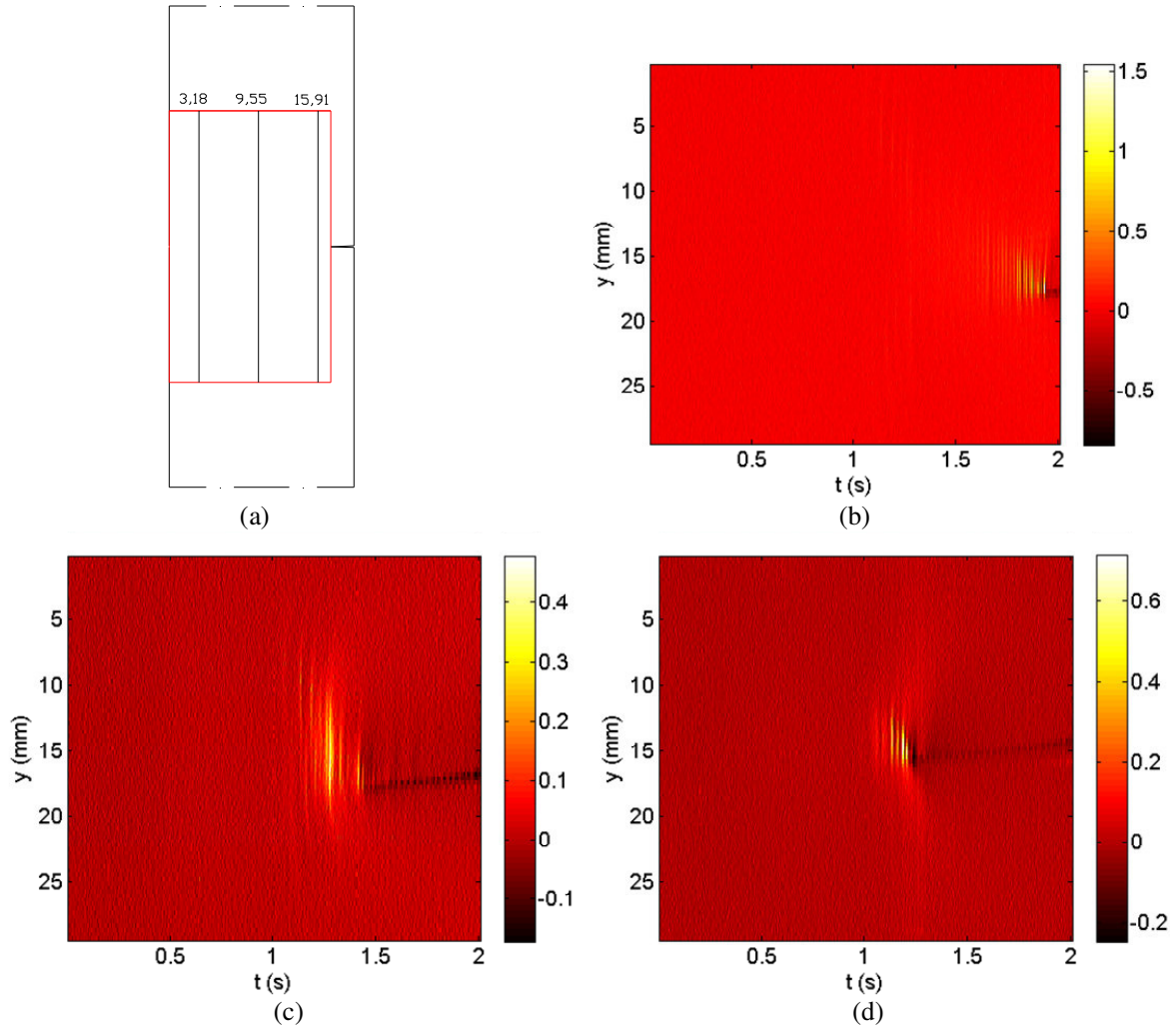


**Figure 12.** (a) Cracked specimen with the imaged area indicating the three vertical lines used for presenting the experimental results; (b) temperature change  $\Delta T(x, y, t)$  measured along the vertical line  $x = 3.18$ ; (c) temperature change  $\Delta T(x, y, t)$  measured along the vertical line  $x = 9.55$ ; (d) temperature change  $\Delta T(x, y, t)$  measured along the vertical line  $x = 15.91$ .

In the case of the cracked specimen (T4), we present in Figure 12 the history of the temperature change  $\Delta T(x, y, t)$  versus time at three different locations on the specimen, namely  $x = 3.18$ ,  $x = 9.55$ , and  $x = 15.91$  (close to the initial crack tip), as depicted in Figure 12a. One observes that there are PLC bands and these bands are stuck in the crack tip. In Figure 12b ( $x = 3.18$ ), to where the crack has propagated, it is only at the end of the test that we could see the traces of deformation bands on the spatiotemporal analysis, when the crack tip has approached this position. In Figures 12c and 12d we observe the progress of the crack, and one can see a similar situation as in Figure 12b. One can also observe that bands do not propagate along the specimen, but are trapped at the crack tip.

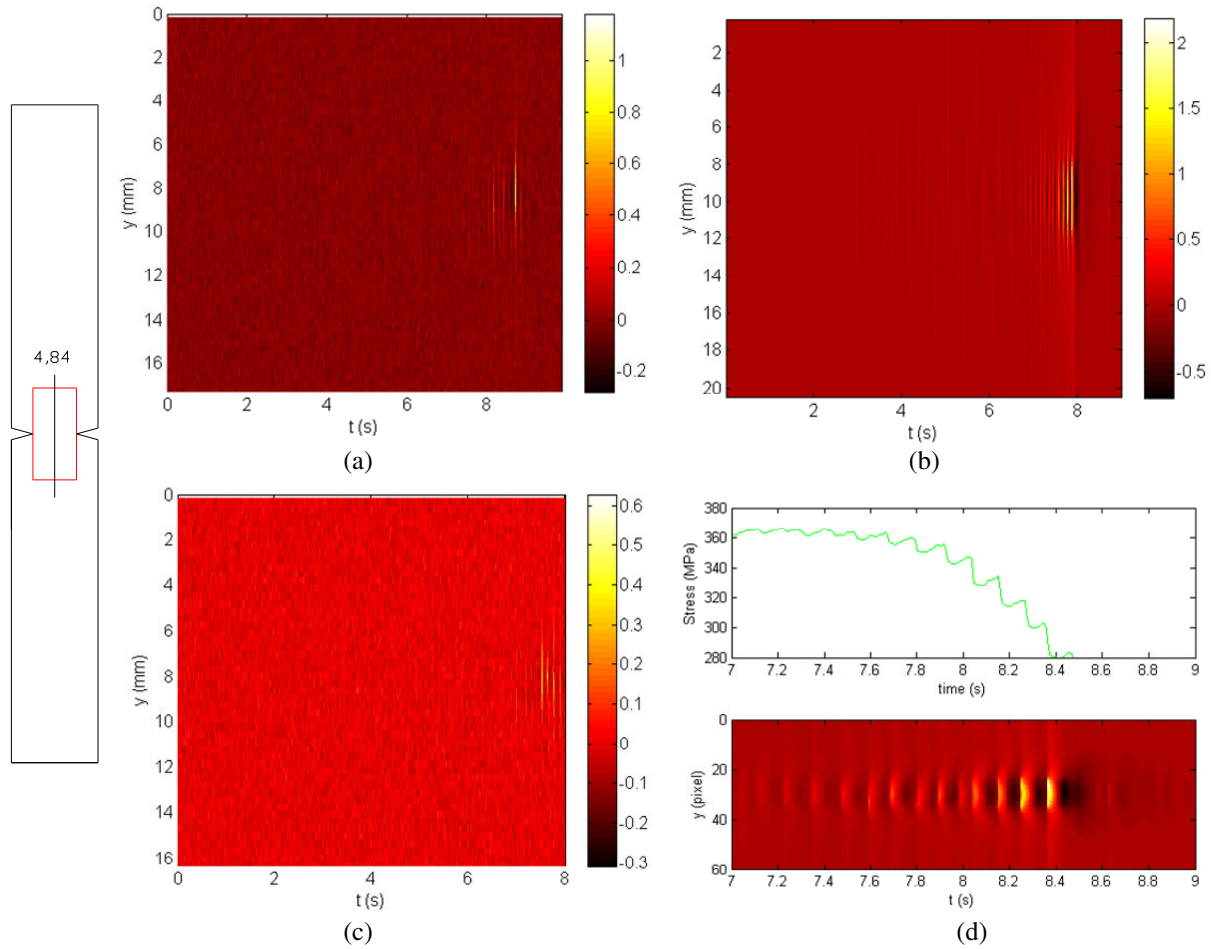


**Figure 13.** Temperature change  $\Delta T(x, y, t)$  measured along the vertical line  $x = 4.84$  for the V-notched specimens: (a) T5 (30°), (b) T6 (45°), (c) T7 (60°), and (d) T6 (V45°), showing its comparison with the response force-time at the end of the test.

Similar representations are provided in Figure 13 for the V-notched specimens.

Figures 14a, 14b, and 14c compare, for the three tests T1, T2, and T3 on U-notched specimens, the incremental strain maps (on the left sides) obtained by DIC and the temperature change  $\Delta T(x, y, t)$  (on the right sides) at different time locations. As seen, the agreement is very good.

At these time locations, a deformation band is seen above or below the minimal section of the specimen. The movement of the band is actually a bowing around and above this minimal section followed by a bowing around and below the minimal section. This is better seen in Figure 11, where in the beginning of the PLC phenomenon a deformation band nucleates in the minimal section of the specimen and bows down until it disappears, after which another band develops, still in the minimal section, and bows up this time until it disappears again. The whole process is repeated again until failure of the specimens in Figure 11 for the three tests.

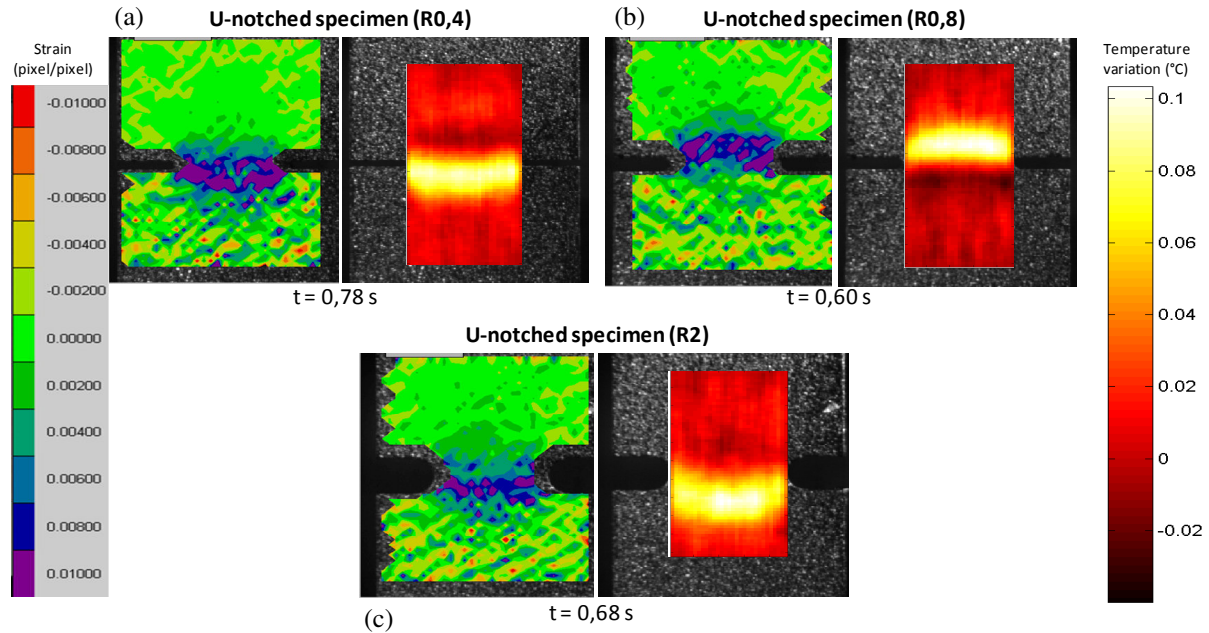


**Figure 14.** Longitudinal strain and temperature change  $\Delta T$  maps as obtained from DIC and DIT on the two opposite sides of each specimen for tests on notched specimens: (a) T1, (b) T2, and (c) T3.

To give more emphasis to the behavior of the bands, we choose T3 and give more details on the movements of the deformation bands. Figure 15 compares the temperature changes observed in the width of the specimen. To that purpose, it displays for the whole test (except for the final part, which includes the fracture of the specimen) the temperature changes  $\Delta T(x, y, t)$  along the vertical lines  $x = 0.65$ ,  $x = 4.84$ , and  $x = 9.68$  of the specimen for the imaged area, shown in Figure 1c. Different levels of temperature are reached from the left to the right of the specimen (with the smallest on the left).

Figures 16 and 17 show the temperature and axial strain ( $\varepsilon_{yy}$ ) histories during the whole test at the same locations mentioned above, the middle and the bottom of the imaged zone shown in Figure 1b. Both strain and temperature histories display the classical staircase behavior characteristic of the PLC

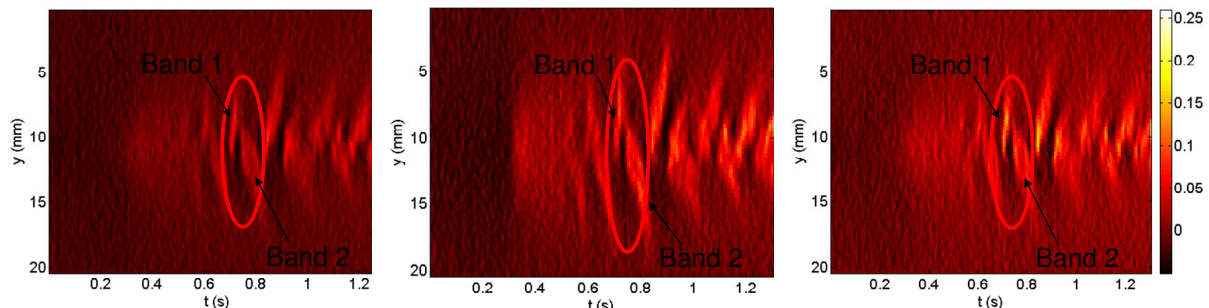


**Figure 15.** Temperature change measured along the vertical lines  $x = 0.65$  (left),  $x = 4.84$  (center), and  $x = 9.68$  (right) for T3.

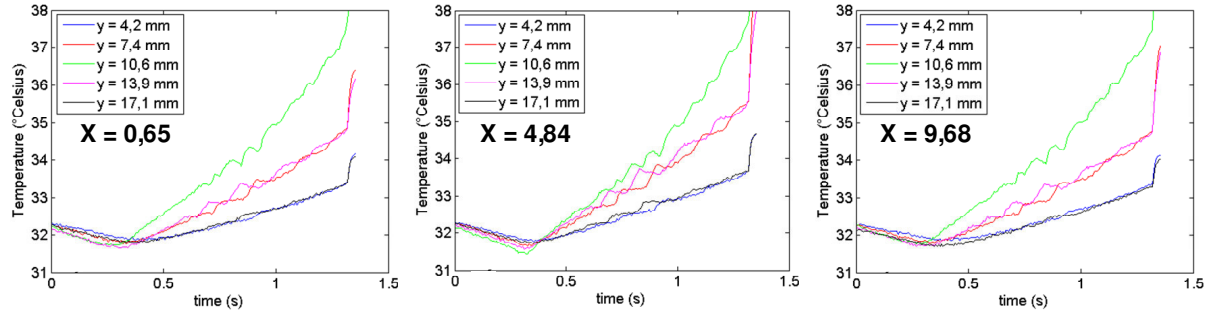


**Figure 16.** Temperature histories for T3 at the different locations indicated in Figure 1b.

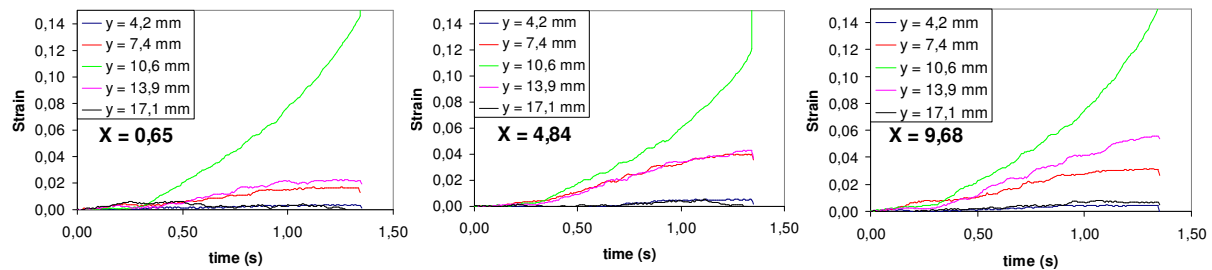


**Figure 17.** Longitudinal strain histories for T3 at the different locations indicated in Figure 1b.

effect, where each stair is the manifestation of a band passing at these locations. Figure 16 shows clearly a higher temperature increase in the minimal section of the specimen ( $y = 10.6$  mm), where the stress concentration is higher. Figure 17 shows that the strain is higher near the notch at the minimal section.

Figures 18 and 19 show the temperature along the three vertical lines ( $x = 0.65$ ,  $x = 4.84$ , and  $x = 9.68$ ) at different time instants. Beside the global rise in temperature due to plasticity, one can also see the propagation of the deformation bands (see the location of the maximum temperature that moves to the left in Figure 18 and to the right in Figure 19). Figure 18 shows a band that propagates from the minimal section (the dashed line) to the top side of the specimen. Figure 19 shows another one that propagates

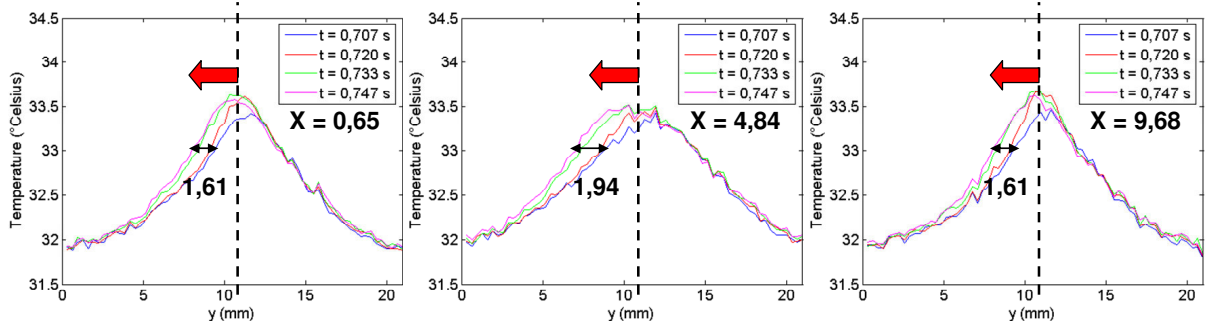


**Figure 18.** Propagation of band 1 shown in Figure 15. The traveling distance of the band is higher in the minimal section ( $x = 4.84$ ) than at the roots of the notches ( $x = 0.65$  and  $x = 9.68$ ) leading to the slightly curved morphology of the band.

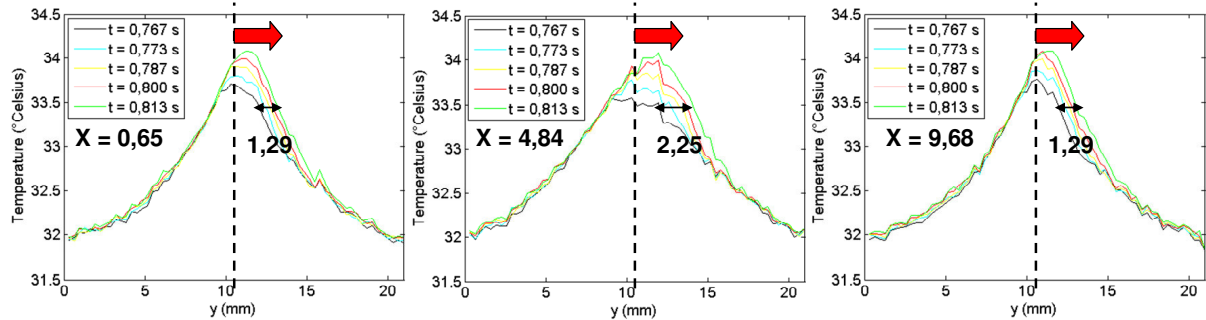


**Figure 19.** Propagation of band 2 shown in Figure 15. The travel distance of the band is higher in the minimal section ( $x = 4.84$ ) than at the roots of the notches ( $x = 0.65$  and  $x = 9.68$ ) leading to the slightly curved morphology of the band.

from the minimal section to the bottom side, as one can also see in Figures 11 and 15. One can also observe the differences in the band propagation, between the centerline of the specimen ( $x = 10.6$ ) and near the roots ( $x = 0.65$  and  $x = 9.68$ ) leading to the bowing of the band around the minimal section.

Figures 20 and 21 give the same results as Figures 18 and 19 but display rather the temperature changes  $\Delta T(x, y, t)$  of relation (1) instead of the temperature. This is more representative of the PLC effect and

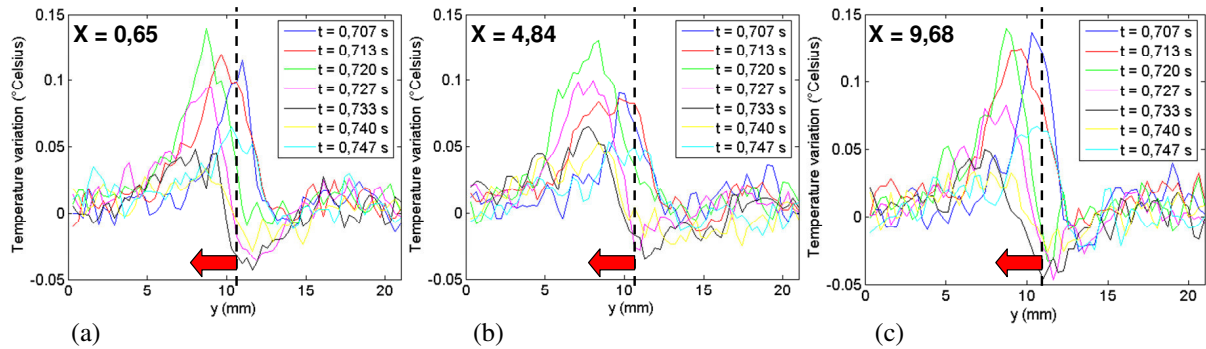


**Figure 20.** Temperature increments  $\Delta T$  profile showing the propagation of band 1 of Figure 15.

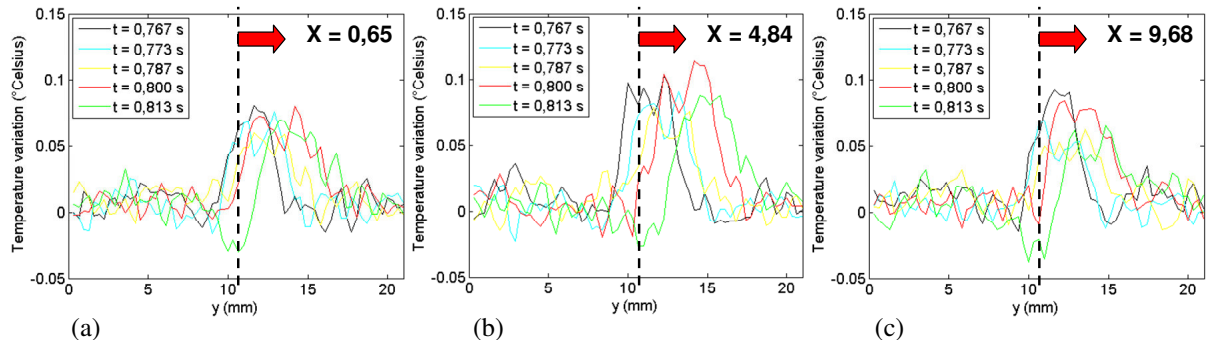


**Figure 21.** Profiles of temperature increments  $\Delta T$  associated with the propagation of band 2 shown in Figure 15.

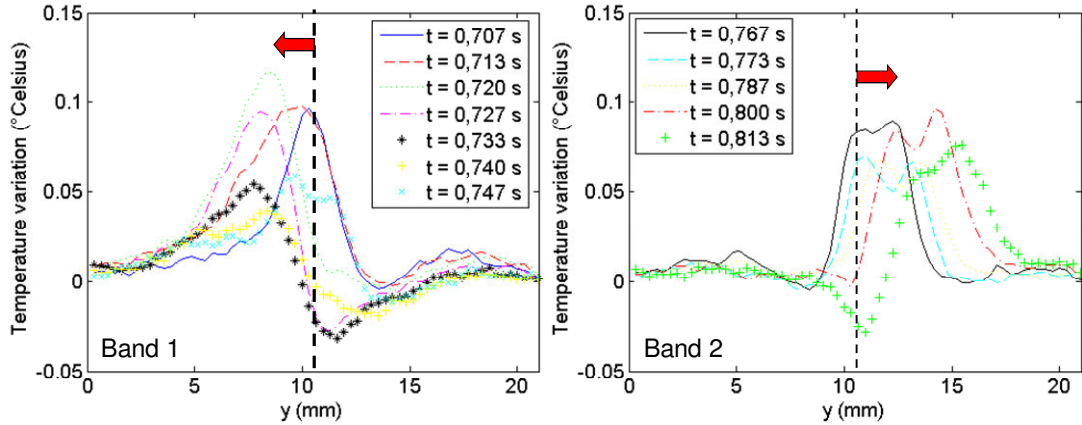


**Figure 22.** Temperature variation as a function of  $y$ , showing the same bands, 1 and 2: average of temperature variations of Figures 20a, 20b, and 20c (left); and average of temperature variations of Figures 21a, 21b, and 21c (right).

is plotted at different times along the lines  $x = 0.65$ ,  $x = 4.84$ , and  $x = 9.68$ . While visible in these figures, the growth (temperature increase), propagation, and decay (temperature decrease) of the bands are better seen in Figure 22, obtained by a filtering of Figures 20 and 21. This filtering is simply carried out by taking the average of the temperature distributions at  $x = 0.65$ ,  $x = 4.84$ , and  $x = 9.68$ . Indeed, on the left of Figure 22, one can clearly distinguish the growth of a band between times  $t = 0.707$  s and  $t = 0.720$  s, and then its decay from  $t = 0.720$  s to  $t = 0.740$  s. During this period, the band moved to the left, then slightly returned at the end. Just after this, another band is seen growing ( $t = 0.747$  s) and continues its growth and decay on the right side of Figure 22 (from  $t = 0.767$  s to  $t = 0.800$  s), but now to the right.

#### 4. Conclusions

Digital infrared thermography and digital image correlation are important tools for observing and evaluating the nucleation, growth, decay, and morphology of Portevin–Le Châtelier deformation bands (as well as other localized and propagating instabilities) under general loading conditions. Application of these tools to various specimens indeed allows exhibiting the main features of the development and propagation of these bands, which, for the cross-head velocity considered here, are seen to be trapped in the vicinity of the minimal cross section and bow up and down around this section for U-notched specimens. In the case of the cracked specimen, bands are stuck at the crack tip. This information is important in modeling dynamic strain aging phenomena and in discriminating between the various proposals existing in the literature. This is currently under investigation.

#### References

- [Benallal et al. 2008a] A. Benallal, T. Berstad, T. Børvik, O. S. Hopperstad, and R. Nogueira de Codes, “Effects of strain rate on the characteristics of PLC deformation bands for AA5083-H116 aluminium alloy”, *Philos. Mag.* **88**:28–29 (2008), 3311–3338.

- [Benallal et al. 2008b] A. Benallal, T. Berstad, T. Børvik, O. S. Hopperstad, I. Koutiri, and R. Nogueira de Codes, “An experimental and numerical investigation of the behaviour of AA5083 aluminium alloy in presence of the Portevin–Le Chatelier effect”, *Int. J. Plast.* **24**:10 (2008), 1916–1945.
- [van den Beukel 1980] A. van den Beukel, “On the mechanism of serrated yielding and dynamic strain ageing”, *Acta Metall.* **28**:7 (1980), 965–969.
- [Clausen et al. 2004] A. H. Clausen, T. Børvik, O. S. Hopperstad, and A. Benallal, “Flow and fracture characteristics of aluminium alloy AA5083-H116 as function of strain rate, temperature and triaxiality”, *Mater. Sci. Eng. A* **364**:1–2 (2004), 260–272.
- [Cottrell 1953a] A. H. Cottrell, *Dislocations and plastic flow in crystals*, University Press, Oxford, 1953.
- [Cottrell 1953b] A. H. Cottrell, “A note on the Portevin–Le Chatelier effect”, *Philos. Mag. (7)* **44**:355 (1953), 829–832.
- [Curtin et al. 2006] W. A. Curtin, D. L. Olmsted, and L. G. Hector, Jr., “A predictive mechanism for dynamic strain ageing in aluminium-magnesium alloys”, *Nat. Mater.* **5**:11 (2006), 875–880.
- [Hild and Roux 2006] F. Hild and S. Roux, “Digital image correlation: from displacement measurement to identification of elastic properties – a review”, *Strain* **42**:2 (2006), 69–80.
- [Hopperstad et al. 2007] O. S. Hopperstad, T. Børvik, T. Berstad, O.-G. Lademo, and A. Benallal, “A numerical study on the influence of the Portevin–Le Chatelier effect on necking in an aluminium alloy”, *Model. Simul. Mater. Sci. Eng.* **15**:7 (2007), 747–772.
- [Kubin and Estrin 1985] L. P. Kubin and Y. Estrin, “Portevin–Le Chatelier effect in deformation with constant stress rate”, *Acta Metall.* **33**:3 (1985), 397–407.
- [McCormick 1988] P. G. McCormick, “Theory of flow localisation due to dynamic strain ageing”, *Acta Metall.* **36**:12 (1988), 3061–3067.
- [Mulford and Kocks 1979] R. A. Mulford and U. F. Kocks, “New observations on the mechanisms of dynamic strain aging and of jerky flow”, *Acta Metall.* **27**:7 (1979), 1125–1134.
- [Nabarro 1948] F. R. N. Nabarro, *Report on strength of solids*, pp. 38, Physical Society, London, 1948.
- [Neuhäuser et al. 2004] H. Neuhäuser, F. B. Klose, F. Hagemann, J. Weidenmüller, H. Dierke, and P. Hähner, “On the PLC effect in strain-rate and stress-rate controlled tests: studies by laser scanning extensometry”, *J. Alloy. Compd.* **378**:1–2 (2004), 13–18.
- [Picu 2004] R. C. Picu, “A mechanism for the negative strain-rate sensitivity of dilute solid solutions”, *Acta Mater.* **52**:12 (2004), 3447–3458.
- [Rizzi and Hähner 2004] E. Rizzi and P. Hähner, “On the Portevin–Le Chatelier effect: theoretical modeling and numerical results”, *Int. J. Plast.* **20**:1 (2004), 121–165.
- [Robinson and Shaw 1994] J. M. Robinson and M. P. Shaw, “Observations on deformation characteristics and microstructure in an Al-Mg alloy during serrated flow”, *Mater. Sci. Eng. A* **174**:1 (1994), 1–7.
- [Sleeswyk 1958] A. W. Sleeswyk, “Slow strain-hardening of ingot iron”, *Acta Metall.* **6**:9 (1958), 598–603.

Received 7 Aug 2010. Revised 30 Nov 2010. Accepted 26 Dec 2010.

RODRIGO NOGUEIRA DE CODES: [nogueira@lmt.ens-cachan.fr](mailto:nogueira@lmt.ens-cachan.fr)

LMT-Cachan, ENS Cachan/CNRS/UPMC/PRES UniverSud Paris, 61 Avenue du Président Wilson, 94235 Cachan, France

AHMED BENALLAL: [benallal@lmt.ens-cachan.fr](mailto:benallal@lmt.ens-cachan.fr)

LMT-Cachan, ENS Cachan/CNRS/UPMC/PRES UniverSud Paris, 61 Avenue du Président Wilson, 94235 Cachan, France

## DISPERSION RELATIONS FOR SH WAVES ON A MAGNETOELECTROELASTIC HETEROSTRUCTURE WITH IMPERFECT INTERFACES

JOSÉ A. OTERO, HÉCTOR CALAS, REINALDO RODRÍGUEZ-RAMOS,  
JULIÁN BRAVO-CASTILLERO, ADAIR R. AGUIAR AND GUILLERMO MONSIVÁIS

The dispersion relations of surface SH waves in an A/B/A heterostructure with magnetoelectroelastic properties and imperfect (electromagnetically permeable or absorbent, mechanically spring-type) bonding at the interfaces are obtained taking the geometric symmetry of the system into account. Consequently, the results for the symmetric and antisymmetric modes are presented. Different limit cases are considered. Numerical calculations for relevant realizations of the heterostructure are investigated for different values of the material parameter describing the assumed mechanically imperfect bonding. In all the studied cases, the propagation velocities of the SH waves increase for increasing values of this parameter and are limited by the velocities on the homogeneous phases A and B.

### 1. Introduction

The development of smart structures is currently receiving widespread attention owing to potential applications in several branches of engineering, such as in integrated control architecture with highly distributed sensors and actuators. More recently, applications can be found in the design of smart materials, where piezoelectric and piezomagnetic properties are involved. The problem of wave propagation in this type of material has been studied by different authors using different geometries. For instance, in [Alshits et al. 1994] the existence of localized acoustic waves was studied on the interface between two piezocrystals of arbitrary anisotropy. In [Pan 2001] an exact closed-form solution was derived for the static deformation of multilayered piezoelectric and piezomagnetic plates based on quasi-Stroh formalism and using the propagator matrix method. In [Pan and Heyliger 2002] the analytical method of [Pan 2001] was extended to the free vibration of three-dimensional, anisotropic linearly magnetoelectroelastic (MEE) simply supported, and multilayered rectangular plates. In [Wang et al. 2003] the state vector equations for three-dimensional, orthotropic, and linearly MEE media were derived. The solution of these equations is based on a mixed formulation, where the basic unknowns are not only the displacements, electrical potential, and magnetic potential, but also the stresses, electric displacements, and magnetic induction. Recently, [Chen et al. 2007] presented an analytical treatment for the propagation of harmonic waves in infinitely extended MEE multilayered plates based on the state vector approach.

---

The authors wish to acknowledge the National Council for Scientific and Technological Development (CNPq), Proc. No. 450462/2009-9, the National Program of Basic Sciences, CITMA, Cuba, PNCIT IBMFQC 0709-0000, CoNaCyT/México project No. 82474 and DGAPA UNAM/México project IN119509, for their support of this research. JBC is also grateful for the support provided by CGCI/CAPES/Brazil project No. 0452-11/2010.

**Keywords:** piezoelectricity, piezomagnetism, magnetoelectroelasticity, dispersion curve, wave propagation, imperfect contact.

The existence of interfaces is a usual feature of both composite materials and structures. Depending on the materials involved and how they are put together (for example, by different glues), a thin layer with its own material properties, which are noticeably different from those of the participating materials, may manifest itself at the interface. The simplest description of the mechanical behavior of an interface is modeled as a layer that geometrically has a zero thickness but still possesses elasticity and interface elastic strain energy, for example, the shear-lag model of [Cheng et al. 1996; Handge 2002], in which the tangential displacement at an interface is allowed to be different from both sides of the interface to account for the deformation of the interface layer. At the same time, the inertia of the interface is neglected so that the traction across the interface is continuous and is proportional to the displacement jump across the interface. In this description, an interface is essentially considered as having many massless springs. A similar description can also be applied in the normal direction of an interface.

In practice, due to various causes such as microdefects, diffusion impurity, damage, weak bonding, et cetera, two dissimilar materials cannot be perfectly bonded, and an interface or transition with thickness in the range of 30–240 nm exists across the contact surfaces [Termonia 1990]. These transition zones weaken the interfacial continuity, and further affect the performance of the heterogeneous structure; in particular, the interfacial characteristics [Margetan et al. 1992; Wu et al. 2002]. An adequate description of such an interface is quite complex. A simplified model consists of considering an imperfect interface with vanishing thickness, at which the stresses can transfer continuously, but the displacements have a jump. In general, linear spring relations are assumed between the normal stress and the displacement jump in the normal direction and between the tangential stress and the displacement jump in the tangential direction [Hashin 1991; Klarbring and Movchan 1998; Zhong et al. 2009]. Using this modeling, the effects of interfacial imperfection on waves propagating in an isotropic elastic bimaterial have been analyzed in [Rokhlin and Wang 1991; Huang and Rokhlin 1992; Deng 2006]. For a class of smart materials, when the bonding interface is fully debonded, a small gap appears; the gap wave propagation has been investigated in [Li and Yang 2006]. The effects of an imperfectly bonded interface of piezoelectric waves near such interface have been studied in [Fan et al. 2006b] and [Yang et al. 2006], respectively, for two bonded piezoelectric materials. For an imperfect interface of a two-phase piezoelectric/piezomagnetic structure, interfacial shear horizontal waves propagating along an imperfect interface have been formulated in [Huang et al. 2009].

Shear-lag type interface models have been mainly used in static analysis. Recently, theoretical analysis was given on vibrations and waves propagating in structures with interfaces described by the shear-lag model [Chen et al. 2004; Yang et al. 2006].

The present work is motivated by recent contributions dealing with the effects of the elastic interface on vibration and wave propagation in composites. For instance, in [Fan et al. 2006a; 2006b; Chen et al. 2008; Melkumyan and Mai 2008] waves propagating in composite structures with imperfectly bonded interfaces were studied. Here, we propose a generalization of [Calas et al. 2008] to the case of imperfect contact conditions. In that study, the authors considered the case of perfect bonding at the interfaces of dissimilar media. In the present contribution, the interface is modeled by the shear-lag model for imperfect bonding. Here, the behavior of stationary SH waves in a heterostructure with MEE materials with imperfect bonding on the interface is studied. In particular, the case of permeable and absorbent interfaces is discussed in detail. The governing system of partial differential equations is solved using the geometric symmetry of the heterostructure and considering the superficial acoustic wave. Solutions

can be separated into symmetric and antisymmetric parts. The dispersion curves and the influence of the imperfection at the interface are shown for some cases.

The work is organized as follows: in Section 2 the governing equations of SH waves propagating in a MEE homogeneous medium with 6 mm hexagonal symmetry are presented. Section 3 is devoted to the formulation of the mean problem of an A/B/A heterostructure considering two types of imperfect interfacial conditions, and to the derivation of the symmetric and antisymmetric solutions of a related auxiliary problem. In Section 4, the dispersion relations are obtained, and different limit cases are described and shown to be in agreement with others reported in the literature. In Section 5 numerical examples are presented and discussed. Finally, some concluding remarks are given in Section 6.

## 2. Wave equation for the SH mode

Consider a MEE material with 6 mm hexagonal symmetry exhibiting magnetization and polarization in the  $z$ -axis direction of an  $xyz$  Cartesian coordinate system. The  $xy$ -plane is the isotropy plane. In this type of material, the SH wave is described by a system of three coupled partial differential equations with three unknowns: the  $z$ -component of the elastic displacement  $u_z$ , the in-plane electric potential  $\varphi$ , and the in-plane magnetic potential  $\psi$  (see, for instance, [Melkumyan 2007; Wang et al. 2007; Calas et al. 2008; Huang and Li 2010]), that is,

$$c\nabla^2 u + e\nabla^2 \varphi + f\nabla^2 \psi = \rho \frac{\partial^2 u}{\partial t^2}, \quad (2-1)$$

$$e\nabla^2 u - \varepsilon\nabla^2 \varphi - g\nabla^2 \psi = 0, \quad (2-2)$$

$$f\nabla^2 u - g\nabla^2 \varphi - \mu\nabla^2 \psi = 0, \quad (2-3)$$

with  $\nabla^2 \equiv \partial^2/\partial x^2 + \partial^2/\partial y^2$ ,  $u \equiv u_z$ , and where  $c \equiv c_{44}$ ,  $e \equiv e_{15}$ ,  $f \equiv f_{15}$ ,  $\varepsilon \equiv \varepsilon_{11}$ ,  $\mu \equiv \mu_{11}$ , and  $g \equiv g_{11}$  are the elastic, piezoelectric, piezomagnetic, dielectric permittivity, magnetic permeability, and magnetoelectric coefficients, respectively. In this study, the in-plane elastic displacements are  $u_x = u_y = 0$ . Equations (2-1)–(2-3) describe the motion of a SH wave in a homogeneous material and, therefore, depend only on  $(x, y, t)$ .

The stress component  $T \equiv T_{zy}$ , the electric displacement  $D \equiv D_y$ , and the magnetic induction  $B \equiv B_y$  are related to  $u$ ,  $\varphi$ , and  $\psi$  by

$$T = c \frac{\partial u}{\partial y} + e \frac{\partial \varphi}{\partial y} + f \frac{\partial \psi}{\partial y}, \quad D = e \frac{\partial u}{\partial y} - \varepsilon \frac{\partial \varphi}{\partial y} - g \frac{\partial \psi}{\partial y}, \quad B = f \frac{\partial u}{\partial y} - g \frac{\partial \varphi}{\partial y} - \mu \frac{\partial \psi}{\partial y}. \quad (2-4)$$

Due to the linearity of the Laplacian operator  $\nabla^2$ , it is possible to write (2-2) and (2-3) in the form

$$\nabla^2 \tilde{\varphi} = 0, \quad \nabla^2 \tilde{\psi} = 0, \quad (2-5)$$

where  $\tilde{\varphi}$  and  $\tilde{\psi}$  are auxiliary potential functions defined by

$$\tilde{\varphi} = \varphi - \frac{e}{\varepsilon} u + \frac{g}{\varepsilon} \psi, \quad \tilde{\psi} = \psi - \frac{f}{\mu} u + \frac{g}{\mu} \varphi. \quad (2-6)$$

Solving (2-6) for the functions  $\varphi$  and  $\psi$ , we find

$$\varphi = \chi \tilde{\varphi} + \frac{\bar{e}}{\varepsilon} u - \frac{\bar{g}}{\varepsilon} \tilde{\psi}, \quad \psi = \chi \tilde{\psi} + \frac{\bar{f}}{\mu} u - \frac{\bar{g}}{\mu} \tilde{\varphi}, \quad (2-7)$$

where

$$\chi = \frac{\varepsilon\mu}{\varepsilon\mu - g^2}, \quad \bar{g} = g\chi, \quad \bar{e} = e\chi - \frac{f}{\mu}\bar{g}, \quad \bar{f} = f\chi - \frac{e}{\varepsilon}\bar{g}. \quad (2-8)$$

Replacing the expressions given by (2-7) into (2-1), the typical wave motion equation for the mechanical displacement  $u$  is given by

$$\left( \nabla^2 - \frac{1}{\bar{v}^2} \frac{\partial^2}{\partial t^2} \right) u = 0, \quad (2-9)$$

where

$$\bar{v} = \sqrt{\bar{c}/\rho} \quad (2-10)$$

is the bulk shear wave speed of the MEE homogeneous medium and

$$\bar{c} = c + e\bar{e}/\varepsilon + f\bar{f}/\mu \quad (2-11)$$

is the magnetoelastically stiffened elastic constant.

In the next section, a heterogeneous medium will be studied (see Figure 1), and (2-5) and (2-9) must be solved in three different homogeneous zones of the  $xy$ -plane. In order to determine  $u$ ,  $\tilde{\varphi}$ , and  $\tilde{\psi}$ , suitable conditions should be employed. Moreover, it is convenient to express the constitutive relations (2-4) in the form

$$T = \bar{c} \frac{\partial u}{\partial y} + \bar{e} \frac{\partial \tilde{\varphi}}{\partial y} + \bar{f} \frac{\partial \tilde{\psi}}{\partial y}, \quad D = -\varepsilon \frac{\partial \tilde{\varphi}}{\partial y}, \quad B = -\mu \frac{\partial \tilde{\psi}}{\partial y}. \quad (2-12)$$

### 3. SH waves in MEE heterostructure

In the  $xy$ -plane, we consider an infinite heterostructure A/B/A formed by two half-spaces ( $y \leq -d/2$  and  $y \geq d/2$ ) and an intermediate layer ( $|y| \leq d/2$ ), as illustrated in Figure 1. Two different homogeneous transversely isotropic MEE materials, with 6 mm symmetry, occupy regions A and B. The magnetization

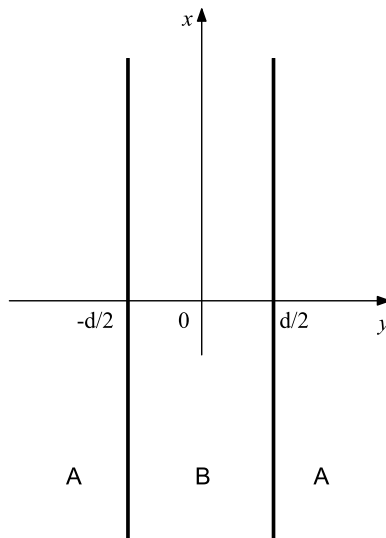


**Figure 1.** Scheme of a heterostructure A/B/A made of two magnetoelastic materials.

and polarization directions are supposed perpendicular to the  $xy$ -plane. Consequently, the equations presented in Section 2 must be satisfied in each one of the phases. We investigate the dispersion relations of SH-wave solutions  $u$ ,  $\varphi$ , and  $\psi$  of (2-1)–(2-3) for two types of imperfect conditions on  $y = \pm d/2$  following a procedure presented in [Calas et al. 2008]. We also investigate classical radiation conditions at infinity through the study of an auxiliary problem involving (2-5) and (2-9).

**3A. Statement of the main problem.** We want to find  $u$ ,  $\varphi$ , and  $\psi$  describing an SH wave propagating in the positive  $x$  direction that satisfy (2-1)–(2-3) in each phase of the heterogeneous structure A/B/A. Since we are interested in the study of confined modes, the functions  $u$ ,  $\varphi$ , and  $\psi$  in media A vanish when  $y \rightarrow \pm\infty$  (evanescent waves in the  $y$  direction). In [Calas et al. 2008] the dispersion relation for the case of perfect contact conditions at the interfaces was studied. Here, two types of imperfect contact conditions will be considered:

- (a) Case of electromagnetically permeable bonding at  $y = \pm d/2$ , for which

$$T_A = T_B = K(u_A - u_B), \quad \varphi_A = \varphi_B, \quad D_A = D_B, \quad \psi_A = \psi_B, \quad B_A = B_B. \quad (3-1)$$

- (b) Case of electromagnetically absorbent bonding at  $y = \pm d/2$ , for which

$$T_A = T_B = K(u_A - u_B), \quad \varphi_A = 0, \quad \varphi_B = 0, \quad \psi_A = 0, \quad \psi_B = 0. \quad (3-2)$$

The variables  $u$ ,  $\varphi$ , and  $\psi$  were introduced before (2-1)–(2-3) and  $T$ ,  $D$ , and  $B$  were introduced before (2-4). Also, the subscripts A and B identify the MEE media A and B, respectively. The first conditions in (3-1) and (3-2) describe an elastic interface with spring constant material parameter  $K > 0$ , which has dimensions of stress divided by length; in particular,  $[K] = \text{GPa}/\text{m}$ . We shall call this constant the interface parameter. With this model, the interface is allowed to deform and the displacement at the interface can be discontinuous. The case  $K \rightarrow \infty$  corresponds to a perfectly bonded interface and the case  $K \rightarrow 0$  corresponds to a mechanically free interface.

**3B. The auxiliary problem.** We now consider harmonic SH waves propagating in the positive  $x$  direction and want to find solutions  $u$ ,  $\tilde{\varphi}$ , and  $\tilde{\psi}$  of (2-5) and (2-9) in regions A and B that satisfy the radiation conditions in regions A, that is, functions  $u$ ,  $\tilde{\varphi}$ , and  $\tilde{\psi}$  vanish for  $y = \pm\infty$ . Using the symmetry properties of the heterostructure, as in [Calas et al. 2008], the MEE fields can be decoupled into symmetric and antisymmetric modes in  $y$ . Indeed, the linear equations (2-5) and (2-9) are invariant under reflections with respect to the  $x$ -axis in both regions A and B. Consequently, the symmetric and antisymmetric parts with respect to  $y$  of the solutions are also solutions of (2-5) and (2-9). In addition, it follows from the linear relations (2-7) and (2-12) that the fields  $\varphi$ ,  $\psi$ ,  $T$ ,  $D$ , and  $B$  are sums of the symmetric and antisymmetric parts of  $u$ ,  $\tilde{\varphi}$ , and  $\tilde{\psi}$ . Consequently, conditions (3-1) and (3-2) at  $y = \pm d/2$  are valid for the symmetric and antisymmetric parts of the solutions.

From (2-5) and (2-9), and taking into account the above considerations, the following solutions are obtained:

$$u = e^{i(\xi x - \omega t)} \begin{cases} U_A e^{\eta_A y}, & y \leq -d/2, \\ U_B \cos(\eta_B y), & |y| \leq d/2, \\ U_A e^{-\eta_A y}, & y \geq d/2, \end{cases} \quad (3-3)$$

$$\tilde{\varphi} = e^{i(\xi x - \omega t)} \begin{cases} \Phi_A e^{\xi y}, & y \leq -d/2, \\ \Phi_B \cosh(\xi y), & |y| \leq d/2, \\ \Phi_A e^{-\xi y}, & y \geq d/2, \end{cases} \quad (3-4)$$

$$\tilde{\psi} = e^{i(\xi x - \omega t)} \begin{cases} \Psi_A e^{\xi y}, & y \leq -d/2, \\ \Psi_B \cosh(\xi y), & |y| \leq d/2, \\ \Psi_A e^{-\xi y}, & y \geq d/2, \end{cases} \quad (3-5)$$

for the symmetric modes in  $y$ , and

$$u = e^{i(\xi x - \omega t)} \begin{cases} U'_A e^{\eta_A y}, & y \leq -d/2, \\ U'_B \sin(\eta_B y), & |y| \leq d/2, \\ -U'_A e^{-\eta_A y}, & y \geq d/2, \end{cases} \quad (3-6)$$

$$\tilde{\varphi} = e^{i(\xi x - \omega t)} \begin{cases} \Phi'_A e^{\xi y}, & y \leq -d/2, \\ \Phi'_B \sinh(\xi y), & |y| \leq d/2, \\ -\Phi'_A e^{-\xi y}, & y \geq d/2, \end{cases} \quad (3-7)$$

$$\tilde{\psi} = e^{i(\xi x - \omega t)} \begin{cases} \Psi'_A e^{\xi y}, & y \leq -d/2, \\ \Psi'_B \sinh(\xi y), & |y| \leq d/2, \\ -\Psi'_A e^{-\xi y}, & y \geq d/2, \end{cases} \quad (3-8)$$

for the antisymmetric modes in  $y$ . Here,  $\omega$ ,  $\xi$ , and  $\eta$  are, respectively, the frequency, the  $x$ -component of the wave vector, and the  $y$ -component of the wave vector, whereas  $U_A$ ,  $U_B$ ,  $\Phi_A$ ,  $\Phi_B$ ,  $\Psi_A$ , and  $\Psi_B$  are the amplitudes of the fields in the medium A and B. The parameters  $\eta_A > 0$ ,  $\eta_B$ ,  $\xi > 0$ , and  $\omega$  appearing in (3-3)–(3-8) are related to each other through the expressions

$$\begin{aligned} (\eta_A)^2 &= (\xi)^2 - (\omega/\bar{v}_A)^2 = \xi^2(1 - v^2/\bar{v}_A^2) > 0, & |y| &\geq d/2, \\ (\eta_B)^2 &= (\omega/\bar{v}_B)^2 - (\xi)^2 = \xi^2(v^2/\bar{v}_B^2 - 1), & |y| &\leq d/2, \end{aligned} \quad (3-9)$$

where  $v = \omega/\xi$  is the phase velocity.

Substituting (3-3)–(3-5) into (2-7), the symmetric parts of the electric and magnetic potentials are given by, respectively,

$$\varphi = e^{i(\xi x - \omega t)} \begin{cases} \frac{\bar{e}_A}{\varepsilon_A} U_A e^{\eta_A y} + \chi_A \Phi_A e^{\xi y} - \frac{\bar{g}_A}{\varepsilon_A} \Psi_A e^{\xi y}, & y \leq -d/2, \\ \frac{\bar{e}_B}{\varepsilon_B} U_B \cos(\eta_B y) + \chi_B \Phi_B \cosh(\xi y) - \frac{\bar{g}_B}{\varepsilon_B} \Psi_B \cosh(\xi y), & |y| \leq d/2, \\ \frac{\bar{e}_A}{\varepsilon_A} U_A e^{-\eta_A y} + \chi_A \Phi_A e^{-\xi y} - \frac{\bar{g}_A}{\varepsilon_A} \Psi_A e^{-\xi y}, & y \geq d/2, \end{cases} \quad (3-10)$$

$$\psi = e^{i(\xi x - \omega t)} \begin{cases} \frac{\bar{f}_A}{\mu_A} U_A e^{\eta_A y} - \frac{\bar{g}_A}{\mu_A} \Phi_A e^{\xi y} + \chi_A \Psi_A e^{\xi y}, & y \leq -d/2, \\ \frac{\bar{f}_B}{\mu_B} U_B \cos(\eta_B y) - \frac{\bar{g}_B}{\mu_B} \Phi_B \cosh(\xi y) + \chi_B \Psi_B \cosh(\xi y), & |y| \leq d/2, \\ \frac{\bar{f}_A}{\mu_A} U_A e^{-\eta_A y} - \frac{\bar{g}_A}{\mu_A} \Phi_A e^{-\xi y} + \chi_A \Psi_A e^{-\xi y}, & y \geq d/2. \end{cases} \quad (3-11)$$

Substituting (3-3)–(3-5) into (2-12), we obtain the following expressions for the symmetric parts of the mechanical stress, electric displacement, and magnetic flux:

$$T = e^{i(\xi x - \omega t)} \begin{cases} U_A \bar{c}_A \eta_A e^{\eta_A y} + (\bar{e}_A \Phi_A + \bar{f}_A \Psi_A) \xi e^{\xi y}, & y \leq -d/2, \\ -U_B \bar{c}_B \eta_B \sin(\eta_B y) + (\bar{e}_B \Phi_B + \bar{f}_B \Psi_B) \xi \sinh(\xi y), & |y| \leq d/2, \\ -U_A \bar{c}_A \eta_A e^{-\eta_A y} - (\bar{e}_A \Phi_A + \bar{f}_A \Psi_A) \xi e^{-\xi y}, & y \geq d/2, \end{cases} \quad (3-12)$$

$$D = e^{i(\xi x - \omega t)} \begin{cases} -\varepsilon_A \xi \Phi_A e^{\xi y}, & y \leq -d/2, \\ -\varepsilon_B \xi \Phi_B \sinh(\xi y), & |y| \leq d/2, \\ \varepsilon_A \xi \Phi_A e^{-\xi y}, & y \geq d/2, \end{cases} \quad (3-13)$$

$$B = e^{i(\xi x - \omega t)} \begin{cases} -\mu_A \xi \Psi_A e^{\xi y}, & y \leq -d/2, \\ -\mu_B \xi \Psi_B \sinh(\xi y), & |y| \leq d/2, \\ \mu_A \xi \Psi_A e^{-\xi y}, & y \geq d/2. \end{cases} \quad (3-14)$$

Analogously, substituting (3-6)–(3-8) into (2-7) and (2-12), the antisymmetric parts of the electric and magnetic potentials, mechanical stress, electric displacement, and magnetic flux are given by

$$\varphi = e^{i(\xi x - \omega t)} \begin{cases} \frac{\bar{e}_A}{\varepsilon_A} U'_A e^{\eta_A y} + \chi_A \Phi'_A e^{\xi y} - \frac{\bar{g}_A}{\varepsilon_A} \Psi'_A e^{\xi y}, & y \leq -d/2, \\ \frac{\bar{e}_B}{\varepsilon_B} U'_B \sin(\eta_B y) + \chi_B \Phi'_B \sinh(\xi y) - \frac{\bar{g}_B}{\varepsilon_B} \Psi'_B \sinh(\xi y), & |y| \leq d/2, \\ -\frac{\bar{e}_A}{\varepsilon_A} U'_A e^{-\eta_A y} - \chi_A \Phi'_A e^{-\xi y} + \frac{\bar{g}_A}{\varepsilon_A} \Psi'_A e^{-\xi y}, & y \geq d/2, \end{cases} \quad (3-15)$$

$$\psi = e^{i(\xi x - \omega t)} \begin{cases} \frac{\bar{f}_A}{\mu_A} U'_A e^{\eta_A y} - \frac{\bar{g}_A}{\mu_A} \Phi'_A e^{\xi y} + \chi_A \Psi'_A e^{\xi y}, & y \leq -d/2, \\ \frac{\bar{f}_B}{\mu_B} U'_B \sin(\eta_B y) - \frac{\bar{g}_B}{\mu_B} \Phi'_B \sinh(\xi y) + \chi_B \Psi'_B \sinh(\xi y), & |y| \leq d/2, \\ -\frac{\bar{f}_A}{\mu_A} U'_A e^{-\eta_A y} + \frac{\bar{g}_A}{\mu_A} \Phi'_A e^{-\xi y} - \chi_A \Psi'_A e^{-\xi y}, & y \geq d/2, \end{cases} \quad (3-16)$$

$$T = e^{i(\xi x - \omega t)} \begin{cases} U'_A \bar{c}_A \eta_A e^{\eta_A y} + (\bar{e}_A \Phi'_A + \bar{f}_A \Psi'_A) \xi e^{\xi y}, & y \leq -d/2, \\ U'_B \bar{c}_B \eta_B \cos(\eta_B y) + (\bar{e}_B \Phi'_B + \bar{f}_B \Psi'_B) \xi \cosh(\xi y), & |y| \leq d/2, \\ U'_A \bar{c}_A \eta_A e^{-\eta_A y} + (\bar{e}_A \Phi'_A + \bar{f}_A \Psi'_A) \xi e^{-\xi y}, & y \geq d/2, \end{cases} \quad (3-17)$$

$$D = e^{i(\xi x - \omega t)} \begin{cases} -\varepsilon_A \xi \Phi'_A e^{\xi y}, & y \leq -d/2, \\ -\varepsilon_B \xi \Phi'_B \cosh(\xi y), & |y| \leq d/2, \\ -\varepsilon_A \xi \Phi'_A e^{-\xi y}, & y \geq d/2, \end{cases} \quad (3-18)$$

$$B = e^{i(\xi x - \omega t)} \begin{cases} -\mu_A \xi \Psi'_A e^{\xi y}, & y \leq -d/2, \\ -\mu_B \xi \Psi'_B \cosh(\xi y), & |y| \leq d/2, \\ -\mu_A \xi \Psi'_A e^{-\xi y}, & y \geq d/2. \end{cases} \quad (3-19)$$

#### 4. Dispersion relations for imperfect contacts

Now, we refer to the conditions at the interface between the layers, which is located at  $y = \pm d/2$ , and the semiinfinite media. Due to the symmetry of the problem, such conditions are restricted to only one interface, and we study the dispersion relation for the imperfect bonding effects defined by (3-1) and (3-2) for the symmetric and antisymmetric solutions.

##### 4A. Dispersion relation for electromagnetically permeable bonding.

*Symmetric modes.* Substituting (3-3) and (3-10)–(3-14) into the interface conditions given by (3-1) for  $y = -d/2$ , an homogeneous system of linear algebraic equations for  $U_A$ ,  $U_B$ ,  $\Phi_A$ ,  $\Phi_B$ ,  $\Psi_A$ , and  $\Psi_B$  is obtained. For nontrivial solutions, the determinant of the principal matrix has to be zero, which leads to the following dispersion relation for the symmetric modes:

$$P_A P_B - Q^2 + K(P_A + P_B + 2Q) = 0, \quad (4-1)$$

where

$$P_A = -\bar{c}_A (\eta_A - \bar{\xi}_{AA}^2 \xi \sinh(\xi d/2)), \quad (4-2)$$

$$P_B = \bar{c}_B (\eta_B \tan(\eta_B d/2) + \bar{\xi}_{BB}^2 \xi \sinh(\xi d/2)), \quad (4-3)$$

$$Q = -\sqrt{\bar{c}_A \bar{c}_B} \bar{\xi}_{AB}^2 \xi \sinh(\xi d/2), \quad (4-4)$$

$$\bar{\xi}_{\alpha\beta}^2 = \frac{1}{\sqrt{\bar{c}_A \bar{c}_B}} \frac{\frac{\bar{e}_\alpha \bar{e}_\beta}{\varepsilon_\alpha \varepsilon_\beta} \Upsilon_{AB}^{(1)} + \frac{\bar{f}_\alpha \bar{f}_\beta}{\mu_\alpha \mu_\beta} \Upsilon_{AB}^{(2)} + \left( \frac{\bar{e}_\alpha \bar{f}_\beta}{\varepsilon_\alpha \mu_\beta} + \frac{\bar{e}_\beta \bar{f}_\alpha}{\varepsilon_\beta \mu_\alpha} \right) \Upsilon_{AB}^{(3)}}{\Upsilon_{AB}^{(1)} \Upsilon_{AB}^{(2)} - (\Upsilon_{AB}^{(3)})^2}, \quad (4-5)$$

$$\Upsilon_{AB}^{(1)} = \frac{\chi_A}{\mu_A} \sinh(\xi d/2) + \frac{\chi_B}{\mu_B} \cosh(\xi d/2), \quad \Upsilon_{AB}^{(2)} = \frac{\chi_A}{\varepsilon_A} \sinh(\xi d/2) + \frac{\chi_B}{\varepsilon_B} \cosh(\xi d/2), \quad (4-6)$$

$$\Upsilon_{AB}^{(3)} = \frac{\bar{g}_A}{\varepsilon_A \mu_A} \sinh(\xi d/2) + \frac{\bar{g}_B}{\varepsilon_B \mu_B} \cosh(\xi d/2). \quad (4-7)$$

Here,  $\bar{\xi}_{\alpha\beta}$ , with  $\alpha\beta = AA, BB, AB$ , is a coupling constant, which depends on the MEE properties of the phases and the thickness  $d$  of the layer.

Let us consider the following limit cases:

- (i) Materials A and B are piezoelectric. Expressions (4-2)–(4-4) reduce to

$$P_A = -\bar{c}_A^e \left( \eta_A - \frac{e_A^2 \xi \bar{\varepsilon}}{\bar{c}_A^e \varepsilon_A (\bar{\varepsilon} + \coth(\xi d/2))} \right), \quad (4-8)$$

$$P_B = \bar{c}_B^e \left( \eta_B \tan(\eta_B d/2) + \frac{e_B^2 \xi}{\bar{c}_B^e \varepsilon_B (\bar{\varepsilon} + \coth(\xi d/2))} \right), \quad (4-9)$$

$$Q = -\frac{e_A e_B \xi}{\varepsilon_A (\bar{\varepsilon} + \coth(\xi d/2))}, \quad (4-10)$$

where  $\bar{c}_\alpha^e = c_\alpha + e_\alpha^2 / \varepsilon_\alpha$  is the piezoelectrically stiffened elastic constant and  $\bar{\varepsilon} = \varepsilon_B / \varepsilon_A$ .

(ii) Materials A and B are piezomagnetic. Expressions (4-2)–(4-4) reduce to

$$P_A = -\bar{c}_A^f \left( \eta_A - \frac{f_A^2 \xi \bar{\mu}}{\bar{c}_A^f \mu_A (\bar{\mu} + \coth(\xi d/2))} \right), \quad (4-11)$$

$$P_B = \bar{c}_B^f \left( \eta_B \tan(\eta_B d/2) + \frac{f_B^2 \xi}{\bar{c}_B^f \mu_B (\bar{\mu} + \coth(\xi d/2))} \right), \quad (4-12)$$

$$Q = -\frac{f_A f_B \xi}{\mu_A (\bar{\mu} + \coth(\xi d/2))}, \quad (4-13)$$

where  $\bar{c}_\alpha^f = c_\alpha + f_\alpha^2 / \mu_\alpha$  is the piezomagnetically stiffened elastic constant and  $\bar{\mu} = \mu_B / \mu_A$ .

- (iii) Material A is piezoelectric and material B is piezomagnetic. Expressions (4-2)–(4-4) reduce to (4-8), (4-12), and  $Q = 0$ , respectively.
- (iv) Material A is piezomagnetic and material B is piezoelectric. Expressions (4-2)–(4-4) reduce to (4-11), (4-9), and  $Q = 0$ , respectively.
- (v) The interface is perfectly bonded. Expression (4-1) reduces to

$$P_A + P_B + 2Q = 0. \quad (4-14)$$

Substituting (4-2)–(4-7) into (4-14), we obtain the dispersion relation [Calas et al. 2008, Equation (59)].

- (vi) The interface has no mechanical interaction,  $K = 0$ , and the media can interact magnetoelectrically. In this case, (4-1) can be written as

$$P_A P_B - Q^2 = 0. \quad (4-15)$$

Substituting (4-2)–(4-7) into (4-15), we obtain

$$(\eta_A - \bar{\xi}_{AA}^2 \xi \sinh(\xi d/2))(\eta_B \tan(\eta_B d/2) + \bar{\xi}_{BB}^2 \xi \sinh(\xi d/2)) = -(\bar{\xi}_{AB}^2 \xi \sinh(\xi d/2))^2, \quad (4-16)$$

which, together with both (3-9) and  $v = \omega/\xi$ , yields

$$\begin{aligned} -\left(\bar{\xi}_{AB}^2 \sinh\left(\frac{1}{v} \frac{\omega d}{2}\right)\right)^2 &= \left(\left(1 - \frac{v^2}{\bar{v}_A^2}\right)^{\frac{1}{2}} - \bar{\xi}_{AA}^2 \sinh\left(\frac{1}{v} \frac{\omega d}{2}\right)\right) \\ &\times \left(\left(\frac{v^2}{\bar{v}_B^2} - 1\right)^{\frac{1}{2}} \tan\left(\left(\frac{v^2}{\bar{v}_B^2} - 1\right)^{\frac{1}{2}} \frac{1}{v} \frac{\omega d}{2}\right) + \bar{\xi}_{BB}^2 \sinh\left(\frac{1}{v} \frac{\omega d}{2}\right)\right). \end{aligned} \quad (4-17)$$

Note from (4-17) that if  $\omega d = 0$ , then  $v$  is given by

$$v = \bar{v}_A, \quad (4-18)$$

which is the bulk shear wave of medium A.

*Antisymmetric modes.* Following a procedure similar to the one used for symmetric modes, we substitute (3-6) and (3-15)–(3-19) into the interface conditions of Case (a) (page (3-1)) at  $y = -d/2$ , and obtain the wave speed equation for the antisymmetric modes in the form of Equation (4-1), where

$$P_A = -\bar{c}_A (\eta_A - \bar{\xi}_{AA}^2 \xi \cosh(\xi d/2)), \quad (4-19)$$

$$P_B = -\bar{c}_B (\eta_B \cot(\eta_B d/2) - \bar{\xi}_{BB}^2 \xi \cosh(\xi d/2)), \quad (4-20)$$

$$Q = -\sqrt{\bar{c}_A \bar{c}_B} \bar{\xi}_{AB}^2 \xi \cosh(\xi d/2), \quad (4-21)$$

and  $\bar{\xi}_{\alpha\beta}$  can be calculated using (4-5), but with  $\Upsilon_{AB}^{(i)}$  ( $i = 1, 2, 3$ ) given by

$$\Upsilon_{AB}^{(1)} = \frac{\chi_A}{\mu_A} \cosh(\xi d/2) + \frac{\chi_B}{\mu_B} \sinh(\xi d/2), \quad \Upsilon_{AB}^{(2)} = \frac{\chi_A}{\varepsilon_A} \cosh(\xi d/2) + \frac{\chi_B}{\varepsilon_B} \sinh(\xi d/2), \quad (4-22)$$

$$\Upsilon_{AB}^{(3)} = \frac{\bar{g}_A}{\varepsilon_A \mu_A} \cosh(\xi d/2) + \frac{\bar{g}_B}{\varepsilon_B \mu_B} \sinh(\xi d/2). \quad (4-23)$$

Let us consider the following limit cases:

- (i) Materials A and B are piezoelectric. Expressions (4-19)–(4-21) reduce to

$$P_A = -\bar{c}_A^e \left( \eta_A - \frac{e_A^2 \xi \bar{\varepsilon}}{\bar{c}_A^e \varepsilon_A (\bar{\varepsilon} + \tanh(\xi d/2))} \right), \quad (4-24)$$

$$P_B = -\bar{c}_B^e \left( \eta_B \cot(\eta_B d/2) - \frac{e_B^2 \xi}{\bar{c}_B^e \varepsilon_B (\bar{\varepsilon} + \tanh(\xi d/2))} \right), \quad (4-25)$$

$$Q = -\frac{e_A e_B \xi}{\varepsilon_A (\bar{\varepsilon} + \tanh(\xi d/2))}. \quad (4-26)$$

- (ii) Materials A and B are piezomagnetic. Expressions (4-19)–(4-21) reduce to

$$P_A = -\bar{c}_A^f \left( \eta_A - \frac{f_A^2 \xi \bar{\mu}}{\bar{c}_A^f \mu_A (\bar{\mu} + \tanh(\xi d/2))} \right), \quad (4-27)$$

$$P_B = -\bar{c}_B^f \left( \eta_B \cot(\eta_B d/2) - \frac{f_B^2 \xi}{\bar{c}_B^f \mu_B (\bar{\mu} + \tanh(\xi d/2))} \right), \quad (4-28)$$

$$Q = -\frac{f_A f_B \xi}{\mu_A (\bar{\mu} + \tanh(\xi d/2))}. \quad (4-29)$$

(iii) Material A is piezoelectric and material B is piezomagnetic. Expressions (4-19)–(4-21) reduce to (4-24), (4-28), and  $Q = 0$ , respectively.

(iv) Material A is piezomagnetic and material B is piezoelectric. Expressions (4-19)–(4-21) reduce to (4-27), (4-25), and  $Q = 0$ , respectively.

(v) The interface is perfectly bonded. Expression (4-1) reduces to (4-14).

(vi) The interface has no mechanical interaction,  $K = 0$ , and the media can interact magnetoelectrically. Equation (4-1) can be written as (4-15). Substituting (4-19)–(4-23) into (4-15), we obtain

$$(\eta_A - \bar{\xi}_{AA}^2 \xi \cosh(\xi d/2))(\eta_B \cot(\eta_B d/2) - \bar{\xi}_{BB}^2 \xi \cosh(\xi d/2)) = (\bar{\xi}_{AB}^2 \xi \cosh(\xi d/2))^2, \quad (4-30)$$

which, together with both (3-9) and  $v = \omega/\xi$ , yields

$$\begin{aligned} \left( \bar{\xi}_{AB}^2 \cosh\left(\frac{1}{v} \frac{\omega d}{2}\right) \right)^2 &= \left( \left(1 - \frac{v^2}{v_A^2}\right)^{\frac{1}{2}} - \bar{\xi}_{AA}^2 \cosh\left(\frac{1}{v} \frac{\omega d}{2}\right) \right) \\ &\quad \times \left( \left( \frac{v^2}{v_B^2} - 1 \right)^{\frac{1}{2}} \cot\left(\left( \frac{v^2}{v_B^2} - 1 \right)^{\frac{1}{2}} \frac{1}{v} \frac{\omega d}{2}\right) - \bar{\xi}_{BB}^2 \cosh\left(\frac{1}{v} \frac{\omega d}{2}\right) \right). \end{aligned} \quad (4-31)$$

Equation (4-31) governs the magnetoelectrical interaction between the three phases. Note from (4-31) that if  $\omega d = 0$ , (4-31) yields the following velocity on the half-spaces ( $|y| > d/2$ ):

$$v^2 = \bar{v}_A^2 (1 - \bar{\xi}_A^4), \quad (4-32)$$

where

$$\bar{\xi}_A^2 = 1 - \frac{c_A}{\bar{c}_A} \quad (4-33)$$

is the limit of  $\bar{\xi}_{AA}$  when  $\omega d \rightarrow 0$ . The magnitude  $v$  defined by (4-32) is the speed of the Bleustein–Gulyaev wave for medium A (see, [Bleustein 1968; Gulyaev 1969]). These results are in agreement with other similar studies, for instance, [Fan et al. 2006a, (15) and (16)] or [Melkumyan and Mai 2008, (27)].

#### 4B. Dispersion relation for electromagnetically absorbent bonding.

*Symmetric modes.* Substituting (3-3) and (3-10)–(3-12) into the interface conditions given by (3-2) for  $y = -d/2$ , we obtain the dispersion relation for the symmetric modes, which is given by

$$P_A P_B + K(P_A + P_B) = 0, \quad (4-34)$$

where

$$P_A = -\bar{c}_A (\eta_A - \bar{\xi}_A^2 \xi), \quad (4-35)$$

$$P_B = \bar{c}_B (\eta_B \tan(\eta_B d/2) + \bar{\xi}_B^2 \xi \tanh(\xi d/2)), \quad (4-36)$$

$$\bar{\xi}_\alpha^2 = 1 - \frac{c_\alpha}{\bar{c}_\alpha}, \quad (4-37)$$

with  $\bar{\xi}_\alpha$ , for  $\alpha = A, B$ , being a coupling constant of the MEE homogeneous medium  $\alpha$ . From (4-37) and using (2-11) on each phase, one can obtain [Huang and Li 2010, (18)].

Let us consider the following special cases:

(i) Materials A and B are piezoelectric. Expressions (4-35) and (4-36) reduce to

$$P_A = -\bar{c}_A^e \left( \eta_A - \frac{e_A^2 \xi}{\bar{c}_A^e \varepsilon_A} \right), \quad (4-38)$$

$$P_B = \bar{c}_B^e \left( \eta_B \tan(\eta_B d/2) + \frac{e_B^2 \xi}{\bar{c}_B^e \varepsilon_B} \tanh(\xi d/2) \right). \quad (4-39)$$

(ii) Materials A and B are piezomagnetic. Expressions (4-35) and (4-36) reduce to

$$P_A = -\bar{c}_A^f \left( \eta_A - \frac{f_A^2 \xi}{\bar{c}_A^f \mu_A} \right), \quad (4-40)$$

$$P_B = \bar{c}_B^f \left( \eta_B \tan(\eta_B d/2) + \frac{f_B^2 \xi}{\bar{c}_B^f \mu_B} \tanh(\xi d/2) \right). \quad (4-41)$$

- (iii) Material A is piezoelectric and material B is piezomagnetic. Expressions (4-35) and (4-36) reduce to (4-38) and (4-41), respectively.
- (iv) Material A is piezomagnetic and material B is piezoelectric. Expressions (4-35) and (4-36) reduce to (4-40) and (4-39), respectively.
- (v) The interface is perfectly bonded. Expression (4-34) reduces to

$$-\bar{c}_A(\eta_A - \bar{\xi}_A^2 \xi) + \bar{c}_B(\eta_B \tan(\eta_B d/2) + \bar{\xi}_B^2 \xi \tanh(\xi d/2)) = 0. \quad (4-42)$$

Equation (4-42) can be written as a function of the normalized velocity  $V_\alpha = v/\bar{v}_\alpha$ ,  $\alpha = A, B$ , and the dimensionless frequency  $\Omega = \omega d/(\pi \bar{v}_B)$  as

$$\bar{c}_B \left( (V_B^2 - 1)^{1/2} \tan \left( \frac{\pi}{2} \frac{\Omega}{V_B} (V_B^2 - 1)^{1/2} \right) + \bar{\xi}_B^2 \tanh \left( \frac{\pi}{2} \frac{\Omega}{V_B} \right) \right) - \bar{c}_A ((1 - V_A^2)^{1/2} - \bar{\xi}_A^2) = 0. \quad (4-43)$$

Setting  $\Omega \rightarrow 0$ , (4-43) reduces to the velocity of the Bleustein–Gulyaev wave given by (4-32) in the two half-spaces  $y > d/2$  and  $y < -d/2$ . These results are in agreement with [Fan et al. 2006b, Equations (10) and (11)] and also [Huang et al. 2009, Equations (19) and (20)].

- (vi) The interface has no mechanical-magnetoelectrical interaction. Equation (4-34) can be written as

$$P_A P_B = 0. \quad (4-44)$$

For  $P_A = 0$ , the phase velocity is identical to (4-32), the velocity of the Bleustein–Gulyaev wave. On the other hand, if  $P_B = 0$ , the velocity in the layer  $|y| < d/2$  satisfies the equation

$$\eta_B \tan(\eta_B d/2) + \bar{\xi}_B^2 \xi \tanh(\xi d/2) = 0. \quad (4-45)$$

The roots of (4-45) determine the dispersion curves for a plate with grounded electrodes. It can be written, in a way similar to [Bleustein 1969, Equation (27)], as

$$\frac{\tan\left(\frac{1}{2}\pi(\Omega^2 - Z^2)^{1/2}\right)}{\tanh\left(\frac{1}{2}\pi Z\right)} = -\frac{\bar{\xi}_B^2 Z}{(\Omega^2 - Z^2)^{1/2}}, \quad (4-46)$$

where the dimensionless wave number ( $Z$ ) in the  $x$  direction is defined by

$$Z = \frac{\xi d}{\pi}. \quad (4-47)$$

In the limit when  $Z \rightarrow 0$ , (4-46) reduces to

$$\tan\left(\frac{\pi}{2}\Omega\right) = 0, \quad \omega d = n\pi \bar{v}_B, \quad n = 0, 2, 4, 6, \dots, \quad (4-48)$$

which is the frequency equation for the symmetric modes of a MEE plate. Equation (4-45) can also be written as a function of the normalized velocity  $V_B$  and the dimensionless wave number  $Z$  as

$$\frac{\tan\left(\frac{1}{2}\pi Z(V_B^2 - 1)^{1/2}\right)}{\tanh\left(\frac{1}{2}\pi Z\right)} = -\frac{\bar{\xi}_B^2}{(V_B^2 - 1)^{1/2}}. \quad (4-49)$$

Taking  $Z \rightarrow 0$ , (4-49) reduces to

$$V_B^2 = (1 - \bar{\xi}_B^2), \quad \text{or} \quad v^2 = \bar{v}_B^2 (1 - \bar{\xi}_B^2). \quad (4-50)$$

Equation (4-45) can also be written as a function of the normalized velocity  $V_B$  and the dimensionless frequency  $\Omega$  as

$$\frac{\tan\left(\frac{1}{2}\pi(\Omega/V_B)(V_B^2 - 1)^{1/2}\right)}{\tanh\left(\frac{1}{2}\pi(\Omega/V_B)\right)} = -\frac{\bar{\xi}_B^2}{(V_B^2 - 1)^{1/2}}. \quad (4-51)$$

Note that (4-51) reduces to (4-50) for  $\Omega \rightarrow 0$ .

*Antisymmetric modes.* Substituting (3-6) and (3-15)–(3-17) into the conditions given by (3-2) for  $y = -d/2$ , the dispersion relation for the antisymmetric modes can be written as (4-34), with

$$P_B = -\bar{c}_B \left( \eta_B \cot(\eta_B d/2) - \bar{\xi}_B^2 \xi \coth(\xi d/2) \right), \quad (4-52)$$

where  $P_A$  and  $\bar{\xi}_\alpha^2$  are given by (4-35) and (4-37), respectively.

Let us consider the following limit cases:

- (i) Materials A and B are piezoelectric. Expression (4-35) becomes (4-38) and (4-52) takes the form

$$P_B = -\bar{c}_B^e \left( \eta_B \cot(\eta_B d/2) - \frac{e_B^2 \xi}{\bar{c}_B^e \varepsilon_B} \coth(\xi d/2) \right). \quad (4-53)$$

- (ii) Materials A and B are piezomagnetic. Expression (4-35) reduces to (4-40) and (4-52) becomes

$$P_B = -\bar{c}_B^f \left( \eta_B \cot(\eta_B d/2) - \frac{f_B^2 \xi}{\bar{c}_B^f \mu_B} \coth(\xi d/2) \right). \quad (4-54)$$

- (iii) Material A is piezoelectric and material B is piezomagnetic. Expressions (4-35) and (4-52) reduce to (4-38) and (4-54), respectively.

- (iv) Material A is piezomagnetic and material B is piezoelectric. Expressions (4-35) and (4-52) reduce to (4-40) and (4-53), respectively.

- (v) The interface is perfectly bonded. Expression (4-34) reduces to

$$-\bar{c}_A \left( (1 - V_A^2)^{1/2} - \bar{\xi}_A^2 \right) = \bar{c}_B \bar{\xi}_B^2 \coth\left(\frac{\pi}{2} \frac{\Omega}{V_B}\right) + \bar{c}_B \left( (V_B^2 - 1)^{1/2} \cot\left(\frac{\pi}{2} \frac{\Omega}{V_B} (V_B^2 - 1)^{1/2}\right) \right). \quad (4-55)$$

Setting  $\Omega \rightarrow 0$ , (4-55) does not have a solution. In fact, dividing by  $\coth\left(\frac{1}{2}\pi(\Omega/V_B)\right)$  and taking the limit for  $\Omega \rightarrow 0$  results in  $\bar{\xi}_B^2 = 1$ , which is not possible.

- (vi) The interface has no mechanical-magnetoelectrical interaction. From (4-34), the expression  $P_A P_B = 0$  is obtained. If  $P_A = 0$ , the phase velocity is identical to (4-32), and if  $P_B = 0$ , the phase velocity for the layer is given by an expression that is similar to [Bleustein 1969, Equation (23)] and is obtained from the dispersion equation

$$\frac{\tan\left(\frac{1}{2}\pi(\Omega^2 - Z^2)^{1/2}\right)}{\tanh\left(\frac{1}{2}\pi Z\right)} = \frac{(\Omega^2 - Z^2)^{1/2}}{\bar{\xi}_B^2 Z}. \quad (4-56)$$

In the limit, as  $Z \rightarrow 0$ , (4-56) reduces to

$$\tan\left(\frac{\pi}{2}\Omega\right) = \frac{\pi\Omega}{2\bar{\xi}_B^2}, \quad (4-57)$$

which is the frequency equation for the antisymmetric modes of a MEE plate. Equation (4-56) can be written as a function of the normalized velocity  $V_B$  and the dimensionless frequency  $\Omega$  as

$$\frac{\tan\left(\frac{1}{2}\pi(\Omega/V_B)(V_B^2 - 1)^{1/2}\right)}{\tanh\left(\frac{1}{2}\pi(\Omega/V_B)\right)} = \frac{(V_B^2 - 1)^{1/2}}{\xi_B^2}. \quad (4-58)$$

When  $\Omega \rightarrow 0$ , (4-58) reduces to  $v = \bar{v}_B$ .

## 5. Numerical examples

We now show dispersion curves for different heterostructures of type A/B/A with MEE properties and discuss quantitative and qualitative aspects of bonding on the dynamic properties of MEE heterostructures. An important aspect is that the behavior of the dispersion curves is strongly dependent on the spring constant material parameter  $K$ .

To perform numerical calculations, we use the piezomagnetic material  $\text{CoFe}_2\text{O}_4$ , the piezoelectric materials  $\text{BaTiO}_3$  and PZT4, and the composite  $\text{BaTiO}_3/\text{CoFe}_2\text{O}_4$  with 30 percent  $\text{BaTiO}_3$  [Bravo-Castillero et al. 2008]. This composite material exhibits MEE properties. We then analyze the dispersion of waves considering the first mode of vibration in the heterostructures  $\text{BaTiO}_3/\text{CoFe}_2\text{O}_4/\text{BaTiO}_3$ ,  $\text{CoFe}_2\text{O}_4/\text{PZT4}/\text{CoFe}_2\text{O}_4$ , and Composite/ $\text{CoFe}_2\text{O}_4$ /Composite with the bonding conditions (3-1), modeling a permeable interface, and (3-2), modeling an absorbent interface. The MEE properties used in the calculations are given in Table 1. The dimensions of the interface parameter  $K$ , which we recall from Section 3A are GPa/m, are omitted in Figures 2–8.

In Figure 2 we show dispersion curves for the symmetric parts of SH waves propagating in the heterostructure of  $\text{BaTiO}_3/\text{CoFe}_2\text{O}_4/\text{BaTiO}_3$  with either a permeable (Figure 2a) or absorbent (Figure 2b) interface for increasing values of the spring constant  $K$ . Observe from Figure 2a that these curves are nonintersecting, nonmonotonic for small values of  $K$ , and both strictly decreasing and convex for large values of  $K$ . These last features can also be observed in [Calas et al. 2008, Figure 2]. In particular, all wave velocities tend to the wave velocity in phase B,  $\bar{v}_{\text{CoFe}_2\text{O}_4}$ , as  $\omega d \rightarrow \infty$ . We conclude from this observation, which is also valid for Figure 2b, that the presence of imperfections at the interfaces does

Properties	$\text{BaTiO}_3$	$\text{CoFe}_2\text{O}_4$	PZT4	Composite
$c$ (GPa)	43	45.3	26	44.58
$e$ ( $\text{C}/\text{m}^2$ )	11.6	0	10.5	3.61
$f$ ( $\text{N}/\text{Am}$ )	0	550	0	378.92
$g$ ( $10^{-9}\text{Ns}/\text{Vm}$ )	0	0	0	-30.67
$\varepsilon$ ( $10^{-9}\text{C}^2/\text{Nm}^2$ )	11.2	0.08	7.124	4.06
$\mu$ ( $10^{-6}\text{Ns}^2/\text{C}^2$ )	5	590	5	415.95
$\rho$ ( $10^3\text{Kg}/\text{m}^3$ )	5.8	5.3	7.5	5.45
$\bar{v}$ ( $10^3\text{m}/\text{s}$ )	3.07981	2.94005	2.35162	2.97348
$\bar{v}_{\text{B-G}}$ ( $10^3\text{m}/\text{s}$ )	3.00547	2.93987	2.18178	2.96514

**Table 1.** Material properties.

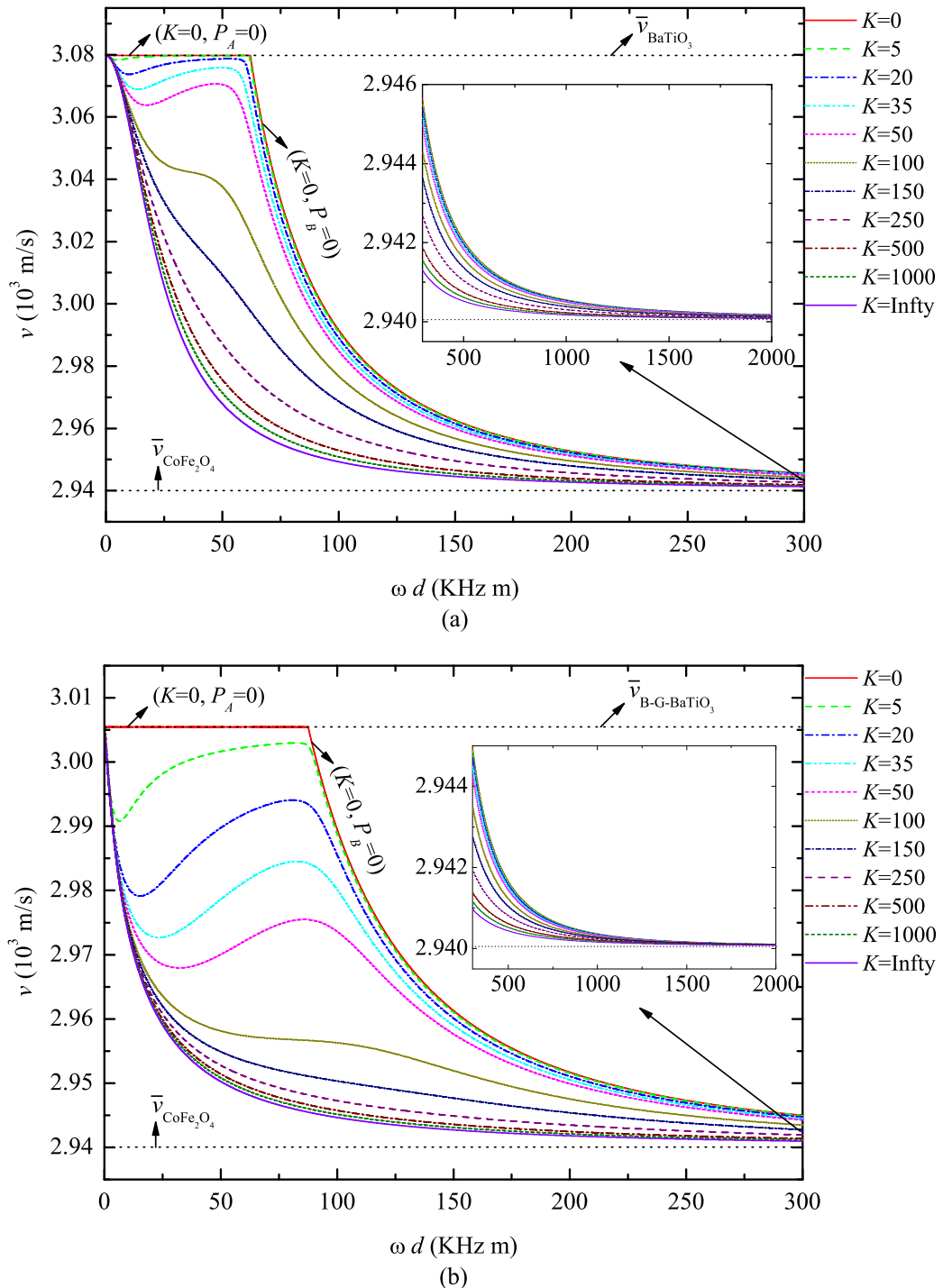


**Figure 2.** Influence of imperfect bonding on the dispersion curves for the symmetric modes in a  $\text{BaTiO}_3/\text{CoFe}_2\text{O}_4/\text{BaTiO}_3$  heterostructure: (a) permeable and (b) absorbent bonding.

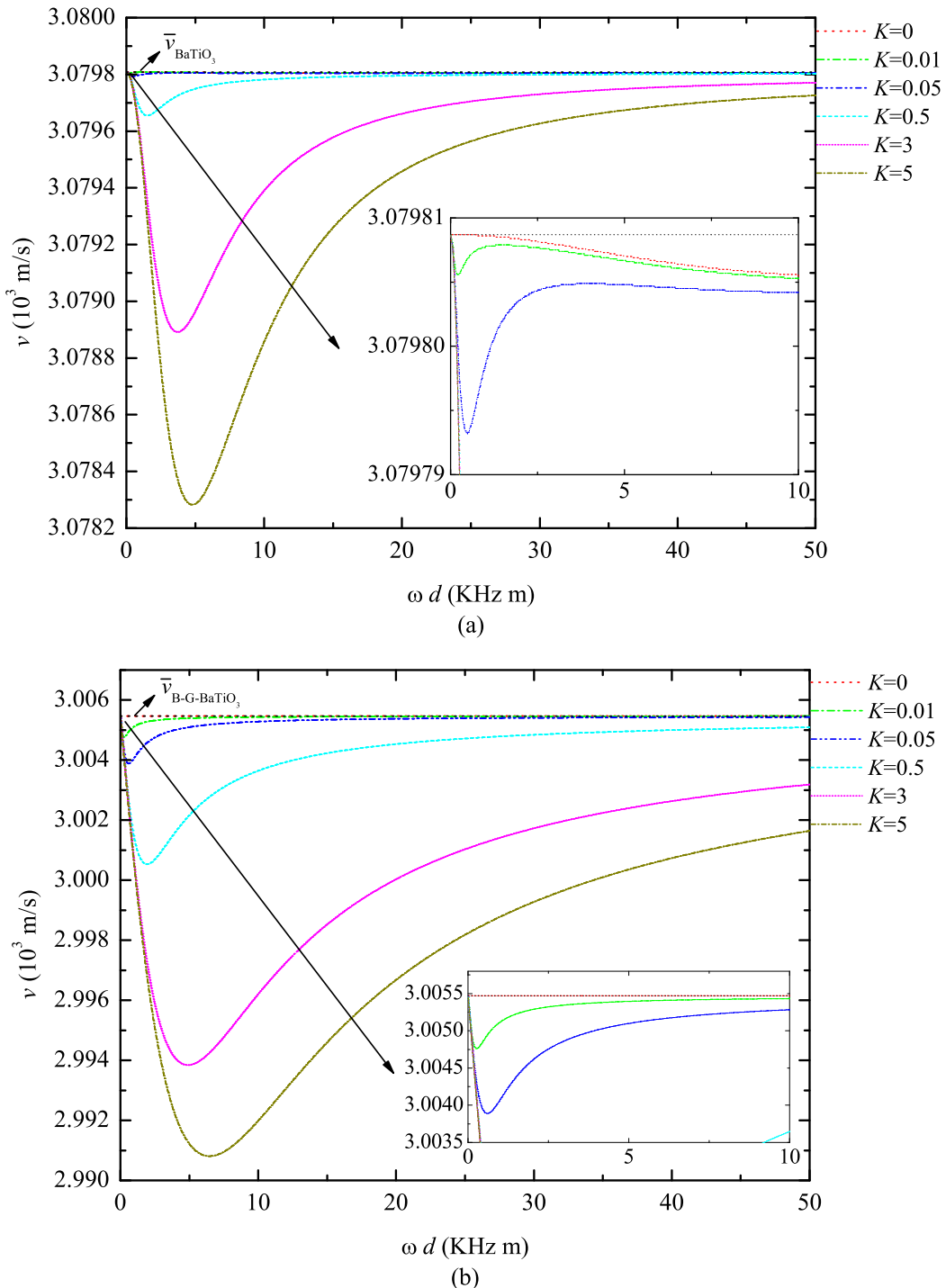


**Figure 3.** Influence of imperfect bonding on the dispersion curves for the symmetric modes in a  $\text{BaTiO}_3/\text{CoFe}_2\text{O}_4/\text{BaTiO}_3$  heterostructure: (a) permeable and (b) absorbent bonding.

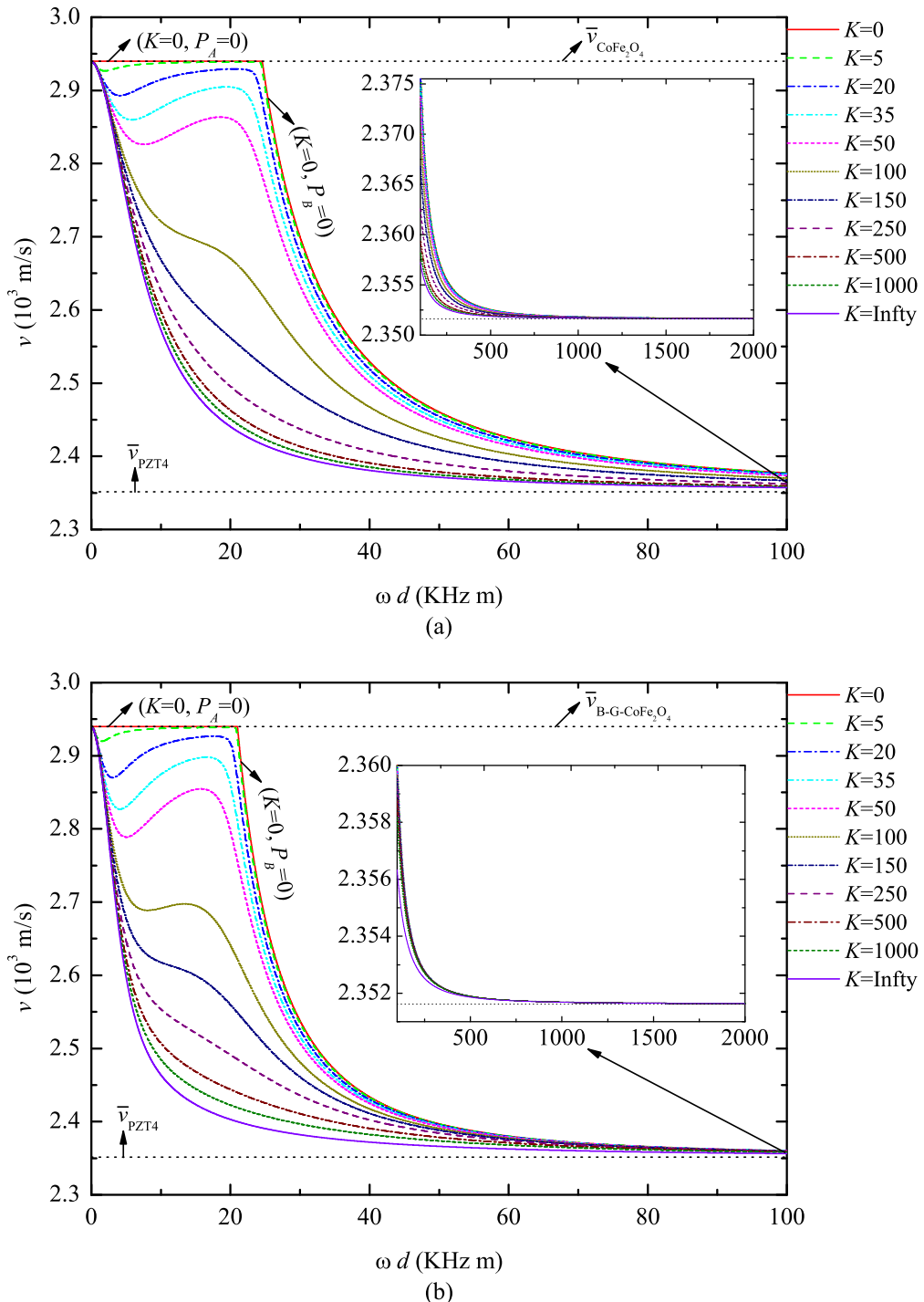


**Figure 4.** Influence of imperfect bonding on the dispersion curves for the symmetric modes in a  $\text{CoFe}_2\text{O}_4/\text{PZT}4/\text{CoFe}_2\text{O}_4$  heterostructure: (a) permeable and (b) absorbent bonding.

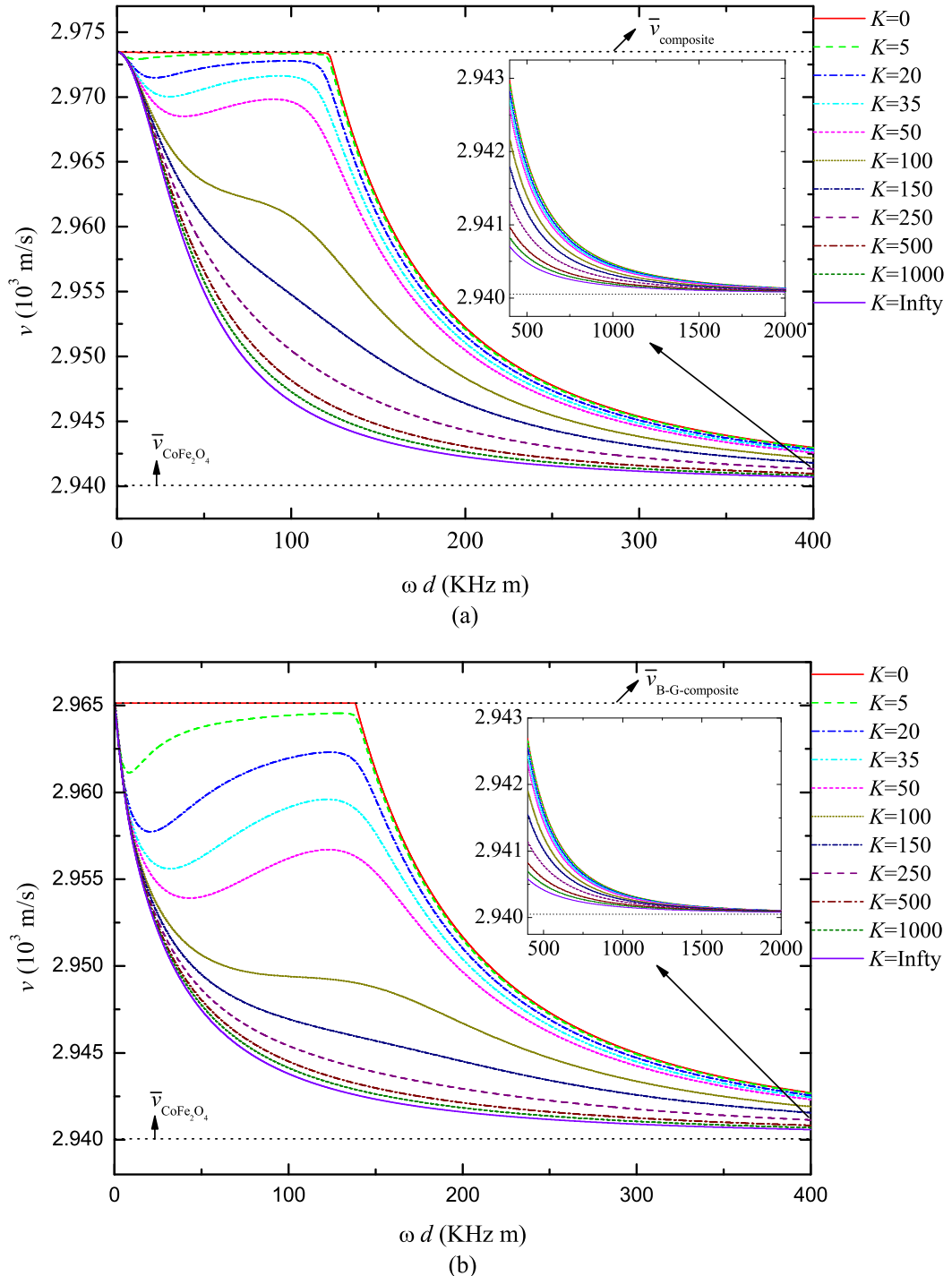


**Figure 5.** Influence of imperfect bonding on the dispersion curves for the symmetric modes in a Composite/Co<sub>Fe<sub>2</sub></sub>O<sub>4</sub>/Composite heterostructure: (a) permeable and (b) absorbent bonding.

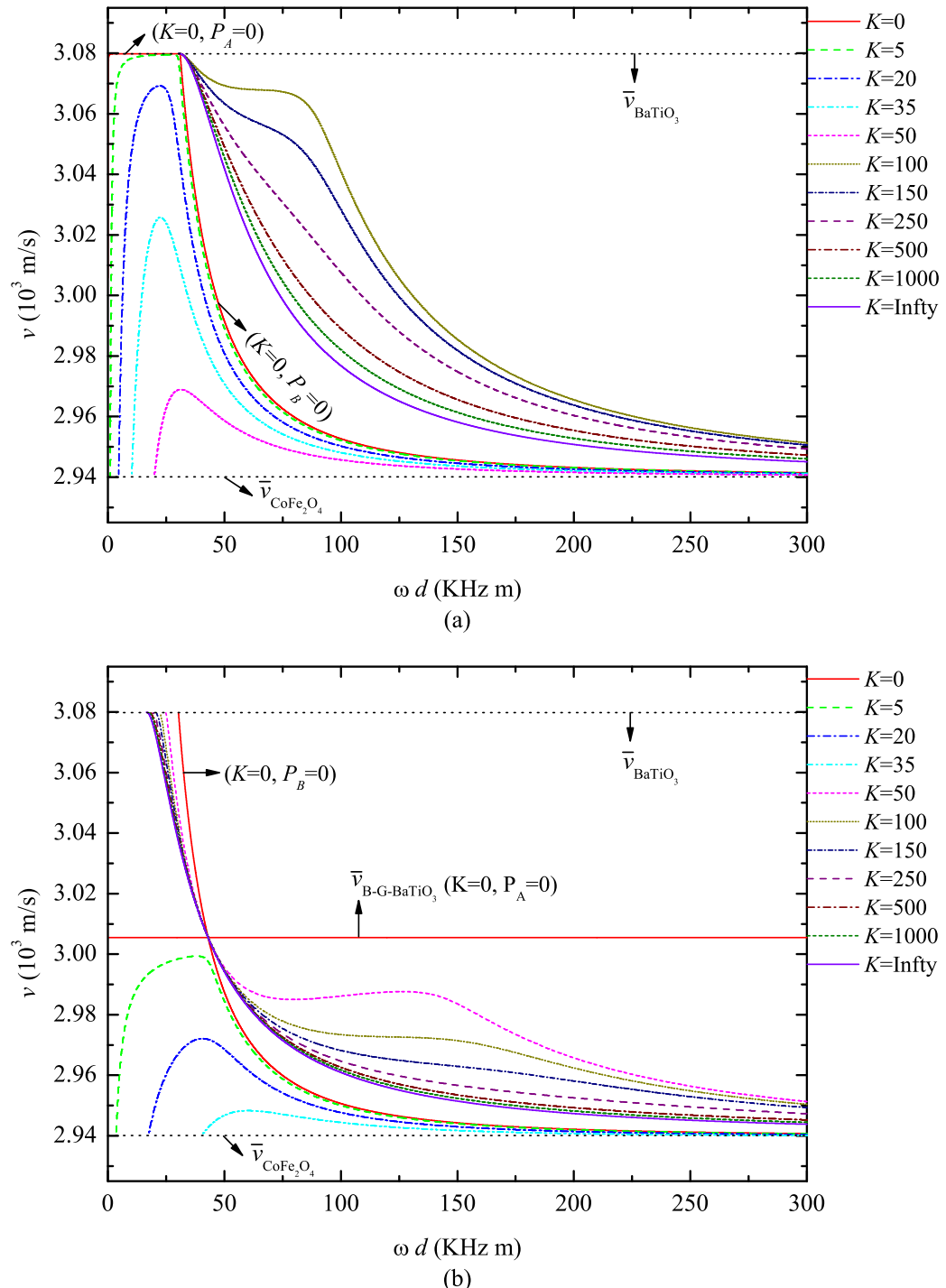


**Figure 6.** Influence of imperfect bonding on the dispersion curves for the antisymmetric modes in a  $\text{BaTiO}_3/\text{CoFe}_2\text{O}_4/\text{BaTiO}_3$  heterostructure: (a) permeable and (b) absorbent bonding.

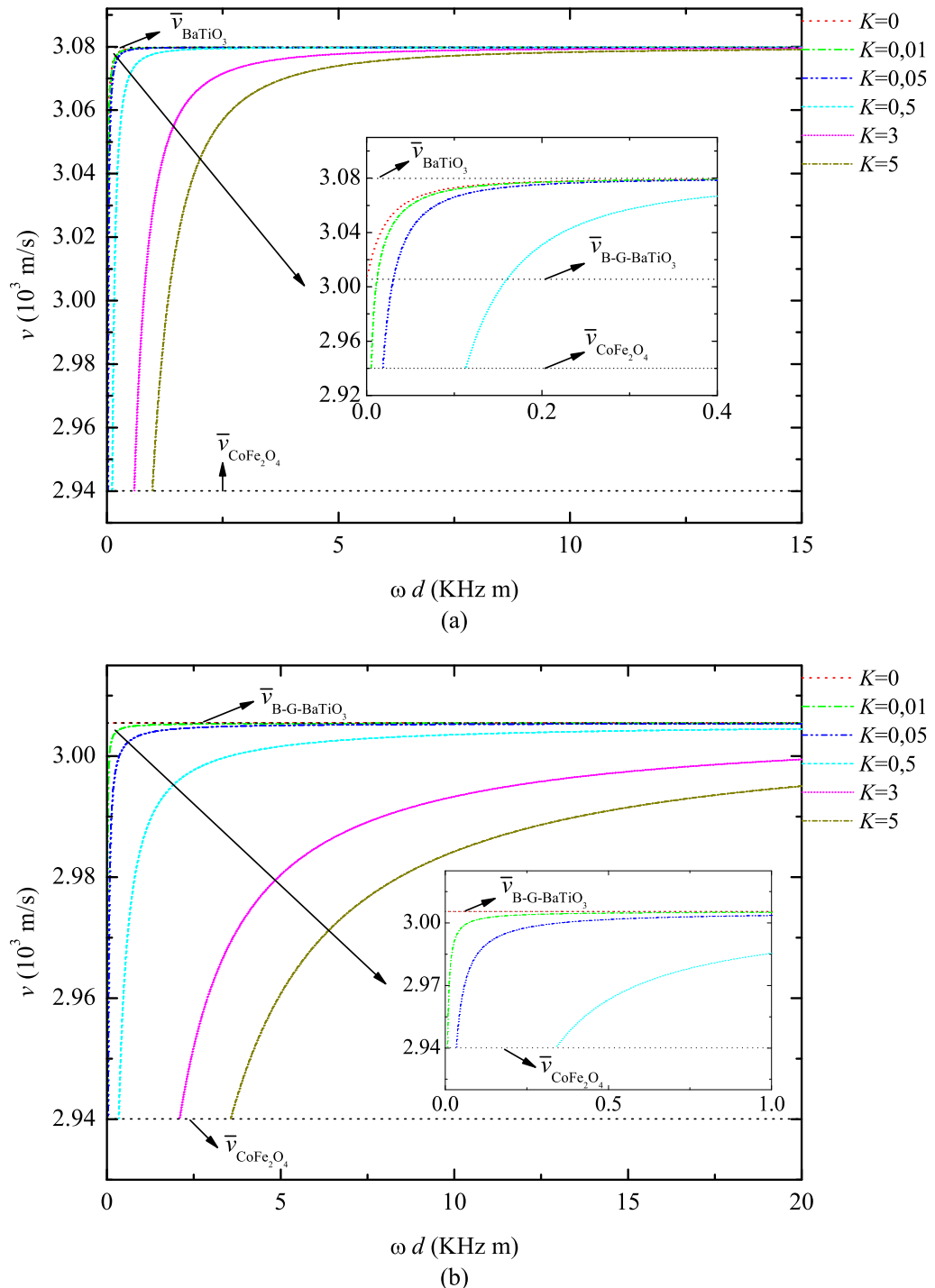


**Figure 7.** Influence of imperfect bonding on the dispersion curves for the antisymmetric modes in a  $\text{BaTiO}_3/\text{CoFe}_2\text{O}_4/\text{BaTiO}_3$  heterostructure: (a) permeable and (b) absorbent bonding.

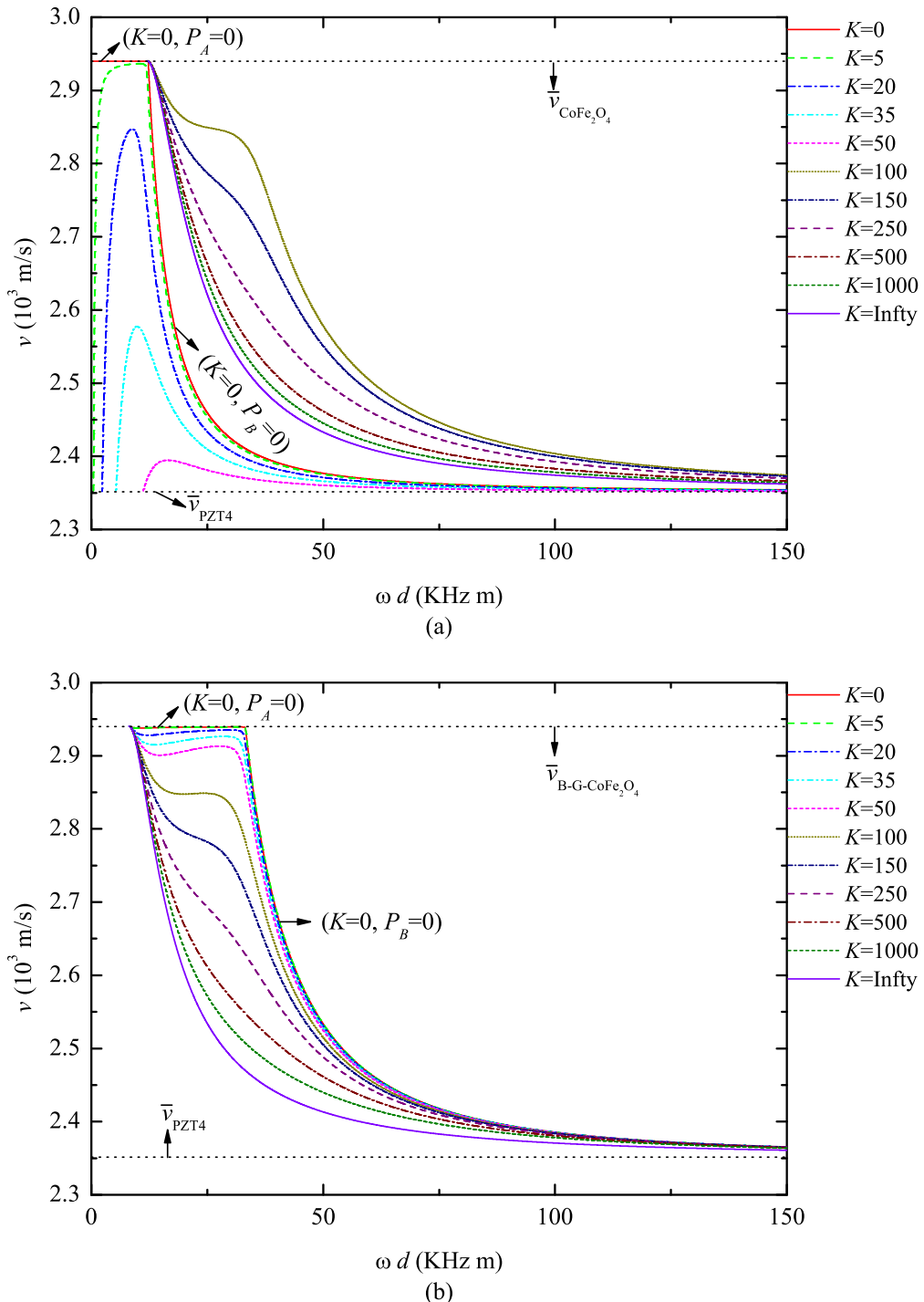


**Figure 8.** Influence of imperfect bonding on the dispersion curves for the antisymmetric modes in a  $\text{CoFe}_2\text{O}_4/\text{PZT}4/\text{CoFe}_2\text{O}_4$  heterostructure: (a) permeable and (b) absorbent bonding.

not affect the wave propagation at high frequency for a given width  $d$ . Observe also from Figure 2a that the velocity  $v$  tends to the velocity in phase A,  $\bar{v}_{\text{BaTiO}_3}$ , as  $K$  tends to zero for  $\omega d$  less than 62.016 KHz m.

To analyze Figure 2b, observe from conditions (3-2)b–(3-2)e that there are neither electrical nor magnetic interactions between phases A,  $\text{BaTiO}_3$ , and B,  $\text{CoFe}_2\text{O}_4$ , across an interface. If  $K = 0$ , recall from (3-2)a that these phases are not bonded at an interface and, therefore, there is no mechanical interaction between them either. In this case, the dispersion relation (4-34) reduces to (4-44), that is,  $P_A P_B = 0$ . The solution  $P_A = 0$  corresponds to the constant phase velocity of the piezoelectric Bleustein–Gulyaev wave for phase A,  $\text{BaTiO}_3$ , which is obtained from (4-32), (4-33), and (2-10), and is given by  $v_{B-G} = \bar{v}_A \sqrt{1 - e_A^4 / (\varepsilon_A \bar{c}_A^e)^2}$ . The dashed straight line in Figure 2b corresponds to this case. On the other hand, the solution  $P_B = 0$  corresponds to a dispersive wave for the  $\text{CoFe}_2\text{O}_4$  medium with velocity determined from (4-45). The dashed line at the bottom of Figure 2b corresponds to this case. Observe from this figure that all other dispersion curves are in between the curve for the Bleustein–Gulyaev wave velocity of the  $\text{BaTiO}_3$  medium and the curve for the wave velocity of phase B, that is,  $\bar{v}_{B-G-\text{BaTiO}_3} < v < \bar{v}_{\text{CoFe}_2\text{O}_4}$ .

We now consider that  $\omega d$  belongs to the interval  $(0, 50)$  in Figure 2 and show dispersion curves in Figure 3 for small values of  $K$  belonging to the set  $\{0, 0.001, 0.005, 0.05, 3, 5\}$ . In the permeable case (Figure 3a) the wave velocity  $v$  tends to the velocity in phase A,  $\bar{v}_{\text{BaTiO}_3}$ , as  $\omega d$  tends to zero, which is an expected result from (4-18). Note from the graph in the lower right-hand corner, for which  $\omega d$  belongs to the interval  $(0, 10)$ , that the wave velocity for  $K = 0$  is both an upper bound and a limit point to which the wave velocity  $v$  tends to as  $K$  tends to zero. In the absorbent case (Figure 3b)  $v$  tends to the Bleustein–Gulyaev velocity of medium A,  $\bar{v}_{B-G-\text{BaTiO}_3}$ , which is obtained from the condition  $P_A = 0$  in (4-44) and is given by (4-32) together with (4-33). Note from both graphs in Figure 3 that  $\bar{v}_{B-G-\text{BaTiO}_3}$  is also an upper bound and a limit point for  $v$  as  $K$  tends to zero.

We now show in Figure 4 dispersion curves for the symmetric modes of SH waves propagating in the heterostructure  $\text{CoFe}_2\text{O}_4/\text{PZT}4/\text{CoFe}_2\text{O}_4$  with either a permeable (Figure 4a) or absorbent (Figure 4b) interface for increasing values of  $K$ . These curves are qualitatively similar to the curves shown in Figure 2. Thus, all wave velocities tend to the wave velocity in phase B,  $\bar{v}_{\text{PZT}4}$ , as  $\omega d \rightarrow \infty$ . As  $\omega d$  tends to zero, these velocities tend to the wave velocity in phase A,  $\bar{v}_{\text{CoFe}_2\text{O}_4}$ , in Figure 4a and tend to the Bleustein–Gulyaev velocity of medium A,  $\bar{v}_{B-G-\text{CoFe}_2\text{O}_4}$ , which is given by  $\bar{v}_A \sqrt{1 - f_A^4 / (\mu_A \bar{c}_A^f)^2}$ . In Figure 4 all the dispersion curves are in a region bounded by curves corresponding to the cases ( $K = 0, P_A = 0$ ), ( $K = 0, P_B = 0$ ), and  $\bar{v}_{\text{PZT}4}$ .

Next, we show in Figure 5 dispersion curves for the symmetric modes of SH waves propagating in the heterostructure Composite/ $\text{CoFe}_2\text{O}_4$ /Composite with either a permeable (Figure 5a) or absorbent (Figure 5b) interface for increasing values of  $K$ . We recall from the beginning of this section that composite stands for the composite  $\text{BaTiO}_3/\text{CoFe}_2\text{O}_4$  with 30 percent  $\text{BaTiO}_3$ . These curves are qualitatively similar to the corresponding curves in both Figure 2 and Figure 3.

Results for the antisymmetric parts of SH waves propagating in the heterostructures  $\text{BaTiO}_3/\text{CoFe}_2\text{O}_4/\text{BaTiO}_3$  and  $\text{CoFe}_2\text{O}_4/\text{PZT}4/\text{CoFe}_2\text{O}_4$  are shown in Figures 6 and 8, respectively, for both types of interface: (a) permeable and (b) absorbent. Observe from Figure 6a that, for the whole range of values of  $\omega d$  shown in the figure and for  $\bar{v}_B \leq v \leq \bar{v}_A$ , the curve corresponding to both  $K = 0$  and  $P_B = 0$  is below the curve corresponding to  $K = \infty$ , there are no other dispersion curves between these two curves, all the curves corresponding to  $K \geq 100$  are above the curve corresponding to  $K = \infty$ , and

all the curves corresponding to  $K \leq 50$  are below the curve corresponding to both  $K = 0$  and  $P_B = 0$ . Similar observations can also be drawn from Figure 8a.

Next, observe from Figure 6b that the curves corresponding to, respectively,  $(K = 0, P_B = 0)$  and  $K = \infty$  intersect each other at  $(\bar{v}_{B-G-BaTiO_3}, \omega d) = (3.00547, 43.02)$ . To the left of  $\omega d = 43.02$  and for  $K \geq 50$ , the dispersion curves are in between the two curves above. To the right of  $\omega d = 43.02$  and for  $K \geq 50$ , these curves are above the curve corresponding to  $K = \infty$ . In both cases, the curves corresponding to  $K \leq 35$  are below all the other curves mentioned above.

In Figure 8b observe that all curves intersect at  $(\bar{v}_{B-G-CoFe_2O_3}, \omega d) = (2.93987, 8.32)$ . For  $\omega d > 8.32$ , observe also that, contrary to the previous figures, the curve corresponding to  $K = \infty$  is below the curve corresponding to  $(K = 0, P_B = 0)$ , and that all the other dispersion curves lie in a region bounded by these two curves.

The behavior of the dispersion curves for small values of  $K$  in the set  $\{0, 0.001, 0.005, 0.05, 3, 5\}$  and for  $0 \leq \omega d \leq 50$  is shown in Figure 7 for the heterostructure  $BaTiO_3/CoFe_2O_4/BaTiO_3$ . Observe from this figure that the curve corresponding to  $K = 0$  is above all the other curves and that the wave velocity for  $K = 0$  tends to the velocity of the Bleustein–Gulyaev wave in phase A as  $\omega d \rightarrow 0$ .

## 6. Conclusions

The effect of imperfect bonding at the interface of a heterostructure A/B/A with magnetoelectroelastic properties on stationary shear (SH) waves has been investigated. Analytical dispersion relations for absorbent and permeable interfaces are obtained. Several numerical examples for the first branches of the dispersion curves are shown in the range of  $\bar{v}_B < v < \bar{v}_A$ . Different limit cases are considered and show a good agreement with corresponding cases reported in recent studies.

Based on numerical examples, the dispersion curves for different values of the material parameter  $K$  are shown. The decreasing of the imperfect bonding parameter  $K$  decreases the propagation velocity. The dispersion curves for the symmetric modes are bounded between the limit cases  $K = 0$  and  $K = \infty$  for both types of interfaces, permeable and absorbent interfaces. The dispersion curves are confined and not intersecting between the velocity of the outer (A) and the inner (B) media. The symmetric and antisymmetric modes for the limit case  $\omega d \rightarrow \infty$  approach asymptotically to  $\bar{v}_B$  for all values of  $K$ . These results were obtained numerically for different combinations of materials.

## References

- [Alshits et al. 1994] V. I. Alshits, D. M. Barnett, A. N. Darinskii, and J. Lothe, “On the existence problem for localized acoustic waves on the interface between two piezocrystals”, *Wave Motion* **20**:3 (1994), 233–244.
- [Bleustein 1968] J. L. Bleustein, “A new surface wave in piezoelectric materials”, *Appl. Phys. Lett.* **13**:12 (1968), 412–413.
- [Bleustein 1969] J. L. Bleustein, “Some simple modes of wave propagation in an infinite piezoelectric plate”, *J. Acoust. Soc. Am.* **45**:3 (1969), 614–620.
- [Bravo-Castillero et al. 2008] J. Bravo-Castillero, R. Rodríguez-Ramos, H. Mechkar, J. A. Otero, and F. J. Sabina, “Homogenization of magneto-electro-elastic multilaminated materials”, *Q. J. Mech. Appl. Math.* **61**:3 (2008), 311–332.
- [Calas et al. 2008] H. Calas, J. A. Otero, R. Rodríguez-Ramos, G. Monsivais, and C. Stern, “Dispersion relations for SH wave in magneto-electro-elastic heterostructures”, *Int. J. Solids Struct.* **45**:20 (2008), 5356–5367.
- [Chen et al. 2004] W. Q. Chen, J. B. Cai, G. R. Ye, and Y. F. Wang, “Exact three-dimensional solutions of laminated orthotropic piezoelectric rectangular plates featuring interlaminar bonding imperfections modeled by a general spring layer”, *Int. J. Solids Struct.* **41**:18-19 (2004), 5247–5263.

- [Chen et al. 2007] J. Chen, E. Pan, and H. Chen, "Wave propagation in magneto-electro-elastic multilayered plates", *Int. J. Solids Struct.* **44**:3-4 (2007), 1073–1085.
- [Chen et al. 2008] J. Chen, W. Wang, J. Wang, Z. Yang, and J. Yang, "A thickness mode acoustic wave sensor for measuring interface stiffness between two elastic materials", *IEEE Trans. Ultrason. Ferroelectr. Freq. Control* **55**:8 (2008), 1678–1681.
- [Cheng et al. 1996] Z.-Q. Cheng, A. K. Jemah, and F. W. Williams, "Theory for multilayered anisotropic plates with weakened interfaces", *J. Appl. Mech. (ASME)* **63**:4 (1996), 1019–1026.
- [Deng 2006] M. Deng, "Analysis of second-harmonic generation of Lamb waves propagating in layered planar structures with imperfect interfaces", *Appl. Phys. Lett.* **88**:22 (2006), 221902.
- [Fan et al. 2006a] H. Fan, J. Yang, and L. Xu, "Antiplane piezoelectric surface waves over a ceramic half-space with an imperfectly bonded layer", *IEEE Trans. Ultrason. Ferroelectr. Freq. Control* **53**:9 (2006), 1695–1698.
- [Fan et al. 2006b] H. Fan, J. Yang, and L. Xu, "Piezoelectric waves near an imperfectly bonded interface between two half-spaces", *Appl. Phys. Lett.* **88**:20 (2006), 203509.
- [Gulyaev 1969] Y. V. Gulyaev, "Surface electroacoustic waves in solids", *J. Exp. Theor. Phys. Lett.* **9** (1969), 37–38.
- [Handge 2002] U. A. Handge, "Analysis of a shear-lag model with nonlinear elastic stress transfer for sequential cracking of polymer coatings", *J. Mater. Sci.* **37**:22 (2002), 4775–4782.
- [Hashin 1991] Z. Hashin, "Thermoelastic properties of particulate composites with imperfect interface", *J. Mech. Phys. Solids* **39**:6 (1991), 745–762.
- [Huang and Li 2010] Y. Huang and X. F. Li, "Shear waves guided by the imperfect interface of two magnetoelectric materials", *Ultrasonics* **50**:8 (2010), 750–757.
- [Huang and Rokhlin 1992] W. Huang and S. I. Rokhlin, "Interface waves along an anisotropic imperfect interface between anisotropic solids", *J. Nondestruct. Eval.* **11**:3-4 (1992), 185–198.
- [Huang et al. 2009] Y. Huang, X.-F. Li, and K. Y. Lee, "Interfacial shear horizontal (SH) waves propagating in a two-phase piezoelectric/piezomagnetic structure with an imperfect interface", *Philos. Mag. Lett.* **89**:2 (2009), 95–103.
- [Klarbring and Movchan 1998] A. Klarbring and A. B. Movchan, "Asymptotic modelling of adhesive joints", *Mech. Mater.* **28**:1-4 (1998), 137–145.
- [Li and Yang 2006] X.-F. Li and J. S. Yang, "Piezoelectric gap waves between a piezoceramic half-space and a piezoceramic plate", *Sens. Actuators A Phys.* **132**:2 (2006), 472–479.
- [Margetan et al. 1992] F. J. Margetan, R. B. Thompson, J. H. Rose, and T. A. Gray, "The interaction of ultrasound with imperfect interfaces: experimental studies of model structures", *J. Nondestruct. Eval.* **11**:3-4 (1992), 109–126.
- [Melkumyan 2007] A. Melkumyan, "Twelve shear surface waves guided by clamped/free boundaries in magneto-electro-elastic materials", *Int. J. Solids Struct.* **44**:10 (2007), 3594–3599.
- [Melkumyan and Mai 2008] A. Melkumyan and Y.-W. Mai, "Influence of imperfect bonding on interface waves guided by piezoelectric/piezomagnetic composites", *Philos. Mag.* **88**:23 (2008), 2965–2977.
- [Pan 2001] E. Pan, "Exact solution for simply supported and multilayered magneto-electro-elastic plates", *J. Appl. Mech. (ASME)* **68**:4 (2001), 608–618.
- [Pan and Heyliger 2002] E. Pan and P. R. Heyliger, "Free vibrations of simply supported and multilayered magneto-electro-elastic plates", *J. Sound Vib.* **252**:3 (2002), 429–442.
- [Rokhlin and Wang 1991] S. I. Rokhlin and Y. J. Wang, "Analysis of boundary conditions for elastic wave interaction with an interface between two solids", *J. Acoust. Soc. Am.* **89**:2 (1991), 503–515.
- [Termonia 1990] Y. Termonia, "Fibre coating as a means to compensate for poor adhesion in fibre-reinforced materials", *J. Mater. Sci.* **25**:1 (1990), 103–106.
- [Wang et al. 2003] J. Wang, L. Chen, and S. Fang, "State vector approach to analysis of multilayered magneto-electro-elastic plates", *Int. J. Solids Struct.* **40**:7 (2003), 1669–1680.
- [Wang et al. 2007] B. L. Wang, Y.-W. Mai, and O. P. Niraula, "A horizontal shear surface wave in magnetoelastic materials", *Philos. Mag. Lett.* **87**:1 (2007), 53–58.
- [Wu et al. 2002] W. Wu, K. Sadeghipour, K. Boberick, and G. Baran, "Predictive modeling of elastic properties of particulate-reinforced composites", *Mater. Sci. Eng. A* **332**:1-2 (2002), 362–370.

[Yang et al. 2006] J. Yang, Y. Hu, Y. Zeng, and H. Fan, “Thickness-shear vibrations of rotated Y-cut quartz plates with imperfectly bonded surface mass layers”, *IEEE Trans. Ultrason. Ferroelectr. Freq. Control* **53**:1 (2006), 241–245.

[Zhong et al. 2009] X.-C. Zhong, X.-F. Li, and K. Y. Lee, “Analysis of a mode-I crack perpendicular to an imperfect interface”, *Int. J. Solids Struct.* **46**:6 (2009), 1456–1463.

Received 11 Nov 2010. Accepted 22 Mar 2011.

JOSÉ A. OTERO: [jaotero@icmf.inf.cu](mailto:jaotero@icmf.inf.cu)

*Instituto de Cibernética, Matemática y Física, Calle 15 No. 551, Habana 4, CP 10400, Cuba*

HÉCTOR CALAS: [hcalass@gmail.com](mailto:hcalass@gmail.com)

*Instituto de Acústica, Consejo Superior de Investigaciones Científicas, Serrano 144, 28006 Madrid, Spain*

REINALDO RODRÍGUEZ-RAMOS: [reinaldo@matcom.uh.cu](mailto:reinaldo@matcom.uh.cu)

*Facultad de Matemática y Computación, Universidad de La Habana, San Lázaro esq. L, Vedado, Habana 4, CP 10400, Cuba*

JULIÁN BRAVO-CASTILLERO: [jbravo@matcom.uh.cu](mailto:jbravo@matcom.uh.cu)

*Facultad de Matemática y Computación, Universidad de La Habana, San Lázaro esq. L, Vedado, Habana 4, CP 10400, Cuba*

ADAIR R. AGUIAR: [aguiarar@sc.usp.br](mailto:aguiarar@sc.usp.br)

*Department of Structural Engineering, University of São Paulo, Av. Trabalhador Sãocarlense, 400, 13566-590 São Carlos, SP, Brazil*

<http://www.set.eesc.usp.br/portal/pt/docentes/110-adair-roberto-aguiar>

GUILLERMO MONSIVAIS: [monsi@fisica.unam.mx](mailto:monsi@fisica.unam.mx)

*Instituto de Física, Universidad Nacional Autónoma de México, Apdo. Postal 20-364, 01000 México, D.F., México*



## NUMERICAL LINEAR STABILITY ANALYSIS OF A THERMOCAPILLARY-DRIVEN LIQUID BRIDGE WITH MAGNETIC STABILIZATION

YUE HUANG AND BRENT C. HOUCHEWS

A full-zone model of a thermocapillary-driven liquid bridge exposed to a steady, axial magnetic field is investigated using a global spectral collocation method for low-Prandtl number ( $\text{Pr}$ ) fluids. Flow instabilities are identified using normal-mode linear stability analyses. This work presents several numerical issues that commonly arise when using spectral collocation methods and linear stability analyses in the solution of a wide range of partial differential equations. In particular, effects such as discontinuous boundary condition regularization, identification of spurious eigenvalues, and the use of pseudospectra to investigate the robustness of the stability analysis are addressed. Physically, this work provides simulations in the practical range of experimentally utilized magnetic field stabilization in optically heated float-zone crystal growth. A second-order vorticity transport formulation enables modeling of the liquid bridge up to these intermediate magnetic field strength ranges, measured by the Hartmann number ( $\text{Ha}$ ). The thermocapillary driving and magnetic stabilization effects are observed up to  $\text{Ha} = 500$  for  $\text{Pr} = 0.001$  and up to  $\text{Ha} = 300$  for  $\text{Pr} = 0.02$ . Prandtl number effects on temperature and flow fields are investigated within  $\text{Pr} \in (10^{-12}, 0.0667)$  and indicate that  $\text{Pr} = 0.001$  is a good representation of the base state in the  $\text{Pr} \rightarrow 0$  limit, at least up to  $\text{Ha} = 300$ .

### 1. Introduction

Float-zone growth processes are methods to grow crystals with the highest purity. A cross-sectional region of a polycrystalline ingot is melted by lateral heating, for example, in an optical heating furnace [Eyer et al. 1979]. This molten region holds itself from spilling by surface tension, forming a liquid bridge between the feed rod and the grown crystal. As the liquid bridge moves through the furnace, the melt resolidifies as a single crystal if properly controlled. Throughout the process the melt never contacts a crucible, and therefore the grown crystal has very low oxygen contamination. Sufficient heat input is required to avoid the onset of morphological instability at the solidification front [Davis 1993]. The thermocapillary effect at the free surface drives a flow within the liquid bridge. This flow is susceptible to instabilities, which result in structural imperfections in grown crystals and uneven dopant distribution for doped crystals [Eyer et al. 1985; Cröll et al. 1994]. Therefore stabilization techniques are typically used in crystal growth practice. For example, two silicon crystal rods were grown in a double ellipsoidal mirror furnace with rod rotation in Spacelab-1 [Martinez and Eyer 1986]. A review of liquid bridge stabilization strategies can be found in [Lappa 2005b]. One strategy for molten semiconductors, which have properties similar to liquid metals, is to apply external magnetic fields to control flow motion.

---

This work was supported by the U.S. Air Force Office of Scientific Research.

**Keywords:** magnetic stabilization, thermocapillary, liquid bridge, linear stability, regularization, pseudospectra.

The optically heated liquid bridge has been studied by the crystal growth community using simpler models such as the half-zone model, resembling one half of a liquid bridge, and the full-zone model. The liquid bridge has a barrel shape in microgravity and a sagged shape under terrestrial conditions. These free-surface shapes have been simulated in both half-zone [Morthland and Walker 1996] and full-zone [Lappa 2004] models, respectively. In [Nakamura et al. 1998],  $m = 1$  and 2 oscillating instability modes were observed in molten silicon in an optically heated half-zone configuration on the TR-IA rocket. The hydrodynamic and hydrothermal instability mechanisms of low and high-Pr liquid bridges, respectively, have been confirmed in [Chen et al. 1997; Lappa 2005a; Bouizi et al. 2007] and elsewhere. Lan and Yeh [2004; 2005] performed quite complete full-zone modeling involving three-dimensional radiation, a deformable free surface and melting interfaces, dopant distribution, and axial and transverse magnetic damping. Prange et al. [1999] studied the half-zone instability with axial magnetic field stabilization up to  $\text{Ha} = 25$ .

This work presents a full-zone liquid bridge model with magnetic stabilization, with a focus on the numerical methods and analyses utilized. The goals of this paper are twofold: first, to provide insight into magnetohydrodynamic control in the liquid bridge problem which will aid in the design of float-zone crystal growth experiments and, second, to demonstrate through example the treatment of several common numerical issues, such as regularization, identification of spurious eigenvalues, and sensitivity of linear stability analyses as quantified by pseudospectral analysis, techniques relevant to a wide array of numerical analysis studies.

## 2. Problem description

**2A. Full-zone model of a liquid bridge.** A liquid bridge of a molten semiconductor is bounded by top and bottom solid boundaries (Figure 1). Both boundaries are assumed flat, electrically insulating, and at the melting temperature  $T_0^*$  of the semiconductor. The lateral cylindrical free surface is assumed nondeformable due to high surface tension and the microgravity environment. The diameter and height

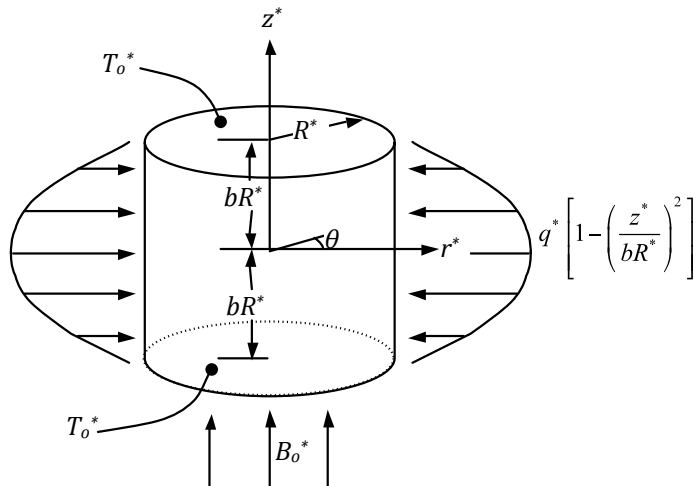


**Figure 1.** Full-zone model of a liquid bridge with a parabolic heat flux at the free surface and an axially applied magnetic field.

of the liquid bridge are  $2R^*$  and  $2bR^*$ , respectively. The aspect ratio  $b$  is held at 1 in this paper. An axisymmetric heat flux is applied at the lateral free surface. This heat flux is approximated with a maximum intensity  $q^*$  at the equatorial plane and parabolic reduction to zero at the top and bottom boundaries. The thermal conductivity of the melt is  $k^*$ . A constant, uniform external magnetic field is applied in the axial direction with a magnetic flux density of  $\mathbf{B}^* = B_o^* \hat{\mathbf{e}}_z$ . Variables with an asterisk superscript are dimensional quantities.

The characteristic length, temperature, and magnetic flux density are  $R^*$ ,  $\Delta T^* = q^* R^* / k^*$ , and  $B_o^*$ , respectively. Temperature is scaled as  $T = (T^* - T_0^*) / \Delta T^*$ . The nondimensional governing equations are incompressible continuity, the Navier–Stokes equations including the electromagnetic body force, the energy equation neglecting viscous dissipation, conservation of charge, and Ohm's law:

$$\nabla \cdot \mathbf{v} = 0, \quad (2-1)$$

$$\frac{\partial \mathbf{v}}{\partial t} + (\mathbf{v} \cdot \nabla) \mathbf{v} = -\nabla P + \nabla^2 \mathbf{v} + \text{Ha}^2 (\mathbf{j} \times \hat{\mathbf{e}}_z), \quad (2-2)$$

$$\text{Pr} \left[ \frac{\partial T}{\partial t} + (\mathbf{v} \cdot \nabla) T \right] = \nabla^2 T, \quad (2-3)$$

$$\nabla \cdot \mathbf{j} = 0, \quad (2-4)$$

$$\mathbf{j} = -\nabla \phi + \mathbf{v} \times \hat{\mathbf{e}}_z, \quad (2-5)$$

where

$$\text{Ha} = \left( \frac{\sigma^*}{\mu^*} \right)^{\frac{1}{2}} B_o^* R^*, \quad \text{Pr} = \frac{\mu^* c_p^*}{k^*}. \quad (2-6)$$

The Hartmann number  $\text{Ha}$  is proportional to the magnetic flux density  $B_o^*$  and measures the ratio of the electromagnetic body forces to the viscous forces. The Prandtl number  $\text{Pr}$  indicates the relative effectiveness of thermal convection to heat conduction in the melt.  $\text{Pr}$  is a material property, where  $c_p^*$  is the specific heat of the melt. For fluids with small Prandtl number (for example,  $\text{Pr}_{\text{silicon}} \approx 0.02$ ), heat conduction is dominant over convection.

Nondimensional boundary conditions include a nondeformable and electrically insulating free surface ( $v_r = 0$  and  $j_r = 0$  at  $r = 1$ ) with flow induced by the thermocapillary boundary conditions, (2-9), and no-slip, no-penetration and electrically insulating top and bottom boundaries ( $\mathbf{v} = 0$  and  $j_z = 0$  at  $z = \pm b$ ) which are maintained at the melting temperature ( $T = 0$  at  $z = \pm b$ ).

The full-zone is a more realistic liquid bridge model for optically heated float-zone crystal growth as compared to the half-zone, though both capture much of the primary physics of the flow field. In the full-zone model the heat flux is input on the free surface, rather than from a hot bottom wall, as in the half-zone. Also, no constraint is enforced at the midplane in the full-zone. Thus the temperature varies at the midplane (see Figures 4a and 4b) and flow is allowed to be nonzero and even cross the midplane (see Figure 6). Note that in this work axial symmetry is assumed in the base flow for computational efficiency, but no boundary condition is imposed at the midplane. Therefore the full-zone character is maintained.

In contrast, the half-zone intends to model one half of the liquid bridge. A no-slip, no-penetration solid boundary at fixed temperature is enforced in the half-zone, at the location of the midplane. A thermally insulating free surface is commonly assumed. The half-zone is driven by the temperature difference

between two bounding disks. Despite these simplifications, the half-zone is an effective liquid bridge model for both experimental and computational studies. However, the onset of flow instabilities tend to be delayed in the half-zone by the presence of the no-slip boundary that replaces the midplane and removes momentum from the flow through viscous effects. An extensive comparison of the half-zone and full-zone models can be found in [Houchens and Walker 2005].

**2B. Thermocapillary-driven flow.** The temperature gradient at the free surface produces surface tension differences, called the thermocapillary or Marangoni effect. The surface tension  $\gamma^*$  drives a flow within the liquid bridge, and is approximated as a linearly decreasing function of temperature:

$$\gamma^*(T^*) = \gamma_0^* + \frac{d\gamma^*}{dT^*}(T^* - T_0^*), \quad (2-7)$$

where  $d\gamma^*/dT^*$  is a negative quantity. With the Newtonian constitutive relations

$$\tau_{rz}^* = \mu^* \left( \frac{\partial v_z^*}{\partial r^*} + \frac{\partial v_r^*}{\partial z^*} \right), \quad \tau_{r\theta}^* = \mu^* \left[ r^* \frac{\partial}{\partial r^*} \left( \frac{v_\theta^*}{r^*} \right) + \frac{1}{r^*} \frac{\partial v_r^*}{\partial \theta} \right], \quad (2-8)$$

the nondimensional thermocapillary boundary conditions become

$$\frac{\partial v_z}{\partial r} = -\text{Re}_{\text{FZ}} \frac{\partial T}{\partial z} \quad \text{at } r = 1, \quad \frac{\partial v_\theta}{\partial r} - \frac{v_\theta}{r} = -\text{Re}_{\text{FZ}} \frac{1}{r} \frac{\partial T}{\partial \theta} \quad \text{at } r = 1, \quad (2-9)$$

where

$$\text{Re}_{\text{FZ}} = \frac{\left| \frac{d\gamma^*}{dT^*} \right| \Delta T^*}{\mu^* V_c^*} = \frac{\rho^* R^* \left| \frac{d\gamma^*}{dT^*} \right| \Delta T^*}{\mu^{*2}}. \quad (2-10)$$

The thermocapillary Reynolds number  $\text{Re}_{\text{FZ}}$  measures the thermocapillary effect. The subscript FZ refers to the full-zone model temperature scaling. The related Marangoni number  $\text{Ma} = \text{Re}_{\text{FZ}} \times \text{Pr}$  is also commonly used in thermocapillary flow studies. The viscous Reynolds number is

$$\text{Re}_{\text{viscous}} = \frac{\rho^* v_{\max}^* R^*}{\mu^*} = \frac{\rho^* v_{\max} V_c^* R^*}{\mu^*} = v_{\max}, \quad (2-11)$$

where  $V_c^* = \mu^* / (\rho^* R^*)$  is the characteristic flow velocity. Thus the maximum dimensionless velocity  $v_{\max}$  is equivalent to the viscous Reynolds number in this scaling.

Figure 2 shows the thermocapillary-driven flow in  $r \in (0, 1)$ ,  $z \in (0, b)$  at some  $\theta$  plane. From  $z = 0 \rightarrow 1$  the temperature decreases along the free surface ( $r = 1$ ), and therefore the surface tension increases. The thermocapillary effect pulls fluid from the equatorial plane toward the top boundary along the free surface. This flow then hits the top boundary, turns inwards and circulates back to the equatorial plane in the interior of the liquid bridge.

### 3. Steady axisymmetric base flow

**3A. Base flow assumptions.** Periodic and/or three-dimensional flow in the liquid bridge results in imperfections in grown crystals such as striations and nonuniform dopant distribution. With sufficient magnetic stabilization, the base flow is steady ( $\partial/\partial t = 0$ ), axisymmetric ( $\partial/\partial\theta = 0$ ) with zero azimuthal velocity

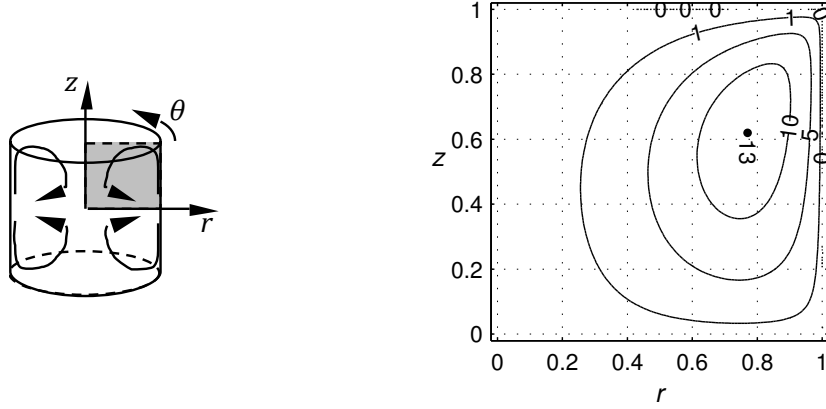


**Figure 2.** Stream function contours of the thermocapillary-driven flow ( $\text{Pr} = 0.02$ ,  $\text{Ha} = 0$ , at the critical  $\text{Re}_{\text{FZ}} = 1546.58$ , flow grid  $r \times z = 35 \times 45$ , temperature grid  $r \times z = 30 \times 30$ ,  $\alpha = 300$ ).

( $v_{\theta 0} = 0$ ), and exhibits axial symmetry about the equatorial plane. For this base flow state the governing equations simplify to

$$\frac{\partial v_{r0}}{\partial r} + \frac{v_{r0}}{r} + \frac{\partial v_{z0}}{\partial z} = 0, \quad (3-1)$$

$$v_{r0} \frac{\partial v_{r0}}{\partial r} + v_{z0} \frac{\partial v_{r0}}{\partial z} = -\frac{\partial P_0}{\partial r} + \frac{\partial^2 v_{r0}}{\partial r^2} + \frac{1}{r} \frac{\partial v_{r0}}{\partial r} - \frac{v_{r0}}{r^2} + \frac{\partial^2 v_{r0}}{\partial z^2} - \text{Ha}^2 v_{r0}, \quad (3-2)$$

$$v_{r0} \frac{\partial v_{z0}}{\partial r} + v_{z0} \frac{\partial v_{z0}}{\partial z} = -\frac{\partial P_0}{\partial z} + \frac{\partial^2 v_{z0}}{\partial r^2} + \frac{1}{r} \frac{\partial v_{z0}}{\partial r} + \frac{\partial^2 v_{z0}}{\partial z^2}, \quad (3-3)$$

$$\text{Pr} \left( v_{r0} \frac{\partial T_0}{\partial r} + v_{z0} \frac{\partial T_0}{\partial z} \right) = \frac{\partial^2 T_0}{\partial r^2} + \frac{1}{r} \frac{\partial T_0}{\partial r} + \frac{\partial^2 T_0}{\partial z^2}, \quad (3-4)$$

with boundary conditions

$$v_{r0} = 0, \quad j_{r0} = 0, \quad \frac{\partial v_{z0}}{\partial r} = -\text{Re}_{\text{FZ}} \frac{\partial T_0}{\partial z} F(z), \quad \frac{\partial T_0}{\partial r} = 1 - \left( \frac{z}{b} \right)^2 \quad \text{at } r = 1, \quad (3-5)$$

$$v_{r0} = 0, \quad v_{z0} = 0, \quad T_0 = 0, \quad j_{z0} = 0 \quad \text{at } z = \pm b, \quad (3-6)$$

where

$$F(z) = 1 - \exp \left\{ -\alpha \left[ 1 - \left( \frac{z}{b} \right)^2 \right]^2 \right\} \quad (3-7)$$

is a regularization function to remove the  $\partial v_{z0}/\partial r$  singularity at  $(r, z) = (1, \pm b)$  between the thermocapillary driving force on the free surface and the no-penetration conditions at the top and bottom boundaries.

Base flow variables are denoted with subscript 0 to differentiate them from perturbation variables (which have subscript 1).

**3B. Second-order vorticity transport formulation.** In [Houchens and Walker 2005], a fourth-order stream function formulation was introduced for the base flow problem, with the stream function  $\psi$  defined as

$$v_{r0} = \frac{1}{r} \frac{\partial \psi}{\partial z}, \quad v_{z0} = -\frac{1}{r} \frac{\partial \psi}{\partial r}. \quad (3-8)$$

The resulting equations were discretized using a global spectral collocation method with Chebyshev basis functions. In this formulation, the momentum equations can be combined into a single fourth-order partial differential equation governing  $\psi$ . Unfortunately, the coefficients on the derivatives of the Chebyshev functions increase dramatically as the derivative order increases. From a numerical standpoint, the combination of order-one coefficients on the first and second derivatives and huge third and fourth derivatives in one equation causes numerical difficulties. This imbalance in fact imposes a constraint on the maximum viable grid resolution in obtaining converged solutions. This consequently limited the maximum magnetic stabilization intensity ( $Ha$ ) that could be studied [Houchens and Walker 2001].

Reducing the maximum Chebyshev derivative order improves the numerical performance, at the expense of more dependent variables. In this work, this is achieved by introducing the azimuthal vorticity  $\omega_\theta$  into the formulation as

$$\omega_\theta = \frac{\partial v_{r0}}{\partial z} - \frac{\partial v_{z0}}{\partial r}. \quad (3-9)$$

The nondimensional governing equations of the second-order vorticity transport formulation are

$$\omega_\theta = \frac{1}{r} \frac{\partial^2 \psi}{\partial r^2} - \frac{1}{r^2} \frac{\partial \psi}{\partial r} + \frac{1}{r} \frac{\partial^2 \psi}{\partial z^2}, \quad (3-10)$$

$$\frac{1}{r} \frac{\partial \psi}{\partial z} \left[ \frac{\partial \omega_\theta}{\partial r} - \frac{\omega_\theta}{r} \right] - \frac{1}{r} \frac{\partial \psi}{\partial r} \left[ \frac{\partial \omega_\theta}{\partial z} \right] = \frac{\partial^2 \omega_\theta}{\partial r^2} + \frac{1}{r} \frac{\partial \omega_\theta}{\partial r} + \frac{\partial^2 \omega_\theta}{\partial z^2} - \frac{\omega_\theta}{r^2} - \frac{Ha^2}{r} \frac{\partial^2 \psi}{\partial z^2}, \quad (3-11)$$

$$\text{Pr} \left( \frac{1}{r} \frac{\partial \psi}{\partial z} \frac{\partial T_0}{\partial r} - \frac{1}{r} \frac{\partial \psi}{\partial r} \frac{\partial T_0}{\partial z} \right) = \frac{\partial^2 T_0}{\partial r^2} + \frac{1}{r} \frac{\partial T_0}{\partial r} + \frac{\partial^2 T_0}{\partial z^2}, \quad (3-12)$$

with boundary conditions

$$\psi = 0, \quad \frac{\partial^2 \psi}{\partial r^2} - \frac{\partial \psi}{\partial r} = \text{Re}_{FZ} \frac{\partial T_0}{\partial z} F(z), \quad \frac{\partial T_0}{\partial r} = 1 - \left( \frac{z}{b} \right)^2, \quad \text{at} \quad r = 1, \quad (3-13)$$

$$\frac{\partial \psi}{\partial z} = 0, \quad \psi = 0, \quad T_0 = 0, \quad \text{at} \quad z = b. \quad (3-14)$$

The base flow variables are represented with Chebyshev polynomials:

$$\psi \left( r, \frac{z}{b} \right) = r^2 \sum_{L=0}^{N_{RF}+1} \sum_{M=0}^{N_{ZF}+1} A_{LM} T_{2L}(r) T_{2M+1} \left( \frac{z}{b} \right), \quad (3-15)$$

$$\omega_\theta \left( r, \frac{z}{b} \right) = r \sum_{L=0}^{N_{RF}} \sum_{M=0}^{N_{ZF}} B_{LM} T_{2L}(r) T_{2M+1} \left( \frac{z}{b} \right), \quad (3-16)$$

$$T_0 \left( r, \frac{z}{b} \right) = \sum_{L=0}^{N_{RT}} \sum_{M=0}^{N_{ZT}} C_{LM} T_{2L}(r) T_{2M} \left( \frac{z}{b} \right), \quad (3-17)$$

where  $T_n(r) = \cos(n \arccos r)$  are the Chebyshev basis functions. As a result of radial symmetry (axisymmetry), only even Chebyshev terms are utilized in  $r$ , with the overall radial symmetry set by the multiple of  $r$  in front of the representation. This corresponds to the behaviors as  $r \rightarrow 0$ , which were investigated for  $\psi$ ,  $\omega_\theta$ , and  $T$  using the Frobenius method. Moreover, due to the axial symmetry, only even or odd Chebyshev terms are nonzero in  $z$ . Taking advantage of axisymmetry and the axial symmetry, the unique

computational domain for the base flow is reduced to  $r \in (0, 1)$ ,  $z \in (0, b)$  at  $\theta = 0$  and is discretized using Gauss–Lobatto collocation grids ( $N_{RF} \times N_{ZF}$  for the flow field and  $N_{RT} \times N_{ZT}$  for the temperature field) given, for example, by

$$r_{IF} = \cos \frac{I_F \pi}{2N_{RF}} \quad \text{for } I_F = 0, 1, 2, \dots, N_{RF}, \quad (3-18)$$

$$z_{KF} = \cos \frac{K_F \pi}{2N_{ZF}} \quad \text{for } K_F = 0, 1, 2, \dots, N_{ZF}. \quad (3-19)$$

These grids weight the finest resolution toward the free surface and the solid boundary where it is most needed.

At  $r = 0$  or  $z = 0$ , the governing equations (3-10) and (3-11) and the first two boundary conditions in (3-13) (at  $z = 0$ ) reduce to  $0 = 0$ . To impose constraints at  $r = 0$  and  $z = 0$ , the first nonzero leading order of these equations are applied. For example, after substituting the representations for  $\psi$  and  $\omega_\theta$  from (3-15) and (3-16), respectively, (3-10) becomes

$$\sum_{L=0}^{N_{RF}} \sum_{M=0}^{N_{ZF}} B_{LM} r T_{2L} T_{2M+1} - \sum_{L=0}^{N_{RF}+1} \sum_{M=0}^{N_{ZF}+1} A_{LM} \frac{r}{b^2} T_{2L} T''_{2M+1} - \sum_{L=0}^{N_{RF}+1} \sum_{M=0}^{N_{ZF}+1} A_{LM} (r T''_{2L} + 3T'_{2L}) T_{2M+1} = 0. \quad (3-20)$$

Equation (3-20) simplifies to  $0 = 0$  at  $r = 0$ . Instead, if the Chebyshev basis functions are expanded in their Taylor series

$$T_{2L}(r) = (-1)^L [1 - 2L^2 r^2 + \frac{2}{3} L^2 (L^2 - 1) r^4 + O(r^6)], \quad (3-21)$$

the coefficients of the nonzero leading order ( $r^1$ ) can be used as a constraint at  $r = 0$ :

$$\sum_{L=0}^{N_{RF}} \sum_{M=0}^{N_{ZF}} B_{LM} \gamma(-1)^L T_{2M+1} - \sum_{L=0}^{N_{RF}+1} \sum_{M=0}^{N_{ZF}+1} A_{LM} \frac{\gamma}{b^2} (-1)^L T''_{2M+1} - \sum_{L=0}^{N_{RF}+1} \sum_{M=0}^{N_{ZF}+1} A_{LM} [\gamma(-1)^L (-4L^2) + 3(-1)^L (-4L^2 \gamma)] T_{2M+1} = 0. \quad (3-22)$$

It was found that the constraints above at  $r = 0$  and  $z = 0$  enhance the accuracy of the solution greatly with minimal additional computational cost. Therefore these constraints were applied in all cases presented here. At the top boundary  $z = b$ , boundary conditions were applied using orthogonality, hence special treatment was not required at  $(r, z) = (0, b)$ .

The  $Re_{FZ}$  is ramped up starting from  $Re_{FZ} < 1$ , where the flow field is almost stagnant, until the desired value is obtained. Solutions for lower  $Re_{FZ}$  cases become initial guesses for larger  $Re_{FZ}$  cases. The governing equations and boundary conditions are solved using the Newton–Raphson iterative method. LU decomposition and back substitution is performed using the DGESV routine [Intel 2008] in LAPACK [Anderson et al. 1999]. The base flow code is written in Fortran 90.

**3C. Magnetic damping.** When exposed to an axial static magnetic field, radial and azimuthal flow motions are damped by the electromagnetic body force. Figure 3 demonstrates this magnetic damping effect by varying the Hartmann number  $Ha$  while keeping the material properties (Pr) and the heat input ( $Re_{FZ}$ ) fixed.

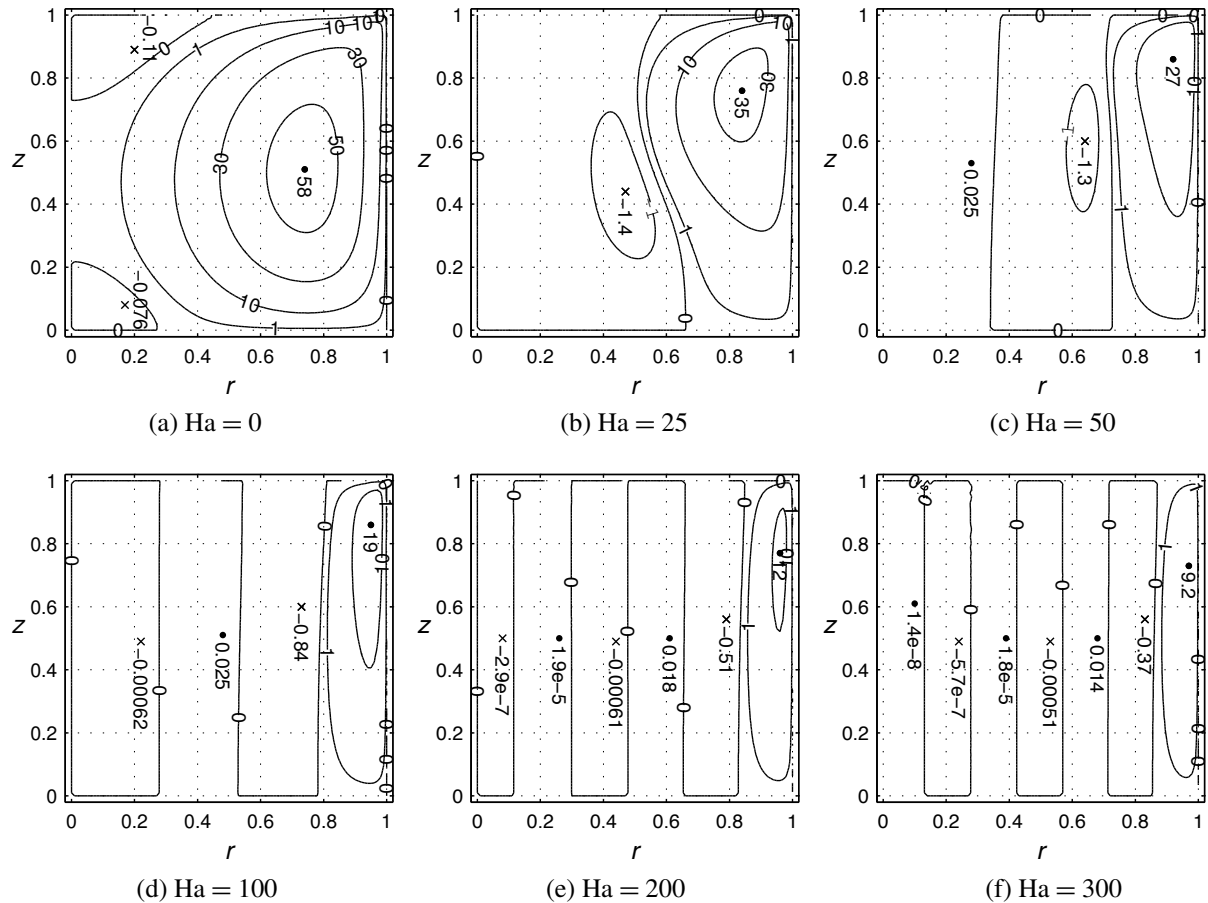


**Figure 3.** Magnetic damping effect on the stream function contours ( $\text{Pr} = 0.02$ ,  $\text{Re}_{FZ} = 21,914.8$ ).

Without magnetic damping ( $\text{Ha} = 0$ ), a primary circulation “cell” forms due to the thermocapillary effect. Flow circulates counterclockwise throughout  $r \in (0, 1)$  in the upper half of the liquid bridge. Small secondary recirculation cells also emerge in the interior due to strong convection. At  $\text{Ha} = 25$ , the electromagnetic effect weakens the primary circulation cell and confines it within  $r \in (0.5, 1)$ . When exposed to a magnetic field in the  $+z$  direction, radial inflow (in the  $-r$  direction) near the  $(r, z) = (1, 1)$  corner induces electric current in the  $+\theta$  direction (into the page). This electric current leads to the Lorentz force exerted in the  $+r$  direction, which opposes the inflow moving in the  $-r$  direction. By continuity, the flow is turned downward and then circulates back as a loop.

As the magnetic field further intensifies, the primary circulation cell is confined more dramatically near the free surface, and more circulation cells develop in the interior. The most significant flow is always within the primary circulation cell. Extremum stream function values within each cell show that the interior of the liquid bridge is effectively stagnant, which is ideal for crystal growth from a melt.

Note that in this example  $Re_{FZ}$  is chosen at 21,914.8, which is near the critical value for  $Pr = 0.02$  at  $Ha = 50$ . This  $Re_{FZ}$  value is well above the critical instability values for  $Ha = 0$  and  $Ha = 25$ ; therefore the actual flow would be perturbed from the base flow states shown here.

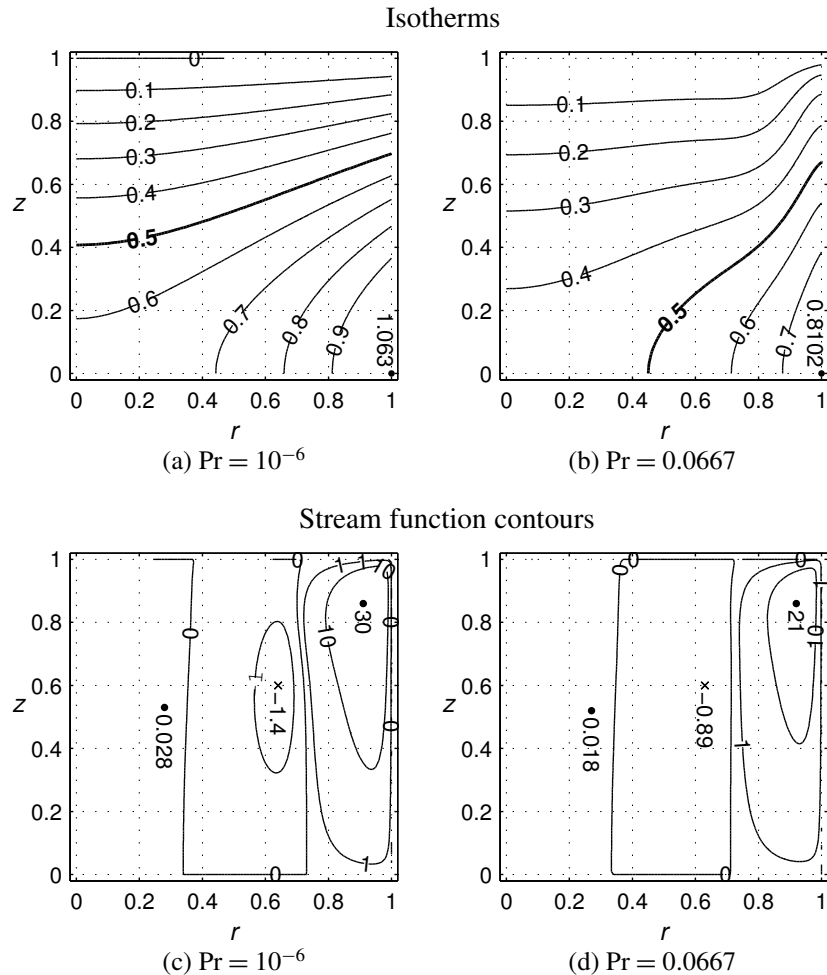


**Figure 4.** Prandtl number effect on the temperature field and the flow field ( $\text{Ha} = 50$ ,  $\text{Re}_{\text{FZ}} = 21,914.8$ ).

**3D. Prandtl number effect.** The crystal growth community has frequently studied the effect of Prandtl number  $\text{Pr}$ , representing different physical materials, in various liquid bridges, typically without magnetic stabilization. For example, Kasperski et al. [2000] first investigated the different characteristics of low and high- $\text{Pr}$  full-zone instabilities. Levenstam et al. [2001] performed a fairly continuous  $\text{Pr}$  study using the half-zone with a focus on the intermediate  $\text{Pr}$  range which bridges the gap between the low and high- $\text{Pr}$  regimes. Bouizi et al. [2007] presented full-zone instabilities over a wide range of  $\text{Pr} \in (0.001, 100)$  by three-dimensional nonlinear spectral computations.

For a liquid bridge with small  $\text{Pr}$ , conduction is dominant over convective heat transfer. In the limit of  $\text{Pr} \rightarrow 0$ , the temperature field is decoupled from the flow field. For example, the isotherms for  $\text{Pr} = 10^{-6}$  (Figure 4a) indicate pure conduction. In this case  $T_{\max} = 1.0633$  remains constant as the magnetic field is varied over  $\text{Ha} \in (0, 300)$  (not shown).  $T_{\max}$  is always located at  $(r, z) = (1, 0)$ , the location of maximum heat flux.

As  $\text{Pr}$  increases,  $T_{\max}$  is reduced due to convective heat transfer (at a fixed  $\text{Ha}$ ) assisting conduction in distributing the thermal energy throughout the domain. At  $\text{Pr} = 0.0667$ , isotherms are bent by convection (Figure 4b). Notice that the  $T = 0.5$  curve shifts by a large amount compared to the case of  $\text{Pr} = 10^{-6}$ .

Compared to the temperature distribution, the Prandtl number has a less significant impact on the flow field with magnetic stabilization. In moving from  $\text{Pr} = 10^{-6}$  to  $\text{Pr} = 0.0667$ , the flow is weakened (see Figures 4c and 4d) due to the weaker thermocapillary driving force resulting from the smaller temperature gradient at the free surface. Otherwise, the cell thicknesses and locations of local extrema change little, primarily because the electromagnetic damping, proportional to the radial flow velocity, increases as the flow intensifies.

The primary flow instabilities for small- $\text{Pr}$  liquid bridges with magnetic stabilization are hydrodynamic in nature. The first instability for  $\text{Pr} < 0.4$  is characterized by stationary disturbances [Bouizi et al. 2007]. Within this range, [Houchens and Walker 2005] further suggested three subregimes with different axial symmetries of the perturbations, which were confirmed in [Bouizi et al. 2007], both in full-zone geometries. In [Levenstam and Amberg 1995; Leypoldt et al. 2000] the secondary instability was found to be three-dimensional and oscillatory in the half-zone.

For high- $\text{Pr}$  liquid bridges, convective heat transfer is dominant over conduction and the instability mechanism is hydrothermal. The base flow first transitions to oscillatory perturbations (see [Leypoldt et al. 2000], for example). Due to strong thermal convection at high  $\text{Pr}$ , isotherms are dramatically distorted such that a large temperature gradient exists at the free surface near the top and bottom boundaries. In reality, the melt-solid interfaces may deform significantly from the assumed rigid plane due to this strong thermal convection. To accurately resolve high- $\text{Pr}$  liquid bridges, more realistic boundary conditions are needed, hence this work is limited to low- $\text{Pr}$  cases.

For a fixed  $\text{Pr} > 0$  (with  $\text{Re}_{\text{FZ}}$  fixed as in Figure 5), increasing  $\text{Ha}$  continuously confines the flow into a narrower region near the free surface and reduces the effectiveness of convective heat transfer into the interior. Thus  $T_{\max}$  increases, which enhances the thermocapillary driving effect. Therefore the flow

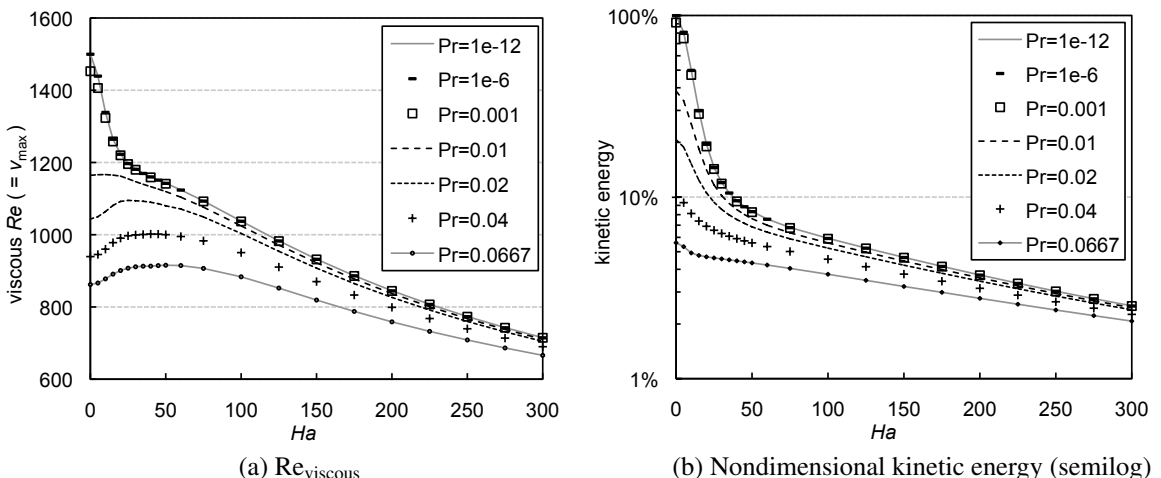


**Figure 5.** Effects of Prandtl number and magnetic damping on viscous Reynolds number and nondimensional kinetic energy ( $\text{Re}_{\text{FZ}} = 21,914.8$  fixed in all cases).

velocity increases at the free surface, but this is limited to a narrow cell due to magnetic damping.  $\text{Re}_{\text{viscous}}$  also increases proportionally to the maximum nondimensional velocity  $v_{\max}$  which always occurs near  $(r, z) = (1, b)$ . This explains the initial increase of  $\text{Re}_{\text{viscous}}$  with  $\text{Ha}$  for  $\text{Pr} \geq 0.02$  in Figure 5a. Eventually magnetic damping is sufficiently large that  $v_{\max}$  is reduced, even though  $T_{\max}$  continues to increase and approach 1.0633 (the value in the limit of no convective heat transfer). Also observe that  $\text{Re}_{\text{viscous}}$  decreases monotonically with increasing  $\text{Ha}$  for  $\text{Pr} \leq 0.001$ . For  $\text{Pr} \leq 0.001$  the temperature field is effectively decoupled from the flow field and  $T_{\max}$  remains constant as  $\text{Ha}$  increases. Therefore increasing  $\text{Ha}$  does not enhance the thermocapillary effect.  $\text{Pr} = 0.01$  marks the division between these two trends.

The nondimensional kinetic energy, computed as the integral of velocity squared over the domain, drops quickly as  $\text{Ha}$  increases (see Figure 5b), which demonstrates the magnetic damping effect. For a fixed  $\text{Re}_{\text{FZ}} (\propto q^* R^* / k^*)$ , the fact that kinetic energy also drops as  $\text{Pr} (= \mu^* c_p^* / k^*)$  increases can be explained as follows. Assume that the dynamic viscosity  $\mu^*$ , specific heat  $c_p^*$ , and radius  $R^*$  remain unchanged. Increasing  $\text{Pr}$  then corresponds to decreasing the thermal conductivity  $k^*$  and consequently a reduction in maximum heat flux  $q^*$  (to maintain a constant  $\text{Re}_{\text{FZ}}$ ). Therefore with less thermocapillary driving force, kinetic energy within the melt is reduced as  $\text{Pr}$  increases. Also note that the  $\text{Pr} = 0.001$ ,  $\text{Pr} = 10^{-6}$  and  $\text{Pr} = 10^{-12}$  curves are virtually indistinguishable, which indicates that  $\text{Pr} = 0.001$  is a good approximation for the limit of  $\text{Pr} \rightarrow 0$ , at least over the range  $0 \leq \text{Ha} \leq 300$ .

#### 4. Normal-mode linear stability analysis

**4A. Disturbances.** Normal-mode linear stability analysis, which compares well with nonlinear simulations in the half-zone [Levenstam et al. 2001], was used to study the stability of the base flow in the full-zone liquid bridge. The base flow was subjected to infinitesimal three-dimensional normal-mode disturbances of the form

$$\xi(r, \theta, z, t) = \xi_0(r, z) + \varepsilon \text{Real}\{\exp(\lambda t + i m \theta)\xi_1(r, z)\} \quad \text{for } \xi = v_r, v_z, P, T, j_\theta, \quad (4-1)$$

$$\zeta(r, \theta, z, t) = \varepsilon \text{Real}\{\exp(\lambda t + i m \theta)i\zeta_1(r, z)\} \quad \text{for } \zeta = v_\theta, \phi, j_r, j_z, \quad (4-2)$$

where  $\varepsilon$  is an infinitesimal magnitude and  $m$  denotes the azimuthal wave number of the disturbance. For uniqueness, disturbance waves must complete themselves as they travel through  $\theta = 0 \rightarrow 2\pi$ , therefore  $m$  is integer valued. Axisymmetric  $m = 0$  cases were not investigated as they have been shown to be very stable in similar systems [Kasperski et al. 2000]. The extra factor of  $i$  in (4-2) accounts for the phase shift in the variables which are zero in the base state, yielding a purely real linear stability problem.

Disturbances adhere to one of two axial symmetries. When perturbation variables have the *same* axial symmetry as their corresponding base flow variables, the mode is denoted as “symmetric”. When perturbation variables have the *opposite* axial symmetry as their corresponding base flow variables, the mode is denoted as “antisymmetric”. Any combination of these disturbance types will result in a critical  $\text{Re}_{\text{FZ}}$  that larger than the smaller  $\text{Re}_{\text{FZ},\text{cr}}$  of these two.

Figure 6 shows an example of streamlines in the base flow along with the disturbed flow. In the axisymmetric base flow state, a weightless fluid particle released at the starting point circulates on the black closed path (the stream function contour) within a fixed  $\theta$  plane. This specific example first transitions to stationary antisymmetric disturbances with  $m = 2$ . At the critical  $\text{Re}_{\text{FZ}}$ , a particle released at the same starting point changes its “orbiting radius” as it circulates, while oscillating within a  $\theta = \pi/m$  wedge.

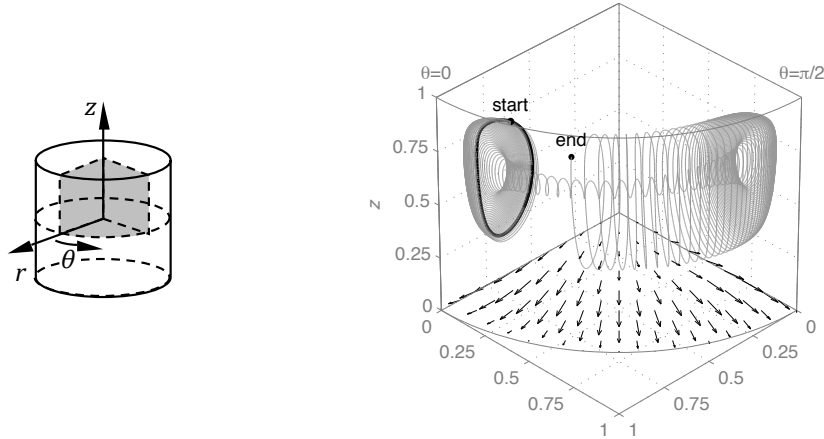


**Figure 6.** Streamlines in the base flow (black closed path) and disturbed flow (gray spiral path), and disturbed flow (vectors) at the midplane ( $\text{Pr} = 0.02$ ,  $\text{Ha} = 0$  at  $\text{Re}_{\text{FZ},\text{cr}} = 1546.58$ , stationary antisymmetric disturbances with  $m = 2$ , base flow grid  $r \times z = 35 \times 45$ , temperature grid  $r \times z = 30 \times 30$ , linear stability grid  $r \times z = 28 \times 28$ ,  $\alpha = 300$ , perturbation versus base flow maximum magnitude ratio 5%).

Note that the path is cut off intentionally at the “end” point to better show its spiral structure. Flow in other wedges and in the lower half of the liquid bridge can be inferred from the symmetry and mode number of the disturbance.

Arrows in the  $z = 0$  plane of Figure 6 show the disturbed flow motion at the liquid bridge midplane. Flow circulates from the liquid bridge interior back to the free surface due to the viscous effect. The flow at  $z = 0$  has no azimuthal component due to the antisymmetric disturbance mode. Perturbed flow crosses the midplane into the upper or lower half of the liquid bridge. In contrast, the half-zone assumes a no-slip, no-penetration midplane.

**4B. Critical thermocapillary Reynolds number.** The critical  $\text{Re}_{\text{FZ},\text{cr}}$  measures the critical point at which the base flow transitions to the first instability. Beyond  $\text{Re}_{\text{FZ},\text{cr}}$ , one or more infinitesimal disturbances grow in time, breaking either the axisymmetry or the axial symmetry or both, and potentially evolving the motion to a periodic flow. The goal is to find the first transition to instability among all possible disturbance modes.

By substituting the disturbance variables of (4-1) and (4-2) into the governing equations and boundary conditions and linearizing (neglecting  $\varepsilon^2$  terms) and discretizing, a generalized eigenvalue problem is obtained:

$$\underline{\mathbf{A}}\underline{\mathbf{M}}\underline{\mathbf{x}} = \lambda \underline{\mathbf{B}}\underline{\mathbf{M}}\underline{\mathbf{x}}, \quad (4-3)$$

The entire generalized system was solved using either the routine RGG in EISPACK or the routine DGGEV in LAPACK [Anderson et al. 1999], with refinement of the critical eigenvectors performed via the inverse iteration method [Saad 1992]. The real part of the leading eigenvalue (or pair)  $\lambda_R$  determines the stability of this system. If the imaginary part of the leading eigenvalue pair  $\lambda_I \neq 0$ , the base flow transitions to a periodic disturbance. Otherwise  $\lambda_I = 0$  and the transition is stationary. For each disturbance

mode ( $\text{Pr}$ ,  $\text{Ha}$ ,  $m$ , antisymmetric or symmetric mode), a neutrally stable mode is found if the leading eigenvalue (or pair) has  $\lambda_R = 0$ . A slight increase in  $\text{Re}_{\text{FZ}}$  causes this mode to become unstable and grow in time.

Finding the  $\text{Re}_{\text{FZ}}$  associated with a neutrally stable mode is an iterative process. Starting from a stable  $\text{Re}_{\text{FZ},s}$  (with  $\lambda_R < 0$ ) and an unstable  $\text{Re}_{\text{FZ},u}$  (with  $\lambda_R > 0$ ), a better approximation  $\text{Re}_{\text{FZ},3}$  is predicted using the regula falsi method. The new  $\lambda_R$  corresponding to  $\text{Re}_{\text{FZ},3}$  is computed using the shifted inverse iteration method. The  $\text{Re}_{\text{FZ},3}$  then replaces either  $\text{Re}_{\text{FZ},s}$  or  $\text{Re}_{\text{FZ},u}$ . In this way the bounds on the neutrally stable  $\text{Re}_{\text{FZ}}$  are narrowed through iterations until convergence. The linear stability analysis code is written in Fortran 90.

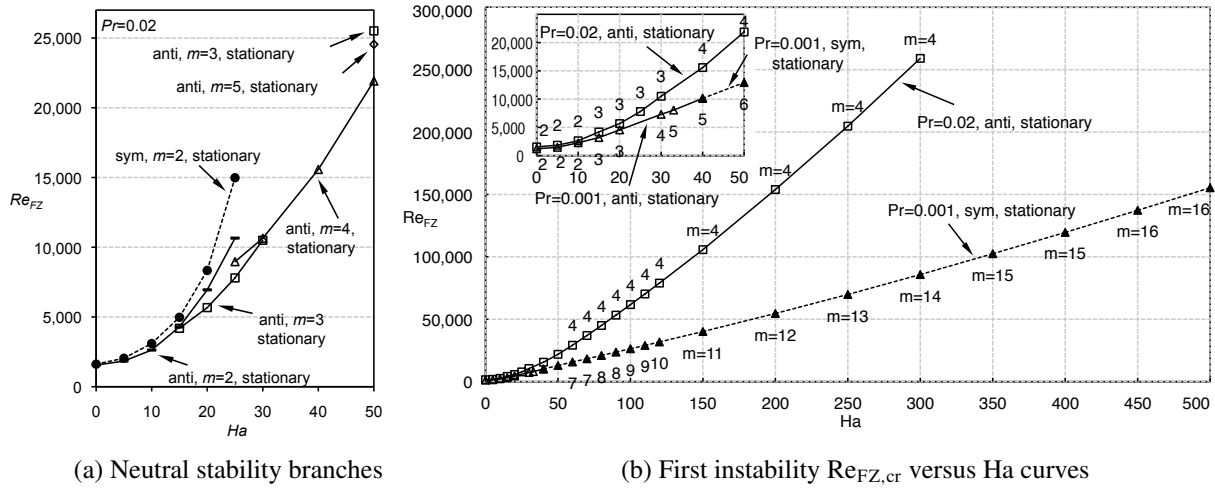
Variables in the linear stability analysis are the velocity perturbations  $v_{r1}$  and  $v_{z1}$ , temperature perturbation  $T_1$ , and electric potential perturbation  $\phi_1$ . Reduction from the 9 primitive stability variables to these four is accomplished using incompressible continuity and  $\theta$  momentum to solve for  $v_{\theta 1}$  and  $P_1$ , respectively. The electric current density perturbations ( $j_{r1}$ ,  $j_{\theta 1}$ , and  $j_{z1}$ ) are solved using Ohm's law and then substituted into conservation of charge. The resulting set of partial differential equations can be found in [Houchens and Walker 2001] for the half-zone. Similarly to the base flow analysis, these variables are represented as Chebyshev polynomials. Only even or odd terms in both  $r$  and  $z$  are nonzero due to the symmetries. In addition, by modeling antisymmetric and symmetric disturbance modes separately, the full-zone liquid bridge domain can be halved at the midplane. The price is that two codes have to be developed. An  $N_R \times N_Z$  Gauss–Lobatto collocation grid is adopted for  $r \in (0, 1)$  and  $z \in (0, b)$ , which is equivalent to a grid resolution of  $r \times z = (2 \times N_R) \times (4 \times N_Z)$  in the full-domain liquid bridge simulation if no symmetries are observed. The finest stability analysis grid used was  $N_R \times N_Z = 50 \times 70$  for high- $\text{Ha}$  cases.

Disturbances with a wide range of azimuthal wave numbers  $m$ , for both the antisymmetric and symmetric modes, are investigated. Axisymmetric disturbances ( $m = 0$ ) are not studied in this work because they are unlikely to be the critical disturbance mode. For example [Bouizi et al. 2007] reported that  $\text{Re}_{\text{FZ},\text{cr}}$  for the  $m = 0$  mode ranges from seven times to thousands of times larger than  $\text{Re}_{\text{FZ},\text{cr}}$  for the critical  $m = 2$  mode for  $\text{Pr} \in (0.001, 0.04)$ .

For a fixed  $\text{Pr}$ , a neutrally stable  $\text{Re}_{\text{FZ}}$  versus  $\text{Ha}$  branch can be obtained for each disturbance mode. The critical  $\text{Re}_{\text{FZ},\text{cr}}$  is the lowest among all neutrally stable  $\text{Re}_{\text{FZ}}$ 's. For example, the neutral stability branches for  $\text{Pr} = 0.02$  (Figure 7a) show how the critical disturbance mode changes from  $m = 2$  to 3 and then 4 for  $\text{Ha} \in (0, 50)$ . The  $m = 2$  symmetric branch (dashed line) deviates from the critical antisymmetric modes as  $\text{Ha}$  increases. Although other stability branches above the critical branch are not valid for predicting a second and third bifurcation, they provide insight into flow stability when subject to these perturbation modes.

Table 1 lists  $\text{Re}_{\text{FZ}}$  values on the  $\text{Pr} = 0.02$  neutral stability branches. For both antisymmetric and symmetric disturbance modes,  $m$  is tracked from 1 to 8 for  $\text{Pr} = 0.02$ , and to at least the critical  $m + 4$  for  $\text{Pr} = 0.001$ .  $\text{Re}_{\text{FZ}}$  values not shown in Table 1 are higher than these listed  $\text{Re}_{\text{FZ}}$ 's for the same  $\text{Ha}$ . The  $m = 5$  antisymmetric branch never becomes critical up to  $\text{Ha} = 300$  for  $\text{Pr} = 0.02$ .

The  $\text{Re}_{\text{FZ},\text{cr}}$  versus  $\text{Ha}$  curves for  $\text{Pr} = 0.02$  and  $\text{Pr} = 0.001$  (see Figure 7b) summarize the first instabilities over a wide  $\text{Ha}$  range. The  $\text{Re}_{\text{FZ},\text{cr}}$  increases quickly with increasing  $\text{Ha}$ , which demonstrates the magnetic stabilization effect. Stronger magnetic fields damp the flow, so that more driving energy must be fed in before the flow trips to an instability. The critical curves determine the minimum magnetic



(a) Neutral stability branches

(b) First instability  $Re_{FZ,cr}$  versus  $Ha$  curves

**Figure 7.** Example of neutral stability branches for  $Pr = 0.02$  and the first instability critical curves for  $Pr = 0.02$  and for  $Pr = 0.001$ .

$Ha$	Antisymmetric				Symmetric
	$m = 2$	$m = 3$	$m = 4$	$m = 5$	$m = 2$
0	<u>1,546.58</u>				1,618.42
5	<u>1,842.97</u>				2,041.81
10	<u>2,629.52</u>				3,098.39
15	4,291.10	<u>4,187.74</u>			4,978.35
20	6,946.57	<u>5,671.88</u>			8,337.20
25	10,653.30	<u>7,800.11</u>	8,964.73		14,980.91
30		<u>10,501.11</u>	10,642.13		
40			<u>15,575.20</u>		
50		25,513.47	<u>21,914.83</u>	24,545.29	
60			<u>29,168.06</u>	30,544.57	
70			<u>36,961.68</u>	37,672.75	
80			<u>44,999.40</u>	45,250.00	
90			<u>53,316.88</u>	53,583.48	
100			<u>61,747.38</u>	62,263.88	
110			<u>70,289.58</u>	71,229.01	
120			<u>79,037.36</u>	80,562.15	
150			<u>105,776.82</u>	109,765.83	
200		162,032.06	<u>153,945.51</u>	204,740.95	225,107.28
250					293,492.96
300		263,317.80	<u>259,068.47</u>		

**Table 1.** Neutrally stable  $Re_{FZ}$ 's for  $Pr = 0.02$  branches ( $Re_{FZ,cr}$ 's are underlined).

field strength required to avoid instabilities in the optically heated float-zone crystal growth process. Note that  $\text{Pr} = 0.001$  is chosen because its critical curve very likely marks the lower limit of critical curves for  $\text{Pr} \rightarrow 0$ . According to [Houchens and Walker 2005], at  $\text{Ha} = 0$  the  $\text{Re}_{\text{FZ},\text{cr}}$  for  $\text{Pr} = 10^{-10}$  is less than 1% smaller than  $\text{Re}_{\text{FZ},\text{cr}}$  for  $\text{Pr} = 0.001$ . Details of the perturbation flow field and the energy analysis between the base state and perturbed field are presented and validated with other liquid bridge studies in [Huang and Houchens 2011]. Here the focus is instead on the numerical issues that arise in the spectral collocation technique and linear stability analyses. The following sections are widely applicable to a range of partial differential equations. First, identification of spurious eigenvalues is discussed. Then, regularization and grid dependence issues are covered. Finally, the use of pseudospectra to investigate the robustness of stability analyses are addressed.

**4C. Identifying spurious eigenvalues.** In the linear stability analysis, unstable systems are identified by positive leading eigenvalues. However, some spurious eigenvalues (usually with very large magnitudes) emerge in the generalized eigenvalue problem, (4-3), bearing no physical meaning regarding system stability. It is crucial to identify and separate them from the remaining legitimate eigenvalues to correctly predict the stability of the system.

Legitimate eigenvalues are independent of linear stability grid resolution. In Table 2, to test if the leading eigenvalue pair  $350.47 \pm 7542.09i$  on a  $30 \times 40$  grid is legitimate or spurious, the linear stability code was run on two other grid sizes,  $28 \times 28$  and  $40 \times 50$ . The fact that  $350.47 \pm 7542.09i$  is not present on these two grids indicates that it is a spurious eigenmode. All other leading eigenvalues agree well, independent of the grid.

As a direct proof, perturbation variable contours are plotted (Figure 8a) using eigenvectors corresponding to the spurious eigenvalue pair  $350.47 \pm 7542.09i$ . The checkerboard pattern has no physical justification, but is rather an oscillation of a high-order mode(s) in each direction between Gauss–Lobatto collocation points. This is clearly shown in the Chebyshev polynomial coefficient plot (Figure 8b) for  $v_{r1}$ , where

$$v_{r1}\left(r, \frac{z}{b}\right) = r^{m-1} \sum_{L=0}^{N_R+1} \sum_{M=0}^{N_Z} \mathcal{A}_{LM} T_{2L}(r) T_{2M}\left(\frac{z}{b}\right). \quad (4-4)$$

Grid size	$r \times z = 28 \times 28$	$r \times z = 30 \times 40$	$r \times z = 40 \times 50$
Leading eigenvalues	<u><math>350.47 \pm 7542.09i</math></u>		
	$-34.61 \pm 9.25i$	$-34.61 \pm 9.26i$	$-34.61 \pm 9.25i$
	$-94.58 \pm 110.75i$	$-94.58 \pm 110.75i$	$-94.58 \pm 110.75i$
	$-113.45 \pm 56.60i$	$-113.46 \pm 56.59i$	$-113.46 \pm 56.60i$
	$-129.35 \pm 175.31i$	$-129.35 \pm 175.31i$	$-129.35 \pm 175.31i$
	$-140.05 \pm 72.15i$	$-140.04 \pm 72.15i$	$-140.04 \pm 72.15i$
	$-197.10 \pm 320.75i$	$-197.10 \pm 320.75i$	$-197.10 \pm 320.75i$
⋮			

**Table 2.** Identification of a spurious eigenvalue (underlined) through grid refinement of the linear stability analysis ( $\text{Pr} = 0.001$ ,  $\text{Ha} = 0$ ,  $\text{Re}_{\text{FZ}} = 1000$ ,  $m = 1$ ,  $\alpha = 400$ , symmetric mode).

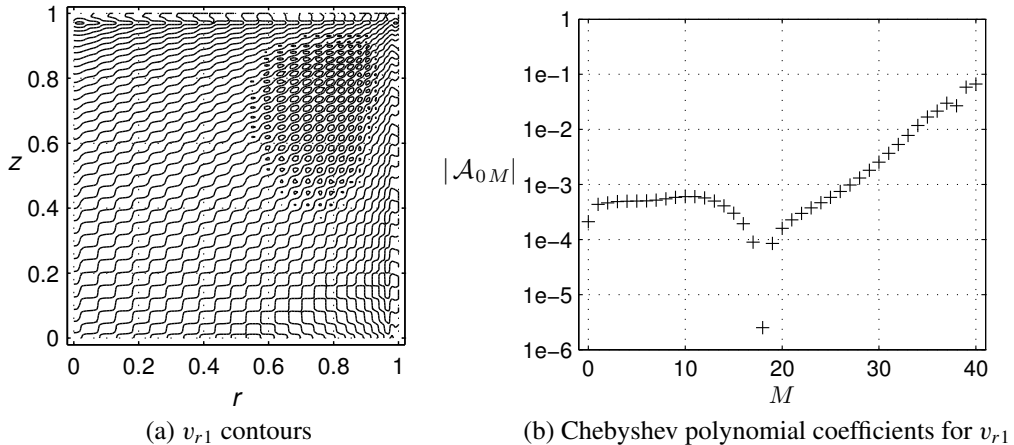


**Figure 8.** Perturbation contours and Chebyshev polynomial coefficients associated with the spurious eigenmode  $350.47 \pm 7542.09i$  in Table 2 ( $\text{Pr} = 0.001$ ,  $\text{Ha} = 0$ ,  $\text{Re}_{\text{FZ}} = 1000$ ,  $m = 1$ ,  $\alpha = 400$ , linear stability grid  $r \times z = 30 \times 40$ ).

The coefficients of the highest-order Chebyshev terms have the largest magnitudes, which are responsible for the high-frequency, oscillating contours. Note that for a legitimate eigenmode, the Chebyshev polynomial coefficients decay exponentially when the representation is sufficient. Therefore, for this case the legitimate leading eigenvalue is a complex pair with negative real part  $-34.61 \pm 9.26i$  as shown in Table 2. The base flow is stable at  $\text{Re}_{FZ} = 1000$  for this branch ( $\text{Pr} = 0.001$ ,  $\text{Ha} = 0$ , and  $m = 1$  symmetric disturbance mode).

## 5. Numerical aspects

**5A. Regularization of the vorticity singularity.** A regularization function  $F(z)$  (from (3-7)) is introduced in the thermocapillary boundary condition to remove the singularity of the velocity gradient at the corner  $(r, z) = (1, b)$ . While  $\partial v_{z0}/\partial r = 0$  at  $(r, z) = (1, b)$  due to the boundary condition  $v_{z0} = 0$  at  $z = b$ , the thermocapillary boundary condition, without regularization, gives a nonzero  $\partial v_{z0}/\partial r$  at  $(r, z) = (1, b)$  due to the nonzero temperature gradient  $\partial T_0/\partial z$  at the free surface. This singularity is removed by multiplying the thermocapillary boundary condition by a function that decays quickly to 0 as  $z \rightarrow b$  but remains equal or close to 1 for the rest of  $z$ .

An optimum value of the regularization parameter  $\alpha$  is achieved when increasing  $\alpha$  further has no measurable impact on the flow and the singularity is effectively removed. Figure 9 shows a test over a wide range of  $\alpha$ . With a sufficiently large value the physics becomes independent of  $\alpha$ , as indicated by the “desired range”. But too large an  $\alpha$  may provide insufficient regularization. In Figure 9, the  $v_{r0}$  contours bear wiggles and circles, indicating  $\alpha = 50,000$  is too large for this case. With even less smoothing (higher  $\alpha$ ), the vorticity singularity may cause the numerical solver to predict the wrong physics, suggested by the sudden drop of the critical  $Re_{FZ}$  beyond  $\alpha = 100,000$ . On the other hand, if the value of  $\alpha$  is too small, the regularization effectively reduces the heat input at the free surface which reduces the driving force and explains the increase of the critical  $Re_{FZ}$  (“too much regularization”) for  $\alpha$  in range 10–100 in Figure 9.

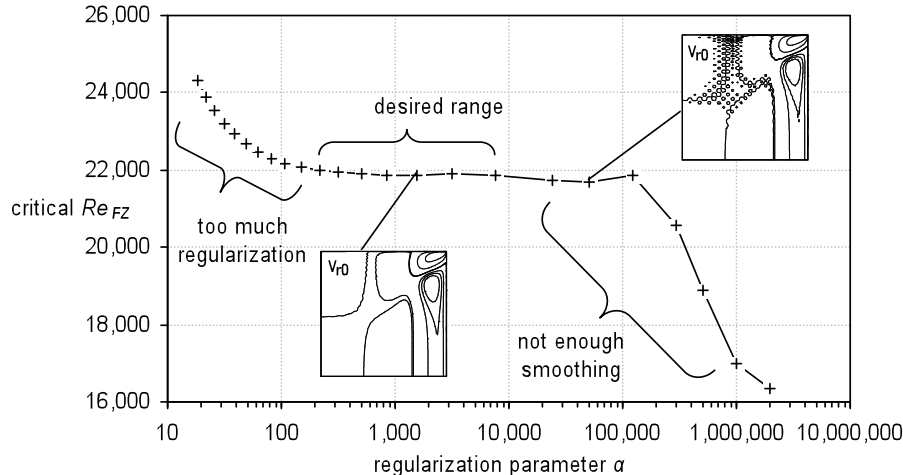


**Figure 9.** Searching for the desired range of regularization parameter  $\alpha$  (semilog plot,  $Pr = 0.02$ ,  $Ha = 50$ , flow grid  $r \times z = 40 \times 40$ , temperature grid  $r \times z = 30 \times 30$ , stability grid  $r \times z = 40 \times 40$ ).

A fast-decaying regularization function is especially important for high- $Pr$  liquid bridge simulation. Due to strong heat convection, the temperature at the free surface varies slowly along  $r = 1$  until very close to  $(r, z) = (1, b)$ . This feature is best preserved by a regularization function that decays quickly near  $(r, z) = (1, b)$ . The choice of regularization function is arbitrary as long as the singularity is removed with minimum modification of the physics. For example, in [Bouizi et al. 2007] a power function regularization function  $F(z) = (1 - z^{2n})^2$  was adopted, where  $n$  is a regularization parameter.

**5B. Grid resolution and independence.** A solution which does not vary with significant further grid refinement indicates that the grid resolution is sufficient and the results are reliable. Table 3 shows such a test based on the critical  $Re_{FZ}$ . Significant resolution increases are introduced for the base flow grids and the stability analysis grid, but the  $Re_{FZ,cr}$  barely changes, demonstrating grid independence was achieved.

More subtle inferences can be made from this test.  $Re_{FZ,cr}$  increased slightly on finer grids in Table 3. This is expected because a fixed regularization parameter ( $\alpha = 400$ ) affects more grid points on a finer axial grid than on a coarser axial grid. The thermocapillary effect is weakened at more collocation

the critical $Re_{FZ}$ for	stability grid ( $r \times z$ )	% difference
flow grid, temperature grid ( $r \times z$ )	$30 \times 75, 25 \times 25$ $70 \times 100, 40 \times 40$	$61,775.37 \quad 61,840.74$ $61,789.51 \quad 61,841.79$
		<b>0.11%</b> <b>0.08%</b>
% difference	<b>0.02%</b>	<b>0.002%</b>

**Table 3.** Grid dependence study based on  $Re_{FZ,cr}$  for  $Pr = 0.02$ ,  $Ha = 100$ ,  $\alpha = 400$ .

points on finer grids, therefore a higher  $\text{Re}_{\text{FZ},\text{cr}}$  is expected. However if this regularization effect were eliminated,  $\text{Re}_{\text{FZ},\text{cr}}$  would be lower on finer grids, because coarser grids tend to smear out the largest gradients, which contribute energy to the instability mechanism. On coarser grids,  $\text{Re}_{\text{FZ},\text{cr}}$  increases to compensate for this smearing effect until the energy is sufficient to trip the instability. Thus, in practice, it is necessary to carry out both grid and regularization dependence studies simultaneously. The regularization parameter must be increased as the grid is refined.

**5C. Model robustness investigated by pseudospectra.** As discussed above, the flow stability in the liquid bridge is determined by its eigenvalues. For the generalized eigenvalue problem, (4-3), each eigenvalue (each black dot in Figure 10) is associated with one flow perturbation eigenmode. Purely real eigenvalues correspond to perturbations in which the base flow transitions to steady, three-dimensional (not axisymmetric) perturbed flow. Complex eigenvalue pairs correspond to perturbations in which the base flow transitions to three-dimensional time-dependent flow, with the imaginary components representing the frequency.

Compared to the simplified numerical full-zone model, real world experiments include many imperfections that are difficult to represent. For example, in experiments the heat flux will not be strictly parabolic or axisymmetric and the free surface will not be exactly cylindrical. It is therefore desirable to predict what impact these imperfections might have, to verify the robustness of the model as compared to the experiment it is intended to represent.

Furthermore, numerical errors in the model may also play a significant but unpredictable role. For example, round-off errors in the eigenvalue problem may accumulate during computation and affect the results. Simulation results are more meaningful provided they are valid even when the model is subject

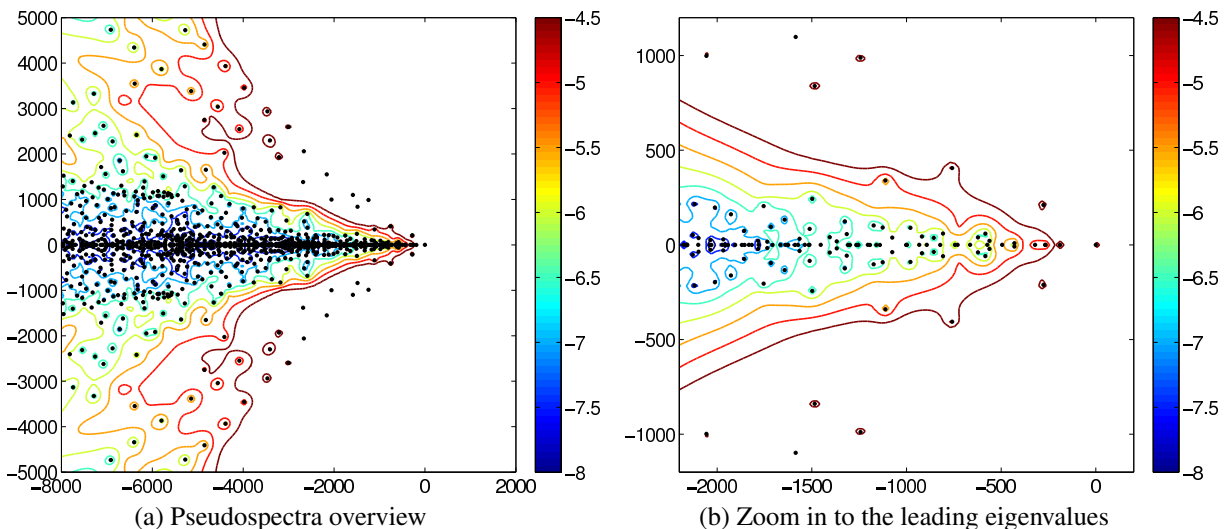


**Figure 10.** Eigenvalues (black dots) and their pseudospectra  $\sigma_\epsilon$  (contours) of the generalized eigenvalue problem (4-3) ( $\text{Pr} = 0.02$ ,  $\text{Ha} = 50$ ,  $\text{Re}_{\text{FZ}} = 21,879.5$ , flow grid  $r \times z = 70 \times 100$ , temperature grid  $r \times z = 40 \times 40$ , stability grid  $r \times z = 35 \times 50$ ,  $\alpha = 1000$ ).

to these minor changes, whether these are purely numerical or result from the inability of the model to represent small imperfections in the experiment.

Pseudospectral analysis provides a quantitative measure to test model robustness. Small numerical errors  $\epsilon$  are purposefully introduced into either or both  $\underline{\underline{AM}}$  and  $\underline{\underline{BM}}$  matrices in the eigenvalue problem  $\underline{\underline{AM}}\underline{x} = \lambda \underline{\underline{BM}}\underline{x}$  (see (4-3)). Note that  $\epsilon$  is different from the  $\varepsilon$  used in the linear stability analysis. In fact,  $\epsilon$  acts like a random perturbation on  $\varepsilon$ . The small errors introduced through  $\epsilon$  can represent physical perturbations on the boundary conditions, geometry, and flow field of the model. They can also be purely numerical perturbations. In this problem such perturbations could be relatively minor (introducing slight curvature in the free surface) or more egregious (violations of conservation of charge).

After introducing these  $\epsilon$  scale errors, the modified generalized eigenvalue problem is solved again to investigate any physically meaningful changes. For example, a possible scenario of significant interest would result if a previously more-stable branch became the critical mode in the modified system. This has tremendous relevance in this problem, as only one known experimental study in a low-Pr fluid in the half-zone configuration has indicated possible observation of the steady, three-dimensional transition before onset of periodicity [Takagia et al. 2001]. In other experiments, the instability has appeared to jump directly to the higher branch associated with the periodic transition, suggesting that the distinction between the preferred modes may be very subtle. Results will show, fortunately or unfortunately, that such sensitivity is not found in the full-zone model.

Introduced in [Reddy and Trefethen 1990], pseudospectra present a systematic method for carrying out such analyses. For an introduction and a simulation method (EigTool) for problems of small or moderate size, the reader is referred to [Embree and Trefethen 2011]. An extensive discussion on pseudospectra, including fluid mechanics applications, can be found in [Trefethen and Embree 2005].

For the large generalized eigenvalue problem in this work the matrix  $\underline{\underline{AM}}$  is perturbed with the random matrix  $\underline{\underline{E}}$  in the way described in [van Dorselaer 1997] using

$$\begin{aligned}\sigma_\epsilon(\underline{\underline{AM}}, \underline{\underline{BM}}) &= \{z \in \mathbf{C} : \|(z \underline{\underline{BM}} - \underline{\underline{AM}})^{-1}\| > 1/\epsilon\} \\ &= \{z \text{ is an eigenvalue of } (\underline{\underline{AM}} + \underline{\underline{E}}, \underline{\underline{BM}}) \text{ for some } \underline{\underline{E}} \text{ with } \|\underline{\underline{E}}\| < \epsilon\}.\end{aligned}\quad (5-1)$$

This analysis must be repeated until representative pseudospectra are obtained. Resulting pseudospectra  $\sigma_\epsilon$  contours indicate the sensitivity of the original eigenvalues to the random noise introduced via  $\epsilon$ . The results of this analysis are given by the color contours in Figure 10. The color gradient indicates the magnitude of the  $\epsilon$  perturbation. The smallest  $\epsilon = 10^{-8}$  perturbations do not affect the leading eigenvalues at a measurable level, hence the blue contours are not visible around these eigenvalues in the complex plane. The first blue envelope that can be observed at this order occurs for eigenvalues with real parts near  $-1500$ . As the order of  $\epsilon$  increases, more eigenvalues are influenced. For example, a perturbation of size  $\epsilon = 10^{-5}$  may move enclosed eigenvalues anywhere within the medium-red regions in Figure 10.

The leading real eigenvalue and complex eigenvalue pair are the most likely to become critical. The linear stability analysis predicts that the real eigenvalue will dominate. This is confirmed by the pseudospectra in Figure 10. Namely, at the largest pseudospectral perturbation of  $\epsilon = 10^{-4.5}$ , the leading real eigenvalue maintains its leading position and explores only a very small region near its origin. In fact, no dark red contours of any eigenvalue extend into the positive half of the real plane. Since the pseudospectra

contours of all the eigenvalues remain behind the leading eigenvalue, the branches associated with these modes will not become critical, even in the modified system. Therefore the critical eigenmode (stationary, antisymmetric disturbances with  $m = 4$  in this example) predicted by the original generalized eigenvalue problem remains valid under such perturbations. Therefore, in careful experiments it would be expected that the stationary mode would be observed first.

To quantitatively or qualitatively relate  $\epsilon = 10^{-4.5}$  numerical perturbations to specific physical changes in the fluid model is appealing, but intractable without imposing further structure on the perturbation. Random changes in matrix elements are often nonphysical, resulting in violations of the conservation of mass, energy, and momentum, and breaking the orthogonality of boundary conditions. Thus even a small  $\epsilon$  may have significant impacts on the physical system. In fact, the entire domain in Figure 10 is contained in the contour  $\sigma_\epsilon(\underline{\mathbf{AM}}, \underline{\mathbf{BM}})$  for  $\epsilon \geq 10^{-4.35}$ . Nevertheless, the pseudospectra suggests the results of the linear stability analysis are quite robust, particularly for the leading eigenvalues which are of most interest.

## 6. Conclusions

A thermocapillary-driven full-zone liquid bridge with magnetic stabilization is modeled numerically. A wide range of three-dimensional flow disturbances are tracked using a normal-mode linear stability analysis. The first instability curve for Prandtl number  $\text{Pr} = 0.02$  (for example, molten silicon) is obtained up to an intermediate Hartmann number of  $\text{Ha} \in (0, 300)$ . Within this range, the steady axisymmetric base flow first transitions to stationary three-dimensional disturbances with axial symmetries opposite to their base flow components (the antisymmetric disturbance mode). Moreover, first instabilities for  $\text{Pr} = 0.001$ , representing the  $\text{Pr} \rightarrow 0$  limit, are presented up to  $\text{Ha} = 500$ . For  $\text{Pr} = 0.001$ , the base flow also first transitions to stationary three-dimensional disturbances. Axial critical disturbance symmetries are antisymmetric below  $\text{Ha} = 40$  and symmetric for  $\text{Ha} \in (40, 500)$ . The critical azimuthal wave number  $m$  increases with  $\text{Ha}$  for both  $\text{Pr} = 0.02$  and  $\text{Pr} = 0.001$ .

Magnetic stabilization effects are observed and quantitatively measured for a steady external magnetic field in the axial direction. The induced Lorentz force acts proportionally against radial flow motion, thus multiple cell-like circulation patterns form within the liquid bridge. The most significant flow is confined to an increasingly narrow region near the free surface as  $\text{Ha}$  increases. At the interior the flow is damped until it is almost stagnant, which provides steady crystal growth conditions at the interface. This damping effect is also confirmed by quantitative studies of the viscous Reynolds number and kinetic energy versus  $\text{Ha}$ . Because the flow disturbances are greatly suppressed by magnetic stabilization, a more intense thermocapillary driving force is needed to trip instabilities within the liquid bridge. For example, the critical thermocapillary Reynolds number  $\text{Re}_{\text{FZ},\text{cr}}$  at  $\text{Ha} = 300$  is two orders of magnitude larger than when no magnetic field ( $\text{Ha} = 0$ ) is applied.

Small-Prandtl number liquid bridges, dominated by heat conduction, are studied over the range  $\text{Pr} \in (10^{-12}, 0.0667)$ . For  $\text{Pr} \leq 0.001$ , the temperature field is effectively decoupled from the flow field, mimicking a pure conduction state such that the temperature distribution is almost unchanged over the range  $\text{Ha} = 0 \rightarrow 300$ . Thermal convection becomes important as  $\text{Pr}$  increases. It helps unify the temperature distribution throughout the domain as suggested by the isotherms. At higher  $\text{Pr}$ , the temperature gradient on the free surface concentrates near the liquid-solid boundaries  $(r, z) = (1, \pm b)$ , which intensifies the

thermocapillary effect in these regions. Interestingly, the flow “circulation cell” thicknesses and locations are almost unaffected by increases in  $\text{Pr}$  over the range studied, mainly because the electromagnetic force, proportional to the radial flow velocity, also increases as convection intensifies.

Numerical techniques and analyses are also highlighted extensively in this work. For example, the vorticity singularity in the spectral scheme is removed by applying an exponential regularization function. The desired range of the regularization parameter  $\alpha$  is determined by balancing the removal of the singularity and the invariance of the physics. The generalized eigenvalue problem  $\underline{\mathbf{A}}\underline{\mathbf{M}}\underline{\mathbf{x}} = \lambda \underline{\mathbf{B}}\underline{\mathbf{M}}\underline{\mathbf{x}}$  in the linear stability analysis is investigated from a numerical perspective. Spurious eigenvalue modes with no physical meaning are identified by a combination of grid dependence studies and plotting of the eigenmodes. The pseudospectra indicate that results predicted by this full-zone model are valid even if the model is subject to minor changes, be they numerical or physical.

**Acknowledgements.** The authors would like to thank Professor Mark Embree at Rice University for providing the pseudospectra plots and insights on the eigenvalue problem and pseudospectra analysis. All tests were run on the Shared University Grid at Rice (SUG@R) cluster. This work was partially supported by the United States Air Force Office of Scientific Research.

## References

- [Anderson et al. 1999] E. Anderson, Z. Bai, C. Bischof, S. Blackford, J. Demmel, J. Dongarra, J. Du Croz, A. Greenbaum, S. Hammarling, A. McKenney, and D. Sorensen, “Linear Algebra PACKage”, 1999, available at <http://www.netlib.org/lapack/lug/index.html>.
- [Bouizi et al. 2007] O. Bouizi, C. Delcarte, and G. Kasperski, “Stability study of the floating zone with respect to the Prandtl number value”, *Phys. Fluids* **19**:11 (2007), 114102.
- [Chen et al. 1997] G. Chen, A. Lizée, and B. Roux, “Bifurcation analysis of the thermocapillary convection in cylindrical liquid bridges”, *J. Cryst. Growth* **180**:3-4 (1997), 638–647.
- [Cröll et al. 1994] A. Cröll, P. Dold, and K. W. Benz, “Segregation in Si floating-zone crystals grown under microgravity and in a magnetic field”, *J. Cryst. Growth* **137**:1-2 (1994), 95–101.
- [Davis 1993] S. H. Davis, “Effects of flow on morphological stability”, pp. 859–897 in *Handbook of crystal growth*, vol. 1B, edited by D. T. J. Hurle, Elsevier, New York, 1993.
- [van Dorsselaer 1997] J. L. M. van Dorsselaer, “Pseudospectra for matrix pencils and stability of equilibria”, *BIT* **37**:4 (1997), 833–845.
- [Embree and Trefethen 2011] M. Embree and L. N. Trefethen, “Pseudospectra gateway”, 2011, available at <http://www.comlab.ox.ac.uk/pseudospectra>.
- [Eyer et al. 1979] A. Eyer, R. Nitsche, and H. Zimmermann, “A double-ellipsoid mirror furnace for zone crystallization experiments in spacelab”, *J. Cryst. Growth* **47**:2 (1979), 219–229.
- [Eyer et al. 1985] A. Eyer, H. Leiste, and R. Nitsche, “Floating zone growth of silicon under microgravity in a sounding rocket”, *J. Cryst. Growth* **71**:1 (1985), 173–182.
- [Houchens and Walker 2001] B. C. Houchens and J. S. Walker, “Magnetic damping of the thermocapillary instability during floating-zone crystal growth in space”, in *Conference and exhibit on international space station utilization* (Cape Canaveral, FL, 2001), AIAA, Reston, VA, 2001. Paper #2001-5053.
- [Houchens and Walker 2005] B. C. Houchens and J. S. Walker, “Modeling the floating zone: instabilities in the half zone and full zone”, *J. Thermophys. Heat Transf.* **19**:2 (2005), 186–198.
- [Huang and Houchens 2011] Y. Huang and B. C. Houchens, “Magnetic stabilization, transition and energy analysis in the Marangoni driven full-zone at low Prandtl numbers”, *Eur. Phys. J. Spec. Top.* **192**:1 (2011), 47–62.
- [Intel 2008] Intel, “Intel math kernel library”, 2008, available at <http://software.intel.com/en-us/intel-mkl>.

- [Kasperski et al. 2000] G. Kasperski, A. Batoul, and G. Labrosse, “Up to the unsteadiness of axisymmetric thermocapillary flows in a laterally heated liquid bridge”, *Phys. Fluids* **12**:1 (2000), 103–119.
- [Lan and Yeh 2004] C. W. Lan and B. C. Yeh, “Three-dimensional simulation of heat flow, segregation, and zone shape in floating-zone silicon growth under axial and transversal magnetic fields”, *J. Cryst. Growth* **262**:1-4 (2004), 59–71.
- [Lan and Yeh 2005] C. W. Lan and B. C. Yeh, “Effects of rotation on heat flow, segregation, and zone shape in a small-scale floating-zone silicon growth under axial and transversal magnetic fields”, *Fluid Dyn. Mater. Process.* **1**:1 (2005), 33–44.
- [Lappa 2004] M. Lappa, “Combined effect of volume and gravity on the three-dimensional flow instability in noncylindrical floating zones heated by an equatorial ring”, *Phys. Fluids* **16**:2 (2004), 331–443.
- [Lappa 2005a] M. Lappa, “Analysis of flow instabilities in convex and concave floating zones heated by an equatorial ring under microgravity conditions”, *Comput. Fluids* **34**:6 (2005), 743–770.
- [Lappa 2005b] M. Lappa, “Review: possible strategies for the control and stabilization of Marangoni flow in laterally heated floating zones”, *Fluid Dyn. Mater. Process.* **1**:2 (2005), 171–188.
- [Levenstam and Amberg 1995] M. Levenstam and G. Amberg, “Hydrodynamical instabilities of thermocapillary flow in a half-zone”, *J. Fluid Mech.* **297** (1995), 357–372.
- [Levenstam et al. 2001] M. Levenstam, G. Amberg, and C. Winkler, “Instabilities of thermocapillary convection in a half-zone at intermediate Prandtl numbers”, *Phys. Fluids* **13**:4 (2001), 807–816.
- [Leypoldt et al. 2000] J. Leypoldt, H. C. Kuhlmann, and H. J. Rath, “Three-dimensional numerical simulation of thermocapillary flows in cylindrical liquid bridges”, *J. Fluid Mech.* **414** (2000), 285–314.
- [Martinez and Eyer 1986] I. Martinez and A. Eyer, “Liquid bridge analysis of silicon crystal growth experiments under microgravity”, *J. Cryst. Growth* **75**:3 (1986), 535–544.
- [Morthland and Walker 1996] T. E. Morthland and J. S. Walker, “Thermocapillary convection during floating-zone silicon growth with a uniform or non-uniform magnetic field”, *J. Cryst. Growth* **158**:4 (1996), 471–479.
- [Nakamura et al. 1998] S. Nakamura, T. Hibiya, K. Kakimoto, N. Imaishi, S. Nishizawa, A. Hirata, K. Mukai, S. Yoda, and T. S. Morita, “Temperature fluctuations of the Marangoni flow in a liquid bridge of molten silicon under microgravity on board the TR-IA-4 rocket”, *J. Cryst. Growth* **186**:1-2 (1998), 85–94.
- [Prange et al. 1999] M. Prange, M. Wanschura, H. C. Kuhlmann, and H. J. Rath, “Linear stability of thermocapillary convection in cylindrical liquid bridges under axial magnetic fields”, *J. Fluid Mech.* **394**:1 (1999), 281–302.
- [Reddy and Trefethen 1990] S. C. Reddy and L. N. Trefethen, “Lax-stability of fully discrete spectral methods via stability regions and pseudo-eigenvalues”, *Comput. Methods Appl. Mech. Eng.* **80**:1-3 (1990), 147–164.
- [Saad 1992] Y. Saad, *Numerical methods for large eigenvalue problems*, Manchester University Press, Manchester, 1992.
- [Takagia et al. 2001] K. Takagia, M. Otaka, H. Natsui, T. Arai, S. Yoda, Z. Yuan, K. Mukai, S. Yasuhiro, and N. Imaishi, “Experimental study on transition to oscillatory thermocapillary flow in a low Prandtl number liquid bridge”, *J. Cryst. Growth* **233**:1-2 (2001), 399–407.
- [Trefethen and Embree 2005] L. N. Trefethen and M. Embree, *Spectra and pseudospectra: the behavior of nonnormal matrices and operators*, Princeton University Press, Princeton, NJ, 2005.

Received 30 Jun 2010. Revised 1 Mar 2011. Accepted 10 Apr 2011.

YUE HUANG: [yue.huang@rice.edu](mailto:yue.huang@rice.edu)

*Department of Mechanical Engineering and Materials Science, Rice University, 6100 Main Street, Houston, TX 77005-1827, United States*

BRENT C. HOUCHENS: [houchens@rice.edu](mailto:houchens@rice.edu)

*Department of Mechanical Engineering and Materials Science, Rice University, 6100 Main Street, Houston, TX 77005-1827, United States*

## NUMERICAL INVESTIGATION OF DIRECTOR ORIENTATION AND FLOW OF NEMATIC LIQUID CRYSTALS IN A PLANAR 1:4 EXPANSION

PEDRO A. CRUZ, MURILO F. TOMÉ, IAIN W. STEWART AND SEAN MCKEE

Numerical solutions to the equations describing Ericksen–Leslie dynamic theory for 2D nematic liquid crystal flows subject to a magnetic field are obtained. The governing equations are solved by a finite difference technique based on the GENSMAC methodology. The resulting numerical technique was verified by comparing numerical solutions for 2D-channel flow by means of mesh refinement. To demonstrate the capabilities of this method, the flow of a nematic liquid crystal in a planar 1:4 expansion was simulated. Calculations were performed for various Ericksen and Reynolds numbers. The results showed that an increase in the Ericksen number caused the appearance of lip and corner vortices.

### 1. Introduction

Although the discovery of liquid crystals is generally attributed to Reinitzer [1888], the term “liquid crystal” was established by Lehmann in 1900, after he originally suggested the term “flowing crystals” [Lehmann 1889]. In [Friedel 1922] different liquid crystal phases were described and three broad categories were proposed: nematic, cholesteric, and smectic. Nematic liquid crystals are characterized by long-range orientational order of the molecules; in other words, the molecular orientation in a nematic liquid crystal exhibits a preferred direction which can be represented by a unit vector  $\mathbf{n}$ , called the director. Gray et al. [1973; 1974] synthesized a nematic liquid crystal that was stable at room temperature and so could be used in display monitors, known as liquid crystal displays; since then, nematic liquid crystals have been rather attractive owing to their applications in high-performance optoelectronic products and their striking rheological properties.

The basic theory that describes the dynamics of nematic liquid crystals is the Ericksen–Leslie dynamic theory, proposed by [Ericksen 1961; Leslie 1966; 1968]. This theory has consistently been applied to many flow problems of nematic liquid crystals, but the equations are complex so that analytic solutions of nematic liquid crystals flows are extremely rare. Consequently, numerical methods are becoming an important tool for solving these highly nonlinear equations.

Many articles treating the flow of nematic liquid crystals can be found (see, for example, [Pieranski and Guyon 1974; Baleo et al. 1992; Chono and Suji 1998; Chono et al. 1998; Carou et al. 2006]). For instance, in [Baleo et al. 1992] elasticity was neglected, in which case the equations reduce to the Ericksen transversely isotropic fluids. In [Chono et al. 1998] the spatial development of the director orientation was studied in tumbling nematic liquid crystals in channel flow. In [Chono and Suji 1998] the flow

---

This work was supported by FAPESP grant number 07/07038-2, CNPq grants numbers 304422/2007-0 and 470764/2007-4, and CAPES grants numbers 4897/09-9 and 2844/10-9. This work was carried out in the framework of the INCT-MACC (CNPq, Brazil).

**Keywords:** nematic liquid crystal, Ericksen–Leslie equations, two-dimensional flow, finite difference.

around a circular cylinder was analyzed. In other studies, such as [Pieranski and Guyon 1974], the investigation was through experimentation. However, to our knowledge, studies using the full Ericksen–Leslie equations for 2D flows are extremely rare.

This paper presents a finite difference technique for solving the full Ericksen–Leslie dynamic equations in two dimensions under the influence of a finite magnetic field.

## 2. Governing equations

We consider the 2D flow of nematic liquid crystals. A magnetic field is applied and we assume the one-constant approximation for the elastic constants. The unitary director  $\mathbf{n}$  and velocity  $\mathbf{v}$  can be written as

$$\mathbf{n} = (\cos \phi, \sin \phi, 0), \quad \phi = \phi(x, y, t), \quad (2-1)$$

$$\mathbf{v} = (u(x, y, t), v(x, y, t), 0), \quad (2-2)$$

where  $\phi$  is the orientation angle of the director. The magnetic field potential (equal to the negative of the magnetic energy) is

$$\Psi = \frac{1}{2}\mu_0\Delta\chi(\mathbf{n} \cdot \mathbf{H})^2, \quad \mathbf{H} = H(\cos \phi_0, \sin \phi_0, 0), \quad |\mathbf{H}| = H < \infty, \quad (2-3)$$

where  $\Delta\chi > 0$  is the magnetic anisotropy,  $H$  is the magnitude of the field, and  $\phi_0$  is a constant. The related external generalized body force  $G_i$  is given by

$$G_i = \frac{\partial \Psi}{\partial n_i} = \mu_0\Delta\chi(\mathbf{n} \cdot \mathbf{H})H_i, \quad (2-4)$$

where  $\mu_0 > 0$  is the permeability of free space.

We shall use the usual Einstein summation convention where appropriate. A comma indicates partial differentiation with respect to the variable it precedes; for example  $n_{i,j}$  denotes the partial derivative of the  $i$ -th component of  $n_i$  with respect to the  $j$ -th variable.

The basic equations for simulating 2D flows of a nematic liquid crystal are the conservation of mass, elastic energy, linear momentum, and angular momentum, which can be written, respectively, in dimensionless form as follows (for details see [Cruz et al. 2010]):

$$u_{,x} + v_{,y} = 0, \quad (2-5)$$

$$(w_F)_{,x} = \frac{1}{\text{ReEr}}[\phi_{,xx} + (\phi_{,y})_{,x}], \quad (w_F)_{,y} = \frac{1}{\text{ReEr}}[(\phi_{,x})_{,y} + \phi_{,yy}], \quad (2-6)$$

$$\begin{aligned} u_{,t} = -(uu)_{,x} - (vu)_{,y} - p_{,x} - w_{F,x} + R_j n_{j,x} + \frac{1}{\text{Re}} & \left[ \frac{1}{2}\alpha_4(u_{,xx} + u_{,yy}) + \Phi_{xx,x} + \Phi_{xy,y} \right] \\ & + \frac{1}{2}\mu_0\Delta\chi H^2 \sin(2(\phi_0 - \phi))\phi_{,x}, \end{aligned} \quad (2-7)$$

$$\begin{aligned} v_{,t} = -(uv)_{,x} - (vv)_{,y} - p_{,y} - w_{F,y} + R_j n_{j,y} + \frac{1}{\text{Re}} & \left[ \frac{1}{2}\alpha_4(v_{,xx} + v_{,yy}) + \Phi_{yx,x} + \Phi_{yy,y} \right] \\ & + \frac{1}{2}\mu_0\Delta\chi H^2 \sin(2(\phi_0 - \phi))\phi_{,y}, \end{aligned} \quad (2-8)$$

$$\begin{aligned} \phi_{,t} = -(u\phi)_{,x} - (v\phi)_{,y} + \frac{1}{\text{Er}\gamma_1} & [\phi_{,xx} + \phi_{,yy}] - \frac{\gamma_2}{2\gamma_1} [(u_{,y} + v_{,x}) \cos(2\phi) + (v_{,y} - u_{,x}) \sin(2\phi)] \\ & - \frac{1}{2}(u_{,y} - v_{,x}) - \frac{\text{Re}}{2\gamma_1}\mu_0\Delta\chi H^2 \sin(2(\phi_0 - \phi)), \end{aligned} \quad (2-9)$$

where  $\text{Re} = \rho UL/\eta$  and  $\text{Er} = UL(\eta/K)$  are the Reynolds and Ericksen numbers, respectively. The coefficient  $\gamma_1 = \alpha_3 - \alpha_2 \geq 0$  is often referred to as the twist or rotational viscosity and the coefficient  $\gamma_2 = \alpha_2 + \alpha_3 = \alpha_6 - \alpha_5$  is called the torsion coefficient. The viscosities  $\alpha_1, \alpha_2, \dots, \alpha_6$  are the Leslie viscosities.

The functions  $\Phi_{xx}, \dots, \Phi_{yy}$  are given by

$$\begin{aligned}\Phi_{xx} = & \alpha_1 \cos^2 \phi (u_{,x} \cos^2 \phi + v_{,y} \sin^2 \phi + \frac{1}{2}(u_{,y} + v_{,x}) \sin(2\phi)) \\ & - (\alpha_2 + \alpha_3) \sin \phi \cos \phi (\phi_{,t} + u\phi_{,x} + v\phi_{,y} + \frac{1}{2}(u_{,y} - v_{,x})) \\ & + (\alpha_5 + \alpha_6)(u_{,x} \cos^2 \phi + \frac{1}{2} \sin \phi \cos \phi (u_{,y} + v_{,x})),\end{aligned}\quad (2-10)$$

$$\begin{aligned}\Phi_{xy} = & \alpha_1 \sin \phi \cos \phi (u_{,x} \cos^2 \phi + v_{,y} \sin^2 \phi + \frac{1}{2}(u_{,y} + v_{,x}) \sin(2\phi)) \\ & + (\alpha_3 \cos^2 \phi - \alpha_2 \sin^2 \phi)(\phi_{,t} + u\phi_{,x} + v\phi_{,y} + \frac{1}{2}(u_{,y} - v_{,x})) \\ & + \frac{1}{2}(\alpha_5 \sin^2 \phi + \alpha_6 \cos^2 \phi)(u_{,y} + v_{,x}) + (\alpha_5 u_{,x} + \alpha_6 v_{,y}) \sin \phi \cos \phi,\end{aligned}\quad (2-11)$$

$$\begin{aligned}\Phi_{yx} = & \alpha_1 \sin \phi \cos \phi (u_{,x} \cos^2 \phi + v_{,y} \sin^2 \phi + \frac{1}{2}(u_{,y} + v_{,x}) \sin(2\phi)) \\ & + (\alpha_2 \cos^2 \phi - \alpha_3 \sin^2 \phi)(\phi_{,t} + u\phi_{,x} + v\phi_{,y} + \frac{1}{2}(u_{,y} - v_{,x})) \\ & + \frac{1}{2}(\alpha_5 \cos^2 \phi + \alpha_6 \sin^2 \phi)(u_{,y} + v_{,x}) + (\alpha_5 v_{,y} + \alpha_6 u_{,x}) \sin \phi \cos \phi,\end{aligned}\quad (2-12)$$

$$\begin{aligned}\Phi_{yy} = & \alpha_1 \sin^2 \phi (u_{,x} \cos^2 \phi + v_{,y} \sin^2 \phi + \frac{1}{2}(u_{,y} + v_{,x}) \sin(2\phi)) \\ & + (\alpha_2 + \alpha_3) \sin \phi \cos \phi (\phi_{,t} + u\phi_{,x} + v\phi_{,y} + \frac{1}{2}(u_{,y} - v_{,x})) \\ & + (\alpha_5 + \alpha_6)(v_{,y} \sin^2 \phi + \frac{1}{2} \sin \phi \cos \phi (u_{,y} + v_{,x})).\end{aligned}\quad (2-13)$$

The terms  $R_j n_{j,x}$  and  $R_j n_{j,y}$  are given by

$$\begin{aligned}R_j n_{j,x} = & \frac{1}{\text{Re}} \left\{ -\gamma_1 \phi_{,x} (\phi_{,t} + u\phi_{,x} + v\phi_{,y} + \frac{1}{2}(u_{,y} - v_{,x})) \right. \\ & \left. - \frac{1}{2} (\gamma_2 \phi_{,x} \cos(2\phi) (u_{,y} + v_{,x}) + \gamma_2 \phi_{,x} \sin(2\phi) (u_{,x} - v_{,y})) \right\},\end{aligned}\quad (2-14)$$

$$\begin{aligned}R_j n_{j,y} = & \frac{1}{\text{Re}} \left\{ -\gamma_1 \phi_{,y} (\phi_{,t} + u\phi_{,x} + v\phi_{,y} + \frac{1}{2}(u_{,y} - v_{,x})) \right. \\ & \left. - \frac{1}{2} (\gamma_2 \phi_{,y} \cos(2\phi) (u_{,y} + v_{,x}) + \gamma_2 \phi_{,y} \sin(2\phi) (u_{,x} - v_{,y})) \right\}.\end{aligned}\quad (2-15)$$

In these equations, the viscosities  $\alpha_1, \dots, \alpha_6$  have been scaled by the factor  $\eta = \alpha_3 - \alpha_2$ .

Equations (2-5) and (2-7)–(2-9) form the complete set of dynamic equations and must be solved subject to suitable boundary conditions in order to find solutions for  $\phi$ ,  $p$ ,  $u$ , and  $v$ .

**2A. Boundary conditions.** To solve (2-5) and (2-7)–(2-9) we impose the following boundary conditions for the velocity field. On rigid boundaries we set  $v_i = 0$  while at fluid entrances (inflows) the normal velocity is specified by  $v_N = V_{\text{inf}}$  and the tangential velocity by  $v_T = 0$ . Here  $N$  denotes normal direction to the boundary and  $T$  denotes the tangential direction. At fluid exits (outflows) the Neumann condition  $v_{i,N} = 0$  is adopted.

The director is strongly anchored on rigid walls. This means that the anchoring angle is set according to the orientation of the rigid wall. Details of this anchoring angle will be given in the section dealing

with numerical results. The choice of the angle of the director at fluid entrances (inflows) is  $\phi = 0$ , and at fluid exits (outflows) we set  $\phi_{,N} = 0$ .

**2B. Numerical procedure.** The numerical method is a standard and robust approach using Chorin's projection method. An interesting but different method was employed in [Svenšek and Žumer 2002]. The momentum equations (2-7) and (2-8), the mass conservation equation (2-5), and the angular momentum equation (2-9) will be solved by a methodology based on the algorithm introduced in [Tomé et al. 2002] as follows.

Assume that, at time  $t_n$ , the velocity field  $v_i(x_k, t_n)$  and the orientation angle of the director  $\phi(x_k, t_n)$  are known and that suitable boundary conditions are provided. To calculate the velocity field  $v_i(x_k, t_{n+1})$ , the pressure  $p(x_k, t_{n+1})$ , the functions  $\Phi_{ij}(x_k, t_{n+1})$ , and the orientation angle of the director  $\phi(x_k, t_{n+1})$ , we proceed in the following manner:

Step 1. Using the values of  $v_i(x_k, t_n)$  and  $\phi(x_k, t_n)$ , solve (2-6) for  $w_F(x_k, t_n)$  and calculate  $w_{F,i}(x_k, t_n)$ ,  $\Phi_{ij}(x_k, t_n)$ , and  $R_j n_{j,i}(x_k, t_n)$  from (2-10)–(2-13), (2-14) and (2-15), respectively.

Step 2. Calculate an intermediate velocity field  $\tilde{v}_i(x_k, t_{n+1})$  from

$$\frac{\partial \tilde{v}_i}{\partial t} = -(v_j v_i)_{,j} - w_{F,i} + R_j n_{j,i} + \frac{1}{2} \mu_0 \Delta \chi H^2 \sin(2(\phi_0 - \phi)) \phi_{,i} + \frac{1}{Re} [\frac{1}{2} \alpha_4 (v_{i,j})_{,j} + \Phi_{ij,j}], \quad (2-16)$$

with  $\tilde{v}_i(x_k, t_n) = v_i(x_k, t_n)$  using the same boundary conditions for the velocity  $v_i(x_k, t_n)$ . This equation is solved by an explicit finite difference method. In [Tomé et al. 1996] it was shown that  $\tilde{v}_i$  possesses the correct vorticity at time  $t_{n+1}$ .

Step 3. Solve the Poisson equation

$$\psi_{,ii}(x_k, t_{n+1}) = \tilde{v}_{i,i}(x_k, t_{n+1}), \quad (2-17)$$

subject to the boundary conditions that  $\psi_{,N} = 0$  on rigid boundaries and inflows and  $\psi = 0$  on outflows [Tomé and McKee 1994].

Step 4. Calculate the final velocity field:

$$v_i(x_k, t_{n+1}) = \tilde{v}_i(x_k, t_{n+1}) - \psi_{,i}(x_k, t_{n+1}). \quad (2-18)$$

Step 5. Determine the pressure field  $p(x_k, t_{n+1})$  [Tomé et al. 1996]:

$$p(x_k, t_{n+1}) = \frac{\psi(x_k, t_{n+1})}{\delta t}. \quad (2-19)$$

Step 6. Calculate the angle of the director  $\phi(x_k, t_{n+1})$  from (2-9). This equation is solved by an explicit finite difference method.

Step 7. Calculate the functions  $\Phi_{ij}(x_k, t_{n+1})$  from (2-10).

### 3. Approximation of the equations by finite differences

The equations contained in the numerical procedure outlined in the previous section are solved by the finite difference method as follows. A staggered grid is employed. This was first introduced in [Harlow and Welch 1965]; it has been used by many investigators because it locally guarantees conservation of mass and momentum while remaining computationally simple.

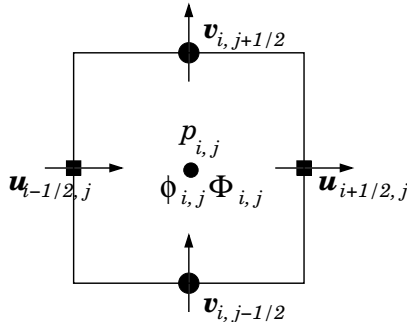


**Figure 1.** 2D staggered cell.

The velocities  $u$  and  $v$  are located at the middle of cell faces while the other quantities ( $\phi$ ,  $\Phi$ ,  $p$ ,  $w_F$ ) are positioned at cell centers. Figure 1 illustrates a typical 2D cell of dimensions  $\delta x \times \delta y$ .

The momentum conservation equations (2-7) and (2-8) and the angular momentum equation (2-9) are solved by the explicit Euler method. The spatial derivatives in the momentum conservation equations are discretized at points  $((i + \frac{1}{2})\delta x, j\delta y)$  and  $(i\delta x, (j + \frac{1}{2})\delta y)$  while the angular momentum equation (2-9), the density of elastic energy (2-6), and the functions  $\Phi_{ij}$  are approximated at cell centers  $(i\delta x, j\delta y)$ . The divergence of  $\Phi_{ij}$ , the gradient of the density of elastic energy  $w_{F,i}$ , and the terms  $R_j n_{j,i}$  are approximated by central differences.

For reasons of space, the details of the finite differences equations involved are not presented here; they can be found in [Cruz et al. 2010].

#### 4. Validation results

The numerical method described in the previous sections was applied to simulate the flow of the nematic liquid crystal MBBA at 25° C. We considered a 2D-channel (see Figure 2) with width  $L$  and length  $C = 10L$ . The boundary conditions for the velocity field were those specified in Section 2A. At the fluid entrance, a fully developed flow was applied:

$$u(y) = -4 \frac{U}{L} \left( y - \frac{L}{2} \right)^2 + U, \quad (4-1)$$

where  $U$  is a prescribed value for velocity.

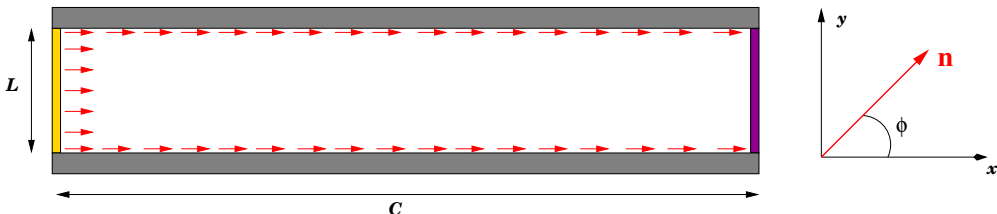


**Figure 2.** Definition of the domain for the simulation of the flow in a 2D channel. The red arrows indicate the boundary conditions used for the calculation of the angle  $\phi$  by means of (2-9).

Leslie viscosities	$\alpha_1$	$\alpha_2$	$\alpha_3$	$\alpha_4$	$\alpha_5$	$\alpha_6$
MBBA near 25° C	-0.0181	-0.1104	-0.001104	0.0826	0.0779	-0.0336
MBBA near 42° C	-0.0036	-0.0310	-0.00218	0.0394	0.0224	-0.01086

**Table 1.** Leslie viscosities for the nematic liquid crystal MBBA, in SI units [Stewart 2004].

Physical parameter	$\Delta\chi$	$\rho$	$\mu_0$	K
Values	$1.219 \times 10^{-6}$	$1088 \text{ kg m}^{-3}$	$12.566 \times 10^{-7} \text{ H m}^{-1}$	$7.5 \times 10^{-12} \text{ N}$

**Table 2.** Physical parameters for the nematic phases of MBBA, in SI units: magnetic anisotropy ( $\Delta\chi$ , unitless) [Stephen and Straley 1974], density ( $\rho$ ) [Stephen and Straley 1974; Stewart 2004], permeability of free space ( $\mu_0$ ), and elastic constant (K). The viscosities at 42° C were taken from [Kneppé et al. 1982].

To simulate this problem, the following input data (specifying the flow) were employed:

- Width of the entry plane  $L = 0.001 \text{ m}$  and velocity scale  $U = 0.00038 \text{ m s}^{-1}$ .

A magnetic field  $H = 1/(4\pi)10^3 \text{ A m}^{-1}$  was applied. The physical parameters, specifying the nematic liquid crystal MBBA at 25°, are given in Tables 1 and 2. With these data we obtain  $\text{Re} = 0.0038$  and  $\text{Er} = 55.38$ . To demonstrate the convergence of the numerical method presented in this paper, we simulated channel flow using four embedded meshes until steady state was achieved. The meshes employed were:

- $M_0$ :  $\delta x = \delta y = 0.000125 \text{ m}$  ( $80 \times 8$  cells),
- $M_1$ :  $\delta x = \delta y = 0.0000625 \text{ m}$  ( $160 \times 16$  cells),
- $M_2$ :  $\delta x = \delta y = 0.00003125 \text{ m}$  ( $320 \times 32$  cells), and
- $M_3$ :  $\delta x = \delta y = 0.000015625 \text{ m}$  ( $640 \times 64$  cells).

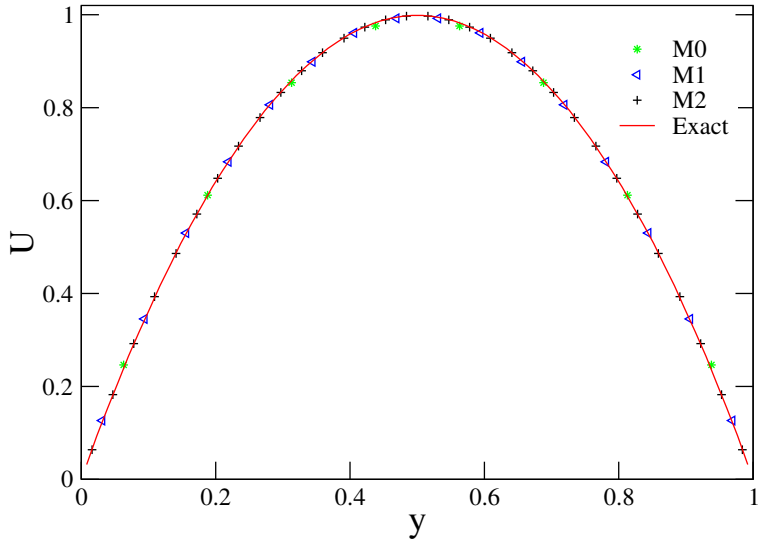
An analytic solution for this problem is not known, so we compared the solutions obtained on meshes  $M_0$ ,  $M_1$ , and  $M_2$  to the solution obtained on the finest mesh,  $M_3$ , which we refer to here to as “exact”.

Figure 3 displays the numerical and the “exact” values of  $u(y)$  at the end of the channel ( $x = 10L$ ). We can see that there is good agreement between the solutions. Moreover, Figure 3 shows that as the mesh is refined the numerical solutions tend to the “exact” solution. Similar results were obtained for the functions  $\Phi_{xx}$ ,  $\Phi_{xy}$ ,  $\Phi_{yx}$ , and  $\Phi_{yy}$ . These results suggest that the numerical method presented in this work is convergent.

## 5. Numerical investigation of nematic liquid crystal flow in a planar 1:4 expansion

In this section we present numerical results from the simulation of the flow of a nematic liquid crystal through a planar 1:4 expansion as illustrated in Figure 4. In this problem, the fluid flows from a channel with width  $2L$  into another channel having width  $8L$ .

This problem is one of the classic benchmarks employed in the study of the development of numerical methods for simulating non-Newtonian fluids. The interest in simulations of this kind of flow comes from the fact that non-Newtonian fluids exhibit a variety of phenomena. A particular point of interest is



**Figure 3.** Numerical simulation of channel flow:  $Re = 0.0038$  and  $Er = 55.38$ . Comparison between the “exact” and the numerical solutions of  $u(y)$  at  $x = 10L$ .

the study of the behavior of vortices in the corners, and vortices that are generated near the expansion entrance (known as lip vortices). The length and intensity of these vortices can be affected by both the Ericksen and Reynolds numbers and the type of expansion as well as by rheological properties of the material such as viscosity and elastic constants.

The boundary conditions for the velocity field were those specified in Section 2A while at the channel entrance the velocity was specified by the fully developed profile given by (4-1).

**Boundary conditions for the angle  $\phi$ .** The boundary conditions for the angle  $\phi$  were specified as follows (for details see Figure 4):

- (1) Along the horizontal walls, the anchoring angle was set to zero, implying parallel alignment to the walls.

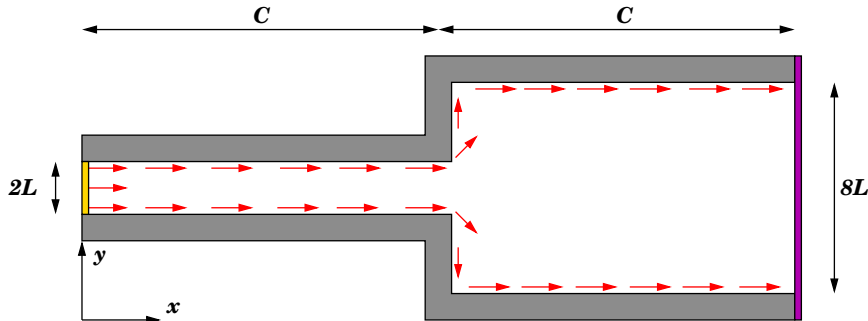


**Figure 4.** Definition of the domain for the simulation of the flow in a 1:4 expansion. The red arrows indicate the boundary conditions used for the calculation of the angle  $\phi$  by (2-9).

- (2) At the expansion entrance, we used:
  - (a)  $\phi = 45^\circ$  (upper lip corner in Figure 4);
  - (b)  $\phi = -45^\circ$  (lower lip corner in Figure 4).
- (3) On the vertical walls (or the expansion walls), we employed:
  - (a)  $\phi = -90^\circ$  at  $x = C$  and  $0 \leq y \leq 3L$ ;
  - (b)  $\phi = 90^\circ$  at  $x = C$  and  $5L \leq y \leq 8L$ .
- (4) At the channel entry defined by  $x = 0$  and  $3L \leq y \leq 5L$ , we set  $\phi = 0$  and at the exit plane,  $x = 2C$  and  $0 \leq y \leq 8L$ , we assumed  $\phi_{,x} = 0$ .

The relevant physical parameters specific to the nematic liquid crystal MBBA at  $25^\circ$  and  $42^\circ$  are presented in Tables 1 and 2, respectively. The remaining parameters specifying the flow were:

- viscosity scales:  $\eta_{25^\circ} = \alpha_3 - \alpha_2 = 0.109296 \text{ Pa}\cdot\text{s}$  and  $\eta_{42^\circ} = \alpha_3 - \alpha_2 = 0.02882 \text{ Pa}\cdot\text{s}$ ;
- mesh (**M**):  $200 \times 40$  cells ( $\delta x = \delta y = 0.0001 \text{ m}$ );
- width of the entry plane:  $2L = 0.001 \text{ m}$ ;

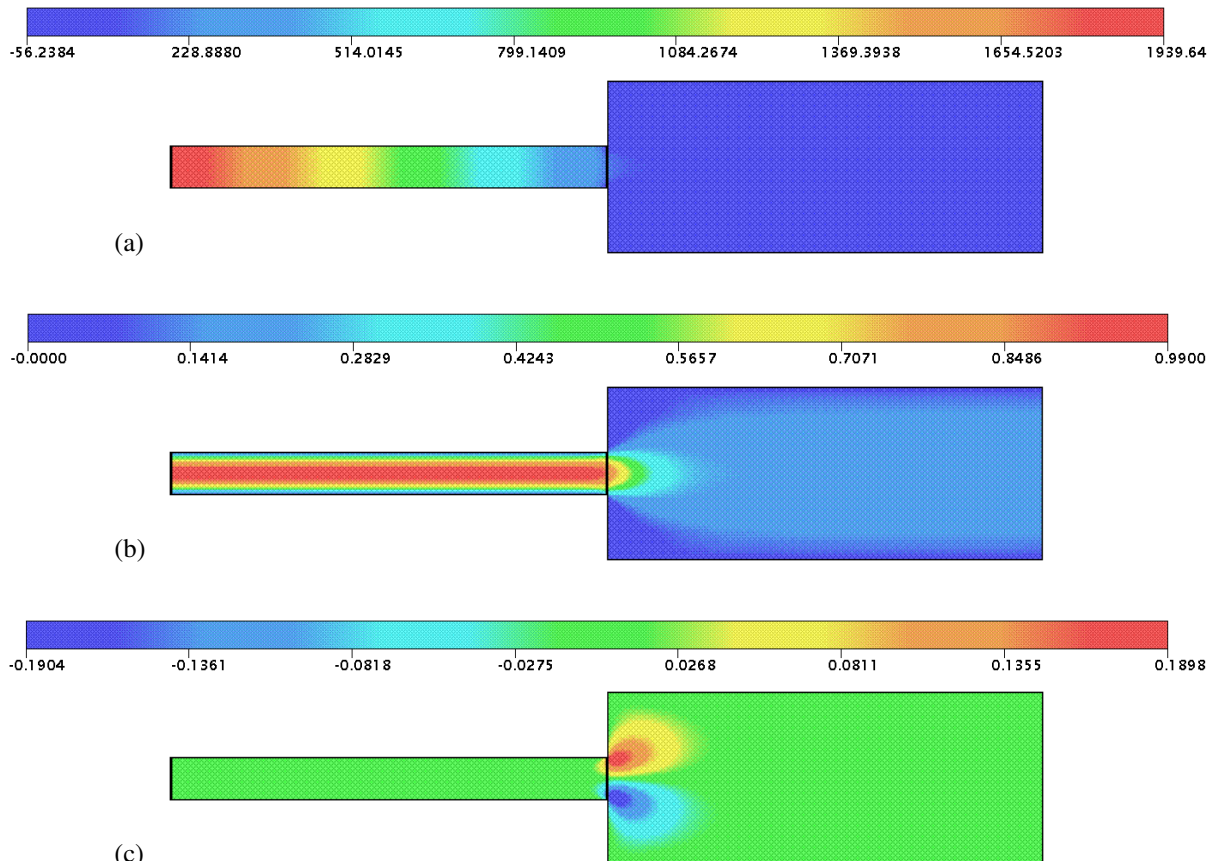


**Figure 5.** Numerical simulation of the flow in a planar 1:4 expansion with  $\text{Re} = 0.005$  and  $\text{Er} = 7.2$  at  $t = 40 \text{ s}$ . Isolines: (a) pressure, (b) velocity  $u$ , and (c) velocity  $v$ .

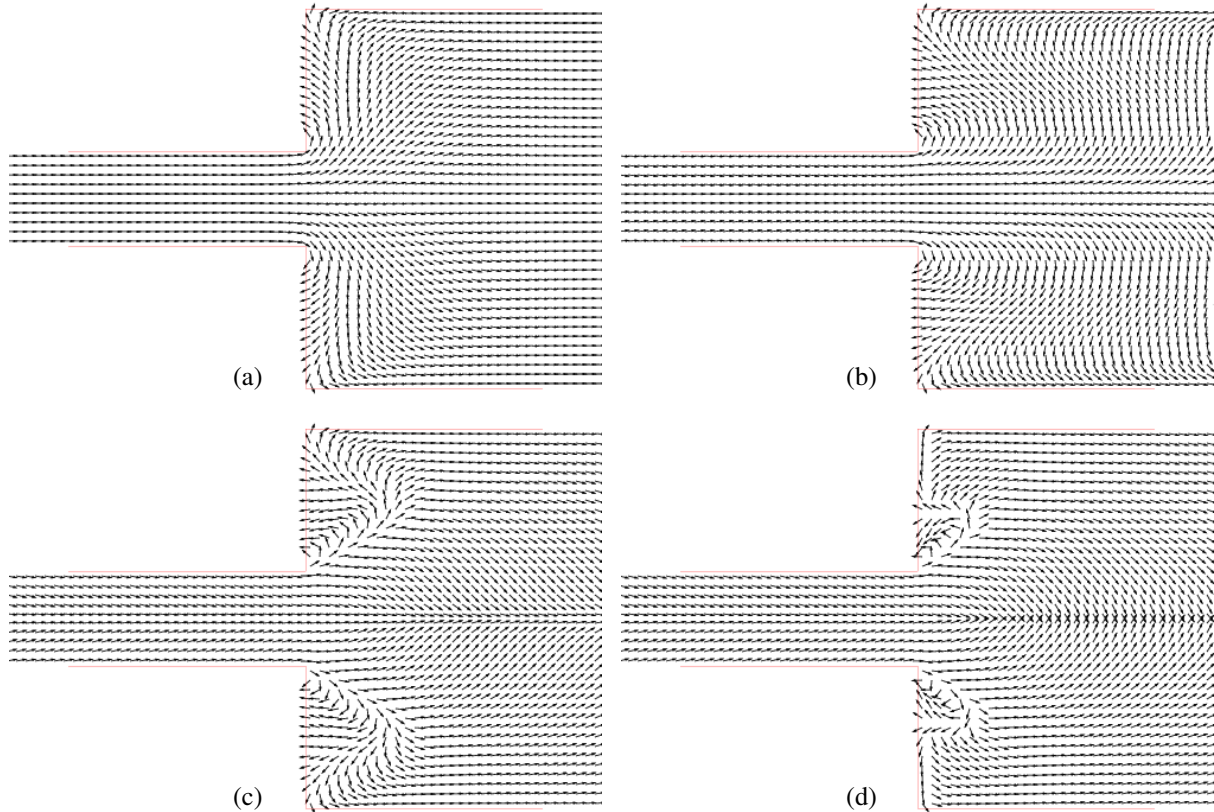


**Figure 6.** Plots of director with  $Re = 0.019$  for different Ericksen numbers: (a)  $Er = 1.9$ , (b)  $Er = 19.2$ , (c)  $Er = 192$ , and (d)  $Er = 1920$ .

- length of the channels:  $C = 0.01 \text{ m}$ ;
- width of the exit plane:  $8L = 0.004 \text{ m}$ ;
- velocity at the entry channel:  $V_{\text{inf}} = 0.00025 \text{ m s}^{-1}$ ;
- velocity scale:  $U = 0.001 \text{ m s}^{-1}$ ;
- length scale:  $L = 0.0005 \text{ m}$ .

The Reynolds number was calculated using the half-width  $L$  of the channel entrance, the velocity scale  $U = 0.001 \text{ m s}^{-1}$ , and the viscosity scales  $\eta_{25^\circ}$  and  $\eta_{42^\circ}$  were selected so that  $Re = 0.005$  and  $Re = 0.019$ , respectively. In the results that follow the following Ericksen numbers ( $Er = UL\eta/K$ ) were employed:

$$Re = 0.005 \quad \begin{cases} K = 7.5 \times 10^{-9} & \Rightarrow Er = 7.2, \\ K = 7.5 \times 10^{-10} & \Rightarrow Er = 72.8, \\ K = 7.5 \times 10^{-11} & \Rightarrow Er = 728, \\ K = 7.5 \times 10^{-12} & \Rightarrow Er = 7286, \end{cases}$$

$$\text{Re} = 0.019 \begin{cases} K = 7.5 \times 10^{-9} & \Rightarrow \text{Er} = 1.9, \\ K = 7.5 \times 10^{-10} & \Rightarrow \text{Er} = 19.2, \\ K = 7.5 \times 10^{-11} & \Rightarrow \text{Er} = 192, \\ K = 7.5 \times 10^{-12} & \Rightarrow \text{Er} = 1920. \end{cases}$$

To observe elastic and viscous effects in the flow, such as the appearance of corner and lip vortices, we simulated this problem for the values of the Reynolds and Erickson numbers given above until a steady state was reached. Each simulation was performed until  $t = 40$  s. Figure 5 displays the isolines of pressure and velocity at time  $t = 40$  s for  $\text{Re} = 0.005$  and  $\text{Er} = 7.2$ . From Figure 5 one can see that the pressure only varies in the  $x$ -direction and the velocity is parabolic within the entrance channel so we can conclude that the steady state has been reached.

A zoom-in on the solutions obtained for the director and the streamlines near the expansion entrance for the case  $\text{Re} = 0.019$  is displayed in Figures 6 and 7 while Figures 8 and 9 show the results obtained with  $\text{Re} = 0.005$ .

For  $\text{Er} = 1.9, 19.2$  (see Figures 6a and 6b) the director profile did not display a great deal of variation: at the centerline the vectors are parallel while away from it, the vectors are diverging pointing to the expansion walls. For  $\text{Er} = 192$  we can observe significant disturbances in the director profile where one

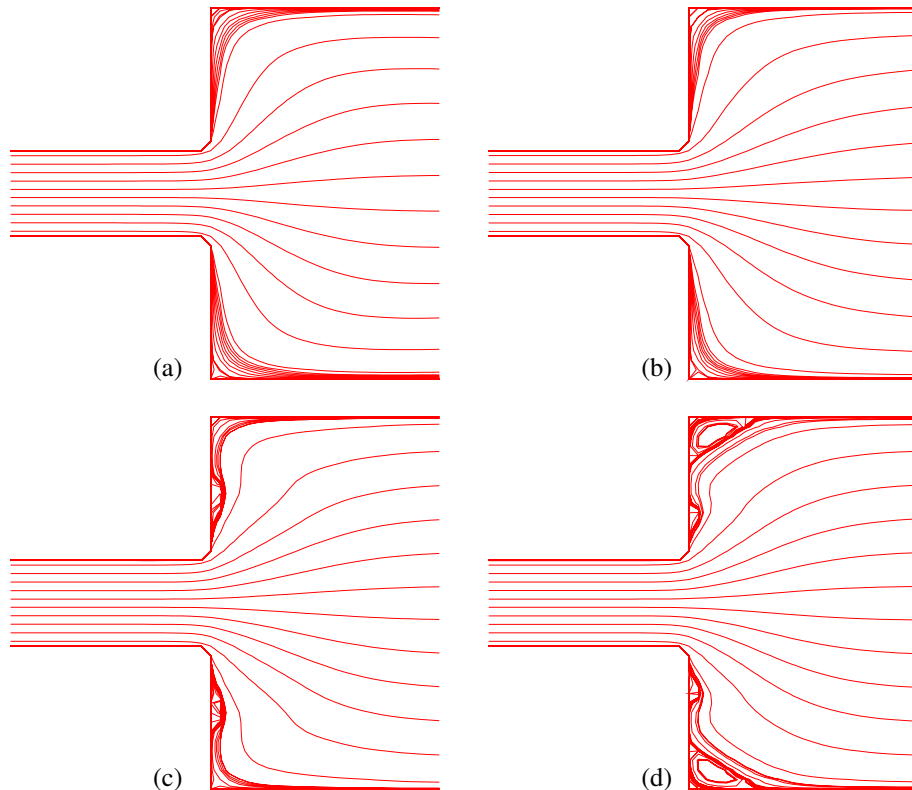


**Figure 7.** Plots of streamlines with  $\text{Re} = 0.019$  for different Erickson numbers: (a)  $\text{Er} = 1.9$ , (b)  $\text{Er} = 19.2$ , (c)  $\text{Er} = 192$ , and (d)  $\text{Er} = 1920$ .

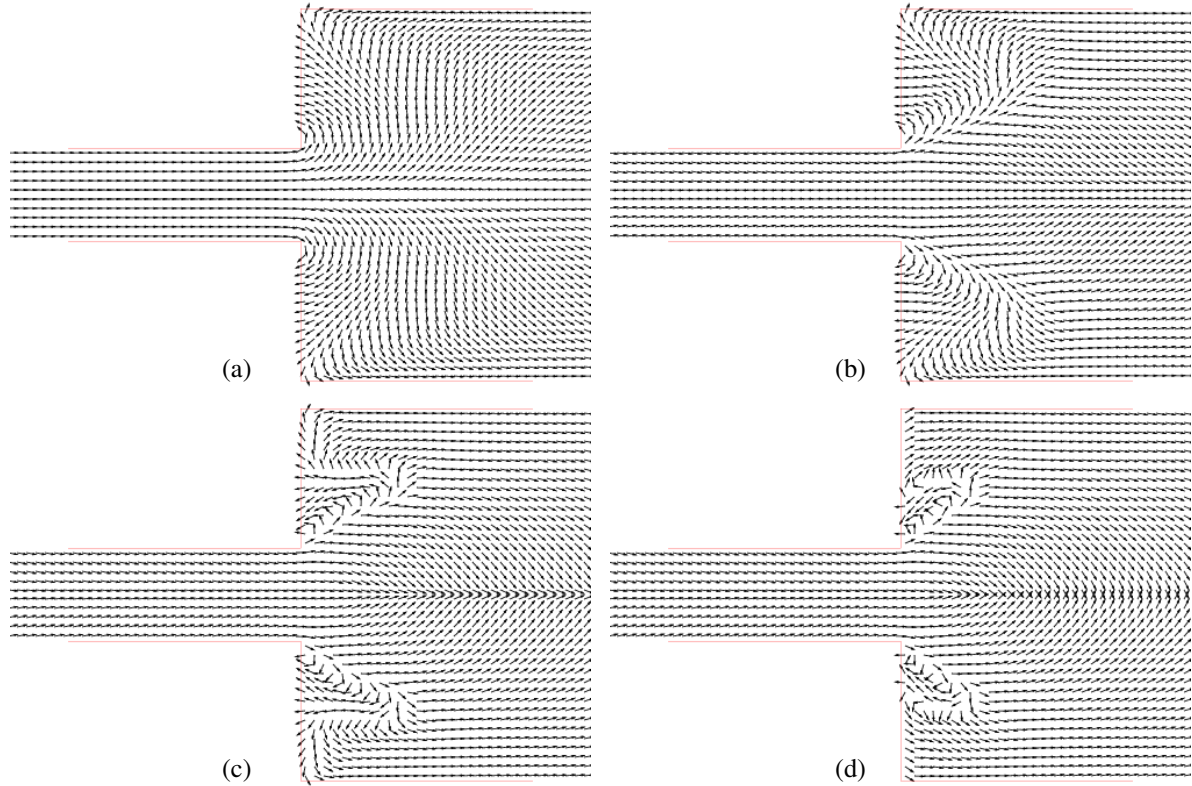


**Figure 8.** Plots of director with  $Re = 0.005$  for different Ericksen numbers: (a)  $Er = 7.2$ , (b)  $Er = 72.8$ , (c)  $Er = 728$ , and (d)  $Er = 7286$ .

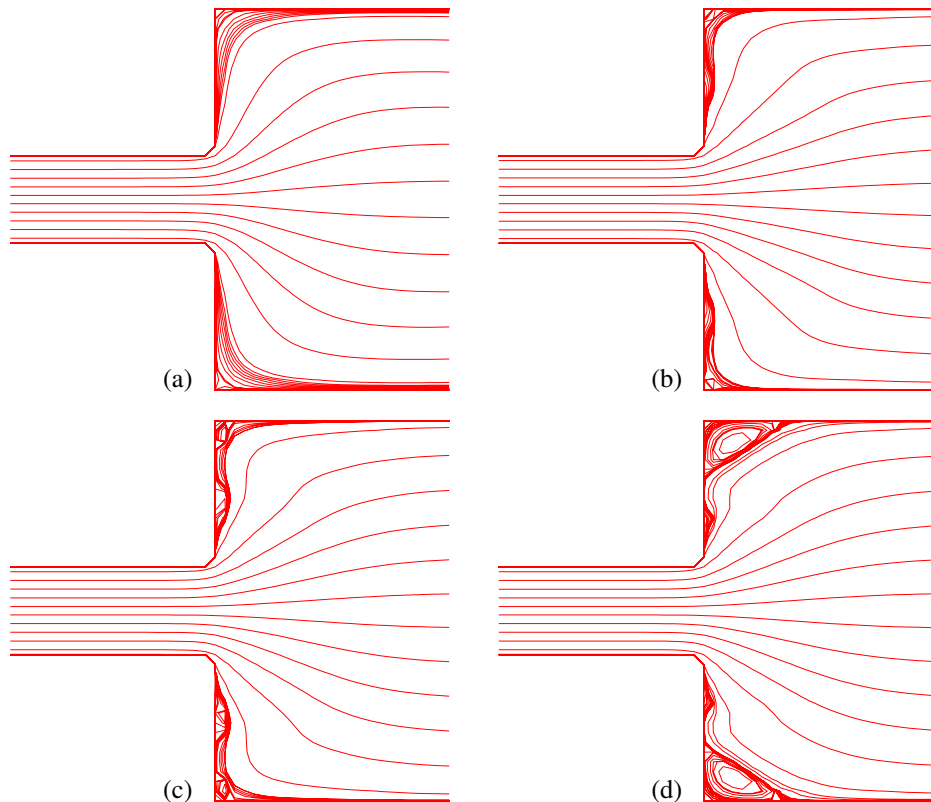
can see the appearance of a small lip vortex (see Figure 6c). Near the symmetry axis, we can see that the director is converging to the centerline. For  $Er = 1920$  (see Figure 6d), the director, at the symmetry axis, is perpendicular to the centerline. We now observe a larger lip vortex concentrated near the entrance of the expansion walls.

The corresponding streamlines displayed in Figure 7 are interesting since they display a lip vortex for  $Er = 192, 1920$  (see Figures 7c and 7d). As the Ericksen number is increased to  $Er = 1920$  a large corner vortex is generated. These results show that the appearance of the lip and corner vortices were caused by an increase in the Ericksen number. This phenomenon is similar to that observed by many authors in certain viscous anisotropic fluids through a 4:1 contraction (for example, [Yoo and Na 1991; Nigen and Walters 2002; Alves et al. 2003]) where the corner vortex decreases with increasing elasticity. The results obtained with  $Re = 0.005$  were similar to those obtained with  $Re = 0.019$  except that the lip vortex appears first at the smaller Ericksen number of  $Er = 72.8$ . The occurrence of the corner vortex is also anticipated (see Figure 9b). Tables 3 and 4 display the size of vortices obtained for each value of the Ericksen number employed in the simulations. We see in these tables that the size of the corner vortices encountered for  $Re = 0.005$  are larger than those obtained with  $Re = 0.019$ . We believe that the appearance of larger corner vortices in the case  $Re = 0.005$  was due to viscous and elastic forces associated with a smaller  $Re$  and higher  $Er$ .

Er	1.9	19.2	192	1920
length	0.0000	0.0000	0.1000	1.441506

**Table 3.** Length of the corner vortices as a function of the Ericksen number for  $Re = 0.019$ .

Er	7.2	72.8	728	7280
length	0.0000	0.0500	0.618543	1.738053

**Table 4.** Length of the corner vortices as a function of the Ericksen number for  $Re = 0.005$ .**Figure 9.** Plots of streamlines with  $Re = 0.005$  for different Ericksen numbers: (a)  $Er = 7.2$ , (b)  $Er = 72.8$ , (c)  $Er = 728$ , and (d)  $Er = 7286$ .

## 6. Conclusions

This paper has dealt with the development of a numerical method for simulating 2D flows of nematic liquid crystals described by the Ericksen–Leslie equations. The numerical technique was based on the method developed in [Tomé et al. 2002] and used the finite difference method. The validation of the technique was performed through the simulation of the flow in a channel using four refined meshes:  $M_0$ ,  $M_1$ ,  $M_2$ , and  $M_3$ . An analytic solution for this problem is not yet available, so we compared the solutions

obtained on meshes  $M_0$ ,  $M_1$ , and  $M_2$  to the solution obtained on the finest mesh  $M_3$ , which we called “exact”. Good agreement was obtained between the numerical solutions on the coarser meshes and the solution on mesh  $M_3$ . We then applied the numerical technique to simulate the flow through a planar 1:4 expansion for various values of the Ericksen number. The results showed that as the Ericksen number is increased interesting effects were observed: the orientation of the director displayed the appearance of a lip vortex while increasing the Ericksen number had the effect of producing a lip vortex at the entrance of the expansion. Increasing the Ericksen number further resulted in the appearance of a corner vortex that increased in size with increasing Ericksen number. The results showed that both elasticity and viscosity had a considerable effect on the formation of corner and lip vortices.

## References

- [Alves et al. 2003] M. A. Alves, P. J. Oliveira, and F. T. Pinho, “Numerical simulation of viscoelastic contraction flows”, pp. 826–829 in *Computational fluid and solid mechanics*, edited by K. Bathe, Elsevier, Amsterdam, 2003.
- [Baleo et al. 1992] J. N. Baleo, M. Vincent, P. Navard, and Y. Demay, “Finite element simulation of flow and director orientation of viscous anisotropic fluids in complex 2D geometries”, *J. Rheol.* **36**:4 (1992), 663–701.
- [Carou et al. 2006] J. Q. Carou, B. R. Duffy, N. J. Mottram, and S. K. Wilson, “Shear-driven and pressure-driven flow of a nematic liquid crystal in a slowly varying channel”, *Phys. Fluids* **18**:2 (2006), article ID 027105.
- [Chono and Suji 1998] S. Chono and T. Suji, “Numerical simulation of nematic liquid crystalline flows around a circular cylinder”, *Mol. Cryst. Liq. Cryst.* **309** (1998), 217–236.
- [Chono et al. 1998] S. Chono, T. Tsuji, and M. M. Denn, “Spatial development of director orientation of tumbling nematic liquid crystals in pressure-driven channel flow”, *J. Non-Newton. Fluid Mech.* **79**:2–3 (1998), 515–527.
- [Cruz et al. 2010] P. A. Cruz, M. F. Tomé, I. W. Stewart, and S. McKee, “Numerical solution of the Ericksen–Leslie dynamic equations for two-dimensional nematic liquid crystal flows”, Report 21, Department of Mathematics and Statistics, University of Strathclyde, Glasgow, 2010.
- [Ericksen 1961] J. L. Ericksen, “Conservation laws for liquid crystals”, *J. Rheol.* **5**:1 (1961), 23–34.
- [Friedel 1922] G. Friedel, “Les états mésomorphes de la matière”, *Annales Physique (Paris)* **18** (1922), 273–474.
- [Gray et al. 1973] G. W. Gray, K. J. Harrison, and J. A. Nash, “New family of nematic liquid crystals for displays”, *Electron. Lett.* **9**:6 (1973), 130–131.
- [Gray et al. 1974] G. W. Gray, K. J. Harrison, J. A. Nash, J. Constant, D. S. Hulme, J. Kirton, and E. P. Raynes, “Stable, low melting nematogens of positive dielectric anisotropy for display devices”, pp. 617–643 in *Liquid crystals and ordered fluids*, vol. 2, edited by J. F. Johnson and R. S. Porter, Plenum Press, New York, 1974.
- [Harlow and Welch 1965] F. H. Harlow and J. E. Welch, “Numerical calculation of time-dependent viscous incompressible flow of fluid with free surface”, *Phys. Fluids* **8**:12 (1965), 2182–2189.
- [Knepp et al. 1982] H. Knepp, F. Schneider, and N. K. Sharma, “Rotational viscosity  $\gamma_1$  of nematic liquid crystals”, *J. Chem. Phys.* **77**:6 (1982), 3203–3208.
- [Lehmann 1889] O. Lehmann, “Über fliessende Krystalle”, *Zeitschrift für physiologische Chemie* **4** (1889), 462–472.
- [Leslie 1966] F. M. Leslie, “Some constitutive equations for anisotropic fluids”, *Q. J. Mech. Appl. Math.* **19**:3 (1966), 357–370.
- [Leslie 1968] F. M. Leslie, “Some constitutive equations for liquid crystals”, *Arch. Ration. Mech. An.* **28**:4 (1968), 265–283.
- [Nigen and Walters 2002] S. Nigen and K. Walters, “Viscoelastic contraction flows: comparison of axisymmetric and planar configurations”, *J. Non-Newton. Fluid Mech.* **102**:2 (2002), 343–359.
- [Pieranski and Guyon 1974] P. Pieranski and E. Guyon, “Transverse effects in nematic flows”, *Phys. Lett. A* **49**:3 (1974), 237–238.
- [Reinitzer 1888] F. Reinitzer, “Beiträge zur kenntniss des cholesterins”, *Monatshefte für Chemie* **9**:1 (1888), 421–441.
- [Stephen and Straley 1974] M. J. Stephen and J. P. Straley, “Physics of liquid crystals”, *Rev. Mod. Phys.* **46**:4 (1974), 617–704.

- [Stewart 2004] I. W. Stewart, *The static and dynamic continuum theory of liquid crystals: a mathematical introduction*, CRC, London, 2004.
- [Svenšek and Žumer 2002] D. Svenšek and S. Žumer, “Hydrodynamics of pair-annihilating disclination lines in nematic liquid crystals”, *Phys. Rev. E* **66**:2 (2002), 021712–021717.
- [Tomé and McKee 1994] M. F. Tomé and S. McKee, “GENSMAC: a computational marker and cell method for free surface flows in general domains”, *J. Comput. Phys.* **110**:1 (1994), 171–186.
- [Tomé et al. 1996] M. F. Tomé, B. Duffy, and S. McKee, “A numerical technique for solving unsteady non-Newtonian free surface flows”, *J. Non-Newton. Fluid Mech.* **62**:1 (1996), 9–34.
- [Tomé et al. 2002] M. F. Tomé, N. Mangiavacchi, J. A. Cuminato, A. Castelo, and S. McKee, “A finite difference technique for simulating unsteady viscoelastic free surface flows”, *J. Non-Newton. Fluid Mech.* **106**:2–3 (2002), 61–106.
- [Yoo and Na 1991] J. Y. Yoo and Y. Na, “A numerical study of the planar contraction flow of a viscoelastic fluid using the SIMPLER algorithm”, *J. Non-Newton. Fluid Mech.* **39**:1 (1991), 89–106.

Received 13 Aug 2010. Revised 13 Dec 2010. Accepted 10 Jan 2011.

PEDRO A. CRUZ: [pedroac@icmc.usp.br](mailto:pedroac@icmc.usp.br)

Department of Applied Mathematics and Statistics, University of São Paulo, Av. Trabalhador São-carlense, 400, 13560-970 São Carlos, SP, Brazil

MURILO F. TOMÉ: [murilo@icmc.usp.br](mailto:murilo@icmc.usp.br)

Department of Applied Mathematics and Statistics, University of São Paulo, Av. Trabalhador São-carlense, 400, 13560-970 São Carlos, SP, Brazil

IAIN W. STEWART: [i.w.stewart@strath.ac.uk](mailto:i.w.stewart@strath.ac.uk)

Department Mathematics and Statistics, University of Strathclyde, Livingstone Tower, 26 Richmond street, Glasgow, G1 1XH, United Kingdom

SEAN MCKEE: [s.mckee@strath.ac.uk](mailto:s.mckee@strath.ac.uk)

Department Mathematics and Statistics, University of Strathclyde, Livingstone Tower, 26 Richmond street, Glasgow, G1 1XH, United Kingdom

## CRITICAL THRESHOLD AND UNDERLYING DYNAMICAL PHENOMENA IN PEDESTRIAN-INDUCED LATERAL VIBRATIONS OF FOOTBRIDGES

STEFANO LENCI AND LAURA MARCHEGGIANI

The problem of lateral vibrations of footbridges due to the synchronization of the pedestrians' motion with that of the supporting structure is analyzed by means of a 3D discrete time model. The map is linear in the mechanical part, and nonlinear in the synchronization part. A very simple and predictive formula is obtained for the critical number of pedestrians, which also takes into account the imperfect resonance between the pedestrians' natural frequencies and the bridge frequency. It is shown that the underlying mechanism triggering the sudden appearance of swaying bridge motion is a perturbation of a pitchfork bifurcation. The results presented in this paper are not related to a specific real case and are based on a quite reasonable hypothesis, and therefore it is expected that they have general validity.

### 1. Introduction

As a consequence of the technological development of new materials and of the architectural trend toward lightness and slenderness, modern footbridges have small natural frequencies, which can resonate with those of the pedestrian-induced load [Živanović et al. 2005; Venuti and Bruno 2009], which are in the range 1.4–2.4 Hz for vertical forcing and in the range 0.7–1.2 Hz for horizontal (lateral) forcing. In this situation unwanted large bridge motions may occur.

Various footbridges have experienced excessive lateral vibrations due to pedestrian-induced loads; the most famous is the London Millennium Bridge, which underwent, on its opening day, large horizontal vibrations due to the synchronization of the pedestrians' motion with the natural modes of the structure [Dallard et al. 2001a; 2001b]. Other bridges which have suffered similar problems are the Toda Park Bridge [Fujino et al. 1993; Nakamura and Kawasaki 2006] and the Maple Valley Bridge [Nakamura and Kawasaki 2006] in Japan, the Solferino Footbridge in Paris [Danbon and Grillaud 2005], and the Alexandra Bridge in Ottawa [Dallard et al. 2001a].

The pedestrian-induced lateral vibrations occurred in bridges of different structural types (suspension, cable-stayed, and steel girder bridges) as well as on footbridges made of different materials (steel, composite steel-concrete, and reinforced and prestressed concrete) [Živanović et al. 2005]. It is therefore confirmed that a large-enough crowd of pedestrians can induce strong lateral vibrations on footbridges of *any* type, although this requires the lateral mode to have a low-enough natural frequency [Dallard et al. 2001a], approximately below 1.2 Hz, as stated.

The phenomenon behind pedestrian-induced lateral vibrations is that of synchronous lateral excitation [Dallard et al. 2001a; Strogatz et al. 2005; Živanović et al. 2005; Eckhardt et al. 2007]. People walking in a crowd exhibit a random level of synchrony, and in general produce a lateral force on the bridge. In fact, even if the bridge is still and the pedestrians are not synchronized at all, due to the

---

**Keywords:** synchronization, discrete time model, Millennium Bridge, lateral induced vibrations, bridge-pedestrian coupling.

stochasticity of the process the net force, which is the sum of all the lateral forces applied to the bridge by the footsteps of pedestrians, is not null, although it is possibly small. This small force produces small oscillations of the bridge.

As soon as the small bridge vibrations become perceptible to the unconscious human cognition processes, pedestrians tend spontaneously to walk in synchrony with the bridge, by slightly changing their walking frequency and phase. Of course, this tendency is somehow proportional to the vibration amplitude, and so it is very small, and possibly negligible, for very small displacements. However, it is believed that this phenomenon starts for very low levels of amplitude of the motion, well below the amplitude threshold perceived by conscious feeling.

This instinctive behavior, which is the mechanism through which the pedestrians interact with the bridge, produces an increase of the synchronization level, and the associated net force grows. This establishes an unwanted positive feedback loop, where the increase in oscillation amplitude causes pedestrians to increase their lateral footfall forcing and their level of synchrony, by following the movements of the deck in order to balance themselves [Dallard et al. 2001a; 2001b]: the more the bridge moves, the more the crowd pushes it to move further.

It has been observed that for potentially susceptible spans there is a critical number of pedestrians  $N_{cr}$  that will cause the vibrations to increase *suddenly* to unacceptable levels. The oscillations are small below  $N_{cr}$  and, due to the synchronization, they increase rapidly above  $N_{cr}$ . This critical threshold is of great practical interest, and its prediction is the goal of almost all studies. This paper aims to provide a simple and reliable analytical prediction of  $N_{cr}$ , as well as to further understanding of the overall phenomenon.

The nature of the problem is nonlinear, as has been confirmed, for example, by tests performed on the London Millennium Bridge [Dallard et al. 2001a]; in spite of this, however, it can be detected within a mechanically linear framework, since even the “large” oscillations are orders of magnitude smaller than the span length. The nonlinearity is only in the interaction between the structure and pedestrians.

Several papers have recently addressed this topic, even if a standard and generally accepted model of pedestrian-induced lateral dynamic loading and of dynamical interaction with the bridge is still missing. Živanović et al. [2005] have performed a comprehensive review of the existing literature on the topic until 2003, while an updated review can be found in [Venuti and Bruno 2009].

Early studies on pedestrian-induced vibrations of footbridges [Blanchard et al. 1977; Matsumoto et al. 1978; Wheeler 1980] concerned only the measurement and modeling of the *vertical* component of pedestrian load on a motionless surface.

Dallard et al. [2001a; 2001b] have conducted a series of controlled crowd tests on the Millennium Bridge and have proposed a load model based on empirical observations. Also a formula has been obtained for the critical number of pedestrians; it actually depends only on the modal damping of the bridge through a proportionality constant which is strictly related to the specific real case-study (the Millennium Bridge). The findings of the present paper extend somewhat these works, by better highlighting the nature of this constant (for example, that it depends on the bridge natural frequency).

Nakamura [2004] has proposed an interactive forcing model analogous to the previous one, but which allows the schematization of the self-limiting nature of the synchronization phenomenon and the prediction of the steady-state amplitude. Also this model is based on coefficients which have been estimated from experimental tests [Fujino et al. 1993; Nakamura and Kawasaki 2006] and cannot easily be generalized to other footbridges.

In [Newland 2003] the problem is approached by referring to the interaction phenomenon between fluid flow and structures which is widely studied in wind engineering and commonly known as lock-in. His model includes the empirical assumption that 40% of the pedestrians are synchronized with the bridge lateral frequency, independent of the amplitude of the oscillations.

Fujino et al. [1993] have adopted a model of harmonic forcing by empirically tuning a synchronization parameter for the lateral vibrations of the Toda Park Bridge (according to their experimental data). This model does not predict any sudden transition to a vibrating state of the bridge but assumes a continuous increase in the vibration amplitude as the number of pedestrians increases.

Roberts [2005] has schematized the interaction between the pedestrians and the footbridge assuming that synchronization occurs when the pedestrians' motion is larger than the bridge motion; from this critical condition, he has obtained a limit number of pedestrians.

In [Ricciardelli and Pizzimenti 2007] a systematic experimental campaign has been performed aimed at characterizing dynamically the lateral force exerted by pedestrians on footbridges, both in the case of a still deck and in the case of a laterally moving deck; deterministic and stochastic lateral loading models for the static case have been provided and the bases have been put in place for more sophisticated dynamic models including crowd-structure interaction. The mechanism of crowd synchronization has been investigated only from the qualitative point of view, deferring quantitative study and modeling until after further measurements.

The excessive lateral vibrations of the Solferino Bridge in Paris have been explained in [Blekherman 2007] on the basis of autoparametric resonance by using a double pendulum model; the process of possible synchronization of pedestrian loading with the relevant vibrational modes, which are nonlinearly coupled in a ratio of 2:1 between their frequencies, depends on the achievement of parametric resonance.

Piccardo and Tubino [2008] have performed an interesting extensive critical analysis of the excitation mechanisms identified in the literature and they have proposed a new forcing model based on experimental tests carried out on harmonically moving platforms [Dallard et al. 2001a]. The force exerted by pedestrians is modeled as harmonic with an amplitude depending on the deck lateral displacement, and a simple criterion defining the limit pedestrian mass is introduced. They mainly ascribe to a mechanism of parametric excitation the lateral sway motion induced by crowds in very flexible, lowly damped footbridges, with a first lateral natural frequency around 0.5 Hz corresponding to half of the first lateral walking frequency.

In Venuti et al. [2007] a first-order model has been developed based on the mass conservation equation, in order to macroscopically describe the dynamics of the crowd in the framework of hydrodynamic modeling. The crowd, considered as a pedestrian flow, is assumed to behave like a continuous compressible fluid; the structural system is modeled by means of a generalized single degree of freedom (SDOF) model. The two-way interaction between the crowd and the structure is studied. This model permits taking into account the triggering of the lock-in and its self-limited nature, previously explained only in [Strogatz et al. 2005]. The effects of the two different kinds of synchronization, that is, between the pedestrians and the structure and among the pedestrians, are introduced; the presence of different frequency components in the overall force exerted by the pedestrians is considered. Some parameters, used in the formulation of the model, come from reasonable qualitative considerations about pedestrian behavior and would require specific experimental tests to be confirmed.

In [Bodgi et al. 2007] a similar approach has been adopted to simulate the mechanics of synchronous lateral excitation induced by pedestrians on footbridges.

Strogatz et al. [2005] have been the first, to the best of our knowledge, to mathematically describe and predict the simultaneous growth of bridge movement and crowd synchronization, an observation that was unexplained in previous models but that is confirmed by analyses of video footage [Arup 2000] recorded during overcrowding conditions on real footbridges [Fujino et al. 1993; Dallard et al. 2001a]. They proposed a model (called SAMEO in [Marcheggiani and Lenci 2010] from the initials of the authors) which is particularly interesting for its contribution to the physical-mathematical explanation of the underlying mechanical event, as well as for the reasonable description of the phenomenon itself.

The SAMEO model is quite simple in its formulation and general enough to be possibly applied to any bridge at risk of synchronous lateral excitation. It models the bridge as a SDOF oscillator that interacts nonlinearly with each pedestrian. The pedestrians are modeled as limit-cycle phase oscillators (this choice comes from a similitude with biological systems, for example, fireflies). The key parameter of the model,  $C$ , measures the pedestrians sensitivity to bridge lateral vibrations; it can be determined only experimentally.

The SAMEO model has been investigated in depth in [Marcheggiani and Lenci 2010], where extensive numerical simulations have been performed in order to detect the effects of the main parameters on the system's response, in particular on the critical threshold. Various extensions have been proposed to model some important aspects not considered in [Strogatz et al. 2005], such as, for example, the self-interaction between pedestrians.

Although the original model and its extensions are simple in their formulation and meaning, they are quite involved in terms of the associated equations of motion, which is a set of  $N + 2$  ( $N$  being the number of pedestrians) nonlinear ordinary differential equations. This system can be fully solved only numerically, although some approximated analytical techniques have been obtained in [Abrams 2006] to get some partial information. This is a limitation of the model, together with the fact that it does not provide immediate information.

In order to overcome the previous drawbacks, in [Lenci and Marcheggiani 2008] a simplified model is proposed and applied with some success to the case of the Millennium Bridge. The main idea is that of passing from ordinary differential equations to maps, that is, from a continuous time system to a discrete time one. In particular, a peak-to-peak map [Candaten and Rinaldi 2000], similar to that introduced by Lorenz in discovering chaotic attractors, has been considered and analyzed in depth. The discrete time permits simple computations (which can be performed by hand), and provides a simple but very predictive formula for  $N_{\text{cr}}$  and a better understanding of the dynamical phenomena lurking in the background.

The work [Lenci and Marcheggiani 2008] is continued in this paper; *another* discrete time model is proposed, now based on the stroboscopic Poincaré map (instead of the peak-to-peak map). The mechanical part is described by the position  $x$  and velocity  $y$ , while the bridge-pedestrian interaction is described by a new state variable  $\sigma$  measuring the degree of synchronization of the pedestrians. We thus get a 3D map, linear in the mechanical part and nonlinear only in the interaction part, whose behavior is analyzed *without* exact knowledge of the evolution law for  $\sigma$ . Just its overall properties and local behavior are used, thus providing a very general analysis, which in particular extends that of [Lenci and Marcheggiani

2008]. The main results are obtained by a bifurcation analysis of the fixed points of the map, which of course is specific to the considered simplified model.

This paper is organized as follows. In Section 2 the mechanical model is illustrated leading to the mechanical part of the discrete time model. Then, the pedestrian-bridge interaction is analyzed in Section 3, where the main properties of the third evolution law are discussed. The fixed points of the map, which are the dynamical behaviors of interest for the computation of the critical threshold, are considered in Section 4, where a simple formula for  $N_{\text{cr}}$  is obtained, and where the effect of imperfections is discussed. Some properties of the map in the resonant case are discussed in Section 5, and conclusions are presented in Section 6.

## 2. Mechanical model

Based on experience in real cases, in particular on that of the London Millennium Bridge mentioned in Section 1, we assume that the phenomenon of *lateral* synchronization involves only one lateral mode  $\varphi(Z)$  of the structure, so that the mechanical equation of motion is

$$M \ddot{X}(T) + B \dot{X}(T) + K X(T) = F(T), \quad (1)$$

where  $M$ ,  $B$ , and  $K$  are the modal mass, damping, and stiffness, respectively, and  $X(T)$  is the modal amplitude. Note that  $M$  includes also the mass of the pedestrians, and in general is not a fixed number. However, in real cases the mass of pedestrians is about 10–15% of the total mass, and so it is expected that it does not play a key role.  $F(T)$  is the modal force, that is, the projection on the considered mode  $\varphi(Z)$  of the force  $\bar{F}(Z, T)$  exerted by pedestrians along the span,  $F(T) = \int_0^L \bar{F}(Z, T) \varphi(Z) dZ$ . In fact, the load of each pedestrian depends not only on the force he applies on the bridge, but also on his position  $Z \in [0, L]$  along the span.

The definitions

$$\Omega = \sqrt{\frac{K}{M}}, \quad t = \Omega T, \quad \xi = \frac{B}{2\sqrt{MK}} = \frac{B\Omega}{2K}, \quad x(t) = X(T), \quad f(t) = \frac{F(T)}{K}, \quad (2)$$

where  $\Omega$  is the natural frequency of the considered mode, permit us to rewrite (1) in the form

$$\ddot{x}(t) + 2\xi\dot{x}(t) + x(t) = f(t), \quad (3)$$

which will be used in the following. Note that the time  $t$  is dimensionless, while  $x$  has the dimension of length.

**2.1. A single pedestrian and the stroboscopic Poincaré map.** We initially consider the effect of a single pedestrian by assuming

$$f(t) = g \sin(\omega_p t - \phi), \quad (4)$$

where:

- $g > 0$  is the dimensionless amplitude, such that  $G = gK \approx 30N$  is the maximum lateral force exerted by a pedestrian [Belli et al. 2001; Marcheggiani and Lenci 2010];
- $\omega_p$  is the dimensionless (circular) frequency, such that  $f_p = \Omega_p/(2\pi) = \Omega\omega_p/(2\pi) = 0.7\text{--}1.2\text{ Hz}$  is the pedestrian footstep native frequency [Živanović et al. 2005]; and

- $\phi \in [0, 2\pi]$  is the pedestrian phase, which depends on the time the pedestrian enters the bridge.

Equation (4) is an approximation of the real force, since experimental data concerning lateral walking forces on a still surface [Bodgi et al. 2007; Ricciardelli and Pizzimenti 2007] have shown that it is much closer to a square wave than to a harmonic force [Belli et al. 2001]. However, expression (4) can be considered as the first term in the Fourier series of the real excitation, thus capturing the most important energy content and maintaining the simple expression needed for analytical computations.

The solution of (3) and (4) starting from  $x(0) = x_n$  and  $\dot{x}(0) = y_n$  is

$$x(t) = e^{-\xi t} [c_1 \sin(t\sqrt{1-\xi^2}) + c_2 \cos(t\sqrt{1-\xi^2})] + g[d_1 \sin(\omega_p t) + d_2 \cos(\omega_p t)], \quad (5)$$

where

$$\begin{aligned} d_1 &= \frac{(1 - \omega_p^2) \cos(\phi) - 2\xi \omega_p \sin(\phi)}{(1 - \omega_p^2)^2 + (2\xi \omega_p)^2}, & d_2 &= \frac{-(1 - \omega_p^2) \sin(\phi) - 2\xi \omega_p \cos(\phi)}{(1 - \omega_p^2)^2 + (2\xi \omega_p)^2}, \\ c_1 &= \frac{\xi x_n + y_n - \omega_p g d_1 - \xi g d_2}{\sqrt{1 - \xi^2}}, & c_2 &= -g d_2 + x_n. \end{aligned} \quad (6)$$

Note that the initial conditions do not modify  $d_1$  and  $d_2$ , only  $c_1$  and  $c_2$ .

After one period  $T_p = 2\pi/\omega_p$  of the excitation we have from (5)

$$x(T_p) = e^{-\xi T_p} [c_1 \sin(T_p \sqrt{1 - \xi^2}) + c_2 \cos(T_p \sqrt{1 - \xi^2})] + g d_2 \quad (7)$$

and

$$\dot{x}(T_p) = e^{-\xi T_p} [(-c_1 \xi - c_2 \sqrt{1 - \xi^2}) \sin(T_p \sqrt{1 - \xi^2}) + (-c_2 \xi + c_1 \sqrt{1 - \xi^2}) \cos(T_p \sqrt{1 - \xi^2})] + g \omega_p d_1. \quad (8)$$

The main idea of this paper consists in moving from a continuous time system, (3), to a discrete one. This can be obtained by introducing an appropriate Poincaré section of the continuous flow, and by considering the associated Poincaré return map [Wiggins 1997].

We use the stroboscopic Poincaré map obtained by sampling the system position and velocity at each *excitation* period  $T_p = 2\pi/\omega_p$ , which is mathematically well defined. It is given by

$$\begin{Bmatrix} x_{n+1} \\ y_{n+1} \end{Bmatrix} = \begin{Bmatrix} f_x(x_n, y_n) \\ f_y(x_n, y_n) \end{Bmatrix} = e^{-\xi T_p} \begin{bmatrix} \alpha_x & \alpha_{xy} \\ -\alpha_{xy} & \alpha_y \end{bmatrix} \begin{Bmatrix} x_n \\ y_n \end{Bmatrix} + g \begin{Bmatrix} \beta_x \\ \beta_y \end{Bmatrix}, \quad (9)$$

where use is made of (7) and (8), and where  $x_{n+1} = x(T_p)$  and  $y_{n+1} = \dot{x}(T_p)$  (see [Wiggins 1997]), the functions  $f_x(x_n, y_n)$  and  $f_y(x_n, y_n)$  are defined by the last equality, and

$$\begin{aligned} \alpha_x &= \xi \frac{\sin(T_p \sqrt{1 - \xi^2})}{\sqrt{1 - \xi^2}} + \cos(T_p \sqrt{1 - \xi^2}), & \alpha_y &= -\xi \frac{\sin(T_p \sqrt{1 - \xi^2})}{\sqrt{1 - \xi^2}} + \cos(T_p \sqrt{1 - \xi^2}), \\ \alpha_{xy} &= \frac{\sin(T_p \sqrt{1 - \xi^2})}{\sqrt{1 - \xi^2}}, & & \\ \beta_x &= e^{-\xi T_p} (-\omega_p d_1 \alpha_{xy} - d_2 \alpha_x) + d_2, & \beta_y &= e^{-\xi T_p} (-\omega_p d_1 \alpha_y + d_2 \alpha_{xy}) + \omega_p d_1. \end{aligned} \quad (10)$$

Note that in the resonant case  $T_p = 2\pi/\sqrt{1 - \xi^2}$  we have  $\alpha_x = \alpha_y = 1$ ,  $\alpha_{xy} = 0$ ,  $\beta_x = d_2(1 - e^{-\xi T_p})$ , and  $\beta_y = \omega_p d_1(1 - e^{-\xi T_p})$ .

**2.2. Crowd of pedestrians.** When a crowd of  $N$  uniformly distributed pedestrians is walking on the bridge the net force is

$$f(t) = \sum_{i=1}^N g_i \sin(\omega_{p,i} t - \phi_i). \quad (11)$$

In principle, the parameters  $g_i$  and  $\omega_{p,i}$  are stochastic variables which depend on the age, health condition, height, etc., of the population of pedestrians. However,  $\phi_i$ , which is also a stochastic variable, depends only on the instant of time the pedestrian enters the bridge, and not on his human characteristics.

Single pedestrian action is modeled by (4) and the action of the crowd by (11); we neglect the interactions between pedestrians, and focus only on the interaction of each pedestrian with the bridge, which is the main mechanism responsible for the considered phenomenon. For the pedestrian-pedestrian interactions, an interesting topic involving complex living systems, but which is out of the scope of this paper, we refer to, for example, [Johansson et al. 2008].

In the following we make the assumption that each pedestrian of the crowd has the same natural frequency,  $\omega_{p,i} = \omega_p$ . This is motivated by the fact that only pedestrians with a natural frequency close to that of the bridge can undergo the synchronization phenomenon we are dealing with, since it involves resonance. This fact is confirmed by the movie of the opening of the Millennium Bridge [Arup 2000], where it is clearly seen that only some pedestrians synchronize (it was estimated at about 40% [Newland 2003]). The others are not influenced by the bridge motion and maintain their natural walking, and so, by stochastic arguments, we can assume that they provide a zero net force on the bridge and thus are not of interest. We conclude that only a narrow band of native frequencies is of real interest, and we consider just one,  $\omega_p$ , in order to fulfill the objective of having a simple, but predictive, model.

By the previous basic hypothesis, which guarantees that the stroboscopic Poincaré map is still well defined, we have that (11) becomes

$$f(t) = \sin(\omega_p t) \sum_{i=1}^N g_i \cos(\phi_i) - \cos(\omega_p t) \sum_{i=1}^N g_i \sin(\phi_i). \quad (12)$$

The summations appearing in (12) depend on the degree of synchronization of the pedestrians, that is, on the degree of correlation of their phases  $\phi_i$ .

In the case of *perfectly asynchronous* pedestrians we have that  $\phi_i$  is a stochastic variable uniformly distributed in  $[0, 2\pi]$ , which implies that

$$\sum_{i=1}^N g_i \cos(\phi_i) = \sum_{i=1}^N g_i \sin(\phi_i) = 0 \quad \Rightarrow \quad f(t) = 0. \quad (13)$$

This can be seen by a standard Monte Carlo analysis. In practice in this case for each pedestrian there exists, on average, a pedestrian with opposite phase.

In the *perfectly synchronous* case pedestrians have exactly the same phase,  $\phi_i = \phi \pm 2n\pi$ , so that

$$\sum_{i=1}^N g_i \cos(\phi_i) = \cos(\phi) \sum_{i=1}^N g_i = \cos(\phi) N g_{av}, \quad \sum_{i=1}^N g_i \sin(\phi_i) = \sin(\phi) \sum_{i=1}^N g_i = \sin(\phi) N g_{av}, \quad (14)$$

and

$$f(t) = N g_{\text{av}} \sin(\omega_p t - \phi). \quad (15)$$

In the previous expressions  $N$  is the number of (synchronized) pedestrians whose frequency is close to  $\omega_p$ , that is, a subset of the total number of pedestrians walking on the bridge (see previous comments); only in calibrated experiments with controlled people is  $N$  the total number of pedestrians. The average force of each pedestrian is  $g_{\text{av}}$ , such that  $G_{\text{av}} = g_{\text{av}} K \cong 30N$  (see Section 2.1), and  $\phi$  is the average phase; its value is inessential, and it will be used in due course to simplify the computations.

From the previous expressions we see that  $f(t)$  ranges from  $f(t) = 0$  (the perfectly asynchronous case) to  $f(t) = N g_{\text{av}} \sin(\omega_p t - \phi)$  (the perfectly synchronous case). In real cases the actual force is in between these two bounds, and depends on the degree of synchronization. Thus we assume

$$f(t) = N g_{\text{av}} \sigma \sin(\omega_p t - \phi), \quad (16)$$

where  $\sigma$  is a dimensionless measure of the degree of synchronization, which ranges from 0 (the perfectly asynchronous case) to 1 (the perfectly synchronous case).

Equation (16) is formally identical to (4), so that mathematically we bring back the crowd case to that of an *equivalent* (single) pedestrian, and we can take advantage of the formulas of Section 2.1. In doing this, we use the “free” overall phase to simplify the expressions. In particular, by assuming (without loss of generality)

$$\sin(\phi) = \frac{-2\xi\omega_p}{\sqrt{(1-\omega_p^2)^2 + (2\xi\omega_p)^2}}, \quad \cos(\phi) = \frac{1-\omega_p^2}{\sqrt{(1-\omega_p^2)^2 + (2\xi\omega_p)^2}}, \quad (17)$$

we have

$$d_1 = \frac{1}{\sqrt{(1-\omega_p^2)^2 + (2\xi\omega_p)^2}}, \quad d_2 = 0, \quad (18)$$

so that

$$\beta_x = -\omega_p d_1 e^{-\xi T_p} \alpha_{xy}, \quad \beta_y = \omega_p d_1 (-e^{-\xi T_p} \alpha_y + 1). \quad (19)$$

The map (9) becomes

$$\begin{Bmatrix} x_{n+1} \\ y_{n+1} \end{Bmatrix} = e^{-\xi T_p} \begin{bmatrix} \alpha_x & \alpha_{xy} \\ -\alpha_{xy} & \alpha_y \end{bmatrix} \begin{Bmatrix} x_n \\ y_n \end{Bmatrix} + \sigma \bar{N} \begin{Bmatrix} -e^{-\xi T_p} \alpha_{xy} \\ 1 - e^{-\xi T_p} \alpha_y \end{Bmatrix}, \quad (20)$$

where

$$\bar{N} = \frac{N g_{\text{av}} \omega_p}{\sqrt{(1-\omega_p^2)^2 + (2\xi\omega_p)^2}}. \quad (21)$$

### 3. Pedestrian-bridge interaction

In the previous section only the mechanical part has been considered. In order to model the dynamical bridge-pedestrian interaction and to describe the natural tendency of the systems to synchronize, we must consider also the human part, starting from the basic observation that the two parts influence each other.

The first step in this direction is to assume that not only  $x_n$  and  $y_n$  vary in (discrete) time, but also the synchronization parameter  $\sigma$ , which is now considered as a state variable,  $\sigma_n$ , and no longer as a (fixed) parameter. Thus, (20) becomes

$$\begin{Bmatrix} x_{n+1} \\ y_{n+1} \end{Bmatrix} = \begin{Bmatrix} f_x(x_n, y_n, \sigma_n) \\ f_y(x_n, y_n, \sigma_n) \end{Bmatrix} = e^{-\xi T_p} \begin{bmatrix} \alpha_x & \alpha_{xy} \\ -\alpha_{xy} & \alpha_y \end{bmatrix} \begin{Bmatrix} x_n \\ y_n \end{Bmatrix} + \sigma_n \bar{N} \begin{Bmatrix} -e^{-\xi T_p} \alpha_{xy} \\ 1 - e^{-\xi T_p} \alpha_y \end{Bmatrix}. \quad (22)$$

Note that the passage from (20) to (22) is not a simple substitution of  $\sigma$  with  $\sigma_n$ , but a conceptual change which, for example, increases the dimension of the dynamical system.

The next step consists in proposing a (discrete time) evolution law for the new state variable  $\sigma_n$ :

$$\sigma_{n+1} = f_\sigma(x_n, y_n, \sigma_n), \quad (23)$$

so that (22) and (23) become a well-defined dynamical system. The choice of the function  $f_\sigma(x_n, y_n, \sigma_n)$  entails modeling the bridge-pedestrian interaction, and so it is the key point. In fact, while for the mechanical part (22) there are physical (Newtonian) laws, for the human part (23) there are no corresponding *axiomatic* laws, and any choice is by definition subjective.

Common sense suggests that the degree of synchronization strongly depends on the amplitude,

$$A_n = \sqrt{x_n^2 + \frac{y_n^2}{\omega_p^2}}, \quad (24)$$

of the bridge motion, and weakly on the current synchronization  $\sigma_n$ . Thus, in this work we assume

$$\sigma_{n+1} = f_\sigma(A_n). \quad (25)$$

The following properties help in the characterization of the nonlinear function  $f_\sigma(A_n)$ :

- (1)  $f_\sigma(0) = 0$ . In fact, in a (mathematically) *perfect* case, in the absence of motion there is no synchronization at all and the force on the bridge is zero. Actually, since the synchronization is a stochastic process, in real (or *imperfect*) cases even if the bridge is still, the lack of synchronization is not perfect, and there is a net force, although very small. This is achieved by assuming  $f_\sigma(0) = \varepsilon$ ,  $|\varepsilon| \ll 1$ . In the sequel we will consider both the perfect and the imperfect cases.
- (2)  $f_\sigma(A_n)$  is a monotonic increasing function, since there is experimental evidence that the degree of synchronization increases with the amplitude of the motion.
- (3)  $f_\sigma(A_n)$  is as simple as possible, since there is no experimental evidence for strange behaviors for certain values of  $A_0$ . Mathematically this property can be formulated by assuming that  $f_\sigma(A_n)$  is smooth, that is, continuously differentiable, in  $]0, \infty[$  and that it has at maximum one inflection point.
- (4)  $\lim_{A_n \rightarrow \infty} f_\sigma(A_n) = 1$ , as, for large excitation amplitudes, *all* the pedestrians synchronize (that is, there is no asymptotic limit less than 1). This property mathematically describes the saturation condition; in practice the rate of convergence toward 1 is important, since it is practically expected that for large but finite values of  $A_n$  we have achieved a practically complete synchronization.

Any function satisfying the previous four points is acceptable in principle.

For the forthcoming developments the most important characteristic of the function  $f_\sigma(A_n)$  is its behavior around the origin  $A_n = 0$ . Without loss of generality we can assume the following local behavior:

$$f_\sigma(A_n) = \varepsilon + \gamma_k(A_n)^k + \dots, \quad (26)$$

where  $\varepsilon$  is the imperfections parameter (see point (1)),  $k$  is a positive real number determining the local rate of convergence toward  $A_n = 0$ , and  $\gamma_k$  is a parameter measuring the “slope” of the local behavior, that is, the sensitivity of the pedestrians to the movement of the bridge. Both  $k$  and  $\gamma_k$  are parameters of the model to be determined theoretically or experimentally.

#### 4. Fixed points

Now that we have the map ((22) and (25)) describing the evolution law for the coupled bridge-pedestrian system we can study its dynamic behavior. We start by considering the fixed points

$$x_0 = f_x(x_0, y_0, \sigma_0), \quad y_0 = f_y(x_0, y_0, \sigma_0), \quad \sigma_0 = f_\sigma(A_0), \quad A_0 = \sqrt{x_0^2 + \frac{y_0^2}{\omega_p^2}}, \quad (27)$$

which correspond to periodic oscillations of the original continuous time system.

Solving the first two equations of (27) yields

$$x_0 = 0, \quad y_0 = \sigma_0 \bar{N} \quad \Rightarrow \quad A_0 = \frac{\sigma_0 \bar{N}}{\omega_p}. \quad (28)$$

Substituting this expression in (27)<sub>3</sub> gives the nonlinear algebraic equations permitting determination of the fixed points:

$$\sigma_0 = f_\sigma\left(\frac{\sigma_0 \bar{N}}{\omega_p}\right) \quad \Rightarrow \quad \frac{\omega_p}{\bar{N}} A_0 = f_\sigma(A_0). \quad (29)$$

Equation (29) can be graphically solved by drawing the graph of  $f_\sigma(A_0)$  and of the straight line  $(\omega_p/\bar{N})A_0$ , as schematically shown in Figure 1. This permits the inference of the main qualitative properties of the solution without exact knowledge of the function  $f_\sigma(A_0)$ .

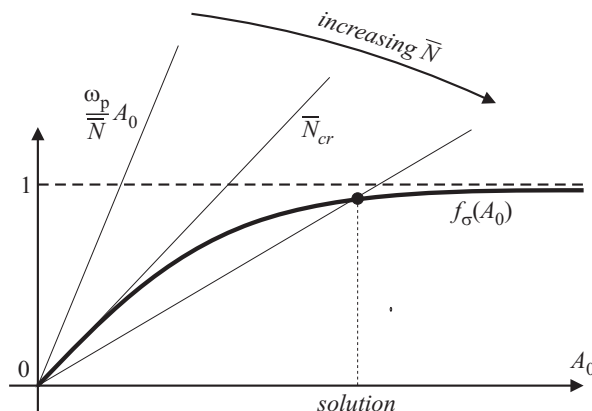


**Figure 1.** A schematic representation of the graphical solution of (29).

The solutions of (29) are now discussed by considering separately the perfect ( $\varepsilon = 0$ , Figure 1) and imperfect ( $\varepsilon \neq 0$ ) cases, and by using  $\bar{N}$  as a varying (driving) parameter for parametric analysis and for bifurcation diagrams.

**4.1. Perfect case.** In the perfect case  $f_\sigma(0) = 0$ , so that we have the trivial (or rest) solution  $A_0 = 0$  corresponding to the still bridge (see (29) and Figure 1). This is the main path of solutions.

To determine if there are secondary solutions bifurcating from the trivial one, we consider the local behavior (26) of  $f_\sigma(A_0)$ , so that (29) becomes

$$\frac{\omega_p}{\bar{N}} A_0 = \gamma_k A_0^k + \dots \quad (30)$$

From the previous equation we conclude that if  $k \neq 1$  there are no solutions in the neighborhood of  $A_0 = 0$  for finite values of  $\bar{N}$ , that is, there are no bifurcation points.

If, on the other hand,  $k = 1$ , then there is a branching at (we write  $\gamma$  instead of  $\gamma_1$  for simplicity)

$$\bar{N}_{\text{cr}} = \frac{\omega_p}{\gamma}, \quad (31)$$

which, as shown in Figure 1, corresponds to the  $\bar{N}$  providing the same slope at the origin for  $f_\sigma(A_0)$  and  $(\omega_p/\bar{N})A_0$ .

Combining (21) and (31) we get

$$N_{\text{cr}} = \frac{\sqrt{(1 - \omega_p^2)^2 + (2\xi\omega_p)^2}}{\gamma g_{\text{av}}}. \quad (32)$$

This expression is the most important result from a practical point of view, since it gives the critical number of pedestrians triggering the phenomenon of lateral synchronization, that is, the maximum number of (synchronizable) pedestrians allowed on the bridge deck. In fact, below this threshold there is only the rest solution, so nothing happens. It is just at this  $N_{\text{cr}}$  that a different solution becomes possible, and the swaying of the bridge appears. This is enough from a designer point of view, and it is valuable because (32) is a very simple formula obtained with reasonable hypotheses. In particular, it does *not* require knowledge of the whole function  $f_\sigma(A_0)$ , but only of its local behavior.

The model parameter  $\gamma$ , which has dimensions of inverse length, measures the sensitivity of the pedestrians to the bridge motion. Its meaning can be understood by considering the following piecewise linear expression, which is the simplest choice for  $f_\sigma(A_0)$ :

$$f_\sigma(A_0) = \begin{cases} \gamma A_0, & \text{for } 0 < A_0 \leq \frac{1}{\gamma}, \\ 1, & \text{for } A_0 \geq \frac{1}{\gamma}. \end{cases} \quad (33)$$

This expression shows that  $1/\gamma$  can be approximately considered as the amplitude such that all the synchronizable pedestrians are actually synchronized. In fact, the limit for  $A_n \rightarrow \infty$  in point (4) is just a mathematical issue, since in practice the phenomenon occurs for small (or moderately small) displacements, justifying the mechanically linear framework used in (1).

Expression (32) provides the critical number as a function of the pedestrians' native frequency  $\omega_p$ . The worst situation corresponds to the resonant case, because in this case each pedestrian has the maximum

effect on the bridge. In fact, by minimizing (32) with respect to  $\omega_p$  we get

$$\omega_{p,\min} = \sqrt{1 - 2\xi^2} = \omega_{\text{res}}, \quad (34)$$

confirming, as expected, that the resonance is the worst situation. By inserting (34) into (32) we obtain

$$N_{\text{cr},\min} = \frac{2\xi}{\gamma g_{\text{av}}} = \frac{B}{\sqrt{MK}} \frac{1}{\gamma} \frac{K}{G_{\text{av}}} = \frac{B\Omega}{\gamma G_{\text{av}}}, \quad (35)$$

where we have assumed  $4\xi^2 - 4\xi^4 \cong 4\xi^2$  due to the smallness of  $\xi$ , and where we remember that  $G_{\text{av}} \cong 30N$  [Belli et al. 2001; Marcheggiani and Lenci 2010].

Expression (35) is the same one obtained in [Lenci and Marcheggiani 2008] with a different model, and agrees with the predictions of the more sophisticated SAMEO model studied in [Marcheggiani and Lenci 2010]. The fact that it is a result of two different models supports its reliability. In fact, in [Lenci and Marcheggiani 2008] it has been shown that it predicts very well experimental results from the literature. Furthermore, based on the results of the London Millennium Bridge, it has been shown that a reasonable value for  $\gamma$ , likely valid in any circumstance, is  $\gamma = 0.14 - 0.17 \text{ cm}^{-1} = 14 - 17 \text{ m}^{-1}$ . This means that there is a complete synchronization for  $\delta = 1/\gamma = 6 - 7 \text{ cm}$  ( $\delta$  refers to the [Lenci and Marcheggiani 2008] notation), a fact that agrees well with experimental observations [Arup 2000; Dallard et al. 2001a; 2001b]. This value also agrees well with the 4.5 cm identified as the limit lateral displacement in [Nakamura and Kawasaki 2006].

Expression (32) is the generalization of (35) to the case of nonperfect resonance, since, contrarily to (35), it permits the detection, still in a simple way, of the effects of  $\omega_p$ .

Formula (35) is now extremely simple, since it requires only the knowledge of the real damping and circular frequency of the involved (lateral) mode

$$N_{\text{cr},\min} = 0.0022B [\text{kg sec}^{-1}] \Omega [\text{sec}^{-1}]. \quad (36)$$

In spite of its straightforwardness, it is very predictive. In fact, we remember that the critical number of pedestrians which destabilized the north span of the London Millennium Bridge was about 155 [Dallard et al. 2001a; 2001b]. Since for the north span we have [Strogatz et al. 2005]  $M = 113000 \text{ kg}$ ,  $K = 4730000 \text{ kg sec}^{-2} \rightarrow \Omega = 6.47 \text{ sec}^{-1}$  (that is, the natural frequency is 1.03 Hz), and  $B = 11000 \text{ kg sec}^{-1}$ , we obtain from (36)  $N_{\text{cr},\min} = 156$ . Note that the mass of the critical number of pedestrians is about  $m = 155 \times 80 = 12480 \text{ kg}$ , that is, 11% of the modal mass.

To further show its reliability, we apply (36) to the Toda Park Bridge, best known as the T-Bridge, a cable-stayed footbridge in Japan. According to [Nakamura and Kawasaki 2006] we have  $M = 237000 \text{ kg}$ ,  $K = 8092000 \text{ kg sec}^{-2} \rightarrow \Omega = 5.84 \text{ sec}^{-1}$  (that is, the natural frequency is 0.93 Hz), and  $B = 22200 \text{ kg sec}^{-1}$ . Therefore the critical number of synchronizable pedestrians is  $N_{\text{cr},\min} = 285$ . In this case we do not have the experimental value of  $N_{\text{cr}}$ , as in the case of the Millennium Bridge, but we know from [Fujino et al. 1993] that with  $N \cong 2000$  pedestrians (an extremely congested situation) the bridge experienced synchronized oscillations. Considering that about 20% of pedestrians synchronized, as explicitly remarked in [Fujino et al. 1993], we have  $N \cong 400$ , which is in good agreement with  $N_{\text{cr},\min} = 285$  (we cannot expect equality, since we have data only for a synchronized situation).

In the case of the Maple Valley cable-stay bridge, also known as the M-Bridge, in Japan, we have that the third asymmetric and, to a minor extent, the fourth symmetric modes are involved in the lateral

synchronization [Nakamura and Kawasaki 2006; Nakamura and Kawasaki 2009]. For the third mode we have synchronization, for example, when there are about 41 pedestrians on the deck (see [Nakamura and Kawasaki 2009, case M-6, Figure 11]). In this case we have [Nakamura and Kawasaki 2009]  $M = 97200 \text{ kg}$ ,  $K = 29648570 \text{ kg sec}^{-2} \rightarrow \Omega = 5.52 \text{ sec}^{-1}$  (that is, the natural frequency is 0.88 Hz), and  $B = 2905 \text{ kg sec}^{-1}$ . Therefore the critical number of synchronizable pedestrians is  $N_{\text{cr,min}} = 35$ .

From the previous work we have seen that the main solution curve has a bifurcation point at  $N_{\text{cr}}$ . The type of bifurcation depends on the higher-order terms of the Taylor expansion (26):

$$f_\sigma(A_0) = \gamma A_0 + \gamma_2(A_0)^2 + \gamma_3(A_0)^3 + \dots, \quad (37)$$

so that from (29) the local behavior of the branching solution is

$$\bar{N}(A_0) = \frac{\omega_p}{\gamma} - \frac{\omega_p \gamma_2}{\gamma^2} A_0 - \frac{\omega_p(\gamma_3 \gamma - \gamma_2^2)}{\gamma^3} (A_0)^2 + \dots \quad (38)$$

From (38) we see that if  $\gamma_2 \neq 0$  we have a transcritical bifurcation. Otherwise, we have a supercritical pitchfork bifurcation if  $\gamma_3 < 0$  or a subcritical pitchfork bifurcation if  $\gamma_3 > 0$  (in this case  $f_\sigma(A_0)$  has an inflection point, which implies that the pitchfork is preceded by a saddle-node bifurcation for a lower value of  $\bar{N}$ , see Figure 2); this is a consequence of the fact that the trivial solution is stable for  $N < N_{\text{cr}}$ . This is obvious by common sense, and can be proved mathematically by noticing that the Jacobian matrix of the map at the rest position is

$$\begin{bmatrix} \alpha_x e^{-\xi T_p} & \alpha_{xy} e^{-\xi T_p} & -\bar{N} \alpha_{xy} e^{-\xi T_p} \\ -\alpha_{xy} e^{-\xi T_p} & \alpha_y e^{-\xi T_p} & \bar{N}(1 - \alpha_y e^{-\xi T_p}) \\ 0 & \frac{\gamma}{\omega_p} & 0 \end{bmatrix}, \quad (39)$$

and the associated characteristic equation is (use is made of the property  $\alpha_x \alpha_y + \alpha_{xy}^2 = 1$ )

$$s^3 - e^{-\xi T_p} (\alpha_x + \alpha_y) s^2 + \left( \frac{\gamma \bar{N}}{\omega_p} (-1 + \alpha_y e^{-\xi T_p}) + e^{-2\xi T_p} \right) s + \frac{\gamma \bar{N} e^{-\xi T_p}}{\omega_p} (-e^{-\xi T_p} + \alpha_x) = 0. \quad (40)$$

In fact, (40) has one solution satisfying  $s = 1$  for  $\bar{N} = \omega_p / \gamma = \bar{N}_{\text{cr}}$ , while below this threshold we have  $|s| < 1$ .

The whole bifurcation scenario for different values of  $\gamma_2$  and  $\gamma_3$  is qualitatively depicted in Figure 3.

It is worth remarking that, again, the most interesting properties are determined only by the *local* behavior of  $f_\sigma(A_0)$ .

Up to now we have considered only the case  $k = 1$ , which is the most interesting from a practical point of view because it is the unique case in which the model has a bifurcation point, which describes well, both qualitatively and quantitatively, the real behavior. For the sake of completeness we consider now also the cases  $k < 1$  and  $k > 1$ . Functions with these characteristics are schematically shown in Figure 2.

By referring to Figure 2 the solution scenarios can be easily understood. For  $k < 1$ , and supposing that  $f_\sigma(A_0)$  has regular behavior with an always negative curvature (as the function in Figure 2, see point (3)), we see that, in addition to  $A_0 = 0$ , for every value of  $\bar{N}$  there is always one and only one solution  $A_0$ . Furthermore, the function  $A_0 = A_0(\bar{N})$  is monotonically increasing and goes to infinity for  $\bar{N} \rightarrow \infty$ .

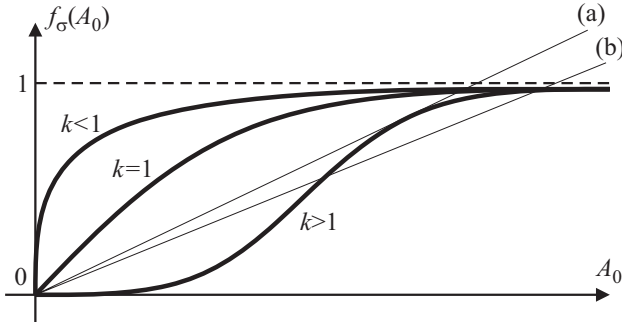


**Figure 2.** A schematic representation of  $f_\sigma(A_0)$  for different values of exponent  $k$  of (26).

The case  $k > 1$  is slightly more involved. In fact we have that for small values of  $\bar{N}$  (that is, very steep straight lines), there are no solutions. When  $\bar{N}$  increases, at a certain threshold the line becomes tangent to the curve  $f_\sigma(A_0)$  (as line (a) in Figure 2), at a point ahead of the unique inflection point. Above this threshold there are always two solutions (see line (b) in Figure 2), one of which approaches zero and the other infinity as  $\bar{N} \rightarrow \infty$ . This is a saddle-node bifurcation, where a solution suddenly appears, far from the main path. This does not seem to capture the behavior observed in real cases, although we cannot exclude in principle that it could happen in different (unobserved up to now) situations. We only note that to detect the saddle-node threshold a local analysis around  $A_0 = 0$  is no longer sufficient.

**4.2. Imperfect case.** In the imperfect case  $f_\sigma(0) = \varepsilon > 0$ , so that  $A_0 = 0$  is no longer a trivial solution. Considering the most interesting case  $k = 1$  we have that

$$\frac{\omega_p}{\bar{N}} A_0 = \varepsilon + \gamma A_0 + \gamma_2(A_0)^2 + \gamma_3(A_0)^3 + \dots, \quad (41)$$

so that locally the solution is

$$\frac{\bar{N}}{\omega_p} = \frac{A_0}{\varepsilon} - \gamma \left( \frac{A_0}{\varepsilon} \right)^2 + (-\gamma_2 \varepsilon + \gamma^2) \left( \frac{A_0}{\varepsilon} \right)^3 - (\gamma_3^2 - 2\gamma \gamma_2 \varepsilon + \gamma^3) \left( \frac{A_0}{\varepsilon} \right)^4 + \dots. \quad (42)$$

The main branch emanating from  $(A_0, \bar{N}) = (0, 0)$  is no longer at rest, although not so far from it, since  $\varepsilon$  is small — otherwise it cannot be considered as an imperfection and must be carefully considered in an appropriate way. There are no longer branching points and branching paths ensuing from the main one, a fact that constitutes the main distinction with respect to the perfect case (Section 4.1).

All possible situations are qualitatively depicted in Figure 3, together with the corresponding perfect scenario. Each case of Figure 3 is clearly an unfolding of a local branching bifurcation, according to the fact that transcritical and pitchfork bifurcations are not structurally stable [Wiggins 1997].

Comparing the pictures of Figure 3 with the numerical simulations of the SAMEO model [Marchegiani and Lenci 2010] and with the experimental outcomes (the results of the Arup tests can be looked up, for example, in [Newland 2001; Abrams 2006]) we see that the situation actually occurring is that of Figure 3c; in fact, for low values of  $N$  there are small (but not null) oscillations, which suddenly but not *instantaneously* (as it would be in the perfect case of a pitchfork bifurcation) increase *around* a critical threshold.

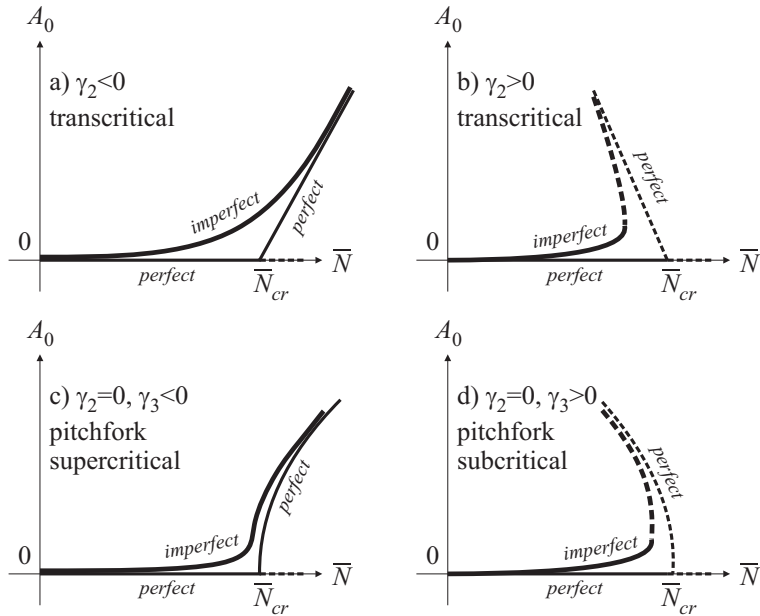


**Figure 3.** Qualitative bifurcation paths for perfect and imperfect cases; stable (solid lines) and unstable (dashed lines).

From the previous considerations we can draw the following conclusions:

- The theoretical critical value  $N_{cr}$  computed in the previous section is a *reference* value, of course of great engineering interest, and not the mathematically exact value of the critical threshold, which actually does not exist.
- The dynamical phenomenon underlying the problem of pedestrian-induced lateral vibrations of footbridges is a perturbation of a pitchfork bifurcation. This result was also obtained in [Lenci and Marcheggiani 2008] and is herein confirmed with a different model.

## 5. The resonant case

We have seen in the previous sections that the resonant case is the worst situation, and thus in this section it is studied in detail.

We start by noticing that the minimum of  $N_{cr}$  for varying  $\omega_p$  is obtained for  $\omega_p = \sqrt{1 - 2\xi^2}$  (see (34)). This is the *mathematical* resonance, corresponding to the maximum of the amplification factor [Clough and Penzien 1975]. The *engineering* resonance is given by  $\omega_p = \sqrt{1 - \xi^2}$  and corresponds to the coincidence between the external (excitation) and internal (natural) frequencies. When  $\xi$  is small, as occurs in practical cases, the difference is negligible.

In the engineering resonance case we have  $\alpha_x = \alpha_y = 1$ ,  $\alpha_{xy} = 0$ , and the map given by (22) and (25) becomes ( $T_p = 2\pi/\sqrt{1 - \xi^2}$ ):

$$x_{n+1} = e^{-\xi T_p} x_n, \quad y_{n+1} = e^{-\xi T_p} y_n + \sigma_n \bar{N} (1 - e^{-\xi T_p}), \quad \sigma_{n+1} = f_\sigma(A_n). \quad (43)$$

From (43)<sub>1</sub> we conclude that, for any trajectory,  $x_n \rightarrow 0$  for  $n \rightarrow \infty$ . This means that the (planar) invariant manifold  $x = 0$  is globally attractive, so that the most interesting dynamics live on it. Note that due to (28)<sub>1</sub> the fixed points obtained in the previous section belong to the manifold.

On the invariant manifold system (43) reduces to the 2D map

$$y_{n+1} = (1 - a)y_n + a\bar{N}\sigma_n, \quad \sigma_{n+1} = f_\sigma\left(\frac{|y_n|}{\omega_p}\right) = f_\sigma\left(\frac{|y_n|}{\sqrt{1-\xi^2}}\right) = \tilde{f}_\sigma(|y_n|), \quad (44)$$

where  $a = 1 - e^{-\xi T_p} = 1 - e^{-2\pi\xi/\sqrt{1-\xi^2}}$  is a positive number less than 1. In real structures it is possibly small,  $a \cong 2\pi\xi$  (and in this case  $f_\sigma$  coincides with  $\tilde{f}_\sigma$ ), but this hypothesis is *not* required here.

Given an initial point  $P_n = (y_n, \sigma_n)$  in the phase space  $(\mathbb{R}, [0, 1])$  of (44), its image  $P_{n+1} = (y_{n+1}, \sigma_{n+1})$  can be obtained by the following graphical procedure, which is a noticeable property of map (44) and which is illustrated in Figure 4:

- (1) From  $P_n$  draw a vertical line and individuate points  $A$  and  $B$  where it intersects line  $r$  of equation  $\sigma_n = y_n/\bar{N}$  and the function  $\tilde{f}_\sigma(|y_n|)$ , respectively.
- (2) From  $A$  draw the line  $s$  of slope  $1/(a\bar{N})$  (which is more steep than line  $r$  since  $a < 1$ ).
- (3) From  $P_n$  draw a horizontal line and individuate the point  $C$  of intersection with  $s$ .
- (4) From  $C$  draw a vertical line and from  $B$  a horizontal line. The intersection point is  $P_{n+1}$ .

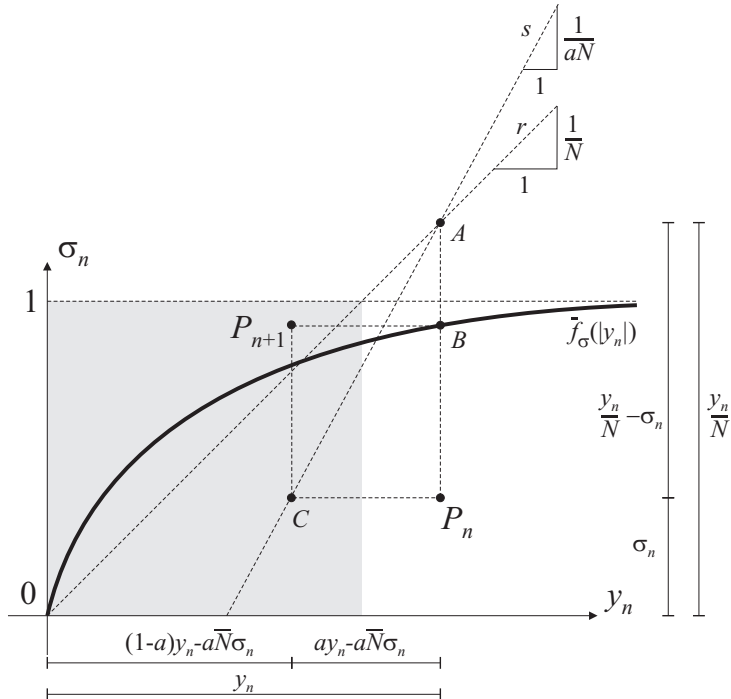


**Figure 4.** Sketch of the graphical construction of the 2D map (44). In gray is attracting region  $R = (y_n, \sigma_n) \in ([0, \bar{N}], [0, 1])$ .

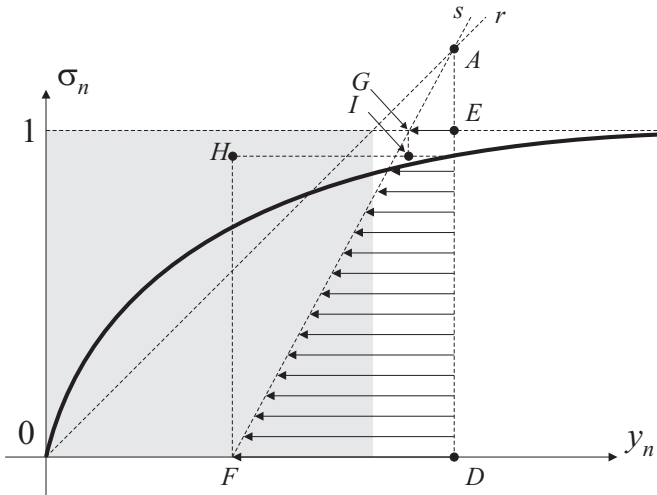


**Figure 5.** Some properties of the map (44).

From the previous graphical construction it is immediately seen that the unique nontrivial fixed point (when it exists, that is, above  $\bar{N}_{\text{cr}}$ ) corresponds to  $y_0$  such that points  $A$  and  $B$  coincide, that is, when line  $r$  intersects  $\bar{f}_\sigma(|y_n|)$ . This corresponds exactly to the point found by the graphical construction of Figure 1.

By using the graphical construction of Figure 4 it is possible to note the following properties, which are illustrated in Figure 5 and which further help in understanding the behavior of the 2D map:

- segment  $F-G$  is the diagram of the horizontal displacements of the points belonging to segment  $D-E$ , that is, the points having a fixed  $y_n$  and varying  $\sigma_n$  and
- the image of segment  $D-E$  is segment  $H-I$ .

It is useful to rewrite (44)<sub>1</sub> in the alternative form

$$\Delta y_n = y_{n+1} - y_n = a(\bar{N}\sigma_n - y_n). \quad (45)$$

Since  $0 \leq \sigma_n \leq 1$ , we have that

$$-ay_n \leq \Delta y_n \leq a(\bar{N} - y_n). \quad (46)$$

From the left-hand side inequality we see that for all negative  $y_n$  the difference  $\Delta y_n$  is positive, so that every point in the region  $y_n < 0$  tends to move toward  $y_n = 0$ . From the right-hand side inequality, on the other hand, we see that for all  $y_n > \bar{N}$  the difference  $\Delta y_n$  is negative, so that every point in the region  $y_n > \bar{N}$  tends to move toward  $y_n = \bar{N}$  (see an example in Figure 5). The conclusion is that the region  $R = (y_n, \sigma_n) \in ([0, \bar{N}], [0, 1])$ , which is shown in gray in Figures 4 and 5, is globally attracting, and the steady-state behavior lies therein. In fact, points belonging to  $R$  do not escape from it, since from  $0 \leq y_n \leq \bar{N}$  and  $0 \leq \sigma_n \leq 1$  it follows (see (44)<sub>1</sub>) that  $0 \leq y_{n+1} \leq \bar{N}$ .

On the attracting region  $R$  the map (44) is *invertible*, because  $\bar{f}_\sigma(y_n)$  is invertible on  $\mathbb{R}^+$  by the assumptions made in Section 3.

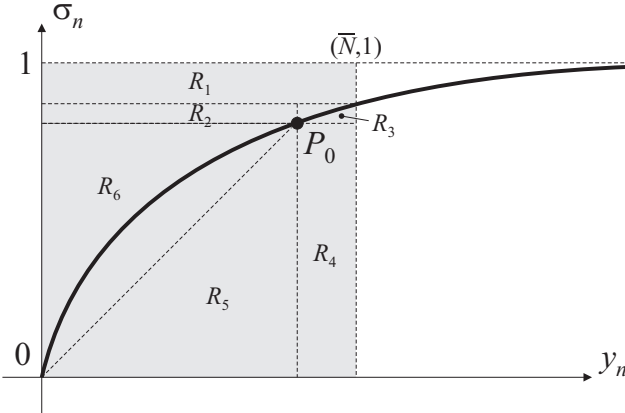


**Figure 6.** The six subregions of the attracting region of the map (44).

In the case  $\bar{N} > \bar{N}_{\text{cr}}$  the region  $R$  can be divided into six subregions, as shown in Figure 6. From the graphical constructions introduced above we see that:

- $R_1 \rightarrow R_3 \cup R_4 \cup R_5 \cup R_6$ ;
- $R_2 \rightarrow R_4 \cup R_5 \cup R_6$ ;
- $R_3 \rightarrow R_3$ ;
- $R_4 \rightarrow R_2 \cup R_3$ ;
- $R_5 \rightarrow R_6$ ;
- $R_6 \rightarrow R_5 \cup R_6$ .

An example is reported in Figure 7 where  $\tilde{f}_\sigma(y) = \tanh(y)$ ,  $\bar{N} = 1.5$  ( $> \bar{N}_{\text{cr}} = 1$ ), and  $a = 0.3$ .

From the previous scheme we conclude that periodic or chaotic solutions (not necessarily stable) are possible only in  $R_3$ , alternating in  $R_2$  and  $R_4$ , and alternating in  $R_5$  and  $R_6$ . These considerations are the starting point for the detailed study of the dynamical behavior of the map (44), which is out of the

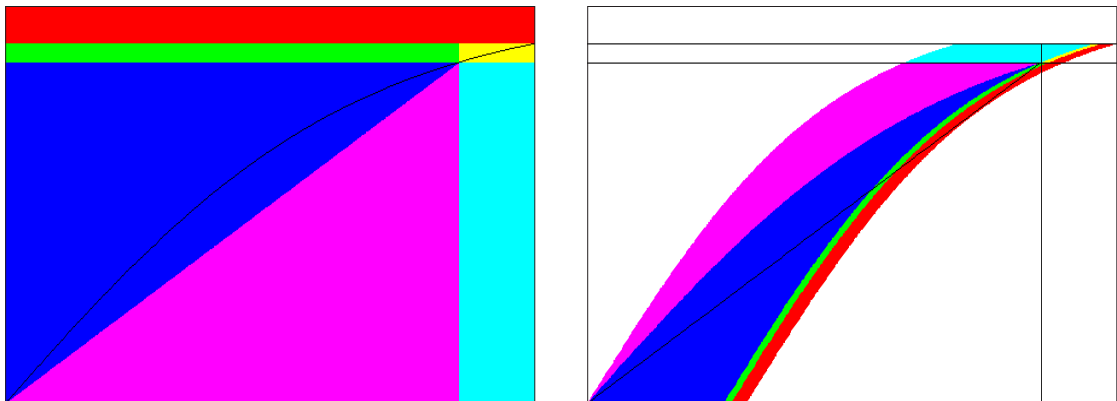


**Figure 7.** The six subregions of the attracting region and their images after one iteration of the map, where  $\tilde{f}_\sigma(y) = \tanh(y)$ ,  $\bar{N} = 1.5$  ( $> \bar{N}_{\text{cr}} = 1$ ), and  $a = 0.3$ .

scope of the present paper and is left for future work. We only note that in some isolated numerical simulations based on the example of Figure 7 we have seen that the bifurcated equilibrium point  $P_0$  is globally attractive for the whole phase space.

## 6. Conclusions

A 3D discrete-time dynamical system has been proposed for studying the pedestrian-induced lateral vibrations of footbridges. For the mechanical part, the model is based on the stroboscopic Poincaré map of the flow of the associated continuous time, one mode system, while the coupling between the pedestrians and the bridge motion has been modeled by assuming that the degree of synchronization of the pedestrians is a function  $f_\sigma$  of the amplitude of the bridge oscillations.

The fixed points of the map have been studied in detail, without exact knowledge of  $f_\sigma$ . Only the local behavior of  $f_\sigma$  around the rest position and some qualitative properties have been used. Both the perfect and the imperfect cases have been considered.

In the perfect case it has been shown that in the unique case of interest in practice (corresponding to  $f'_\sigma(0) = \gamma \in ]0, \infty[$ ) there is a main path of rest solutions. When the number of pedestrians  $N$  increases, at a certain threshold  $N_{cr}$  a secondary path bifurcates from the previous one, thus allowing for “large” oscillations of the bridge. This is the threshold of activation of the unwanted lateral oscillations, and it is of primary importance in practice. With the proposed model a very simple, predictive, and general formula is obtained for  $N_{cr}$ , a fact that constitutes the main result of this paper.

The imperfect case has been considered, by including the effect of small imperfections. It has been shown how the four possible fixed-points scenarios are modified by the imperfections. The one corresponding to a perturbation of a pitchfork bifurcation is noted to agree with experimental observations on real cases (the Arup experiments on the Millennium Bridge) and with numerical simulations of a more sophisticated model. Thus, it is concluded that the dynamical phenomenon underlying the synchronization problem is a perturbation of the pitchfork bifurcation.

The present paper is devoted to the construction of the model and to the study of the fixed points, which is sufficient to obtain the desired formula for the critical number of pedestrians and to understand the main dynamical aspects. The detailed study of the whole dynamics of the system, including more complex phenomena such as chaos, is worthwhile but out of the scope of this work, and is left for future work.

## Acknowledgements

Lenci thanks the Organizing Committee of PACAM XI, and its President Adair Aguiar, for supporting his participation in the Congress. Thanks are also gratefully due to Carlos Mazzilli and Paulo Gonçalves for supporting a post-Congress visit at USP and PUC, during which part of this work has been developed.

## References

- [Abrams 2006] D. M. Abrams, *Two coupled oscillator models: the Millennium Bridge and the Chimera state*, Ph.D. thesis, Theoretical and Applied Mechanics, Cornell University, Ithaca, NY, 2006, available at <http://hdl.handle.net/1813/3271>.
- [Arup 2000] Arup Group, “The Millennium Bridge”, 2000. <http://www.arup.com/MillenniumBridge/indepth/video.html>.

- [Belli et al. 2001] A. Belli, P. Bui, A. Berger, A. Geyssant, and J.-R. Lacour, “A treadmill ergometer for three-dimensional ground reaction forces measurement during walking”, *J. Biomech.* **34**:1 (2001), 105–112.
- [Blanchard et al. 1977] J. Blanchard, B. L. Davies, and J. W. Smith, “Design criteria and analysis for dynamic loading of footbridges”, pp. 90–107 in *Symposium on Dynamic Behaviour of Bridges* (Crowthorne, 1977), TRRL Supplementary Report **275**, Transport and Road Research Laboratory, Crowthorne, U.K., 1977.
- [Blekherman 2007] A. N. Blekherman, “Autoparametric resonance in a pedestrian steel arch bridge: Solferino bridge, Paris”, *J. Bridge Eng.* **12**:6 (2007), 669–676.
- [Bodgi et al. 2007] J. Bodgi, S. Erlicher, and P. Argoul, “Lateral vibration of footbridges under crowd-loading: continuous crowd modeling approach”, *Key Eng. Mater.* **347** (2007), 685–690.
- [Candaten and Rinaldi 2000] M. Candaten and S. Rinaldi, “Peak-to-peak dynamics: a critical survey”, *Int. J. Bifurc. Chaos* **10**:8 (2000), 1805–1820.
- [Clough and Penzien 1975] R. Clough and J. Penzien, *Dynamics of structures*, McGraw-Hill, New York, 1975.
- [Dallard et al. 2001a] P. Dallard, A. J. Fitzpatrick, A. Flint, S. Le Bourva, A. Low, R. M. R. Smith, and M. Willford, “The London Millennium Footbridge”, *Struct. Eng.* **79**:22 (2001), 17–33.
- [Dallard et al. 2001b] P. Dallard, A. J. Fitzpatrick, A. Flint, A. Low, R. M. R. Smith, M. Willford, and M. Roche, “London Millennium Bridge: pedestrian-induced lateral vibration”, *J. Bridge Eng.* **6**:6 (2001), 412–417.
- [Danbon and Grillaud 2005] F. Danbon and G. Grillaud, “Dynamic behaviour of a steel footbridge: characterization and modelling of the dynamic loading induced by a moving crowd on the Solferino Footbridge in Paris”, in *Proceedings of Footbridge 2005: 2nd International Conference* (Venice, 2005), Office Technique pour l’Utilisation de l’Acier, Puteaux, 2005.
- [Eckhardt et al. 2007] B. Eckhardt, E. Ott, S. H. Strogatz, D. M. Abrams, and A. McRobie, “Modeling walker synchronization on the Millennium Bridge”, *Phys. Rev. E* **75**:2 (2007), 021110.
- [Fujino et al. 1993] Y. Fujino, B. M. Pacheco, S.-I. Nakamura, and P. Warnitchai, “Synchronization of human walking observed during lateral vibration of a congested pedestrian bridge”, *Earthq. Eng. Struct. Dyn.* **22**:9 (1993), 741–758.
- [Johansson et al. 2008] A. Johansson, D. Helbing, H. Z. Al-Abideen, and S. Al-Bosta, “From crowd dynamics to crowd safety: a video-based analysis”, *Adv. Complex Syst.* **11**:4 (2008), 497–527.
- [Lenci and Marcheggiani 2008] S. Lenci and L. Marcheggiani, “A discrete-time model for the phenomenon of synchronous lateral excitation due to pedestrians motion on footbridges”, in *Proceedings of Footbridge 2008: Footbridge for urban renewal: 3rd International Conference* (Porto, 2008), edited by E. de Sá Caetano and Á. Cunha, University of Porto, College of Engineering (FEUP), Porto, 2008.
- [Marcheggiani and Lenci 2010] L. Marcheggiani and S. Lenci, “On a model for the pedestrians-induced lateral vibrations of footbridges”, *Meccanica (Milano)* **45**:4 (2010), 531–551.
- [Matsumoto et al. 1978] Y. Matsumoto, T. Nishioka, H. Shiojiri, and K. Matsuzaki, “Dynamic design of footbridges”, *IABSE Proc.* **2** (1978), 1–15. Paper P-17/78.
- [Nakamura 2004] S.-I. Nakamura, “Model for lateral excitation of footbridges by synchronous walking”, *J. Struct. Eng. (ASCE)* **130**:1 (2004), 32–37.
- [Nakamura and Kawasaki 2006] S.-I. Nakamura and T. Kawasaki, “Lateral vibration of footbridges by synchronous walking”, *J. Constr. Steel Res.* **62**:11 (2006), 1148–1160.
- [Nakamura and Kawasaki 2009] S.-I. Nakamura and T. Kawasaki, “A method for predicting the lateral girder response of footbridges induced by pedestrians”, *J. Constr. Steel Res.* **65**:8-9 (2009), 1705–1711.
- [Newland 2001] D. E. Newland, “Vibration: problem and solution”, pp. 88–93 in *Blade of light: the story of London’s Millennium Bridge*, edited by D. Sudjic, Penguin/Millennium Bridge Trust, London, 2001.
- [Newland 2003] D. E. Newland, “Pedestrian excitation of bridges: recent results”, pp. 1–15 in *Proceedings of the Tenth International Congress on Sound and Vibration (ICSV-10)* (Stockholm, 2003), edited by A. Nilsson and H. Boden, International Institute of Acoustics and Vibration (IIAV), Stockholm, 2003.
- [Piccardo and Tubino 2008] G. Piccardo and F. Tubino, “Parametric resonance of flexible footbridges under crowd-induced lateral excitation”, *J. Sound Vib.* **311**:1-2 (2008), 353–371.

- [Ricciardelli and Pizzimenti 2007] F. Ricciardelli and A. D. Pizzimenti, “Lateral walking-induced forces on footbridges”, *J. Bridge Eng.* **12**:6 (2007), 677–688.
- [Roberts 2005] T. M. Roberts, “Lateral pedestrian excitation of footbridges”, *J. Bridge Eng.* **10**:1 (2005), 107–112.
- [Strogatz et al. 2005] S. H. Strogatz, D. M. Abrams, A. McRobie, B. Eckhardt, and E. Ott, “Theoretical mechanics: crowd synchrony on the Millennium Bridge”, *Nature* **438**:7064 (2005), 43–44.
- [Venuti and Bruno 2009] F. Venuti and L. Bruno, “Crowd-structure interaction in lively footbridges under synchronous lateral excitation: a literature review”, *Phys. Life Rev.* **6**:3 (2009), 176–206.
- [Venuti et al. 2007] F. Venuti, L. Bruno, and N. Bellomo, “Crowd dynamics on a moving platform: mathematical modelling and application to lively footbridges”, *Math. Comput. Model.* **45**:3-4 (2007), 252–269.
- [Wheeler 1980] J. E. Wheeler, “Pedestrian induced vibration in footbridges”, Technical report 15, Main Roads Department, Perth, 1980.
- [Wiggins 1997] S. Wiggins, *Introduction to applied nonlinear dynamical systems and chaos*, Texts in Applied Mathematics **2**, Springer, New York, 1997.
- [Živanović et al. 2005] S. Živanović, A. Pavic, and P. Reynolds, “Vibration serviceability of footbridges under human-induced excitation: a literature review”, *J. Sound Vib.* **279**:1-2 (2005), 1–74.

Received 23 Jun 2010. Revised 26 Nov 2010. Accepted 30 Nov 2010.

STEFANO LENCI: [lenci@univpm.it](mailto:lenci@univpm.it)

Dipartimento di Ingegneria Civile, Edile e Architettura, Università Politecnica delle Marche, via Brecce Bianche,  
I-60131 Ancona, Italy

LAURA MARCHEGGIANI: [1.marcheggiani@univpm.it](mailto:1.marcheggiani@univpm.it)

Dipartimento di Ingegneria Civile, Edile e Architettura, Università Politecnica delle Marche, via Brecce Bianche,  
I-60131 Ancona, Italy



## FREE VIBRATION OF A SIMULATION CANDU NUCLEAR FUEL BUNDLE STRUCTURE INSIDE A TUBE

XUAN ZHANG AND SHUDONG YU

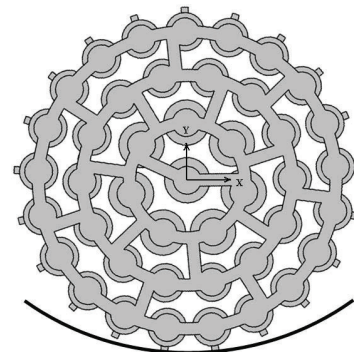
This paper presents a numerical rigid-elasto model for vibration of a simulation nuclear fuel bundle structure confined in a circular tube. The model is developed using the finite element method combined with the floating frame formulation. The nonlinear dynamic equations are derived using the Lagrange equations. Small-amplitude vibration about the static equilibrium position is obtained through linearization. Numerical results show that the fundamental mode is a rocking-like mode, in which rigid body translation and rotation are coupled with elastic deformations. Gravity is found to reduce the frequency of the fundamental mode without affecting the higher modes. Experiments are conducted for a single fuel bundle structure to validate the numerical results.

### 1. Introduction

Horizontally placed CANDU<sup>1</sup> fuel bundles in a circular tube are used in the Canadian nuclear industry. During operation, the fuel bundles experience small-amplitude flow-induced vibration, which can result in significant wear to the supporting structures over a period of time.

Static deformations of fuel bundle structures have been investigated in [Cho et al. 2000; Horhoianu and Ionescu 2006]. Dynamic models of a horizontally placed rod bundle sitting on the inner surface of a tube have not been seen before in the literature.

A 43-element simulation fuel bundle is shown in Figure 1 on the next page. The bundle has 43 rods distributed in 3 rings and at the center. The rods are interconnected by two endplates. Each endplate consists of 3 circular rings and 16 ribs/webs. The weight of the bundle is supported by the bearing pads on the bottom rods in the outer ring, as shown on the right. Ideally there are four bearing pads in contact with the tube surface and supporting the bundle weight. The radial gaps between the tube surface and the bearing pads on the rods next to the bottom rods are about 30–50  $\mu\text{m}$ , which permits small-amplitude bundle vibration without impacting the supporting structure. This small-amplitude vibration results in a relatively large motion in the top parts of the bundle due to the large bundle diameter. When disturbed or excited, the bundle vibrates about its equilibrium position.



Fuel channel inspections at the Darlington nuclear station indicated that bundle vibrations, for example, rocking, induced by the coolant flow were responsible for the fretting between the pressure tube spacer sleeve and the inlet bundle bearing pads [Judah 1992]. Modeling the bundle vibration requires

*Keywords:* multibody dynamics, floating frame, fuel bundle structure, vibration.

<sup>1</sup>CANadian Deuterium and Uranium, a registered trademark of Atomic Energy of Canada Ltd.

formulation of the rigid-elastic motions of a 3D bundle structure. The superimposition method [Schwab and Meijaard 2002] and the floating frame formulation [Shabana 2005] have been used to deal with rigid and elastic motions of a 3D body.

Extending from [Zhang and Yu 2010a], this paper presents a numerical procedure for modeling the rod bundles using the floating frame formulation. A rigid-elastodynamic model is established and applied to the study of the fundamental mode of a single bundle. The influence of gravity is discussed based on the simulation results. The simulation results are compared to experimental results.

## 2. Finite element model in the floating frame formulation

The floating frame formulation used in multibody dynamics is employed to couple the rigid body motion and the elastic deformation of the bundle. Nonlinear equations of motion are obtained for the bundle vibration, and then simplified to a set of linear equations for the small-amplitude vibrations about the equilibrium.

As shown in Figure 1, left, a global inertia frame is chosen in such a way that the  $X$ -axis is horizontal and the  $Y$ -axis is vertical. The origin of the global frame is chosen to be the center of the upstream endplate. To describe the rigid body motion, a reference frame  $x$ - $y$ - $z$  is also defined in the figure. The frame is rigidly attached to the mass center of the bundle so that it moves and rotates with the bundle. This frame is regarded as the body frame of the bundle.

The bundle is discretized using two types of finite elements. The rods are modeled using a three-node higher-order beam element in conjunction with Euler–Bernoulli theory [Meirovitch 2001]. The endplates are modeled using a special nine-node isoparametric plate element [Yu and Wen 2007] in conjunction with the third-order thick plate theory of [Reddy 1984]. The finite element model is shown in Figure 1, right. The endplate is regarded as massless because its mass is significantly smaller than the mass of the rods. Therefore the stiffness of the endplate can be condensed using static substructuring. A superelement can then be achieved for each endplate using the procedures described in [Zhang and Yu 2010b].

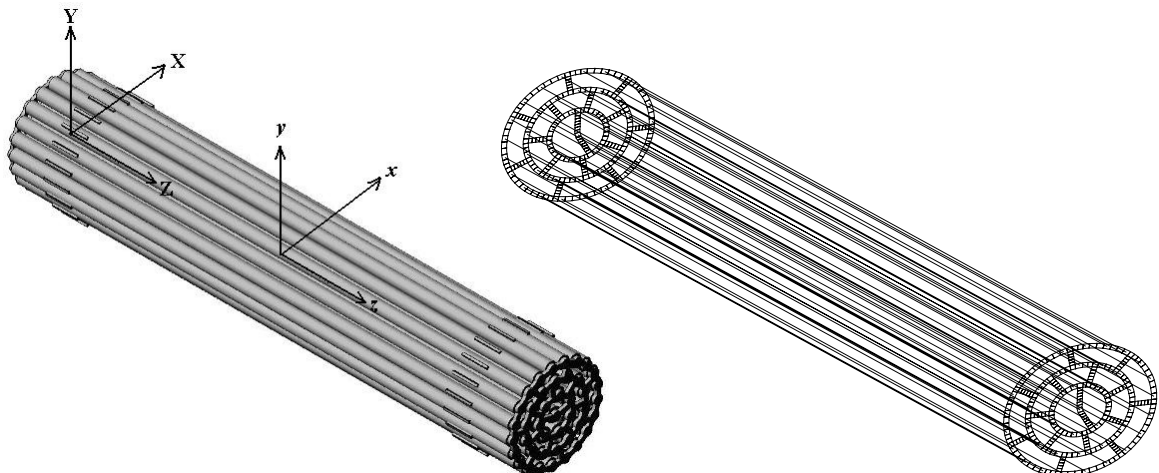


**Figure 1.** Rod bundle: isoparametric view (left) and finite-element mesh (right).

Two sets of degrees of freedom (DOFs) are considered in this model. The first set is the rigid body (body frame) displacement including translations  $\mathbf{u}_c$  and rotations  $\boldsymbol{\phi}$  measured in the global frame X-Y-Z. The second set is the deformation-induced displacement  $\mathbf{u}_f$  measured in the body frame. In the floating frame formulation [Shabana 2005], the displacement of an arbitrary material point on the bundle can be expressed as

$$\mathbf{u} = \mathbf{u}_c + [\mathbf{A}(\boldsymbol{\phi}) - \mathbf{A}_0]\mathbf{x} + \mathbf{A}(\boldsymbol{\phi})\mathbf{u}_f,$$

where  $\mathbf{A}(\boldsymbol{\phi}) = \mathbf{A}_3\mathbf{A}_2\mathbf{A}_1$  is the Euler rotation matrix,

$$\mathbf{A}_3 = \begin{bmatrix} \cos \varphi_3 & -\sin \varphi_3 & 0 \\ \sin \varphi_3 & \cos \varphi_3 & 0 \\ 0 & 0 & 1 \end{bmatrix}, \quad \mathbf{A}_2 = \begin{bmatrix} \cos \varphi_2 & 0 & \sin \varphi_2 \\ 0 & 1 & 0 \\ -\sin \varphi_2 & 0 & \cos \varphi_2 \end{bmatrix}, \quad \mathbf{A}_1 = \begin{bmatrix} 1 & 0 & 0 \\ 0 & \cos \varphi_1 & -\sin \varphi_1 \\ 0 & \sin \varphi_1 & \cos \varphi_1 \end{bmatrix}.$$

$\varphi_1$ ,  $\varphi_2$ , and  $\varphi_3$  are three Euler angles.  $\mathbf{A}^0$  is the initial value of  $\mathbf{A}$  and is equal to the identity matrix  $\mathbf{I}$ ;  $\mathbf{u}_f$  can be further expressed in terms of the finite element nodal displacement  $\bar{\mathbf{u}}_f$  as

$$\mathbf{u}_f = \mathbf{t}^T \mathbf{N}(x) \mathbf{T} \bar{\mathbf{u}}_f,$$

where  $\mathbf{N}(x)$  is the shape function of the beam element, while  $\mathbf{t}$  and  $\mathbf{T}$  are the transformation matrices between the element local frame and the body frame coordinates for the material point and the nodal DOFs, respectively. Vector  $\mathbf{x}$  is the distance vector from the body frame origin to the material point measured in the body frame. Vector  $\mathbf{x}$  can be expressed as  $\mathbf{x} = \mathbf{x}_E^{(b)} + \mathbf{t}^T \mathbf{x}^{(e)}$ , where  $\mathbf{x}_E^{(b)}$  is the distance vector from the body frame origin to the element local frame origin measured in the body frame and  $\mathbf{x}^{(e)}$  is the distance vector from the element local frame origin to the material point measured in the element local frame.

The velocity of the arbitrary material point is

$$\dot{\mathbf{u}} = \dot{\mathbf{u}}_c + \dot{\mathbf{A}}(\mathbf{x} + \mathbf{u}_f) + \mathbf{A}\dot{\mathbf{u}}_f = [\mathbf{L}_r \ \tilde{\mathbf{L}}_f] \begin{Bmatrix} \dot{\mathbf{u}}_r \\ \dot{\mathbf{u}}_f \end{Bmatrix} = \mathbf{L}\dot{\mathbf{q}},$$

where

$$\begin{aligned} \mathbf{q} &= \{\mathbf{u}_r^T \ \bar{\mathbf{u}}_f^T\}^T, \quad \mathbf{u}_r = \{\mathbf{u}_c^T \ \boldsymbol{\phi}^T\}^T, \quad \mathbf{L}_r = [\mathbf{I} \ \mathbf{B}], \quad \tilde{\mathbf{L}}_f = [\tilde{\mathbf{A}}] = [\mathbf{A}\mathbf{t}^T \mathbf{N}(x) \mathbf{T} \bar{\mathbf{u}}_f], \\ \mathbf{B} &= \left[ \mathbf{A}_3 \mathbf{A}_2 \frac{\partial \mathbf{A}_1}{\partial \varphi_1} \mathbf{u}^* \ \mathbf{A}_3 \frac{\partial \mathbf{A}_2}{\partial \varphi_2} \mathbf{A}_1 \mathbf{u}^* \ \frac{\partial \mathbf{A}_3}{\partial \varphi_3} \mathbf{A}_2 \mathbf{A}_1 \mathbf{u}^* \right] = \mathbf{B}(\boldsymbol{\phi}, \mathbf{u}^*), \\ \mathbf{u}^* &= \mathbf{x} + \mathbf{u}_f = \mathbf{x} + \mathbf{t}^T \mathbf{N}(x) \mathbf{T} \bar{\mathbf{u}}_f. \end{aligned}$$

The kinetic energy of the system can then be expressed as

$$T = \int_V \frac{1}{2} \rho \dot{\mathbf{u}}^T \dot{\mathbf{u}} dV = \frac{1}{2} \begin{Bmatrix} \dot{\mathbf{u}}_r \\ \dot{\mathbf{u}}_f \end{Bmatrix}^T \begin{bmatrix} \mathbf{M}_{rr} & \mathbf{M}_{rf} \\ \mathbf{M}_{fr} & \mathbf{M}_{ff} \end{bmatrix} \begin{Bmatrix} \dot{\mathbf{u}}_r \\ \dot{\mathbf{u}}_f \end{Bmatrix} = \frac{1}{2} \dot{\mathbf{q}}^T \mathbf{M} \dot{\mathbf{q}}, \quad (1)$$

where

$$\mathbf{M}_{rr} = \int_V \rho \mathbf{L}_r^T \mathbf{L}_r dV, \quad \mathbf{M}_{rf} = \int_V \rho \mathbf{L}_r^T \tilde{\mathbf{L}}_f dV, \quad \mathbf{M}_{fr} = \int_V \rho \tilde{\mathbf{L}}_f^T \mathbf{L}_r dV, \quad \mathbf{M}_{ff} = \int_V \rho \tilde{\mathbf{L}}_f^T \tilde{\mathbf{L}}_f dV.$$

The potential energy of the system is simply the summation of the elastic potential energy  $V_e$  and the gravity potential energy  $V_g$ :

$$V = V_e + V_g, \quad V_e = \frac{1}{2} \begin{Bmatrix} \mathbf{u}_r \\ \bar{\mathbf{u}}_f \end{Bmatrix}^T \begin{bmatrix} \mathbf{0} & \mathbf{0} \\ \mathbf{0} & \mathbf{K}_{ff} \end{bmatrix} \begin{Bmatrix} \mathbf{u}_r \\ \bar{\mathbf{u}}_f \end{Bmatrix} = \frac{1}{2} \mathbf{q}^T \mathbf{K} \mathbf{q}, \quad V_g = \int_V \rho g [0 \ 1 \ 0] \mathbf{r} dV, \quad (2)$$

where  $\mathbf{K}_{ff}$  is the stiffness matrix obtained using the finite element method for the bundle and  $\mathbf{r}$  is the distance vector from the global origin to the arbitrary material point.

The bundle is assumed to be constrained at the four bearing pad locations. The bundle cannot move due to the large weight and the frictional force between the bundle and the hosting tube. It is justified to consider the nodes as simply supported at the four bearing pad locations when small oscillatory motion is studied. Therefore, the following constraint conditions apply:

$$\mathbf{u}^{(i)} = \mathbf{u}_c + [\mathbf{A}(\phi) - \mathbf{A}^0] \mathbf{x}^{(i)} + \mathbf{A}(\phi) \bar{\mathbf{u}}_f^{(i)} = \mathbf{0}, \quad (3)$$

where superscript  $(i)$  represents the  $i$ -th constrained node ( $i = 1, \dots, 4$ ).

According to the free and constrained DOFs, (1) and (2) can be partitioned

$$T = \frac{1}{2} \begin{Bmatrix} \dot{\mathbf{u}}_r \\ \dot{\bar{\mathbf{u}}}_{fc} \\ \dot{\bar{\mathbf{u}}}_{fi} \end{Bmatrix}^T \begin{bmatrix} \mathbf{M}_{11} & \mathbf{M}_{12} & \mathbf{M}_{13} \\ \mathbf{M}_{21} & \mathbf{M}_{22} & \mathbf{M}_{23} \\ \mathbf{M}_{31} & \mathbf{M}_{32} & \mathbf{M}_{33} \end{bmatrix} \begin{Bmatrix} \dot{\mathbf{u}}_r \\ \dot{\bar{\mathbf{u}}}_{fc} \\ \dot{\bar{\mathbf{u}}}_{fi} \end{Bmatrix}, \quad V_e = \frac{1}{2} \begin{Bmatrix} \mathbf{u}_r \\ \bar{\mathbf{u}}_{fc} \\ \bar{\mathbf{u}}_{fi} \end{Bmatrix}^T \begin{bmatrix} \mathbf{K}_{11} & \mathbf{K}_{12} & \mathbf{K}_{13} \\ \mathbf{K}_{21} & \mathbf{K}_{22} & \mathbf{K}_{23} \\ \mathbf{K}_{31} & \mathbf{K}_{32} & \mathbf{K}_{33} \end{bmatrix} \begin{Bmatrix} \mathbf{u}_r \\ \bar{\mathbf{u}}_{fc} \\ \bar{\mathbf{u}}_{fi} \end{Bmatrix}, \quad (4)$$

where  $\bar{\mathbf{u}}_{fc} = \{\bar{\mathbf{u}}_f^{(1)T} \ \bar{\mathbf{u}}_f^{(2)T} \ \bar{\mathbf{u}}_f^{(3)T} \ \bar{\mathbf{u}}_f^{(4)T}\}^T$  represents the DOFs corresponding to the constrained nodes and  $\bar{\mathbf{u}}_{fi}$  represents the unconstrained DOFs.

From (3),  $\bar{\mathbf{u}}_{fc}$  can be expressed in terms of  $\mathbf{u}_r$ . The independent DOFs become  $\tilde{\mathbf{q}} = \{\mathbf{u}_r^T \ \bar{\mathbf{u}}_{fi}^T\}^T$ . Substituting into (4), the kinetic energy and elastic potential energy become

$$\begin{aligned} T &= \frac{1}{2} \dot{\tilde{\mathbf{q}}}^T \begin{bmatrix} \mathbf{M}_{11} & \mathbf{M}_{13} \\ \mathbf{M}_{31} & \mathbf{M}_{33} \end{bmatrix} \dot{\tilde{\mathbf{q}}} + \bar{T}(\dot{\tilde{\mathbf{q}}}, \tilde{\mathbf{q}}) = \frac{1}{2} \dot{\tilde{\mathbf{q}}}^T \mathbf{M}_s \dot{\tilde{\mathbf{q}}} + \bar{T}(\dot{\tilde{\mathbf{q}}}, \tilde{\mathbf{q}}), \\ V_e &= \frac{1}{2} \tilde{\mathbf{q}}^T \begin{bmatrix} \mathbf{K}_{11} & \mathbf{K}_{13} \\ \mathbf{K}_{31} & \mathbf{K}_{33} \end{bmatrix} \tilde{\mathbf{q}} + \bar{V}_e(\tilde{\mathbf{q}}) = \frac{1}{2} \tilde{\mathbf{q}}^T \mathbf{K}_s \tilde{\mathbf{q}} + \bar{V}_e(\tilde{\mathbf{q}}), \end{aligned} \quad (5)$$

where

$$\begin{aligned} \bar{T}(\dot{\tilde{\mathbf{q}}}, \tilde{\mathbf{q}}) &= \frac{1}{2} (\dot{\mathbf{u}}_r^T \mathbf{M}_{12} \dot{\bar{\mathbf{u}}}_{fc} + \dot{\bar{\mathbf{u}}}_{fc}^T \mathbf{M}_{21} \dot{\mathbf{u}}_r + \dot{\bar{\mathbf{u}}}_{fi}^T \mathbf{M}_{32} \dot{\bar{\mathbf{u}}}_{fc} + \dot{\bar{\mathbf{u}}}_{fc}^T \mathbf{M}_{23} \dot{\mathbf{u}}_r + \dot{\bar{\mathbf{u}}}_{fc}^T \mathbf{M}_{22} \dot{\bar{\mathbf{u}}}_{fc}), \\ \bar{V}_e(\tilde{\mathbf{q}}) &= \frac{1}{2} (\mathbf{u}_r^T \mathbf{K}_{12} \bar{\mathbf{u}}_{fc} + \bar{\mathbf{u}}_{fc}^T \mathbf{K}_{21} \mathbf{u}_r + \bar{\mathbf{u}}_{fi}^T \mathbf{K}_{32} \bar{\mathbf{u}}_{fc} + \bar{\mathbf{u}}_{fc}^T \mathbf{K}_{23} \mathbf{u}_r + \bar{\mathbf{u}}_{fc}^T \mathbf{K}_{22} \bar{\mathbf{u}}_{fc}). \end{aligned}$$

Gravity potential can also be expressed as a composite function of  $\tilde{\mathbf{q}}$ :

$$V_g = V_g[\mathbf{u}_r, \bar{\mathbf{u}}_{fc}(\mathbf{u}_r), \bar{\mathbf{u}}_{fi}] = V_g(\tilde{\mathbf{q}}).$$

Assuming no nonconservative load, the equations of motion of the system can be obtained using the Lagrange equations [Meirovitch 2001]:

$$\frac{d}{dt} \left( \frac{\partial T}{\partial \dot{\tilde{\mathbf{q}}}} \right)^T - \left( \frac{\partial T}{\partial \tilde{\mathbf{q}}} \right)^T + \left( \frac{\partial V_e}{\partial \tilde{\mathbf{q}}} \right)^T + \left( \frac{\partial V_g}{\partial \tilde{\mathbf{q}}} \right)^T = \mathbf{0}. \quad (6)$$

Substituting (2)–(4) into (6), notice that  $\mathbf{M}_s$  depends on  $\tilde{\mathbf{q}}$  while  $\mathbf{K}_s$  is a constant. The equations of motion become

$$\mathbf{M}_s \ddot{\tilde{\mathbf{q}}} + \dot{\mathbf{M}}_s \dot{\tilde{\mathbf{q}}} + \frac{d}{dt} \left( \frac{\partial \bar{T}}{\partial \dot{\tilde{\mathbf{q}}}} \right) - \frac{\partial}{\partial \tilde{\mathbf{q}}} \left( \frac{1}{2} \dot{\tilde{\mathbf{q}}} \mathbf{M}_s \dot{\tilde{\mathbf{q}}} \right)^T - \frac{\partial \bar{T}}{\partial \tilde{\mathbf{q}}} + \mathbf{K}_s \tilde{\mathbf{q}} + \mathbf{R}(\tilde{\mathbf{q}}) + \mathbf{H}(\tilde{\mathbf{q}}) = \mathbf{0},$$

where  $\mathbf{R}$  represents the nonlinear term from the derivative of the elastic potential energy and  $\mathbf{H}$  represents the force and moment induced by gravity:

$$\begin{aligned} \mathbf{R}(\tilde{\mathbf{q}}) &= \frac{\partial \bar{V}_e}{\partial \tilde{\mathbf{q}}} = \begin{bmatrix} \mathbf{K}_{12} \bar{\mathbf{u}}_{fc} + \left( \frac{\partial \bar{\mathbf{u}}_{fc}}{\partial \mathbf{u}_r} \right)^T \mathbf{K}_{21} \mathbf{u}_r + \left( \frac{\partial \bar{\mathbf{u}}_{fc}}{\partial \mathbf{u}_r} \right)^T \mathbf{K}_{23} \bar{\mathbf{u}}_{fi} + \left( \frac{\partial \bar{\mathbf{u}}_{fc}}{\partial \mathbf{u}_r} \right)^T \mathbf{K}_{22} \bar{\mathbf{u}}_{fc} \\ \mathbf{K}_{32} \bar{\mathbf{u}}_{fc} \end{bmatrix} = \begin{bmatrix} \mathbf{R}_r \\ \mathbf{R}_{fi} \end{bmatrix}, \\ \mathbf{H}(\tilde{\mathbf{q}}) &= \frac{\partial V_g}{\partial \tilde{\mathbf{q}}} = \left\{ \left( \frac{\partial V_g}{\partial \mathbf{u}_r} + \frac{\partial V_g}{\partial \bar{\mathbf{u}}_{fc}} \frac{\partial \bar{\mathbf{u}}_{fc}}{\partial \mathbf{u}_r} \right)^T, \left( \frac{\partial V_g}{\partial \bar{\mathbf{u}}_{fi}} \right)^T \right\}^T, \end{aligned}$$

where

$$\frac{\partial V_g}{\partial \mathbf{u}_r} = \int_V \rho g [0 \ 1 \ 0] [\mathbf{I} \ \mathbf{B}] dV, \quad \frac{\partial V_g}{\partial \bar{\mathbf{u}}_{fc}} = \int_V \rho g [0 \ 1 \ 0] [\tilde{\mathbf{A}}] dV,$$

and  $\tilde{\mathbf{A}}$  is a fraction of  $\mathbf{A}$  which corresponds to the constraint DOFs  $\mathbf{u}_{fc}$ . From (3), it can be obtained that

$$\frac{\partial \bar{\mathbf{u}}_{fc}}{\partial \mathbf{u}_r} = -\mathbf{A}^{-1} [\mathbf{I} \ \mathbf{B}(\mathbf{u}_c^*)],$$

where  $\mathbf{u}_c^* = \mathbf{x} + \bar{\mathbf{u}}_{fc}(\tilde{\mathbf{q}})$ .

The damping effect caused by the velocity terms is not within the scope of this paper. Ignoring the velocity terms  $\dot{\mathbf{M}}_s \dot{\tilde{\mathbf{q}}}$ ,  $(\partial/\partial \tilde{\mathbf{q}})(\frac{1}{2} \dot{\tilde{\mathbf{q}}} \mathbf{M}_s \dot{\tilde{\mathbf{q}}})$ ,  $\partial \bar{T}/\partial \tilde{\mathbf{q}}$ , and those in  $(d/dt)(\partial \bar{T}/\partial \dot{\tilde{\mathbf{q}}})$ , the governing equations become

$$\mathbf{M}_s \ddot{\tilde{\mathbf{q}}} + \mathbf{K}_s \tilde{\mathbf{q}} + \mathbf{S}(\tilde{\mathbf{q}}, \tilde{\mathbf{q}}) + \mathbf{R}(\tilde{\mathbf{q}}) + \mathbf{H}(\tilde{\mathbf{q}}) = \mathbf{0}, \quad (7)$$

where

$$\mathbf{S}(\tilde{\mathbf{q}}, \tilde{\mathbf{q}}) = \begin{bmatrix} \mathbf{M}_{12} \ddot{\bar{\mathbf{u}}}_{fc} + \left( \frac{\partial \bar{\mathbf{u}}_{fc}}{\partial \mathbf{u}_r} \right)^T \mathbf{M}_{21} \ddot{\mathbf{u}}_r + \left( \frac{\partial \bar{\mathbf{u}}_{fc}}{\partial \mathbf{u}_r} \right)^T \mathbf{M}_{23} \ddot{\mathbf{u}}_{fi} + \left( \frac{\partial \bar{\mathbf{u}}_{fc}}{\partial \mathbf{u}_r} \right)^T \mathbf{M}_{22} \ddot{\bar{\mathbf{u}}}_{fc} \\ \mathbf{M}_{32} \ddot{\bar{\mathbf{u}}}_{fc} \end{bmatrix} = \begin{bmatrix} \mathbf{S}_r \\ \mathbf{S}_{fi} \end{bmatrix}.$$

If the dynamic terms in (7) are dropped, a static equilibrium solution of the system  $\tilde{\mathbf{q}}^0$  can be obtained through iteration. A Fortran90 code is implemented to solve for the equilibrium solution. For a convergence criterion of 0.001 for the L2 norm of the displacement vector, it takes two steps to reach the converged equilibrium solution. Figure 2 shows the scaled global deformation of the bundle at three different locations for the equilibrium solution.

Denoting  $\boldsymbol{\delta}$  as the deviation from the equilibrium position, the generalized coordinates can be expressed as  $\tilde{\mathbf{q}} = \tilde{\mathbf{q}}^0 + \boldsymbol{\delta}$ . Substituting this equation into (7), dropping the constant terms and linearizing the nonlinear terms with a Taylor expansion at  $\tilde{\mathbf{q}}^0$ , the governing equation for oscillation about the equilibrium can be obtained as

$$\mathbf{M}_s \ddot{\boldsymbol{\delta}} + \mathbf{S}(\boldsymbol{\delta}, \tilde{\mathbf{q}}^0) + \left( \mathbf{K}_s + \frac{\partial \mathbf{R}}{\partial \tilde{\mathbf{q}}}(\tilde{\mathbf{q}}^0) + \frac{\partial \mathbf{H}}{\partial \tilde{\mathbf{q}}}(\tilde{\mathbf{q}}^0) \right) \boldsymbol{\delta} = \mathbf{0}. \quad (8)$$

The term  $\mathbf{S}(\ddot{\delta}, \tilde{\mathbf{q}}^0)$  can be further linearized using the Taylor expansion at  $\ddot{\delta} = \mathbf{0}$ , and (8) becomes

$$\left( \mathbf{M}_s + \frac{\partial \mathbf{S}}{\partial \ddot{\delta}}(\mathbf{0}, \tilde{\mathbf{q}}^0) \right) \ddot{\delta} + \left( \mathbf{K}_s + \frac{\partial \mathbf{R}}{\partial \tilde{\mathbf{q}}}(\tilde{\mathbf{q}}^0) + \frac{\partial \mathbf{H}}{\partial \tilde{\mathbf{q}}}(\tilde{\mathbf{q}}^0) \right) \delta = \mathbf{0}, \quad (9)$$

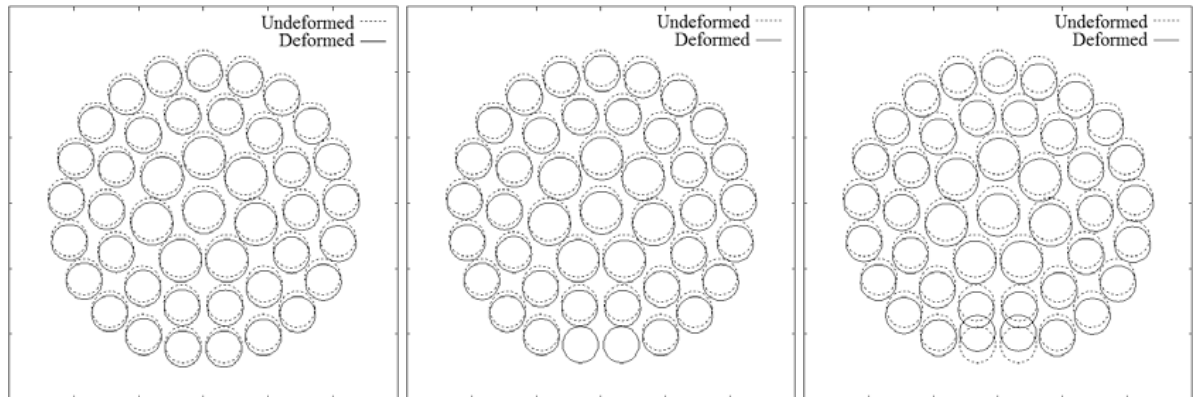
where

$$\begin{aligned} \frac{\partial \mathbf{S}}{\partial \ddot{\delta}}(\mathbf{0}, \tilde{\mathbf{q}}^0) &= \begin{bmatrix} \frac{\partial \mathbf{S}_r}{\partial \ddot{\mathbf{u}}_r} & \left( \frac{\partial \ddot{\mathbf{u}}_{fc}}{\partial \ddot{\mathbf{u}}_r} \right)^T \mathbf{M}_{23} \\ \mathbf{M}_{32} \left( \frac{\partial \ddot{\mathbf{u}}_{fc}}{\partial \ddot{\mathbf{u}}_r} \right) & \mathbf{0} \end{bmatrix}_{\substack{\ddot{\delta}=\mathbf{0} \\ \tilde{\mathbf{q}}=\tilde{\mathbf{q}}^0}}, \quad \frac{\partial \mathbf{R}}{\partial \tilde{\mathbf{q}}}(\tilde{\mathbf{q}}^0) = \begin{bmatrix} \frac{\partial \mathbf{R}_r}{\partial \mathbf{u}_r} & \left( \frac{\partial \bar{\mathbf{u}}_{fc}}{\partial \mathbf{u}_r} \right)^T \mathbf{K}_{23} \\ \mathbf{K}_{32} \left( \frac{\partial \bar{\mathbf{u}}_{fc}}{\partial \mathbf{u}_r} \right) & \mathbf{0} \end{bmatrix}_{\substack{\ddot{\delta}=\mathbf{0} \\ \tilde{\mathbf{q}}=\tilde{\mathbf{q}}^0}}, \\ \frac{\partial \ddot{\mathbf{u}}_{fc}}{\partial \ddot{\mathbf{u}}_r} &\doteq \begin{bmatrix} -\mathbf{A}^{-1} - \mathbf{A}^{-1} \mathbf{B}(\varphi, \mathbf{u}^{(1)}) \\ \vdots \\ -\mathbf{A}^{-1} - \mathbf{A}^{-1} \mathbf{B}(\varphi, \mathbf{u}^{(4)}) \end{bmatrix}, \quad \frac{\partial \mathbf{u}_{fc}}{\partial \mathbf{u}_r} \doteq \begin{bmatrix} -\mathbf{A}^{-1} - \mathbf{A}^{-1} \mathbf{B}(\varphi, \mathbf{u}^{*(1)}) \\ \vdots \\ -\mathbf{A}^{-1} - \mathbf{A}^{-1} \mathbf{B}(\varphi, \mathbf{u}^{*(4)}) \end{bmatrix}, \\ \frac{\partial \mathbf{H}}{\partial \tilde{\mathbf{q}}} &= \sum_{i=1}^{Ne} \int_{V_i} \begin{bmatrix} \mathbf{0} & \mathbf{0} & \mathbf{0} \\ \mathbf{0} & \frac{\partial \mathbf{B}_{2,:}}{\partial \boldsymbol{\phi}} & \frac{\partial \mathbf{B}_{2,:}}{\partial \mathbf{u}_f} \\ \mathbf{0} & \frac{\partial \tilde{\mathbf{A}}_{2,:}}{\partial \boldsymbol{\phi}} & \mathbf{0} \end{bmatrix}_{\tilde{\mathbf{q}}=\tilde{\mathbf{q}}^0} dV, \end{aligned}$$

and where the subscript  $(2, :)$  represents the second row of the matrix.  $\frac{\partial \mathbf{S}_r}{\partial \ddot{\mathbf{u}}_r}$  and  $\frac{\partial \mathbf{R}_r}{\partial \mathbf{u}_r}$  are  $6 \times 6$  matrices.

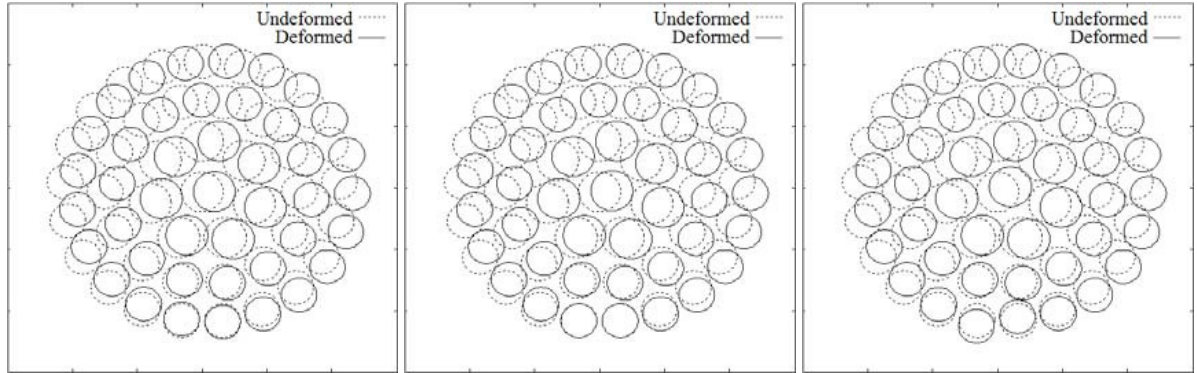
### 3. Numerical solutions and discussion

A numerical solution to the governing equations of motion, (9), is sought. The geometry and material properties of the bundle are listed in Table 1. The numerical solution shows that the fundamental natural frequency is 6.1 Hz. After normalizing the eigenvector, it is found that the  $Z$ -direction rigid body rotation is the primary dominant component and the  $X$ -direction rigid body translation is the secondary. The



**Figure 2.** Scaled deformation in equilibrium at different locations: bundle ends (left), bearing pads (middle), and midspan (right).

Parameter	Symbol	Value
Bundle length (mm)	$L$	500.0
Outer ring mean radius (mm)	$R_1$	42.5
Intermediate ring mean radius (mm)	$R_2$	30.0
Inner ring mean radius (mm)	$R_3$	16.5
Ring and rib width (mm)	$b$	3.4
Endplate thickness (mm)	$t$	3.0
Young's modulus (GPa)	$E$	200.0
Poisson's ratio	$\nu$	0.3
Shear modulus (GPa)	$G$	76.9

**Table 1.** Geometric dimensions and material properties.**Figure 3.** Scaled deviation of the rocking mode at different locations: bundle ends (left), bearing pads (middle), and midspan (right).

elastic DOFs are negligibly small except those on the two supporting rods at the bottom. To visualize the solution, the mode shape of the small deviation is shown in Figure 3. The total displacement, which is the static deformation superposed with the scaled deviation eigenvector, is shown in Figure 4. The mode exhibits a rocking motion in terms of the total displacement.

It is necessary to validate the accuracy of the meshing scheme and the numerical methods used in this paper against independent finite element code. Most general finite element codes do not incorporate the floating frame formulation; therefore comparison can be made on a conventional finite element model of the bundle structure. The above rigid-elasto model is degraded to a conventional finite element model by removing the floating frame formulation. The modal solution from this model is compared to that of an independent finite element model developed in ANSYS®ED 8.0 using straight beam elements. The comparison of the natural frequencies is shown in Table 2.

From the above solutions, it can be seen that the rigid body motion and gravity have a significant influence on the rocking frequency. The structural solution, which does not include the rigid body DOFs and the gravity terms, shows a frequency of 7.7 Hz, while the rigid-elasto solution shows a frequency of

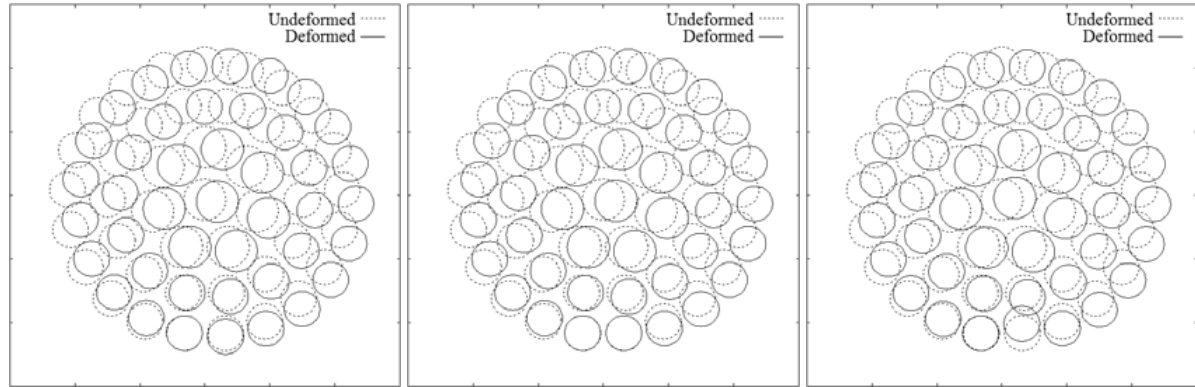


**Figure 4.** Scaled total displacement of the rocking mode at different locations: bundle ends (left), bearing pads (middle), and midspan (right).

Mode	Natural frequencies (Hz)	
	This paper	ANSYS ED 8.0
1	7.7	7.5
2	50.8	50.0
3	93.0	87.7
4	93.8	93.2
5	94.3	93.6
6	94.8	94.0

**Table 2.** Validation on the current finite element model (without floating frame formulation) against ANSYS ED 8.0.

Mode	Frequencies (Hz)		Difference (%)	
	With			
	Without			
1	6.1	7.7	20.8	
2	50.4	50.8	0.8	
3	91.9	93.0	1.2	
4	93.8	93.8	0.0	
5	94.2	94.3	0.1	
6	94.4	94.8	0.4	

**Table 3.** Influence of gravity. Frequencies are shown for with and without floating frame formulation and gravity.

6.1 Hz. The difference is 20.8%. It can be seen in Table 3 that the influence of gravity is only significant on the fundamental mode. This is because the fundamental mode is related to rigid body rotations and gravity does positive work when the bundle rocks from the equilibrium position to either side. The

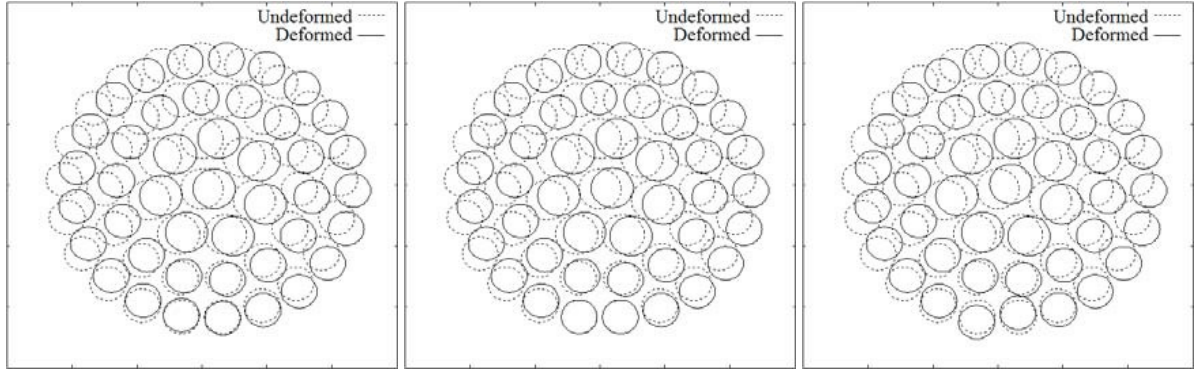


**Figure 5.** Scaled deformation of the rocking mode at different locations without floating frame formulation and nonlinear terms: bundle ends (left), bearing pads (middle), and midspan (right).

second mode is a pure vertical motion and the gravity work cancels itself in the motion. Higher modes are characterized by the bending deformation of the rods, and thus receive little influence from gravity. The fundamental mode of the structural solution is also shown in Figure 5 for comparison.

Although the influence of gravity is important, it needs to be clarified that the impact is delivered “indirectly”. The major influence of gravity is enforced through the equilibrium solution hidden in the nonlinear terms  $\partial \mathbf{S} / \partial \ddot{\boldsymbol{\delta}}$  and  $\partial \mathbf{R} / \partial \tilde{\boldsymbol{q}}$ , especially the latter. The  $\partial \mathbf{R}_r / \partial \mathbf{u}_r$  term in  $\partial \mathbf{R} / \partial \tilde{\boldsymbol{q}}$  can be further expressed as

$$\begin{aligned} \frac{\partial \mathbf{R}_r}{\partial \mathbf{u}_r} = & \left[ \mathbf{K}_{12} \frac{\partial \mathbf{u}_{fc}}{\partial \mathbf{u}_r} + \left( \frac{\partial \mathbf{u}_{fc}}{\partial \mathbf{u}_r} \right)^T \mathbf{K}_{21} + 2 \left( \frac{\partial \mathbf{u}_{fc}}{\partial \mathbf{u}_r} \right)^T \mathbf{K}_{22} \frac{\partial \mathbf{u}_{fc}}{\partial \mathbf{u}_r} \right]_{\tilde{\boldsymbol{q}}^0} \\ & + \left[ \mathbf{u}_r^T \frac{\partial \mathbf{h}_i^A}{\partial \mathbf{u}_r} + \frac{\partial}{\partial \mathbf{u}_r} (\mathbf{h}_i^B \mathbf{u}_{fi}) + \mathbf{u}_r^T \frac{\partial \mathbf{h}_i^C}{\partial \mathbf{u}_r} \right]_{\tilde{\boldsymbol{q}}^0}, \quad (10) \end{aligned}$$

where  $\mathbf{h}_i^A$ ,  $\mathbf{h}_i^B$ , and  $\mathbf{h}_i^C$  are the  $i$ -th rows of  $(\partial \mathbf{u}_{fc} / \partial \mathbf{u}_r)^T \mathbf{K}_{21}$ ,  $(\partial \mathbf{u}_{fc} / \partial \mathbf{u}_r)^T \mathbf{K}_{23}$ , and  $(\partial \mathbf{u}_{fc} / \partial \mathbf{u}_r)^T \mathbf{K}_{22}$ , respectively. The terms in the second set of brackets in (10) contain the equilibrium solution which is a consequence of gravity. If this term is dropped, the rocking frequency will increase to a value which is almost identical to the structural solution. It should be noticed that the coupling term between the constraint DOF and the rigid body DOF terms  $\mathbf{K}_{12}$  and  $\mathbf{K}_{21}$  is actually zero; therefore, the corresponding terms in the second set of brackets are dominant. Even a small quantity in the second set of brackets may have a strong influence on the result. Dissimilarly to this, the contributions from the nonlinear terms in  $\partial \mathbf{S} / \partial \ddot{\boldsymbol{\delta}}$  are very small compared to those from  $\mathbf{M}_{12}$  and  $\mathbf{M}_{21}$ , and hence have little influence on the result.

Influences from the nonlinearity in the Euler rotation matrix  $\mathbf{A}$ , the derivative matrix  $\mathbf{B}$ , and the constraint equations are relatively small compared to the indirect influence of gravity. However, if the constraint equations are linearized so that  $\partial \mathbf{u}_{fc} / \partial \mathbf{u}_r$  becomes a constant, then the derivatives of  $\mathbf{h}_i^A$ ,  $\mathbf{h}_i^B$ , and  $\mathbf{h}_i^C$  in (10) will become zero and hence the influence from gravity will be lost.

There is also a “direct” influence of gravity, the  $\partial \mathbf{H} / \partial \tilde{\mathbf{q}}$  term. This represents the rate of change in the gravity-induced moment with respect to the displacement. Although this term is derived from the gravity potential, its impact is negligible in this application, because the rods in the bundle are almost evenly distributed. Numerical solution shows that the values of the elements in the  $\partial \mathbf{H} / \partial \tilde{\mathbf{q}}$  term are a few orders lower in magnitude than those in the  $\mathbf{K}_s$  and  $\partial \mathbf{R} / \partial \tilde{\mathbf{q}}$  terms.

#### 4. Experiment

An experiment was carried out to determine the rocking frequency of the bundle. Lateral oscillation in the horizontal direction of the bundle may be related to the rocking motion of the bundle. Its frequency can be obtained by monitoring the oscillatory motion of a point on the outer ring of the bundle near the end. Instead of using accelerometers, a noncontact displacement sensor is used for vibration measurement. This type of sensor is more sensitive to low frequency, relatively large displacement vibrations.

To measure the bundle vibration, a 43-rod bundle is placed inside a 4-inch PVC tube supported by strong steel columns, as shown in Figure 6. A noncontact differential variable reluctance transducer (MicroStrain NC-DVRT-1.5) is used to record the lateral displacement of the bundle. The sensor detects the distance between a target object and the face of the transducer head. The reluctance of the coils within the sensor is changed when the face of the transducer is in close proximity to a ferrous or highly conductive material. The transducer outputs a voltage signal that is a nonlinear function of the distance. The typical repeatability of this transducer is  $\pm 2 \mu\text{m}$  and the frequency range is 0 to 800 Hz. The transducer is mounted at one side of the tube near the end of the bundle. The transducer head penetrates the tube wall and approaches the rod around the 4 o’clock position. The initial gap from the head of the transducer is around  $200 \mu\text{m}$  for the best gain factor in the output. The time-domain voltage signal is sampled with a sampling rate of 5 kHz and recorded using a data acquisition system. The voltage signal is then converted to gap distance and analyzed using code written in Matlab to obtain the spectral information.

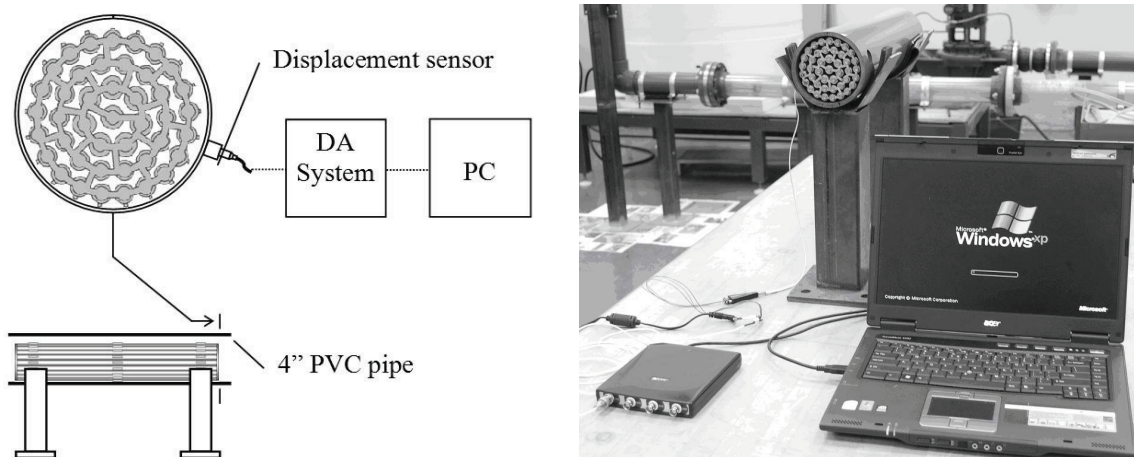


**Figure 6.** Experimental setup.

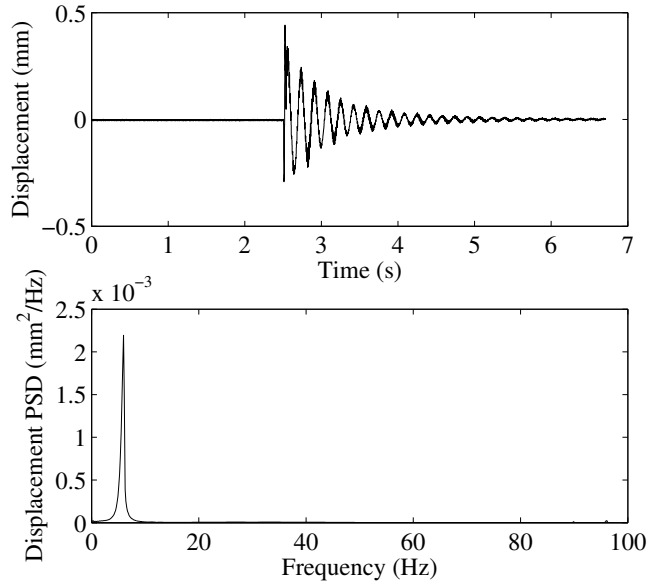


**Figure 7.** The response of the bundle to an impulse.

The response of the bundle to an impulse is recorded and analyzed. The time-domain displacement of the monitored point and its power spectral density are shown in Figure 7. The response of the rocking mode is found to be clear and free of noise from higher modes, such as the 90–100 Hz mode group corresponding to the first bending mode of the rods. The rocking mode frequency is 6.0 Hz. The damping ratio calculated from the difference between the peaks in the time-domain signal is about 0.05. For such a low damping ratio, the effect of damping on natural frequencies is negligible.

The tube is built from PVC, a material softer than steel. When the steel bearing pads contact the tube inner surface, the soft material will deform. This deformation leads to a contact stiffness and may have an influence on the fundamental frequency. It is necessary to examine the contact stiffness and compare it to the overall equivalent stiffness that relates to the bundle deformation with the current boundary conditions. The Boussinesq point contact solution [Johnson 1985] is used to estimate the order of magnitude of the normal contact stiffness  $k_C$ . Based on the solution, the normal elastic deformation  $w$  at the contact location when a point object indents on a semiinfinite elastic space in the normal direction can be expressed as

$$w = \frac{2P(1-\nu)}{4\pi Gr}, \quad (11)$$

where  $P$  is the normal contact force,  $r$  is the contact point radius,  $G$  is the shear modulus of the elastic space ( $G = 1$  GPa for PVC), and  $\nu$  is the Poisson's ratio of the elastic space ( $\nu = 0.41$  for PVC). The order of magnitude of the contact stiffness on one bearing pad can then be estimated as  $k_{C,1} \sim P/w = \pi Gr/(1-\nu) \approx 10^7$ . The overall contact stiffness provided by the contact of the four bearing pads is  $k_C = 4k_{C,1} \sim 4 \times 10^7$ . Because the most potential energy in the rocking mode comes from the deformation of the two rods that contact the tube through bearing pads, it is reasonable to compare  $k_C$  with the equivalent stiffness of these rods. The equivalent stiffness can be conveniently estimated by dividing the weight of the bundle and the vertical displacement of its mass center from a static analysis.

The order of magnitude of the equivalent stiffness is obtained as  $k_E \sim 1 \times 10^6$ , which is far smaller than  $k_C$ . This indicates that the contact stiffness can be considered infinite and the tube can be regarded as rigid with regards to the lower bundle vibration modes.

## 5. Conclusions

The vibration of a 43-rod simulation CANDU fuel bundle horizontally placed in a supporting tube is studied through numerical models and experiments. The floating frame formulation and nonlinear constraint conditions are employed in a finite element model to predict the natural frequencies of the small-amplitude oscillations about the equilibrium position. The fundamental mode is found to be a low frequency rocking mode, which is a combination of rigid body motion and elastic deformation, but is dominated by the rigid body rotation about a bundle axis. Gravity is found to influence the rocking motion, and to reduce the frequency. The simulation results are in good agreement with experimental results.

## References

- [Cho et al. 2000] M.-S. Cho, K.-S. Sim, H. C. Suk, and S.-K. Chang, “Static strength analysis of CANDU-6 reactor fuel bundle”, *Nucl. Eng. Des.* **200**:3 (2000), 407–419.
- [Horhoianu and Ionescu 2006] G. Horhoianu and D. V. Ionescu, “A finite element model for static strength analysis of CANDU fuel bundle”, *Kerntechnik* **71**:4 (2006), 203–207.
- [Johnson 1985] K. L. Johnson, *Contact mechanics*, Cambridge University Press, London, 1985.
- [Judah 1992] J. Judah, “Overview of fuel inspections at the Darlington nuclear generating station”, pp. 1–22 in *3rd International CNS CANDU Fuel Conference* (Chalk River, 1992), Canadian Nuclear Society, Toronto, ON, 1992.
- [Meirovitch 2001] L. Meirovitch, *Fundamentals of vibrations*, McGraw-Hill, Boston, 2001.
- [Reddy 1984] J. N. Reddy, “A simple higher-order theory for laminated composite plates”, *J. Appl. Mech. (ASME)* **51**:4 (1984), 745–752.
- [Schwab and Meijaard 2002] A. L. Schwab and J. P. Meijaard, “Small vibrations superimposed on a prescribed rigid body motion”, *Multibody Syst. Dyn.* **8**:1 (2002), 29–49.
- [Shabana 2005] A. A. Shabana, *Dynamics of multibody systems*, 3rd ed., Cambridge University Press, Cambridge, 2005.
- [Yu and Wen 2007] S. D. Yu and D. C. Wen, “An efficient plate finite element and its application to three-dimensional deformations of CANDU fuel endplate rings”, *Nucl. Eng. Des.* **237**:4 (2007), 342–352.
- [Zhang and Yu 2010a] X. Zhang and S. D. Yu, “Theoretical and experimental investigations of oscillatory rolling motion of a rod bundle inside a tube”, in *Proceedings of 11th Pan-American Congress of Applied Mechanics (PACAM XI)* (Foz do Iguaçu, 2010), edited by A. R. Aguiar and T. L. Attard, Brazilian Society of Mechanical Sciences and Engineering, Rio de Janeiro, 2010. Paper #PAC0512.
- [Zhang and Yu 2010b] X. Zhang and S. D. Yu, “A thick plate model for bending and twisting of CANDU fuel endplates”, *Nucl. Eng. Des.* **240**:10 (2010), 2565–2570.

Received 5 Mar 2010. Revised 3 Jun 2010. Accepted 12 Nov 2010.

XUAN ZHANG: [x8zhang@ryerson.ca](mailto:x8zhang@ryerson.ca)

*Department of Mechanical and Industrial Engineering, Ryerson University, 350 Victoria Street, Toronto, ON M5B 2K3, Canada*

SHUDONG YU: [syu@ryerson.ca](mailto:syu@ryerson.ca)

*Department of Mechanical and Industrial Engineering, Ryerson University, 350 Victoria Street, Toronto, ON M5B 2K3, Canada*

## NONLINEAR DYNAMICS AND SENSITIVITY TO IMPERFECTIONS IN AUGUSTI'S MODEL

DIEGO ORLANDO, PAULO BATISTA GONÇALVES, GIUSEPPE REGA AND STEFANO LENCI

The influence of geometric imperfections on the nonlinear behavior and stability of Augusti's model under static and dynamic loads is analyzed. This 2-DOF lumped-parameter system is an archetypal model of modal interaction in stability theory representing a large class of structural problems. When the system displays coincident buckling loads, several postbuckling paths emerge from the bifurcation point (critical load) along the fundamental path, in particular coupled unstable postbuckling paths that control the nonlinear dynamics of the system for load levels lower than the critical load. Systems displaying unstable postbuckling behavior are particularly sensitive to initial imperfections. They decrease the static buckling load and distort the topology of the safe potential well. Herein, coupled/uncoupled dynamic responses, bifurcations, escape from the prebuckling potential well, stability, space-time-varying displacements, and attractor-manifold-basin phase portraits are numerically evaluated with the aim of enlightening the effect of system imperfection sensitivity. In particular, the investigation of the reduction of escape load for several varying system parameters highlights the remarkable loss of safety and dynamic integrity of the structure due to penetration of eroding fractal tongues into the safe basin.

### 1. Introduction

The influence of imperfections on bifurcations can be traced back at least to [Koiter 1945] in problems of elastic stability and [Zocher 1933] in problems involving liquid crystals. A mathematical treatment of the problem can be found, for example, in [Iooss and Joseph 1980]. Analysis of the imperfection sensitivity of simplified models exhibiting different types of bifurcation under static loads can be found in [Croll and Walker 1972; Thompson and Hunt 1973; 1984; Naschie 1990], among others. These models have been used to demonstrate the nonlinear behavior and stability of several classes of structures. The influence of imperfection is particularly important in systems liable to postbuckling behavior. One area where the study of imperfection sensitivity is essential is the analysis of systems where the interaction of different buckling modes with equal or nearly equal bifurcation loads may conspire to increase or even generate unstable postbuckling paths.

Augusti's model constitutes an archetypal model for this class of problems [Augusti 1964]. Static analysis of this model can be found in, for example, [Croll and Walker 1972; Bažant and Cedolin 1991; Pignataro et al. 1991; Raftoyiannis and Kounadis 2000]. Augusti's model represents a large class of structures where the postbuckling behavior is controlled by modal coupling. This model may present two equal or nearly equal critical loads associated with two different critical modes. When the modes

---

The authors acknowledge the financial support of the Brazilian research agencies CAPES, CNPq and FAPERJ-CNE..

**Keywords:** Augusti's model, modal coupling, nonlinear oscillations, imperfection sensitivity, dynamic instability, load-carrying capacity.

are analyzed separately, the structure exhibits a stable symmetric postbuckling behavior. However, when the modal coupling is taken into account, apart from the uncoupled solutions, which become unstable, new coupled unstable paths emerge from the bifurcation points. These unstable coupled paths delimit the safe prebuckling well and the magnitude of the perturbations that the structure can withstand without escaping from the safe well. Continuous structures displaying coincident or nearly coincident buckling loads, are, among others, plates, shells, cold-formed struts, and some frame structures [Tvergaard 1973; Bažant and Cedolin 1991; Kiymaz 2005; Chen and Yu 2006; Brubak and Hellesland 2007; Dinis et al. 2007; Kołakowski 2007; Quinn et al. 2007]. A particularly notorious case is the cylindrical shell under axial compression, which, as shown in [Koiter 1945], may display for certain geometries an infinite number of coincident buckling loads [Heijden 2008]. Another interesting model in the static context proposed by Augusti was thoroughly investigated in [Elishakoff et al. 1996].

The influence of modal coupling on the nonlinear dynamics of Augusti's model has been addressed in [Gonçalves et al. 2009]. Here, upon formulating the mechanical problem for the system with imperfections (Section 2), a detailed parametric analysis shows the influence of geometric imperfections on the buckling and postbuckling behavior of Augusti's model and how the unstable solutions control the global behavior of the system (Section 3.1). The analysis of the system under harmonic base excitation and different forcing directions clarifies the importance of the imperfections on the dynamics through the analysis of bifurcation diagrams and the evolution of basins of attraction, focusing on the evaluation of system load-carrying capacity (Section 3.2). Although this constitutes an important issue in nonlinear structural dynamics, little is known on the influence of imperfections on the nonlinear dynamics of structures liable to unstable postbuckling behavior.

## 2. Formulation of the problem

Figure 1a illustrates Augusti's model. It is an inverted spatial pendulum composed of a slender, rigid (but massless) bar of length  $l$ , with a tip-mass  $m$ , pinned at the base, where two rotational springs with constant stiffnesses  $k_1$  and  $k_2$  initially act in perpendicular planes and rotate with the bar. The angles

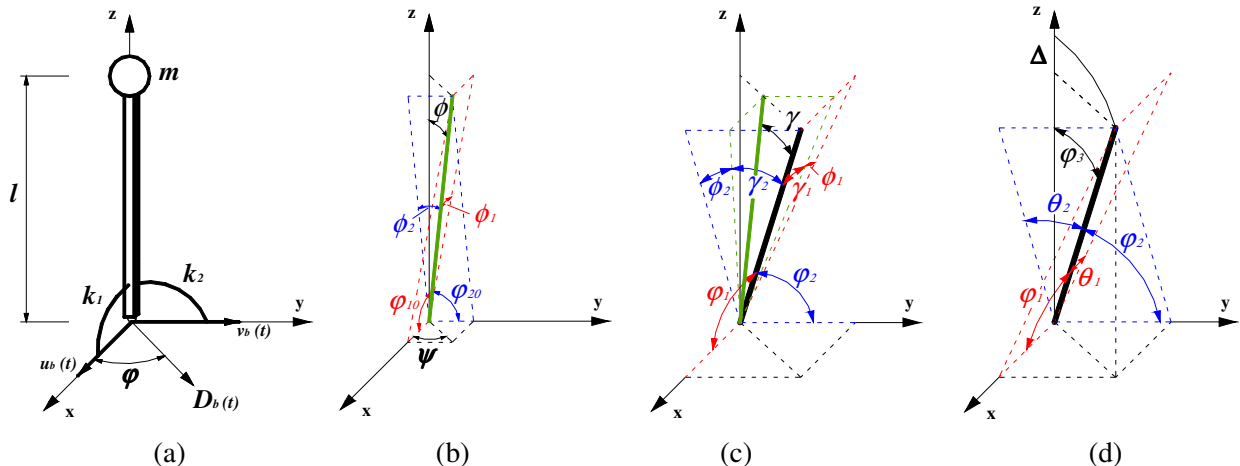


**Figure 1.** Augusti's 2-DOF model. Perfect system: undeformed (a) and deformed (d); imperfect system: undeformed (b) and deformed (c, d).

$\theta_1$  and  $\theta_2$  (Figure 1d) are chosen as the two DOFs. Figure 1a shows the system under a harmonic base excitation  $D_b(t)$ , acting at an angle  $\varphi$  with respect to the  $x$  axis. The force  $D_b(t)$  is decomposed into two components,  $u_b(t)$  in the  $x$  direction and  $v_b(t)$  in the  $y$  direction. These components are given by  $u_b = F_b \cos \varphi \sin(\omega_e t)$  and  $v_b = F_b \sin \varphi \sin(\omega_e t)$ , where  $F_b$  is the forcing magnitude and  $\omega_e$  is the forcing frequency. Figure 1 shows the auxiliary variables necessary for the derivation of the equations of motion of the imperfect system. The initial configuration of the geometrically imperfect column is defined by the angles  $\phi$  and  $\psi$  shown in Figure 1b, where the two angles  $\varphi_{10}$  and  $\varphi_{20}$  are also reported. The angles  $\phi_1$  and  $\phi_2$  are the geometric imperfections of the two torsional springs and  $\gamma_1$  and  $\gamma_2$  are their deformations in the  $\theta_1$  and  $\theta_2$  directions (see Figure 1c). The following expressions hold:

$$\varphi_3 = \phi + \gamma, \quad \theta_1 = \phi_1 + \gamma_1, \quad \theta_2 = \phi_2 + \gamma_2, \quad (1)$$

$\varphi_1$ ,  $\varphi_2$ , and  $\varphi_3$  being the angles of the imperfect pendulum with the three axes in the deformed configuration (Figure 1d).

The dimensionless total potential energy of the system is given by [Orlando 2010]

$$\bar{V} = \frac{V}{ml^2} = \frac{1}{2} \frac{\omega_p^2}{\lambda} (\theta_1 - \phi_1)^2 + \frac{1}{2} \frac{\omega_p^2}{\lambda} (\theta_2 - \phi_2)^2 - \omega_p^2 \left( \sqrt{1 - \sin^2 \phi_1 - \sin^2 \phi_2} - \sqrt{1 - \sin^2 \theta_1 - \sin^2 \theta_2} \right), \quad (2)$$

where  $P = mg$ ,  $\omega_p^2 = g/l$ ,  $\lambda = P/P_{\text{cr}}$ ,  $k/ml^2 = \omega_p^2/\lambda$ ,  $k_1 = k_2 = k$ , and  $P_{\text{cr1}} = P_{\text{cr2}} = P_{\text{cr}} = k/l$ , with  $\omega_p$  and  $P_{\text{cr}}$  being the pendulum natural frequency and buckling load, respectively, while the dimensionless kinetic energy is written as

$$\bar{T} = \frac{T}{ml^2} = \frac{1}{2l^2} \left( (l\dot{\theta}_1 \cos \theta_1 + \dot{u}_b)^2 + (l\dot{\theta}_2 \cos \theta_2 + \dot{v}_b)^2 + \frac{l^2(\dot{\theta}_1 \cos \theta_1 \sin \theta_1 + \dot{\theta}_2 \cos \theta_2 \sin \theta_2)^2}{\cos^2 \theta_1 + \cos^2 \theta_2 - 1} \right), \quad (3)$$

where the dot indicates differentiation with respect to time  $t$ .

Using Hamilton's principle of least action, the equations of motion of the system are obtained as the extremals of the functional  $\Phi = \int_{t_1}^{t_2} L dt$ ,  $L$  being the Lagrangian. Then the evolution of  $\theta_i$  with time is subjected to the Euler–Lagrange equations of motion:

$$\frac{d}{dt} \frac{\partial(\bar{T})}{\partial \dot{\theta}_i} - \frac{\partial(\bar{T})}{\partial \theta_i} + \frac{\partial(\bar{V})}{\partial \theta_i} = 0. \quad (4)$$

Considering also a viscous damping for the geometrically imperfect Augusti's model, the equations of motion in terms of the generalized coordinates  $\theta_1$  and  $\theta_2$  are given explicitly by [Orlando 2010]

$$\begin{aligned} & (\ddot{\theta}_1(-\cos^2 \theta_1 \cos^2 \theta_2 + \cos^4 \theta_1 \cos^2 \theta_2 + \cos^2 \theta_1 \cos^4 \theta_2) + \ddot{\theta}_2(-\cos \theta_1 \sin \theta_1 \cos \theta_2 \sin \theta_2 \\ & + \cos^3 \theta_1 \sin \theta_1 \cos \theta_2 \sin \theta_2 + \cos \theta_1 \sin \theta_1 \cos^3 \theta_2 \sin \theta_2) + \dot{\theta}_1^2(-\cos \theta_1 \sin \theta_1 \cos^4 \theta_2 + \cos \theta_1 \sin \theta_1 \cos^2 \theta_2) \\ & + \dot{\theta}_2^2(\cos \theta_1 \sin \theta_1 - 2 \cos \theta_1 \sin \theta_1 \cos^2 \theta_2 - \cos^3 \theta_1 \sin \theta_1 + 2 \cos^3 \theta_1 \cos^2 \theta_2 \sin \theta_1 + \cos \theta_1 \cos^4 \theta_2 \sin \theta_1) \\ & + \dot{\theta}_1 \dot{\theta}_2(2 \cos^2 \theta_1 \cos \theta_2 \sin \theta_2 - 2 \cos^4 \theta_1 \cos \theta_2 \sin \theta_2)) + \left( \frac{2\xi_1}{\Omega} \dot{\theta}_1 + \frac{\theta_1 - \phi_1}{\lambda \Omega^2} - \frac{1}{\Omega^2} \frac{\cos \theta_1 \sin \theta_1}{\sqrt{1 - \sin^2 \theta_1 - \sin^2 \theta_2}} \right) \\ & \times (1 - 2 \cos^2 \theta_1 - 2 \cos^2 \theta_2 + \cos^4 \theta_1 + \cos^4 \theta_2 + 2 \cos^2 \theta_1 \cos^2 \theta_2) \\ & = F \cos \varphi \sin \tau \cos \theta_1(1 - 2 \cos^2 \theta_1 - 2 \cos^2 \theta_2 + \cos^4 \theta_1 + \cos^4 \theta_2 + 2 \cos^2 \theta_1 \cos^2 \theta_2), \quad (5) \end{aligned}$$

$$\begin{aligned}
& (\ddot{\theta}_2(-\cos^2 \theta_1 \cos^2 \theta_2 + \cos^4 \theta_1 \cos^2 \theta_2 + \cos^2 \theta_1 \cos^4 \theta_2) + \ddot{\theta}_1(-\cos \theta_1 \sin \theta_1 \cos \theta_2 \sin \theta_2 \\
& + \cos^3 \theta_1 \sin \theta_1 \cos \theta_2 \sin \theta_2 + \cos \theta_1 \sin \theta_1 \cos^3 \theta_2 \sin \theta_2) + \dot{\theta}_2^2(-\cos^4 \theta_1 \cos \theta_2 \sin \theta_2 + \cos^2 \theta_1 \cos \theta_2 \sin \theta_2) \\
& + \dot{\theta}_1^2(\cos \theta_2 \sin \theta_2 - 2 \cos^2 \theta_1 \cos \theta_2 \sin \theta_2 - \cos^3 \theta_2 \sin \theta_2 + 2 \cos^2 \theta_1 \cos^3 \theta_2 \sin \theta_2 + \cos^4 \theta_1 \cos \theta_2 \sin \theta_2) \\
& + \dot{\theta}_1 \dot{\theta}_2(2 \cos \theta_1 \sin \theta_1 \cos^2 \theta_2 - 2 \cos \theta_1 \sin \theta_1 \cos^4 \theta_2)) + \left( \frac{2\xi_2}{\Omega} \dot{\theta}_2 + \frac{\theta_2 - \phi_2}{\lambda \Omega^2} - \frac{1}{\Omega^2} \frac{\cos \theta_2 \sin \theta_2}{\sqrt{1 - \sin^2 \theta_1 - \sin^2 \theta_2}} \right) \\
& \quad \times (1 - 2 \cos^2 \theta_1 - 2 \cos^2 \theta_2 + \cos^4 \theta_1 + \cos^4 \theta_2 + 2 \cos^2 \theta_1 \cos^2 \theta_2) \\
& = F \sin \varphi \sin \tau \cos \theta_1 (1 - 2 \cos^2 \theta_1 - 2 \cos^2 \theta_2 + \cos^4 \theta_1 + \cos^4 \theta_2 + 2 \cos^2 \theta_1 \cos^2 \theta_2), \quad (6)
\end{aligned}$$

where the dot now denotes  $d/d\tau$ , with  $\tau = \omega_e t$ ,  $\Omega = \omega_e/\omega_p$ ,  $F = F_b/l$ , and  $C_i/ml^2 = 2\xi_i/\Omega$  ( $\xi_i$  are the damping factors). Geometrical and inertial nonlinearities are seen to occur in (5) and (6).

### 3. Nonlinear behavior and imperfection sensitivity analysis

**3.1. Static analysis.** The nonlinear behavior of the imperfect system in the absence of dynamic excitation can be described by the following set of two coupled nonlinear equations obtained from (2)

$$(\theta_1 - \phi_1) - \lambda \frac{\cos \theta_1 \sin \theta_1}{\sqrt{1 - \sin^2 \theta_1 - \sin^2 \theta_2}} = 0, \quad (\theta_2 - \phi_2) - \lambda \frac{\cos \theta_2 \sin \theta_2}{\sqrt{1 - \sin^2 \theta_1 - \sin^2 \theta_2}} = 0. \quad (7)$$

When  $k_1 = k_2 = k$ , the perfect model ( $\phi = \psi = 0$ ) displays two coincident buckling loads,  $P_{\text{cr}1} = P_{\text{cr}2} = P_{\text{cr}} = k/l$ , and orthogonal buckling modes  $\theta_1, \{1, 0\}^T$ , and  $\theta_2, \{0, 1\}^T$ . Figure 2a shows the fundamental path ( $\theta_1 = \theta_2 = 0$ ) for the perfect system, which is stable up to the static critical load ( $\lambda = 1$ ), and the four possible postbuckling paths: the two ascending unstable paths, which correspond to the two uncoupled solutions (either  $\theta_1$  or  $\theta_2$  is zero), and the two descending unstable orthogonal paths at  $45^\circ$ , which are the solutions of the coupled system (7). The important fact to note is that interaction of the buckling modes  $\theta_1$  and  $\theta_2$  conspires to produce the descending unstable paths and imperfection sensitivity, although each mode taking place alone exhibits no imperfection sensitivity [Bažant and Cedolin 1991]. Figure 2b shows the nonlinear behavior of the imperfect system considering  $\phi = 1^\circ$  and  $\psi = 0^\circ$ . The multiple bifurcation in Figure 2a is destroyed by the imperfection. In this case, the imperfect column under increasing static loading displays a stable nonlinear equilibrium path contained in the  $x \times z$  plane since  $\psi = 0^\circ$  (see Figure 1), which becomes unstable due to a subcritical pitchfork bifurcation. The critical load is lower than that of the perfect system. Several unstable complementary paths corresponding to the perturbed unstable postbuckling paths of Figure 1a are observed. These unstable paths control the global dynamics of the system. Figure 2c shows the response of the imperfect system with  $\phi = 1^\circ$  and  $\psi = 45^\circ$ . In this case, the nonlinear stable path loses stability at a limit point and the maximum load is even lower than in the previous case. Again, several unstable complementary paths are observed. The load-carrying capacity of the system decreases as  $\phi$  and  $\psi$  increase, as illustrated by the imperfection sensitivity curves shown in Figure 3, where the critical load of the imperfect system is plotted as a function of the imperfection magnitude  $\phi$  for selected values of  $\psi$ . The lowest critical loads are obtained for  $\psi = 45^\circ$  when the maximum modal coupling occurs.

Much of the global behavior and dynamics of a structural system can be understood from the topological structure of its potential energy function. For a static load level  $\lambda = 0.9$ , Figure 4 shows the

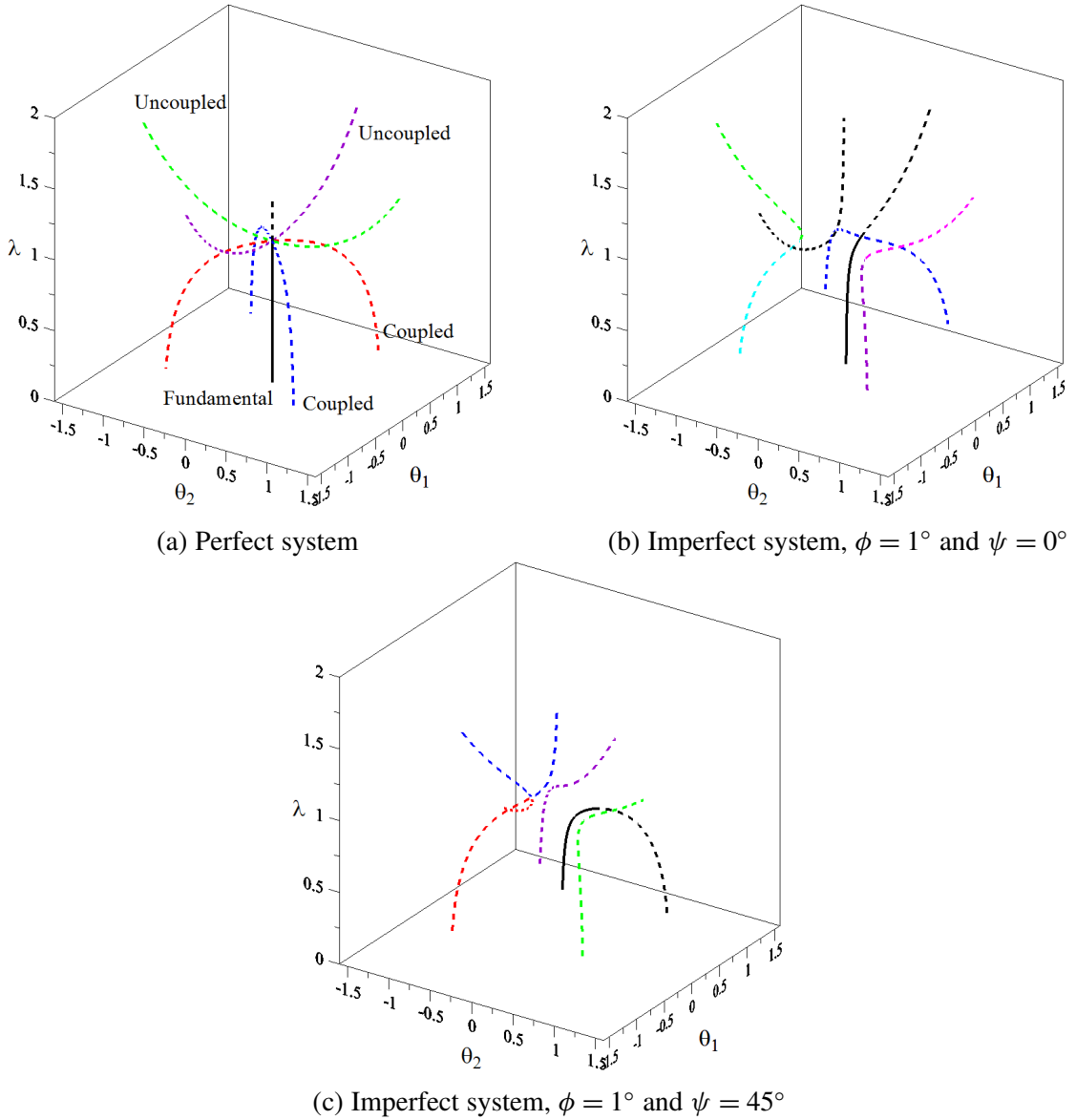


**Figure 2.** Equilibrium paths of the perfect and imperfect systems.

equipotential curves for the three cases analyzed in Figure 2. The perfect system, Figure 4a, displays the four symmetric saddles corresponding to the four unstable postbuckling descending branches shown in Figure 2a and a minimum corresponding to the stable prebuckling solution. The saddles and their invariant manifolds separate the initial conditions that lead to bounded solutions surrounding the prebuckling configuration—which identify the so-called safe region [Soliman and Thompson 1989; Rega and Lenci 2005]—from the unbounded escape solutions. For  $\phi = 1^\circ$  and  $\psi = 0^\circ$ , Figure 4b shows that the safe region is bounded by the two saddles corresponding to the blue equilibrium path in Figure 2b. There is a significant decrease in the area of the safe region due to the imperfection. For  $\phi = 1^\circ$  and

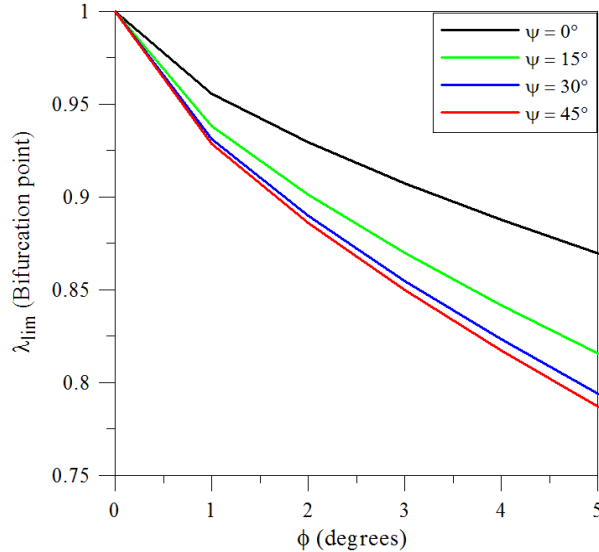


**Figure 3.** Imperfection sensitivity of Augusti's model.

$\psi = 45^\circ$ , as shown in Figure 4c, the safe region is bounded by the saddle with the lowest potential energy among the four saddles and is much smaller than in the previous case. The saddle corresponds to the unstable black equilibrium path in Figure 2c. As illustrated by these results, the imperfections not only decrease the load-carrying capacity of the structure, but also the set of initial conditions that lead to safe bounded motions around the equilibrium configuration. The knowledge of these frontiers helps the designer to separate the phase space into safe and unsafe domains and evaluate the degree of safety of the system. The frontiers are associated with the stable and unstable manifolds of the saddles in the conservative system, whose two-dimensional projections are shown in Figure 5. For the perfect system there are two pairs of heteroclinic orbits, each pair connecting two opposite saddles at  $\pm 45^\circ$  (Figure 5a). For the imperfect system with  $\phi = 1^\circ$  and  $\psi = 0^\circ$ , Figure 5b shows that the safe region is bounded by two homoclinic orbits, while for  $\phi = 1^\circ$  and  $\psi = 45^\circ$ , Figure 5c shows that there is only one homoclinic orbit. In each case, the relevant manifolds lie on a four-dimensional hypersurface that bounds the initial conditions leading to bounded solutions around the trivial prebuckling solution, that is, the interior of this region is filled with a continuous family of stable trajectories. The equation of this surface can be obtained by the principle of conservation of total energy, equating the sum of expressions (2) and (3) to the value of the total energy at one of the relevant saddles, that is

$$T(\theta_i, \dot{\theta}_i) + V(\theta_i) = V_{\text{saddle}}. \quad (8)$$

Three-dimensional sections  $(\theta_1 \times \theta_2 \times \dot{\theta}_1)$  of this four-dimensional region are shown in Figure 6, considering  $\lambda = 0.9$  and  $\omega_p = 1.0 \text{ s}^{-1}$ . These sections show clearly the sharp decrease in the safe region with the imperfection. This safe hypervolume decreases swiftly as the static load increases and vanishes at the critical point. So, near a bifurcation point, even very small perturbations may lead to escape from the prebuckling well. Since all structures work in a dynamical environment, an appropriate safety

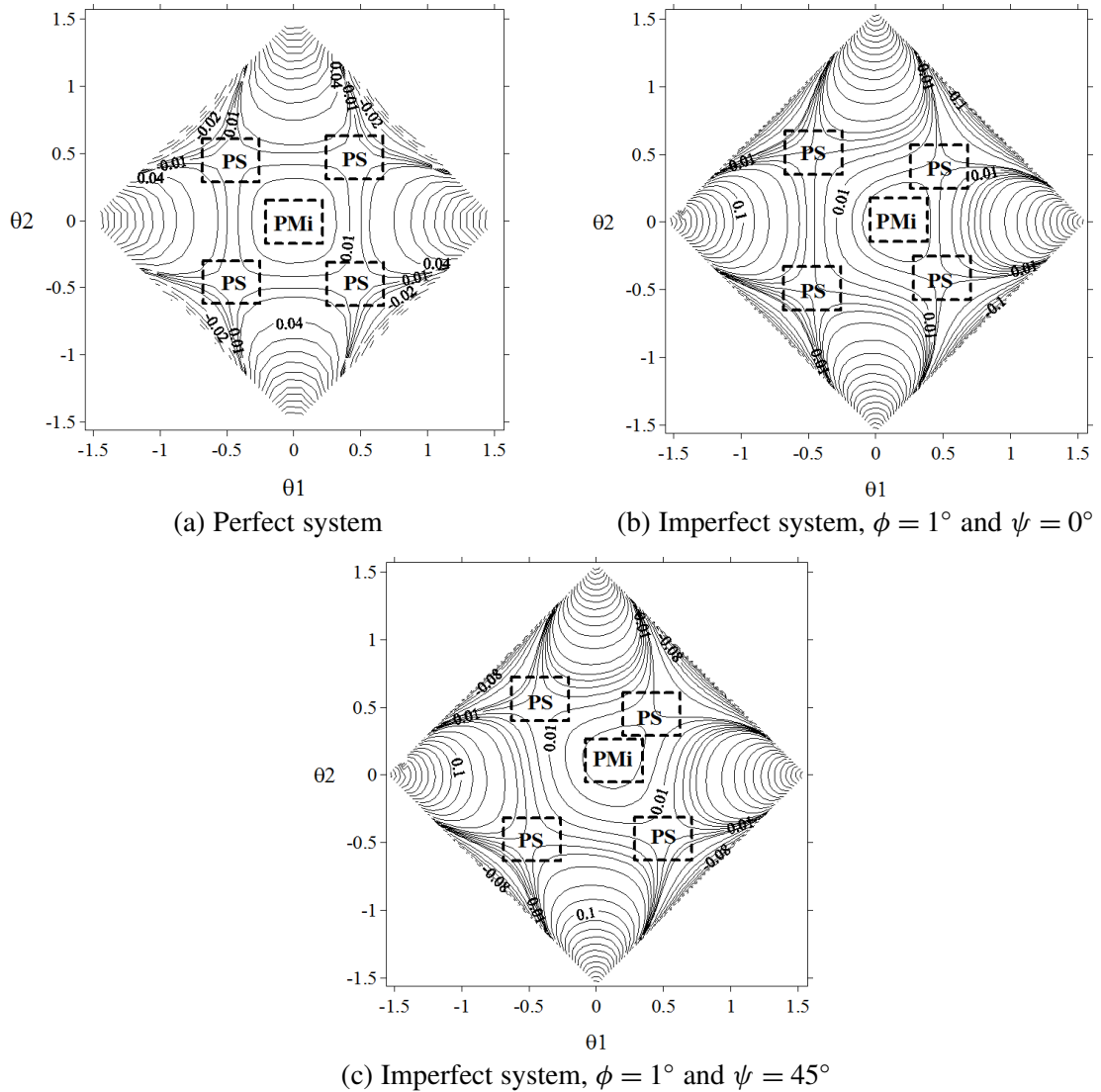


**Figure 4.** Curves of equal potential energy for  $\lambda = 0.9$ . PS: Saddles. PMi: Stable position corresponding to a local minimum.

factor based on the geometry and size of the safe region and its variation with load and imperfections must be used in design. Moreover, as structural systems are usually lightly damped, the response of the real structure will only depart lightly from the conservative case. An analysis of the safe region gives information on the maximum allowable displacements and velocities. These quantities must also be referred to in vibration control to specify the upper bound of allowable disturbances.

**3.2. Nonlinear dynamic analysis.** Figure 7 shows the stability boundaries in force frequency-amplitude control space for the perfect system and a forcing direction  $\varphi = 0^\circ$ . The escape load,  $F_{\text{esc}}$ , corresponds to escape of the response from the prebuckling potential well in a slowly evolving system (dynamic

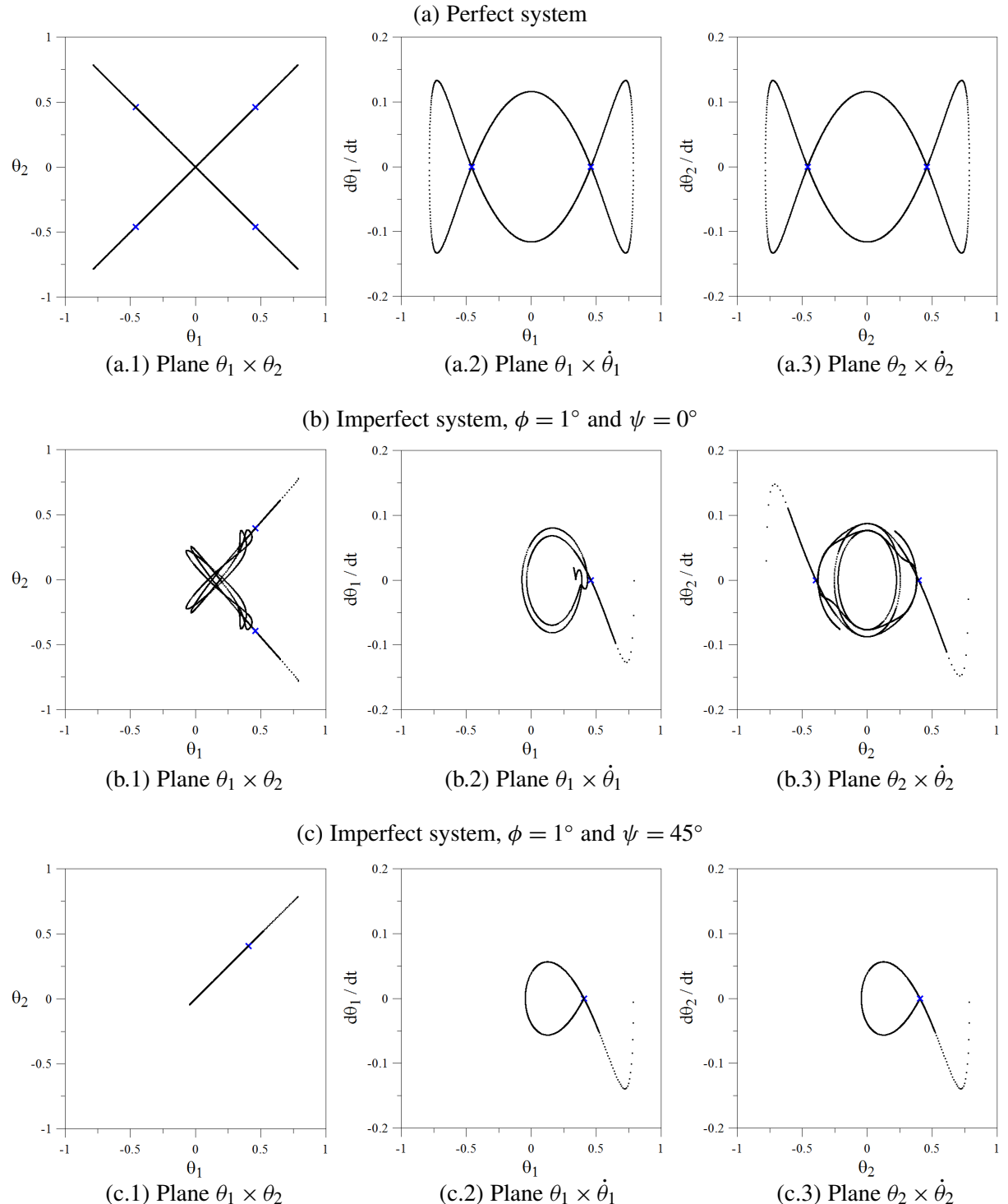


**Figure 5.** Two-dimensional projections of the stable and unstable manifold of the saddles that limit the safe region for  $\lambda = 0.9$  and  $\omega_p = 1.0$  /s.

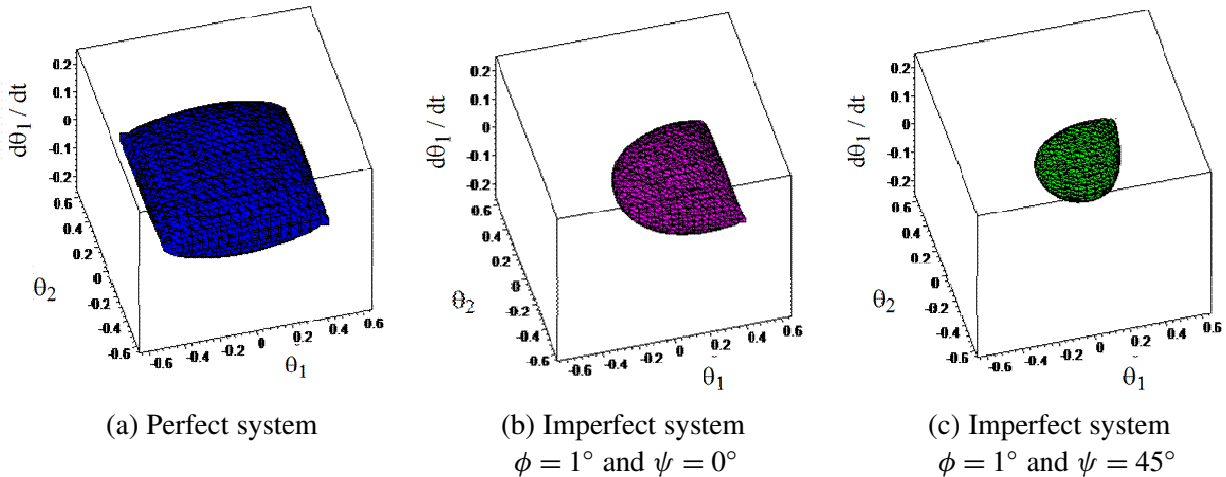


**Figure 6.** Three-dimensional sections of safe prebuckling region.  $\lambda = 0.9$  and  $\omega_p = 1.0/\text{s}$ .

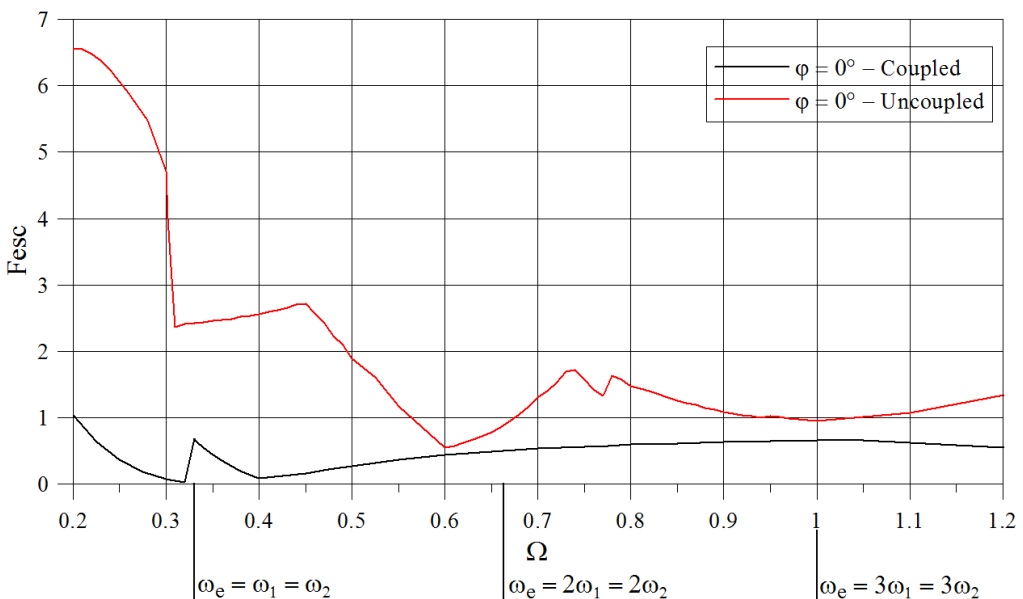


**Figure 7.** Stability boundaries in force control space (load versus forcing frequency) for the forcing direction  $\varphi = 0^\circ$ , considering the coupled and uncoupled cases.  $F_{\text{esc}}$ : escape load.

buckling). These curves ensue from several bifurcation diagrams obtained by increasing slowly the forcing amplitude while holding the frequency constant [Gonçalves et al. 2009; Orlando 2010]. Denoting with  $\omega_i$ ,  $i = 1, 2$ , the natural frequencies of the two linear vibration modes of the system, a large range of forcing frequencies is considered, which includes the fundamental parametric resonances ( $\omega_e = \omega_i$ ) of the two modes and their principal subharmonic parametric resonances, of order  $\frac{1}{2}$  (that is,  $\omega_e = 2\omega_i$ ) and  $\frac{1}{3}$  ( $\omega_e = 3\omega_i$ ). For the perfect system  $\omega_1 = \omega_2$ , the fundamental and principal resonances correspond

to the nondimensional forcing frequency values  $\Omega = \frac{1}{3}$ ,  $\Omega = \frac{2}{3}$ , and  $\Omega = 1$ , respectively, whereas for the imperfect system the two natural frequencies differ from each other [Orlando 2010] and the same occurs for the relevant resonant conditions.

Two cases are considered in Figure 7: the uncoupled case, when perturbations only in  $\theta_1$  and  $\dot{\theta}_1$  are considered and only these coordinates are excited, and the coupled case, when very small perturbations in  $\theta_2$  and  $\dot{\theta}_2$  are also considered after each load step ( $\theta_2 = \dot{\theta}_2 = 0.001$ ), causing the coupling of the two modes. For the uncoupled case, the lowest values of the escape load occur in the neighborhood of

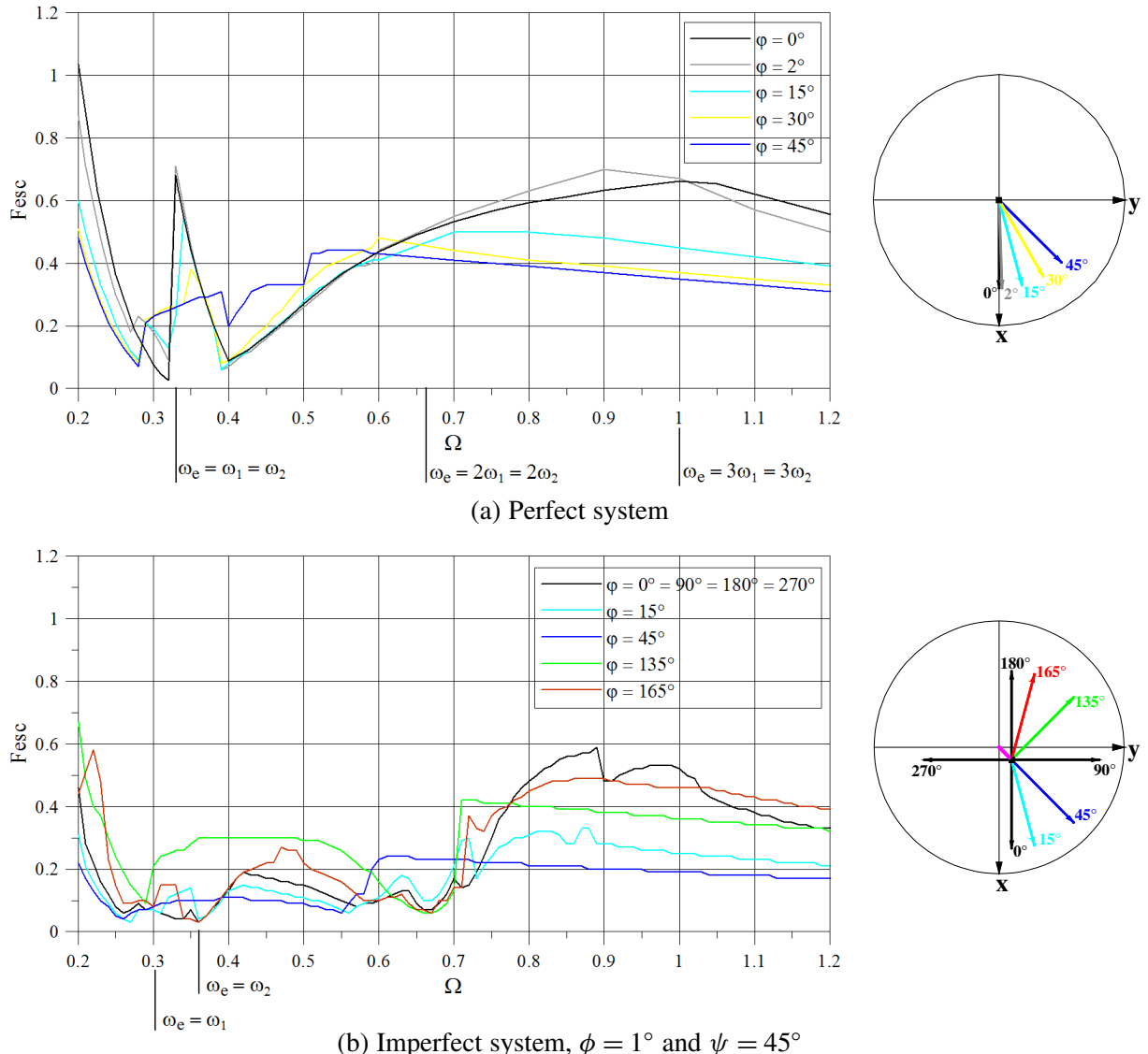


**Figure 8.** Stability boundaries in force control space (load versus forcing frequency) for different values of the forcing direction  $\varphi$  (polar diagram) for perfect and imperfect systems.  $F_{\text{esc}}$ : escape load)

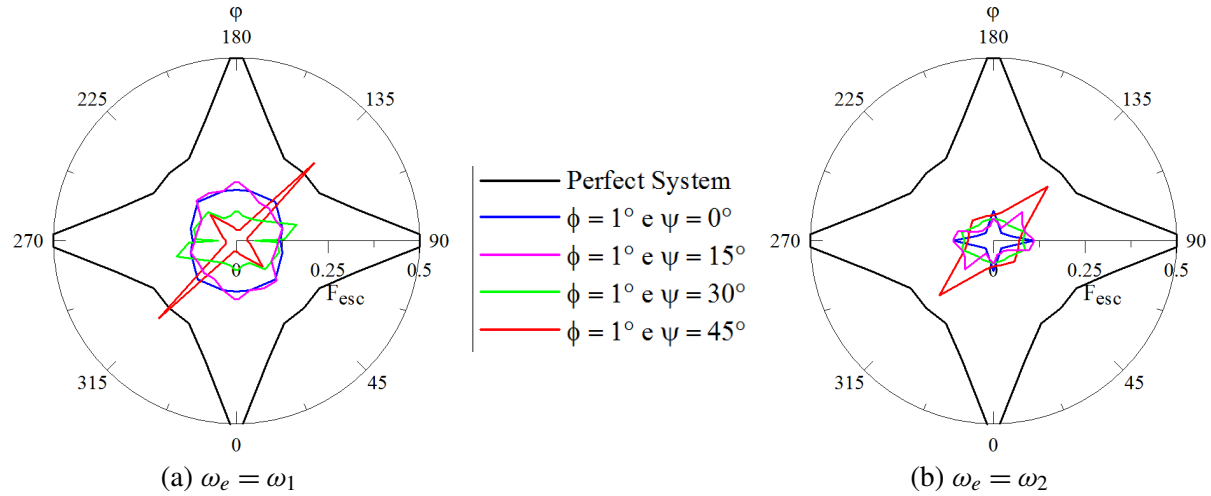


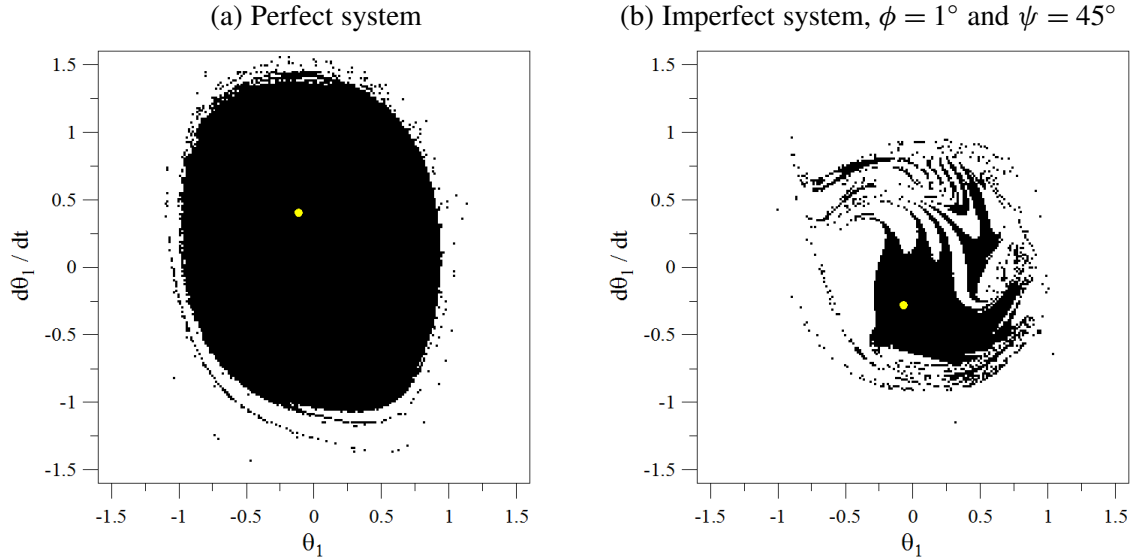
**Figure 9.** Variation of the escape load with the forcing direction  $\varphi$  for the resonance regions.

the principal resonances ( $\Omega = \frac{2}{3}$  and  $\Omega = 1$ ) of the two coinciding modes, as expected in a condition of parametric excitation. In contrast, quite high  $F_{\text{esc}}$  values do occur in the region of fundamental resonance ( $\Omega = \frac{1}{3}$ ). But for even very small values of  $\theta_2$  and  $\dot{\theta}_2$ , which entail coupling of the two modes, a drastic reduction in the escape load is observed in the latter region along with an overall reduction in the whole excitation frequency range here analyzed. Indeed, there is a marked difference between the relevant stability boundaries in the two cases, corroborating the importance of modal coupling in Augusti's model.

Figure 8 shows the stability boundaries for different values of the forcing direction  $\varphi$ , respectively for the perfect system (Figure 8a) and for the imperfect system considering  $\phi = 1^\circ$  and  $\psi = 45^\circ$  (Figure 8b). Figure 8a shows that, as soon as coupling comes into play due to the excitation ( $\varphi \neq 0^\circ$ ), the escape load decreases mostly in the larger frequency range, where it is higher for  $\varphi \neq 0^\circ$ , with the major reduction occurring for  $\varphi = 45^\circ$ , namely, when the coupling effect is the highest. When imperfection is added (Figure 8b), a significant decrease of the dynamic buckling load is observed with respect to the perfect system (Figure 8a) for any value of the forcing frequency  $\Omega$ , with the maximum reduction still occurring for  $\varphi = 45^\circ$ , as expected, owing to the considered  $\psi = 45^\circ$  imperfection value.

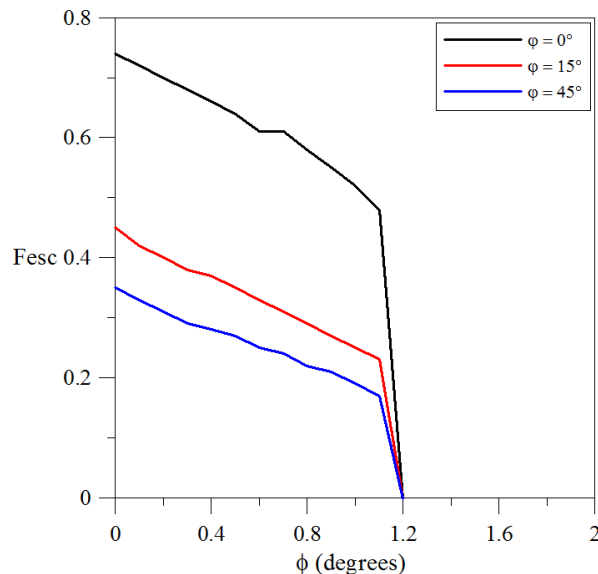
Overall, as in the static case, the dynamic buckling load displays high imperfection sensitivity with drastic effects on the safety of the system. Figure 9 shows the variation of the escape load,  $F_{\text{esc}}$ , for the perfect and imperfect columns with the forcing direction  $\varphi$ , by distinguishing between the regions of fundamental resonance of the two DOFs, which do coincide in the perfect system (see Figure 8a) but are slightly different in the imperfect one (Figure 8b). For the imperfect case, different values of the imperfection direction  $\psi$  are considered and an initial column inclination  $\phi = 1^\circ$  is adopted. The results show a high imperfection sensitivity for all values of  $\varphi$ . It is observed that the results are also sensitive to the imperfection direction  $\psi$ , with the ensuing coupling effect entailing the strongest reduction of escape load with respect to the perfect system when the latter exhibits no coupling, that is, for  $\varphi = 0^\circ$ .

Figure 10 shows the variation of the basin of attraction of the bounded solution between perfect and imperfect systems, when considering a forcing direction  $\varphi = 0^\circ$ , a forcing magnitude  $F = 0.1$ , and a forcing frequency  $\Omega = \frac{1}{3}$ . The cross section of the basin of attraction of the perfect system (Figure 10a)



**Figure 10.** Variation of the basin of attraction with the geometric imperfection ( $\Omega = \frac{1}{3}$ ,  $F = 0.1$ ,  $\varphi = 0^\circ$ ).

is still relatively integer (nonfractal) since the considered  $F = 0.1$  value is below the escape threshold (see Figure 8a). In contrast, for the imperfect system with  $\phi = 1^\circ$  and  $\psi = 45^\circ$  (Figure 10b), a drastic reduction of the safe basin area is observed, since the forcing magnitude is now slightly smaller than the corresponding escape load (see Figure 8b;  $F_{\text{esc}} = 0.11$ ).



**Figure 11.** Variation of the escape load with the column initial inclination  $\phi$  for  $\Omega = 1$  and  $\psi = 45^\circ$ .

Finally, Figure 11 shows the variation of the escape load with the column initial inclination  $\phi$ . The escape load reduction already occurring for the perfect system owing to the  $\varphi \neq 0^\circ$  excitation direction is clearly visible for  $\phi = 0^\circ$ . As the initial inclination  $\phi$  increases the escape load smoothly decreases, but at  $\phi = 1.2^\circ$  it suddenly falls down to zero, which corresponds to the complete annihilation of the basin of attraction for any excitation direction (also for the uncoupled case,  $\varphi = 0^\circ$ ). This shows that even very small imperfections may have a remarkable influence on the stability and safety of the structure and, in particular, that the residual dynamic integrity of the system [Rega and Lenci 2005] associated with the nonvanishing value of the escape load for  $\phi = 1^\circ$  actually corresponds to a very dangerous system configuration from a nonlinear dynamics viewpoint.

#### 4. Conclusions

In this paper the influence of geometric imperfections on the static and dynamic behavior of Augusti's model is studied through a detailed parametric analysis. The inherent strong modal coupling of the model leads to various unstable postbuckling solutions that control the geometry of the safe prebuckling potential well and, consequently, the global behavior of the system under dynamic loads. The initial imperfections not only decrease the load-carrying capacity of the structure, but also decrease substantially the safe region where initial conditions lead to bounded solutions within the prebuckling well. This region is swiftly reduced as the static load approaches the critical value.

The results also highlight the influence of the imperfections on the forced response of the system under harmonic base excitation with varying the horizontal direction. For any excitation frequency and for all nonvanishing forcing directions, the imperfection considerably reduces the escape load and the safe basin area, decreasing the safety of the system.

The analysis of Augusti's model, as an archetypal model of a large class of structures liable to buckling that display a strong modal coupling and imperfection sensitivity, illustrates the tools and steps necessary for a rational evaluation of system safety and dynamic integrity.

#### References

- [Augusti 1964] G. Augusti, "Stabilità elastiche elementari in presenza di grandi spostamenti", *Atti. Accad. Sci. Fis. Mat. Napoli Ser. 3a* **4**:5 (1964).
- [Bažant and Cedolin 1991] Z. P. Bažant and L. Cedolin, *Stability of structures*, Oxford University Press, Oxford, 1991.
- [Brubak and Hellesland 2007] L. Brubak and J. Hellesland, "Semi-analytical postbuckling and strength analysis of arbitrarily stiffened plates in local and global bending", *Thin-Walled Struct.* **45**:6 (2007), 620–633.
- [Chen and Yu 2006] H. Chen and W. Yu, "Postbuckling and mode jumping analysis of composite laminates using an asymptotically correct, geometrically non-linear theory", *Int. J. Non-Linear Mech.* **41**:10 (2006), 1143–1160.
- [Croll and Walker 1972] J. G. Croll and A. C. Walker, *Elements of structural stability*, 1st ed., Macmillan, London, 1972.
- [Dinis et al. 2007] P. B. Dinis, D. Camotim, and N. Silvestre, "FEM-based analysis of the local-plate/distortional mode interaction in cold-formed steel lipped channel columns", *Comput. Struct.* **85**:19–20 (2007), 1461–1474.
- [Elishakoff et al. 1996] I. Elishakoff, S. Marcus, and J. H. Starnes, Jr., "On vibrational imperfection sensitivity of Augusti's model structure in the vicinity of a non-linear static state", *Int. J. Non-Linear Mech.* **31**:2 (1996), 229–236.
- [Gonçalves et al. 2009] P. B. Gonçalves, D. Orlando, G. Rega, and S. Lenci, "Influence of modal coupling on the nonlinear dynamics of Augusti's model", *ASME Conf. Proc.* **2009**:49019 (2009), 1351–1358.
- [Heijden 2008] A. M. A. Van der Heijden, *W. T. Koiter's elastic stability of solids and structures*, Cambridge University Press, Cambridge, 2008.

- [Iooss and Joseph 1980] G. Iooss and D. D. Joseph, *Elementary stability and bifurcation theory*, Springer, New York, 1980. 2nd ed. published in 1990.
- [Kiymaz 2005] G. Kiymaz, “FE based mode interaction analysis of thin-walled steel box columns under axial compression”, *Thin-Walled Struct.* **43**:7 (2005), 1051–1070.
- [Koiter 1945] W. T. Koiter, *Over de stabiliteit van het elastisch evenwicht*, Ph.D. thesis, Delft University of Technology, 1945, available at <http://tinyurl.com/Koiter-WT-1945-Thesis>. Translated in *On the stability of elastic equilibrium*, NASA Technical Translation NASA-TT-F-10833 (1967) and *The stability of elastic equilibrium*, Air Force Flight Dynamics Laboratory report AFFDL TR 70-25 (1970), <http://contrails.iit.edu/DigitalCollection/1970/AFFDLTR70-025.pdf>.
- [Kołakowski 2007] Z. Kołakowski, “Some aspects of dynamic interactive buckling of composite columns”, *Thin-Walled Struct.* **45**:10–11 (2007), 866–871.
- [Naschie 1990] M. S. El Naschie, *Stress, stability and chaos in structural engineering, an energy approach*, McGraw-Hill, London, 1990.
- [Orlando 2010] D. Orlando, *Dinâmica não-linear, instabilidade e controle de sistemas estruturais com interação modal*, Ph.D. thesis, Pontifícia Universidade Católica, Rio de Janeiro, 2010.
- [Pignataro et al. 1991] M. Pignataro, N. Rizzi, and A. Luongo, *Stability, bifurcation and postcritical behaviour of elastic structures*, Developments in Civil Engineering **39**, Elsevier, Amsterdam, 1991.
- [Quinn et al. 2007] D. D. Quinn, J. P. Wilber, C. B. Clemons, G. W. Young, and A. Buldum, “Buckling instabilities in coupled nano-layers”, *Int. J. Non-Linear Mech.* **42**:4 (2007), 681–689.
- [Raftoyiannis and Kounadis 2000] I. G. Raftoyiannis and A. N. Kounadis, “Dynamic buckling of 2-DOF systems with mode interaction under step loading”, *Int. J. Non-Linear Mech.* **35**:3 (2000), 531–542.
- [Rega and Lenci 2005] G. Rega and S. Lenci, “Identifying, evaluating, and controlling dynamical integrity measures in non-linear mechanical oscillators”, *Nonlinear Anal. Theory Methods Appl.* **63**:5–7 (2005), 902–914.
- [Soliman and Thompson 1989] M. S. Soliman and J. M. T. Thompson, “Integrity measures quantifying the erosion of smooth and fractal basins of attraction”, *J. Sound Vib.* **135**:3 (1989), 453–475.
- [Thompson and Hunt 1973] J. M. T. Thompson and G. W. Hunt, *A general theory of elastic stability*, Wiley, London, 1973.
- [Thompson and Hunt 1984] J. M. T. Thompson and G. W. Hunt, *Elastic instability phenomena*, Wiley, London, 1984.
- [Tvergaard 1973] V. Tvergaard, “Imperfection-sensitivity of a wide integrally stiffened panel under compression”, *Int. J. Solids Struct.* **9**:1 (1973), 177–192.
- [Zocher 1933] H. Zocher, “The effect of a magnetic field on the nematic state”, *Trans. Faraday Soc.* **29**:140 (1933), 945–957.

Received 23 Jun 2010. Revised 17 Sep 2010. Accepted 15 Nov 2010.

DIEGO ORLANDO: [dgorlando@gmail.com](mailto:dgorlando@gmail.com)

*Department of Civil Engineering, Pontifical Catholic University, Rio, Rua Marquês de São Vicente, 225, Gávea, 22453-900 Rio de Janeiro-RJ, Brazil*

PAULO BATISTA GONÇALVES: [paulo@puc-rio.br](mailto:paulo@puc-rio.br)

*Department of Civil Engineering, Pontifical Catholic University, Rio, Rua Marquês de São Vicente, 225, Gávea, 22453-900 Rio de Janeiro-RJ, Brazil*

GIUSEPPE REGA: [giuseppe.rega@uniroma1.it](mailto:giuseppe.rega@uniroma1.it)

*Dipartimento di Ingegneria Strutturale e Geotecnica, Università degli Studi di Roma ‘La Sapienza’, via Eudossiana 18, I-00184 Roma, Italy*

STEFANO LENCI: [lenci@univpm.it](mailto:lenci@univpm.it)

*Dipartimento di Architettura, Costruzioni e Strutture, Università Politecnica delle Marche, via Brecce Bianche, I-60131 Ancona, Italy*

## ACTIVE CONTROL OF VORTEX-INDUCED VIBRATIONS IN OFFSHORE Catenary Risers: A NONLINEAR NORMAL MODE APPROACH

CARLOS E. N. MAZZILLI AND CÉSAR T. SANCHES

Offshore catenary risers are used in the exploitation of deep-water oil and gas fields. They are subjected to severe dynamical loads, such as high-pressure inside-flow of fluids, sea-current external flow, and sea-wave motion of the floating production platform. This paper addresses the dynamic instability caused by vortex-induced vibrations (VIV). For simplicity, the touchdown-point motion and the mooring compliance are neglected in this introductory study. The nonlinear normal modes of a finite element model of the riser are determined, following the invariant manifold procedure, and a mode that is particularly prone to be excited by VIV is selected. A reduced mathematical model that couples the structural response and the fluid dynamics is used to foresee the vibration amplitudes when the instability caused by VIV takes over. Active control is introduced and the linear quadratic regulator is employed to determine gain matrices for the system and the observer. Results are compared with those from a linear analysis.

### 1. Introduction

The oil and gas industry has faced new challenges since several onshore and offshore fields have matured, aggravated by the growing global demand for energy and the volatility in oil prices. This scenario has led the operating companies to focus on deep and ultradeep water exploitation, bringing forth new concerns on reducing costs via advanced technological developments. Consequently, the offshore industry has increased its attention to new realms of research such as nonlinear dynamics of structures and computational fluid dynamics.

If subsea exploration has always been a complex and demanding activity, from now on, in view of the upcoming developments in deep and ultradeep water, it will be even more challenging. In fact, the offshore industry has already begun to explore in water depths at the limits of current technology and has plans to access depths over 2,500 m. It is already developing subsea production systems in preparation for ultradeep water production that include more flexible and lighter risers that operate under harsher environmental conditions. From this standpoint, nonlinear effects are expected to play a major role in riser global dynamics.

The objective of this paper is to present a numerical study on the fluid-structure interaction and structural nonlinear dynamic behavior of a deep-water catenary riser subjected to in-plane vortex-induced vibration (VIV), employing the van der Pol oscillator proposed in [Blevins 1990] to represent the fluid dynamics and to the nonlinear modal analysis technique, respectively. A computational model is initially proposed using the finite element method. Geometrically nonlinear finite elements are employed so that the equations of motion take into consideration quadratic and cubic nonlinearities, expressed in terms

---

The first author acknowledges the support of CNPq under Grant 301942/2009-9.

**Keywords:** catenary risers, VIV, nonlinear modes, finite element method, active control.

of third and fourth-order tensors, respectively. These nonlinear equations allow for the assessment of both cable and beam behavior. In this work, the motion of the floating production unit (FPU) and the unilateral contact at the touchdown zone (TDZ) have been neglected. Hence, the catenary riser has been modeled with fixed pinned ends, just allowing for rotation. Further advances, regarding a numerical approach for the TDZ, are under development, since considerable programming effort is required to take into consideration contact at the TDZ. It is worth mentioning that an analytical study of the local dynamics of steel catenary risers (SCR), considering unilateral contact at the TDZ, led to an approximate evaluation of the associated nonlinear normal modes of vibration [Mazzilli and Lenci 2008]. Nonlinear modes seem to play an important role in the structural representation of deep-water risers by models with small numbers of degrees of freedom. A free-hanging catenary is addressed in a case study, considering a certain nonlinear normal mode of vibration, which is seen to be relevant for the analysis of the VIV motion. The ultimate goal is to develop a coupled fluid-riser low-dimensional model, to which active control can be added in a simple way.

## 2. Nonlinear modes

This paper should be regarded as an initial effort to assess the nonlinearly coupled fluid-riser interaction. The riser will be modeled as a plane frame with geometric nonlinearities due to the coupling of tangential and transversal displacements. Material linearity will be assumed. Torsion and 3D effects, as well as FPU motion and unilateral contact at the TDZ, will be neglected.

Although internal resonance may come into play, which would require the consideration of the so-called nonlinear multimodes, the paper will concentrate on the nonlinear normal modes.

It is believed that the nonlinear normal modes and multimodes may play an important role in generating reliable models with few degrees of freedom, still keeping the essential behavior of risers under different sea-loading conditions, such as in cases of high-frequency VIV and low-frequency drifting.

**2.1. FEM formulation.** Typically, the equations of motion of a general  $n$ -degree of freedom finite element model of an elastic plane frame with geometric nonlinearities under free vibrations read [Soares and Mazzilli 2000]:

$$M_{rs} \ddot{p}_s + D_{rs} \dot{p}_s + K_{rs} p_s = 0, \quad r, s = 1, \dots, n, \quad (1)$$

where Einstein's convention for summation is employed;  $p_s$  are the generalized coordinates. The matrices of mass  $M_{rs}$ , equivalent damping  $D_{rs}$ , and stiffness  $K_{rs}$  depend on the generalized coordinates and velocities as follows:

$$\begin{aligned} M_{rs} &= {}^0M_{rs} + {}^1M_{rs}^i p_i + {}^2M_{rs}^{ij} p_i p_j, \\ D_{rs} &= {}^0D_{rs} + {}^1D_{rs}^i \dot{p}_i + {}^2D_{rs}^{ij} \dot{p}_i p_j, \\ K_{rs} &= {}^0K_{rs} + {}^1K_{rs}^i p_i + {}^2K_{rs}^{ij} p_i p_j, \end{aligned} \quad (2)$$

where  ${}^0M_{rs}$ ,  ${}^1M_{rs}^i$ ,  ${}^2M_{rs}^{ij}$ ,  ${}^0D_{rs}$ ,  ${}^1D_{rs}^i$ ,  ${}^2D_{rs}^{ij}$ ,  ${}^0K_{rs}$ ,  ${}^1K_{rs}^i$ , and  ${}^2K_{rs}^{ij}$  ( $r, s, i, j = 1, \dots, n$ ) are constants.

**2.2. Linear and nonlinear modes.** During a modal motion, the phase trajectories of a discretized linear system remain confined to a 2D eigenplane, in much the same way as the phase trajectory of a one-degree-of-freedom system with generalized coordinate  $x$  remains confined to the plane  $x \times \dot{x}$ . Due to this invariance property, such an eigenplane is an invariant manifold of the dynamical system.

In nonlinear systems the invariant manifolds are no longer planes, and the motions whose trajectories are confined to them are called nonlinear normal modes. Normally, there are  $n$  invariant manifolds, each one corresponding to a different mode; these manifolds contain the equilibrium point at which they are tangent to the eigenplanes of the linearized system.

Such a geometric characterization of a modal motion suggests the so-called invariant-manifold procedure to determine normal modes, which was proposed in [Shaw and Pierre 1993] and applied to systems of few degrees of freedom. In [Soares and Mazzilli 2000] the procedure was extended to full finite element models of plane frames.

An alternative technique to evaluate nonlinear normal modes of finite element models was proposed in [Mazzilli and Baracho Neto 2002], based on the method of multiple scales.

To handle cases of coupled modal motions of nonlinear systems subjected to internal resonance, the multiple-scales procedure has also been successfully extended in [Baracho Neto and Mazzilli 2005]. Here, the ensuing vibration takes place in an invariant manifold embedded in the phase space, whose dimension is twice the number of the normal modes that interact. This manifold contains a stable equilibrium point at which it is tangent to the subeigenspace of the linearized system, which characterizes the corresponding coupled linear modes. On this manifold, the system behaves like an  $M$ -degree of freedom oscillator, where  $M$  is the number of coupled normal modes.

**2.3. Invariant manifold procedure.** Here, the fundamental steps of the invariant-manifold procedure are followed [Shaw and Pierre 1993], keeping in mind its application to finite element models of risers.

Introducing the notation  $x_i = p_i$  and  $y_i = \dot{p}_i = \dot{x}_i$ , the system (1) can be written in first-order form as

$$\dot{x}_i = y_i, \quad \dot{y}_i = f_i(x_1, \dots, x_n, y_1, \dots, y_n), \quad i = 1, \dots, n. \quad (3)$$

Series expansions for the functions  $f_i(x_1, \dots, x_n, y_1, \dots, y_n)$  in the neighborhood of the equilibrium point are introduced in (4):

$$\begin{aligned} f_i(x_1, \dots, x_n, y_1, \dots, y_n) = & B_{ij}x_j + C_{ij}y_j + E_{ijm}x_jx_m + F_{ijm}x_jy_m + G_{ijm}y_jy_m \\ & + H_{ijmp}x_jx_mx_p + L_{ijmp}x_jx_my_p + N_{ijmp}x_jy_my_p + R_{ijmp}y_jy_my_p, \end{aligned} \quad (4)$$

where  $B_{ij}$ ,  $C_{ij}$ ,  $E_{ijm}$ ,  $F_{ijm}$ ,  $G_{ijm}$ ,  $H_{ijmp}$ ,  $L_{ijmp}$ ,  $N_{ijmp}$ , and  $R_{ijmp}$  ( $i, j, m, p = 1, \dots, n$ ) are known constants that depend on the previously introduced  ${}^0M_{rs}$ ,  ${}^1M_{rs}^i$ ,  ${}^2M_{rs}^{ij}$ ,  ${}^0D_{rs}$ ,  ${}^1D_{rs}^i$ ,  ${}^2D_{rs}^{ij}$ ,  ${}^0K_{rs}$ ,  ${}^1K_{rs}^i$ , and  ${}^2K_{rs}^{ij}$  ( $r, s, i, j = 1, \dots, n$ ), as detailed in [Soares and Mazzilli 2000].

If, during a modal motion, the trajectory of the solution in the phase-space is restricted to a 2D surface, then it must be possible to express each generalized displacement or velocity as a function of two of them, for instance  $u = x_k$  and  $v = y_k$ , for a certain degree of freedom  $k$ , at least in the neighborhood of the equilibrium point.

By substituting the expressions

$$x_i(t) = X_i(u(t), v(t)), \quad y_i(t) = Y_i(u(t), v(t)), \quad i = 1, \dots, n, \quad (5)$$

in (3), one arrives at

$$\begin{aligned} \frac{\partial X_i}{\partial u}v + \frac{\partial X_i}{\partial v}f_k(X_1, \dots, X_n, Y_1, \dots, Y_n) &= Y_i, \\ \frac{\partial Y_i}{\partial u}v + \frac{\partial Y_i}{\partial v}f_k(X_1, \dots, X_n, Y_1, \dots, Y_n) &= f_i(X_1, \dots, X_n, Y_1, \dots, Y_n), \quad i = 1, \dots, n, \end{aligned} \quad (6)$$

which is a nonlinear system of partial differential equations having the functions  $X_i$  and  $Y_i$  as unknowns, which may be as difficult to solve as the original equations. However, if we look for an approximate solution, these functions can be written as polynomials up to cubic terms:

$$\begin{aligned} X_i(u, v) &= a_{1i}u + a_{2i}v + a_{3i}u^2 + a_{4i}uv + a_{5i}v^2 + a_{6i}u^3 + a_{7i}u^2v + a_{8i}uv^2 + a_{9i}v^3, \\ Y_i(u, v) &= b_{1i}u + b_{2i}v + b_{3i}u^2 + b_{4i}uv + b_{5i}v^2 + b_{6i}u^3 + b_{7i}u^2v + b_{8i}uv^2 + b_{9i}v^3, \end{aligned} \quad (7)$$

where  $a_{ji}$  and  $b_{ji}$  ( $j = 1, \dots, 9$  and  $i = 1, \dots, n$ ) are constants to be determined.

Now, if we substitute (7) and (4) in (6), a system of nonlinear polynomial equations having the  $a$ 's and  $b$ 's as unknowns is formed. In general, there are  $n$  solutions to this system, each one corresponding to a different set of modal relations (5), that is, a different invariant manifold. Moreover, substituting any one of these solutions in (7) and the resulting expressions in (5), the  $k$ -th equation in (3)–(4)—called the modal oscillator equation—characterizes the dynamics of the corresponding mode.

Details of the procedure just outlined are avoided here for brevity, but can be found in [Soares and Mazzilli 2000], where it is also shown that the solution of the system of nonlinear polynomial equations mentioned above can be avoided, provided the eigenvalues and eigenvectors of the linearized system are known.

### 3. Fluid-structure interaction

Among the possible scenarios for the fluid-structure interaction, the case of vortex-induced vibrations (VIV) is here addressed [Williamson and Govardhan 2004]. In the subcritical regime, the flow with free-stream velocity  $U = U_\infty$  around a circular cylinder of diameter  $D$  forms a von Kármán vortex street as the one shown in Figure 1 [Assi 2009]. The Strouhal number,  $St$ , is the predominant frequency of vortex shedding  $f_s$  multiplied by the cylinder diameter  $D$  and divided by the free-stream velocity:

$$St = \frac{f_s D}{U}. \quad (8)$$

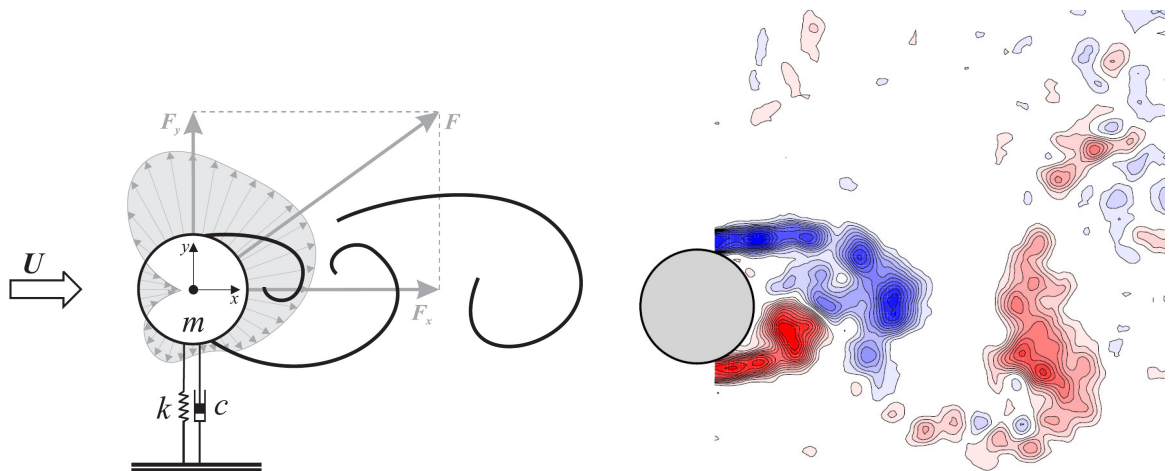


**Figure 1.** Visualization of von Kármán vortex street [Assi 2009].

In the subcritical regime, the Reynolds number,  $\text{Re}$ , based on the cylinder diameter is in the range  $200 \leq \text{Re} \leq 5 \times 10^5$ . In this range, experimental results found in the literature indicate that the Strouhal number is almost constant  $\text{St} = 0.20$  and the drag coefficient is  $C_d = 1.2$ .

A classical approach to characterizing the dynamics of the coupled fluid-structure system [Facchinetto et al. 2004] is to employ phenomenological models, a thorough review of which can be found in [Gabbai and Benaroya 2005]. In this paper a very simple phenomenological model based in [Blevins 1990] has been considered, leading to the following system of differential equations, the first of which refers to the nonlinear dynamics of the reduced-order model of the structural system and the second of which to the fluid dynamics:

$$\frac{d^2u}{dt^2} + 2\omega_n(\zeta_s + \zeta_F)\frac{du}{dt} + \omega_n^2 u + \text{nonlinear terms} = \left(\frac{\rho D^2}{m}\right) \frac{U}{D} a_4 \frac{dw}{dt}, \quad (9)$$

$$\frac{d^2w}{dt^2} + \omega_s^2 w = \left(\frac{a_1 - a_4}{a_0}\right) \frac{U}{D} \frac{dw}{dt} - \frac{a_2}{a_0} \frac{1}{UD} \left(\frac{dw}{dt}\right)^3 + \frac{a_4}{a_0} \frac{U}{D} \frac{du}{dt}, \quad (10)$$

where  $u$ , as before, is the modal generalized coordinate,  $\omega_n$  is the linear natural frequency of the chosen vibration mode,  $\zeta_s$  is the structural damping ratio,  $\zeta_F$  is the fluid damping ratio,  $\rho$  is the seawater specific mass,  $m$  is the modal mass including both the structure and the fluid added mass,  $w$  is the fluid hidden variable [Blevins 1990],  $\omega_s = 2\pi f_s$  is the vortex shedding frequency, and  $a_0, a_1, a_2$ , and  $a_4$  are known constants.

In this paper, (9) is sought by using the invariant manifold approach. Therefore, second and third-order nonlinear terms will arise as a consequence of the nonlinear structural formulation.

#### 4. Case study: Part A

Table 1 presents the riser data used to model the structural system. Figure 2 shows the riser finite element model with 77 degrees of freedom and 26 nonlinear Bernoulli–Euler-based elements. The reduced number of elements used is due to the considerable computational effort required to work out third and fourth-order tensors that led this FEM model to allocate approximately 2 GB of RAM. It took 17 hours of processing time using a 1.6 GHz processor to obtain the nonlinear normal modes of the system.

Young's modulus	$E = 2.1 \times 10^{11} \text{ N/m}^2$
Riser length	$l = 1,800 \text{ m}$
Cross-section area	$A = 1.1021 \times 10^{-2} \text{ m}^2$
Cross-section moment of inertia	$I = 4.72143 \times 10^{-5} \text{ m}^4$
Riser external diameter	$D = 2.032 \times 10^{-1} \text{ m}$
Riser thickness	$e = 19.05 \text{ mm}$
Initial tension (at the top)	$T_{0t} = 2 \times 10^6 \text{ N}$
Initial tension (at the bottom)	$T_{0b} = 6.914 \times 10^5 \text{ N}$
Riser mass per unit length (water inside and added mass)	$m = 108 \text{ kg/m}$
Riser weight per unit length	$p = 727 \text{ N/m}$

**Table 1.** Typical steel riser data.

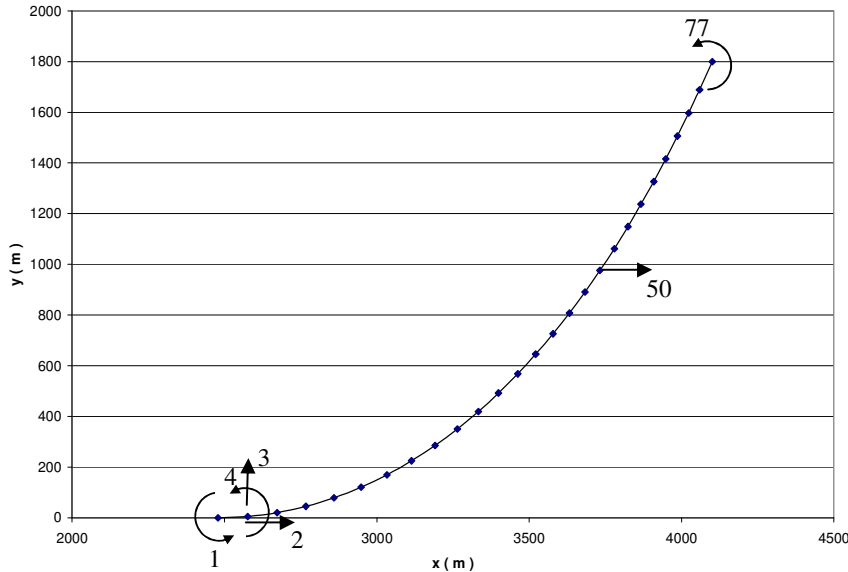


**Figure 2.** Riser finite element model and the chosen modal variable  $u = p_{50}$ .

VIV calculations were performed assuming the Strouhal number to be  $St = 0.20$  and the free-stream velocity  $U = 0.5 \text{ m/s}$  (normal to the motion plane). Taking this into account, the vortex-shedding frequency approaches the natural frequency of the 26th vibration mode. Therefore, it is assumed that the lock-in occurs for this mode. As a result, the following system of equations is sought to represent the dynamics of the coupled fluid-structure system herein addressed:

$$\ddot{u} + 8.1921u + 39v + 22.16u^2 - 3.0673v^2 - 70.823u^3 + 533.54uv^2 = 38.95\dot{w}, \quad (11)$$

$$\ddot{w} + 9.8696w = 4.17\dot{w}^3 + 0.3125\dot{w} + 1.98v, \quad (12)$$

where  $u$  and  $v$  are respectively the modal displacement and the modal velocity, so  $\dot{u} = v$ . The chosen modal displacement is  $u = p_{50}$ , as shown in Figure 2.

In Figure 3, a phase portrait, for both “linear” and nonlinear responses, can be observed. The “linear” response is the response of the coupled fluid-structure system when only the structural system is linearized. Thus, the dynamics of the fluid remain nonlinear even when the linear structural system is considered. The total nonlinear amplitude amounts to 0.565 m whilst the “linear” response leads to a total amplitude of 0.567 m. Although there is no noteworthy difference in the total amplitudes, it’s interesting to stress that the nonlinear amplitude extremes are different with the maximum of 0.3057 m and the minimum of -0.2596 m. On the other hand, the “linear” system gives the same absolute values for the extremes (0.2834 m and -0.2834 m). Hence, the nonlinear system is able to capture the asymmetric stiffness, due to the riser static curvature.

## 5. Active control

The Luenberger observer [Luenberger 1979] is employed in what follows. Here, only one specific nonlinear normal mode will be considered when modeling the controlled system. Therefore, this should

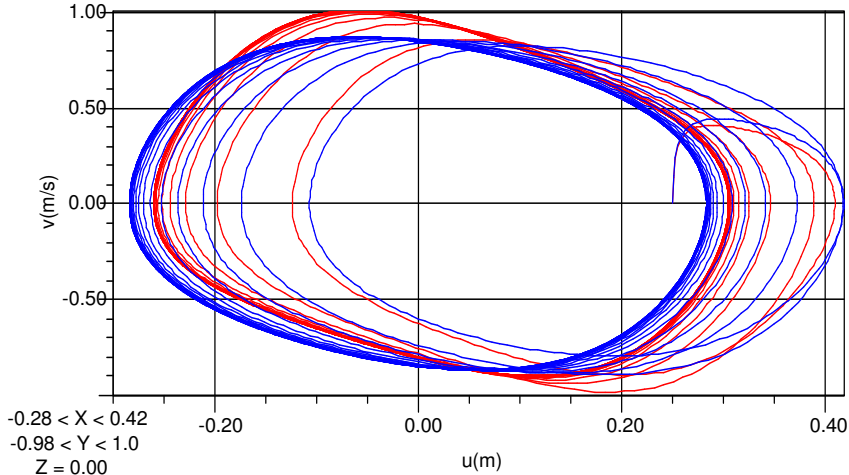


**Figure 3.** Phase portrait (“linear” in blue, nonlinear in red).

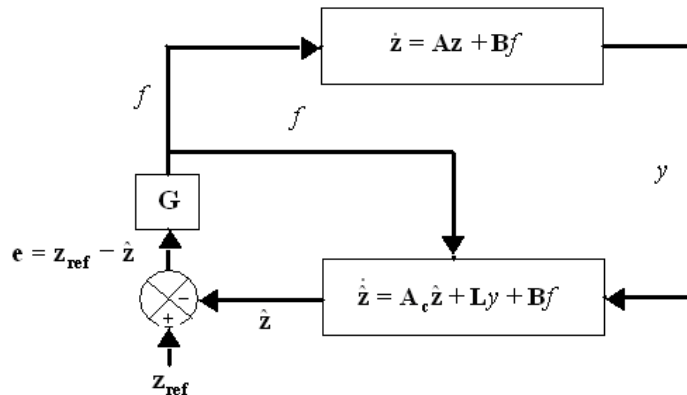


**Figure 4.** The control system.

be regarded as an initial investigation of the behavior of a SCR riser under VIV. Emphasis is placed on the system design, namely the system and the observer gain matrices. Considerations regarding actuators, sensors, or physical installations are not within the scope of this work. A simple example regarding controlled VIV will be addressed in Section 6. Although the structural system will be modeled as nonlinear, the employed observer will still be assumed to be linear. A nonlinear observer would lead to a much more complex model, but the control system would present a larger stability window. However, it will be seen that the linear observer already leads to stable responses, even when large amplitudes and considerable nonlinear effects are taken into consideration. Optimal control is employed via the linear quadratic regulator [Ogata 1995; Preumont 2002]. Figure 4 represents the control system.

The matrix equation of the structural system with the actuator term can be written as

$$\dot{z} = Az + Bf, \quad (13)$$

where  $z = \{\{\tilde{x}\}^T \{\dot{\tilde{x}}\}^T\}^T$  is the  $2n \times 1$  phase-space vector for a  $n$ -degree of freedom system,  $\tilde{x}$  is the  $n \times 1$

vector of principal generalized coordinates in the configuration space,  $f = \mathbf{G}(z_{\text{ref}} - \hat{z})$  is the input control force,  $\mathbf{G}$  is the  $1 \times 2n$  system gain matrix, and  $\mathbf{A} = \mathbf{A}(z)$  is the  $2n \times 2n$  nonlinear system matrix. Let  $\mathbf{T}$  be the  $n \times n$  linear eigenvector matrix of the structural system and  $\mathbf{b} = \mathbf{T}^T \mathbf{n}$  an  $n \times 1$  vector, where  $\mathbf{n}$  is the  $n \times 1$  actuator position vector. Hence, the  $2n \times 1$  vector  $\mathbf{B} = \{\{\mathbf{b}\}^T \{\mathbf{0}\}^T\}^T$  is defined.

The system of differential equations presented in Figure 4 can be rewritten as follows:

$$\begin{Bmatrix} \dot{z} \\ \dot{\hat{z}} \end{Bmatrix} = \begin{bmatrix} \mathbf{A} & -\mathbf{B}\mathbf{G} \\ \mathbf{LC} & \mathbf{A}_c - \mathbf{B}\mathbf{G} \end{bmatrix} \begin{Bmatrix} z \\ \hat{z} \end{Bmatrix} + \begin{Bmatrix} \mathbf{B} \\ \mathbf{B} \end{Bmatrix} f_{\text{ref}}, \quad (14)$$

where  $\mathbf{A}_c = \mathbf{A} - \mathbf{LC}$ ,  $f_{\text{ref}}$  is an arbitrary force related to an arbitrary state vector  $z_{\text{ref}}$ , and  $\mathbf{L}$  is the  $2n \times 1$  observer gain matrix. Defining the  $1 \times 2n$  matrix  $\mathbf{C} = \{\mathbf{c} \quad \mathbf{0}\}$ , where  $\mathbf{c} = \mathbf{h}^T \mathbf{T}$  is a  $1 \times n$  matrix and  $\mathbf{h}$  is the  $n \times 1$  sensor position vector, then  $y = \mathbf{C}z$ . For further details see [Ogata 1995]. The solution of (14) is pursued via the Runge–Kutta method.

**5.1. Linear quadratic regulator.** A linear state feedback with constant system gain  $\mathbf{G}$  is sought, such that the following quadratic cost functional is minimized:

$$\min J = \int_0^\infty \left( \frac{1}{2} z^T \mathbf{Q} z + \frac{1}{2} f^T \mathbf{R} f \right) dt, \quad \text{such that } \dot{z} = \mathbf{A}z + \mathbf{B}f, \quad (15)$$

where  $\mathbf{Q}$  is semipositive definite and  $\mathbf{R}$  is strictly positive definite. The matrices  $\mathbf{Q}$  and  $\mathbf{R}$  are, at first, unknown and should be calibrated according to experimental results [Preumont 2002]. It is possible to show that the system gain matrix ends up being

$$\mathbf{G} = \mathbf{R}^{-1} \mathbf{B}^T \mathbf{P}, \quad (16)$$

where  $\mathbf{P}$  is a symmetric positive definite matrix that can be obtained from Riccati's equation:

$$\mathbf{Q} + \mathbf{A}^T \mathbf{P} + \mathbf{P} \mathbf{A} - \mathbf{P} \mathbf{B} \mathbf{R}^{-1} \mathbf{B}^T \mathbf{P} = \mathbf{0}. \quad (17)$$

## 6. Case study: Part B

To provide an introductory example of a forced controlled system, the coupled structural and fluid equations (accordingly to Section 3) for a SCR are written as follows:

$$\begin{aligned} \ddot{u} + 8.1921u + 39v + 22.216u^2 - 3.0673v^2 - 70.823u^3 + 533.54uv^2 &= 38.95\dot{w} + f_u, \\ \ddot{w} + 9.8696w &= 0.3125\dot{w} + 4.17\dot{w}^3 + 1.98v, \end{aligned} \quad (18)$$

where  $u$  is the chosen modal displacement,  $v = \dot{u}$  the respective modal velocity,  $f_u$  the actuator modal force, and  $w$  the fluid hidden variable. As before, the data for the SCR are from Table 1 and Figure 2 depicts the finite element model. The nonlinear modal oscillator, (18), was obtained via the invariant manifold technique. It corresponds to the 26th nonlinear vibration mode. The control influence is introduced in the system as, mainly, a variation in the riser tension. As seen in Section 4, the simulation of the uncontrolled system, considering the nonlinear structural behavior, leads to a maximum displacement of 0.3057 m and a minimum displacement of -0.2596 m. The time response and the phase diagram for the controlled system are presented in Figure 5, from which it is seen that the maximum displacement for the controlled system, considering the nonlinear structural behavior, is 0.2571 m and the minimum is

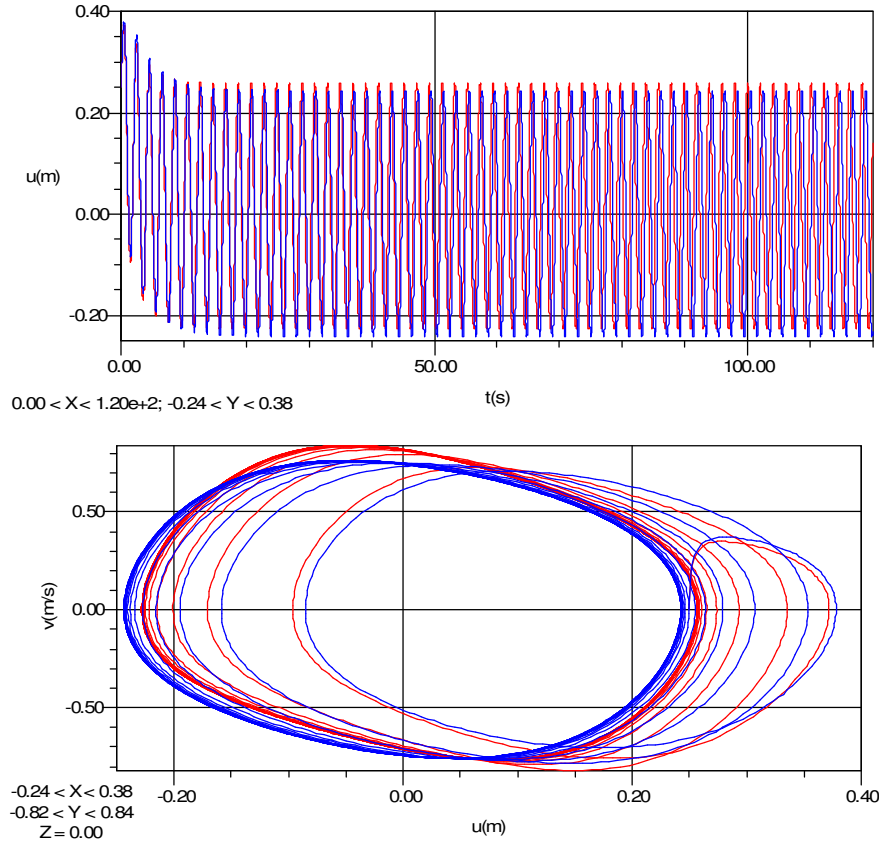


**Figure 5.** SCR time response and phase portrait (blue for linear and red for nonlinear).

–0.2277 m. Therefore, the amplitude of the controlled system is 14.16% smaller than the uncontrolled, but in order to reach such an amplitude reduction, an increase of approximately 50% in the riser tension is seen to be necessary. Consequently, it is questionable if the adoption of the riser tension as a control parameter is suitable for SCRs. It could be further argued that the tension variation for control purposes would affect the riser natural frequencies, so that the vortex shedding frequency might be detuned with respect to the previously locked-in mode, but could be tuned to another nearby mode. Of course, this behavior cannot be detected by the single-degree of freedom reduced-order model considered here and would require a more realistic analysis [Silveira et al. 2007; Josefsson and Dalton 2010].

## 7. Conclusion

We introduce tools of nonlinear dynamics, such as nonlinear normal modes and reduced-order modeling, based on which the analysis of offshore risers, considering geometrical nonlinearities, vortex-induced vibrations, and active control, may be pursued in a simple way. The case study addresses the response of a SCR, revealing not only remarkable quantitative differences in the estimates of maximum amplitudes between linear and nonlinear, uncontrolled and controlled models, but also qualitatively distinct behavior, due to the nonlinear effect of the riser statical curvature.

## References

- [Assi 2009] G. R. S. Assi, *Mechanisms for flow-induced vibration of interfering bluff bodies*, Ph.D., Imperial College, Department of Aeronautics, London, 2009, available at [http://www.ndf.poli.usp.br/~gassi/GAssi\\_PhD\\_2009.pdf](http://www.ndf.poli.usp.br/~gassi/GAssi_PhD_2009.pdf).
- [Baracho Neto and Mazzilli 2005] O. G. P. Baracho Neto and C. E. N. Mazzilli, “Evaluation of multi-modes for finite-element models: systems tuned into 1:2 internal resonance”, *Int. J. Solids Struct.* **42**:21-22 (2005), 5795–5820.
- [Blevins 1990] R. D. Blevins, *Flow-induced vibration*, 2nd ed., Van Nostrand Reinhold, New York, 1990.
- [Facchinetti et al. 2004] M. L. Facchinetti, E. de Langre, and F. Biolley, “Coupling of structure and wake oscillators in vortex-induced vibrations”, *J. Fluids Struct.* **19**:2 (2004), 123–140.
- [Gabbai and Benaroya 2005] R. D. Gabbai and H. Benaroya, “An overview of modeling and experiments of vortex-induced vibration of circular cylinders”, *J. Sound Vib.* **282**:3-5 (2005), 575–616.
- [Josefsson and Dalton 2010] P. M. Josefsson and C. Dalton, “An analytical/computational approach in assessing vortex-induced vibration of a variable tension riser”, *J. Offshore Mech. Arct. Eng.* **132**:3 (2010), article ID 031302-1/7.
- [Luenberger 1979] D. G. Luenberger, *Introduction to dynamic systems: theory, models, and applications*, Wiley, New York, 1979.
- [Mazzilli and Baracho Neto 2002] C. E. N. Mazzilli and O. G. P. Baracho Neto, “Evaluation of non-linear normal modes for finite-element models”, *Comput. Struct.* **80**:11 (2002), 957–965.
- [Mazzilli and Lenci 2008] C. E. N. Mazzilli and S. Lenci, “Normal vibration modes of a slender beam on elastic foundation with unilateral contact”, in *XXII ICTAM* (Adelaide, Australia, 2008), IUTAM - International Union of Theoretical and Applied Mechanics, 2008.
- [Ogata 1995] K. Ogata, *Discrete-time control system*, Prentice Hall, Englewood Cliffs, 1995.
- [Preumont 2002] A. Preumont, *Vibration control of active structures: an introduction*, Kluwer, Dordrecht, 2002.
- [Shaw and Pierre 1993] S. W. Shaw and C. Pierre, “Normal modes for non-linear vibratory systems”, *J. Sound Vib.* **164**:1 (1993), 85–124.
- [Silveira et al. 2007] L. M. Y. Silveira, C. M. Martins, L. D. Cunha, and C. P. Pesce, “An investigation on the effect of tension variation on the VIV of risers”, in *Proceedings of the 26th International Conference on Offshore Mechanics and Arctic Engineering*, San Diego, 2007.
- [Soares and Mazzilli 2000] M. E. S. Soares and C. E. N. Mazzilli, “Nonlinear normal modes of planar frames discretised by the finite element method”, *Comput. Struct.* **77**:5 (2000), 485–493.
- [Williamson and Govardhan 2004] C. H. K. Williamson and R. Govardhan, “Vortex-induced vibrations”, *Annu. Rev. Fluid Mech.* **36** (2004), 413–455.

Received 16 Jun 2010. Revised 2 Dec 2010. Accepted 17 Jan 2011.

CARLOS E. N. MAZZILLI: [cenmazzi@usp.br](mailto:cenmazzi@usp.br)

*Department of Structural and Geotechnical Engineering, Polytechnic School, University of São Paulo,  
Av. Prof. Almeida Prado, trav. 2 n. 83, 05508-900 São Paulo-SP, Brasil*

CÉSAR T. SANCHES: [cesar.sanches@gmail.com](mailto:cesar.sanches@gmail.com)

*Department of Structural and Geotechnical Engineering, Polytechnic School, University of São Paulo,  
Av. Prof. Almeida Prado, trav. 2 n. 83, 05508-900 São Paulo-SP, Brasil*

## NONLINEAR ELECTROMECHANICAL FIELDS AND LOCALIZED POLARIZATION SWITCHING OF PIEZOELECTRIC MACROFIBER COMPOSITES

YASUHIDE SHINDO, FUMIO NARITA, KOJI SATO AND TOMO TAKEDA

This paper examines theoretically and experimentally the nonlinear electromechanical response of piezoelectric macrofiber composites. 3D finite element analysis was carried out to study the strain versus electric field curve and the internal electromechanical fields near interdigitated electrodes in the macrofiber composites by introducing a model for polarization switching. The piezoelectric fibers in the macrofiber composite are partially or fully poled. Results on the strain versus electric field curves from microelectromechanical models and simple experiments were also presented, and comparison was made with the finite element solutions.

### 1. Introduction

Piezoelectric macrofiber composite (MFC) elements, developed at NASA Langley Research Center for aerospace applications, are gaining increasing interest for applications in structural health monitoring [Brunner et al. 2009] and energy harvesting [Song et al. 2009] systems. The development of the MFC helps to overcome some of the limitations of conventional lead zirconate titanate (PZT) ceramics, especially brittleness, lack of reliability, and conformability. In [Williams et al. 2006] the actuation behavior of MFC under electromechanical loading was investigated analytically and experimentally, and the piezoelectric and electrostrictive coefficients were discussed. Also, in [Bilgen et al. 2010] the structural response of MFC actuated clamped-free thin cantilever beams was studied.

In some MFC applications, high values of stress and electric fields arise in the neighborhood of electrode tips in PZT fibers, and the field concentrations can result in electromechanical degradation [Shindo et al. 2004; Narita et al. 2007]. There is also another problem related to the manufacturing process. A PZT wafer is first diced into rectangular fibers. This fiber arrangement is infiltrated with resin and cured together with interdigitated Kapton electrode sheets in a high-precision lamination pressing machine. After this, in a final step, the MFC is polarized with high voltages for about 10 minutes at room temperature. With these fabrication techniques, the resulting polarization of the PZT fibers will inevitably be partial. Due to the presence of interdigitated electrode (IDE) edges and the resulting inhomogeneity of the constituents, piezoelectric MFCs can suffer damage prematurely during service. It is therefore important to understand electromechanical field concentrations near IDEs in piezoelectric MFCs.

In this paper, we investigate the electromechanical response of piezoelectric MFCs. Recent works [Dano and Jullière 2007; Deraemaeker et al. 2009] used the linear constitutive relations for coupling

---

The authors thank Smart Material Corp. for providing useful information regarding piezoelectric MFCs.

**Keywords:** piezomechanics, finite element method, material testing, piezoelectric composites, electromechanical field concentrations, smart materials and structures.

response in MFCs; hence the novelty of this work consists of exploration of the nonlinear behavior during the polarization switching process and comparison of the numerical values with the experimental data. In Section 2, the basic equations for piezoelectric materials are described. A nonlinear 3D finite element model incorporating the polarization switching mechanism is also presented to predict the strain versus electric field curve and internal electromechanical fields near IDEs in piezoelectric MFCs. The piezoelectric fibers in the MFC are partially or fully poled. In addition, the effective longitudinal piezoelectric constant of the MFC with fully poled PZT fibers is derived analytically using microelectromechanical models. In Section 3, the electric field-induced strain is measured. Test results on the strain versus electric field curve are compared to predictions in Section 4. The finite element results on the internal electromechanical fields are then discussed. Our conclusions are summarized in Section 5.

## 2. Analysis

**2.1. Basic equations.** Consider a piezoelectric material with no body force and free charge. The governing equations in the Cartesian coordinates  $x_i$  ( $i = 1, 2, 3$ ) are

$$\sigma_{ji,j} = 0, \quad D_{i,i} = 0, \quad (1)$$

where  $\sigma_{ij}$  is the stress tensor,  $D_i$  is the electric displacement vector, a comma denotes partial differentiation with respect to the coordinate  $x_i$ , and Einstein summation convention over repeated indices is used. The relation between the strain tensor  $\varepsilon_{ij}$  and the displacement vector  $u_i$  is given by

$$\varepsilon_{ij} = \frac{1}{2}(u_{j,i} + u_{i,j}), \quad (2)$$

and the electric field intensity vector is  $E_i = -\phi_{,i}$ , where  $\phi$  is the electric potential. In a ferroelectric material, domain switching leads to changes in the remanent strain  $\varepsilon_{ij}^r$  and remanent polarization  $P_i^r$ . The constitutive relations can be written as

$$\sigma_{ij} = c_{ijkl}(\varepsilon_{kl} - \varepsilon_{kl}^r) - e_{kij}E_k, \quad D_i = e_{ikl}(\varepsilon_{kl} - \varepsilon_{kl}^r) + \epsilon_{ik}E_k + P_i^r. \quad (3)$$

In (3),  $c_{ijkl}$  and  $e_{ikl}$  are the elastic and piezoelectric tensors, and  $\epsilon_{ik}$  is the dielectric permittivity tensor. Valid symmetry conditions for the material constants are

$$c_{ijkl} = c_{jikl} = c_{ijlk} = c_{klij}, \quad e_{kij} = e_{kji}, \quad \epsilon_{ik} = \epsilon_{ki}. \quad (4)$$

The constitutive equations (3) for piezoelectric material poled in the  $x_3$ -direction are found in Appendix A.

Although there are many criteria that can be used to predict polarization switching in piezoelectric materials, we choose the switching criterion proposed in [Hwang et al. 1995]. This is due to the fact that the model is simple and quite successful at predicting the homogeneous average response of PZT material systems [Steinkopff 1999; Hayashi et al. 2003]. In this model, the direction of a spontaneous polarization  $P^s$  of each grain can change by  $90^\circ$  or  $180^\circ$  for ferroelectric switching induced by a sufficiently large electric field.  $90^\circ$  ferroelastic switching is induced by a sufficiently large stress field. This criterion requires that a polarization switches when the combined electrical and mechanical work exceeds a critical value; that is,

$$\sigma_{ij}\Delta\varepsilon_{ij} + E_i\Delta P_i \geq 2P^sE_c, \quad (5)$$

where  $E_c$  is a coercive electric field, and  $\Delta\varepsilon_{ij}$  and  $\Delta P_i$  are the changes in the spontaneous strain and spontaneous polarization during switching, respectively. The values of  $\Delta\varepsilon_{ij}$  and  $\Delta P_i$  are given in Appendix B. The constitutive equations (3) after polarization switching are given by

$$\sigma_{ij} = c_{ijkl}(\varepsilon_{kl} - \varepsilon_{kl}^r) - e'_{kij}E_k, \quad D_i = e'_{ikl}(\varepsilon_{kl} - \varepsilon_{kl}^r) + \epsilon_{ik}E_k + P_i^r. \quad (6)$$

The new piezoelectric constant  $e'_{ikl}$  is given in Appendix C.

**2.2. Model.** Consider a M-4010-P1 MFC (Smart Material Corp., Sarasota, FL) with overall dimensions of about  $50\text{ mm} \times 22\text{ mm} \times 0.3\text{ mm}$ . The MFC is comprised of very thin PZT-5A fibers (width  $2w_p$ , thickness  $2h_p$ ) that are unidirectionally aligned in an epoxy matrix and sandwiched between two sets of copper IDE (width  $2w_e$ , thickness  $h_e$ ) patterns as shown in Figure 1a. The IDE patterns are printed on a Kapton film (thickness  $h_k$ ). The MFC has an IDE spacing of about 0.5 mm and has an active area of about  $40\text{ mm} \times 10\text{ mm}$ . The material characteristics of PZT-5A are listed in Table 1, and the coercive electric field is approximately  $E_c = 1.5\text{ MV/m}$ . The Young's modulus  $E$  and Poisson's ratio  $\nu$  of the epoxy, copper, and Kapton are listed in Table 2 [Deraemaeker et al. 2009].

Figure 1b illustrates the repeating unit of the MFC. A rectangular Cartesian coordinate system O-xyz is used with the z-axis coinciding with the PZT fiber direction. The repeating unit of the MFC occupies the region  $(0 \leq x \leq W, 0 \leq y \leq H, 0 \leq z \leq L)$ . The model consists of rectangular PZT fiber (width  $w_p$ , length  $L$ ) embedded in an epoxy matrix and Kapton film (width  $W$ , length  $L$ ). Electrodes 1 and 3 of area  $W \times w_e$  and electrode 2 of area  $W \times 2w_e$  are also incorporated into the model. The total thickness of the model is  $H = h_p + h_e + h_k$ .

With the IDEs, the electric field  $E_0$  is applied along the PZT fibers (the z-direction) which produces much higher in-plain actuation strain  $\varepsilon_0$  than traditional monolithic PZT poled through-the-thickness (see Figure 2) [Bent and Hagood 1997; Williams et al. 2004; Paradies and Melnykowycz 2007]. We consider the following electrical boundary conditions: the electric potentials on the interface between the PZT fiber and electrode 1 (that is,  $0 \leq x \leq w_p, y = h_p, 0 \leq z \leq w_e$ ) and the interface between the PZT fiber and electrode 3 (that is,  $0 \leq x \leq w_p, y = h_p, L - w_e \leq z \leq L$ ) equal the applied voltage,  $\phi = V_0$ , and the interface between the PZT fiber and electrode 2 (that is,  $0 \leq x \leq w_p, y = h_p, L/2 - w_e \leq z \leq L/2 + w_e$ ) is connected to the ground, so that  $\phi = 0$ . The applied electric field  $E_0$  can be estimated to be the voltage  $V_0$

	Elastic stiffnesses ( $\times 10^{10}\text{ N/m}^2$ )					Piezoelectric coefficients ( $\text{C/m}^2$ )			Dielectric constants ( $\times 10^{-10}\text{ C/V m}$ )	
	$c_{11}$	$c_{33}$	$c_{44}$	$c_{12}$	$c_{13}$	$e_{31}$	$e_{33}$	$e_{15}$	$\epsilon_{11}$	$\epsilon_{33}$
PZT-5A	12.0	11.1	2.1	7.51	7.51	-3.05	21.1	11.8	81.1	73.5

**Table 1.** Material properties of PZT-5A fiber.

	Young's modulus $E$ ( $\times 10^{10}\text{ N/m}^2$ )	Poisson's ratio $\nu$
Epoxy	0.29	0.30
Copper	11.7	0.31
Kapton	0.28	0.30

**Table 2.** Material properties of nonpiezoelectric constituents.

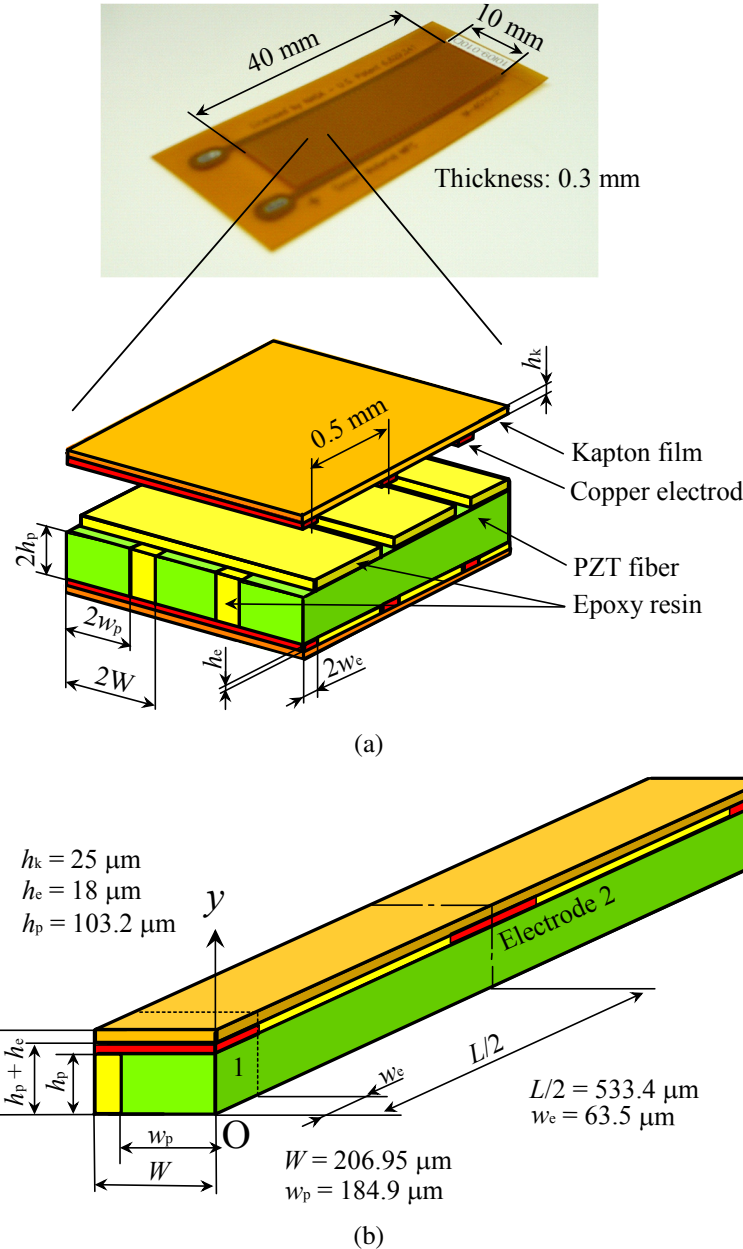


**Figure 1.** Schematic drawing of MFC: (a) lay-up and geometry and (b) repeating unit.

divided by the IDE spacing  $L/2$ . The mechanical boundary conditions include the traction-free condition on the top surface at  $y = H$  and the zero-displacement conditions on the  $x = 0$ ,  $y = 0$ , and  $z = 0$  faces. Also included are the symmetry conditions on the side surfaces at  $x = W$  and  $z = L$ .

Consider two types of poling. The first is partially poled. For partially poled PZT fibers, a matrix of crystalline grains with an idealized microstructure [Dent et al. 2007] is first considered, where each grain has a random polarization obtained using statistical procedures [Swain and Swain 1980]. The resulting

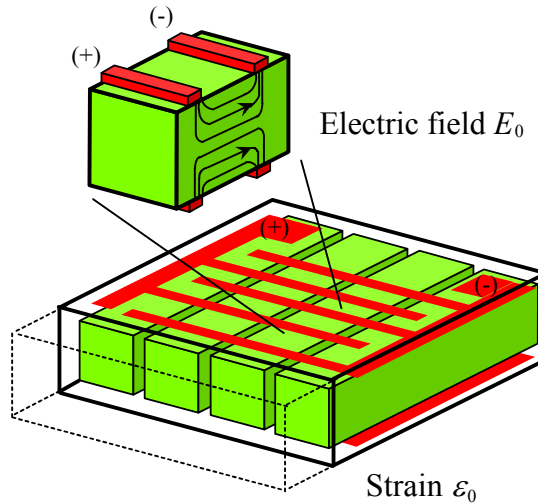


**Figure 2.** Strain and electric field of MFC with IDE.

material is equivalent to an unpoled piezoelectric [Shindo et al. 2009]. Figure 3a shows a typical model ( $x = 0$  plane) with a fine microstructure. The grain polarizations are quantized to just six orientations, corresponding to the two directions along the three principal axes. Other directions are not considered here for simplicity. High voltage is next applied through finite element analysis (FEA), and the PZT fiber model is partially polarized. The second has fully poled PZT fibers (see Figure 3b).

Each element consists of many grains, and each grain is modeled as a uniformly polarized cell that contains a single domain. The model neglects domain wall effects and interaction among different domains. In reality, this is not true, but the assumption does not affect the macroscopic behavior of the MFC. The polarization switching is defined for each element. The voltage  $V_0$  is applied, and the

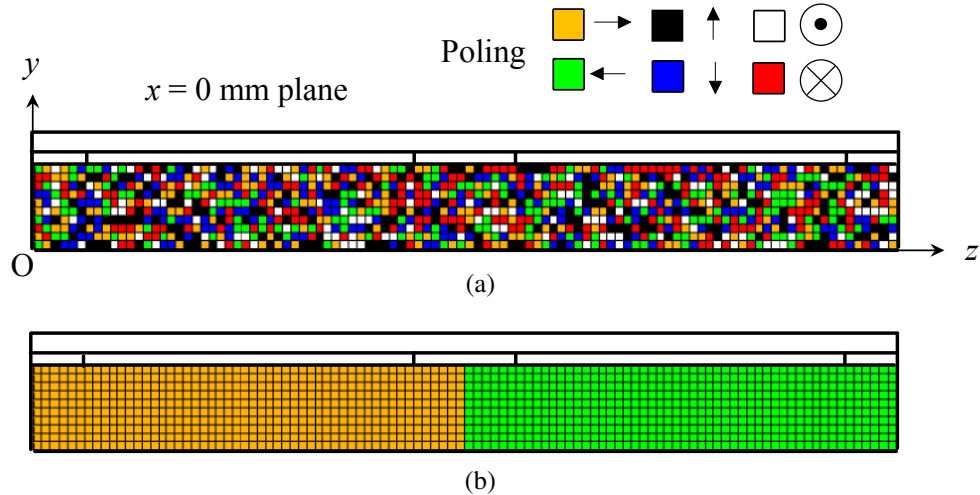


**Figure 3.** Models of (a) unpoled and (b) fully poled PZT fibers.

electromechanical fields of each element are computed from the FEA. The switching criterion of (5) is checked for every element to see if switching will occur. After all possible polarization switches have occurred, the piezoelectricity tensor of each element is rotated to the new polarization direction. The electromechanical fields are recalculated, and the process is repeated until the solution converges. The macroscopic response of the MFC is determined by the finite element model.

The finite element computations by ANSYS were provided by modifying the program with routines developed in our previous work (for example, [Shindo et al. 2004]). The spontaneous polarization  $P^s$  and strain  $\gamma^s$  were assigned representative values of  $0.3 \text{ C/m}^2$  and  $0.004$ , respectively, based on the experimental data [Hwang et al. 1995]. Simulations were also run with the spontaneous polarization and strain values varying, though the results are not shown here since changing these values did not impact the results. Each element was defined by an eight-node 3D coupled field solid for the PZT fiber and an eight-node 3D structural solid for the epoxy matrix, Kapton film, and copper electrodes.

The strain  $\varepsilon_0^e$  of the repeating unit for the fully poled PZT fiber under stress-free conditions is related to the electric field  $E_0$  by the expression [Deraemaeker et al. 2009]:

$$\varepsilon_0^e = d_{33}^e E_0. \quad (7)$$

Here, the effective longitudinal piezoelectric coefficient  $d_{33}^e$  is obtained, using microelectromechanics models based on the uniform field assumptions [Tan and Tong 2001]. Assuming that  $90^\circ$  switching does not occur, the effective coefficient for the repeating unit without Kapton film or copper/epoxy layer is given by

$$d_{33}^e = \begin{cases} e_{31}^e s_{13}^e + e_{32}^e s_{23}^e + e_{33}^e s_{33}^e & \text{if } E_0 > -E_c, \\ -(e_{31}^e s_{13}^e + e_{32}^e s_{23}^e + e_{33}^e s_{33}^e) & \text{if } E_0 \leq -E_c, \end{cases} \quad (8)$$

where  $e_{31}^e$ ,  $e_{32}^e$ ,  $e_{33}^e$ ,  $s_{13}^e$ ,  $s_{23}^e$ , and  $s_{33}^e$  are given in Appendix D.

### 3. Experimental procedure

The free strain ( $\varepsilon$ ) response of the M-4010-P1 MFC (see Figure 1a) was measured. Strain gages were bonded symmetrically at the center of the active area on both sides of the piezoelectric MFC. Voltage was applied using a power supply for voltages up to  $1.25 \text{ kV/DC}$  in order to generate the strain versus electric field curve. A plot of applied voltage versus time during the test is shown in Figure 4. The MFC

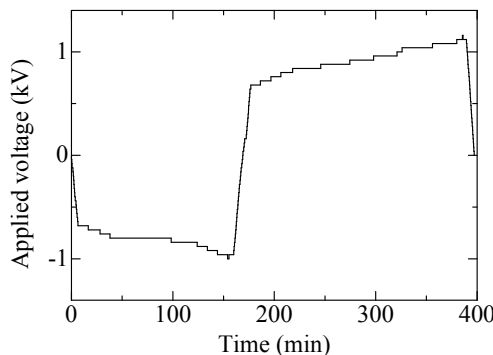


**Figure 4.** Applied voltage versus time.

was then cut and observed using a digital microscope. The measured entities were statistically analyzed to obtain realistic geometrical parameters. The main values are represented in Figure 1b.

#### 4. Results and discussion

Figure 5 shows the FEA results for the distribution of poled areas at the  $x = 0$  mm plane for the PZT fiber under the electric field for  $E_0 = E_c = 1.5$  MV/m and for  $E_0 = 2E_c = 3$  MV/m. The unpoled areas are observed under the coercive electric field. Moreover, at an electric field of  $2E_c$ , there are some areas where the pole is not aligned. Figure 6 provides the strain versus electric field for the piezoelectric MFCs. The solid and dot-dashed lines represent the strain  $\varepsilon_{zz}$  at  $x = 0$ ,  $y = H$ , and  $z = 0$  for MFCs with partially and fully poled PZT fibers from the FEA while the open circle represents the test data  $\varepsilon$ . The partially poled PZT fiber is obtained under  $E_0 = 2E_c$  (see Figure 5b). Also shown is the analytical data  $\varepsilon_0^e$  obtained from the microelectromechanics models (dashed line). The FEA results show that as the electric field  $E_0$

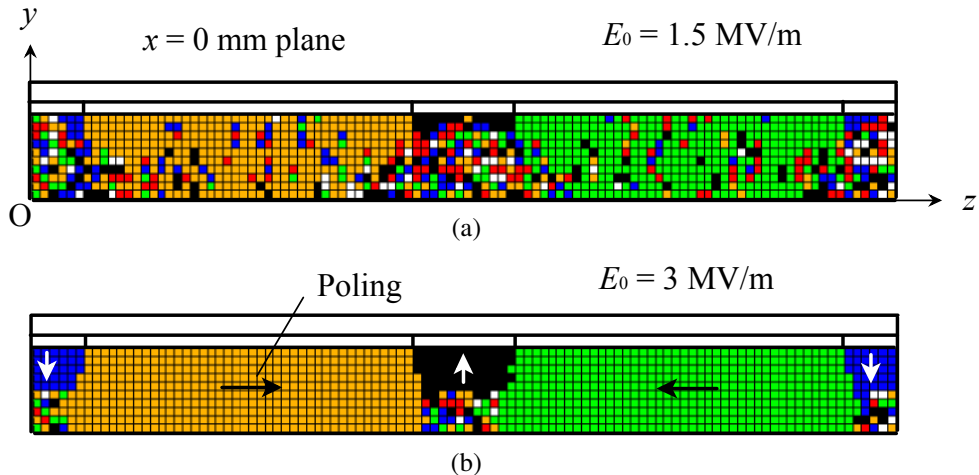


**Figure 5.** Images of poling for PZT fiber at (a)  $E_0 = E_c = 1.5$  MV/m and (b)  $E_0 = 2E_c = 3$  MV/m.

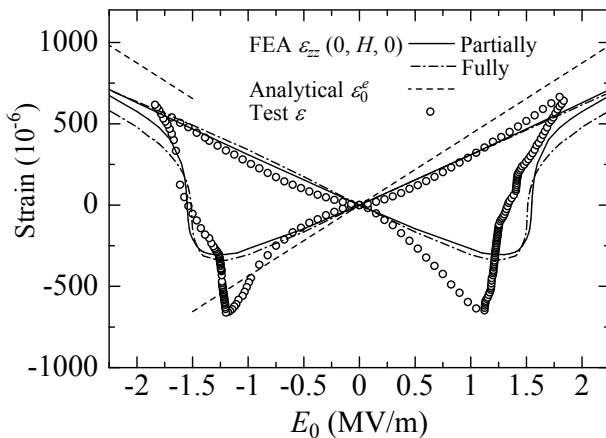


**Figure 6.** Strain versus electric field for piezoelectric MFCs.

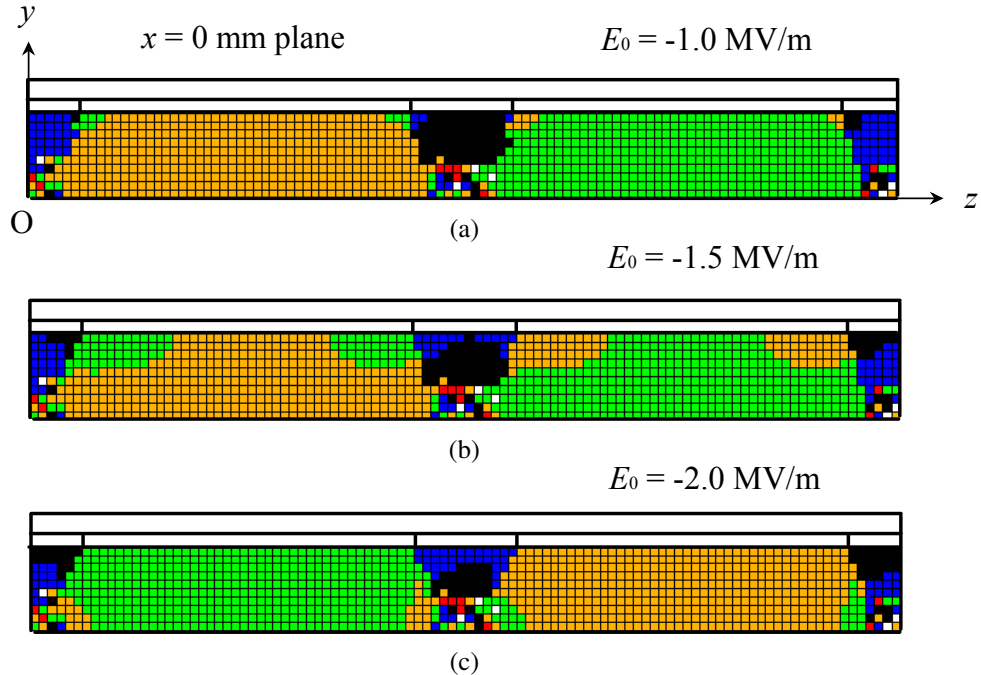


**Figure 7.** Polarization switching zone induced by electric field of (a)  $E_0 = -1.0 \text{ MV/m}$ , (b)  $E_0 = -1.5 \text{ MV/m}$ , and (c)  $E_0 = -2.0 \text{ MV/m}$  at the  $x = 0 \text{ mm}$  plane for MFC with partially poled PZT fibers.

is increased from zero initially, the tensile strain increases linearly due to the piezoelectric effect. On the other hand, the compressive strain increases nonlinearly as the electric field is lowered from zero; then, the compressive strain reaches maximum at about  $E_0 = -1.25 \text{ MV/m}$  as localized depolarization occurs. The compressive strain then decreases, and the tensile strain rises as the negative remanent polarization develops. As polarization reversal takes place, the piezoelectric coefficients of the PZT fiber change their signs. This leads to a reversal of the macroscopic piezoelectric effect. The tensile strain decreases as the negative electric field is gradually decreased. As the electric field is cycled, the butterfly loop is repeated. Note that there is a good agreement between the FEA and the test. Also, little difference in the strain versus electric field curve is observed between the MFCs with partially and fully poled PZT fibers. Although the strain obtained from the microelectromechanics models is larger than that from the FEA due to neglecting the Kapton film and copper/epoxy layer, the microelectromechanics models may serve to predict roughly the strain response of the MFCs. Figure 7 shows the polarization switching zones at the  $x = 0 \text{ mm}$  plane of the MFC with partially poled PZT fibers. The original poled state is shown in Figure 5b. Under the electric field,  $E_0 = -1.0 \text{ MV/m}$ , below the coercive field strength  $E_c = 1.5 \text{ MV/m}$ , polarization switching occurs near the IDE tip. It seems that the switching expands along the region near the interface between the PZT fiber and epoxy layer. The size of the  $180^\circ$  switching zone increases with increasing electric field opposite to the original poling direction. The above numerical and experimental results show that if MFCs are operated under negative electric fields, the polarization switching effect is by no means negligible, and designers need to be aware of the nonlinear behavior.

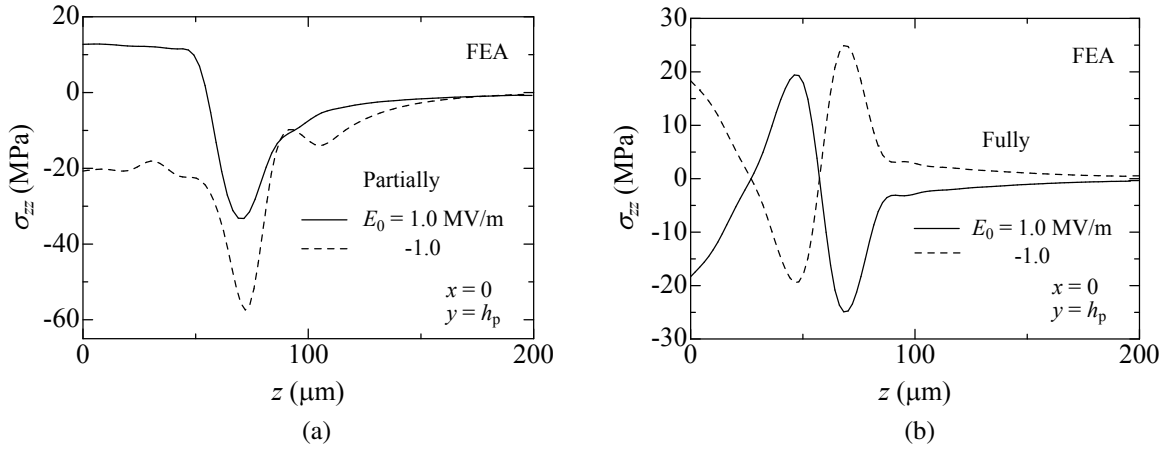


**Figure 8.** Variation of normal stress  $\sigma_{zz}$  as a function of  $z$  for MFCs with (a) partially and (b) fully poled PZT fibers;  $x = 0 \text{ mm}$  and  $y = h_p$ .

The normal stress  $\sigma_{zz}$  as a function of  $z$  at the  $x = 0 \text{ mm}$  plane of the MFC with partially poled PZT fibers is shown in Figure 8a for  $y = h_p$  under an electric field  $E_0 = \pm 1.0 \text{ MV/m}$ . When a positive  $E_0$  of  $1.0 \text{ MV/m}$  is applied, the normal stress in the neighborhood of the IDE tip changes from tensile to compressive and the maximum value of the compressive stress occurs at about  $z = 70 \mu\text{m}$ . It is interesting to note that under  $E_0 = -1.0 \text{ MV/m}$ , the highest compressive stress occurs at about  $z = 75 \mu\text{m}$ . Figure 8b shows similar results for the MFC with fully poled PZT fibers. The maximum values of the compressive and tensile stresses occur under  $E_0 = 1.0$  and  $-1.0 \text{ MV/m}$ , respectively, at about  $z = 70 \mu\text{m}$ . Figure 9 shows the shear stress  $\sigma_{yz}$  as a function of  $z$  at the  $x = 0 \text{ mm}$  plane of the MFCs with partially and fully poled PZT fibers for  $y = h_p$  under an electric field  $E_0 = 1.0 \text{ MV/m}$ . The peak values of  $\sigma_{yz}$  for the MFCs with partially and fully poled PZT fibers occur at different locations, and the maximum shear stress for the MFC with partially poled PZT fibers is larger than that for the MFC with fully poled PZT fibers. Figure 10 shows the normal stress  $\sigma_{yy}$  as a function of  $z$  at the  $x = 0 \text{ mm}$  plane of the MFCs with

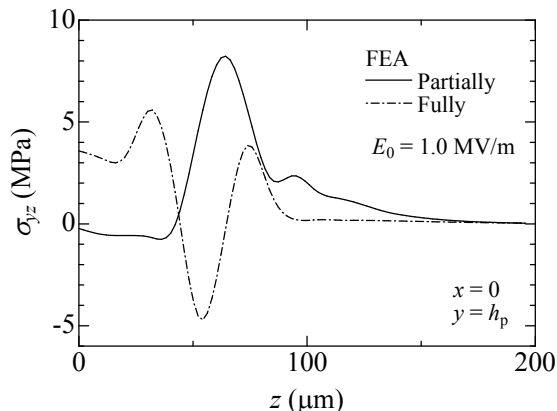


**Figure 9.** Variation of shear stress  $\sigma_{yz}$  as a function of  $z$  for MFCs with partially and fully poled PZT fibers;  $x = 0 \text{ mm}$  and  $y = h_p$ .

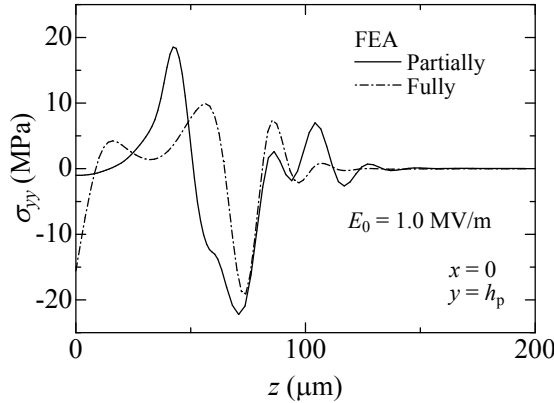


**Figure 10.** Variation of normal stress  $\sigma_{yy}$  as a function of  $z$  for MFCs with partially and fully poled PZT fibers;  $x = 0$  mm and  $y = h_p$ .

partially and fully poled PZT fibers for  $y = h_p$  under an electric field  $E_0 = 1.0$  MV/m. The maximum value of the tensile stress for the MFC with partially poled PZT fibers is about twice that for the MFC with fully poled PZT fibers. A comparison between the results for MFCs with partially and fully poled PZT fibers indicates that the inhomogeneity near the IDE of the MFC has little effect on the strain versus electric field curve but affects the internal stresses.

## 5. Conclusions

This paper presents the results of numerical and experimental study in piezoelectric macrofiber composites (MFCs). The developed finite element model quantitatively predicted the strain versus electric field curve and captured the nonlinear electromechanical phenomena. We showed that the inhomogeneity near the interdigitated electrode (IDE) tip in the MFCs leads to dramatic differences in the internal stresses. By knowing how the partially poled lead zirconate titanate (PZT) fiber, IDE, and matrix constituents interact, we can design a MFC to achieve particular overall properties. The results of this study will help to offer a basis for optimizing piezoelectric MFC performance by selecting the optimal microstructure and properties of composite constituents.

## Appendix A

For piezoelectric ceramics which exhibit hexagonal crystal symmetry of class 6 mm with respect to the principal  $x_1$ ,  $x_2$ , and  $x_3$  axes, the constitutive relations can be written in the form

$$\begin{Bmatrix} \sigma_1 \\ \sigma_2 \\ \sigma_3 \\ \sigma_4 \\ \sigma_5 \\ \sigma_6 \end{Bmatrix} = \begin{Bmatrix} c_{11} & c_{12} & c_{13} & 0 & 0 & 0 \\ c_{12} & c_{11} & c_{13} & 0 & 0 & 0 \\ c_{13} & c_{13} & c_{33} & 0 & 0 & 0 \\ 0 & 0 & 0 & c_{44} & 0 & 0 \\ 0 & 0 & 0 & 0 & c_{44} & 0 \\ 0 & 0 & 0 & 0 & 0 & c_{66} \end{Bmatrix} \begin{Bmatrix} \varepsilon_1 - \varepsilon_1^r \\ \varepsilon_2 - \varepsilon_2^r \\ \varepsilon_3 - \varepsilon_3^r \\ \varepsilon_4 - \varepsilon_4^r \\ \varepsilon_5 - \varepsilon_5^r \\ \varepsilon_6 - \varepsilon_6^r \end{Bmatrix} - \begin{Bmatrix} 0 & 0 & e_{31} \\ 0 & 0 & e_{31} \\ 0 & 0 & e_{33} \\ 0 & e_{15} & 0 \\ e_{15} & 0 & 0 \\ 0 & 0 & 0 \end{Bmatrix} \begin{Bmatrix} E_1 \\ E_2 \\ E_3 \end{Bmatrix}, \quad (\text{A.1})$$

$$\begin{Bmatrix} D_1 \\ D_2 \\ D_3 \end{Bmatrix} = \begin{bmatrix} 0 & 0 & 0 & 0 & e_{15} & 0 \\ 0 & 0 & 0 & e_{15} & 0 & 0 \\ e_{31} & e_{31} & e_{33} & 0 & 0 & 0 \end{bmatrix} \begin{Bmatrix} \varepsilon_1 - \varepsilon_1^r \\ \varepsilon_2 - \varepsilon_2^r \\ \varepsilon_3 - \varepsilon_3^r \\ \varepsilon_4 - \varepsilon_4^r \\ \varepsilon_5 - \varepsilon_5^r \\ \varepsilon_6 - \varepsilon_6^r \end{Bmatrix} + \begin{bmatrix} \epsilon_{11} & 0 & 0 \\ 0 & \epsilon_{11} & 0 \\ 0 & 0 & \epsilon_{33} \end{bmatrix} \begin{Bmatrix} E_1 \\ E_2 \\ E_3 \end{Bmatrix} + \begin{Bmatrix} P_1^r \\ P_2^r \\ P_3^r \end{Bmatrix}, \quad (\text{A.2})$$

where

$$\sigma_1 = \sigma_{11}, \sigma_2 = \sigma_{22}, \quad \sigma_3 = \sigma_{33}, \quad \sigma_4 = \sigma_{23} = \sigma_{32}, \quad \sigma_5 = \sigma_{31} = \sigma_{13}, \quad \sigma_6 = \sigma_{12} = \sigma_{21}, \quad (\text{A.3})$$

$$\varepsilon_1 = \varepsilon_{11}, \varepsilon_2 = \varepsilon_{22}, \quad \varepsilon_3 = \varepsilon_{33}, \quad \varepsilon_4 = 2\varepsilon_{23} = 2\varepsilon_{32}, \quad \varepsilon_5 = 2\varepsilon_{31} = 2\varepsilon_{13}, \quad \varepsilon_6 = 2\varepsilon_{12} = 2\varepsilon_{21}, \quad (\text{A.4})$$

$$\varepsilon_1^r = \varepsilon_{11}^r, \varepsilon_2^r = \varepsilon_{22}^r, \quad \varepsilon_3^r = \varepsilon_{33}^r, \varepsilon_4^r = 2\varepsilon_{23}^r = 2\varepsilon_{32}^r, \quad \varepsilon_5^r = 2\varepsilon_{31}^r = 2\varepsilon_{13}^r, \quad \varepsilon_6^r = 2\varepsilon_{12}^r = 2\varepsilon_{21}^r, \quad (\text{A.5})$$

$$\begin{aligned} c_{11} &= c_{1111} = c_{2222}, c_{12} = c_{1122}, \quad c_{13} = c_{1133} = c_{2233}, c_{33} = c_{3333}, \\ c_{44} &= c_{2323} = c_{3131}, c_{66} = c_{1212} = \frac{1}{2}(c_{11} - c_{12}), \end{aligned} \quad (\text{A.6})$$

$$e_{15} = e_{131} = e_{223}, \quad e_{31} = e_{311} = e_{322}, \quad e_{33} = e_{333}. \quad (\text{A.7})$$

The remanent strain and polarization are present in the piezoelectric material poled in the positive  $x_3$ -direction but because the remanent state is the reference for the measurement of strain and polarization,  $\varepsilon_{ij}^r$  and  $P_i^r$  are numerically equal to zero for the polarized state.

## Appendix B

The values of  $\Delta\varepsilon_{ij} = \varepsilon_{ij}^r$  and  $\Delta P_i = P_i^r$  for  $180^\circ$  switching can be expressed as

$$\Delta\varepsilon_{11} = 0, \quad \Delta\varepsilon_{22} = 0, \quad \Delta\varepsilon_{33} = 0, \quad \Delta\varepsilon_{12} = 0, \quad \Delta\varepsilon_{23} = 0, \quad \Delta\varepsilon_{31} = 0, \quad (\text{B.1})$$

$$\Delta P_1 = 0, \quad \Delta P_2 = 0, \quad \Delta P_3 = -2P^s. \quad (\text{B.2})$$

For  $90^\circ$  switching in the  $x_3x_1$  plane, the changes are

$$\Delta\varepsilon_{11} = \gamma^s, \quad \Delta\varepsilon_{22} = 0, \quad \Delta\varepsilon_{33} = -\gamma^s, \quad \Delta\varepsilon_{12} = 0, \quad \Delta\varepsilon_{23} = 0, \quad \Delta\varepsilon_{31} = 0, \quad (\text{B.3})$$

$$\Delta P_1 = \pm P^s, \quad \Delta P_2 = 0, \quad \Delta P_3 = -P^s, \quad (\text{B.4})$$

where  $\gamma^s$  is a spontaneous strain. For  $90^\circ$  switching in the  $x_2x_3$  plane, we have

$$\Delta\varepsilon_{11} = 0, \quad \Delta\varepsilon_{22} = \gamma^s, \quad \Delta\varepsilon_{33} = -\gamma^s, \quad \Delta\varepsilon_{12} = 0, \quad \Delta\varepsilon_{23} = 0, \quad \Delta\varepsilon_{31} = 0, \quad (\text{B.5})$$

$$\Delta P_1 = 0, \quad \Delta P_2 = \pm P^s, \quad \Delta P_3 = -P^s. \quad (\text{B.6})$$

### Appendix C

The new piezoelectric constant  $e'_{ikl}$  is related to the elastic and direct piezoelectric constants by

$$\begin{aligned} e'_{111} &= d'_{111}c_{11} + d'_{122}c_{12} + d'_{133}c_{13}, & e'_{122} &= d'_{111}c_{12} + d'_{122}c_{11} + d'_{133}c_{13}, \\ e'_{133} &= d'_{111}c_{13} + d'_{122}c_{13} + d'_{133}c_{33}, & e'_{123} &= 2d'_{123}c_{44}, \quad e'_{131} = 2d'_{131}c_{44}, \quad e'_{112} = 2d'_{112}c_{66}, \\ e'_{211} &= d'_{211}c_{11} + d'_{222}c_{12} + d'_{233}c_{13}, & e'_{222} &= d'_{211}c_{12} + d'_{222}c_{11} + d'_{233}c_{13}, \\ e'_{233} &= d'_{211}c_{13} + d'_{222}c_{13} + d'_{233}c_{33}, & e'_{223} &= 2d'_{223}c_{44}, \quad e'_{231} = 2d'_{231}c_{44}, \quad e'_{212} = 2d'_{212}c_{66}, \\ e'_{311} &= d'_{311}c_{11} + d'_{322}c_{12} + d'_{333}c_{13}, & e'_{322} &= d'_{311}c_{12} + d'_{322}c_{11} + d'_{333}c_{13}, \\ e'_{333} &= d'_{311}c_{13} + d'_{322}c_{13} + d'_{333}c_{33}, & e'_{323} &= 2d'_{323}c_{44}, \quad e'_{331} = 2d'_{331}c_{44}, \quad e'_{312} = 2d'_{312}c_{66}. \end{aligned} \quad (\text{C.1})$$

The components of the piezoelectricity tensor  $d'_{ikl}$  are

$$d'_{ikl} = \{d_{333}n_i n_k n_l + d_{311}(n_i \delta_{kl} - n_i n_k n_l) + d_{131}(\delta_{ik} n_l - 2n_i n_k n_l + \delta_{il} n_k)\}, \quad (\text{C.2})$$

where  $n_i$  is the unit vector in the poling direction,  $\delta_{ij}$  is the Kronecker delta,  $d_{333} = d_{33}$ ,  $d_{311} = d_{31}$ , and  $d_{131} = d_{15}/2$  are the direct piezoelectric constants, and

$$d_{33} = \frac{(c_{11} + c_{12})e_{33} - 2c_{13}e_{31}}{\{(c_{11} + c_{12})c_{33} - 2c_{13}^2\}}, \quad d_{31} = \frac{c_{33}e_{31} - c_{13}e_{33}}{\{(c_{11} + c_{12})c_{33} - 2c_{13}^2\}}, \quad d_{15} = \frac{e_{15}}{c_{44}}. \quad (\text{C.3})$$

### Appendix D

In (8),  $e_{31}^e$ ,  $e_{32}^e$ ,  $e_{33}^e$ ,  $s_{13}^e$ ,  $s_{23}^e$ , and  $s_{33}^e$  are

$$e_{31}^e = e_{31} \frac{c_{11m}w_p/W}{c_{11m}w_p/W + c_{11}(1 - w_p/W)}, \quad (\text{D.1})$$

$$e_{32}^e = e_{31}^e \frac{c_{11m}w_p/W + (c_{11} - c_{12} + c_{12m})(1 - w_p/W)}{c_{11m}}, \quad (\text{D.2})$$

$$e_{33}^e = e_{33}w_p/W + e_{31}^e \frac{(c_{12m} - c_{13})(1 - w_p/W)}{c_{11m}}, \quad (\text{D.3})$$

$$s_{13}^e = \frac{C_{12}C_{23} - C_{13}C_{22}}{(C_{11}C_{22} - C_{12}^2)C_{33} - C_{11}C_{23}^2 + 2C_{12}C_{13}C_{23} - C_{13}^2C_{22}}, \quad (\text{D.4})$$

$$s_{23}^e = \frac{C_{12}C_{13} - C_{11}C_{23}}{(C_{11}C_{22} - C_{12}^2)C_{33} - C_{11}C_{23}^2 + 2C_{12}C_{13}C_{23} - C_{13}^2C_{22}}, \quad (\text{D.5})$$

$$s_{33}^e = \frac{C_{11}C_{22} - C_{22}^2}{(C_{11}C_{22} - C_{12}^2)C_{33} - C_{11}C_{23}^2 + 2C_{12}C_{13}C_{23} - C_{13}^2C_{22}}, \quad (\text{D.6})$$

where

$$C_{11} = \frac{c_{11}c_{11m}}{c_{11m}w_p/W + c_{11}(1-w_p/W)}, \quad (\text{D.7})$$

$$C_{12} = \frac{c_{12}c_{11m}w_p/W + c_{11}c_{12m}(1-w_p/W)}{c_{11m}w_p/W + c_{11}(1-w_p/W)}, \quad (\text{D.8})$$

$$C_{13} = \frac{c_{13}c_{11m}w_p/W + c_{11}c_{12m}(1-w_p/W)}{c_{11m}w_p/W + c_{11}(1-w_p/W)}, \quad (\text{D.9})$$

$$C_{22} = c_{11}w_p/W + c_{11m}(1-w_p/W) + \frac{C_{12}^2}{C_{11}} - \left\{ \frac{c_{12}^2w_p/W}{c_{11}} + \frac{c_{12m}^2(1-w_p/W)}{c_{11m}} \right\}, \quad (\text{D.10})$$

$$C_{23} = c_{13}w_p/W + c_{12m}(1-w_p/W) + \frac{C_{12}C_{13}}{C_{11}} - \left\{ \frac{c_{12}c_{13}w_p/W}{c_{11}} + \frac{c_{12m}^2(1-w_p/W)}{c_{11m}} \right\}, \quad (\text{D.11})$$

$$C_{33} = c_{33}w_p/W + c_{11m}(1-w_p/W) + \frac{C_{13}^2}{C_{11}} - \left\{ \frac{c_{13}^2w_p/W}{c_{11}} + \frac{c_{12m}^2(1-w_p/W)}{c_{11m}} \right\}, \quad (\text{D.12})$$

and

$$c_{11m} = \frac{E_m(1-\nu_m)}{(1+\nu_m)(1-2\nu_m)}, \quad c_{12m} = \frac{E_m\nu_m}{(1+\nu_m)(1-2\nu_m)}. \quad (\text{D.13})$$

$E_m$  and  $\nu_m$  in (D.13) are the Young's modulus and Poisson's ratio of the epoxy matrix.

## References

- [Bent and Hagood 1997] A. A. Bent and N. W. Hagood, "Piezoelectric fiber composites with interdigitated electrodes", *J. Intell. Mater. Syst. Struct.* **8**:11 (1997), 903–919.
- [Bilgen et al. 2010] O. Bilgen, A. Erturk, and D. J. Inman, "Analytical and experimental characterization of macro-fiber composite actuated thin clamped-free unimorph benders", *J. Vib. Acoust. (ASME)* **132**:5 (2010), 051005.
- [Brunner et al. 2009] A. J. Brunner, M. Birchmeier, M. M. Melnykowycz, and M. Barbezat, "Piezoelectric fiber composites as sensor elements for structural health monitoring and adaptive material systems", *J. Intell. Mater. Syst. Struct.* **20**:9 (2009), 1045–1055.
- [Dano and Jullière 2007] M.-L. Dano and B. Jullière, "Active control of thermally induced distortion in composite structures using macro fiber composite actuators", *Smart Mater. Struct.* **16**:6 (2007), 2315–2322.
- [Dent et al. 2007] A. C. Dent, C. R. Bowen, R. Stevens, M. G. Cain, and M. Stewart, "Effective elastic properties for unpoled barium titanate", *J. Eur. Ceram. Soc.* **27**:13–15 (2007), 3739–3743.
- [Deraemaeker et al. 2009] A. Deraemaeker, H. Nasser, A. Benjeddou, and A. Preumont, "Mixing rules for the piezoelectric properties of macro fiber composites", *J. Intell. Mater. Syst. Struct.* **20**:12 (2009), 1475–1482.
- [Hayashi et al. 2003] K. Hayashi, Y. Shindo, and F. Narita, "Displacement and polarization switching properties of piezoelectric laminated actuators under bending", *J. Appl. Phys.* **94**:7 (2003), 4603–4607.
- [Hwang et al. 1995] S. C. Hwang, C. S. Lynch, and R. M. McMeeking, "Ferroelectric/ferroelastic interactions and a polarization switching model", *Acta Metall. Mater.* **43**:5 (1995), 2073–2084.
- [Narita et al. 2007] F. Narita, Y. Shindo, and M. Mikami, "Electroelastic field concentrations and polarization switching induced by circular electrode at the interface of piezoelectric disk composites", *Eur. J. Mech. A Solids* **26**:3 (2007), 394–404.
- [Paradies and Melnykowycz 2007] R. Paradies and M. Melnykowycz, "Numerical stress investigation for piezoelectric elements with a circular cross section and interdigitated electrodes", *J. Intell. Mater. Syst. Struct.* **18**:9 (2007), 963–972.
- [Shindo et al. 2004] Y. Shindo, M. Yoshida, F. Narita, and K. Horiguchi, "Electroelastic field concentrations ahead of electrodes in multilayer piezoelectric actuators: experiment and finite element simulation", *J. Mech. Phys. Solids* **52**:5 (2004), 1109–1124.

- [Shindo et al. 2009] Y. Shindo, F. Narita, and M. Hirama, “Electromechanical field concentrations near the electrode tip in partially poled multilayer piezo-film actuators”, *Smart Mater. Struct.* **18**:8 (2009), 085020.
- [Song et al. 2009] H. J. Song, Y.-T. Choi, A. S. Purekar, and N. M. Wereley, “Performance evaluation of multi-tier energy harvesters using macro-fiber composite patches”, *J. Intell. Mater. Syst. Struct.* **20**:17 (2009), 2077–2088.
- [Steinkopff 1999] T. Steinkopff, “Finite-element modelling of ferroic domain switching in piezoelectric ceramics”, *J. Eur. Ceram. Soc.* **19**:6–7 (1999), 1247–1249.
- [Swain and Swain 1980] C. G. Swain and M. S. Swain, “A uniform random number generator that is reproducible, hardware-independent, and fast”, *J. Chem. Inf. Comput. Sci.* **20**:1 (1980), 56–58.
- [Tan and Tong 2001] P. Tan and L. Tong, “Micro-electromechanics models for piezoelectric-fiber-reinforced composite materials”, *Compos. Sci. Technol.* **61**:5 (2001), 759–769.
- [Williams et al. 2004] R. B. Williams, D. J. Inman, M. R. Schultz, M. W. Hyer, and W. K. Wilkie, “Nonlinear tensile and shear behavior of macro fiber composite actuators”, *J. Compos. Mater.* **38**:10 (2004), 855–869.
- [Williams et al. 2006] R. B. Williams, D. J. Inman, and W. K. Wilkie, “Nonlinear response of the macro fiber composite actuator to monotonically increasing excitation voltage”, *J. Intell. Mater. Syst. Struct.* **17**:7 (2006), 601–608.

Received 26 Jun 2010. Revised 10 Dec 2010. Accepted 13 Dec 2010.

YASUHIDE SHINDO: [shindo@material.tohoku.ac.jp](mailto:shindo@material.tohoku.ac.jp)

Department of Materials Processing, Graduate School of Engineering, Tohoku University, Aoba-yama 6-6-02, Sendai 980-8579, Japan

FUMIO NARITA: [narita@material.tohoku.ac.jp](mailto:narita@material.tohoku.ac.jp)

Department of Materials Processing, Graduate School of Engineering, Tohoku University, Aoba-yama 6-6-02, Sendai 980-8579, Japan

KOJI SATO: Department of Materials Processing, Graduate School of Engineering, Tohoku University, Aoba-yama 6-6-02, Sendai 980-8579, Japan

TOMO TAKEDA: [takeda-t@material.tohoku.ac.jp](mailto:takeda-t@material.tohoku.ac.jp)

Department of Materials Processing, Graduate School of Engineering, Tohoku University, Aoba-yama 6-6-02, Sendai 980-8579, Japan

## THREE-DIMENSIONAL BEM ANALYSIS TO ASSESS DELAMINATION CRACKS BETWEEN TWO TRANSVERSELY ISOTROPIC MATERIALS

NICOLÁS O. LARROSA, JHONNY E. ORTIZ AND ADRIÁN P. CISILINO

Beyond the inherent attribute of reducing the dimensionality of the problem, the attraction of the boundary element method (BEM) for dealing with fracture mechanic problems is its accuracy in solving strong geometrical discontinuities. Within this context, a three-dimensional implementation of the energy domain integral (EDI) for the analysis of interface cracks in transversely isotropic bimaterials is presented in this paper. The EDI allows extending the two-dimensional  $J$ -integral to three dimensions by means of a domain representation naturally compatible with the BEM, in which the required stresses, strains, and derivatives of displacements are evaluated using their appropriate boundary integral equations. To this end, the BEM implementation uses a set of recently introduced fundamental solutions for transversely isotropic materials. Several examples are solved in order to demonstrate the efficiency and accuracy of the implementation for solving straight and curved crack-front problems.

### 1. Introduction

High-performance composite materials possess excellent mechanical properties such as strength, toughness, and fatigue resistance. Composite materials are ideal for components which require high strength per weight and stiffness per weight ratios. By choosing an appropriate combination of reinforcement and matrix material, manufacturers can produce materials with mechanical properties that fit the requirements for a particular purpose. Commonly, high strength and stiffness are required in various directions within a plane. A solution is to stack and weld together a number of plies, each having with the fibers oriented in a different direction. Such a stack is termed a laminate. The individual plies present a macroscopic transversely isotropic behavior with the symmetry axis in the direction of the fibers [Gibson 2007].

However, the application of composite materials in critical components has lagged due to the lack of sufficient knowledge about composite damage tolerance properties. Delamination, for example, is one of the areas that still demand a lot of work. Delamination consists in the nucleation of interface cracks between the plies of the laminate as a consequence of thermomechanical fatigue, impact, or material degradation [Gibson 2007]. Progress in the mechanics of interface fracture has been generally focused on the two-dimensional idealization of an interface crack, and not until recently has major effort been conducted on the three-dimensional aspect of interface fracture. That is in part due to the complexity of such problems and the very large computational effort required for their numerical analysis. However,

---

This work has been partially supported by the Agencia Nacional de Promoción Científica y Tecnológica (ANPCyT) of Argentina through grant PICT 2007 No. 1154. J. E. Ortiz has been supported by the Programa Ramón y Cajal of the Spanish Ministry of Science and Innovation.

**Keywords:** three-dimensional interface cracks, transversely isotropic bimaterials, energy domain integral, boundary element method.

given the material mismatch at the interface boundary, it is expected that the three-dimensional effects play a more significant role in laminate structures than in homogeneous structures.

The numerical analysis of interface cracks in transversely isotropic materials has been traditionally addressed using finite element analysis; see, for example, [Boniface and Banks-Sills 2002; Freed and Banks-Sills 2005]. There is also the alternative of using the boundary element method (BEM). The attraction of the BEM can be largely attributed to the reduction in the dimensionality of the problem; this means that, compared to finite-element domain-type analysis, BEM analysis results in a substantial reduction in data preparation. At the same time, due to the inherent characteristics of its formulation, BEM provides very accurate results for problems containing strong geometrical discontinuities. Fracture mechanical analysis of three-dimensional transversely isotropic materials using BEM has been reported in [Sáez et al. 1997; Ariza and Dominguez 2004a; 2004b], which modeled static and dynamic crack problems, [Zhao et al. 2007], which derived the displacement discontinuity boundary integral equation, and more recently in [Chen et al. 2009], which studied the stress intensity factors of a central square crack in a transversely isotropic cuboid with arbitrary material orientations. To our knowledge, there is no published material about three-dimensional BEM modeling of interface cracks in dissimilar transversely isotropic bimaterials.

A number of techniques have been proposed for the evaluation of fracture parameters of interface cracks using FEM and BEM. They are, among others, the virtual crack extension approach [So et al. 2004], contour and domain path-independent integrals [Chow and Atluri 1998; Freed and Banks-Sills 2005; Ortiz and Cisilino 2005; Shah et al. 2006], displacement extrapolation techniques [Tan and Gao 1990; Mao and Sun 1995; Freed and Banks-Sills 2005], and special crack-tip elements [He et al. 1994]. In particular, path-independent integral techniques are derived from the  $J$ -integral proposed in [Rice 1968]. Being an energy approach, path-independent integrals eliminate the need to solve local crack tip fields accurately. If the integration domain is defined over a relatively large portion of the mesh, accurate modeling of the crack tip is unnecessary because the crack tip field contribution to the overall energy is not significant. At the same time, the  $J$ -integral approach developed in [Rice 1968] characterizes the crack driving force for two-dimensional problems. Therefore, for general three-dimensional cases involving cracks of arbitrary shape an alternative form for the  $J$ -integral is needed.

Three basic schemes have evolved for the numerical computation of the  $J$ -integral in three dimensions: virtual crack extension methods, generalization of Rice's contour integral, and domain integral methods [Anderson 2005]. Domain integrals are equivalent to the virtual crack extension technique and are better suited for numerical analysis than contour integral methods. Among the available domain integral methods (see for example, [Nikishkov and Atluri 1987; Feijoó et al. 2000]), the energy domain integral (EDI) of [Moran and Shih 1987] was chosen for this work.

The EDI can be formulated by applying the divergence theorem to Rice's  $J$ -integral. It produces a domain-independent integral defined over finite volumes enclosing some portion of the crack front [Moran and Shih 1987]. Previous works by the authors of this paper have demonstrated the versatility and efficiency of the BEM implementation of the EDI for assessing three-dimensional cracks in elastic [Cisilino et al. 1998], elastoplastic [Cisilino and Aliabadi 1999], and thermoelastic bodies [Balderrama et al. 2006; 2008] and for interface cracks in dissimilar isotropic bimaterials [Ortiz and Cisilino 2005].

This work introduces the BEM implementation of the EDI for the computation of the  $J$ -integral in three-dimensional interface cracks in transversely isotropic bimaterials. The BEM implementation uses

the fundamental solutions recently introduced in [Távara et al. 2008]. The BEM solution strategy for the fracture problem and the EDI implementation is an extension of that proposed in [Ortiz and Cisilino 2005] for interface cracks in dissimilar isotropic bimaterials. Several examples are solved and the results compared to those available in the literature.

## 2. Transversely isotropic materials

The basic constitutive expressions governing the elastic behavior of transversely isotropic materials are reviewed, following [Ting 1996]. The general constitutive law of the anisotropic material is

$$\sigma_{ij}(x) = C_{ijkl}(x)\varepsilon_{kl}(x) = C_{ijkl}(x)u_{k,l}(x), \quad (1)$$

where, relative to a fixed rectangular Cartesian coordinate system,  $\sigma_{ij}(x)$  are the components of the stress tensor,  $\varepsilon_{ij}(x)$  are the components of the infinitesimal strain tensor, and  $u_k(x)$  are the components of the displacement vector. Partial derivatives are indicated using comma notation. The  $C_{ijkl}(x)$  are the components of the fourth-order constitutive tensor  $C$ , defined in terms of 21 independent elasticity constants.

Transversely isotropic materials are those with an axis of symmetry such that all directions perpendicular to that axis are on a plane of isotropy. In such a case the constitutive tensor can be defined in terms of only 5 independent elasticity constants. Using the Voigt reduced notation, the fourth-order constitutive tensor  $C_{ij}$  ( $i, j = 1, \dots, 6$ ) for a transversely isotropic material with the axis of symmetry coincident with the Cartesian axis  $x_3$  can be expressed in terms of the following five elastic constants:

$$C_{1111} = C_{11}, \quad C_{3333} = C_{33}, \quad C_{1122} = C_{12}, \quad C_{1133} = C_{13}, \quad C_{2323} = C_{44}. \quad (2)$$

Due to symmetry with respect to  $x_3$ ,  $C_{66} = (C_{11} - C_{12})/2$ .

The coefficients of the constitutive tensor  $C_{ij}$  can be written in terms of the elastic engineering constants as follows:

$$C_{11} = \frac{E(n - \nu'^2)}{\lambda(1 + \nu)}, \quad C_{12} = \frac{E(n + \nu'^2)}{\lambda(1 + \nu)}, \quad C_{13} = \frac{Ev'}{\lambda}, \quad C_{33} = \frac{E(1 + \nu)}{\lambda}, \quad C_{44} = \mu', \quad (3)$$

where

$$\lambda = n(1 - \nu) - 2\nu'^2, \quad n = E/E', \quad (4)$$

and

- $E$  and  $E'$  are the Young's moduli in the plane of isotropy and in the direction normal to it, respectively,
- $\nu$  is the Poisson's ratio that represents the strain response in the plane of isotropy due to an action parallel to it and  $\nu'$  is the lateral strain response for the planes normal to the plane of isotropy, and
- $\mu'$  is the shear modulus for the planes normal to the planes of transverse isotropy.

## 3. The energy domain integral

Consider a three-dimensional crack front with a continuously turning tangent as depicted in Figure 1a with a local coordinate system  $x^*$  at position  $\eta$ , given by  $x_1^*$  normal to the crack front,  $x_2^*$  normal to

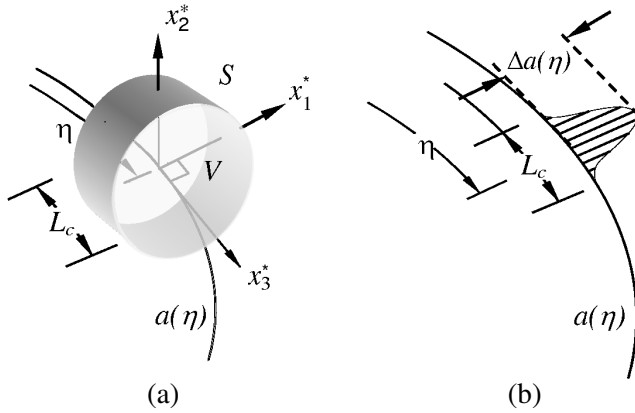


**Figure 1.** (a) Definition of the local orthogonal Cartesian coordinates at point  $\eta$  on the crack front and integration volume, and (b) virtual crack front advance.

the crack plane, and  $x_3^*$  tangent to the crack front. In addition, a tubular domain  $V$  surrounds the crack segment  $L_c$  which contains the position  $\eta$ .

Following [Nahta and Moran 1993], the  $J$ -integral at the position  $\eta$  can be computed using the EDI:

$$J(\eta) = \frac{\bar{G}(\eta)}{\int_{L_c} \Delta a(\eta) dl}, \quad (5)$$

where  $\bar{G}(\eta)$  gives the total energy released when the finite segment  $L_c$  undergoes the virtual displacement,  $\Delta a(\eta)$ , in the plane of the crack (see Figure 1b).

The expression of the energy release rate is

$$\bar{G}(\eta) = \int_V (\sigma_{ij}^* u_{j,k}^* - w \cdot \delta_{ki}) q_{k,i} dV, \quad (6)$$

where  $w$  is the strain energy density,  $\sigma_{ij}^*$  and  $u_{j,k}^*$  are Cartesian components of stress and displacement derivatives expressed in the system  $x^*$ , the integration domain  $V$  is the volume of the tubular domain that surrounds the crack segment  $L_c$ , and  $q$  is an auxiliary vector function used to represent the virtual crack advance as follows (see Figure 1b):

$$q_k = \begin{cases} \Delta a(\eta) \cdot \xi_k(\eta) & \text{on } L_c, \\ 0 & \text{on } S. \end{cases} \quad (7)$$

The function  $q$  must be smooth in  $V$ , possess a maximum at the position  $\eta$ , and vanishes on the surfaces of  $V$ . The symbol  $\xi_k(\eta)$  in (7) stands for the  $k$ -th component of the unit outward normal to the crack front in the crack plane  $x_1^*-x_3^*$ .

Analogously to the path-independence of its classical two-dimensional counterpart, the EDI formulation of the  $J$ -integral is independent of the integration volume  $V$  [Nahta and Moran 1993].

#### 4. Boundary element formulation and implementation

In order to account for the nonhomogeneous material properties, a multidomain BEM formulation is used for the problem solution. The modeling strategy is illustrated in the schematic representation in Figure 2 for a model consisting of two subdomains,  $\Omega_I(x)$  and  $\Omega_{II}(x)$ , with external boundaries  $\Gamma_I(x)$  and  $\Gamma_{II}(x)$ , respectively. Both subdomains share a common interface  $\Gamma_{I-II}(x)$ , a portion of which is debonded, and thus an interface crack is introduced. The subdomains possess linear transversely isotropic material behaviors as described in Section 2. The orientation of the material is specified using a local Cartesian system  $(x_1^0, x_2^0, x_3^0)$  for each subdomain. In every case the direction of the symmetry axis of the material is chosen coincident with the direction  $x_3^0$  (see Figure 2). In this way, it is possible to model interface cracks lying between laminates with arbitrary relative orientations.

The standard BEM uses the displacement boundary integral equation to relate the displacement and traction fields,  $u(x)$  and  $t(x)$ , over the model boundary in the global coordinate system (see [Aliabadi 2002]):

$$c_{ik}(x')u_i(x') + \int_{\Gamma} T_{ik}(x, x')u_i(x) d\Gamma(x) = \int_{\Gamma} U_{ik}(x, x')t_i(x) d\Gamma(x), \quad (8)$$

where  $U_{ik}(x, x')$  and  $T_{ik}(x, x')$  are the displacement and traction fundamental solutions for transversely isotropic materials, respectively. The fundamental solutions account for the solution of the  $i$ -th component of the displacement and traction fields,  $u_i(x)$  and  $t_i(x)$ , at the field point,  $x$ , due to the action of a unit load acting in the direction  $j$  at the source point,  $x'$  (see the next section for the details about the fundamental solutions used in this work). The symbol  $c_{ik}$  is the so-called jump term which depends on the local geometry at the source point,  $x'$ , only.

BEM models are discretized using 9-node quadrilateral elements. Continuous elements are used everywhere in the model, except at the intersections of the interface and the crack faces with the model

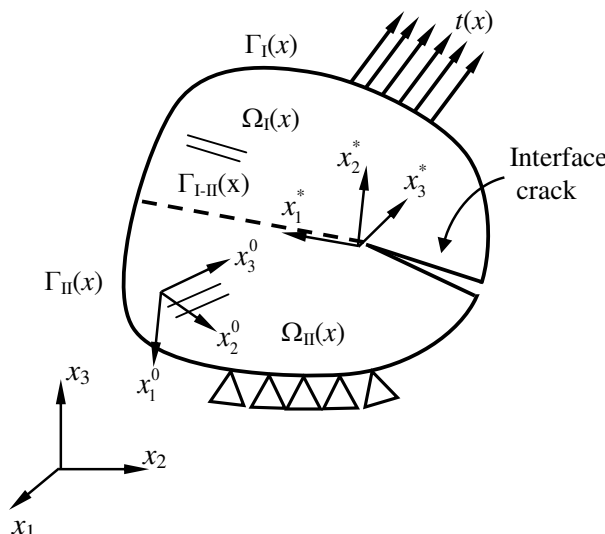


**Figure 2.** Schematic two-dimensional representation of the multidomain BEM model with an interface crack.

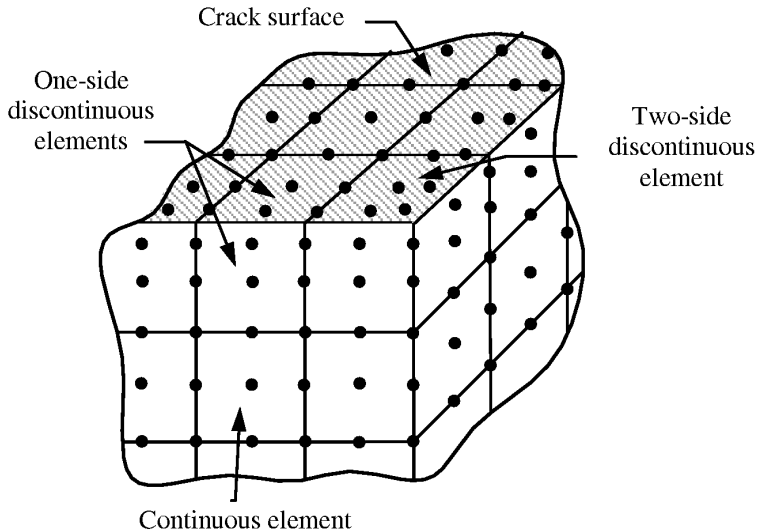


**Figure 3.** Model discretization strategy using continuous and one and two-side discontinuous elements.

outer surface. In such cases one and two-side discontinuous elements are used in order to avoid common nodes at the intersections (see Figure 3). It is worth noting that, although discontinuous elements are not strictly necessary to solve most of the practical bimaterial crack problems, they have been implemented in this work in order to develop a versatile and robust discretization strategy capable of dealing with general multiple subdomain problems (including the case of more than two subdomains sharing a single edge). At the same time, the implementation remains open to introduce further extensions to account for crack propagation which could require automatic model remeshing.

The regular BEM integrals over continuous and discontinuous elements are evaluated using standard Gaussian quadrature. In the case of nearly singular integrals an adaptive element subdivision technique is also employed. On the other hand, the Cauchy principal-value integrals and the free terms are evaluated using the rigid-body motion approach (see [Aliabadi 2002]). Singular integrals are computed using the variable transformation technique of [Lachat and Watson 1976].

The equilibrium and continuity conditions are enforced at the nodes lying on the interface  $\Gamma_{I-II}$  shared by the two regions. In the case that no external forces are applied on the interface, the equilibrium condition is  $t_I = -t_{II}$ . The continuity condition is  $u_I = u_{II}$ . For further details on the multidomain BEM formulation and implementation the reader is referred to [Aliabadi 2002].

Comninou [1977] showed that the solution of the stress fields for a crack between dissimilar materials always predicts a contact zone between the crack surfaces at the crack tip. However, according to [Rice 1988] elastic fracture mechanics procedures are still valid when the inevitable nonlinear contact-zone size is small compared with the crack size. It is assumed in this work that this condition is always satisfied, and so the BEM implementation does not account for contact between the crack surfaces.

The computation of the  $J$ -integral is included in the BEM code as a postprocessing procedure, and so it could be applied to the results from a particular model at a later stage. The required stresses, strains, and derivatives of displacements at internal points are directly obtained from their boundary integral

representations [Aliabadi 2002]:

$$u_{i,m}(X') = \int_{\Gamma} U_{ij,m}(x, X') t_j(x) d\Gamma(x) - \int_{\Gamma} T_{ij,m}(x, X') u_j(x) d\Gamma(x), \quad (9)$$

where  $X'$  is the coordinate of the internal point, and  $U_{ij,m}(x, X')$  and  $T_{ij,m}(x, X')$  are the derivatives of the fundamental displacement and traction fundamental solutions. The boundary  $\Gamma$  corresponds to the boundary of the subdomain which the internal point  $X'$  lies on. Strains and stresses at internal points can then be easily computed using the definition of the infinitesimal strain tensor  $\varepsilon_{ij} = (u_{i,j} + u_{j,i})/2$  and the constitutive relations in (1).

On the other hand, the derivatives of the displacements, strains, and displacements for boundary points are evaluated from the boundary displacements and tractions by means of a procedure similar to that usually used for finite elements. For further details the reader is referred to [Ortiz and Cisilino 2005].

Finally, in order to proceed with the  $J$ -integral computation, the resultant displacement derivatives, strains, and stresses for both internal and boundary points are transformed to the local crack-front coordinate system  $(x_1^*, x_2^*, x_3^*)$  introduced in Section 3 using the standard transformation rule for second-order tensors; see [Ting 1996].

### 5. The fundamental solutions for transversely isotropic materials

There are several expressions for the fundamental solutions for transversely isotropic materials; see, for example, [Pan and Chou 1976; Lolo 2000]. However, these solutions could be cumbersome to implement in a BEM code because of the multiple cases to consider due to all the possible material orientations and the relative positions of the source and field points.

Távara et al. [2008] have recently derived completely general and unique expressions valid for all possible configurations given in terms of real functions only. These fundamental solutions are presented in what follows.

The Green's function for a linearly elastic anisotropic medium using the Barnett–Lothe tensor is [Lifshitz and Rozentsveig 1947]

$$U^0(x) = \frac{1}{4\pi r} H(x), \quad (10)$$

where  $x$  is the position vector and the matrix  $H(x)$  defined by

$$H(x) = \frac{1}{\pi} \int_{-\infty}^{+\infty} \Gamma^{-1}(p) dp. \quad (11)$$

The integrand  $\Gamma(p)$  is the  $3 \times 3$  matrix

$$\Gamma(p) = Q + p(R + R^T) + p^2 T, \quad (12)$$

where superscript  $T$  means transpose, and the matrices  $Q$ ,  $R$ , and  $T$  are defined by

$$Q_{ij} = C_{ijks} n_j n_s, \quad R_{ik} = C_{ijks} n_j m_s, \quad T_{ik} = C_{ijks} m_j m_s, \quad (13)$$

for  $n$  and  $m$  orthogonal unit vectors in the plane normal to the position vector  $x$ . The matrices  $Q$  and  $T$  are symmetric and positive definite if the deformation energy of the material is positive. Considering (12) and (13), the matrix  $H(x)$  is also symmetric and depends on the direction of the position vector  $x$ ,

but not on its magnitude. Using residues theory,  $H(x)$  in (11) can be expressed in the same form as (10) and (12):

$$H(x) = 2i \sum_{v=1}^3 \frac{\hat{\Gamma}(p_v)}{|\Gamma(p)|'}, \quad (14)$$

where  $\hat{\Gamma}(p_v)$  is the adjunct of the matrix of  $\Gamma(p)$  defined in (12) and  $|\Gamma(p)|$  is its determinant. The values  $p_v$  are the so-called Stroh eigenvalues of the sextic equation:

$$|\Gamma(p)| = 0. \quad (15)$$

The eigenvalues of (15) can be represented as  $p_v = \alpha_v + i\beta_v$  where both  $\alpha_v$  and  $\beta_v$  are real with  $\beta_v > 0$  ( $v = 1, 2, 3$ ). Although there are explicit solutions for (14) in terms of the eigenvalues,  $p_v$ , and for the Green's function in (10), they are not of practical use here because they are not general and they do not hold for the degenerate cases  $p_1 = p_2$  and  $p_1 = p_2 = p_3$ . Alternatively, a simplified solution for (14) can be obtained when (15) is a cubic equation in  $p^2$  of the form

$$|\Gamma(p)| = |T|(p^2 - p_1^2)(p^2 - p_2^2)(p^2 - p_3^2). \quad (16)$$

In this case, (15) can be expressed as

$$[p^4 + (g^2 - 2h)p^2 + h^2][p^2 + \beta_3^2] = 0, \quad (17)$$

where  $g$ ,  $h$ , and  $\beta_3$  are defined in the Appendix.

A new expression for  $H(x)$  is obtained for any anisotropic linear elastic material

$$H(x) = \frac{1}{|T|} \sum_{n=0}^4 p^n \hat{\Gamma}^{(n)}. \quad (18)$$

Using (16) and (18) with (14), the following expression results:

$$H(x) = \frac{1}{|T|\xi} \left\{ \frac{\zeta}{h\beta_3} \hat{\Gamma}^{(0)} + \hat{\Gamma}^{(2)} + \delta \hat{\Gamma}^{(4)} \right\}, \quad (19)$$

where

$$\zeta = -i(p_1 + p_2 + p_3) = g + \beta_3, \quad (20)$$

$$\delta = -(p_1 p_2 + p_2 p_3 + p_3 p_1) = h + g\beta_3, \quad (21)$$

$$\xi = i(p_1 + p_2)(p_2 + p_3)(p_1 + p_3) = g(h + g\beta_3 + \beta_3^2). \quad (22)$$

The terms  $\zeta$ ,  $\delta$ , and  $\xi$  depend only on  $p_1 + p_2$ ,  $p_1 p_2$ , and  $p_3$ ; therefore, it is not necessary to calculate all the eigenvalues. The solution to (19) is valid for degenerate and nondegenerate cases. The terms  $\beta_3$ ,  $h$ , and  $g$  can be computed using (17).

A relatively simple and general expression for  $H(x)$  for transversely isotropic materials can be obtained using the auxiliary vector  $\hat{x} = (r_{12}, 0, x_3^2)$ , where  $r_{12} = [(x_1^0)^2 + (x_2^0)^2]^{1/2}$ ,  $(x_1^0, x_2^0, x_3^0)$  is the local coordinate system, and the triad  $[n, m, \hat{x}/r]$ , with  $n = (c, 0, -s)$  and  $m = (0, 1, 0)$ , where  $c = \cos \phi = x_3^0/r$ ,

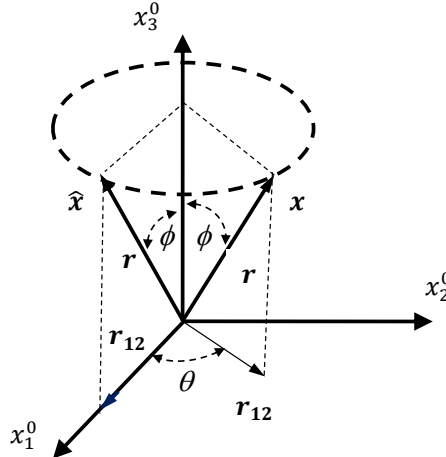


**Figure 4.** Points  $x$  and  $\hat{x}$  associated with a transversely isotropic material.

$s = \sin \phi = r_{12}/r$ , and  $0 \leq \phi \leq \pi$ , is illustrated in Figure 4. For such a coordinate system, the only nonzero coefficients are given by

$$\begin{aligned} H_{11} &= \frac{1}{C_{66}\beta_3} + \frac{C_{44}c^2 + C_{33}s^2}{C_{11}C_{44}gh} - \frac{f}{\xi}, & H_{22} &= \frac{1}{C_{11}g} + \frac{f}{\xi}, \\ H_{33} &= \frac{1}{gh} \left\{ \frac{h+c^2}{C_{44}} + \frac{s^2}{C_{11}} \right\}, & H_{13} &= \frac{(C_{13} + C_{44})sc}{C_{11}C_{44}gh}. \end{aligned} \quad (23)$$

The additional terms in (23) are given in the Appendix. The general expression of the tensor  $H(x)$  for any  $x$  can be obtained by transformation of the components:

$$H_{ij}(x) = \Omega_{ik}\Omega_{js}H_{ks}(\hat{x}), \quad (24)$$

where the rotation matrix  $\Omega_{ij}$  is

$$\Omega_{ij} = \begin{pmatrix} \cos \theta & -\sin \theta & 0 \\ \sin \theta & \cos \theta & 0 \\ 0 & 0 & 1 \end{pmatrix}. \quad (25)$$

The derivatives of the fundamental solution for the displacement can be expressed using the modulation function  $\hat{U}_{ij,k}(x)$ :

$$U_{ij,k}^0(x) = \frac{\hat{U}_{ij,k}(x)}{4\pi r^2}. \quad (26)$$

$\hat{U}_{ij,k}(x)$  is an odd function, which depends on the direction of  $x$  but not on its magnitude, that is,  $\hat{U}_{ij,k}(x) = -\hat{U}_{ij,k}(-x/r)$ . Using the transformation in (24), the derivatives of the displacement fundamental solution are:

$$\hat{U}_{ij,k}(x) = \Omega_{ia}\Omega_{jb}\Omega_{kc}\hat{U}_{ab,c}(\hat{x}). \quad (27)$$

The closed-form expressions of  $\hat{U}_{ij,k}(\hat{x})$  can be found in [Távara et al. 2008].

The fundamental solution for the stresses,  $\Sigma_{ijk}(x)$ , can be obtained by applying Hooke's law for transversely isotropic material, yielding

$$\Sigma_{ijk}^0(x) = \frac{\hat{\Sigma}_{ijk}(x)}{4\pi r^2}, \quad (28)$$

where  $\hat{\Sigma}_{ijk}(x)$  is an odd symmetric function. So, the stress fundamental solution can be expressed in a similar form to (27):

$$\hat{\Sigma}_{ijk}(x) = \Omega_{ia}\Omega_{jb}\Omega_{kc}\hat{\Sigma}_{abc}(\hat{x}). \quad (29)$$

The closed-form expressions of  $\hat{\Sigma}_{ijk}(\hat{x})$  can be found in [Távara et al. 2008]. The traction fundamental solution associated with the normal vector  $n_j(x)$  can be obtained directly using

$$T_{ik}^o(x) = \Sigma_{ijk}^0(x)n_j(x). \quad (30)$$

Finally, the fundamental solutions  $U_{ik}(x)$  and  $T_{ik}(x)$  have to be transformed from the local coordinate system,  $(x_1^0, x_2^0, x_3^0)$ , to the global in order to assemble the boundary integral (8). The fundamental solutions are transformed from the local coordinate system to the global via the standard transformations for second order tensors (see [Ting 1996]):

$$U_{ij}(x) = a_{ik}a_{jl}U_{kl}^o(x), \quad T_{ij}(x) = a_{ik}a_{jl}T_{kl}^o(x), \quad (31)$$

where  $a_{ik}$  are the coefficients of the transformation matrix.

## 6. *J*-integral computation

The computation of the EDI was included in the BEM code as a postprocessing procedure, and so it could be applied to the results from a particular model at a later stage. As stated in Section 3, (5) allows the computation of the *J*-integral at any position  $\eta$  on the crack front. In each case, this requires the evaluation of a volume integral over a domain that encloses a segment of the crack front,  $L_c$ . A natural choice here is to make  $\eta$  coincident with the element nodes on the crack front, while  $L_c$  is taken as the element or element sides where the point  $\eta$  lies. As depicted in Figure 5, three different cases are considered depending on whether the node  $M$  at the location of the crack front position  $\eta$  is a midside node, is shared by two elements, or is located coincident with the external surface (a surface node). If the

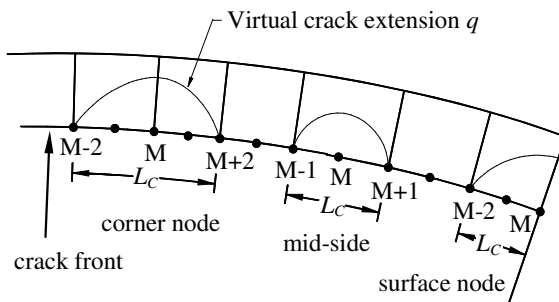


**Figure 5.** Schematic of the crack front region illustrating the  $q$ -function assimilated to the virtual crack extensions for a corner node, a midnode, and a surface node.

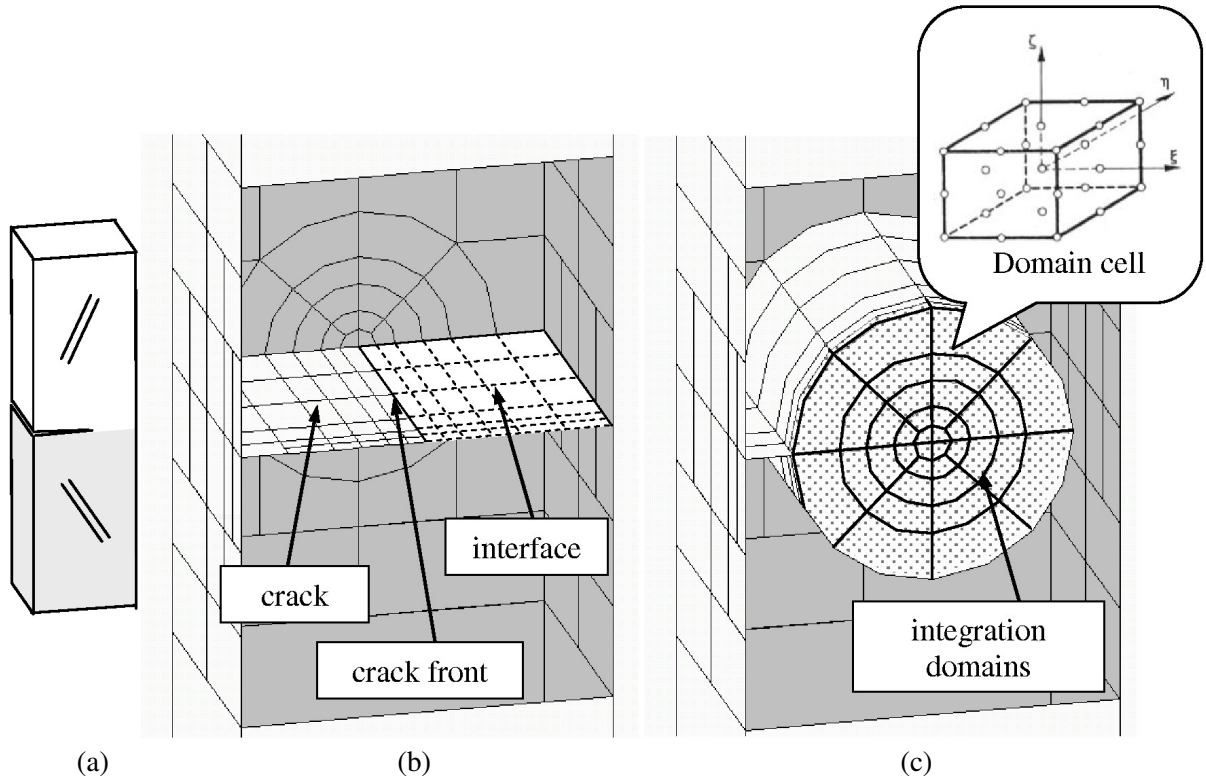


**Figure 6.** (a) Problem geometry, (b) boundary element discretization, and (c) integration domains. Note in (c) the detail illustrating the 27-node isoparametric (brick) cells. The dotted region indicates the volume cells defining the integration volumes used for the computation of the  $J$ -integral for the crack-front node on the specimen surface (see surface node in Figure 5).

node  $M$  is a midside node or surface node,  $L_c$  (the width of the integration domain) spans one element, connecting nodes  $M - 1$ ,  $M$ , and  $M + 1$  and nodes  $M - 2$ ,  $M - 1$ , and  $M$ , respectively. On the other hand, if node  $M$  is shared by two elements,  $L_c$  spans both elements, connecting nodes from  $M - 2$  to  $M + 2$ .

The boundary mesh is designed to have a web pattern around the crack front in order to build the integration domains for the evaluation of the EDI in the shape of cylinders. The integration volumes are discretized using 27-node isoparametric (brick) cells. This is illustrated in Figure 6, where a portion of the model surface has been removed to show the discretizations of the crack and of the integration domains.

Stresses, strains, and derivatives of displacements at cell nodes are computed using the procedures introduced in Section 4, and then transformed to the local crack-front coordinate system,  $(x_1^*, x_2^*, x_3^*)$ , using the standard transformation rule for second-order tensors. The stresses, strains, and displacements derivatives are approximated within cell domains by products of the cell interpolation functions,  $\psi_i$ , and the nodal values of  $\sigma_{ij}^*$ ,  $\varepsilon_{ij}^*$ , and  $u_{i,m}^*$ .

A central point in the implementation of the EDI is the specification of the values for the function  $q$ . Following the definition introduced in (7), the value of  $q_k$  is specified equal to one for the cell node coincident with the position  $\eta$  on the crack front where the EDI is evaluated, and equal to zero for all the cell nodes located on the surface of the integration volume. For the implementation used in this work, the function  $q$  is chosen to vary quadratically in the directions tangential and normal to the crack front: this is schematically illustrated in Figure 5 for the tangential direction on the  $x_1^*x_3^*$ -plane. This biquadratic definition of  $q$  has been employed with excellent results in the computation of EDI for a variety of problems in previous works [Cisilino et al. 1998; Cisilino and Aliabadi 1999; Ortiz and Cisilino 2005; Balderrama et al. 2006; 2008]. Thus, considering that the evaluation point  $\eta$  is at the middle of the crack front segment,  $L_c$ , and that  $r_0$  is the radius of the integration domain, the function  $q$  is written as

$$q(x^*) = \left| 1 - \left( \frac{x_3^*}{L_c/2} \right)^2 \right| \cdot \left[ 1 - \left( \frac{r}{r_0} \right)^2 \right], \quad (32)$$

where  $r$  is the distance from the crack front in the  $x_1^*x_3^*$ -plane (see Figure 1).

Equation (32) is used to specify the value of  $q$  for all the cell nodes within the integration domain. Then, consistent with the isoparametric formulation, the  $q$ -values are interpolated within each volume cell using

$$q = \sum_{i=1}^{27} \psi_i Q^i, \quad (33)$$

where the  $\psi_i$  are the shape functions and  $Q^i$  is the  $q$ -value for the  $i$ -th node. Following standard manipulations, the derivatives of  $q$  are

$$q_{k,j} = \sum_{i=1}^{27} \sum_{l=1}^3 \frac{\partial \psi_i}{\partial \zeta_l} \frac{\partial \zeta_l}{\partial x_j^*} Q^i, \quad (34)$$

where  $\zeta_k$  are the coordinates in the cell isoparametric space and  $\partial \zeta_k / \partial x_j^*$  is the Jacobian matrix of the transformation.

Finally, if Gaussian integration is used, the discretized form of (6) is

$$\bar{G}(\eta) = \sum_{\text{cells in } V} \sum_{p=1}^m \left\{ (\sigma_{ij}^* u_{j,k}^* - \sigma_{ij}^* \varepsilon_{ij}^* \delta_{ki}) q_{k,j} \det \left( \frac{\partial x_j}{\partial \zeta_k} \right) \right\}_p w_p, \quad (35)$$

where  $m$  is the number of Gaussian points per cell and the  $w_p$  are their weighting factors.

## 7. Application examples

**7.1. Thick bimaterial plate in tension with a center interface crack.** A thick bimaterial plate containing a through crack on the interface is considered in the first example. A schematic representation of the problem geometry, dimensions, and boundary conditions is depicted in Figure 7. The model discretization is similar to that depicted in Figure 6. It consists of 658 elements and 2855 nodes. Eighteen elements are placed along the crack front and a total of 126 elements are used in the crack discretization. Five rings of cells with normalized radii  $r/a = 0.1, 0.2, 0.3, 0.44$ , and  $0.64$  are used around the crack front for  $J$  computations. For this purpose 648 cells and 6438 nodes are employed.

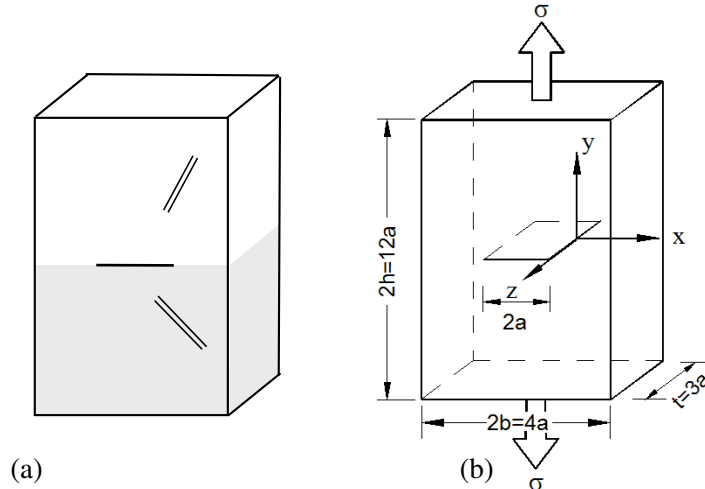


**Figure 7.** (a) Schematic representation of a thick tension plate with a center interface crack and (b) model dimensions.

In order to validate the code, the problem was solved first for homogeneous cases, that is, the material elastic constants and orientations were set the same for both subdomains. Thus, the direction of the axis of symmetry,  $x_3^0$ , was chosen to be parallel to the crack plane, that is, coincident with the global directions  $x$  and  $z$ . The material elastic constants were chosen to be the same as those used for the laminated case in [Ariza and Dominguez 2004b]. The five independent values of the elastic constants  $C_{ij}$  in (3) are

$$C_{11} = 5.37 \text{ GPa}, \quad C_{12} = 1.34 \text{ GPa}, \quad C_{13} = 3.35 \text{ GPa}, \quad C_{33} = 251.168 \text{ GPa}, \quad C_{44} = 5 \text{ GPa}. \quad (36)$$

The associated elastic properties are:  $E = 5 \text{ GPa}$ ,  $E' = 247.83 \text{ GPa}$ ,  $\nu = 0.245$ ,  $\nu' = 0.01$ , and  $\mu' = 2.5$ . The material orientation is specified for each subdomain by means of the angles which define the orientation of the material axis of symmetry,  $x_3^0$ , with respect to the global coordinate system ( $x$ ,  $y$ ,  $z$ ). In this way, for the material axis of symmetry oriented in the global direction  $x$ , the orientation angles are  $0^\circ/90^\circ/90^\circ$ , while for the material axis of symmetry oriented in the global direction  $z$ , the angles are  $90^\circ/90^\circ/0^\circ$ .

The computed results along the crack front are presented in Figure 8. In order to compare with other results, the data in Figure 8 is presented in terms of normalized stress intensity factors (SIF),  $K_I/K_0$ , where  $K_0 = \sigma \sqrt{\pi a}$ . To compute the SIF from the  $J$  results the expressions of [Chu and Hong 1990] are used:

$$\begin{aligned} J_1 &= a_{11} K_I^2 + a_{12} K_I K_{II} + a_{22} K_{II}^2, \\ J_2 &= b_{11} K_I^2 + b_{12} K_I K_{II} + b_{22} K_{II}^2, \end{aligned} \quad (37)$$

where the coefficients  $a_{ij}$  and  $b_{ij}$  depend on the elastic material properties and the material orientation. The coefficients  $a_{12}$  and  $a_{22}$  and the three coefficients  $b_{ij}$  are zero when one of the principal axes of the material is parallel to the crack plane. Thus, for the cases considered in this work,

$$J_1 = a_{11} K_I^2. \quad (38)$$

These are the values of the coefficient  $a_{11}$  and the ratio  $E_x/E_y$  between Young's moduli:

$$\text{Material symmetry in } x\text{-direction: } a_{11} = 0.112 \times 10^{-9} \quad E_x/E_y = 49.57$$

$$\text{Material symmetry in } z\text{-direction: } a_{11} = 0.2 \times 10^{-9} \quad E_x/E_y = 1$$

It can be seen in Figure 8 that, excepting only the regions next to the lateral faces of the specimen (say,  $|z/t| > 0.45$ ) where the boundary layer effect takes place, the SIF value is nearly constant along the crack front. Two sets of results obtained from a two-dimensional high-resolution finite element model are also shown in Figure 8. The finite element model was solved using ABAQUS [2009], and was discretized using a fine regular mesh consisting of 9,600 8-node biquadratic, plane stress elements (CPS8R). The SIF were computed using the ABAQUS built-in  $J$ -integral procedure. The resultant normalized SIF are  $K_I/K_0 = 1.124$  and  $K_I/K_0 = 1.184$  for the material axis of symmetry oriented in the global directions  $x$  and  $z$ , respectively. The maximum difference between the BEM and FEM results along the crack front in the interior of the specimen (that is, excluding the regions next to the lateral faces) is less than 2%.

The final case consists of a heterogeneous plate with the axis of symmetry of the material oriented in the global directions  $z$  and  $y$  for subdomains I and II, respectively; that is,  $90^\circ/90^\circ/0^\circ$  for subdomain I and  $90^\circ/0^\circ/90^\circ$  for subdomain II. The material elastic properties are the same as in the previous cases. Computed results are presented in Table 1. The results are normalized with respect to  $J_0 = \sigma^2 \pi a / E'$ . It can be seen that the  $J$  value is nearly constant along the complete crack front. Besides, the path independence is found to be excellent, with a standard deviation of around 5% for the results computed using the domains with radii  $r/a \geq 0.20$ . The only exceptions are the positions next to the lateral face of

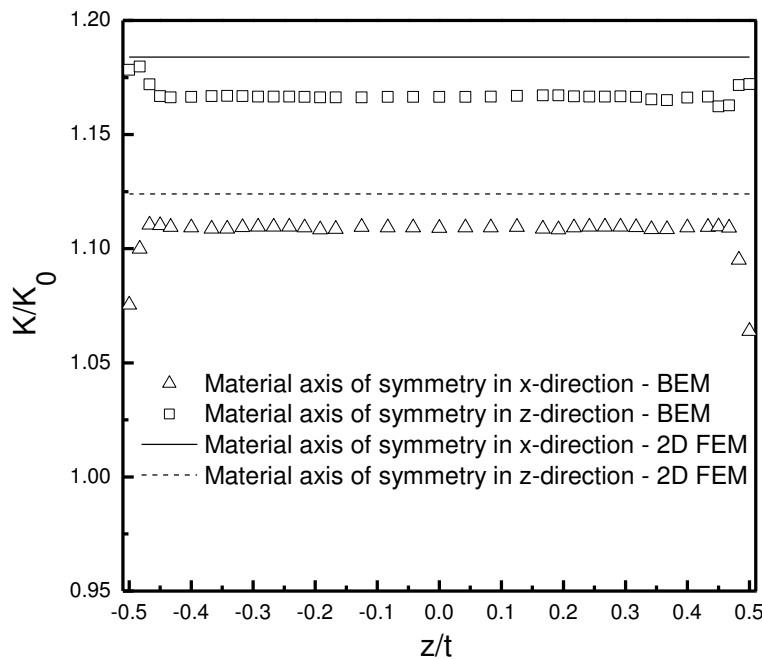


**Figure 8.** Normalized SIF results along the crack front for homogeneous transversely isotropic center crack specimen.

$z/t$	$r/a =$						Std. dev.
	0.10	0.20	0.30	0.44	0.64	Average	
0.000	25.6382	30.4503	30.7658	30.7658	30.6081	30.5613	0.49
0.042	25.6382	30.4503	30.7658	30.7658	30.6081	30.5566	0.49
0.083	25.6382	30.4503	30.7658	30.7658	30.6081	30.5512	0.49
0.125	25.6382	30.4503	30.7658	30.7658	30.6081	30.5452	0.49
0.167	25.6382	30.4503	30.7658	30.7658	30.6081	30.5384	0.49
0.192	25.6382	30.4503	30.6869	30.7658	30.6081	30.5306	0.44
0.217	25.6382	30.4503	30.6869	30.7658	30.6081	30.5231	0.44
0.242	25.6382	30.4503	30.6869	30.7658	30.6081	30.5144	0.44
0.267	25.6382	30.4503	30.6869	30.7658	30.6081	30.5041	0.44
0.292	25.6382	30.4503	30.6869	30.7658	30.6081	30.4917	0.44
0.317	25.6382	30.3714	30.6869	30.6869	30.5292	30.4766	0.50
0.342	25.6382	30.3714	30.6081	30.6869	30.4503	30.4651	0.47
0.367	25.6382	30.3714	30.6081	30.6081	30.4503	30.4559	0.39
0.400	25.5593	30.3714	30.6081	30.6081	30.4503	30.4470	0.39
0.433	25.5593	30.2925	30.6081	30.6081	30.4503	30.4345	0.50
0.450	25.5593	30.2925	30.5292	30.6081	30.4503	30.4207	0.44
0.467	25.4804	30.2925	30.6869	30.7658	30.6869	30.4043	0.70
0.483	25.0071	29.9770	30.7658	31.1603	31.2391	30.3024	1.91
0.500	23.5871	28.5570	29.7403	30.3714	30.6081	29.8192	3.08

**Table 1.** Normalized  $J$ -integral results for the heterogeneous plate as a function of the integration domain size. The results for the smallest integration domains,  $r/a = 0.1$  (shaded column in the table) are excluded for the computation of the average value and the standard deviation.

the specimen, where the boundary layer effect takes place and the applicability of the  $J$ -integral is not strictly valid. The smallest integration domains with  $r/a = 0.10$  do not provide accurate results. This is attributed to the fact that these domains are discretized using a single cell in the radial direction. Similar behaviors were found by the authors previously [Cisilino et al. 1998; Ortiz and Cisilino 2005].

**7.2. Bimaterial laminate with an edge interface crack.** In this example the analysis of an edge crack in a bimaterial laminate is considered. The model geometry and discretization are shown in Figure 9. The model dimensions are: crack length  $a = 10$  mm, specimen width  $b = 4a$ , height  $h = a$ , and thickness  $2t = 1.5a$ . The material properties are the same ones used in the previous example. The discretization consists of 596 elements. Five rings of cells with normalized radii  $r/a = 0.05, 0.1, 0.15, 0.22$ , and  $0.32$  are used around the crack front for the  $J$  computations. 504 cells are used in the construction of the integration domains.

The model was solved for a number of relative orientations of the axis of symmetry of the material in both subdomains. The computed results are reported in Figure 10. The  $J$ -results in Figure 10 are normalized with respect to  $J_0 = \sigma^2 \pi a / E'$ . It can be seen that when one of the principal axes of the material is specified perpendicular to the crack front direction for both subdomains, the  $J$ -integral results

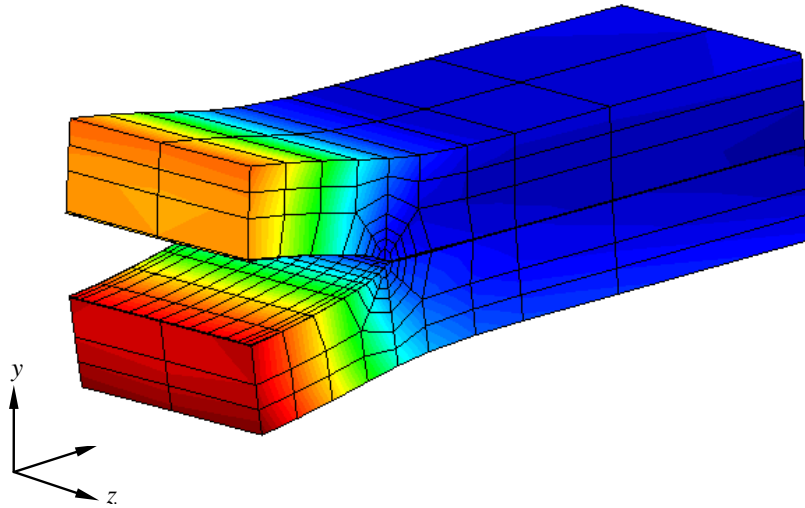


**Figure 9.** Bimaterial laminate with an edge crack (deformed geometry).

along the crack front are symmetric with respect to the specimen midplane ( $z/t = 0$ ). This is the case for the results labeled  $90/90/00-90/90/00$  and  $0/90/90-90/90/00$  in the figure. On the other hand, when there is no principal axis of the material oriented perpendicular to the crack front in at least one of the subdomains, the  $J$ -integral results are not symmetric with respect to the specimen midplane. The extreme values for the  $J$ -integral are attained at the free surface.

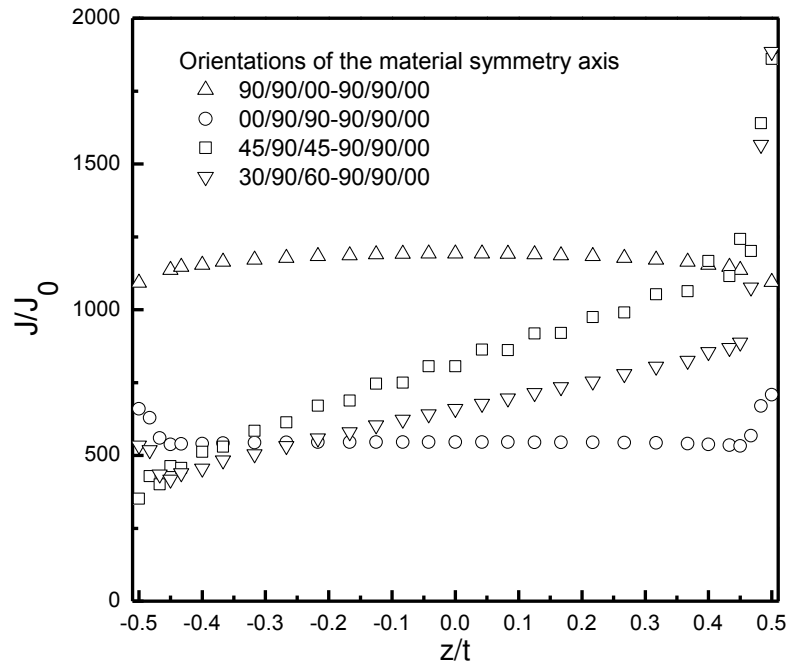


**Figure 10.** Normalized  $J$ -integral results along the crack front of the edge crack in the ply.

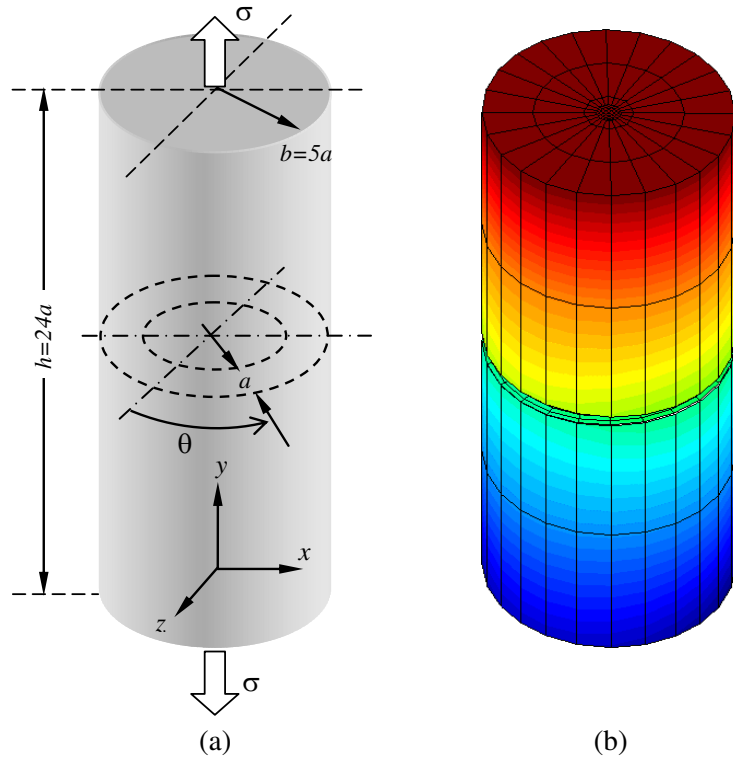


**Figure 11.** External circumferential interface crack in a cylindrical bimaterial bar.  
(a) Model geometry and dimensions and (b) model discretization (deformed mesh).

**7.3. A circumferential interface crack in a cylindrical bimaterial bar.** The last example consists of a cylindrical bimaterial bar containing a circumferential crack subjected to remote axial tension  $\sigma$ , as illustrated in Figure 11a. The radius of the bar is  $b = 5a$  and its height is  $h = 24a$ , with  $a$  being the crack depth. A total of 684 elements are employed in the model discretization. Four rings of cells with radii  $r/a = 0.25, 0.5, 0.75$ , and 1 are used around the crack front for the  $J$  computations. The integration domains are constructed using 672 cells. The model discretization is illustrated in Figure 11b. The material properties are the same reported for the previous examples.

The problem was solved considering different material orientations. The results are shown in Figure 12. In every case the results are normalized with respect to  $J_0 = \sigma^2 \pi a / E'$ . The first solution is for an isotropic homogeneous material and was used for validation purposes. The  $J$  result is constant along the complete crack front. Also plotted in Figure 12 is the result of [Murakami and Okazaki 1976], which possesses a reported accuracy of 3%. The difference between the computed result and that of the reference is 5%. The second solution is for a homogeneous transversely isotropic case, with the material symmetry axis specified coincident with the direction  $y$  for both subdomains (results labeled  $90^\circ/0^\circ/90^\circ-90^\circ/0^\circ/90^\circ$  in Figure 12). Once again, and as was expected, the computed  $J$  values are constant along the complete crack front. In the third case the orientation of the material axes of symmetry are different in each subdomain: for subdomain I the material axis of symmetry is oriented in the  $z$ -direction, while for subdomain II it is oriented in the  $y$ -direction (results labeled  $90^\circ/90^\circ/0^\circ-90^\circ/0^\circ/90^\circ$  in Figure 12). The

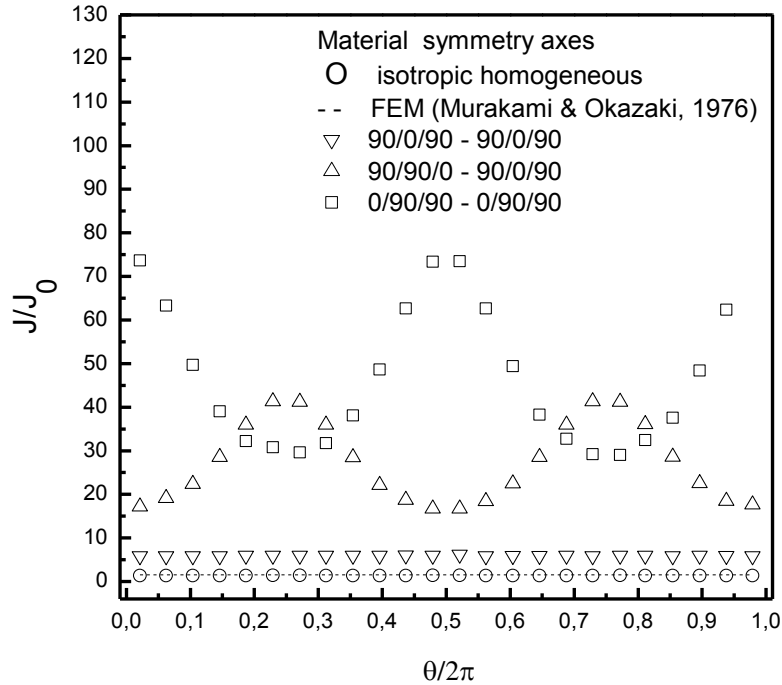


**Figure 12.** Normalized  $J$ -integral results along the crack front of the circumferential crack in the biomaterial bar.

$J$  results exhibit a periodic variation along the crack front. The minimum values occur in the positions coincident with the direction of the  $z$ -axis, while the maximum values are in the positions coincident with the direction of the  $x$ -axis. In the last case, the orientation of the material axis of symmetry is specified in the  $x$ -direction for both subdomains (results labeled  $0^\circ/90/90^\circ-0^\circ/90/90^\circ$  in Figure 12). As for the previous case, the  $J$  results exhibit a periodic variation along the crack front. However, in this case minimum values occur in the positions coincident with the direction of the  $x$ -axis, while the maximums are in the positions coincident with the direction of the  $z$ -axis.

## 8. Conclusions

A boundary element implementation of the energy domain integral (EDI) for the computation of the  $J$ -integral of three-dimensional interface cracks in transversely isotropic bimaterials has been presented in this paper. The analysis is addressed using a multidomain boundary element method (BEM) formulation in order to account for the different material properties at both sides of the crack. The  $J$ -integral computation is implemented as a postprocessing technique, and so it can be applied to the results from a particular model at a later stage. The BEM uses a versatile set of fundamental solutions given only in terms of real functions which are valid for all possible material configurations. The implementation takes advantage of the efficiency of the boundary integral equation to directly obtain the required displacement derivatives, stress, and strain fields from their boundary integral representations.

The efficiency and accuracy of the proposed implementation has been addressed by analyzing a number of examples with straight and curved crack fronts. The computed results compare very well with those

reported in the literature for benchmark problems. In addition, the implemented algorithm allowed for studying the effect of the relative orientations of the materials on both sides of the crack on the  $J$  integral values.

Maximum errors and dependence of the computed results on the integration paths occur for surface cracks at the intersection of the crack front with a free surface. This behavior is attributed to the boundary layer effect taking place at the intersection of the crack front and a free surface. Under these circumstances, the EDI is not strictly applicable. This problem remains unsolved in this work. Following previous work [Ortiz and Cisilino 2005], alternative approaches for the selection of the auxiliary function  $q$  for the implementation of the EDI could be explored to improve the accuracy of the computations.

## Appendix

Additional terms of the components of the tensor  $H(\hat{x})$ :

$$\beta_3 = \left\{ \frac{C_{44}c^2 + C_{33}s^2}{C_{66}} \right\}^{1/2}, \quad h = \left\{ c^4 + \frac{\eta s^2 c^2}{C_{11}C_{44}} + \frac{C_{33}s^4}{C_{11}} \right\}^{1/2}, \quad g = \left\{ 2(h + c^2) + \frac{\eta s^2}{C_{11}C_{44}} \right\}^{1/2},$$

$$\xi = g(h + g\beta_3 + \beta_3^2), \quad \eta = C_{11}C_{33} - C_{13}^2 - 2C_{13}C_{44}, \quad f = \frac{h+c^2}{C_{66}} + \frac{gh}{C_{66}\beta_3} + \frac{C_{33}s^2}{C_{11}C_{44}},$$

where  $c = \cos \phi = x_3/r$ ,  $s = \sin \phi = r_{12}/r$ , the angle  $\phi$  being as in Figure 4.

## References

- [ABAQUS 2009] ABAQUS, Version 6.9-1, Dassault Systèmes, Providence, RI, 2009.
- [Aliabadi 2002] M. H. Aliabadi, *The boundary element method, 2: Applications in solids and structures*, Wiley, Chichester, 2002.
- [Anderson 2005] T. L. Anderson, *Fracture mechanics: fundamentals and applications*, 3rd ed., CRC Press, Boca Raton, FL, 2005.
- [Ariza and Dominguez 2004a] M. P. Ariza and J. Dominguez, “Dynamic BE analysis of 3-D cracks in transversely isotropic solids”, *Comput. Methods Appl. Mech. Eng.* **193**:9–11 (2004), 765–779.
- [Ariza and Dominguez 2004b] M. P. Ariza and J. Dominguez, “Boundary element formulation for 3D transversely isotropic cracked bodies”, *Int. J. Numer. Methods Eng.* **60**:4 (2004), 719–753.
- [Balderrama et al. 2006] R. Balderrama, A. P. Cisilino, and M. Martinez, “Boundary element method analysis of three-dimensional thermoelastic fracture problems using the energy domain integral”, *J. Appl. Mech. (ASME)* **73**:6 (2006), 959–969.
- [Balderrama et al. 2008] R. Balderrama, A. P. Cisilino, and M. Martinez, “Boundary element analysis of three-dimensional mixed-mode thermoelastic crack problems using the interaction and the energy domain integrals”, *Int. J. Numer. Methods Eng.* **74**:2 (2008), 294–320.
- [Boniface and Banks-Sills 2002] V. Boniface and L. Banks-Sills, “Stress intensity factors for finite interface cracks between a special pair of transversely isotropic materials”, *J. Appl. Mech. (ASME)* **69**:3 (2002), 230–239.
- [Chen et al. 2009] C.-S. Chen, C.-H. Chen, and E. Pan, “Three-dimensional stress intensity factors of a central square crack in a transversely isotropic cuboid with arbitrary material orientations”, *Eng. Anal. Bound. Elem.* **33**:2 (2009), 128–136.
- [Chow and Atluri 1998] W. T. Chow and S. N. Atluri, “Stress intensity factors as the fracture parameters for delamination crack growth in composite laminates”, *Comput. Mech.* **21**:1 (1998), 1–10.
- [Chu and Hong 1990] S. J. Chu and C. S. Hong, “Application of the  $J_k$  integral to mixed mode crack problems for anisotropic composite laminates”, *Eng. Fract. Mech.* **35**:6 (1990), 1093–1103.
- [Cisilino and Aliabadi 1999] A. P. Cisilino and M. H. Aliabadi, “BEM implementation of the energy domain integral for the elastoplastic analysis of 3D fracture problems”, *Int. J. Fract.* **96**:3 (1999), 229–245.

- [Cisilino et al. 1998] A. P. Cisilino, M. H. Aliabadi, and J. L. Otegui, "Energy domain integral applied to solve center and double-edge crack problems in three dimensions", *Theor. Appl. Fract. Mech.* **29**:3 (1998), 181–194.
- [Comninou 1977] M. Comninou, "The interface crack", *J. Appl. Mech. (ASME)* **44**:4 (1977), 631–636.
- [Feijoó et al. 2000] R. A. Feijoó, C. Padra, R. Saliba, E. Taroco, and M. J. Vénere, "Shape sensitivity analysis for energy release rate evaluation and its application to the study of three-dimensional cracked bodies", *Comput. Methods Appl. Mech. Eng.* **188**:4 (2000), 649–664.
- [Freed and Banks-Sills 2005] Y. Freed and L. Banks-Sills, "A through interface crack between a  $\pm 45^\circ$  transversely isotropic pair of materials", *Int. J. Fract.* **133**:1 (2005), 1–41.
- [Gibson 2007] R. F. Gibson, *Principles of composite material mechanics*, 2nd ed., CRC Press, Boca Raton, FL, 2007.
- [He et al. 1994] W. J. He, J. E. Bolander, Jr., D. S. Lin, and H. J. Ding, "A boundary element for crack analysis at a bimaterial interface", *Eng. Fract. Mech.* **49**:3 (1994), 405–410.
- [Lachat and Watson 1976] J. C. Lachat and J. O. Watson, "Effective numerical treatment of boundary integral equations: a formulation for three-dimensional elastostatics", *Int. J. Numer. Methods Eng.* **10**:5 (1976), 991–1005.
- [Lifshitz and Rozentsveig 1947] I. M. Lifshitz and L. N. Rozentsveig, "Construction of the Green tensor for the fundamental equation of elasticity theory in the case of an unbounded elastically anisotropic medium", *Zh. Èksper. Teor. Fiz.* **17** (1947), 783–791.
- [Loloi 2000] M. Loloi, "Boundary integral equation solution of three-dimensional elastostatic problems in transversely isotropic solids using closed-form displacement fundamental solutions", *Int. J. Numer. Methods Eng.* **48**:6 (2000), 823–842.
- [Mao and Sun 1995] R. Mao and G. Sun, "A study of the interaction between matrix crack and matrix-fibre interface", *Eng. Fract. Mech.* **51**:3 (1995), 469–477.
- [Moran and Shih 1987] B. Moran and C. F. Shih, "A general treatment of crack tip contour integrals", *Int. J. Fract.* **35**:4 (1987), 295–310.
- [Murakami and Okazaki 1976] Y. Murakami and Y. Okazaki, "A simple procedure for the accurate determination of stress intensity factors by finite element method", *Trans. Jpn. Soc. Mech. Eng.* **42**:364 (1976), 3679–3687.
- [Nahta and Moran 1993] R. Nahta and B. Moran, "Domain integrals for axisymmetric interface crack problems", *Int. J. Solids Struct.* **30**:15 (1993), 2027–2040.
- [Nikishkov and Atluri 1987] G. P. Nikishkov and S. N. Atluri, "Calculation of fracture mechanics parameters for an arbitrary three-dimensional crack, by the 'equivalent domain integral' method", *Int. J. Numer. Methods Eng.* **24**:9 (1987), 1801–1821.
- [Ortiz and Cisilino 2005] J. E. Ortiz and A. P. Cisilino, "Boundary element method for J-integral and stress intensity factor computations in three-dimensional interface cracks", *Int. J. Fract.* **133**:3 (2005), 197–222.
- [Pan and Chou 1976] Y.-C. Pan and T.-W. Chou, "Point force solution for an infinite transversely isotropic solid", *J. Appl. Mech. (ASME)* **43**:4 (1976), 608–612.
- [Rice 1968] J. R. Rice, "A path independent integral and the approximate analysis of strain concentration by notches and cracks", *J. Appl. Mech. (ASME)* **35**:2 (1968), 379–386.
- [Rice 1988] J. R. Rice, "Elastic fracture mechanics concepts for interfacial cracks.", *J. Appl. Mech. (ASME)* **55**:1 (1988), 98–103.
- [Sáez et al. 1997] A. Sáez, M. P. Ariza, and J. Dominguez, "Three-dimensional fracture analysis in transversely isotropic solids", *Eng. Anal. Bound. Elem.* **20**:4 (1997), 287–298.
- [Shah et al. 2006] P. D. Shah, C. L. Tan, and X. Wang, "Evaluation of T-stress for an interface crack between dissimilar anisotropic materials using the boundary element method", *Comput. Model. Eng. Sci.* **13**:3 (2006), 185–198.
- [So et al. 2004] W. M. G. So, K. J. Lau, and S. W. Ng, "Determination of stress intensity factors for interfacial cracks using the virtual crack extension approach", *Comput. Model. Eng. Sci.* **5**:3 (2004), 189–200.
- [Tan and Gao 1990] C. L. Tan and Y. L. Gao, "Treatment of bimaterial interface crack problems using the boundary element method", *Eng. Fract. Mech.* **36**:6 (1990), 919–932.
- [Távara et al. 2008] L. Távara, J. E. Ortiz, V. Mantič, and F. París, "Unique real-variable expressions of displacement and traction fundamental solutions covering all transversely isotropic elastic materials for 3D BEM", *Int. J. Numer. Methods Eng.* **74**:5 (2008), 776–798.

[Ting 1996] T. C.-T. Ting, *Anisotropic elasticity: theory and applications*, Oxford Engineering Science Series **45**, Oxford University Press, New York, 1996.

[Zhao et al. 2007] M. H. Zhao, C. Y. Fan, T. Liu, and F. Yang, “Extended displacement discontinuity Green’s functions for three-dimensional transversely isotropic magneto-electro-elastic media and applications”, *Eng. Anal. Bound. Elem.* **31**:6 (2007), 547–558.

Received 19 Jun 2010. Revised 11 Dec 2010. Accepted 4 Feb 2011.

NICOLÁS O. LARROSA: [nlarrosa@us.es](mailto:nlarrosa@us.es)

Departamento de Ingeniería Mecánica y de los Materiales, Escuela Técnica Superior de Ingeniería, Universidad de Sevilla, Camino Descubrimientos, s/n, 41092 Sevilla, Spain

JHONNY E. ORTIZ: [jortiz@us.es](mailto:jortiz@us.es)

Departamento de Mecánica de Medios Continuos, Escuela Técnica Superior de Ingeniería, Universidad de Sevilla, Camino Descubrimientos, s/n, 41092 Sevilla, Spain

ADRIÁN P. CISILINO: [cisilino@fimdp.edu.ar](mailto:cisilino@fimdp.edu.ar)

División Soldadura y Fractomecánica, Instituto de Investigaciones en Ciencia y Tecnología de Materiales, Facultad de Ingeniería, Universidad Nacional de Mar del Plata - Consejo Nacional de Investigaciones Científicas, Av. Juan B. Justo 4302, B7608FDQ Mar del Plata, Argentina



## PORCINE DERMIS IN UNIAXIAL CYCLIC LOADING: SAMPLE PREPARATION, EXPERIMENTAL RESULTS AND MODELING

ALEXANDER E. EHRET, MARC HOLLENSTEIN, EDOARDO MAZZA AND MIKHAIL ITSKOV

We present a straightforward technique to prepare thin samples of planar or bulky soft tissue with very accurate geometry. The experimental procedure includes the preparation of thin slices of tissue by means of a surgical dermatome and specimen extraction by die cutters. We illustrate this method in application to porcine dermal tissue. The prepared specimens were subjected to uniaxial cyclic tension along and across the lines of cleavage with increasing upper stretch limits. Besides a distinct anisotropic and nonlinear behavior, cyclic loading caused considerable preconditioning effects including softening and substantial residual deformations. This observed behavior is well represented by a recently proposed constitutive model accounting for the elastic and dissipative behavior of soft tissues.

### 1. Introduction

Skin provides the barrier of the body to the surrounding environment and is for this reason, more directly than any other organ, subject to external loads, possibly going beyond the physiological level. A comprehensive understanding of the mechanical properties of skin is thus of major importance. Moreover, skin is widely used as an autograft in reconstructive surgery, for example, for treating burn wounds. In this field, as well as in plastic surgery, techniques and results can be improved taking the mechanical characteristics of the skin into account. These properties may also serve as an indicator for connective tissue disorders which alter the constitution of the skin. Like the majority of soft biological tissues, skin is a composite material containing a large amount of fibrous proteins, in particular collagen, which, due to a preferred alignment, induce anisotropic material properties. This anisotropy was already discovered in the early 19th century when Dupuytren [1834] investigated the apparent discrepancy between the circular cross-section of a weapon injuring the skin and the resulting elliptic shape of the wound. The preferred directions of this anisotropy coincide with the lines of cleavage of the skin referred to as Langer's lines [Langer 1861].

For the mechanical characterization of skin, a number of experiments have been proposed using in vivo methods such as indentation [Delalleau et al. 2006] and suction [Alexander and Cook 1977], as well as dedicated extension [Alexander and Cook 1977; Khatyr et al. 2004]. The most common in vitro experiment is the uniaxial tension test. Ridge and Wright [1966] carried out uniaxial tensile experiments on human skin specimens and confirmed the anisotropy of skin by a stress response, which was remarkably stiffer along than across the Langer's lines. Further uniaxial tension tests were performed, for example, on the skin of cats [Veronda and Westmann 1970], rats [Haut 1989; Eshel and Lanir 2001;

---

The advice and support of Prof. Dr. med. A. Prescher, University Hospital Aachen, and Dr. med. M. Guggenheim, University Hospital Zurich, concerning the histology of skin and the proper use of the surgical dermatome is gratefully acknowledged. For technical assistance with the parameter identification process, we thank A. R. Elliott. The work of MH and EM was partially supported by the Swiss National Science Foundation (NCCR CO-ME).

**Keywords:** dermis, anisotropy, constitutive modeling, preconditioning, soft tissues, mechanical testing, cyclic loading.

Delalleau et al. 2006], and mice [Del Prete et al. 2004; Muñoz et al. 2008]. Since physiologically relevant loading states are of a biaxial nature, Lanir and Fung [1974] investigated the biaxial viscoelastic stress response of rectangular rabbit skin samples, the width of which was fixed during elongation. By means of a multiaxial testing device, the planar orthotropic elastic properties of human skin were studied in [Reihsner et al. 1995], which confirmed only small deviations of the principal stress directions from the Langer's lines. For an overview of available testing methods, the reader is also referred to the review articles [Payne 1991; Edwards and Marks 1995; Xu et al. 2008].

While the majority of investigations focus on elastic and viscoelastic properties as well as on failure, the anisotropic inelastic softening and, in particular, the preconditioning behavior of skin occurring during the initial few applied load cycles have rarely been the scientific focus. In this regard, Muñoz et al. [2008] have presented an interesting study on the inelastic behaviour of murine skin subject to uniaxial cyclic loading, where the load was successively increased in each step. Besides remarkable residual strains growing with the achieved maximal stretch, they found softening characteristics which clearly resemble the Mullins effect [Mullins 1947] in rubber-like materials. The anisotropic preconditioning behavior of thin porcine dermis samples subject to pure shear loading has recently been investigated in [Hollenstein et al. 2011] and this study will be extended to the case of uniaxial tension in the present work.

After preconditioning, the response of skin is characterized by a stable hysteresis loop [Tong and Fung 1976]. Accordingly, hyperelastic and viscoelastic models dominate the constitutive modeling approaches, including both phenomenological and microstructural strategies; see [Xu et al. 2008] for a review. As for most other tissues, the transient softening behavior during initial load cycles is often treated as a side effect and is only addressed in few works. For example, preconditioning has been modeled for tendon [Sverdlik and Lanir 2002], liver [Nava et al. 2004], and ventricular myocardium [Emery et al. 1997]. In all three works, quasilinear viscoelastic models were enriched either by a plastic or a softening variable to capture the observed softening effects. Under unphysiological conditions, the stress softening is mostly related to tissue damage and consequently is modeled in the framework of continuum damage mechanics, as, for example, applied to overstretched arteries [Balzani et al. 2006] or ligaments [Calvo et al. 2007]. Rubin and Bodner [2002] proposed a viscoplastic model for skin and the underlying fascial tissue, which has recently been applied to simulate the aging skin of the human face [Barbarino et al. 2009].

In the present work, we apply a novel method to excise thin specimens of accurate geometry from planar or bulky soft tissues [Hollenstein et al. 2011]. By using a surgical dermatome, 500  $\mu\text{m}$ -thick samples of porcine dermis were prepared and subjected to cyclic quasistatic uniaxial loading. The observed stress-response is modeled by a recently proposed modeling framework to capture preconditioning and softening effects [Ehret and Itskov 2009].

## 2. Materials and methods

The preparation of the specimens was carried out according to a protocol recently presented in conjunction with a pure shear test series of porcine dermal tissue and is briefly summarized in this section. For a detailed description and technical specifications please refer to [Hollenstein et al. 2011]. All experiments were performed in accordance with Swiss federal ethical research standards.

**2A. Sample preparation.** Porcine skin is anatomically subdivided into the epidermal, dermal, and subcutaneous layers, with respective thicknesses of about 30–140  $\mu\text{m}$ , 1–2 mm, and up to 12 mm or more,

depending on sex, anatomical site, and nutritional state of the pig [Vardaxis et al. 1997]. Light and scanning electron microscopy [Meyer et al. 1982] as well as confocal laser scanning microscopy [Vardaxis et al. 1997] reveal that porcine dermal tissue is mainly composed of a dense three-dimensional network of collagen fibers and thick fiber bundles crossing each other in two main directions. Ridge and Wright [1966] have suggested a simplified planar lattice structure in which these preferred fiber directions of skin form an angle of “somewhat less than 45°” to the Langer’s lines. The resulting axes of orthotropy along and across the Langer’s lines indeed coincide well with experimental results (see, for example, [Rehsner et al. 1995]). Depending on the anatomical site, a substantial amount of elastic fibers are also present [Meyer et al. 1981]. The two proteins collagen and elastin constitute about 70–80% and 4% of the dry weight, respectively [Mathews 1975; Fung 1993].

Skin pieces from the snout and head region of female domestic pigs (*Sus scrofa domestica*) were obtained from the slaughterhouse immediately after animal slaughter. The pieces were approximately 300×300 mm large with a thickness of about 10–15 mm, containing the subcutaneous layer. After carefully being rinsed with water, the pieces were shaved and finally stored in saline-soaked cloths at 4°C.

Following the protocol proposed in [Hollenstein et al. 2011], the pieces were first nailed under slight tension on a foam damping pad and paraffin oil was applied to the skin surface. Thereafter 500 µm-thick and 80 mm-wide slices were extracted by means of a surgical dermatome (Figure 1a). The second and third layers extracted in this way consisted completely of dermal tissue and were used for testing.

Finally, rectangular specimens were punched out of the dermis sections by the use of a 10×80 mm die cutter (Figure 1b) and shortened to a length of 50 mm with the aid of a scalpel. To obtain longitudinal and transversal specimens, respectively, the die was aligned with its long side either along or perpendicular to the optically observable crease lines, which coincide well with the cleavage lines [Cox 1941].

**2B. Experimental setup and test realization.** Uniaxial tension tests were performed on a custom-made testing device with two horizontally arranged hydraulic actuators with an available piston rod stroke of 100 mm. Load cells with a capacity of 100 N were installed at the end of each actuator. Custom-made

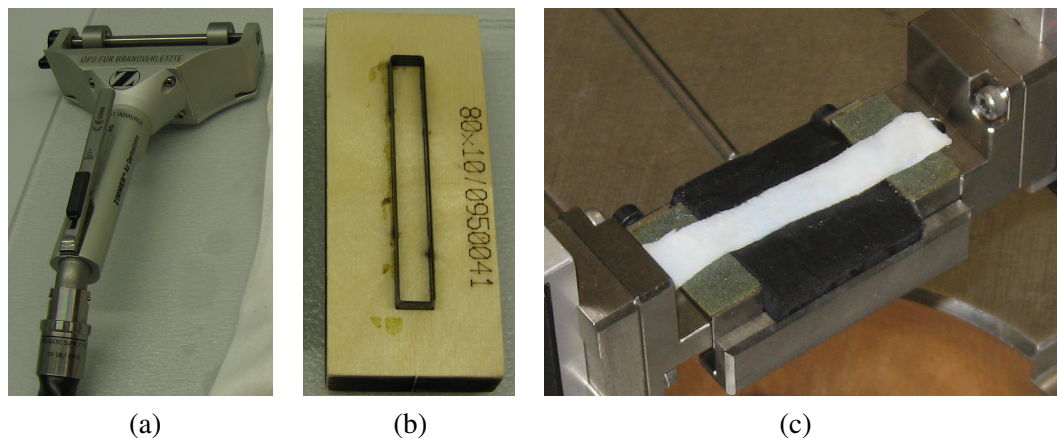


**Figure 1.** (a) Surgical air-dermatome. (b) Custom-made die cutter for excision of uniaxial specimens. (c) Dermis specimen on the supporting table before mounting the upper grips.

titanium clamps equipped with sandpaper allowed for specimen fixation by closing a knurled thumb screw. The force  $F$  acting on the fixed actuator and the displacement of the moving actuator relative to its initial position were recorded.

For precise spreading of the specimens on the grip surfaces, a small supporting table was installed in between the clamps while the actuator piston rods were in their initial testing position, providing a distance of 30 mm (Figure 1c). After the closing of the clamps and removal of the table, the specimens were hanging slightly slack in between the two clamps, and a preload of 0.05 N was applied to straighten the sample. The resulting length is considered as the reference length. Note that the choice of this preload thus has significant influence on the stretch calculation. Before and during testing, the samples were sprayed with physiological saline in order to keep them moist.

The induced nominal strain  $\varepsilon_n(t)$ , the stretch ratio  $\lambda_n(t)$ , and the nominal stress  $P$  were computed as [Hollenstein et al. 2011]

$$\varepsilon_n(t) = \frac{d(t)}{l_0}, \quad \lambda_n(t) = 1 + \varepsilon_n(t), \quad P = \frac{F}{A_0}, \quad (2-1)$$

where  $d(t)$  is the displacement of the actuator,  $A_0$  the initial cross-sectional area,  $l_0$  the free gauge length at preload, and  $F$  the measured force.

We performed the tests in a displacement-controlled mode, where the protocol was defined based on the nominal strain and its rate. The lower cycle-reversal points, however, were enforced when the measured force became less than 0.05 N in order to prevent the tissue from becoming slack during the cyclic loading. The preconditioning protocol contained five sets of five cycles, respectively, with increasing upper strain levels of 2.9%, 5.7%, 8.5%, 11.4%, and 14.3%. The highest strain level was chosen well below the rupture strain in preceding tension-to-failure experiments and the lower levels were obtained by appropriate scaling. All tests were run with  $\dot{\varepsilon}_n = 0.1\% \text{ s}^{-1}$ . In previous experiments, we found that further decreasing the rate below this value had negligible influence on the tissue response, which was thus considered quasistatic.

### 3. Experimental results

In Figure 2 the nominal stress  $P$  in the loading direction is plotted against the applied stretch ratio for a longitudinal and a transversal specimen cut from the same skin sample. As typical for the majority of soft biological tissues each stress-stretch curve is characterized by a *J*-shaped form with a distinct toe region. Comparison between the two graphs reveals the distinct anisotropy of the tissue, with a much stiffer response for loading along the direction of the cleavage lines.

All specimens showed substantial preconditioning effects. This includes stress softening and a tendency to stabilise after some cycles if the upper stretch limit is kept constant. Increasing this limit, however, the tissue again undergoes several preconditioning cycles until a reasonably stable response is reached. It is remarked that even for loading at these low strain rates, the stabilized loading-unloading cycles demonstrate hysteresis, in line with the phenomenon of pseudoelasticity [Fung 1993]. Along with the softening, both longitudinal and transversal samples accumulate remarkably large residual strains of approximately 60% of the applied strain after removing the load. The observed phenomena, in particular the strong effect of the previous loading history, bear a tremendous resemblance to stress softening characteristics of rubber-like materials such as the Mullins effect [Mullins 1947].

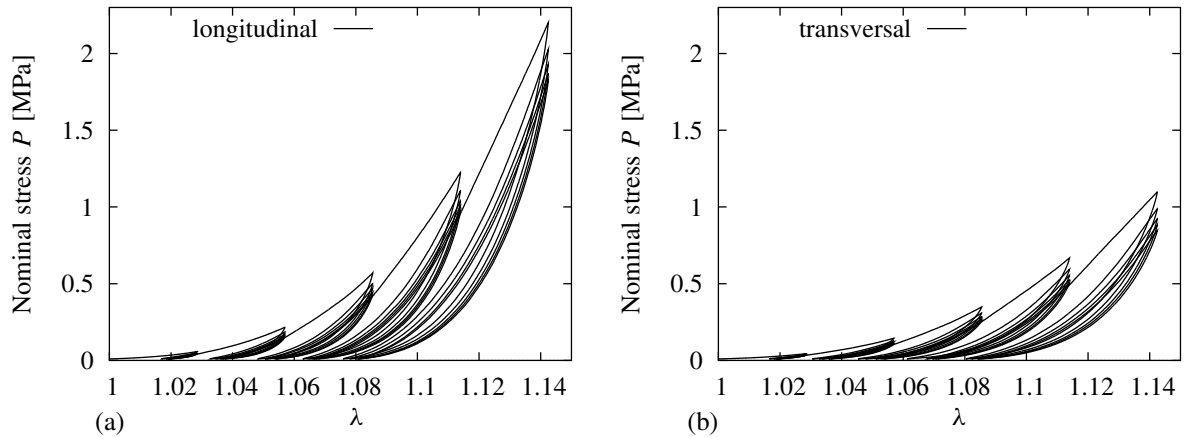


**Figure 2.** Nominal stress response of two dermis specimens cut either (a) along or (b) perpendicular to the cleavage lines of the skin.

#### 4. Constitutive modeling

In order to interpret the observed anisotropic softening behavior, we consider a recently proposed dissipative modeling framework for anisotropic materials [Ehret and Itskov 2009]. The model treats soft biological tissues in the framework of classical invariant theory of fiber-reinforced materials consisting of an isotropic matrix and  $n$  families of collagen fibers, the alignment of which is specified by unit vectors  $\mathbf{a}_i$ ,  $i = 1, 2, \dots, n$ . Based on these fiber vectors, the structural tensors  $\mathbf{L}_i = \mathbf{a}_i \otimes \mathbf{a}_i$  are introduced and, by means of the second-order identity tensor  $\mathbf{I}$ , additionally  $\mathbf{L}_0 = \mathbf{I}/3$ , which accounts for the isotropic matrix. A set of suitable invariants to formulate the free energy function is given in terms of the structural tensors and the right Cauchy–Green tensor  $\mathbf{C}$  as (for details, refer to [Ehret and Itskov 2007])

$$I_i = \text{tr}(\mathbf{C}\mathbf{L}_i), \quad J_i = \text{tr}[(\text{cof } \mathbf{C})\mathbf{L}_i], \quad \text{III}_{\mathbf{C}} = \det \mathbf{C}, \quad i = 0, 1, \dots, n, \quad (4-1)$$

where  $\text{cof } \mathbf{C} = \mathbf{C}^{-1} \det \mathbf{C}$ . In the case  $i = 0$ , one finds  $I_0 = \text{I}_{\mathbf{C}}/3$  and  $J_0 = \text{II}_{\mathbf{C}}/3$ , where  $\text{I}_{\mathbf{C}}$  and  $\text{II}_{\mathbf{C}}$  denote the first and second principal invariants of  $\mathbf{C}$ . Moreover, for  $i = 1, 2, \dots, n$ ,  $I_i$  describes the change in squared length of a line element aligned with the vector  $\mathbf{a}_i$ . Using Nanson's formula, one further realises that  $J_i$  accounts for the change in squared area of an element with the surface normal  $\mathbf{a}_i$  in the reference state [Schröder and Neff 2003]. Under the incompressibility constraint  $\det \mathbf{C} = 1$ , the invariants (4-1) take the form

$$I_i = \text{tr}(\mathbf{C}\mathbf{L}_i), \quad K_i = \text{tr}[\mathbf{C}^{-1}\mathbf{L}_i], \quad \text{III}_{\mathbf{C}} = 1, \quad i = 0, 1, \dots, n, \quad (4-2)$$

where the second set of invariants is denoted by  $K_i$  in this case. Taking into account that the isotropic matrix and various fibers may have different influences on the deformation behavior, generalized invariants are postulated as linear combinations of the form [Ehret and Itskov 2007]

$$\tilde{I} = \sum_{i=0}^n u_i I_i, \quad \tilde{K} = \sum_{i=0}^n v_i K_i, \quad (4-3)$$

where  $u_i$  and  $v_i$  denote nonnegative weight factors controlling the influence of the different constituents, respectively. As a result of the kinematic interpretation of the invariants (4-2),  $u_i$  is associated with longitudinal characteristics, while  $v_i$  relates to cross-sectional properties. The inelastic modeling concept is based on the idea that structural alterations of a constituent  $i$  must be reflected in a change of the associated weight factor. Treating the weight factors as internal variables characterising the structural state of the tissue, its free energy  $\Psi$  per unit volume is represented in the incompressible case ( $\det \mathbf{C} = 1$ ) by [Itskov and Ehret 2009]

$$\Psi = \tilde{\Psi}(\tilde{I}, \tilde{K}) = \hat{\Psi}(I_i, K_i, u_i, v_i) = \frac{\mu}{4} \left\{ \frac{1}{\alpha} [e^{\alpha(\tilde{I}-1)} - 1] + \frac{1}{\beta} [e^{\beta(\tilde{K}-1)} - 1] \right\}, \quad (4-4)$$

where  $\mu$  has dimensions of stress and  $\alpha > 0$  and  $\beta > 0$  denote dimensionless material constants. Keeping the weight factors constant, the free energy function (4-4) reduces to the incompressible representation of a recently proposed polyconvex and coercive strain-energy function [Ehret and Itskov 2007]. In the elastic case, this property guarantees material stability as well as the existence of the global minimiser of the total elastic energy, which is an important prerequisite for the solution of boundary value problems [Ball 1977; Ciarlet 1988; Schröder and Neff 2003].

Inserting (4-4) into the Clausius–Duhem inequality and regarding the incompressibility constraint yields the second Piola–Kirchhoff stress tensor as  $S = 2\partial\Psi/\partial\mathbf{C} - p\mathbf{C}^{-1}$  where  $p$  is an arbitrary scalar. Furthermore, one obtains a dissipation inequality that guarantees a nonnegative rate of entropy production [Truesdell and Noll 1965]. Borrowing methods from strain space plasticity [Naghdi and Trapp 1975], one can set up evolution criteria and suitable rate equations for the weight factors so that the latter inequality is satisfied and the model is thermodynamically consistent. The evolution equations are formulated in terms of the thermodynamic forces " $u\varphi_i = \partial\Psi/\partial u_i$ " and " $v\varphi_i = \partial\Psi/\partial v_i$ ", work-conjugate to  $u_i$  and  $v_i$ , respectively. In the special case of a continuously softening material, these evolution equations take the form [Ehret and Itskov 2009]

$$\dot{u}_i = \begin{cases} {}^u d_i {}^u \dot{\varphi}_i & \text{if } {}^u \dot{\varphi}_i > 0 \wedge I_i > 1, \\ 0 & \text{else,} \end{cases} \quad \dot{v}_i = \begin{cases} {}^v d_i {}^v \dot{\varphi}_i & \text{if } {}^v \dot{\varphi}_i > 0 \wedge K_i > 1, \\ 0 & \text{else,} \end{cases} \quad (4-5)$$

for  $i = 0, 1, \dots, n$ , where the superposed circle indicates  $\dot{x} = \partial x / \partial \mathbf{C} : \dot{\mathbf{C}}$ , and " $d_i \leq 0$ " and " $v d_i \leq 0$ " denote softening functions.

A structural initial state is introduced such that the tissue is energy and stress-free in the reference configuration with  $\mathbf{C} = \mathbf{I}$ . Considering the latter relation in (4-4) and the resulting second Piola–Kirchhoff stress tensor, one easily confirms that the tissue is energy and stress-free if [Itskov and Ehret 2009]

$$u_i = v_i = w_i, \quad \sum_{i=0}^n w_i = 1, \quad (4-6)$$

which will be referred to as the virgin state of the material.

## 5. Comparison with experimental data

**5A. Model specification.** Taking the initially discussed arrangement of collagen fibers in the dermis into account, we adopt the simplified fiber structure suggested in [Ridge and Wright 1966] and model the tissue as a fiber-reinforced material with two fiber families forming an angle of  $\pm\theta$  with the cleavage

lines. Introducing the vectors  $\mathbf{e}_1$  along and  $\mathbf{e}_2$  across these lines, as well as  $\mathbf{e}_3$  in the thickness direction, they form an orthonormal basis with respect to which the two fiber vectors are specified as

$$\mathbf{a}_1 = \cos(\theta)\mathbf{e}_1 + \sin(\theta)\mathbf{e}_2, \quad \mathbf{a}_2 = \cos(\theta)\mathbf{e}_1 - \sin(\theta)\mathbf{e}_2. \quad (5-1)$$

For loading along and across the fiber directions, the nominal stresses can thus be calculated in terms of the principal stretches  $\lambda_k$ ,  $k = 1, 2, 3$ , by

$$P_k = \frac{\partial \Psi}{\partial \lambda_k} - p\lambda_k^{-1},$$

where  $p$  denotes an arbitrary parameter which is determined by the assumption of stress-free lateral boundaries during the uniaxial tests. As a result of the incompressibility condition, the principal stretches are related by  $\lambda_3 = 1/(\lambda_1\lambda_2)$ , so that the nominal stresses may be expressed in the form  $P_k = \bar{P}_k(\lambda_1, \lambda_2)$ .

We assign the observed softening exclusively to alterations of the longitudinal fiber properties; the bulk and cross-sectional properties remain unchanged so that  $u_0 = v_0 = w_0$  and  $v_i = w_i$ ,  $i = 1, 2$ . Thus it remains to specify the softening functions in the evolution equations (4-5)<sub>1</sub> for  $u_i$ ,  $i = 1, 2$ , where with minor changes the form proposed in [Ehret and Itskov 2009] is adopted as

$${}^u d_i = \frac{4{}^u k_i}{\mu} (\bar{u}_i - u_i), \quad \bar{u}_i = w_i \exp \left[ -{}^u c_i \left( \frac{{}^u \bar{\varphi}_i}{\mu/4} \right)^{{}^u b_i} \right], \quad {}^u \bar{\varphi}_i = \max_{\tau \in (-\infty, t]} [{}^u \varphi_i(\tau)], \quad (5-2)$$

where  ${}^u \bar{\varphi}_i$  indicates the maximum of the thermodynamic force reached in the past loading history, and  ${}^u k_i$ ,  ${}^u b_i$ , and  ${}^u c_i$  are dimensionless constants. In the virgin state, the two fiber families are assumed to be mechanically equivalent, and thus  $w_1 = w_2 = (1 - w_0)/2$ , in view of (4-6). This equivalence also motivates the evolution of these factors being governed by analogous evolution equations so that  ${}^u k_i$ ,  ${}^u b_i$ , and  ${}^u c_i$  take the same value for  $i = 1$  and  $i = 2$ , respectively. Thus altogether there are three constants characterising the anisotropic softening as well as the parameters  $\mu$ ,  $\alpha$ ,  $\beta$ , and  $w_0$  and the angle  $\theta$  controlling the elastic response.

**5B. Parameter identification.** In order to determine the aforementioned parameters in comparison with the uniaxial tension tests, the constitutive equations were implemented in a Maple 10 worksheet. By this means, the model response was simulated for the applied stretch history in the loading direction. For each stretch increment, the evolution equations were solved implicitly and the stretch in the lateral direction was computed from the condition that this direction be stress-free. With these values at hand, the stress in loading direction was calculated. The model does, however, account only for the dissipative processes, inducing softening, and not for the hysteresis loops formed by unloading and subsequent reloading curves. For this reason, the difference between the model and experiment was only taken into account for the 25 unloading paths, where  $N_l^k$  data points for longitudinal and  $N_t^k$  data points for transversal loading were considered on the  $k$ -th unloading curve. Based on these differences, a least-squares objective function of the general form

$$\Omega = \sum_{k=1}^{25} \left\{ \frac{\omega_l^k}{N_l^k} \sum_{i=1}^{N_l^k} [\bar{P}_1(\lambda_l^{k,i}, \lambda_2^{k,i}) - P_l^{k,i}]^2 + \frac{\omega_t^k}{N_t^k} \sum_{i=1}^{N_t^k} [\bar{P}_2(\lambda_1^{k,i}, \lambda_t^{k,i}) - P_t^{k,i}]^2 \right\} \quad (5-3)$$

was defined and subjected to an optimization procedure. Here  $(\lambda_l^{k,i}, P_l^{k,i})$  and  $(\lambda_t^{k,i}, P_t^{k,i})$  are experimental data pairs,  $\lambda_{1,2}^{k,i}$  denote the computed lateral stretches, and  $\omega_{l,t}^k$  are weighting factors.

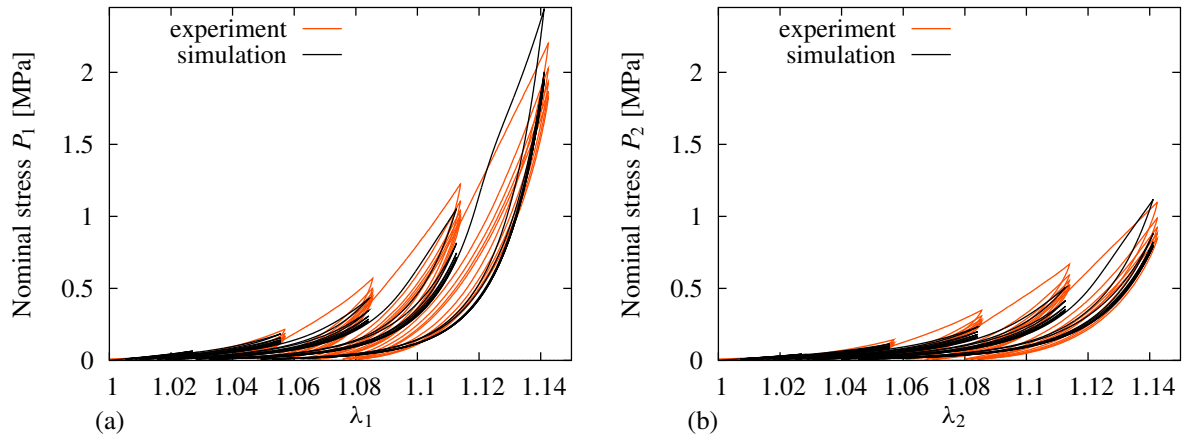


**Figure 3.** Comparison of the simulated stress response based on the parameters obtained by the fitting procedure with experimental data for loading (a) along and (b) across the lines of cleavage. Material parameters:  $\mu = 0.9545$  MPa,  $\alpha = 146.2$ ,  $\beta = 170.0$ ,  $w_0 = 0.2348$ ,  $\theta = 42.44^\circ$ ,  ${}^w k_1 = 0.1420$ ,  ${}^w b_1 = 0.4453$ , and  ${}^w c_1 = 0.01306$ .

Based on the parameter values obtained through the fitting procedure, we simulated the model stress response to the protocol applied in the experiments. The simulation results displayed in Figure 3 (the black solid lines) show fair agreement with the experimental stresses, where we emphasise once again that the hysteresis loops formed by the successive reloading paths are not taken into account by the model. Note that, although the angle between fiber bundles and Langer's lines was estimated at close to  $\theta = 45^\circ$ , the responses for loading along and across these lines differ remarkably, which is explained by the strong nonlinearity of the model.

## 6. Conclusions

In the present paper, we used a novel and robust protocol for the preparation of uniaxial tension specimens of accurately defined dimensions. Sample preparation from soft biological tissues is challenging: shape and structure of the available sample material limit possible geometries and thus applicable extraction procedures. During cutting, the tissue is locally disrupted and new boundaries are created. This may lead to artefactual behavior which affects the results of the mechanical characterization. Thus, gently prepared samples with exact geometry are highly valuable for in vitro testing.

The key features of the preparation protocol include the use of a surgical dermatome in combination with punching dies. The dermatome allows for obtaining thin and thus relatively homogeneous tissue sections. The punching tools guarantee a precise planar geometry of the specimens. Dermatomes are designed to perform extremely smooth sectioning in plastic and reconstructive surgery, and are thus highly suitable for the preparation of evenly shaped specimens for materials testing. Therefore, we argue that, due to the precise geometry of the samples obtained, the proposed method of sample preparation leads to a general reduction in systematic errors, which will have to be proven statistically on a broader database in the future.

Concerning components and structure, dermal tissue is representative of many soft biological tissues and exhibits typical characteristics such as pronounced preconditioning and a response differing in

loading and unloading, a phenomenon known as pseudoelasticity. The remarkable residual deformations demonstrated by the dermis samples in the present study are in line with recent observations on skin specimens including all layers [Muñoz et al. 2008].

The observed inelastic behavior was taken into account by a constitutive model that regards softening as structural alterations of the longitudinal and cross-sectional fiber properties. The model in its present form accounts only for the softening including residual deformations, not, however, for the hysteresis formed due to pseudoelastic behavior of the tissue during reloading. Consequently, the model was calibrated only against the unloading part of the stress-strain cycles, while neglecting the stiffening during reloading. Bearing this in mind, the obtained agreement between simulation and experiment is remarkable and reveals the potential of the model for future developments.

## References

- [Alexander and Cook 1977] H. Alexander and T. H. Cook, "Accounting for natural tension in the mechanical testing of human skin", *J. Investig. Dermatol.* **69** (1977), 310–314.
- [Ball 1977] J. M. Ball, "Convexity conditions and existence theorems in nonlinear elasticity", *Arch. Ration. Mech. An.* **63**:4 (1977), 337–403.
- [Balzani et al. 2006] D. Balzani, J. Schröder, and D. Gross, "Simulation of discontinuous damage incorporating residual stresses in circumferentially overstretched atherosclerotic arteries", *Acta Biomater.* **2**:6 (2006), 609–618.
- [Barbarino et al. 2009] G. G. Barbarino, M. Jabareen, J. Trzewik, A. Nkengne, G. Stamatias, and E. Mazza, "Development and validation of a three-dimensional finite element model of the face", *J. Biomech. Eng. (ASME)* **131**:4 (2009), 041006.
- [Calvo et al. 2007] B. Calvo, E. Peña, M. A. Martinez, and M. Doblaré, "An uncoupled directional damage model for fibred biological soft tissues: formulation and computational aspects", *Int. J. Numer. Methods Eng.* **69**:10 (2007), 2036–2057.
- [Ciarlet 1988] P. G. Ciarlet, *Mathematical elasticity, I: Three-dimensional elasticity*, 2nd ed., Studies in Mathematics and its Applications **20**, North-Holland, Amsterdam, 1988.
- [Cox 1941] H. T. Cox, "The cleavage lines of the skin", *Br. J. Surg.* **29**:114 (1941), 234–240.
- [Del Prete et al. 2004] Z. Del Prete, S. Antoniucci, A. H. Hoffman, and P. Grigg, "Viscoelastic properties of skin in Mov-13 and Tsk mice", *J. Biomech.* **37**:10 (2004), 1491–1497.
- [Delalleau et al. 2006] A. Delalleau, G. Josse, J.-M. Lagarde, H. Zahouani, and J.-M. Bergheau, "Characterization of the mechanical properties of skin by inverse analysis combined with the indentation test", *J. Biomech.* **39**:9 (2006), 1603–1610.
- [Dupuytren 1834] G. Dupuytren, *Traité théorique et pratique des blessures par armes de guerre*, J.-B. Baillière, Paris, 1834.
- [Edwards and Marks 1995] C. Edwards and R. Marks, "Evaluation of biomechanical properties of human skin", *Clin. Dermatol.* **13**:4 (1995), 375–380.
- [Ehret and Itsikov 2007] A. E. Ehret and M. Itsikov, "A polyconvex hyperelastic model for fiber-reinforced materials in application to soft tissues", *J. Mater. Sci.* **42**:21 (2007), 8853–8863.
- [Ehret and Itsikov 2009] A. E. Ehret and M. Itsikov, "Modeling of anisotropic softening phenomena: application to soft biological tissues", *Int. J. Plast.* **25**:5 (2009), 901–919.
- [Emery et al. 1997] J. L. Emery, J. H. Omens, and A. D. McCulloch, "Strain softening in rat left ventricular myocardium", *J. Biomech. Eng. (ASME)* **119**:1 (1997), 6–12.
- [Eshel and Lanir 2001] H. Eshel and Y. Lanir, "Effects of strain level and proteoglycan depletion on preconditioning and viscoelastic responses of rat dorsal skin", *Ann. Biomed. Eng.* **29**:2 (2001), 164–172.
- [Fung 1993] Y. C. Fung, *Biomechanics: mechanical properties of living tissues*, 2nd ed., Springer, New York, 1993.
- [Haut 1989] R. C. Haut, "The effects of orientation and location on the strength of dorsal rat skin in high and low speed tensile failure experiments", *J. Biomech. Eng. (ASME)* **111**:2 (1989), 136–140.
- [Hollenstein et al. 2011] M. Hollenstein, A. E. Ehret, M. Itsikov, and E. Mazza, "A novel experimental procedure based on pure shear testing of dermatome-cut samples applied to porcine skin", *Biomech. Model. Mechanobiol.* **10**:5 (2011), 651–661.

- [Itskov and Ehret 2009] M. Itskov and A. E. Ehret, "A universal model for the elastic, inelastic and active behaviour of soft biological tissues", *GAMM-Mitt.* **32**:2 (2009), 221–236.
- [Khatyr et al. 2004] F. Khatyr, C. Imberdis, P. Vescovo, D. Varchon, and J.-M. Lagarde, "Model of the viscoelastic behaviour of skin *in vivo* and study of anisotropy", *Skin Res. Technol.* **10**:2 (2004), 96–103.
- [Langer 1861] K. Langer, "Zur Anatomie und Physiologie der Haut, I: Über die Spaltbarkeit der Cutis", *Sitzungsber. Kais. Akad. Wiss. Math.-Naturwiss. Kl.* **44** (1861), 19–46. In German; translated in "On the anatomy and physiology of the skin, I: The cleavability of the cutis", *Br. J. Plast. Surg.* **31**:1 (1978), 3–8.
- [Lanir and Fung 1974] Y. Lanir and Y. C. Fung, "Two-dimensional mechanical properties of rabbit skin, II: Experimental results", *J. Biomech.* **7**:2 (1974), 171–182.
- [Mathews 1975] M. B. Mathews, *Connective tissue: macromolecular structure and evolution*, edited by A. Kleinzeller et al., Molecular Biology, Biochemistry and Biophysics **19**, Springer, Berlin, 1975.
- [Meyer et al. 1981] W. Meyer, K. Neurand, and B. Radke, "Elastic fibre arrangement in the skin of the pig", *Arch. Dermatol. Res.* **270**:4 (1981), 391–401.
- [Meyer et al. 1982] W. Meyer, K. Neurand, and B. Radke, "Collagen fibre arrangement in the skin of the pig", *J. Anat.* **134**:1 (1982), 139–148.
- [Muñoz et al. 2008] M. J. Muñoz, J. A. Bea, J. F. Rodríguez, I. Ochoa, J. Grasa, A. Pérez del Palomar, P. Zaragoza, R. Osta, and M. Doblaré, "An experimental study of the mouse skin behaviour: damage and inelastic aspects", *J. Biomech.* **41**:1 (2008), 93–99.
- [Mullins 1947] L. Mullins, "Effect of stretching on the properties of rubber", *J. Rubber Res.* **16** (1947), 275–289.
- [Naghdi and Trapp 1975] P. M. Naghdi and J. A. Trapp, "The significance of formulating plasticity theory with reference to loading surfaces in strain space", *Int. J. Eng. Sci.* **13**:9–10 (1975), 785–797.
- [Nava et al. 2004] A. Nava, E. Mazza, O. Haefner, and M. Bajka, "Experimental observation and modelling of preconditioning in soft biological tissues", *Lect. Notes Comput. Sci.* **3078** (2004), 1–9.
- [Payne 1991] P. A. Payne, "Measurement of properties and function of skin", *Clin. Phys. Physiol. Meas.* **12**:2 (1991), 105–129.
- [Reihsner et al. 1995] R. Reihsner, B. Balogh, and E. J. Menzel, "Two-dimensional elastic properties of human skin in terms of an incremental model at the *in vivo* configuration", *Med. Eng. Phys.* **17**:4 (1995), 304–313.
- [Ridge and Wright 1966] M. D. Ridge and V. Wright, "The directional effects of skin: a bio-engineering study of skin with particular reference to Langer's lines", *J. Investig. Dermatol.* **46**:4 (1966), 341–346.
- [Rubin and Bodner 2002] M. B. Rubin and S. R. Bodner, "A three-dimensional nonlinear model for dissipative response of soft tissue", *Int. J. Solids Struct.* **39**:19 (2002), 5081–5099.
- [Schröder and Neff 2003] J. Schröder and P. Neff, "Invariant formulation of hyperelastic transverse isotropy based on polyconvex free energy functions", *Int. J. Solids Struct.* **40**:2 (2003), 401–445.
- [Sverdlik and Lanir 2002] A. Sverdlik and Y. Lanir, "Time-dependent mechanical behavior of sheep digital tendons, including the effects of preconditioning", *J. Biomech. Eng. (ASME)* **124**:1 (2002), 78–84.
- [Tong and Fung 1976] P. Tong and Y.-C. Fung, "The stress-strain relationship for the skin", *J. Biomech.* **9**:10 (1976), 649–657.
- [Truesdell and Noll 1965] C. Truesdell and W. Noll, *Die nicht-linearen Feldtheorien der Mechanik*, edited by S. Flügge, Handbuch der Physik **III/3**, Springer, Berlin, 1965.
- [Vardaxis et al. 1997] N. J. Vardaxis, T. A. Brans, M. E. Boon, R. W. Kreis, and L. M. Marres, "Confocal laser scanning microscopy of porcine skin: implications for human wound healing studies", *J. Anat.* **190**:4 (1997), 601–611.
- [Veronda and Westmann 1970] D. R. Veronda and R. A. Westmann, "Mechanical characterization of skin: finite deformations", *J. Biomech.* **3**:1 (1970), 111–124.
- [Xu et al. 2008] F. Xu, T. J. Lu, and K. A. Seffen, "Biothermomechanical behavior of skin tissue", *Acta Mech. Sinica* **24**:1 (2008), 1–23.

Received 1 Jul 2010. Revised 10 Dec 2010. Accepted 10 Jan 2011.

ALEXANDER E. EHRET: ehret@km.rwth-aachen.de

*Department of Continuum Mechanics, RWTH Aachen University, 52056 Aachen, Germany*

MARC HOLLENSTEIN: [mhollenstein@ethz.ch](mailto:mhollenstein@ethz.ch)

*Institute for Mechanical Systems, ETH Zurich, 8092 Zurich, Switzerland*

EDOARDO MAZZA: [emazza@ethz.ch](mailto:emazza@ethz.ch)

*Institute for Mechanical Systems, ETH Zurich, 8092 Zurich, Switzerland*

and

*EMPA, 8600 Dübendorf, Switzerland*

MIKHAIL ITSKOV: [itskov@km.rwth-aachen.de](mailto:itskov@km.rwth-aachen.de)

*Department of Continuum Mechanics, RWTH Aachen University, 52056 Aachen, Germany*



## ANALYSIS OF NONSTATIONARY RANDOM PROCESSES USING SMOOTH DECOMPOSITION

RUBENS SAMPAIO AND SERGIO BELLIZZI

Orthogonal decompositions provide a powerful tool for stochastic dynamics analysis. The most popular decomposition is the Karhunen–Loëve decomposition (KLD), also called proper orthogonal decomposition. KLD is based on the eigenvectors of the correlation matrix of the random field. Recently, a modified KLD called smooth Karhunen–Loëve decomposition (SD) has appeared in the literature. It is based on a generalized eigenproblem defined from the covariance matrix of the random process and the covariance matrix of the associated time-derivative random process. SD appears to be an interesting tool to extend modal analysis. Although it does not satisfy the optimality relation of KLD, and maybe is not as good a candidate for building reduced models as KLD is, SD gives access to the modal vectors independently of the mass distribution. In this paper, the main properties of SD for nonstationary random processes are explored. A discrete nonlinear system is studied through its linearization, for uncorrelated and correlated excitation, and the SD of the nonlinear system and of the linearization are compared. It seems that SD detects not only mass inhomogeneities but also nonlinearities.

### 1. Introduction

The Karhunen–Loëve decomposition (KLD) method has been extensively used as a tool for analyzing random fields [Holmes et al. 1996; Lin et al. 2002; Wolter et al. 2002; Kerschen et al. 2005]. KLD reveals some coherent structures which have been advantageously used in different domains such as, for example, the stochastic finite elements method, simulation of random fields, modal analysis of nonlinear systems, and construction of reduced-order models. Depending on the discipline and the properties of the random field under study, but also on the averaging operator used to build the KLD [Bellizzi and Sampaio 2006; 2007], this decomposition has been called principal component analysis, singular value decomposition (these two in finite dimensions), and proper orthogonal decomposition. In the definition of KLD there are two inner products, one given by the normalization condition involving the standard inner product and another by the correlation; the latter, like the former, is a symmetric operator. Orthogonality is meant with respect to the normalization condition. In structural vibration, KLD has been principally applied to the displacement field, but it can be applied also to the velocity, acceleration, and displacement-velocity fields [Bellizzi and Sampaio 2009a].

Recently, a new multivariable data analysis method called smooth orthogonal decomposition (SOD) has been proposed [Chelidze and Zhou 2006]. SOD is defined from a maximization problem associated with a scalar time series of measurement but subject to a minimization constraint acting on the associated

---

The authors gratefully acknowledge the financial support of CNPq, Faperj, and the cooperation project 672/10 financed by CAPES and COFECUB..

**Keywords:** smooth decomposition, output only modal analysis, linear and nonlinear systems.

time derivative of the time series. SOD can be used to extract normal modes and natural frequencies of multi-degree of freedom vibration systems [Zhou 2006]. Free and forced sinusoidal responses have been considered in [Chelidze and Zhou 2006] and randomly excited systems have been analyzed in [Farooq and Feeny 2008]. SOD has been formulated in term of a smooth Karhunen–Loève decomposition (SKLD) to analyze time-continuous stationary random processes in [Bellizzi and Sampaio 2009b]. The SKLD is obtained solving a generalized eigenproblem defined from the covariance matrix of the random process and the covariance matrix of its time derivative. In this paper the SKLD will be referred to as smooth decomposition (SD) since it neither has the properties of a Karhunen–Loève decomposition nor is it orthogonal in the sense of the standard inner product. There is, indeed, orthogonality with respect to inner products defined by the two correlations, displacement and velocity, as we shall see.

This work presents and discusses a nontrivial generalization of SD for time-continuous nonstationary random processes. This generalization is based on an averaging operator combining the temporal mean and mathematical expectation to build the covariance matrices of the random process and of its time derivative.

This paper is organized as follows: Section 2 extends the SD for nonstationary processes, Section 3 extends the proprieties of the SD for the nonstationary case, Section 4 gives a mechanical interpretation of the SD, Section 5 shows some numerical examples, and, finally, Section 6 presents some conclusions.

## 2. Smooth decomposition

Our goal here is to extend to nonstationary time processes the smooth decomposition introduced in [Bellizzi and Sampaio 2009b] as a smooth Karhunen–Loève decomposition for stationary random processes.

Let  $\{\mathbf{U}(t), t \in \mathbb{R}\}$  be a  $\mathbb{R}^n$ -valued random process indexed by  $\mathbb{R}$ . We assume that  $\{\mathbf{U}(t), t \in \mathbb{R}\}$  is a second-order process and admits a time-derivative process  $\{\dot{\mathbf{U}}(t), t \in \mathbb{R}\}$  which is also a second-order process. With these assumptions, the covariance matrices of  $\{\mathbf{U}(t), t \in \mathbb{R}\}$  and  $\{\dot{\mathbf{U}}(t), t \in \mathbb{R}\}$ , denoted  $\mathbf{R}_U(t) = \mathbb{E}(\mathbf{U}(t)^T \mathbf{U}(t))$  and  $\mathbf{R}_{\dot{U}}(t) = \mathbb{E}(\dot{\mathbf{U}}(t)^T \dot{\mathbf{U}}(t))$ , respectively, are time dependent. Without loss of generality, we will also assume that  $\{\mathbf{U}(t), t \in \mathbb{R}\}$  is a zero-mean random process and that  $\mathbf{R}_U(t)$  and  $\mathbf{R}_{\dot{U}}(t)$  are symmetric positive definite.

In the case of stationary processes (that is,  $\mathbf{R}_U(t)$  and  $\mathbf{R}_{\dot{U}}(t)$  do not depend on time), the smooth decomposition of  $\{\mathbf{U}(t), t \in \mathbb{R}\}$  is defined (see [Bellizzi and Sampaio 2009b]) recursively by the maximum optimization problem

$$\max_{\Gamma \in \mathbb{R}^n} \frac{\mathbb{E}(\langle \mathbf{U}(t), \Gamma \rangle^2)}{\mathbb{E}(\langle \dot{\mathbf{U}}(t), \Gamma \rangle^2)}, \quad (2-1)$$

where  $\langle \cdot \rangle$  denotes the inner product in  $\mathbb{R}^n$ .

In the case of nonstationary processes, the objective function (see (2-1)) is time dependent and as in [Bellizzi and Sampaio 2006], where KLD has been proposed for nonstationary random processes, the time variable has to be included in the averaging operation. Let  $t_i$  and  $t_f$  be two positive constants with  $t_i < t_f$ . The ratio

$$\frac{\frac{1}{t_f - t_i} \int_{t_i}^{t_f} \mathbb{E}(\langle \mathbf{U}(t), \Gamma \rangle^2) dt}{\frac{1}{t_f - t_i} \int_{t_i}^{t_f} \mathbb{E}(\langle \dot{\mathbf{U}}(t), \Gamma \rangle^2) dt} \quad (2-2)$$

can be considered to define the smooth decomposition. The objective function (2-2) can be written

$$\frac{\Gamma^T \mathfrak{R}_U^{t_i, t_f} \Gamma}{\Gamma^T \mathfrak{R}_{\dot{U}}^{t_i, t_f} \Gamma}, \quad (2-3)$$

where

$$\mathfrak{R}_U^{t_i, t_f} = \frac{1}{t_f - t_i} \int_{t_i}^{t_f} \mathbf{R}_U(t) dt, \quad \mathfrak{R}_{\dot{U}}^{t_i, t_f} = \frac{1}{t_f - t_i} \int_{t_i}^{t_f} \mathbf{R}_{\dot{U}}(t) dt, \quad (2-4)$$

showing that the quotient depends on the covariance matrices of  $\{\mathbf{U}(t), t \in [t_f, t_i]\}$  and  $\{\dot{\mathbf{U}}(t), t \in [t_f, t_i]\}$ . The vectors that yield the extrema of

$$\max_{\Gamma \in \mathbb{R}^n} \frac{\Gamma^T \mathfrak{R}_U^{t_i, t_f} \Gamma}{\Gamma^T \mathfrak{R}_{\dot{U}}^{t_i, t_f} \Gamma} \quad (2-5)$$

are solutions of the eigenproblem

$$\mathfrak{R}_U^{t_i, t_f} \Gamma_k = \sigma_k \mathfrak{R}_{\dot{U}}^{t_i, t_f} \Gamma_k. \quad (2-6)$$

The SD of the random process will then be given by

$$\mathbf{U}(t) = \sum_{k=1}^n \zeta_k(t) \Gamma_k, \quad (2-7)$$

where the vectors  $\Gamma_k$  solve the generalized eigenproblem (2-6) and the scalar random processes,  $\zeta_k(t)$ , are given by

$$\zeta_k(t) = \frac{\Gamma_k^T \mathfrak{R}_U^{t_i, t_f} \mathbf{U}(t)}{\Gamma_k^T \mathfrak{R}_{\dot{U}}^{t_i, t_f} \Gamma_k} = \frac{\Gamma_k^T \mathfrak{R}_{\dot{U}}^{t_i, t_f} \mathbf{U}(t)}{\Gamma_k^T \mathfrak{R}_{\dot{U}}^{t_i, t_f} \Gamma_k}. \quad (2-8)$$

Note that the scalar processes  $\{\zeta_k(t)\}$  can be defined from either  $\mathfrak{R}_{\dot{U}}^{t_i, t_f}$  or  $\mathfrak{R}_U^{t_i, t_f}$ ; that is, they do not depend on which of these two covariance matrices is used.

The following notation is used: the eigenvalues  $\sigma_k$  are called the smooth values (SVs) ( $\Sigma = \text{diag}(\sigma_k)$ ), the eigenvectors  $\Gamma_k$  are called the smooth modes (SMs) ( $\Gamma = [\Gamma_1 \Gamma_2 \cdots \Gamma_n]$ ), and the scalar random processes  $\{\zeta_k(t)\}$  are called the smooth components (SCs). All these quantities depend on the time interval  $[t_i, t_f]$ .

The generalized eigenproblem (2-6) is a *temporal* version (for nonstationary random processes) of the generalized eigenvalue problem introduced in [Bellizzi and Sampaio 2009b] to characterize the SD of the stationary process. In addition, in the definition (2-6) only the *generalized* covariance matrices  $\mathfrak{R}_U^{t_i, t_f}$  and  $\mathfrak{R}_{\dot{U}}^{t_i, t_f}$  are used, no other operator is necessary. It is important (and trivial) to note that, if the random process is stationary, the covariance matrices reduce to the stationary ones (as described in [Bellizzi and Sampaio 2009b]) and, if the vector signal is deterministic, the covariance matrices reduce to the time-average ones (as described in [Chelidze and Zhou 2006]). We will show that the results are, of course, similar to the ones presented in [Chelidze and Zhou 2006; Farooq and Feeny 2008; Bellizzi and Sampaio 2009b], but now, since one relies on the covariance matrices, one has a powerful computation tool not available before (see, for example, [Quaranta et al. 2008]).

Finally, the quotient used to define the SD differs significantly from that used to define the classical Karhunen–Loëve decomposition [Bellizzi and Sampaio 2006]. In the SD case, the denominator takes

the covariance matrix of the time-derivative process  $\{\dot{\mathbf{U}}(t), t \in \mathbb{R}\}$  into account which justifies the name *smooth* decomposition since the idea is to have a small rate-of-variation of the process.

### 3. Some properties of smooth decomposition

The classical properties as established in the case of stationary processes [Bellizzi and Sampaio 2009b] are extended to the nonstationary case.

**3A. Properties of SV, SM, and SC.** The matrices  $\mathfrak{R}_U^{t_i, t_f}$  and  $\mathfrak{R}_{\dot{U}}^{t_i, t_f}$  being symmetric positive definite implies that all the SVs (eigenvalues)  $\nu_k$  are strictly positive and the set of the vectors  $\boldsymbol{\Gamma}_k$  (the SMs) constitutes a basis which is orthogonal with respect to both covariance matrices  $\mathfrak{R}_U^{t_i, t_f}$  and  $\mathfrak{R}_{\dot{U}}^{t_i, t_f}$ . Note that the SMs are unique up to a scaling constant.

The scalar processes  $\{\zeta_k(t), t \in \mathbb{R}\}$  are correlated:

$$\frac{1}{t_f - t_i} \int_{t_i}^{t_f} \mathbb{E}(\zeta_k(t)\zeta_l(t)) dt = \frac{\boldsymbol{\Gamma}_k^T \mathfrak{R}_U^{t_i, t_f} \mathfrak{R}_U^{t_i, t_f} \mathfrak{R}_U^{t_i, t_f} \boldsymbol{\Gamma}_l}{\boldsymbol{\Gamma}_k^T \mathfrak{R}_U^{t_i, t_f} \boldsymbol{\Gamma}_k \boldsymbol{\Gamma}_l^T \mathfrak{R}_U^{t_i, t_f} \boldsymbol{\Gamma}_l} = \frac{\boldsymbol{\Gamma}_k^T \mathfrak{R}_{\dot{U}}^{t_i, t_f} \mathfrak{R}_{\dot{U}}^{t_i, t_f} \mathfrak{R}_{\dot{U}}^{t_i, t_f} \boldsymbol{\Gamma}_l}{\boldsymbol{\Gamma}_k^T \mathfrak{R}_{\dot{U}}^{t_i, t_f} \boldsymbol{\Gamma}_k \boldsymbol{\Gamma}_l^T \mathfrak{R}_{\dot{U}}^{t_i, t_f} \boldsymbol{\Gamma}_l}. \quad (3-1)$$

So, the SVs are not related to energy distribution and, of course, the SD does not satisfy the standard optimality relationship as the Karhunen–Loëve decomposition does. So, properly speaking, the SD is not a Karhunen–Loëve decomposition. The introduction of regularity has then its drawbacks.

**3B. Linear transformation of the SD.** Let  $\{\mathbf{V}(t), t \in [t_i, t_f]\}$  be a  $\mathbb{R}^n$ -valued random process defined as

$$\mathbf{V}(t) = \mathbf{A}\mathbf{U}(t), \quad (3-2)$$

where  $\mathbf{A}$  is an invertible matrix.

From the relations  $\mathbf{R}_V(t) = \mathbf{A}\mathbf{R}_U(t)\mathbf{A}^T$  and  $\mathbf{R}_{\dot{V}}(t) = \mathbf{A}\mathbf{R}_{\dot{U}}(t)\mathbf{A}^T$  it can be shown that the SVs of  $\{\mathbf{V}(t), t \in [t_i, t_f]\}$  coincide with the SVs of  $\{\mathbf{U}(t), t \in [t_i, t_f]\}$  and the sets of the SMs satisfy

$$\boldsymbol{\Gamma}_k(V) = \mathbf{A}^{-T} \boldsymbol{\Gamma}_k(U), \quad (3-3)$$

where  $\boldsymbol{\Gamma}_k(U)$  (respectively,  $\boldsymbol{\Gamma}_k(V)$ ) denotes a SM of  $\{\mathbf{U}(t), t \in [t_i, t_f]\}$  (respectively, of  $\{\mathbf{V}(t), t \in [t_i, t_f]\}$ ). Finally, following (2-8), the SCs are invariant with respect to linear change of variables if and only if  $\mathbf{A}\mathbf{A}^T = \mathbf{I}$ .

### 4. Mechanical interpretation of the SD

**4A. Discrete linear case.** Consider a discrete mechanical system with  $n$  degrees of freedom. Let  $\mathbf{U}(t)$  be the displacement vector at instant  $t$ . We assume that  $\mathbf{U}(t)$  satisfies the initial-value problem

$$\mathbf{M}\ddot{\mathbf{U}}(t) + \mathbf{C}\dot{\mathbf{U}}(t) + \mathbf{K}\mathbf{U}(t) = \mathbf{F}(t), \quad t \in [0, t_f], \quad (4-1)$$

$$\mathbf{U}(0) = \mathbf{U}_0, \quad \dot{\mathbf{U}}(0) = \dot{\mathbf{U}}_0, \quad (4-2)$$

where  $\mathbf{M}$ ,  $\mathbf{C}$ , and  $\mathbf{K}$  are symmetric square matrices with dimensions  $n \times n$ . The vectors  $\mathbf{U}_0$  and  $\dot{\mathbf{U}}_0$  define the initial conditions of the motion at  $t = 0$ , and  $\{\mathbf{F}(t), t \in [0, t_f]\}$  is a random vector process. Without loss of generality, we have assumed that  $t_i = 0$ .

The linear normal modes (LNM) are classically defined from the free responses of the associated undamped system as

$$\mathbf{K}\mathbf{8} = \mathbf{M}\mathbf{8}\Omega^2,$$

where  $\mathbf{8} = [\mathbf{8}_1 \cdots \mathbf{8}_i \cdots \mathbf{8}_n]$  denotes the modal matrix with the normalization condition  $\mathbf{8}^T \mathbf{M} \mathbf{8} = \mathbf{I}$  which implies that  $\mathbf{8}^T \mathbf{K} \mathbf{8} = \Omega^2 = \text{diag}(\omega_i^2)$  ( $\omega_i^2$  and  $\mathbf{8}_i$  denote the squared resonance frequencies and the associated normal-mode vectors).

Here we focus on (4-1) with proportional damping. Note that in this case the matrix  $\mathbf{8}^T \mathbf{C} \mathbf{8}$  is also diagonal. In this section the aim is to establish when and how the SMs and the SVs, defined in Section 2 (which were based on forced responses), can be used to determine the LNM. This part of the study, which is in line with the results presented in [Kerschen and Golinval 2002; Wolter et al. 2002; Feeny and Liang 2003; Chelidze and Zhou 2006], will be restricted to the case where the excitation is a white-noise random process with zero mean (that is,  $\mathbf{R}_F(\tau) = \mathbb{E}(\mathbf{F}(t + \tau)\mathbf{F}^T(t)) = \mathbf{S}_F\delta(\tau)$ , where  $\mathbf{S}_F$  is a constant symmetric matrix) and the initial conditions ( $\mathbf{U}_0$  and  $\dot{\mathbf{U}}_0$ ) are two random vectors with zero mean.

**4A1. SD and modal analysis.** Introducing the modal-displacement vector  $\mathbf{Q}(t)$  with

$$\mathbf{U}(t) = \Phi \mathbf{Q}(t) = \sum_{i=1}^n \Phi_i Q_i(t), \quad (4-3)$$

the equation of motion (4-1) can be equivalently replaced by

$$\ddot{\mathbf{Q}}(t) + \Theta \dot{\mathbf{Q}}(t) + \Omega^2 \mathbf{Q}(t) = \Phi^T \mathbf{F}(t), \quad t \in [0, t_f], \quad (4-4)$$

with  $\Theta = \Phi^T \mathbf{C} \Phi = \text{diag}(2\tau_i \omega_i)$ .

The evolution of the covariance matrix,  $\mathbf{R}_{\mathbb{Q}}(t) = \mathbb{E}(\mathbb{Q}(t)\mathbb{Q}^T(t))$ , of  $\mathbb{Q}(t) = (\mathbf{Q}^T(t), \dot{\mathbf{Q}}^T(t))^T$  is given by (see, for example, in [Bellizzi and Sampaio 2006])

$$\dot{\mathbf{R}}_{\mathbb{Q}}(t) = \mathbf{A}_{\mathbb{Q}} \mathbf{R}_{\mathbb{Q}}(t) + \mathbf{R}_{\mathbb{Q}}(t) \mathbf{A}_{\mathbb{Q}}^T + \mathbf{D}_{\mathbb{Q}}, \quad t \in [0, t_f], \quad (4-5)$$

$$\mathbf{R}_{\mathbb{Q}}(0) = \mathbf{R}_{\mathbb{Q}_0}, \quad (4-6)$$

where

$$\mathbf{A}_{\mathbb{Q}} = \begin{pmatrix} \mathbf{0} & \mathbf{I} \\ -\Theta & -\Omega^2 \end{pmatrix}, \quad \mathbf{D}_{\mathbb{Q}} = \begin{pmatrix} \mathbf{0} & \mathbf{0} \\ \mathbf{0} & \Phi^T \mathbf{S}_F \Phi \end{pmatrix},$$

and  $\mathbf{R}_{\mathbb{Q}_0}$  is easily deduced from  $\mathbf{R}_{\mathbb{U}_0} = \mathbb{E}(\mathbb{U}_0 \mathbb{U}_0^T)$  with  $\mathbb{U} = (\mathbf{U}_0^T, \dot{\mathbf{U}}_0^T)^T$ .

If the matrix  $\Phi^T \mathbf{S}_F \Phi$  is diagonal (that is, if the modal-excitation terms  $\Phi_i^T \mathbf{F}(t)$  in (4-4) are uncorrelated) and if  $\mathbf{R}_{\mathbb{Q}_0}$  is also diagonal then, from (4-5), it can be shown that the covariance matrix  $\mathbf{R}_{\mathbb{Q}}(t)$  is partitioned into four blocks and each block is a  $n \times n$  diagonal matrix. Hence, for all  $t \in [0, t_f]$ , the covariance matrices  $\mathbf{R}_{\mathbf{Q}}(t)$  and  $\mathbf{R}_{\dot{\mathbf{Q}}}(t)$  of the transient responses  $\{\mathbf{Q}(t), t \in [0, t_f]\}$  and  $\{\dot{\mathbf{Q}}(t), t \in [0, t_f]\}$  are diagonal. Integrating over  $[0, t_f]$  we deduce that the generalized covariance matrices  $\mathfrak{R}_{\mathbf{Q}}^{0,t_f}$  and  $\mathfrak{R}_{\dot{\mathbf{Q}}}^{0,t_f}$  are also diagonal.

Solving (2-6), the SMs associated with  $\{\mathbf{Q}(t), t \in [0, t_f]\}$  are equal to the vectors of the canonical basis of  $\mathbb{R}^n$ . Now using the linear relation (4-3), we can easily deduce (see (3-3)) that the SMs of  $\{\mathbf{U}(t), t \in [0, t_f]\}$  are given by

$$\boldsymbol{\Gamma} = \Phi^{-T}, \quad \text{where } \boldsymbol{\Gamma} = [\boldsymbol{\Gamma}_1 \cdots \boldsymbol{\Gamma}_n]. \quad (4-7)$$

We have here extended the result established in [Bellizzi and Sampaio 2009b] for the stationary case. Unfortunately, in the case of transient responses, it is not possible to relate the SVs ( $\Sigma$ ) to natural frequencies of the mechanical system as it is the case for stationary responses where, under the same assumption on  $\Phi^T \mathbf{S}_F \Phi$ , the following relationship holds:

$$\Sigma = (\Omega^2)^{-1}. \quad (4-8)$$

It is interesting to note that, as indicated in [Chelidze and Zhou 2006], no assumption on the mass matrix  $\mathbf{M}$  is needed to relate the LNM to the SMs.

**4A2. Influence of the mass inhomogeneity on the SM.** An interesting property of the SMs is their sensitivity to mass inhomogeneity. Combining the two equations

$$\Gamma = \Phi^{-T}, \quad \Phi^T \mathbf{M} \Phi = \mathbf{I},$$

the SM matrix reads as  $\Gamma = \mathbf{M} \Phi$ . In the case of mass inhomogeneity—that is, when the mass matrix is diagonal with entries  $m_i$ , with not all the  $m_i$  equal—then each SM  $\Gamma_k$  differs from a LNM  $\Phi_k$  by a scaling vector factor characterizing the mass inhomogeneity, that is,

$$\Gamma_k = \mathbf{V}_{\mathbf{M}} \cdot \Phi_k, \quad (4-9)$$

where  $\mathbf{V}_{\mathbf{M}} = (m_1, \dots, m_n)^T$  and “.” denotes the element-by-element product.

This relationship can be used in practice to localize the mass dispersion comparing the SMs and the column vectors of  $\Gamma^{-T}$ . This analysis can be implemented knowing only the covariance matrices of the displacement and velocity processes.

**4A3. Influence of the correlation coefficient between modal excitation terms.** As we have seen above SD can be used to obtain the LNM if the modal excitation terms  $\Phi_i^T \mathbf{F}(t)$  are uncorrelated. In this section we will discuss the influence of the correlation coefficient between modal excitation terms considering transient responses.

Let us take a two-degree of freedom linear system of (4-1) and (4-2) with proportional damping. We assume that the matrix  $\Phi^T \mathbf{S}_F \Phi$  is not diagonal and reads

$$\Phi^T \mathbf{S}_F \Phi = \begin{pmatrix} \sigma_{11} & \rho \sqrt{\sigma_{11}\sigma_{22}} \\ \rho \sqrt{\sigma_{11}\sigma_{22}} & \sigma_{22} \end{pmatrix}, \quad (4-10)$$

where  $\sigma_{11}$  and  $\sigma_{22}$  denote the modal input level and  $\rho$  the associated correlation coefficient.

We focus on the associated modal equation (4-4) where  $\omega_i$  and  $\tau_i$  (for  $i = 1, 2$ ) denote the resonance frequencies and the associated damping ratios.

We first consider the stationary case. The covariance matrix  $\hat{\mathbf{R}}_{\mathbb{Q}}$  of the stationary response is defined from the following Lyapunov equation:

$$\mathbf{A}_{\mathbb{Q}} \hat{\mathbf{R}}_{\mathbb{Q}} + \hat{\mathbf{R}}_{\mathbb{Q}} \mathbf{A}_{\mathbb{Q}}^T + \mathbf{D}_{\mathbb{Q}} = 0. \quad (4-11)$$

Solving (4-11) gives for  $\hat{\mathbf{R}}_Q$  and  $\hat{\mathbf{R}}_{\dot{Q}}$ :

$$\hat{R}_{Q_{11}} = \frac{\sigma_{11}}{4\tau_1\omega_1^3}, \quad \hat{R}_{Q_{22}} = \frac{\sigma_{22}}{4\tau_2\omega_2^3}, \quad \hat{R}_{Q_{12}} = \rho_{Q_{12}}\sqrt{\hat{R}_{Q_{11}}\hat{R}_{Q_{22}}}, \quad (4-12)$$

$$\hat{R}_{\dot{Q}_{11}} = \frac{\sigma_{11}}{4\tau_1\omega_1}, \quad \hat{R}_{\dot{Q}_{22}} = \frac{\sigma_{22}}{4\tau_2\omega_2}, \quad \hat{R}_{\dot{Q}_{12}} = \rho_{\dot{Q}_{12}}\sqrt{\hat{R}_{\dot{Q}_{11}}\hat{R}_{\dot{Q}_{22}}}, \quad (4-13)$$

with

$$\rho_{Q_{12}} = \rho \frac{8\tau_1^2 r_\omega \sqrt{r_\tau r_\omega} (1 + r_\tau r_\omega)}{(1 - r_\omega^2)^2 + 4\tau_1^2(1 + r_\tau r_\omega)(r_\tau + r_\omega)r_\omega}, \quad \rho_{\dot{Q}_{12}} = \rho \frac{4\sqrt{r_\tau r_\omega}}{1 + r_\tau r_\omega}, \quad r_\tau = \frac{\tau_2}{\tau_1}, \quad r_\omega = \frac{\omega_2}{\omega_1}.$$

Introducing the ratio  $r_\sigma = \sigma_{22}/\sigma_{11}$ , the stationary covariance matrices take the form

$$\hat{\mathbf{R}}_Q = \frac{\sigma_{11}}{4\tau_1\omega_1^3} \begin{pmatrix} 1 & \rho_{Q_{12}}\sqrt{\frac{r_\sigma}{r_\tau r_\omega^3}} \\ \rho_{Q_{12}}\sqrt{\frac{r_\sigma}{r_\tau r_\omega^3}} & \frac{r_\sigma}{r_\tau r_\omega^3} \end{pmatrix}, \quad \hat{\mathbf{R}}_{\dot{Q}} = \frac{\sigma_{11}}{4\tau_1\omega_1} \begin{pmatrix} 1 & \rho_{\dot{Q}_{12}}\sqrt{\frac{r_\sigma}{r_\tau r_\omega}} \\ \rho_{\dot{Q}_{12}}\sqrt{\frac{r_\sigma}{r_\tau r_\omega}} & \frac{r_\sigma}{r_\tau r_\omega} \end{pmatrix}, \quad (4-14)$$

showing that the SVs of the stationary response defined from the generalized eigenproblem,

$$\hat{\mathbf{R}}_Q \Gamma_k = \sigma_k \hat{\mathbf{R}}_{\dot{Q}} \Gamma_k, \quad (4-15)$$

depend only on the modal damping  $(\tau_1, \tau_2)$ , modal frequency ratio  $r_\omega$ , modal input level ratio  $r_\sigma$ , and the correlation coefficient  $\rho$ . Moreover, the SMs (that is, the eigenvectors  $\Gamma_k$ ) do not depend on the absolute values of the modal frequencies  $(\omega_1, \omega_2)$ .

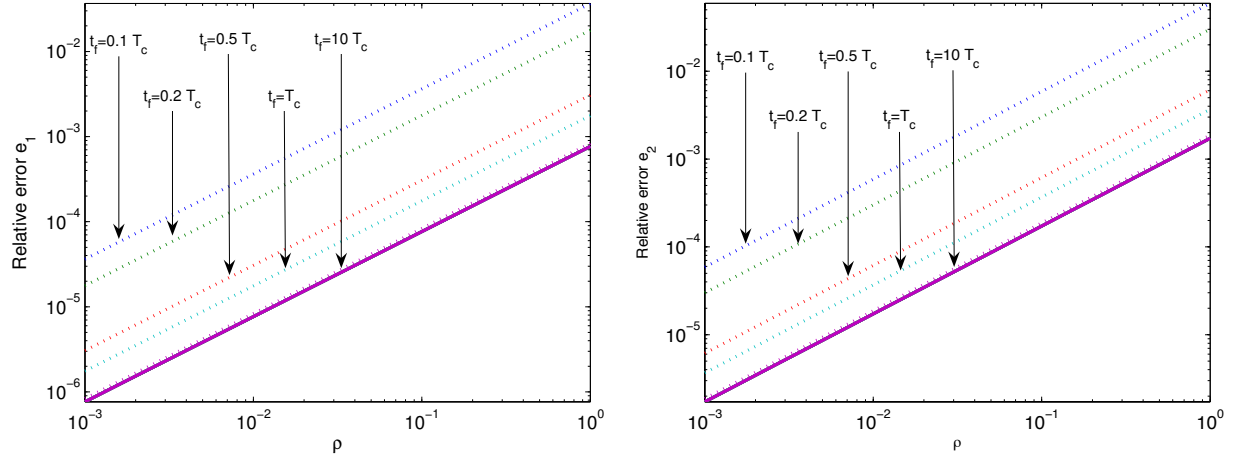
We now consider the nonstationary case assuming zero initial conditions ( $\mathbf{Q}(t) = 0$  and  $\dot{\mathbf{Q}}(t) = 0$ ). As introduced in Section 2, the SD is defined from the generalized covariance matrices

$$\mathfrak{R}_Q^{0,t_f} = \frac{1}{t_f} \int_0^{t_f} \mathbf{R}_Q(t) dt, \quad \mathfrak{R}_{\dot{Q}}^{0,t_f} = \frac{1}{t_f} \int_0^{t_f} \mathbf{R}_{\dot{Q}}(t) dt, \quad (4-16)$$

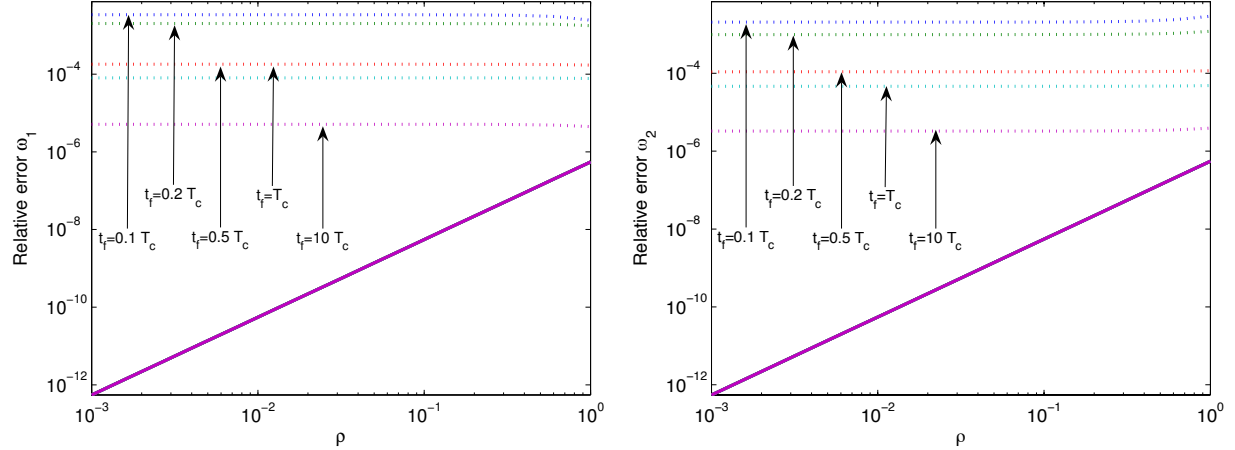
where  $\mathbf{R}_Q(t)$  and  $\mathbf{R}_{\dot{Q}}(t)$  solve (4-5) over  $[0, t_f]$ . Numerical investigations are reported below for  $\omega_1 = 1$ ,  $r_\omega = 1.5$ ,  $\tau_1 = 0.01$ ,  $r_\tau = 1$ ,  $\sigma_{11} = 1$ , and  $r_\sigma = 1$ . We discuss the influence of the correlation coefficient  $\rho$  between the modal excitations and the influence of  $t_f$  on the SD. The time constant of the mechanical system is used as a time unit. The time constant is defined by  $T_c = \max(1/(\tau_1\omega_1), 1/(\tau_2\omega_2))$ .

Figure 1 shows the relative errors between the canonical vectors  $e_1 = (1, 0)^T$  and  $e_2 = (0, 1)^T$  (the LNMs of (4-4)) and the approximations of these LNMs given by the SMs of the transient response  $\{\mathbf{Q}(t), t \in [0, t_f]\}$  using (4-7), plotted versus the correlation coefficient  $\rho$  and for different values of  $t_f$  ( $t_f = 0.1T_c, 0.2T_c, 0.5T_c, T_c$ , and  $10T_c$ ). First of all, in all the simulation results, the relative errors are small (less than 0.1) and, of course, the worse case corresponds to  $\rho = 1$  and  $t_f$  small. As expected, for a given  $t_f$ , the relative error decreases as  $\rho$  decreases. When  $t_f$  increases the SD coincides with the SD given by the stationary response (see the continuous line in Figure 1).

Under the same simulation conditions, Figure 2 shows the relative errors between the resonance frequencies  $\omega_1 = 1$  and  $\omega_2 = 1.5$  and the approximation of these resonance frequencies given by the SMs of the transient response  $\{\mathbf{Q}(t), t \in [0, t_f]\}$  using (4-8). Here also the relative errors are very small (less than 0.001). Moreover, for fixed  $t_f$ , the relative error does not depend on  $\rho$  and decreases when  $t_f$  increases.



**Figure 1.** Relative error (using Euclidean norm vector) between the canonical vector ( $e_1 = (1, 0)^T$  (left) and  $e_2 = (0, 1)^T$  (right)) and the approximation of these LNM given by the SMs of the transient response  $\{Q(t), t \in [0, t_f]\}$  using (4-7) (dotted lines) and the approximation of these LNM given by the SMs of the stationary response (continuous line).



**Figure 2.** Relative error between the natural resonance-frequency vector ( $\omega_1$  (left) and  $\omega_2$  (right)) and the approximation of these LNM given by the SMs of the transient response  $\{Q(t), t \in [0, t_f]\}$  using (4-8) (dotted lines) and the approximation of these LNM given by the SMs of the stationary response (continuous line).

**4B. Discrete nonlinear case.** Consider a discrete mechanical system with  $n$  degrees of freedom. Let  $\mathbf{U}(t)$  be the displacement vector at the instant  $t$ . We assume that  $\mathbf{U}(t)$  satisfies the initial-value problem

$$\mathbf{M}\ddot{\mathbf{U}}(t) + \mathbf{H}(\dot{\mathbf{U}}(t), \mathbf{U}(t)) = \mathbf{F}(t), \quad t \in [0, t_f] \quad (4-17)$$

$$\mathbf{U}(0) = \mathbf{U}_0, \quad \dot{\mathbf{U}}(0) = \dot{\mathbf{U}}_0, \quad (4-18)$$

where  $\mathbf{M}$  is a symmetric square matrix with dimension  $n \times n$  and  $\mathbf{H}$  is a  $n$ -vector smooth nonlinear function. The vectors  $\mathbf{U}_0$  and  $\dot{\mathbf{U}}_0$  define the initial conditions of the motion at  $t = 0$ , and  $\{\mathbf{F}(t), t \in [0, t_f]\}$  is a random vector process.

One rather interesting result was the difference between the SM obtained using the SD of the stationary response of the nonlinear system and the SM obtained using the SD of the stationary response of the equivalent linear system obtained using statistical linearization, as described in [Kozin 1988].

Rewriting (4-17) as a nonlinear first-order differential equation (for  $\mathbb{U}(t) = (\mathbf{U}(t)^T, \dot{\mathbf{U}}(t)^T)^T$ )

$$\dot{\mathbb{U}}(t) = \mathbf{N}(\mathbb{U}(t)) + \mathbf{G}(t), \quad (4-19)$$

with external random excitation  $\mathbf{G}(t) = (0, (\mathbf{M}^{-1}\mathbf{F}(t))^T)^T$ . A suitable equivalent linear system can be written as

$$\dot{\mathbb{U}}(t) = \mathbf{L}_{\text{eq}}\mathbb{U}(t) + \mathbf{G}(t), \quad (4-20)$$

where the constant matrix  $\mathbf{L}_{\text{eq}}$  is determined by

$$\min_{\mathbf{L}} E(\|\mathbf{N}(\mathbb{U}(t)) - \mathbf{L}\mathbb{U}(t)\|^2). \quad (4-21)$$

Under the assumption that the nonlinear system (4-19) admits a stationary ergodic probability measure, it can be shown [Kozin 1988] that the stationary covariance matrix of the nonlinear response (4-19) coincides with the stationary covariance matrix of the equivalent linear response (4-20). Hence, the SD analysis of the stationary response of the nonlinear system (4-17) gives the same results as the SD analysis of the stationary response of the equivalent linear system except for the SCs. Following the modal analysis described in the previous sections, the SD can also be viewed as a tool for modal analysis of the nonlinear system, the SMs and SVs of the nonlinear system being interpreted as in reference to the modal characteristics of the linearized system.

## 5. Numerical example

We consider a finite chain of  $n$  mass points with the first one linked by a linear spring to a fixed point, the others consecutively linked one to the other, and the last one linked only to the previous mass. All the stiffness coefficients of the strings are equal and their common value is 1. The mass values are denoted by  $m_i$  ( $m_i > 0$ ). The system can also include isolated nonlinearities between consecutive masses of the form  $\lambda_i(U_i(t) - U_{i-1}(t))^3$  for  $i = 2, \dots, n$ . The associated equations of motion are of the form of (4-17), with

$$\mathbf{M} = \begin{pmatrix} m_1 & 0 & 0 & \cdots & 0 & 0 \\ 0 & m_2 & 0 & & 0 & 0 \\ 0 & 0 & m_3 & & 0 & 0 \\ \vdots & & & & \vdots & \\ 0 & 0 & 0 & & m_{n-1} & 0 \\ 0 & 0 & 0 & \cdots & 0 & m_n \end{pmatrix}, \quad \mathbf{K} = \begin{pmatrix} 2 & -1 & 0 & \cdots & 0 & 0 \\ -1 & 2 & -1 & & 0 & 0 \\ 0 & -1 & 2 & & 0 & 0 \\ \vdots & & & & \vdots & \\ 0 & 0 & 0 & & 2 & -1 \\ 0 & 0 & 0 & \cdots & -1 & 1 \end{pmatrix}. \quad (5-1)$$

$\mathbf{H}$ , which only depends on  $\mathbf{U}(t)$ , is easily deduced from the form of the nonlinearity. The damping matrix is chosen to be  $\mathbf{C} = 2\tau_1\omega_1\mathbf{M}$ , with  $\tau_1 > 0$ , which assures that the damping is proportional and

fixes the damping ratio of the first linear mode. Note that the linear version of this system has been discussed in [Farooq and Feeny 2008].

Two excitation conditions will be considered:

- Uncorrelated excitation: the system is excited by a standard vector-valued white-noise process with matrix intensity

$$\mathbf{S}_F = S_0 \mathbf{M}, \quad (5-2)$$

with  $S_0 > 0$ . This choice ensures that, for all mass values  $m_i$ ,  $\Phi^T \mathbf{S}_F \Phi = S_0 \mathbf{I}$  is always diagonal.

- Correlated excitation: the system is excited by a white-noise scalar process applied to the mass numbered  $i_{\text{excit}}$ , that is,

$$\mathbf{F}(t) = (0 \cdots 0 1 0 \cdots 0)^T f(t) = \mathbf{P} f(t), \quad (5-3)$$

with  $\{f(t), t \in \mathbb{R}\}$  being a white-noise process with intensity  $S_0 > 0$ . The intensity matrix of  $\{\mathbf{F}(t), t \in \mathbb{R}\}$  is given by  $\mathbf{S}_F = S_0 \mathbf{P} \mathbf{P}^T$  and hence  $\Phi^T \mathbf{S}_F \Phi = S_0 (\Phi_{i_{\text{excit}}} \Phi_{j_i})$  is not a diagonal matrix.

The displacement and velocity histories were obtained from excitation histories by solving (4-17) over  $[0, t_f]$  numerically using the Newmark method. The excitation histories were simulated using the procedure described in [Poirion and Soize 1989]. The following values of parameters were used:  $n = 10$ ,  $m_2 = 2$ , and  $m_i = 1$  for  $i \neq 2$ ,  $\tau_1 = 0.05$ ,  $\lambda_5 = 10$ , and  $\lambda_i = 0$  for  $i \neq 5$ ,  $S_0 = 1$ , and for the correlated case,  $i_{\text{excit}} = 1$ . Zero initial displacement and velocity were assumed. The time-discretization parameter value was chosen equal to  $\Delta t = 0.1$  (that is,  $f_e = 10$ ) and 65536 instants were simulated. The last-half points of the displacement and velocity histories were used to approximate the covariance matrices  $\mathbf{R}_U$  and  $\mathbf{R}_{\dot{U}}$  of the stationary response. The simulated data were also used to estimate  $\mathbf{L}_{\text{eq}}$  solving (4-21) and the SDs of the stationary response of the equivalent linear system (4-20) were computed solving the associated equation (4-11).

The estimated values of the resonance frequencies obtained from SD analysis are reported in Table 1. Note that the expression “resonance frequency” is a misnomer because the system is nonlinear; we will

Underlying linear system	SD from: (4-17)	Uncorrelated case		Correlated case	
		(4-20)	(4-17)	(4-20)	(4-17)
$\omega_1$	0.0236	0.0246	0.0246	0.0243	0.0243
$\omega_2$	0.0665	0.0705	0.0706	0.0696	0.0696
$\omega_3$	0.1068	0.1077	0.1074	0.1076	0.1073
$\omega_4$	0.1515	0.1656	0.1655	0.1626	0.1626
$\omega_5$	0.1960	0.1984	0.1983	0.1977	0.1978
$\omega_6$	0.2327	0.2430	0.2429	0.2418	0.2417
$\omega_7$	0.2491	0.2519	0.2521	0.2513	0.2514
$\omega_8$	0.2740	0.2862	0.2866	0.2850	0.2850
$\omega_9$	0.2980	0.3010	0.3013	0.2996	0.2997
$\omega_{10}$	0.3132	1.0234	1.0240	0.4533	0.4533

**Table 1.** Estimated values of the resonance frequencies obtained from SD analysis.

use it in reference to the associated linearized system. As expected in the uncorrelated case, the estimates obtained from the nonlinear system coincide with those given by the linearized system. These values are very close to the resonance-frequency values of the underlying linear system (that is, with  $\lambda_5 = 0$ ) except for the last value which is larger due to the nonlinear term. The same comments hold also for the correlated case showing that the SD properties are robust to the loss of the noncorrelation assumption. Here also the numerical value of  $\omega_{10}$  is large, resulting in the effect of the nonlinear term which is however smaller than the uncorrelated case.

For the uncorrelated case, the SMs obtained from the stationary responses of the nonlinear system and the linearized system are plotted in Figure 3. As expected in the uncorrelated case (see Section 4A1), the SMs obtained from the nonlinear system coincide with those given by the linearized system. The SMs differ significantly from the normal modes of the underlying linear system, also plotted in the figure. For the first modes, the difference occurs only around the mass number 2 where the mass inhomogeneity is

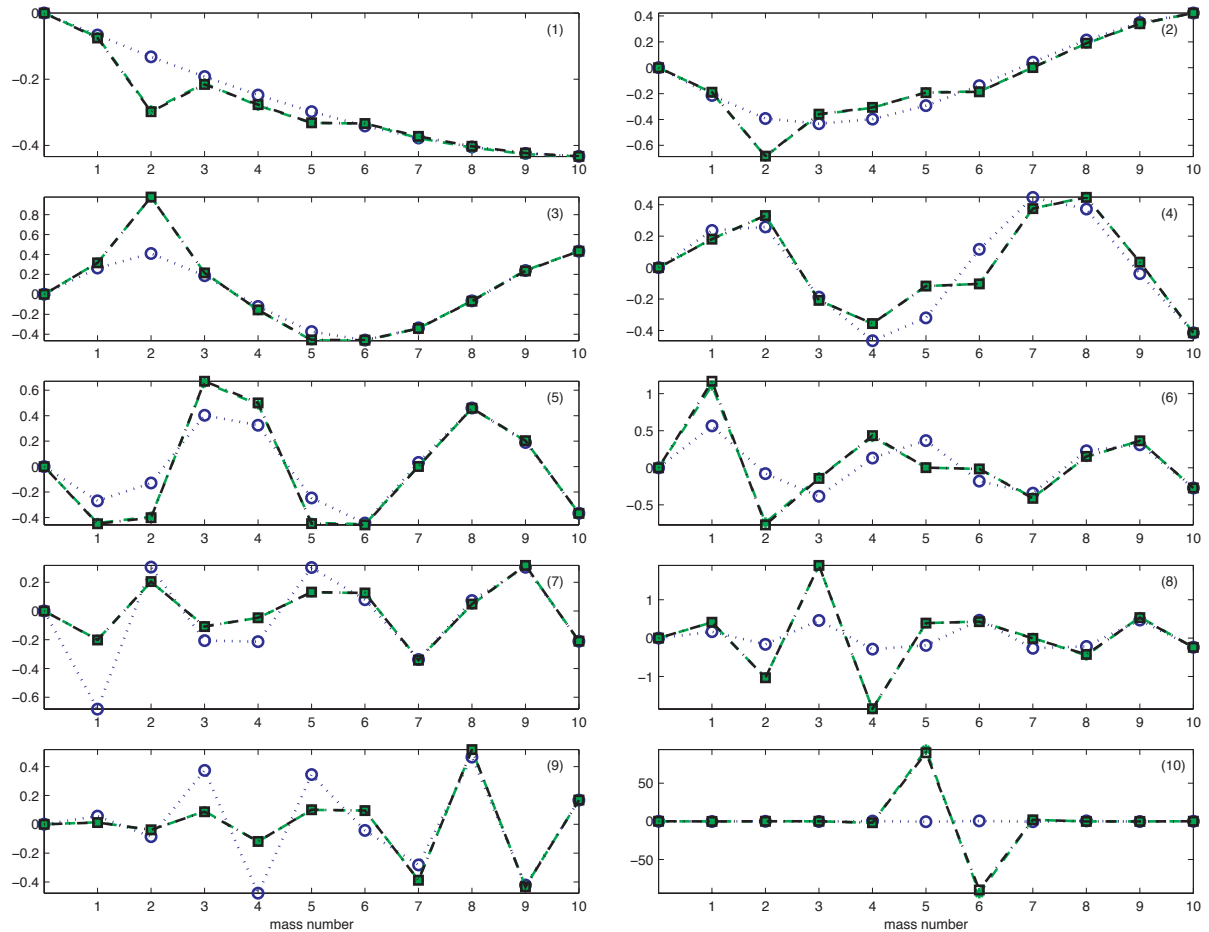


**Figure 3.** Uncorrelated case: the SMs (dashed lines and point markers) and the associated normal modes given by  $\Gamma^{-T}$  (dotted-dashed lines and square markers), see (4-7), obtained from the nonlinear system. The normal modes of the underlying linear system are also reported (dotted lines and circle markers).

present. The relationship between the normal modes and the SMs is in line with (4-9). For the last mode (corresponding to  $\omega_{10}$ ), the difference between the normal mode and the SM occurs around the mass numbers 5 and 6, where there is local nonlinearity. At these two masses the amplitudes of the SMs are very large and have opposite signs. The SMs, then, seem to be also sensitive to the nonlinearity of the system. In Figure 4, the modes obtained from the SMs of the stationary responses of the nonlinear system and the linearized system are plotted and compared to the normal modes of the underlying linear system. The first modes are very similar. The difference increases for the middle and higher modes. For the correlated case, the SMs obtained from the stationary responses of the nonlinear system and the linearized system are plotted in Figure 5 and compared to the normal modes of the underlying linear system. For the middle modes (vector 4 to vector 8), the nonlinear SMs differ from the linearized SMs. Here also, the SMs differ from the normal modes of the underlying linear system where the mass inhomogeneity is present (mass number 2) and where the local nonlinear term acts (mass numbers 5 and 6).

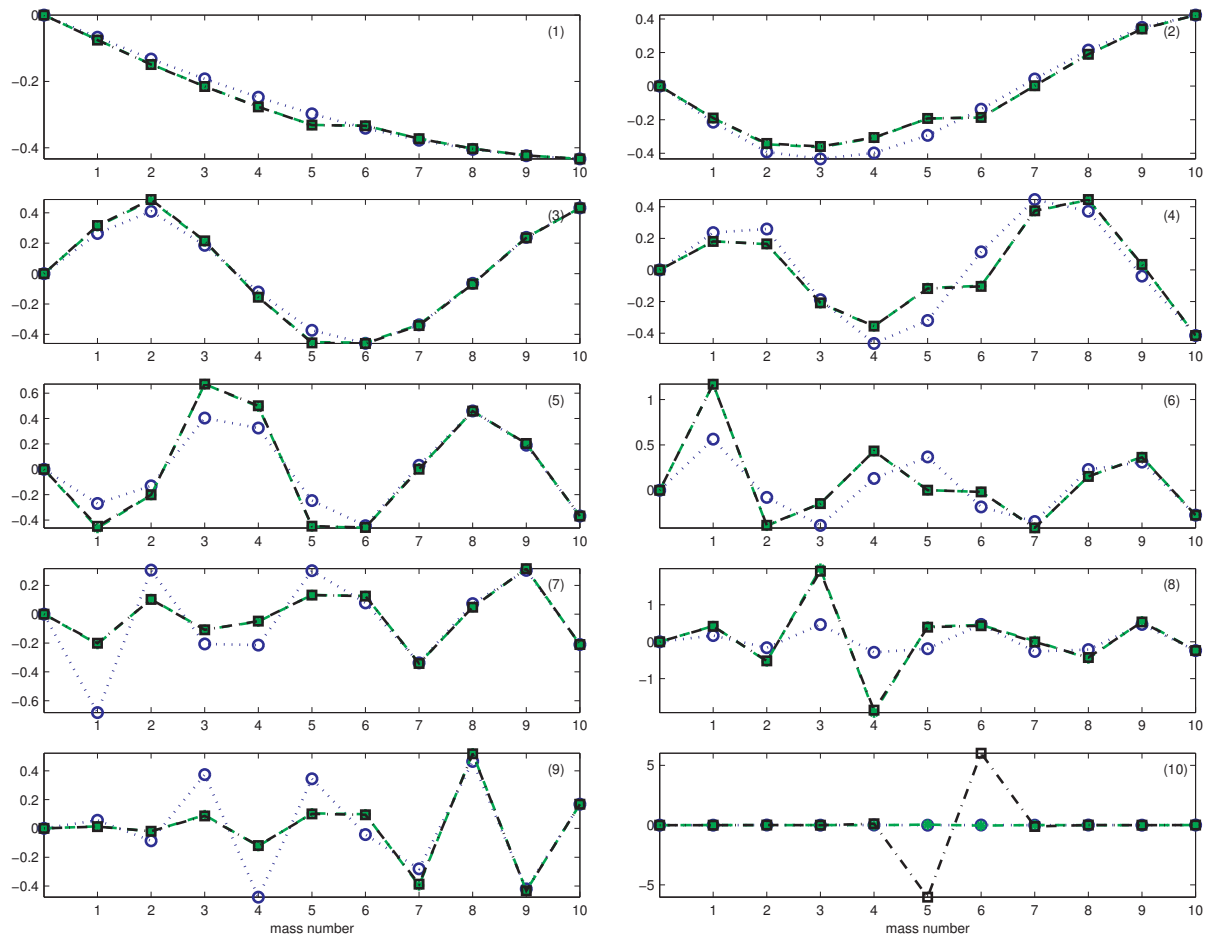


**Figure 4.** Uncorrelated case: the normal modes obtained from the nonlinear system (dashed lines and point markers),  $\Gamma^{-T}$  (see (4-7)), and form the linearized system (dotted-dashed lines and square markers). The normal modes of the underlying linear system are also reported (dotted lines and circle markers).

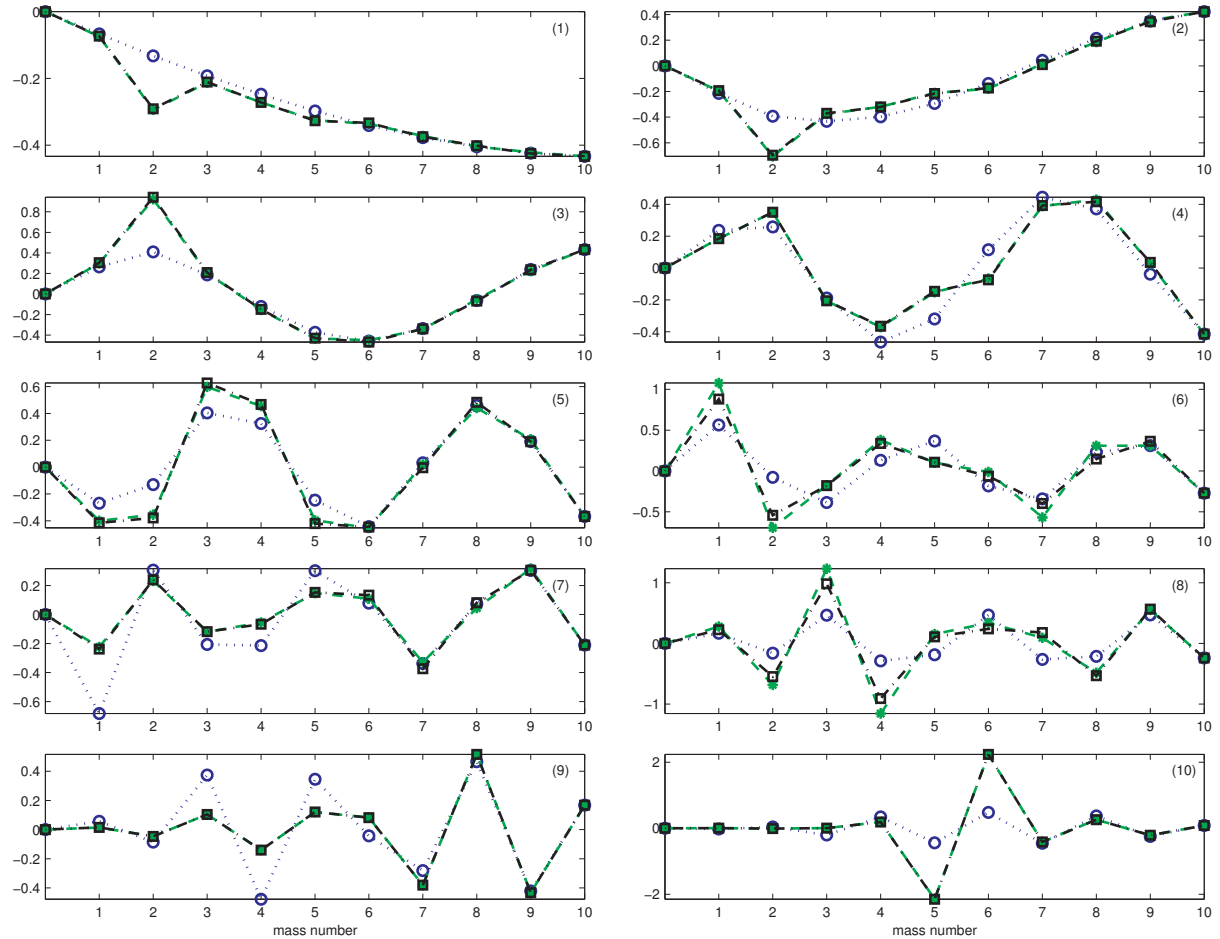


**Figure 5.** Correlated case: the SMs (dashed lines and point markers) and the associated normal modes given by  $\Gamma^{-T}$  (dotted-dashed lines and square markers), see (4-7), obtained from the nonlinear system. The normal modes of the underlying linear system are also reported (dotted lines and circle markers).

In Figure 6, the SMs of the stationary responses of the nonlinear system are compared to the modes obtained from the SMs of the stationary responses of the nonlinear system. Here also, the SMs differ from the approximate normal modes where the mass inhomogeneity is present (mass number 2) and where the local nonlinear term acts (mass numbers 5 and 6). Note that these modes have been obtained only from data. This shows the ability of SD analysis to extract frequency, mode, and mass information.

## 6. Conclusions

In this paper, the smooth orthogonal decomposition method introduced in [Chelidze and Zhou 2006] was formulated in terms of a smooth decomposition (SD) (also called smooth Karhunen–Loëve decomposition in [Bellizzi and Sampaio 2009b]) to analyze time-continuous nonstationary random processes. The SD is obtained by solving a generalized eigenproblem defined by combining the covariance matrix

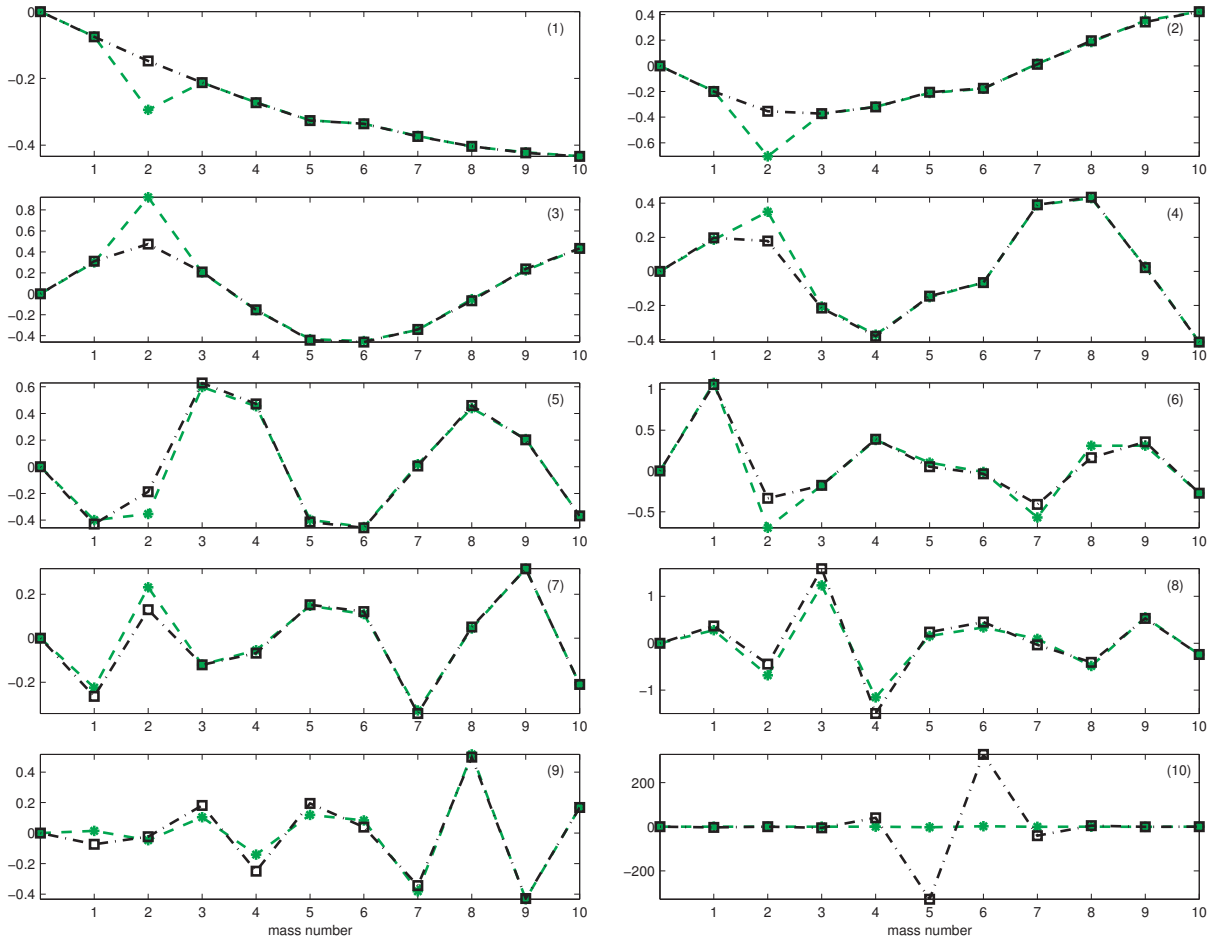


**Figure 6.** Correlated case: the SMs obtained from the nonlinear system (dashed lines and point markers) and the associated normal modes given by  $\Gamma^{-T}$  (dotted-dashed lines and square markers), see (4-7).

of the random field with that of the associated time-derivative random field, a constraint in the rate of variation of the field that originates the term *smooth*. The covariance operator is defined from an averaging operator combining the temporal mean and mathematical expectation which reduces to the mathematical expectation in the case of time-stationary random processes. Note that in this case, the definition has several computational advantages, for example, the use of Lyapunov equations to compute the covariances (see [Bellizzi and Sampaio 2006]). SD does not have the best-decomposition properties of the Karhunen–Loëve decomposition (KLD) and its orthogonality is with respect to the two covariance matrices used in its definition. In the context of output-only modal analysis (that is, without excitation data), SD has several advantages with respect to KLD. If the modal forcing components are not correlated and if the damping is proportional it is possible to estimate, without condition on the mass distribution, normal modes and also, in the stationary case, resonance frequencies directly. This is true independently of the damping level. Note that if the modal forcing components are correlated, the efficiency of the SD

method to estimate resonance frequencies and normal modes rapidly decreases when the damping level increases. Beyond the modal analysis, another interesting property of the SD is that it is possible to extract the mass distribution from the SD comparing the smooth modes (SMs) and the normal modes estimated also from the SMs. Finally, the SD can also be viewed as a tool for modal analysis of nonlinear systems. In the stationary case, the SMs and smooth values (SVs) of the nonlinear response coincide with the SMs and SVs of the response of the equivalent linear system obtained by a statistical linearization approach. Moreover under a constant mass matrix assumption, the SMs give access to the mass distribution.

## References

- [Bellizzi and Sampaio 2006] S. Bellizzi and R. Sampaio, “POMs analysis of randomly vibrating systems obtained from Karhunen–Loève expansion”, *J. Sound Vib.* **297**:3–5 (2006), 774–793.
- [Bellizzi and Sampaio 2007] S. Bellizzi and R. Sampaio, “Analysis of randomly vibrating systems using Karhunen–Loève expansion”, pp. 1387–1395 in *Proceedings of the ASME International Design Engineering Technical Conferences & Computers and Information in Engineering Conference* (Las Vegas, NV, 2007), vol. 1, ASME, New York, 2007. Paper #DETC2007-34431.
- [Bellizzi and Sampaio 2009a] S. Bellizzi and R. Sampaio, “Karhunen–Loève modes obtained from displacement and velocity fields: assessments and comparisons”, *Mech. Syst. Signal Process.* **23**:4 (2009), 1218–1222.
- [Bellizzi and Sampaio 2009b] S. Bellizzi and R. Sampaio, “Smooth Karhunen–Loève decomposition to analyze randomly vibrating systems”, *J. Sound Vib.* **325**:3 (2009), 491–498.
- [Chelidze and Zhou 2006] D. Chelidze and W. Zhou, “Smooth orthogonal decomposition-based vibration mode identification”, *J. Sound Vib.* **292**:3–5 (2006), 461–473.
- [Farooq and Feeny 2008] U. Farooq and B. F. Feeny, “Smooth orthogonal decomposition for modal analysis of randomly excited systems”, *J. Sound Vib.* **316**:1–5 (2008), 137–146.
- [Feeny and Liang 2003] B. F. Feeny and Y. Liang, “Interpreting proper orthogonal modes of randomly excited vibration systems”, *J. Sound Vib.* **265**:5 (2003), 953–966.
- [Holmes et al. 1996] P. Holmes, J. L. Lumley, and G. Berkooz, *Turbulence, coherent structures, dynamical systems and symmetry*, Cambridge University Press, Cambridge, 1996.
- [Kerschen and Golinval 2002] G. Kerschen and J.-C. Golinval, “Physical interpretation of the proper orthogonal modes using the singular value decomposition”, *J. Sound Vib.* **249**:5 (2002), 849–865.
- [Kerschen et al. 2005] G. Kerschen, J.-C. Golinval, A. F. Vakakis, and L. A. Bergman, “The method of proper orthogonal decomposition for dynamical characterization and order reduction of mechanical systems: an overview”, *Nonlinear Dyn.* **41**:1–3 (2005), 147–169.
- [Kozin 1988] F. Kozin, “The method of statistical linearization for nonlinear stochastic vibrations”, pp. 45–56 in *Nonlinear stochastic dynamic engineering systems (IUTAM Symposium)* (Innsbruck, 1987), edited by F. Ziegler and G. I. Schuëller, Springer, Berlin, 1988.
- [Lin et al. 2002] W. Z. Lin, K. H. Lee, P. Lu, S. P. Lim, and Y. C. Liang, “The relationship between eigenfunctions of Karhunen–Loève decomposition and the modes of distributed parameter vibration system”, *J. Sound Vib.* **256**:4 (2002), 791–799.
- [Poirion and Soize 1989] F. Poirion and C. Soize, “Simulation numérique des champs stochastiques Gaussiens homogènes et non homogènes”, *Rech. Aéosp.* **1** (1989), 41–61.
- [Quaranta et al. 2008] G. Quaranta, P. Maserati, and P. Mantegazza, “Continuous-time covariance approaches for modal analysis”, *J. Sound Vib.* **310**:1–2 (2008), 287–312.
- [Wolter et al. 2002] C. Wolter, M. A. Trindade, and R. Sampaio, “Obtaining mode shapes through the Karhunen–Loève expansion for distributed-parameter linear systems”, *Shock Vib.* **9**:4–5 (2002), 177–192.
- [Zhou 2006] W. Zhou, *Multivariate analysis in vibration modal parameter identification*, Ph.D. thesis, University of Rhode Island, 2006, Available at <http://gradworks.umi.com/32/48/3248248.html>.

Received 20 May 2010. Revised 27 Sep 2010. Accepted 14 Nov 2010.

RUBENS SAMPAIO: [rsampaio@puc-rio.br](mailto:rsampaio@puc-rio.br)

Departamento de Engenharia Mecânica, PUC-Rio, Rua Marquês de São Vicente, 225, 22453-900 Rio de Janeiro-RJ, Brazil

SERGIO BELLIZZI: [bellizzi@lma.cnrs-mrs.fr](mailto:bellizzi@lma.cnrs-mrs.fr)

Laboratoire de Mécanique et d'Acoustique - CNRS, 31 chemin Joseph Aiguier, 13402 Marseille, France

## PERTURBATION STOCHASTIC FINITE ELEMENT-BASED HOMOGENIZATION OF POLYCRYSTALLINE MATERIALS

SEVERINE LEPAGE, FERNANDO V. STUMP, ISAIAH H. KIM AND PHILIPPE H. GEUBELLE

This work presents a study of the influence on the macroscopic (homogenized) elastic properties of polycrystalline materials induced by uncertainties in the material texture and microstructure geometry. Since many microelectromechanical systems are made of materials deposited as thin films with  $\langle 111 \rangle$  fiber texture, we study the variance of the homogenized elastic properties of the material around its nominal  $\langle 111 \rangle$  texture. To perform this analysis, the perturbation stochastic finite element method (PSFEM) is coupled to the mathematical theory of homogenization leading to a second-order perturbation-based homogenization method. This method is able to evaluate the mean and variance of a given homogenized property as a function of the grain property uncertainty. The multiscale formulation is implemented in a plane-stress linear elastic finite element framework based on a multigrain periodic unit cell generated by Voronoi tessellation. This perturbation-based homogenization method is verified against Monte Carlo simulations, showing its effectiveness and limitations. Then, through applications, it is evaluated how different levels of uncertainty in grains induce uncertainty in the macroscopic elastic properties of the polycrystalline material. In particular, the influence of the unit cell is studied. Finally, by coupling the PSFEM with the Monte Carlo method, the effects on the macroscopic properties of uncertainty of both the geometry and orientation of the grains is estimated.

### 1. Introduction

The performance of a microelectromechanical system (MEMS) is affected by uncertainties. Manufacturing processes may leave substantial uncertainties in the shape and geometry of the device, while the material properties of a component are inherently subject to scattering. Moreover, microscale properties are extremely sensitive to process variations. Accuracy and precision of standard processes are difficult to control, so properties vary by recipe, by fabrication run, wafer-to-wafer, and across the wafer. The design of accurate MEMS has to take into account the influence of these uncertainties. This paper focuses on the prediction of material property variability that is inherent in MEMS due to their microfabrication processes. The materials making up MEMS are deposited as thin films. In particular, this work is motivated by the study of texturized gold thin films which are common MEMS materials. Although the electric characterization of metallic thin films is well established, the mechanical characterization of the same films is still a challenge. Moreover, the material properties are dependent on the fabrication process and therefore are not the same as those for the bulk material. The material properties can even be different between runs of the same fabrication process.

One approach to investigating property variability of metallic thin films is to use homogenization methods that allow the evaluation of the macroscopic properties based on the polycrystalline microstructure.

---

*Keywords:* perturbation stochastic finite element, homogenization, Monte Carlo method, polycrystalline material.

By that approach the microscopic features, which are defined by the microfabrication processes, can be taken into account to calculate the macroscopic properties of the film.

The mathematical theory of homogenization (MTH) is a well established multiscale method that provides the equivalent homogeneous material properties for heterogeneous material when the separation of scales works [Bensoussan et al. 1978; Sanchez-Palencia and Zaoui 1987]. The MTH provides the deterministic model which the stochastic finite element scheme will be built upon.

Stochastic finite element methods can be classified into two main categories based on the kind of results they yield. Firstly, reliability methods aim at calculating the failure probability, and hence focus on the tails of the probability density function of the response. Secondly, other methods aim at calculating the probabilistic characterization of the response. In this category, some methods, such as that presented hereafter, determine only the first two statistical moments of the response. For details, see first two statistical moments of the response. For more details, the reader should refer to [Schueller 1997; 2001; Manohar and Ibrahim 1999; Sudret and der Kiureghian 2000; van den Nieuwenhof 2003].

Monte Carlo simulations have the major advantage that accurate statistical solutions can be obtained for any problem whose deterministic solution is known, since they statistically converge to the correct solution provided that a large number of simulations is employed. Indeed, the basic principle of direct Monte Carlo simulation is to generate a sampling of the input parameters according to their probability distributions and correlations. For each input sample, a deterministic finite element analysis is carried out, giving an output sample. Finally, a response sampling is obtained, from which the mean and the standard deviation of the response can be derived. The disadvantage of the direct Monte Carlo method is that it is usually extremely computationally demanding due to the very large number of analyses that have to take place. The convergence rate of the estimator does not only increase by increasing the number of samples but also by decreasing the variance  $\sigma_y^2$ . Variance reduction techniques exploit additional a priori information to reduce the necessary sample size  $n$  for a specified confidence level. Stratification techniques widely used in practice, such as Latin hypercube sampling (LHS) [McKay et al. 1979], use conditional expectations to reduce the variance of the estimator.

The basics of the perturbation stochastic finite element method (PSFEM) are expounded in [Kleiber and Hien 1992]. This method consists in a deterministic analysis complemented by a sensitivity analysis with respect to the random parameters. This permits the development of a Taylor series expansion of the response, from which the mean and variance of the response can be derived knowing the mean, variance, and correlation structure of the random parameters. Depending on the expansion order of the Taylor series expansion (1 or 2), the statistical moments of the response are first or second-order accurate and the method is called the first-order second moment (FOSM) or second-order second moment (SOSM) method, respectively. The main advantages of the PSFEM are its simplicity and applicability to a wide range of problems at low cost. It has been used in static and dynamic elastic analyses [Hien and Kleiber 1990; Kleiber and Hien 1992], buckling analyses [Altus and Totry 2003], composite ply failure problems [Onkar et al. 2007], inelastic deformation studies [Doltsinis and Kang 2006], linear transient heat transfer problems [Hien and Kleiber 1997], the analysis of free vibration of composite cantilevers [Oh and Librescu 1997], nonlinear dynamics [Lei and Qiu 2000], and the study of eigenvalues of structures with uncertain boundary conditions [Huang et al. 2007]. Due to the Taylor series expansion, accurate results are expected only in case of relatively small variability of the parameters and for nearly linear problems. The derivatives of the structural matrices have to be calculated with respect to the random

variables. This can be done analytically, semianalytically, or by finite difference. These computations can be time-consuming, particularly when the second-order terms are included.

The PSFEM has been applied to the homogenization of elastic properties of composite materials such as a bicomponent 1D bar [Kaminski 2000] and unidirectional fiber-reinforced composites [Kaminski and Kleiber 2000; Sakata et al. 2008]. All these applications use random variables which are related to inherent material properties of the composite components. This paper considers polycrystalline material and in particular accounts for the uncertainty resulting from the scattering of constitutive grain orientation. Moreover, the effect of the unit cell size on the macroscopic (homogenized) property variation is investigated as well as the geometry of the grains generated by Voronoi tessellation. The aim of this study is not only to quantify the uncertainty in the macroscopic polycrystalline elastic properties but also to gain confidence in the minimum size required to consider the unit cell as a representative volume element (RVE) of the polycrystalline material. An unit cell is considered as a RVE when the standard deviation of the homogenized properties is below a threshold defined by the analyst. In that case, the unit cell is stochastically representative of the material behavior, that is, the standard deviation of the output represents the uncertainty resulting from the input uncertainty.

After a review of the basics of the finite element implementation of the classical MTH in Section 2, the perturbation stochastic finite element-based homogenization formulation is derived by applying the PSFEM to the homogenization scheme in Section 3. In Section 4, the obtained methodology is first verified against Monte Carlo results for a unit cell of 4 grains in which one random variable is considered. Then, the methodology is applied on multigrain unit cells made of textured gold. This application investigates the influence of unit cell size, grain geometry, and orientation randomness on the macroscopic (homogenized) elastic properties.

## 2. Multiscale model

As described in the previous section, the focus of this work is on quantifying the stochastic nature of the elastic properties of polycrystalline media. More precisely, we aim at assessing how the uncertainties in the material texture (that is, the grain orientation and stiffness) impact its homogenized macroscopic elastic properties. As indicated earlier, the homogenization scheme adopted in this study is based on the finite element implementation of the classical mathematical theory of homogenization (MTH). In this section, the MTH is summarized and the grain-level anisotropic response is described.

Following the classic work [Bensoussan et al. 1978] as well as [Guedes and Kikuchi 1990], we start from a  $y$ -periodic asymptotic expansion of the displacement field

$$\mathbf{u}(\mathbf{x}, \mathbf{y}) \approx \mathbf{u}^{(0)}(\mathbf{x}, \mathbf{y}) + \xi^1 \mathbf{u}^{(1)}(\mathbf{x}, \mathbf{y}) + \xi^2 \mathbf{u}^{(2)}(\mathbf{x}, \mathbf{y}) + \dots, \quad (2-1)$$

where the superscripts in parentheses represent the level in the multiscale expansion, and  $\mathbf{x}$  and  $\mathbf{y}$  label the material points at the macro and microscale, respectively (see Figure 1). The relation between the two scales is defined by the asymptotic parameter  $\xi$  as  $\mathbf{y} = \mathbf{x}/\xi$ , where  $\xi$  roughly corresponds to the size of the periodic unit cell that serves as the basis of the homogenization scheme. Applying the chain rule,

$$\frac{d\varphi(\mathbf{x}, \mathbf{y})}{d\mathbf{x}} = \frac{\partial\varphi(\mathbf{x}, \mathbf{y})}{\partial\mathbf{x}} + \frac{1}{\xi} \frac{\partial\varphi(\mathbf{x}, \mathbf{y})}{\partial\mathbf{y}}, \quad (2-2)$$

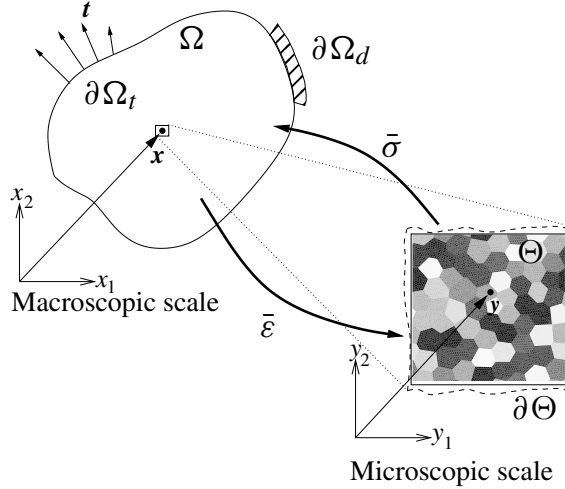


**Figure 1.** Schematic view of the homogenization scheme, with the microscopic scale showing the polycrystalline periodic unit cell.

we obtain the corresponding expansion for the strain tensor

$$\varepsilon_{ij} \approx \xi^{-1} \left( \frac{\partial^S u_i^{(0)}}{\partial y_j} \right) + \xi^0 \left( \frac{\partial^S u_i^{(0)}}{\partial x_j} + \frac{\partial^S u_i^{(1)}}{\partial y_j} \right) + \xi^1 \left( \frac{\partial^S u_i^{(1)}}{\partial x_j} + \frac{\partial^S u_i^{(2)}}{\partial y_j} \right) + \dots, \quad (2-3)$$

where we adopt the symmetric gradient tensor notation

$$\frac{\partial^S \bullet_i}{\partial x_j} = \frac{1}{2} \left( \frac{\partial \bullet_i}{\partial x_j} + \frac{\partial \bullet_j}{\partial x_i} \right). \quad (2-4)$$

For the elastic problem characterized by a local fourth-order material stiffness tensor  $D_{ijkl}$  and tractions  $t$  applied along the portion  $\partial\Omega_t$  of the boundary  $\partial\Omega$ , the principle of virtual work takes the form

$$\int_{\Omega} D_{ijkl} \frac{\partial^S v_i}{\partial x_j} d\Omega - \int_{\partial\Omega_t} t_i v_i d\Omega = 0 \quad (2-5)$$

for all admissible displacements  $v$  satisfying

$$v \in [H^1]^2, \quad v = 0 \text{ on } \partial\Omega_d = \partial\Omega \setminus \partial\Omega_t, \quad (2-6)$$

where  $[H^1]^2$  is the Sobolev space for the 2D problem. Combining (2-3) and (2-5) and grouping the terms by powers of  $\xi$  leads to

$$\frac{1}{\xi^2} \int_{\Omega} D_{ijkl} \frac{\partial^S u_k^{(0)}}{\partial y_l} \frac{\partial^S v_i}{\partial y_j} d\Omega = 0, \quad (2-7)$$

$$\frac{1}{\xi} \int_{\Omega} D_{ijkl} \left[ \left( \frac{\partial^S u_k^{(0)}}{\partial x_l} + \frac{\partial^S u_k^{(1)}}{\partial y_l} \right) \frac{\partial^S v_i}{\partial y_j} + \frac{\partial^S u_k^{(0)}}{\partial y_l} \frac{\partial^S v_i}{\partial x_j} \right] d\Omega = 0, \quad (2-8)$$

$$\int_{\Omega} D_{ijkl} \left[ \left( \frac{\partial^S u_k^{(1)}}{\partial x_l} + \frac{\partial^S u_k^{(2)}}{\partial y_l} \right) \frac{\partial^S v_i}{\partial y_j} + \left( \frac{\partial^S u_k^{(0)}}{\partial x_l} + \frac{\partial^S u_k^{(1)}}{\partial y_l} \right) \frac{\partial^S v_i}{\partial x_j} \right] d\Omega = \int_{\partial\Omega_t} t_i v_i d\Omega. \quad (2-9)$$

As shown in [Guedes and Kikuchi 1990], we establish from (2-7) that  $\mathbf{u}^{(0)}$  is exclusively a function of  $\mathbf{x}$ , that is,

$$\mathbf{u}^{(0)}(\mathbf{x}, \mathbf{y}) = \mathbf{u}^{(0)}(\mathbf{x}), \quad (2-10)$$

while (2-8) leads to the following expression of the equilibrium at the microscale:

$$\frac{1}{|\Theta|} \int_{\Theta} D_{ijkl} \left[ \left( \frac{\partial^S u_k^{(0)}}{\partial x_l} + \frac{\partial^S u_k^{(1)}}{\partial y_l} \right) \frac{\partial^S v_i}{\partial y_j} \right] d\Theta = 0, \quad (2-11)$$

where  $\Theta$  denotes the volume of the periodic unit cell.

Defining the macroscopic strain  $\bar{\epsilon} = \partial^S \mathbf{u}^{(0)} / \partial \mathbf{x}$  and the fluctuation strain  $\tilde{\epsilon} = \partial^S \mathbf{u}^{(1)} / \partial \mathbf{y}$ , we recast (2-11) as

$$\frac{1}{|\Theta|} \int_{\Theta} D_{ijkl} \tilde{\epsilon}_{kl} \frac{\partial^S v_i}{\partial y_j} d\Theta = - \frac{1}{|\Theta|} \int_{\Theta} D_{ijkl} \frac{\partial^S v_i}{\partial y_j} d\Theta \bar{\epsilon}_{kl}, \quad (2-12)$$

where we observe that the macroscopic strain serves as a loading term in the solution for the fluctuation strain. Relation (2-12) allows us to solve for the fluctuation strain at every point in the periodic unit cell, defining the strain localization operator  $G_{ijkl}$  as

$$\tilde{\epsilon}_{ij}(\mathbf{x}, \mathbf{y}) = G_{ijkl}(\mathbf{x}, \mathbf{y}) \bar{\epsilon}_{kl}. \quad (2-13)$$

Finally, the homogenized elastic properties of the polycrystalline material can be extracted from the equilibrium equation (2-9). Assuming that  $v_i$  is a function of  $\mathbf{x}$  only, (2-9) reduces to [Guedes and Kikuchi 1990]

$$\int_{\Omega} \left[ \frac{1}{|\Theta|} \int_{\Theta} D_{ijkl} (\bar{\epsilon}_{kl} + \tilde{\epsilon}_{kl}) d\Theta \right] \frac{\partial^S v_i}{\partial x_j} d\Omega = \int_{\partial\Omega} t_i v_i d\partial\Omega, \quad (2-14)$$

or, combining with (2-13),

$$\int_{\Omega} \left[ \frac{1}{|\Theta|} \int_{\Theta} D_{ijkl} (I_{klmn} + G_{klmn}) d\Theta \right] \bar{\epsilon}_{mn} \frac{\partial^S v_i}{\partial x_j} d\Omega = \int_{\partial\Omega} t_i v_i d\partial\Omega, \quad (2-15)$$

where  $I_{klmn} = \frac{1}{2} (\delta_{km} \delta_{ln} + \delta_{kn} \delta_{lm})$ . From (2-15), we identify the homogenized elastic tensor  $D_{ijkl}^h$  as

$$D_{ijmn}^h = \frac{1}{|\Theta|} \int_{\Theta} D_{ijkl} (I_{klmn} + G_{klmn}) d\Theta. \quad (2-16)$$

For the finite element implementation of this homogenization scheme, it is more convenient to recast (2-16) using the Voigt formulation (that is, in matrix notation) as

$$\mathbf{D}^h = \frac{1}{|\Theta|} \sum_{e=1}^n \int_{\Theta^e} (\mathbf{D}^e \mathbf{I} + \mathbf{D}^e \mathbf{G}^e) d\Theta, \quad (2-17)$$

where the domain  $\Theta$  has been subdivided into  $n$  elements and the superscript  $e$  denotes the local value in element  $e$ .

In this notation, the stiffness tensor of a material with cubic symmetry, such as the face centered cubic material of interest in this work, is given by

$$\mathbf{D}_c^e = \begin{bmatrix} C_{11} & C_{12} & C_{12} & 0 & 0 & 0 \\ C_{12} & C_{11} & C_{12} & 0 & 0 & 0 \\ C_{12} & C_{12} & C_{11} & 0 & 0 & 0 \\ 0 & 0 & 0 & C_{44} & 0 & 0 \\ 0 & 0 & 0 & 0 & C_{44} & 0 \\ 0 & 0 & 0 & 0 & 0 & C_{44} \end{bmatrix}, \quad (2-18)$$

in a coordinate system attached to each crystal (or grain) as denoted by the subscript  $c$ . To transform the stiffness matrix into the sample coordinate system (denoted by the subscript  $s$ ), we adopt the Bunge convention and introduce the triad  $(\phi_1, \theta, \phi_2)$ , defining the individual rotation matrices

$$\mathbf{R}_1 = \begin{bmatrix} \cos \phi_1 & \sin \phi_1 & 0 \\ -\sin \phi_1 & \cos \phi_1 & 0 \\ 0 & 0 & 1 \end{bmatrix}, \quad \mathbf{R}_2 = \begin{bmatrix} 1 & 0 & 0 \\ 0 & \cos \theta & \sin \theta \\ 0 & -\sin \theta & \cos \theta \end{bmatrix}, \quad \mathbf{R}_3 = \begin{bmatrix} \cos \phi_2 & \sin \phi_2 & 0 \\ -\sin \phi_2 & \cos \phi_2 & 0 \\ 0 & 0 & 1 \end{bmatrix}.$$

The resulting rotation matrix from the crystal coordinate system to the sample one is given by

$$\mathbf{Q} = (\mathbf{R}_3 \mathbf{R}_2 \mathbf{R}_1)^T. \quad (2-19)$$

The rotation of the forth-order tensor  $D_{ijmn}$  denoted  $\mathbf{D}$  in matrix notation is then expressed as

$$\mathbf{D}_s^e = \mathbf{K} \mathbf{D}_c^e \mathbf{K}^T, \quad (2-20)$$

while the compliance matrix  $\mathbf{S}_c^e = (\mathbf{D}_c^e)^{-1}$  is transformed as

$$\mathbf{S}_s^e = (\mathbf{K}^{-1})^T \mathbf{S}_c^e \mathbf{K}^{-1}. \quad (2-21)$$

In (2-20) and (2-21),  $\mathbf{K}$  is given by [Ting 1996]

$$\mathbf{K} = \begin{bmatrix} \mathbf{K}_1 & 2\mathbf{K}_2 \\ \mathbf{K}_3 & \mathbf{K}_4 \end{bmatrix}, \quad (2-22)$$

where

$$\mathbf{K}_1 = \begin{bmatrix} Q_{11}^2 & Q_{12}^2 & Q_{13}^2 \\ Q_{21}^2 & Q_{22}^2 & Q_{23}^2 \\ Q_{31}^2 & Q_{32}^2 & Q_{33}^2 \end{bmatrix}, \quad \mathbf{K}_2 = \begin{bmatrix} Q_{12}Q_{13} & Q_{13}Q_{11} & Q_{11}Q_{12} \\ Q_{22}Q_{23} & Q_{23}Q_{21} & Q_{21}Q_{22} \\ Q_{32}Q_{33} & Q_{33}Q_{31} & Q_{31}Q_{32} \end{bmatrix}, \quad \mathbf{K}_3 = \begin{bmatrix} Q_{21}Q_{31} & Q_{22}Q_{32} & Q_{23}Q_{33} \\ Q_{31}Q_{11} & Q_{32}Q_{12} & Q_{33}Q_{13} \\ Q_{11}Q_{21} & Q_{12}Q_{22} & Q_{13}Q_{23} \end{bmatrix},$$

$$\mathbf{K}_4 = \begin{bmatrix} Q_{22}Q_{33} + Q_{23}Q_{32} & Q_{23}Q_{31} + Q_{21}Q_{33} & Q_{21}Q_{32} + Q_{22}Q_{31} \\ Q_{32}Q_{13} + Q_{33}Q_{12} & Q_{33}Q_{11} + Q_{31}Q_{13} & Q_{31}Q_{12} + Q_{32}Q_{11} \\ Q_{12}Q_{23} + Q_{13}Q_{22} & Q_{13}Q_{21} + Q_{11}Q_{23} & Q_{11}Q_{22} + Q_{12}Q_{21} \end{bmatrix},$$

with  $Q_{ij}$  denoting the components of  $\mathbf{Q}$  defined in (2-19). To perform the analysis in a plane-stress framework, the compliance matrix is first expressed in the sample coordinate system using (2-21). The

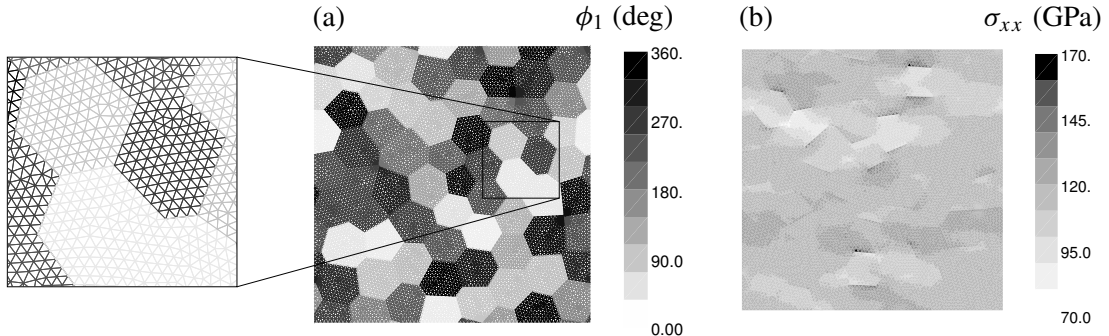


**Figure 2.** For a unit cell with 64 grains: (a) typical  $\phi_1$  distribution and finite element mesh and (b) stress field ( $\sigma_{xx}$ ). The right figure emphasizes the heterogeneous nature of the stress field in the RVE.

plane-stress compliance matrix is then obtained as

$$\mathbf{S}_{s,2D}^e = \begin{bmatrix} S_{s,11} & S_{s,12} & S_{s,16} \\ S_{s,21} & S_{s,22} & S_{s,26} \\ S_{s,61} & S_{s,62} & S_{s,66} \end{bmatrix}, \quad (2-23)$$

where  $S_{s,ab}$  represents component  $ab$  of the 3D compliance matrix  $\mathbf{S}_s^e$  given by (2-21). Finally, the stiffness matrix is found by inverting the compliance matrix:

$$\mathbf{D}_{s,2D}^e = (\mathbf{S}_{s,2D}^e)^{-1}.$$

As stated in Section 1, this work is motivated by the study of textured gold thin films. In this particular case, the material constants are  $C_{11} = 186$  GPa,  $C_{12} = 157$  GPa, and  $C_{44} = 42$  GPa. To represent the  $\langle 111 \rangle$  fiber texture only two Euler angles need to be specified,  $\theta = 54.7^\circ$  and  $\phi_2 = 45^\circ$ . The third angle  $\phi_1$  is not defined and can assume any value, as all grains have the  $\langle 111 \rangle$  pole normal to the surface and the in-plane rotations are random. Here it is important to stress that the  $\phi_1$  values used in the application cases in Section 4 have been randomly chosen. However,  $\phi_1$  is not considered as a random variable of interest in this work since it does not describe the uncertainty of the material texture.

A typical result obtained with the multiscale scheme is presented in Figure 2 for the case of a 64-grain RVE and a macroscopic strain  $\bar{\epsilon}_{xx}$  equal to 1%. The heterogeneous stress field due to angles mismatch for a macroscopic strain of 1% presents a ratio of approximately 2.4 between the maximum and minimum stress values in the RVE.

### 3. Perturbation stochastic FE formulation

A set of stochastic variables enter the finite element-based homogenization scheme described in previous section. These random variables, denoted hereafter by  $\zeta$ , include quantities such as the stiffness and orientation of the grains that compose the periodic unit cell. Our goal in this section is to derive the key quantities entering the PSFEM formulation of the MTH scheme summarized in Section 2. We start from

the stochastic form of the homogenized stiffness matrix (2-17) which is given by

$$\mathbf{D}^h(\zeta) = \frac{1}{|\Theta|} \sum_{e=1}^n \int_{\Theta^e} (\mathbf{D}^e(\zeta) \mathbf{I} + \mathbf{D}^e(\zeta) \mathbf{G}^e(\zeta)) d\Theta, \quad (3-1)$$

where  $\mathbf{G}$  implicitly depends on the uncertainty through

$$\frac{1}{|\Theta|} \int \mathbf{B}^T \mathbf{D}(\zeta) \mathbf{G}^e(\zeta) d\Theta = \frac{1}{|\Theta|} \int \mathbf{B}^T \mathbf{D}(\zeta) d\Theta, \quad (3-2)$$

with  $\mathbf{B}$  denoting the traditional strain-displacement matrix.

The perturbation method considers the random design variables  $b_i$  as perturbed from their expectation  $\bar{b}_i$ , so that the random variables  $b_i$  are written as the sum of a deterministic value  $\bar{b}_i$  and a zero-mean random variable  $\Delta b_i$  as

$$b_i = \bar{b}_i + \Delta b_i. \quad (3-3)$$

The covariance matrix  $\mathbf{C}$  of the random variables  $b_i$  is related to the zero-mean random variables as

$$C_{ij} = \text{Cov}(b_i, b_j) = E[\Delta b_i \Delta b_j]. \quad (3-4)$$

The perturbation method consists in expanding the random quantities about their expectations via a truncated Taylor series expansion. The second-order Taylor expansion about the nominal value  $\bar{\mathbf{b}}$  with respect to the random variables  $b_i$  is given by

$$\mathbf{D}^h(\bar{\mathbf{b}}) \approx \bar{\mathbf{D}}^h + \sum_{i=1}^n \mathbf{D}_{,i}^h \Delta b_i + \frac{1}{2} \sum_{i=1}^n \sum_{j=1}^n \mathbf{D}_{,ij}^h \Delta b_i \Delta b_j, \quad (3-5)$$

where the subscript  $,i$  denotes the derivative with respect to random variable  $b_i$ . Since the random variables  $\Delta b_i$  are zero-mean random variables of known covariance, the expectation of the homogenized property matrix is

$$E[\mathbf{D}^h(\bar{\mathbf{b}})] \approx \bar{\mathbf{D}}^h + \sum_{i=1}^n \mathbf{D}_{,i}^h E[\Delta b_i] + \frac{1}{2} \sum_{i=1}^n \sum_{j=1}^n \mathbf{D}_{,ij}^h E[\Delta b_i \Delta b_j] = \bar{\mathbf{D}}^h + \frac{1}{2} \sum_{i=1}^n \sum_{j=1}^n \mathbf{D}_{,ij}^h \text{Cov}(b_i, b_j), \quad (3-6)$$

while the variance of the homogenized property matrix is expressed as

$$\text{Var}(\mathbf{D}^h(\bar{\mathbf{b}})) = E[(\mathbf{D}^h(\bar{\mathbf{b}}) - E[\mathbf{D}^h(\bar{\mathbf{b}})])^2] \approx \sum_{i=1}^n \sum_{j=1}^n \mathbf{D}_{,i}^h \mathbf{D}_{,j}^h E[\Delta b_i \Delta b_j] = \sum_{i=1}^n \sum_{j=1}^n \mathbf{D}_{,i}^h \mathbf{D}_{,j}^h \text{Cov}(b_i, b_j). \quad (3-7)$$

The mean is second-order accurate with no first-order term in its expression, while the variance is first-order accurate since no second-order term appears in its expression. The variance expression will be the same whether a first-order or a second-order approximation is used in the perturbation method.

The first-order sensitivity of the homogenized property matrix has to be computed. Differentiating (2-17) with respect to  $b_i$  gives

$$\mathbf{D}_{,i}^h(\zeta) = \sum_{e=1}^n \int_{\Theta_e} (\mathbf{D}_{,i}^e(\zeta) \mathbf{I} + \mathbf{D}_{,i}^e(\zeta) \mathbf{G}^e(\zeta) + \mathbf{D}^e(\zeta) \mathbf{G}_{,i}^e(\zeta)) d\Theta, \quad (3-8)$$

where  $\mathbf{G}_{,i}$  is computed by differentiating (3-2) as

$$\int \mathbf{B}^T \mathbf{D}(\zeta) \mathbf{G}_{,i}(\zeta) d\Theta = \int \mathbf{B}^T \mathbf{D}_{,i}(\zeta) d\Theta - \int \mathbf{B}^T \mathbf{D}_{,i}(\zeta) \mathbf{G}(\zeta) d\Theta. \quad (3-9)$$

Similarly, (3-8) gives the second-order sensitivity of  $\mathbf{D}^h$ :

$$\begin{aligned} \mathbf{D}_{,ij}^h(\zeta) &= \sum_{e=1}^n \int_{\Theta^e} (\mathbf{D}_{,ij}^e(\zeta) \mathbf{I} + \mathbf{D}_{,ij}^e(\zeta) \mathbf{G}^e(\zeta)) d\Theta \\ &\quad + \sum_{e=1}^n \int_{\Theta^e} (\mathbf{D}_{,i}^e(\zeta) \mathbf{G}_{,j}^e(\zeta) + \mathbf{D}_{,j}^e(\zeta) \mathbf{G}_{,i}^e(\zeta)) d\Theta + \sum_{e=1}^n \int_{\Theta^e} (\mathbf{D}^e(\zeta) \mathbf{G}_{,ij}^e(\zeta)) d\Theta, \end{aligned} \quad (3-10)$$

where  $\mathbf{G}_{,ij}$  is computed by differentiating (3-9)

$$\begin{aligned} \int \mathbf{B}^T \mathbf{D}(\zeta) \mathbf{G}_{,ij}(\zeta) d\Theta &= \int \mathbf{B}^T \mathbf{D}_{,ij}(\zeta) d\Theta - \int \mathbf{B}^T \mathbf{D}_{,ij}(\zeta) \mathbf{G}(\zeta) d\Theta \\ &\quad - \int \mathbf{B}^T \mathbf{D}_{,i}(\zeta) \mathbf{G}_{,j}(\zeta) d\Theta - \int \mathbf{B}^T \mathbf{D}_{,j}(\zeta) \mathbf{G}_{,i}(\zeta) d\Theta. \end{aligned} \quad (3-11)$$

The quantities of interest, that is, the expectation of the homogenized property (3-6) and its variance (3-7), are obtained by evaluating (3-8) and (3-10) in a finite element framework.

#### 4. Verification

The second-order PSFEM is applied to analyze the influence of uncertainty on the behavior of a cubic material in  $\langle 111 \rangle$  texture. The objective of this section is to verify the PSFEM formulation by comparing its results against Monte Carlo (MC) simulations. For this purpose, we chose to study a small unit cell composed of only 4 grains, shown in Figure 3.

Using the material constants introduced at the end of Section 2, the 2D nominal stiffness matrix of each grain is given by

$$\bar{\mathbf{D}}^c = \begin{bmatrix} 186 & 157 & 0 \\ 157 & 186 & 0 \\ 0 & 0 & 42 \end{bmatrix} \quad (\text{GPa}), \quad (4-1)$$

expressed in its material axes. The Euler angles are set to  $\theta = 54.7^\circ$  and  $\phi_2 = 45^\circ$ , and  $\phi_1$  has randomly assigned values of  $188^\circ$ ,  $289^\circ$ ,  $294^\circ$ , and  $68^\circ$  for grains 1, 2, 3, and 4, respectively.  $C_{11}$ , the first

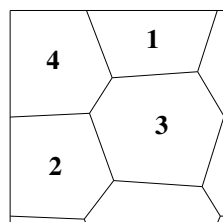


**Figure 3.** Periodic unit cell composed of 4 grains used to perform the verification test case of PSFEM.

CoV (%)	$E[C_{11}^h]$ (GPa) (PSFEM)	$E[C_{11}^h]$ (GPa) (MC, 2000 samples)	$\sqrt{\text{Var}[C_{11}^h]}$ (GPa) (PSFEM)	$\sqrt{\text{Var}[C_{11}^h]}$ (GPa) (MC, 2000 samples)
2	120.0338	120.0052	0.5410	0.5529
4	120.0235	119.8789	1.0820	1.1930
6	120.0133	119.6227	1.6229	2.1429

**Table 1.** Verification test case based on Figure 3 unit cell: PSFEM and MC results for coefficients of variance of 2%, 4%, and 6% of the random variable  $C_{11}$  of grain 1.

component of the stiffness matrix expressed in the material axes of grain 1, is considered as a Gaussian random variable. The effect of the level of uncertainty is studied by successively considering a coefficient of variation,  $\text{CoV}(C_{11})$ , of 2%, 4%, and 6%.

The unit cell is loaded with a tensile strain in direction 1 of the sample coordinate system. This loading allows us to quantify the effect of uncertainty on the first column of the homogenized stiffness matrix expressed in the unit cell axes. The mean and the standard deviation of the homogenized stiffness matrix of the unit cell are computed using (3-6) and (3-7). In this paper, the results are presented for the first component of the homogenized stiffness matrix,  $C_{11}^h$ .

In order to verify the validity of the PSFEM approach, the results are compared to the MC results. A Latin hypercube sampling (LHS) method is used to generate 2000 samples of  $C_{11}$  whose mean and standard deviation correspond to the values specified in the PSFEM study. LHS generates samples of a normally distributed random variable  $s$  with a mean of zero and a standard deviation of one.  $C_{11}$  is then expressed as a function of  $s$ :

$$C_{11} = \bar{C}_{11}(1 + \text{CoV}(C_{11})s). \quad (4-2)$$

Then, the homogenized stiffness matrix is computed for each value of  $C_{11}$ . Finally, the mean and standard deviation of the 2000 samples of  $C_{11}^h$  are computed and compared to PSFEM results.

Table 1 compares the PSFEM and MC values of the mean and standard deviation of  $C_{11}^h$  for the three values of the coefficient of variation. The nominal value of  $C_{11}^h$  is equal to 120.044 GPa, that is, the value of the deterministic analysis. As the coefficient of variation increases, the mean value increasingly deviates from the nominal value even if this difference is not significant. This variation is a quadratic function, as explained previously and shown in Figure 4, left.

Figure 4, right, shows the variation of the relative error of the mean and standard deviation of  $C_{11}^h$  computed by PSFEM with respect to MC values, which are considered as reference values. PSFEM estimation error in both the mean and the standard deviation increases as the coefficient of variation increases because the approximation of the variation of  $C_{11}^h$  as a quadratic function with respect to the uncertainty becomes less appropriate as the level of uncertainty increases.

The error in the mean is smaller than in the standard deviation. This is explained by the fact that the mean estimation is second-order accurate while the standard deviation estimation is only first-order accurate. The error is due to the fact that PSFEM approximates the variation of  $C_{11}^h$  as a second-order polynomial function while, as shown in the left part of Figure 4, the actual variation of  $C_{11}^h$  is more complex. This approximation is thus adequate in the vicinity of the nominal value.

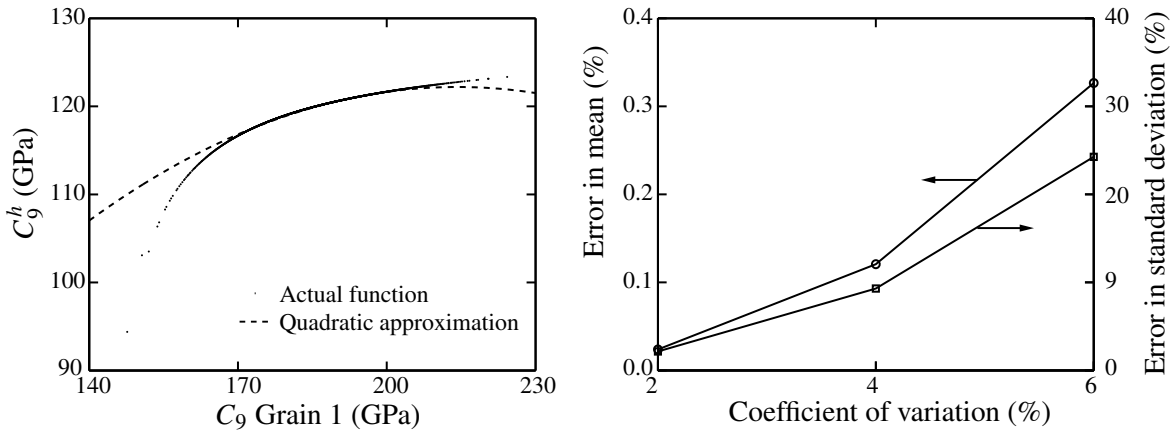


**Figure 4.** Verification test case based on Figure 3 unit cell. Left: variation of  $C_{11}^h$  as a function of the random variable, that is,  $C_{11}$  of grain 1. Right: percentage errors of  $C_{11}^h$  mean and standard deviation between MC and PSFEM analyses for various  $C_{11}$  coefficients of variation.

Another verification test case is to analyze the unit cell represented in Figure 3 assuming  $C_{11}$  of each grain to be a random variable with a coefficient of variation of 3%. The uncertainty is thus characterized by 4 random variables. The correlation between them is modeled by a correlation matrix. Three different correlation matrices are successively investigated. First, the correlation is supposed to be a matrix full of ones, which means that the four random variables are fully correlated and represent one and only one random variable. The opposite case is to set the correlation matrix to be the identity matrix, which is equivalent to considering 4 independent uncorrelated random variables. An intermediate correlation matrix is also studied:

$$\begin{bmatrix} 1 & 0.5 & 0.25 & 0 \\ 0.5 & 1 & 0.5 & 0.25 \\ 0.25 & 0.5 & 1 & 0.5 \\ 0 & 0.25 & 0.5 & 1 \end{bmatrix}. \quad (4-3)$$

Note that such a correlation matrix could result from the representation of  $C_{11}$  as a random field.

Both the mean and standard deviation increase as the correlation of the random variables increases, as can be observed in Figure 5. The reduction of the variance due to the fact that the random parameter is modeled by a random field instead of one random variable is also called the compensation effect on the variability. The verification demonstrates that PSFEM is a suitable tool to quantify the uncertainty of homogenized properties due to microstructural uncertainty. This method also allows us to evaluate the effect of different levels of correlation between the random variables on the macroscopic response.

## 5. Study of geometry and material uncertainty

The second-order PSFEM is applied to the analysis of several unit cells of a cubic material with a  $\langle 111 \rangle$  texture. As explained in Section 2, for  $\langle 111 \rangle$  texture, the Euler angles are  $\theta = 54.7^\circ$  and  $\phi_2 = 45^\circ$ , and  $\phi_1$  has random assigned values. The influence of uncertainty in the  $\theta$  angle of each grain is studied on

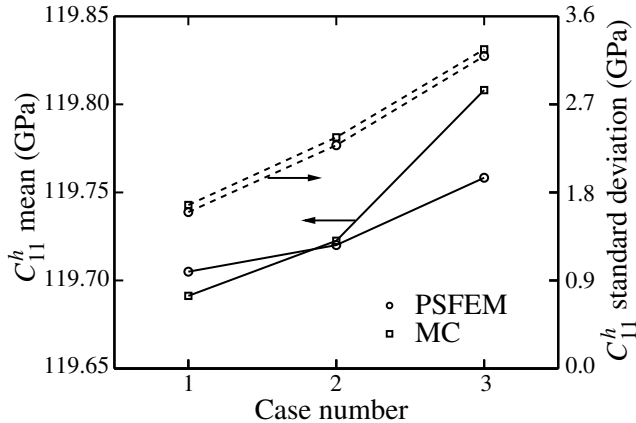


**Figure 5.** Effect of the correlation of random variables on the mean and standard deviation of  $C_{11}^h$ . Case 1: four independent random variables; case 2: correlation matrix (4-3); case 3: one random variable.

the material behavior of periodic unit cells from 4 to 64 grains. In particular, the mean and standard deviation of the homogenized  $C_{11}^h$  are quantified.

**5A. Influence of material texture uncertainty.** To study the influence of texture uncertainty, a unit cell with 16 grains and 16 random variables (one per grain) is generated. The angle  $\theta$  which controls the perpendicularity of the  $\langle 111 \rangle$  pole with respect to the surface of the thin film is chosen as the random variable. The random variables are assumed to be independent. The standard deviation of  $\theta$  is varied from  $2^\circ$  to  $10^\circ$ . In each case, the mean and standard deviation of  $C_{11}^h$  of the unit cell are computed using PSFEM and are compared to the values obtained from MC analysis using 15000 samples. The same finite element model, that is, with the same mesh and grain geometry, is used for the PSFEM and MC analyses.

Figure 6 shows that as the standard deviation increases, the error of the PSFEM approximation increases. The error on the mean remains lower than one percent while the error on the standard deviation varies from 0.73% to 9.84%. As explained previously, PSFEM method relies on a second-order approximation of the response, and so its accuracy is limited within a neighborhood of the expectation value of the random variable. This analysis shows that for the particular problem of interest, the error on the PSFEM is less than 0.73% for the mean and standard deviation when  $\theta$  has a standard deviation of at most  $2^\circ$ . The error on the means remains low for  $\theta$  standard deviation up to  $10^\circ$ , that is, less than one percent, while the error on the standard deviation becomes not negligible, that is, above 5%, once the  $\theta$  standard deviation reaches  $7^\circ$ . This analysis allows us to quantify the limitation of PSFEM on the quantification of the influence of material texture uncertainty.

It should be noted that the CPU requirement associated with the PSFEM is substantially lower than for the MC method since considerably less homogenization problems have to be solved. Therefore, even if PSFEM approximates the response statistics, it allows us to gain valuable knowledge on the macroscopic property uncertainty induced by grain-level uncertainties at a lower cost than the classical MC method. However, it should be noted that if the number of random variables becomes really large, PSFEM's computational cost may be such that using the MC method would be more advantageous.

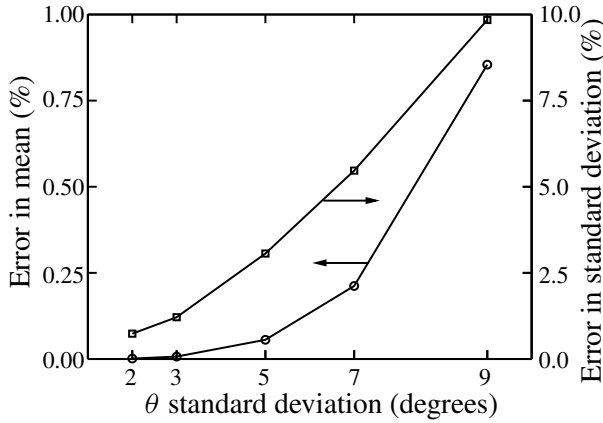


**Figure 6.** Material texture uncertainty study: Percentage errors of  $C_{11}^h$  mean and standard deviation between MC and PSFEM analyses for various  $\theta$  standard deviations on a 16 grain unit cell.

To study the effect of the unit cell size, for a fixed standard deviation of  $\theta$ , the number of grains of the unit cell is varied from 4 to 64. For each unit cell, the mean and standard deviation of  $C_{11}^h$  are evaluated using PSFEM and the MC method. For each unit cell size, MC analyses have been performed for three LHS sets of 8000, 12000, and 15000 samples, respectively. The statistics for  $C_{11}^h$  were obtained from those of the three sets. The results of both methodologies are presented in Figure 7. The maximum error on the mean is 0.0084% while for the standard deviation it is 8.1%. As the unit cell size increases, the standard deviation of  $C_{11}^h$  decreases up to a threshold of 0.31 GPa. The influence of the unit cell size on the standard deviation of  $C_{11}^h$  provides an important parameter to decide to what extent a unit cell can be considered as a RVE. Once the standard deviation of the output reaches a threshold, the unit cell

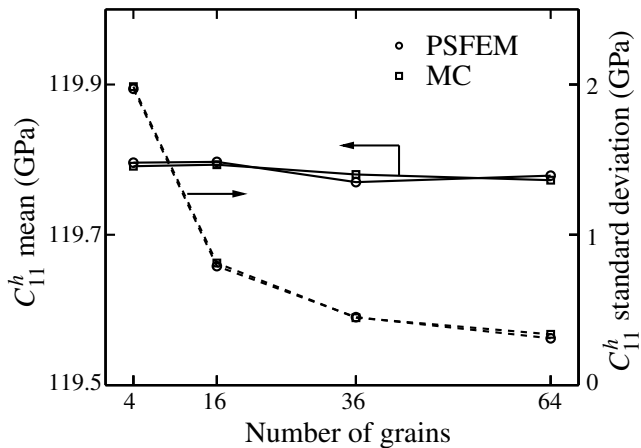


**Figure 7.** Material texture uncertainty study: Effect of unit cell size on MC and PSFEM prediction of the mean (solid curves) and standard deviation (dashed curves) for  $C_{11}^h$  with a standard deviation of  $2^\circ$  in  $\theta$ .

Parameter	Mean (GPa)	Standard deviation (GPa)
$C_{11}^h$	119.782	0.311
$C_{12}^h$	68.2993	0.088
$C_{21}^h$	68.2993	0.088
$C_{22}^h$	119.7785	0.3356

**Table 2.** PSFEM mean and standard deviation of effective components of homogenized stiffness matrix of a unit cell composed of 64 grains with a standard deviation of  $2^\circ$  in  $\theta$ .

can be considered stochastically representative, that is, the standard deviation threshold value represents the uncertainty resulting from the input uncertainty. For this particular case, when the unit cell contains more than 64 grains, it is observed that a textural uncertainty, characterized by a  $2^\circ$  standard deviation, introduces an uncertainty on  $C_{11}^h$  characterized by a 0.31 GPa standard deviation.

All aforepresented results relate to  $C_{11}^h$ . Table 2 lists the mean and standard deviation obtained for other effective components of the homogenized stiffness matrix. The results are for a unit cell composed of 64 grains. For each grain, its  $\theta$  angle is considered as a random variable characterized by a  $2^\circ$  standard deviation. These 64 random variables are considered as independent, which means that their correlation matrix is equal to the identity matrix. The uncertainty introduced on  $C_{11}^h$  and  $C_{22}^h$  are similar: 0.31 GPa and 0.33 GPa, respectively. Conclusions based on one or on the other would be the same. The means of  $C_{12}^h$  and  $C_{21}^h$  are equal as well as their standard deviation. The relative importance of the standard deviation with respect to the mean is twice larger on the diagonal components than on the off-diagonal ones. Based on these facts, the study will hereafter focus on  $C_{11}^h$  results.

**5B. Combining PSFEM and Monte Carlo methods to evaluate geometry and texture uncertainty.** So far, only uncertainty in the material parameters has been considered and PSFEM and MC analyses have been carried out on only one representation of the unit cell. In order to take into account the geometric uncertainty of grains as well as the grains material property randomness, MC and PSFEM are coupled. A standard deviation of  $10^\circ$  is considered for  $\theta$ . The geometry variation is taken into account by using the Monte Carlo method. For each geometry sample, a PSFEM analysis is carried out in order to take into account the material property uncertainty. Using the law of total expectation, the output mean is computed by averaging over the geometry samples the mean obtained by PSFEM:

$$\bar{S} = \frac{\sum_{i_{\text{geo}}}^{n_{\text{geo}}} \bar{S}_{\text{PSFEM}}}{n_{\text{geo}}}. \quad (5-1)$$

By applying the law of total variance, we get the value of the variance of the output as

$$\text{Var}(S) = \text{Var}(\bar{S}_{\text{PSFEM}}) + E[\text{Var}(S)_{\text{PSFEM}}]. \quad (5-2)$$

It is assumed that the randomness of the material properties and the grain geometry are independent.

Monte Carlo analyses are performed for unit cells composed of 4, 16, 36, and 64 grains. For each unit cell size, 100 different geometry samples are generated by an in-house Voronoi tessellation software which can control the mean size of the grains. In this study, the mean grain size is defined as 21.36 nm. The grain size is defined as the diameter of a circle whose area is equal to the grain's area. The randomness

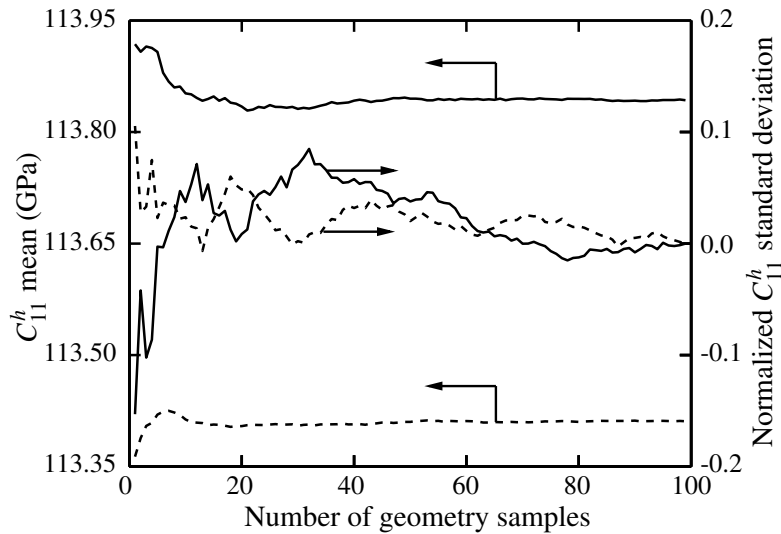


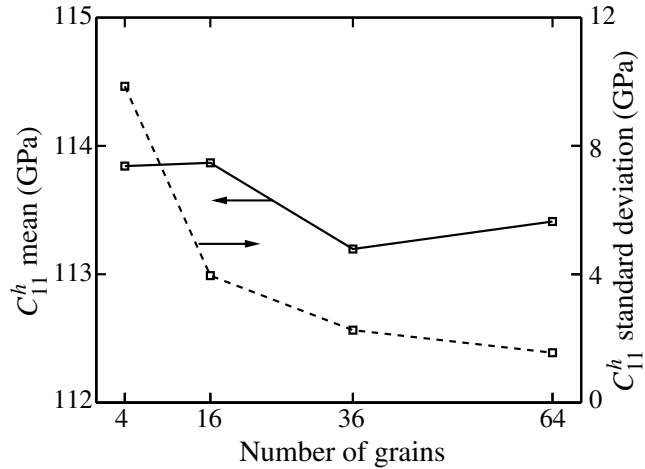
**Figure 8.** Geometry and texture uncertainty study: Variation of  $C_{11}^h$  mean and normalized standard deviation for unit cell composed of 4 (solid curves) and 64 (dotted curves) grains with a standard deviation of  $10^\circ$  in  $\theta$ .

on the grain distribution inside the unit cell is obtained by randomly assigning the seed point of the Voronoi tessellation.

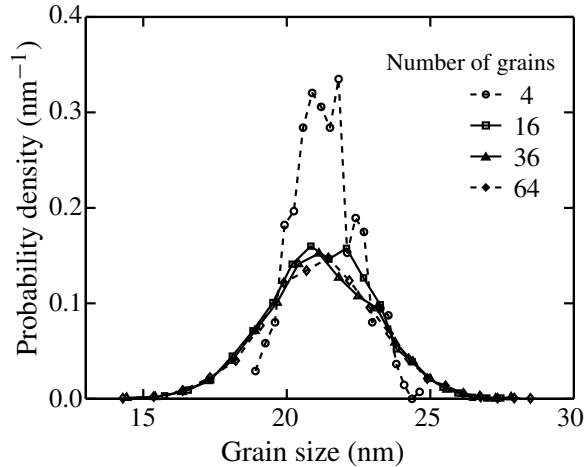
Figure 8 presents the mean and standard deviation of  $C_{11}^h$  versus the number of geometry samples considered for the unit cells of 4 and 64 grains. The standard deviation was normalized with respect to the standard deviations obtained using 100 samples. Those standard deviations were 9.86 GPa and 1.56 GPa for 4 and 64 grains, respectively. 20 geometric samples are sufficient to get a converged mean. For the standard deviation, convergence occurs from 80 samples. In the following, results are those obtained from 100 samples since they can be assumed as converged.

Figure 9 presents the mean and standard deviation of  $C_{11}^h$  when considering geometric and material uncertainties. It is observed that the mean oscillates between 113 and 114 GPa, while the standard deviation decreases as the number of grains in the unit cell increases. The standard deviation is an important parameter for deciding to what extent a unit cell can be considered as a RVE. From this graph, it is concluded that for unit cells composed of 64 or more grains, the uncertainty in the homogenized properties is less than 1.56 GPa, that is, about 1.4% of the  $C_{11}^h$  mean. From a practical point of view, this application shows that a unit cell of 64 grains can be considered as an RVE for the quantification of the uncertainty of the macroscopic elastic properties of a polycrystalline material induced by uncertainties on its grain geometry and texture.

To estimate the uncertainty of the geometry, the approximated grain size probability density function is plotted in Figure 10. The probability density is obtained by discretizing the grain size into 20 segments. The number of grains in each segment was counted and a value of the area of that segment was obtained; these values were normalized by the total area of the histogram. Figure 10 shows that the probability density functions for unit cells of 16 or more grains are similar. This guarantees that the comparison between the unit cells with 16, 36, and 64 grains is meaningful since all of them have the same input



**Figure 9.** Geometry and texture uncertainty study: Effect of the unit cell size on  $C_{11}^h$  mean (solid curves) and standard deviation (dashed curves) with a standard deviation of  $10^\circ$  in  $\theta$ .



**Figure 10.** Probability density of grain size distribution for various RVE units. The mean grain sizes are 21.41, 21.36, 21.36, and 21.35 nm and the standard deviations are 8.03, 16.09, 18.04, and 19.30 nm for the unit cells composed of 4, 16, 36, and 64 grains, respectively.

uncertainty. So the differences in mean and standard deviation in this case can be attributed to the set of grain orientations and the unit cell size.

## 6. Conclusion

This work presents the application of a perturbation-based stochastic method in the study of uncertainty in homogenized elastic properties of polycrystalline materials. The perturbation stochastic finite element

method (PSFEM) has been applied to the mathematical theory of homogenization. The formulation obtained has been used to study the influence of geometry and material texture uncertainties at the grain level on the macroscopic polycrystalline material properties.

By comparing the results with Monte Carlo results on verification test cases, it has been shown that the PSFEM approximation errors depend on the problem of interest and the coefficient of variation for the input random variables. In the case of homogenization of gold polycrystalline structures, the limitation of PSFEM on the computation of the influence of material texture uncertainty has been quantified. The error on the  $C_{11}^h$  standard deviation remains below 5% for a standard deviation in the Euler angle defining the  $\langle 111 \rangle$  texture up to  $7^\circ$ .

By combining Monte Carlo and PSFEM, the uncertainty of the geometry of the grains has been taken into account on top of the material texture uncertainty. The convergence of this approach has been demonstrated by numerical examples. The results show that for gold thin films, a unit cell with 64 grains or more predicts an uncertainty characterized by a coefficient of variation of 1.4% on  $C_{11}^h$  for a standard deviation of  $10^\circ$  in the Euler angle defining the  $\langle 111 \rangle$  texture.

The proposed approach is a general tool for quantifying the uncertainty of the elastic properties of polycrystalline materials as a function of the grain geometric and material properties and the unit cell size. Moreover, this study can provide better confidence on the necessary representative volume element size.

### Acknowledgments

The authors gratefully acknowledge the support from DARPA through the MEMS/NEMS S&T Fundamentals Program, from the Beckman Institute of Advanced Science and Technology, from NSF through Grant CMMI 09-27149 ARRA and from the Illinois Space Grant Consortium.

### References

- [Altus and Totry 2003] E. Altus and E. M. Totry, "Buckling of stochastically heterogeneous beams, using a functional perturbation method", *Int. J. Solids Struct.* **40**:23 (2003), 6547–6565.
- [Bensoussan et al. 1978] A. Bensoussan, J.-L. Lions, and G. Papanicolaou, *Asymptotic analysis for periodic structures*, Studies in Mathematics and its Applications **5**, North-Holland, Amsterdam, 1978.
- [Doltsinis and Kang 2006] I. Doltsinis and Z. Kang, "Perturbation-based stochastic FE analysis and robust design of inelastic deformation processes", *Comput. Methods Appl. Mech. Eng.* **195**:19–22 (2006), 2231–2251.
- [Guedes and Kikuchi 1990] J. M. Guedes and N. Kikuchi, "Preprocessing and postprocessing for materials based on the homogenization method with adaptive finite element methods", *Comput. Methods Appl. Mech. Eng.* **83**:2 (1990), 143–198.
- [Hien and Kleiber 1990] T. D. Hien and M. Kleiber, "Finite element analysis based on stochastic Hamilton variational principle", *Comput. Struct.* **37**:6 (1990), 893–902.
- [Hien and Kleiber 1997] T. D. Hien and M. Kleiber, "Stochastic finite element modelling in linear transient heat transfer", *Comput. Methods Appl. Mech. Eng.* **144**:1–2 (1997), 111–124.
- [Huang et al. 2007] B. Huang, Q. S. Li, W. H. Shi, and Z. Wu, "Eigenvalues of structures with uncertain elastic boundary restraints", *Appl. Acoust.* **68**:3 (2007), 350–363.
- [Kaminski 2000] M. Kaminski, "Homogenization of 1D elastostatics by the stochastic second order approach", *Mech. Res. Commun.* **27**:3 (2000), 273–280.
- [Kaminski and Kleiber 2000] M. Kaminski and M. Kleiber, "Perturbation based stochastic finite element method for homogenization of two-phase elastic composites", *Comput. Struct.* **78**:6 (2000), 811–826.

- [Kleiber and Hien 1992] M. Kleiber and T. D. Hien, *The stochastic finite element method: basic perturbation technique and computer implementation*, Wiley, Chichester, 1992.
- [Lei and Qiu 2000] Z. Lei and C. Qiu, “A stochastic variational formulation for nonlinear dynamic analysis of structure”, *Comput. Methods Appl. Mech. Eng.* **190**:5–7 (2000), 597–608.
- [Manohar and Ibrahim 1999] C. S. Manohar and R. A. Ibrahim, “Progress in structural dynamics with stochastic parameter variations: 1987–1998”, *Appl. Mech. Rev. (ASME)* **52**:5 (1999), 177–197.
- [McKay et al. 1979] M. D. McKay, R. J. Beckman, and W. J. Conover, “A comparison of three methods for selecting values of input variables in the analysis of output from a computer code”, *Technometr.* **21**:2 (1979), 239–245.
- [van den Nieuwenhof 2003] B. van den Nieuwenhof, *Stochastic finite elements for elastodynamics: random field and shape uncertainty modelling using direct and modal perturbation-based approaches*, Ph.D. thesis, Catholic University of Louvain, 2003, available at <http://hdl.handle.net/2078.1/4995>.
- [Oh and Librescu 1997] D. H. Oh and L. Librescu, “Free vibration and reliability of composite cantilevers featuring uncertain properties”, *Reliab. Eng. Syst. Saf.* **56**:3 (1997), 265–272.
- [Onkar et al. 2007] A. K. Onkar, C. S. Upadhyay, and D. Yadav, “Probabilistic failure of laminated composite plates using the stochastic finite element method”, *Compos. Struct.* **77**:1 (2007), 79–91.
- [Sakata et al. 2008] S. Sakata, F. Ashida, T. Kojima, and M. Zako, “Three-dimensional stochastic analysis using a perturbation-based homogenization method for elastic properties of composite material considering microscopic uncertainty”, *Int. J. Solids Struct.* **45**:3–4 (2008), 894–907.
- [Sanchez-Palencia and Zaoui 1987] E. Sanchez-Palencia and A. Zaoui (editors), *Homogenization techniques for composite media* (Udine, 1985), Lecture Notes in Physics **272**, Springer, Berlin, 1987.
- [Schueller 1997] G. I. Schueller, “A state-of-the-art report on computational stochastic mechanics”, *Probab. Eng. Mech.* **12**:4 (1997), 197–321.
- [Schueller 2001] G. I. Schueller, “Computational stochastic mechanics: recent advances”, *Comput. Struct.* **79**:22–25 (2001), 2225–2234.
- [Sudret and der Kiureghian 2000] B. Sudret and A. der Kiureghian, “Stochastic finite element methods and reliability: a state-of-the-art report”, Report No. UCB/SEMM-2000/08, Department of Civil and Environmental Engineering, University of California, Berkeley, November 2000, available at <http://tinyurl.com/UCB-SEMM-2000-08>.
- [Ting 1996] T. C. T. Ting, *Anisotropic elasticity: theory and applications*, Oxford Engineering Science Series **45**, Oxford University Press, New York, 1996.

Received 6 Apr 2010. Revised 5 Oct 2010. Accepted 12 Nov 2010.

SEVERINE LEPAGE: [severine.lepage@e-xstream.com](mailto:severine.lepage@e-xstream.com)

*Beckman Institute for Advanced Science and Technology, University of Illinois at Urbana-Champaign, 405 N. Mathews Av., Urbana, IL 61801, United States*

*Current address: Present address:, e-Xstream engineering (L) sarl, ZI Bommelscheuer, L-4940 Bascharage, Luxembourg*

FERNANDO V. STUMP: [fstump2@illinois.edu](mailto:fstump2@illinois.edu)

*Department of Mechanical Science and Engineering, University of Illinois at Urbana-Champaign, 1206 W. Green St., Urbana, IL 61801, United States*

ISAIAH H. KIM: [hdkim1@illinois.edu](mailto:hdkim1@illinois.edu)

*Department of Mechanical Science and Engineering, University of Illinois at Urbana-Champaign, 1206 W. Green St., Urbana, IL, 61801, United States*

PHILIPPE H. GEUBELLE: [geubelle@illinois.edu](mailto:geubelle@illinois.edu)

*Department of Aerospace Engineering, University of Illinois at Urbana-Champaign, 104 S. Wright St., Urbana, IL 61801, United States*

## A COLLOCATION APPROACH FOR SPATIAL DISCRETIZATION OF STOCHASTIC PERIDYNAMIC MODELING OF FRACTURE

GEORGIOS I. EVANGELATOS AND POL D. SPANOS

In this paper a collocation approach is presented for spatial discretization of the partial integrodifferential equation arising in a peridynamic formulation in stochastic fracture mechanics. In the formulation nodes are distributed inside the domain forming a grid, and the inverse multiquadric radial basis functions are used as interpolation functions inside the domain. Due to this discretization the peridynamic stiffness is generated in a manner similar to the finite element method. Further, any discontinuity in the domain is included in this discretized form and affects only the peridynamic stiffness of the adjacent nodes. Using this approach as a tool, the probability density function of the energy release rate can be determined at a given crack tip point for all possible crack paths. Thus, the crack propagation direction can be probabilistically identified. This is accomplished by numerical evaluation of the requisite Neumann expansion using pertinent Monte Carlo simulations. Specific examples of applications are included.

### 1. Introduction

The problem of modeling dynamic or static systems that contain discontinuities is fundamental in mechanics. Fractured surfaces and propagating cracks are discontinuities which disrupt the domains of differential equations and create mathematical singularities. There are several approaches to dealing with these kinds of discontinuities. Two classical ones are the finite element method (FEM), with remeshing of the continuous domain, and the extended finite element method (XFEM), which circumvents the constant remeshing of the domain and uses the same mesh by simply adjusting the stiffness of the cracked element [Zi and Belytschko 2003]. Further, mesh-free techniques have been applied to the same problem with quite reasonable results [Belytschko et al. 1994; 1995]. However, all of these approaches have been based on local mechanics theory. In local mechanics theory, a single point in the medium is in direct contact with only its immediate neighboring points, and thus spatial derivatives exist in such a continuum. In nonlocal mechanics, however, a single point in the medium is in direct contact with points further away in addition to its immediate neighboring points. Nonlocal theories were initially developed in [Kröner 1967; Eringen et al. 1977] and since then several researchers have contributed to this concept.

In a pioneering publication, S. A. Silling extended the concept of nonlocal mechanics. Until then the concept of nonlocality was used as a generalization of local mechanics and it was assumed that spatial derivatives of a certain finite neighborhood around the point of interest could be used. Silling [2000] proposed a fully nonlocal peridynamic modeling in which no spatial derivatives are needed, and therefore the inherent problem of a discontinuity in the domain can be circumvented. The model involves the formulation of a partial integrodifferential equation that holds for discontinuous domains with no additional treatment such as enrichment.

---

*Keywords:* peridynamics, fracture mechanics, radial basis functions, stochastic medium, collocation method.

Since this pioneering work, several publications have focused on the application of this approach to a wide spectrum of problems. In [Silling et al. 2003] the deformation of an infinite bar was investigated using peridynamic theory. In [Silling et al. 2007] a generalization of the original peridynamics framework was proposed to extend the kinds of materials that can be modeled by peridynamic theory. In [Bobaru et al. 2009] adaptive refinement was proposed and the uniform convergence of peridynamic theory to classical mechanics was shown for dynamic and static 1D solutions when the horizon is approaching zero. In [Warren et al. 2009] the previous peridynamic theory was extended to handle Poisson ratios other than  $\frac{1}{4}$  and to allow bonds to exhibit noncentral forces. In [Macek and Silling 2007] peridynamic theory was extended beyond EMU meshless formulations to FEM by incorporating truss elements. In [Bobaru 2007] the peridynamic method was used to analyze the effect of van der Waals forces on the mechanical behavior, strength, and toughness of 3D nanofiber networks. In the benchmark study, the fracture was introduced at the microstructural level using the concept of bonds; it was concluded that two main mechanisms control the deformation: fiber reorientation and fiber accretion. In [Silling and Askari 2005] a numerical mesh-free method for solving the partial integrodifferential equation arising from peridynamic theory was proposed and examples of modeling crack growth in brittle materials were presented. In [Zhou and Du 2010] a mathematically based approach for linear peridynamic FEMs was introduced.

In this paper a peridynamic modeling of systems with stochastic material properties exposed to stochastic excitations is considered. Proceeding to this task, a novel spatial discretization of the peridynamic equation is applied which allows for the stochastic extension of the model. The governing partial integrodifferential equation is treated by the Kansa collocation method [Kansa 1990a; 1990b] using inverse multiquadric (IMQ) radial basis functions (RBF). In this formulation the direction and length of the crack propagation is not governed by the nodal density and positioning of the nodes as it is in the usual mesh-free peridynamic approach. The approach is quite similar to the XFEM [Zi and Belytschko 2003] where the crack is influencing only one finite element and the stiffness of the current element through which the crack is going needs only to be determined. Further, the boundary conditions are imposed in a simpler manner than in peridynamic theory; it is quite similar to FEM. Finally, after having established a reliable collocation method to treat the deterministic problem, the stochastic problem is considered and is solved utilizing the concept proposed in the stochastic finite element method (SFEM) [Ghanem and Spanos 1991]. The reliability of the system is evaluated by calculating the probability density function (PDF) of the energy release rate around the crack tip.

## 2. Peridynamic formulation

**2.1. The peridynamic partial integrodifferential equation.** Consider a mechanical component having one dimension significantly smaller than the other two, and operating under an excitation in the plane defined by its two significant dimensions. Obviously, the significant displacements of the vibrating medium are lying on the same 2D plane. Next, consider nonlocal peridynamic theory for modeling the behavior of the medium. The nonlocal theory of peridynamics involves a partial integrodifferential equation for dynamic problems [Emmrich and Weckner 2007b]. Specifically, this equation is a second-order differential equation with respect to time, and an integral equation with respect to space. In this context, the governing equation of motion of any particle inside the vibrating 2D medium is given by the

equation

$$\rho \begin{bmatrix} \ddot{u}(\underline{x}, t) \\ \ddot{v}(\underline{x}, t) \end{bmatrix} + \int_{H(\underline{x})} f \left( \begin{bmatrix} u(\underline{x}, t) - u(\hat{\underline{x}}, t) \\ v(\underline{x}, t) - v(\hat{\underline{x}}, t) \end{bmatrix}, \underline{x} - \hat{\underline{x}} \right) dV_{\hat{\underline{x}}} = \begin{bmatrix} b_x(\underline{x}, t) \\ b_y(\underline{x}, t) \end{bmatrix}, \quad (1)$$

where  $\ddot{u}$  and  $\ddot{v}$  denote the second-order derivatives of  $u$  and  $v$  with respect to time, and the vectors  $\underline{x}$  and  $\hat{\underline{x}}$  are defined by the equations

$$\underline{x} = \begin{pmatrix} x \\ y \end{pmatrix} \quad (2)$$

and

$$\hat{\underline{x}} = \begin{pmatrix} \hat{x} \\ \hat{y} \end{pmatrix}. \quad (3)$$

Note that  $\rho$  is the material density,  $b_x(\underline{x}, t)$  and  $b_y(\underline{x}, t)$  are the force densities,  $u(\underline{x})$  and  $v(\underline{x})$  denote the displacements of the point  $\underline{x}$  on the  $x$  and  $y$  axes respectively,  $f$  denotes the force function measured in force per unit volume squared exerted on the point  $\underline{x}$  by the point  $\hat{\underline{x}}$ , and  $H(\underline{x})$  is the domain of integration. Note that the force function  $f$  may depend on the partial derivatives of the displacement with respect to the directions  $x$  and  $y$ , and thus (1) is a partial integrodifferential equation. In peridynamic theory the domain of  $\hat{\underline{x}}$  is restricted by the position of  $\underline{x}$  by defining the relative position

$$\underline{\xi} = \underline{x} - \hat{\underline{x}} \quad (4)$$

such that

$$|\underline{\xi}| < \delta. \quad (5)$$

The distance  $\delta$  is called the horizon and represents the distance of the nonlocal approximation. The domain  $H(\underline{x})$  for every given point  $\underline{x}$  is defined by the equation

$$H(\underline{x}) = \{ \hat{\underline{x}} : |\underline{x} - \hat{\underline{x}}| < \delta \}, \quad (6)$$

and yields a circular disc centered at  $\underline{x}$  of radius  $\delta$ ; Figure 1 helps to elucidate this concept.

Further, the pairwise force function  $f$  represents the force between two particles separated by a distance of length  $\xi$  [Silling 2000]. Thus it must exhibit the properties

$$f(-\underline{\eta}, -\underline{\xi}) = -f(\underline{\eta}, \underline{\xi}), \quad (7)$$

$$(\underline{\xi} + \underline{\eta}) \otimes f(\underline{\eta}, \underline{\xi}) = 0, \quad (8)$$

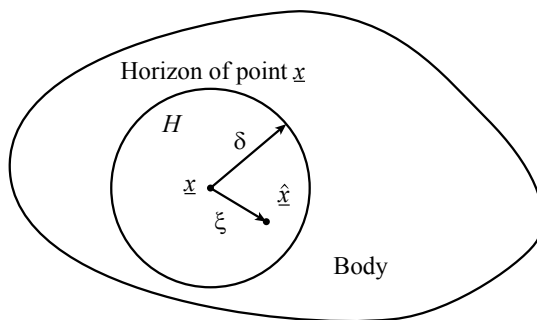


**Figure 1.** Each point  $\underline{x}$  in the body  $\Omega$  interacts directly with the points  $\hat{\underline{x}}$  in the circular disc  $H(\underline{x})$  through bonds.

where  $\otimes$  is the symbol of the tensor product, and the vector  $\underline{\eta}$  is defined by the equation

$$\underline{\eta} = \begin{bmatrix} u(\underline{x}) - u(\hat{\underline{x}}) \\ v(\underline{x}) - v(\hat{\underline{x}}) \end{bmatrix}. \quad (9)$$

These restrictions ensure the conservation of angular momentum and the collinearity of the force with respect to the relative position of the particles. Details on the force function can be found in [Silling 2000]. Next, for the linearized pairwise force function introduced in that reference, the force yields

$$f(\underline{\eta}, \underline{\xi}) = C(\underline{\xi})\underline{\eta}, \quad (10)$$

where the micromodulus  $C$  satisfies the condition

$$C(-\underline{\xi}) = C(\underline{\xi}). \quad (11)$$

A fundamental measure of peridynamic theory is the bond stretch given by the formula

$$s = \frac{|\underline{\xi} + \underline{\eta}| - |\underline{\xi}|}{|\underline{\xi}|}. \quad (12)$$

Specifically, stretch is used to determine whether the bond has failed or not, and thus it is the measure governing the force between the particles, like strain in classical mechanics theory. Bonds which have exceeded the predetermined value of  $s_0$  are damaged. In quantifying the damage on a specific point  $\underline{x}$  from the points in the horizon of  $\underline{x}$  the function

$$\phi(\underline{x}, t) = 1 - \frac{\int_{H(\underline{x})} \mu(\underline{x}, t, \underline{\xi}) dV_{\hat{\underline{x}}}}{\int_{H(\underline{x})} dV_{\hat{\underline{x}}}} \quad (13)$$

is used, where the damage can be assumed to cause total failure of the bond by

$$\mu(\underline{\xi}, t) = \begin{cases} 1 & \text{if } s(t, \underline{\xi}) < s_0, \\ 0 & \text{otherwise.} \end{cases} \quad (14)$$

In linear peridynamics, the pairwise force amplitude is given by the equation [Silling 2000; Silling and Askari 2005]

$$|f(\underline{\eta}, \underline{\xi})| = c \frac{|\underline{\eta}|}{|\underline{\xi}|}, \quad (15)$$

where the force vector  $f$  is aligned with the vector  $\underline{\xi} + \underline{\eta}$ , and for a 2D plate problem the constant  $c$  is given by

$$c = \frac{9E}{2\pi\delta^3}, \quad (16)$$

where  $k$  is the bulk modulus of the material in [Emmrich and Weckner 2007a]. Several other formulations can be found in [Silling 2000] regarding the pairwise force function.

**2.2. Polar coordinate transformation.** Equation (1) can also be cast into polar coordinates, yielding

$$\rho \begin{bmatrix} \ddot{u}(\underline{x}, t) \\ \ddot{v}(\underline{x}, t) \end{bmatrix} + \int_{H(\theta, r)} f \left( \begin{bmatrix} u(\underline{x}, t) - u(\underline{x} + \underline{r}, t) \\ v(\underline{x}, t) - v(\underline{x} + \underline{r}, t) \end{bmatrix}, -\underline{r} \right) |J| d\theta dr = \begin{bmatrix} b_x(\underline{x}, t) \\ b_y(\underline{x}, t) \end{bmatrix}, \quad (17)$$

where

$$|J| = -r, \quad (18)$$

$$\underline{r} = -\xi, \quad (19)$$

$$\underline{r} = r \begin{pmatrix} \cos \theta \\ \sin \theta \end{pmatrix}. \quad (20)$$

Note that (9) in polar coordinates yields

$$\underline{\eta} = \begin{bmatrix} u(\underline{x}) - u(\underline{x} + \underline{r}) \\ v(\underline{x}) - v(\underline{x} + \underline{r}) \end{bmatrix}, \quad (21)$$

and equivalently (15) yields

$$|f(\underline{\eta}, \underline{r})| = \frac{c}{r} |\underline{\eta}|. \quad (22)$$

For purposes of elucidation, the displacements  $u$  and  $v$  of a bond are shown in Figure 2.

Adopting the linearized pairwise force function, and using the fact that the horizon  $\delta$  is a small distance, the total stretch of the bond can be approximated quite accurately by just the collinear component of the vector  $\underline{r}$ . The contribution to the extension of the bond from the perpendicular displacements with respect to the vector  $\underline{r}$  shown in Figure 2 can be neglected for small distances  $r$ . This is due to the assumption that small rigid body rotations of the bond can be neglected (see Appendix C). With this assumption and since this force is in the direction of the vector  $\underline{r}$  the forces per unit volume in the  $x$  and  $y$  directions

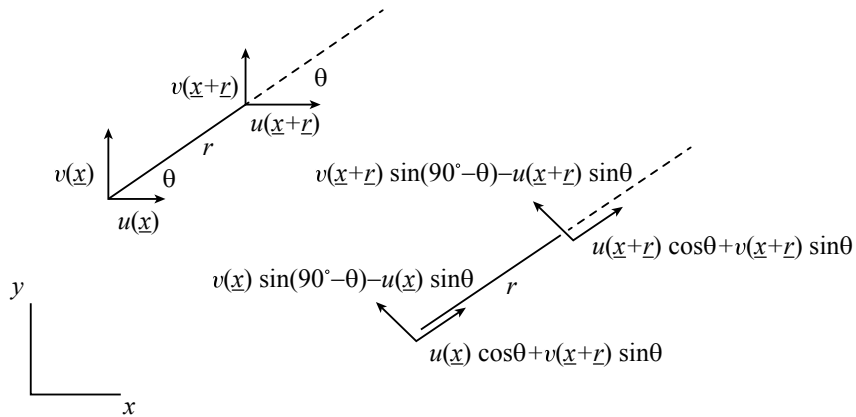


**Figure 2.** A bond of length  $r$  and angle  $\theta$  with respect to the global coordinate system.

yield

$$\begin{aligned} \text{force}_x &= \frac{c}{r} ((u(\underline{x}) - u(\underline{x} + \underline{r})) dV_{\underline{x}+\underline{r}} \cos \theta + (v(\underline{x}) - v(\underline{x} + \underline{r})) dV_{\underline{x}+\underline{r}} \sin \theta) \cos \theta, \\ \text{force}_y &= \frac{c}{r} ((v(\underline{x}) - v(\underline{x} + \underline{r})) dV_{\underline{x}+\underline{r}} \cos \theta + (v(\underline{x}) - v(\underline{x} + \underline{r})) dV_{\underline{x}+\underline{r}} \sin \theta) \sin \theta. \end{aligned} \quad (23)$$

These equations represent the force in the  $x$  and  $y$  directions due to one bond formed from two particles at distance  $r$  and at angle from the reference point  $\theta$ . Since (17) is given in polar coordinates, (1) can be cast as

$$\rho \begin{bmatrix} \ddot{u}(\underline{x}, t) \\ \dot{v}(\underline{x}, t) \end{bmatrix} + \int_0^\delta \int_0^{2\pi} \frac{c}{r} \begin{bmatrix} \cos^2 \theta & \cos \theta \sin \theta \\ \cos \theta \sin \theta & \sin^2 \theta \end{bmatrix} \begin{pmatrix} u(\underline{x}, t) - u(\underline{x} + \underline{r}, t) \\ v(\underline{x}, t) - v(\underline{x} + \underline{r}, t) \end{pmatrix} |J| d\theta dr = \begin{bmatrix} b_x(\underline{x}, t) \\ b_y(\underline{x}, t) \end{bmatrix}. \quad (24)$$

### 3. Spatial discretization

**3.1. Radial basis function expansion.** Having derived (24), we proceed to use the Kansa collocation method for its spatial discretization; see [Kansa 1990a; 1990b]. In implementing the Kansa collocation method, a series of nodes is distributed in the domain forming a grid of points. Inverse multiquadric (IMQ) radial basis functions (RBFs) are used as defined in those references; they correspond to the inverse of the Euclidean distance of the point  $\underline{x}$  from the collocation node  $k$ :

$$g_k(\vec{x}) = \frac{1}{\sqrt{(x - x_k)^2 + (y - y_k)^2 + \psi_k^2}}, \quad (25)$$

where the distance  $\psi_k$  is a local shape parameter regulating the shape of the basis. Large values of this parameter contribute to smoother shapes and are quite accurate approximations of flat and slowly varying solutions. However, small parameters represent sharper shapes and are particularly good for peaks and steep slopes. The IMQ function attains its maximum at the node and monotonically decreases as the distance from the node increases. Next, using the same IMQs for both the  $u$  and  $v$  displacements yields

$$u(\underline{x}) = \sum_{k=1}^N a_{1k} g_k(\underline{x}) + \sum_{j=1}^M a_{2j} q_j(\underline{x}), \quad v(\underline{x}) = \sum_{k=1}^N d_{1k} g_k(\underline{x}) + \sum_{j=1}^M d_{2j} q_j(\underline{x}). \quad (26)$$

Further, the polynomials  $q$  that correspond to the  $a$  and  $d$  coefficients can be arbitrarily chosen. Note that details on the Kansa collocation method and the IMQ RBFs are included in Appendix B. Next, (26) on the collocation points with time-dependent coefficients can be cast in the form

$$\begin{bmatrix} u(\underline{x}_1, t) \\ v(\underline{x}_1, t) \\ \vdots \\ 0 \\ \vdots \end{bmatrix} = \begin{bmatrix} g_1(\underline{x}_1) & 0 & \dots & q_1(\underline{x}_1) & 0 & \dots \\ 0 & g_1(\underline{x}_1) & \dots & 0 & q_1(\underline{x}_1) & \dots \\ \vdots & \vdots & \vdots & \vdots & \vdots & \vdots \\ q_1(\underline{x}_1) & q_1(\underline{x}_2) & q_1(\underline{x}_3) & \dots & 0 & 0 \\ \vdots & \vdots & \vdots & \vdots & \vdots & \ddots \end{bmatrix} \begin{bmatrix} a_{11}(t) \\ d_{11}(t) \\ \vdots \\ a_{21}(t) \\ d_{21}(t) \\ \vdots \end{bmatrix}. \quad (27)$$

Equation (27) is the basis upon which the 2D solution of the integrodifferential equation is expanded. The difference in the displacements of a bond, denoted by the vector  $\underline{\eta}$  and shown in (21), is obtained

using (26). Specifically, the vector  $\underline{\eta}$  with time dependence yields

$$\underline{\eta}(\underline{x}, \underline{r}, t) = \begin{bmatrix} G_1(\underline{x}, \underline{r}) & 0 & G_2(\underline{x}, \underline{r}) & \dots & Q_1(\underline{x}, \underline{r}) & 0 & \dots \\ 0 & G_1(\underline{x}, \underline{r}) & 0 & \dots & 0 & Q_1(\underline{x}, \underline{r}) & \dots \end{bmatrix} \begin{bmatrix} a_{11}(t) \\ d_{11}(t) \\ \vdots \\ a_{21}(t) \\ d_{21}(t) \\ \vdots \end{bmatrix}, \quad (28)$$

where

$$G_k(\underline{x}, \underline{r}) = g_k(\underline{x}) - g_k(\underline{x} + \underline{r}), \quad Q_j(\underline{x}, \underline{r}) = q_j(\underline{x}) - q_j(\underline{x} + \underline{r}). \quad (29)$$

**3.2. Stiffness determination.** Having represented the displacements by linear combinations of the basis functions, an approach similar to the one of FEM is followed. It is assumed that the displacement of any given point inside the domain is captured by interpolating the four adjacent nodes surrounding the point. Figure 3, left, elucidates this interpolation scheme.

It is clear that for any point that belongs in the square, the four adjacent nodes contribute to its displacement. This leads to a quite convenient and efficient way to integrate over the horizon of each node. Figure 3, right, shows the horizon of each node in a specific element.

Obviously the integration of (1) can be performed using a finite element approximation inside an element. Specifically, integration over the horizon is required only for one element and its four nodes. Then, the integration over the horizon of each node is performed by merely adding the nodal values of the elements, identically as done in FEM. Therefore combining (21), (24), and (28), the peridynamic stiffness density of the node  $i$  is given as

$$K = \int_0^\delta \int_0^{2\pi} \frac{c}{r} \begin{bmatrix} \cos^2 \theta & \cos \theta \sin \theta \\ \cos \theta \sin \theta & \sin^2 \theta \end{bmatrix} \begin{bmatrix} G_i(\underline{x}_i) & 0 & \dots & Q_1(\underline{x}_i) & 0 & \dots \\ 0 & G_i(\underline{x}_i) & \dots & 0 & Q_1(\underline{x}_i) & \dots \end{bmatrix} |J| d\theta dr. \quad (30)$$

In this regard, combining (30) with (18) yields the second-order micromodulus tensor

$$C(\underline{\xi}) = c \begin{bmatrix} \cos^2 \theta & \cos \theta \sin \theta \\ \cos \theta \sin \theta & \sin^2 \theta \end{bmatrix}, \quad (31)$$

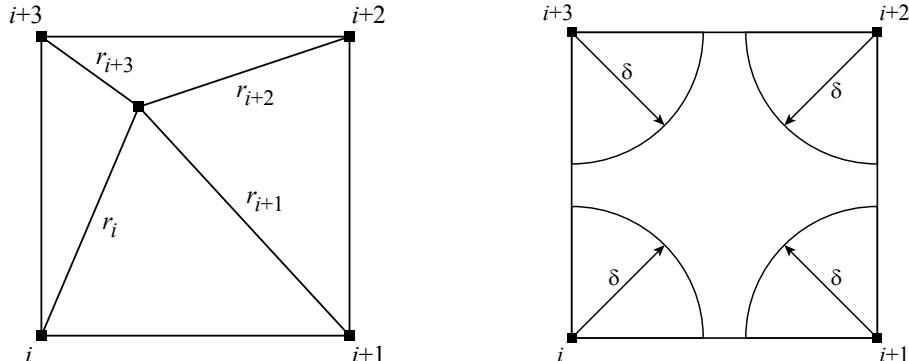


**Figure 3.** Left: a point of interest surrounded by its four closest nodes. Right: horizon of each node in a square element formed by four grid points.

and combining (4), (19), and (20), (31) can be cast in a form identical to that of [Silling 2000] as

$$C(\underline{\xi}) = \frac{c}{|\underline{\xi}|^2} \underline{\xi} \otimes \underline{\xi}. \quad (32)$$

Next, the stiffness density matrix corresponding to the  $g$  basis functions for a four-node element consists of  $4 \times 4$  blocks of  $2 \times 2$  matrices and yields

$$K_G = - \int_0^\delta \left[ \begin{array}{c} \int_0^{\pi/2} C(\theta, r) [G_i(\underline{x}_i, r, \theta) \ G_{i+1}(\underline{x}_i, r, \theta) \ G_{i+2}(\underline{x}_i, r, \theta) \ G_{i+3}(\underline{x}_i, r, \theta)] d\theta \\ \int_{\pi/2}^\pi C(\theta, r) [G_i(\underline{x}_{i+1}, r, \theta) \ G_{i+1}(\underline{x}_{i+1}, r, \theta) \ G_{i+2}(\underline{x}_{i+1}, r, \theta) \ G_{i+3}(\underline{x}_{i+1}, r, \theta)] d\theta \\ \int_\pi^{3\pi/2} C(\theta, r) [G_i(\underline{x}_{i+2}, r, \theta) \ G_{i+1}(\underline{x}_{i+2}, r, \theta) \ G_{i+2}(\underline{x}_{i+2}, r, \theta) \ G_{i+3}(\underline{x}_{i+2}, r, \theta)] d\theta \\ \int_{3\pi/2}^{2\pi} C(\theta, r) [G_i(\underline{x}_{i+3}, r, \theta) \ G_{i+1}(\underline{x}_{i+3}, r, \theta) \ G_{i+2}(\underline{x}_{i+3}, r, \theta) \ G_{i+3}(\underline{x}_{i+3}, r, \theta)] d\theta \end{array} \right] dr. \quad (33)$$

Further, the stiffness density matrix corresponding to the  $q$  basis functions for the node  $i$  consists of a  $2 \times M$  matrix, where  $M$  is the number of the  $q$  functions, and yields

$$K_Q = - \int_0^\delta \left[ \int_0^{2\pi} C(\theta, r) [Q_1(\underline{x}_i, r, \theta) d\theta \ \dots \ Q_M(\underline{x}_i, r, \theta)] d\theta \right] dr. \quad (34)$$

#### 4. Implementation aspect

**4.1. Linear differential equations.** Utilizing the concept shown in Figure 3 and combining (1), (33), and (34) yields a set of linear differential equations. Specifically, the set of linear second-order differential equations can be cast in the matrix form as

$$\begin{bmatrix} \sum_i \rho_i G_i & \sum_j \rho_j Q_j \\ \sum_j Q_j^T & 0 \end{bmatrix} \begin{bmatrix} a_{11} \\ d_{11} \\ \vdots \\ a_{21} \\ d_{21} \\ \vdots \end{bmatrix} + \begin{bmatrix} \sum_i K_{Gi} & \sum_j K_{Qi} \\ \sum_j Q_j^T & 0 \end{bmatrix} \begin{bmatrix} a_{11} \\ d_{11} \\ \vdots \\ a_{21} \\ d_{21} \\ \vdots \end{bmatrix} = \begin{bmatrix} b \\ 0 \end{bmatrix}, \quad (35)$$

where  $\sum_i \rho_i G_i$  is a  $2N \times 2N$  square matrix representing the nodal material density related to the  $g$  basis functions,  $\sum_j \rho_j Q_j$  is a  $2N \times 2M$  rectangular matrix representing the nodal material density related to the additional basis functions  $q$ ,  $\sum_j Q_j^T$  is a  $2M \times 2N$  rectangular matrix and is called the regularization condition, and finally 0 is a  $2M \times 2M$  zero matrix. More details on the regularization conditions can be found in [Kansa 1990a; 1990b] and in Appendix B. Equivalently  $\sum_i K_{Gi}$ , which is a square  $2N \times 2N$  matrix, is the stiffness density related to the  $g$  basis functions,  $\sum_j K_{Qi}$  is the  $2N \times 2M$  stiffness density matrix related to the  $q$  basis functions, and  $\begin{bmatrix} b \\ 0 \end{bmatrix}$  is the  $2N \times 1$  loading vector on top of a  $2M \times 1$  zero vector representing the regularization conditions. Further, (35) is a  $2(N + M) \times 2(N + M)$  system of second-order linear differential equations and can be readily integrated in time using a time

integration scheme. Note that since the quantities at (30), (33), and (34) represent the stiffness density, this collocation approach is different from FEM.

**4.2. Crack-inclusion treatment.** Next, we proceed to address the crack growth or crack initiation problem utilizing the preceding peridynamic theory. In this regard, assume that a crack exists in a specific position in the medium. With the above formulation this crack will affect only the peridynamic stiffness of the surrounding nodes. Naturally the cracks interrupt the horizon of the nodes surrounding them; Figure 4 shows how the horizon of node  $i + 1$  is affected.

It is perhaps easier to appreciate from Figure 4 how powerful the peridynamic formulation becomes when it comes to dealing with discontinuities in the domain. The crack essentially describes the bond failure at these points and therefore node  $i + 1$  along with the other nodes cannot “see” past the crack, thus inducing less stiffness density. This is implemented by using the same equations as before, only with different integration limits in (33) and (34). The integration over the discontinuous horizon poses many difficulties; it is carried out numerically in Appendix A. Gaussian quadrature is used for the element  $K_G$  referring to the healthy part of the domain, shown in Appendix A. Despite the fact that a more laborious numerical integration is needed for the cracked element, peridynamic modeling through this approach is quite efficient since a uniform grid of points would have only one kind of element and thus no other integration is needed. For the integration over the horizon of the functions  $Q$ , closed-form solutions are available for “healthy” bonds around the nodes, but for discontinuities numerical integration is again needed, as shown in Appendix A.

Keeping in mind that the collocation approach yields stiffness density, in contrast to the finite element formulation, which yields stiffness, note that the weak form of the problem, given in [Emmrich and Weckner 2007b], is

$$\begin{aligned} \int_R \rho(\underline{x}) \partial_t^2 \begin{pmatrix} u(\underline{x}) \\ v(\underline{x}) \end{pmatrix} w(\underline{x}) dV_{\underline{x}} + \frac{1}{2} \int_R \int_{H(\underline{x})} \begin{pmatrix} u(\hat{\underline{x}}) \\ v(\hat{\underline{x}}) \end{pmatrix} C(\underline{x}, \hat{\underline{x}}) w(\underline{x}) dV_{\underline{x}} dV_{\hat{\underline{x}}} \\ = \int_R \begin{pmatrix} b_x(\underline{x}, t) \\ b_y(\underline{x}, t) \end{pmatrix} w(\underline{x}) dV_{\underline{x}}. \quad (36) \end{aligned}$$

In this equation  $w$  denotes the weight function, and substituting the displacement function in (36) yields the Galerkin approximation, which leads to FEM. As is clear for the stiffness expression, a double

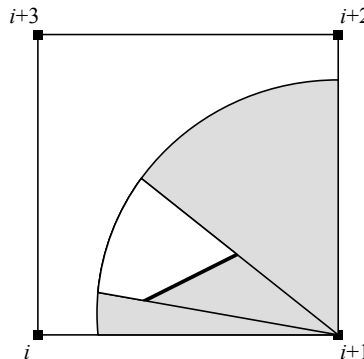


**Figure 4.** The disrupted horizon of node  $i + 1$ , as it is modeled in peridynamics.

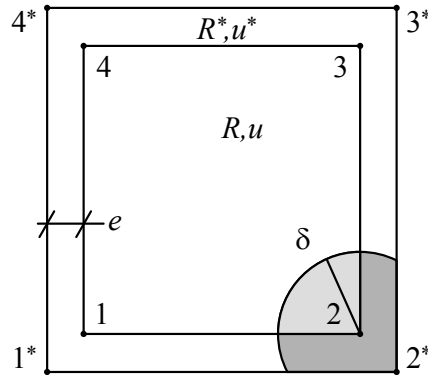


**Figure 5.** The additional layer of material  $R^*$  needed for implementing the boundary conditions.

integration is involved, one on the domain  $R$  and one in the horizon domain  $H$ . This emphasizes that in the formulation of (33) and (34), the stiffness density at a collocation point is calculated. Therefore (1) is solved not in terms of displacements and nodal forces as it is from (36), but rather in terms of loading density at the collocation points and displacements. Utilizing this formulation, the peridynamic boundary conditions are applied in a much simpler way since the input loading is actually a load density. Further, two consecutive integrations over the discontinuous domains  $R$  and  $H$  are quite laborious. This is in fact the reason why the finite element formulation is substituting the large number of bonds in an equivalently large number of truss elements in [Macek and Silling 2007]. The formulation proposed herein is quite similar to the truss approach; each node is virtually connected to all the trusses inside its horizon and its stiffness is obtained by direct integration without the actual introduction of the trusses. Further, since the crack is handled geometrically inside the element, there is no need of checking all the bonds inside the domain. The displacements inside the domain are interpolated from the nodal displacements and are directly obtained. Then, the energy release rate is calculated around the crack independently from the mesh size. Naturally, for a more accurate approximation around the crack tip, enrichment of the  $q$  functions according to [Fleming et al. 1997] is available in addition to the grid refinement.

**4.3. Peridynamic boundary conditions.** Having derived the governing equation as a set of linear second-order differential equations in matrix form, we proceed to incorporate the boundary conditions. Details on incorporating boundary conditions in peridynamic theory are covered in [Silling 2000]. However, due to this formulation the implementation of boundary conditions becomes readily available. Specifically, an additional layer of material is added to the external part of the elements standing on the boundaries of the domain; it is denoted by  $R^*$  in [Silling 2000]. The corresponding displacements of the additional layer are decomposed on the same  $g$  and  $q$  basis functions and therefore the displacements of the material  $R^*$ , denoted by  $u^*$  in [Silling 2000], are given from (26). Figure 5 shows the additional layer of material  $R^*$  that needs to be added on the boundaries.

Next, the stiffness density related to the lightly shaded area has been already calculated from the preceding equations. However, the stiffness density related to a small layer of thickness  $e$  and shown in Figure 5 with the darker shade needs to be added to the stiffness density of the nodes. In this regard, since the displacements  $u^*$  are decomposed into the same basis as the displacements  $u$ , the boundary

conditions, such as simple supports, etc., can be applied on the external nodes  $1^*$ ,  $2^*$ , etc., by utilizing the expansion basis and the displacements of these nodes. Next, for imposing certain boundary conditions on the collocation nodes of the Kansa method, specific rows in the matrices shown in (35) are changed to account for the imposed constraints. Details can be found on the implementation of boundary conditions of the Kansa collocation method in [Kansa 1990a; 1990b]. Note that the governing equation is solved in terms of displacements  $u(x)$  and  $v(x)$  and force density  $b(x)$ , and since the force loading conditions by definition are force densities, the boundary conditions are imposed readily using the basis functions. For comparison with any theoretical models involving stress applied on the above described example, the loading density  $b(x)$  must be multiplied by the layer thickness  $e$  to yield force per unit area.

## 5. Illustrative example

To illustrate the applicability of the proposed approach, a deterministic problem is considered. In this regard, a square 2D plate of dimensions  $1\text{ cm} \times 1\text{ cm}$  and bulk modulus  $k = 1\text{ N/cm}^2$  under tensile stress is modeled with FEM and peridynamic theory. The tension is of unitary amplitude  $\sigma = 1\text{ N/cm}^2$  and the displacements obtained by peridynamic theory are compared to the FEM displacements. Figure 6 shows the equivalent modeling of this simple problem with FEM and the proposed peridynamic theory involving the Kansa collocation method.

For FEM, the nodal forces are readily calculated using the stress applied on that edge. In peridynamic theory, however, the nodal forces are force densities and  $b^*e = \sigma$  thus the force density simply depends on the additional layer thickness. The displacements given by the finite element model are compared to the ones obtained from the proposed formulation in Table 1 on the next page; a layer of thickness  $e = \delta/5$  is assumed for the numerical calculations.

Next, a cracked element is considered. Figure 7 shows a simple patch test used to verify displacements for a cracked square plate under tension.

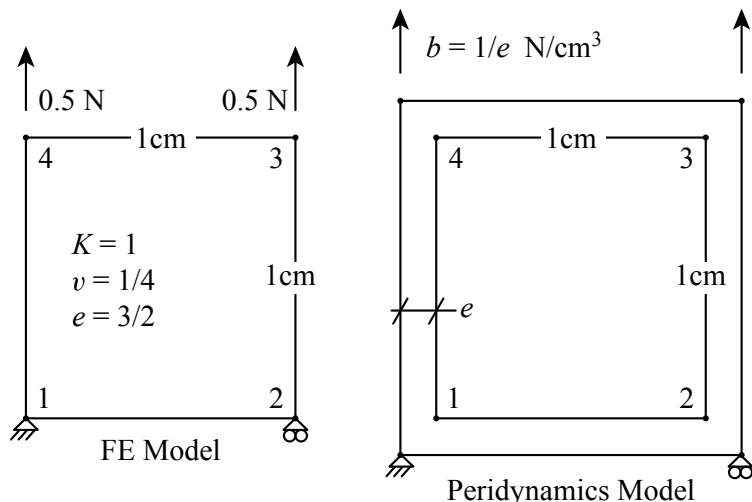


**Figure 6.** A simple 2D plate of unit thickness under tension of  $\sigma = 1\text{ N/cm}^2$ , modeled via FEM and peridynamic theory by the Kansa collocation method.

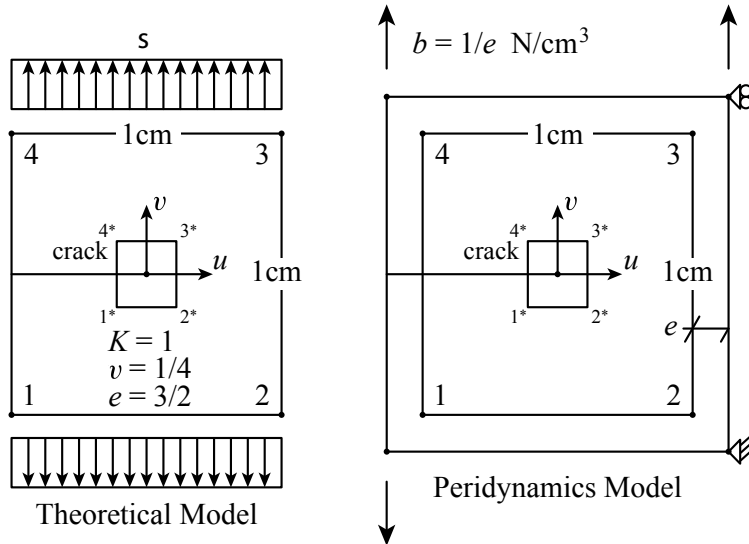


**Figure 7.** A cracked square plate under uniform tension modeled via peridynamic theory and the Kansa collocation method.

The displacements of the theoretical solution are given by the closed-form equations in [Gdoutos 1990] and yield

$$u(x) = \frac{k_1}{2\mu} \sqrt{\frac{r}{2\pi}} \cos\left(\frac{\theta}{2}\right) \left[ k_2 - 1 + 2 \sin\left(\frac{\theta}{2}\right) \right], \quad v(x) = \frac{k_1}{2\mu} \sqrt{\frac{r}{2\pi}} \sin\left(\frac{\theta}{2}\right) \left[ k_2 + 1 - 2 \cos\left(\frac{\theta}{2}\right) \right]. \quad (37)$$

Taking into account the symmetry of the loading, and transforming the coordinate system, the displacements of the two models are compared for the displacements  $u$  and  $v$ . The symbol  $k_1$  stands for the first mode stress intensity factor,  $r$  is the distance from the center of the element,  $\mu$  stands for the shear modulus,  $\theta$  is the angle with respect to the initial crack, and  $k_2$  is a parameter depending on the Poisson ratio and the crack geometry. For the element in Figure 7 the theoretical displacements are compared with the results of the peridynamic formulation. However, the peridynamic results with this formulation were not accurate. A more accurate approximation of the displacements around the crack tip points is achieved through the enrichment of the basis functions  $q$  from [Fleming et al. 1997] with the basis

$$q_5 = \sqrt{r} \cos \frac{\theta}{2}, \quad q_6 = \sqrt{r} \sin \frac{\theta}{2}, \quad q_7 = \sqrt{r} \sin \frac{\theta}{2} \sin \theta, \quad q_8 = \sqrt{r} \cos \frac{\theta}{2} \sin \theta. \quad (38)$$

Peridynamics via Kansa collocation method					FEM displacements				
Node	$u$ (cm)	$v$ (cm)	$\epsilon_x$	$\nu$	Node	$u$ (cm)	$v$ (cm)	$\epsilon_x$	$\nu$
1	-0.027	0.112	-0.160	0.237	1	0	0	-0.167	0.250
2	-0.187	0.112			2	-0.167	0		
3	-0.026	0.787	$\epsilon_y$		3	0	0.667	$\epsilon_y$	
4	-0.187	0.787	0.674		4	-0.167	0.667	0.667	

**Table 1.** Comparison of displacements for a plate under uniform tension.

Peridynamics via Kansa collocation method			Theoretical displacements		
Node*	$u$ (cm)	$v$ (cm)	Node*	$u$ (cm)	$v$ (cm)
1	0.128	-0.31	1	0.1354	-0.3269
2	0.179	-0.078	2	0.1706	-0.0707
3	0.178	0.079	3	0.1706	0.0707
4	0.126	0.31	4	0.1354	0.3269

**Table 2.** Comparison of displacements for a cracked plate under uniform tension.

The problem of obtaining the displacements around the crack tip was encountered in [Fleming et al. 1997] and the results were accurate enough when the basis was expanded with the basis containing the displacements near the crack tip. Thus, the linear functions  $q$  are enriched with an additional four basis functions for the crack tip. For the simple example shown in Figure 7, Table 2 summarizes the results for the corners of the square inside the element with side length 0.2 cm.

The numerical results obtained prior to the basis enrichment are omitted due to their poor accuracy. However, it has been seen that the numerical results after the enrichment are significantly better than the ones obtained without the basis enrichment. Further, there are persistent errors which must be addressed. The horizon  $\delta$  that has been used in both examples is  $\delta = 1$  cm and the solution of the first example remains constant for any  $\delta$  value less than 1 cm. The displacements obtained from the cracked domain appear to be dependent on the horizon length for values larger than  $\delta = 0.80$  cm, which is another issue that needs to be addressed. Integration over the horizon for the IMQ basis functions is achieved by implementing the “visibility” criterion, extensively described in [Fleming et al. 1997]. That is, the crack interrupts the horizon and thus the values of the  $g$  basis functions beyond the crack line are set equal to zero. The same concept holds for all the  $q$  basis functions.

## 6. Stochastic peridynamic theory

**6.1. Maximum energy release rate criterion.** The reliability of a structure including a crack or initiating a crack is considered in this section. Specifically, the probability of crack propagation and the direction in which the crack will propagate is of particular interest. For this, the position of the propagating or initiating fracture can be determined by the maximum energy release rate for brittle materials in [Gdoutos 1990]. To obtain the energy release rate, the length of the crack propagation is preselected as  $\delta\alpha$  and therefore points to be checked lay on the circular area given by the selected equation

$$\underline{x}_{\text{test}} = \underline{x}_c + \delta\alpha \begin{pmatrix} \cos \phi \\ \sin \phi \end{pmatrix} \quad (39)$$

for  $\phi \in [0, 2\pi]$ , where  $\underline{x}_{\text{test}}$  is the position of the potential next crack tip and  $\underline{x}_c$  is the position of the current crack tip. Since the points on the circle  $\underline{x}_{\text{test}}$  and the crack tip  $\underline{x}_c$  form potential fracture surfaces, the work of all the tensile bonds per unit area of potential fracture can be directly calculated by (see [Silling and Askari 2005])

$$G_E = \int_z \int_{V'} w(\underline{\eta}, \underline{\xi}) dV' dz. \quad (40)$$

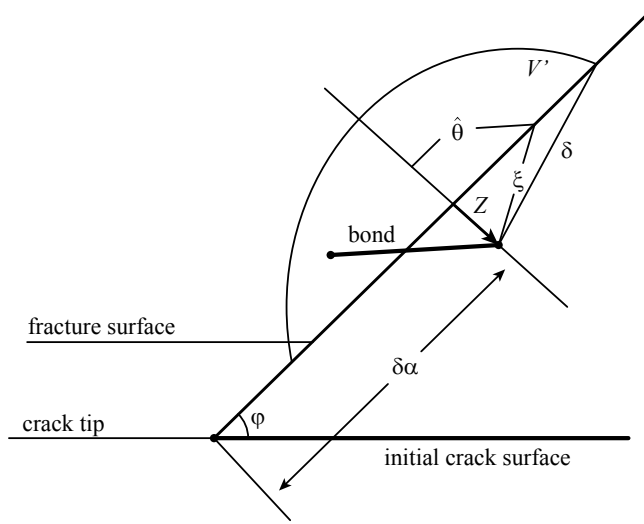


**Figure 8.** The propagating fracture of length  $\delta\alpha$  at angle  $\phi$  from the initial crack and the calculation of the energy release rate per unit of fractured area.

In this equation  $z$  denotes the perpendicular distance of a point from the fractured surface and  $V'$  is the volume of integration. Figure 8 helps to elucidate the concept of the distance  $z$  and the volume of integration. For the linearized pairwise force function, the work of a single bond yields

$$w(\underline{\eta}, \underline{\xi}) = \frac{1}{2} c s^2 |\underline{\xi}|, \quad (41)$$

and utilizing (19) yields the energy per unit surface area of a 2D plate with unit thickness:

$$G_E = \int_0^\delta \int_z^\delta \int_{-\cos^{-1}(z/r)}^{\cos^{-1}(z/r)} \frac{1}{2} c s^2 r^2 d\hat{\theta} dr dz. \quad (42)$$

Figure 8 also helps visualize the concept of bonds breaking and forming a cracked surface. Obviously, the energy per unit surface area depends on the initial crack tip, the angle  $\phi$ , and the length  $\delta\alpha$ , since the stretch  $s$  depends on these parameters. From the assumption of a linear pairwise force function and small rigid body rotations shown in Appendix C, the stretch of the bonds can be calculated from a simpler form than (12). This form is

$$s(\underline{x}, \underline{r}, \theta) = \frac{1}{r} [\cos \theta \ \sin \theta] \begin{bmatrix} u(\underline{x}) - u(\underline{x} + \underline{r}) \\ v(\underline{x}) - v(\underline{x} + \underline{r}) \end{bmatrix}, \quad (43)$$

and Figure 2 helps to illustrate this concept. Next, combining (43), (42), and (39) and correlating the angles  $\hat{\theta}$ ,  $\phi$ , and  $\theta$  through the simple equation

$$\pi/2 - \hat{\theta} + \phi = \theta \quad (44)$$

yields

$$G_E(\delta\alpha, \phi, \underline{x}_c) = \int_0^\delta \int_z^\delta \int_{\phi+\sin^{-1}(z/r)}^{\phi+\pi-\sin^{-1}(z/r)} |\underline{\eta}(\theta, \underline{\xi}, z, \delta\alpha, \phi, \underline{x}_c)|^2 d\theta dr dz, \quad (45)$$

where  $|\underline{\eta}|$  is given for the linearized pairwise force function shown in Appendix C as

$$|\underline{\eta}| = s|\underline{\xi}|. \quad (46)$$

Naturally, the angle at which the tensile energy per unit area is the maximum can be chosen as the fracture propagation angle; see [Gdoutos 1990]. Further, in brittle materials the energy release is a measurable quantity and can be used in real applications as a threshold for fracture. Figure 8 can be used to clarify this concept; see also [Silling and Askari 2005].

**6.2. Stochastic fracture on elastostatic peridynamic theory.** Having derived the energy release rate as a function of the crack tip  $\underline{x}_c$ , propagating crack length  $\delta\alpha$ , and propagating crack angle  $\phi$ , we proceed to probabilistically identify the propagation angle. In this context, in classical mechanics, materials with random properties are modeled by expressing the Young's modulus as a random process. However, in the peridynamic approach this must be modified. The fact that each node is connected with an infinite number of points belonging in the node's horizon should make the random process which represents the micromodulus of the bonds depend both on the angle  $\theta$  and on the distance  $r$  in the polar coordinate system. In this paper, the bond micromodulus is treated as a random process depending only on the distance from the node  $r$ . Therefore, the micromodulus coefficient  $c$  is a random process  $c(r, \vartheta)$  where  $\vartheta$  is the random parameter. Further, the loading of the structure involves uncertainties which are specified in terms of a random variable. The PDF of the energy release rate  $G_E$  given in (45) must be calculated in order for the reliability of the crack propagation to be calculated. Naturally the PDF of the coefficients for the static case can be obtained by utilizing (35), which yields

$$\begin{bmatrix} a_{11} \\ d_{11} \\ \vdots \\ a_{21} \\ d_{21} \\ \vdots \end{bmatrix} = \begin{bmatrix} \sum_i K_{Gi} & \sum_j K_{Qi} \\ \sum_j Q_j^T & 0 \end{bmatrix}^{-1} \begin{bmatrix} b \\ 0 \end{bmatrix}. \quad (47)$$

Obviously, the equation above includes a random matrix inversion and a multiplication by a random forcing vector. In this context, (46) combined with (43) can be cast in the form

$$|\underline{\eta}| = \sum_{i=1}^n \alpha_i \beta_i, \quad (48)$$

where  $\alpha_i = [a \dots d]$  is the set of the random coefficients, and

$$\beta_i = [G_1(\underline{x}_{\text{test}} + \underline{z}, \underline{r}) \cos \theta \dots Q_4(\underline{x}_{\text{test}} + \underline{z}, \underline{r}) \sin \theta]$$

is the set of the deterministic functions which depend on the angle  $\phi$  and the length  $\delta\alpha$ . Clearly,

$$|\underline{\eta}|^2 = \sum_{i=1}^n (\alpha_i \beta_i)^2 + 2 \sum_{i=1}^{n-1} \sum_l^n \alpha_i \alpha_l \beta_i \beta_l, \quad (49)$$

where  $l > i$ . In this case, the PDF of the energy release at a given orientation can be determined by combining (49) and (45) and yields

$$G_E(\delta\alpha, \phi, x_c) = \int_0^\delta \int_z^\delta \int_{\phi+\sin^{-1}(z/r)}^{\phi+\pi-\sin^{-1}(z/r)} [\beta_1(\theta, r, z)^2 \dots \beta_n(\theta, r, z)^2] d\theta dr dz \begin{bmatrix} \alpha_1^2 \\ \vdots \\ \alpha_n^2 \end{bmatrix} + 2 \int_0^\delta \int_z^\delta \int_{\phi+\sin^{-1}(z/r)}^{\phi+\pi-\sin^{-1}(z/r)} [\beta_1 \beta_2(\theta, r, z) \dots \beta_{n-1} \beta_n(\theta, r, z)] d\theta dr dz \begin{bmatrix} \alpha_1 \alpha_2 \\ \vdots \\ \alpha_{n-1} \alpha_n \end{bmatrix}. \quad (50)$$

Equation (50) involves a summation of products of deterministic coefficients multiplied by random variables and yields the energy release rate for a given probable fracture surface. Having samples of the random variables leads to the determination of the energy release rate PDF for any direction of propagation and length since the deterministic coefficients depend only on  $\phi$ ,  $\delta\alpha$ , and  $x_c$ .

Assuming now that the micromodulus function is of the form of (31), the coefficient  $c$  of (15) can be taken as a random process such as

$$c(r, \vartheta) = \tilde{c}_0 + \hat{c}(r, \vartheta), \quad (51)$$

where  $\tilde{c}_0$  is the mean value.

The stiffness density of (33) and (34) involve integration over the horizon  $\delta$ . Thus, the random process can be decomposed by the Karhunen–Loève expansion in a way extensively described in stochastic finite element methods (SFEM) in [Ghanem and Spanos 1991]. In this study, the Monte Carlo simulation (MCS) technique is pursued for the determination of the energy PDF, and thus, the random process shown in (51) is sampled for the construction of the stiffness density. Due to the computational intensity of MCS, only the static case with initial fracture inside the domain is addressed in this study. In this context, (47), which involves the inversion of a random matrix, is obtained using the inverse Neumann expansion used in SFEM [Ghanem and Spanos 1991]. This yields

$$\begin{bmatrix} a_{11} \\ d_{11} \\ \vdots \\ a_{21} \\ d_{21} \\ \vdots \end{bmatrix} = \sum_{j=0}^{N_e} \begin{bmatrix} \left[ \sum_i \tilde{K}_{Gi} \sum_j \tilde{K}_{Qi} \right]^{-1} & \left[ \sum_i K_{Gi} \sum_j K_{Qi} \right] \\ \left[ \sum_j Q_j^T \quad 0 \right] & \left[ \sum_j Q_j^T \quad 0 \right] \end{bmatrix}^j \begin{bmatrix} \left[ \sum_i \tilde{K}_{Gi} \sum_j \tilde{K}_{Qi} \right]^{-1} \\ \left[ \sum_j Q_j^T \quad 0 \right] \end{bmatrix} \begin{bmatrix} b \\ 0 \end{bmatrix}, \quad (52)$$

where  $N_e$  is the order of the Neumann expansion,  $\tilde{K}_G$  and  $\tilde{K}_Q$  are the average stiffness densities corresponding to the mean value of the random field, and  $K_G$  and  $K_Q$  are the stiffness densities corresponding to the zero mean random field. Note that a quite large sample of the coefficients must be calculated by pertinent MC simulations in order for the PDF of the energy release rate to be available for all lengths and angles of the crack propagation.

**6.3. Monte Carlo application.** For the example shown in Figure 9 with initial crack of 2 mm in the middle of the domain,  $\delta\alpha = 1$  mm, the PDF of the energy release rate at angles  $\phi = \pi$  and  $\phi = 3\pi/4$  is

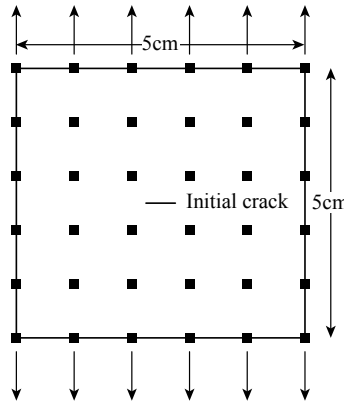


**Figure 9.** A  $5\text{ cm} \times 5\text{ cm}$  plate under tension, including an initial crack in the center.

calculated by extensive MC simulations of (50) and (52). White Gaussian noise is used for the random process describing the micromodulus coefficient  $c$  with mean value obtained from (16) for bulk modulus  $k = 1\text{ N/cm}^2$ . The horizon is discretized using 100 points, and thus 100 identical independent Gaussian random variables are considered. The inversion of the random matrix is obtained by a fourth-order Neumann expansion and the loading is perturbed by an additional white Gaussian noise with standard deviation 20% of the mean value which is taken to be equal to  $1\text{ N/cm}^2$ .

After a large enough sample of the coefficients is obtained by pertinent MCS of (52), the probability density function of fracture in omnidirectional propagation orientations can be calculated by the deterministic integration of the coefficients of (50) for any angle  $\phi$ , propagation length  $\delta\alpha$ , and initial crack tip point  $x_c$ . Figure 10 shows one realization of the random micromodulus coefficient with variance 20% of the mean value shown in (51). Figure 11 summarizes the results for the two approaches. The state of the art mesh-free numerical method is considered the method described in [Silling and Askari 2005].

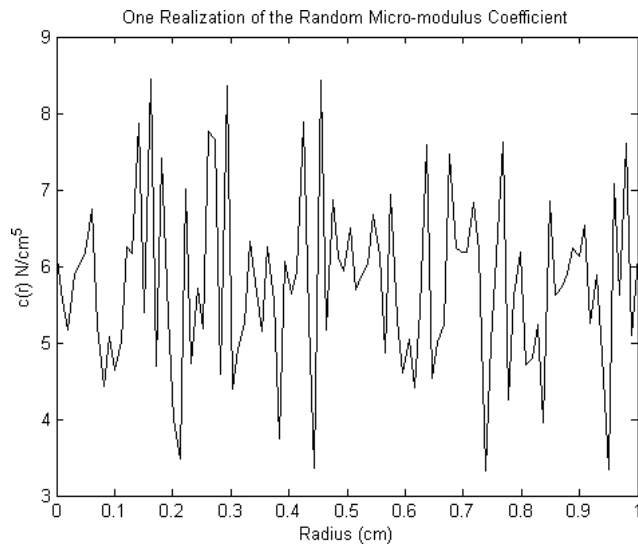


**Figure 10.** Random micromodulus coefficient spanning the horizon from 0 to  $\delta$ .

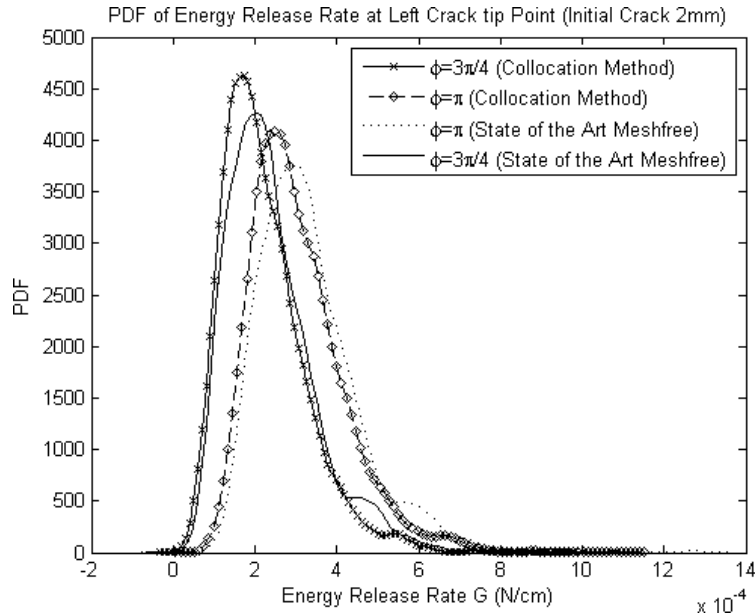


**Figure 11.** The PDF of the energy release rate for the left crack tip point estimated by 6000 Monte Carlo simulations.

The grid used for the mesh-free numerical method is  $\Delta x = 0.01$  cm and thus 10201 nodes have been used. The horizon  $\delta = 5\Delta x$  and the force constant  $c$  is sampled from a Gaussian distribution.

The PDFs obtained from 6000 MC simulations using the two methods are in reasonable agreement. However, the difference of the PDFs shown in Figure 11 is attributed to the fact that the methods do not produce identical results around the crack tip. Obviously, a finer grid of nodes will produce more accurate results for the Kansa collocation method. Further, for slightly different cracks inside the element the results deviate from the ones obtained by closed-form solutions. A possible resolution of this issue is the refinement of the grid by adding more nodes on the cracked element. However, in this paper, the introduction of a novel spatial discretization for deterministic/stochastic peridynamic modeling is the primary concern, and further work is warranted towards the direction of specifically describing the enrichment efficiency vis a vis the node refinement. In this model, node refinement was not considered due to the nature and simplicity of the numerical example and due to the fact that the enrichment of the  $q$  basis [Fleming et al. 1997] provided quite accurate results for the specific example. However, for more elaborate cracks and medium shapes, node refinement is the most convenient option to achieve accuracy at the expense of additional computation cost.

## 7. Concluding remarks

In this work the application of peridynamic modeling to stochastic systems incorporating discontinuities has been considered. A novel approach for the spatial discretization of the integrodifferential equation arising from peridynamic theory that allows for stochastic extension has been devised. This spatial discretization has been based on the inverse multiquadric radial basis functions enriched with polynomials

from the finite element method. Due to this formulation the stochastic problem has been solved in a manner similar to the stochastic finite element method, with some minor differences arising from the peridynamic stiffness density formulation. Following this similar path to the finite element method, the stiffness density of each element surrounded by four nodes has been constructed incorporating the fracture inside. The discontinuity inside the element has been handled by applying the visibility criterion and by changing the integration limits in the polar coordinate system. After formulating the stiffness density of the healthy and cracked elements, the global stiffness density matrix on the collocation points has been assembled and the system has become readily solvable. Next, the idea that the crack propagates in such a way that the energy release rate attains its maximum value has been adopted. In this context, since a continuous approximation has been devised for the displacements inside the domain, the energy release rate has been calculated progressively around the crack tip. For systems with random material properties under random excitations the PDF of the energy release rate has been obtained by Monte Carlo simulation of the requisite Neumann expansion. Further, having the PDF of the energy release for the area around the crack tip determines whether the crack propagates and in which direction with respect to the initial crack surface. Furthermore, this formulation has the advantage that the equilibrium equation is formed in terms of force density and displacement. Thus, there is no need for a double integration over the discontinuous medium. In the preceding regard, this is the first paper correlating the peridynamic formulation with reliability of failure. Specifically, stochastic fracture propagation and stochastic response of systems modeled utilizing the peridynamic formulation has been presented and results have demonstrated the effectiveness of the proposed approach.

### Appendix A: Numerical integration for stiffness determination

For elements that do not include fracture or any kind of discontinuity the integrations of (33) are carried out by Gaussian quadrature using  $2 \times 2$  points. Figure A.1 shows the Gaussian quadrature points.

Integrating the function  $f(r, \theta)$  on a 2D rectangular domain  $H = [\theta_1, \theta_2] \times [r_1, r_2]$  yields

$$\int_{r_1}^{r_2} \int_{\theta_1}^{\theta_2} f(r, \theta) dr d\theta = \frac{r_2 - r_1}{2} \frac{\theta_2 - \theta_1}{2} \int_{-1}^1 \int_{-1}^1 f\left(\frac{r_2 - r_1}{2}\hat{r} + \frac{r_2 + r_1}{2}, \frac{\theta_2 - \theta_1}{2}\hat{\theta} + \frac{\theta_2 + \theta_1}{2}\right) d\hat{r} d\hat{\theta}. \quad (\text{A.1})$$

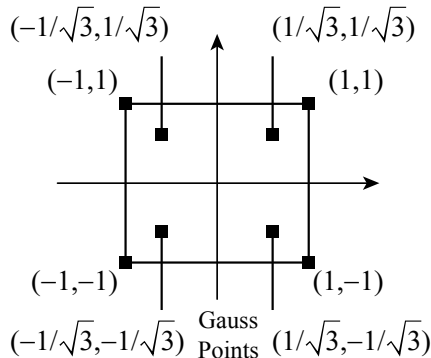


**Figure A.1.** Gaussian quadrature of  $2 \times 2$  points of weight 1.

Applying Gaussian quadrature of  $2 \times 2$  points for the numerical integration of (A.1) yields

$$\int_{r_1}^{r_2} \int_{\theta_1}^{\theta_2} f(r, \theta) dr d\theta = \frac{r_2 - r_1}{2} \frac{\theta_2 - \theta_1}{2} \sum_{i,j=1}^2 \left( \frac{r_2 - r_1}{2} \hat{r}_i + \frac{r_2 + r_1}{2}, \frac{\theta_2 - \theta_1}{2} \hat{\theta}_i + \frac{\theta_2 + \theta_1}{2} \right). \quad (\text{A.2})$$

Next, for elements including fracture and discontinuity, numerical integration on a refined grid of points is needed. Figure A.2 shows an example of a refined grid.

The accurate determination of the fracture contour in polar coordinates is considered herein; specifically the determination of the curve  $AB$  shown in Figure A.2. For the purposes of elucidation consider the initial crack shown in Figure A.3. Next, the position of the initial crack is known, therefore the vectors shown in Figure A.3 can be obtained;  $\underline{z}_1$  and  $\underline{z}_2$  are the vectors from the node of interest to the crack tips and  $\underline{u}$  is the vector aligned with the crack with orientation from one crack tip to the other. The

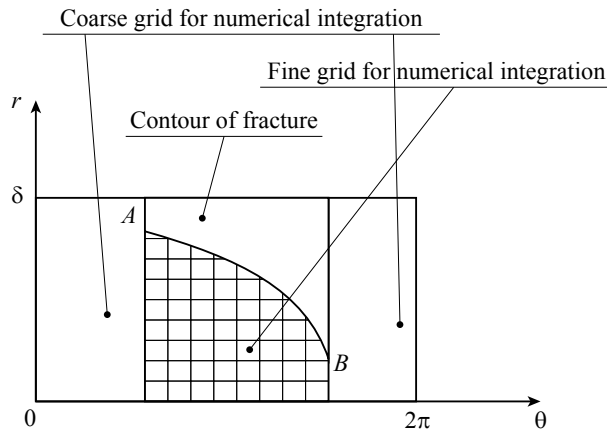


**Figure A.2.** Refined discretization for the numerical evaluation of the stiffness density of a fractured element.

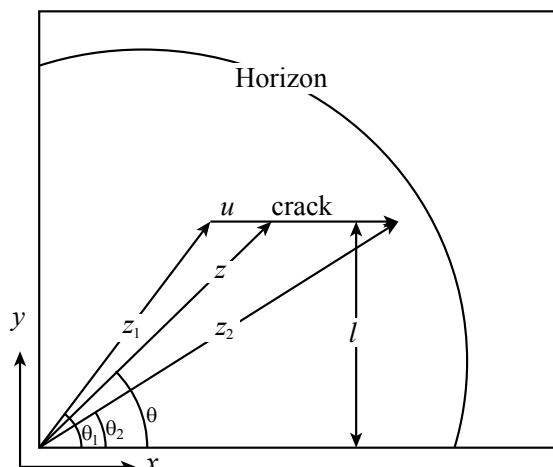


**Figure A.3.** Determination of the fractured contour of a cracked element.

tangent of the angle of a vector  $\underline{z}$  shown in Figure A.3 is given by

$$\tan \theta(a) = \frac{l}{|\underline{z}_1| \cos \theta_1 + \alpha |\underline{u}|}, \quad (\text{A.3})$$

where  $\alpha$  is a coefficient such that  $\alpha \in [0, 1]$ . Next, the partial derivative of (A.3) with respect to the coefficient  $\alpha$  yields

$$\frac{d\theta}{d\alpha} \frac{1}{\cos^2 \theta(\alpha)} = -\frac{l|\underline{u}|}{(|\underline{z}_1| \cos \theta_1 + \alpha |\underline{u}|)^2}. \quad (\text{A.4})$$

Carrying out the calculations yields a simplified expression for (A.4):

$$d\theta = -\frac{l|\underline{u}|}{(|\underline{z}_1| \cos \theta_1 + \alpha |\underline{u}|)^2 + l^2} d\alpha. \quad (\text{A.5})$$

Obviously, as the vector  $\alpha \vec{u}$  approaches the crack tip on the right, the rate of the angle is changing. Thus, the curve  $AB$  shown in Figure A.2 is obtained numerically by fixing the  $d\alpha$  value. Specifically, for a certain  $d\alpha$  value,  $\alpha_j$  is defined as

$$\alpha_j = j \cdot d\alpha, \quad (\text{A.6})$$

where  $j = 1, \dots, 1/d\alpha$  and thus  $d\theta_j$  is defined as

$$d\theta_j = -\frac{l|\underline{u}|}{(|\underline{z}_1| \cos \theta_1 + \alpha_j |\underline{u}|)^2 + l^2} d\alpha. \quad (\text{A.7})$$

Numerically integrating (A.7) by fixing  $d\alpha$  yields

$$\theta_j = \theta_1 - \sum_j \frac{l|\underline{u}|}{(|\underline{z}_1| \cos \theta_1 + \alpha_j |\underline{u}|)^2 + l^2} d\alpha. \quad (\text{A.8})$$

Next, the corresponding length  $r_j$  to the angle  $\theta_j$  shown in Figure A.2 yields

$$r_j = |\underline{z}_1 + \alpha_j \underline{u}|. \quad (\text{A.9})$$

In this way the curve  $AB$  is obtained as points  $\theta_j$  and  $r_j$  for  $\alpha_j \in [0, 1]$ , and thus the contour of integration is determined for the numerical integration. For purposes of elucidation, points  $A$  and  $B$  in Figure A.2 correspond to the crack tips  $\underline{z}_2$  and  $\underline{z}_1$  shown in Figure A.3. In the same way (34) is numerically evaluated for elements including cracks. However, for healthy elements, polynomial functions  $q$ , and the micromodulus function shown in (31), the integration has a closed-form solution. Specifically, consider the first four linear functions of FEM as the  $q$  functions

$$q_1(\underline{x}) = 1, \quad q_2(\underline{x}) = x, \quad q_3(\underline{x}) = y, \quad q_4(\underline{x}) = xy. \quad (\text{A.10})$$

Combining (29), (34), and (A.10) yields

$$K_Q = c \int_0^\delta \left[ \int_0^{2\pi} \begin{bmatrix} \cos^2 \theta & \cos \theta \sin \theta \\ \cos \theta \sin \theta & \sin^2 \theta \end{bmatrix} [0 \ r \cos \theta \ r \sin \theta \ (x + r \cos \theta)(y + r \sin \theta) - xy] d\theta \right] dr,$$

expanding which yields

$$K_Q = c [K_{Q1} \ K_{Q2} \ K_{Q3} \ K_{Q4}], \quad (\text{A.11})$$

where

$$K_{Q1} = \begin{bmatrix} 0 & 0 \\ 0 & 0 \end{bmatrix}, \quad K_{Q2} = \left[ \begin{array}{cc} \frac{\cos^2 \theta \sin \theta}{3} + \frac{2 \sin \theta}{3} & -\frac{\cos^3 \theta}{3} \\ -\frac{\cos^3 \theta}{3} & \frac{\sin^3 \theta}{3} \end{array} \right] \Big|_0^{2\pi} \frac{r^2}{2} \Big|^{\delta},$$

$$K_{Q3} = \left[ \begin{array}{cc} -\frac{\cos^3 \theta}{3} & \frac{\sin^3 \theta}{3} \\ \frac{\sin^3 \theta}{3} & \frac{\cos \theta \sin^2 \theta}{3} - \frac{2 \cos \theta}{3} \end{array} \right] \Big|_0^{2\pi} \frac{r^2}{2} \Big|^{\delta},$$
(A.12)

and finally

$$K_{Q4} = \left[ \begin{array}{cc} -\frac{\cos^4 \theta}{4} & -\frac{\sin^2 \theta \cos^3 \theta}{4} + \frac{\theta}{8} + \frac{\sin 2\theta}{16} \\ -\frac{\sin^2 \theta \cos^3 \theta}{4} + \frac{\theta}{8} + \frac{\sin 2\theta}{16} & \frac{\sin^4 \theta}{4} \end{array} \right] \Big|_0^{2\pi} \frac{r^3}{3} \Big|^{\delta} + xK_{Q3} + yK_{Q2}. \quad (\text{A.13})$$

## Appendix B: Kansa collocation method

The Kansa collocation method in 1D, for a set of  $N = L/\Delta x + 1$  equally spaced grid points of distance  $\Delta x$ , yields the equations in the following form:

$$\begin{bmatrix} u(0) \\ u(\Delta x) \\ u(2\Delta x) \\ \vdots \\ 0 \\ 0 \end{bmatrix} = \begin{bmatrix} g_1(0) & g_1(0) & \dots & g_N(0) & q_0(0) & \dots \\ g_1(\Delta x) & g_1(\Delta x) & \dots & g_N(\Delta x) & q_0(\Delta x) & \dots \\ g_1(2\Delta x) & g_1(2\Delta x) & \dots & g_N(2\Delta x) & q_0(2\Delta x) & \dots \\ \vdots & \vdots & \vdots & \vdots & \vdots & \vdots \\ q_1(0) & q_1(\Delta x) & q_1(2\Delta x) & \dots & 0 & 0 \\ \vdots & \vdots & \vdots & \vdots & 0 & 0 \end{bmatrix} \begin{bmatrix} a_{11} \\ a_{12} \\ \vdots \\ a_{1N} \\ a_{21} \\ \vdots \end{bmatrix}. \quad (\text{B.1})$$

The last  $M$  rows represent the regularization equations of the coefficients which state that

$$\sum_{k=1}^N q_j(\underline{x}_k) d_{2k} = 0 \quad \text{and} \quad \sum_{k=1}^N q_j(\underline{x}_k) d_{2k} = 0 \quad \text{for } j = 1, \dots, M, \quad (\text{B.2})$$

where  $M$  is the number of the additional basis functions  $q$ .

Assuming that the displacements of a point in the domain of Figure B.1 can be approximated by the adjacent nodes, (26) yields the displacement for a point inside the upper right square:

$$u(\underline{x}_i + \underline{r}) = \sum_{k=i}^{i+3} a_{1k} g_k(\underline{x}_i + \underline{r}) + \sum_{j=1}^M a_{2j} q_j(\underline{x}_i + \underline{r}),$$

$$v(\underline{x}_i + \underline{r}) = \sum_{k=i}^{i+3} d_{1k} g_k(\underline{x}_i + \underline{r}) + \sum_{j=1}^M d_{2j} q_j(\underline{x}_i + \underline{r}).$$
(B.3)

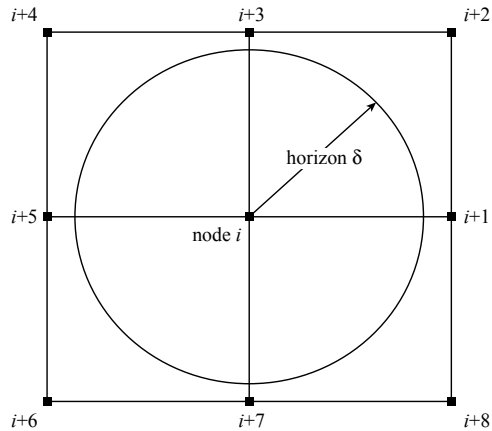


**Figure B.1.** The horizon of one node over four elements, the stiffness density of the node  $i$  is calculated through (33) and (34).

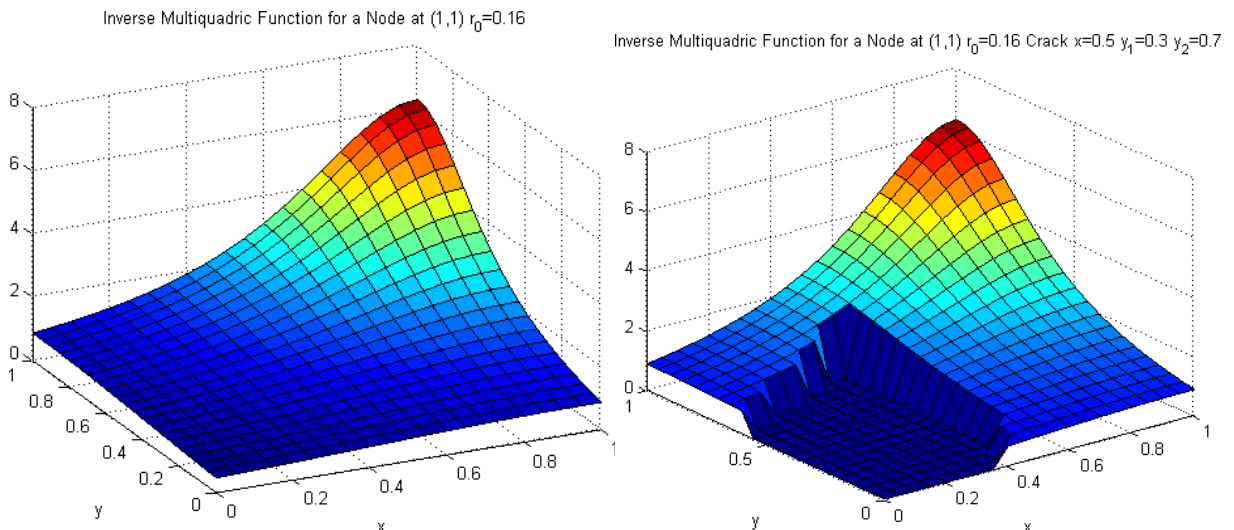


**Figure B.2.** IMQ basis function of the corresponding node on a four-node element, with and without a crack inside the horizon.

Figure B.2 shows the IMQ function for the same node, both for a healthy and a cracked four-node element. It can be seen that the visibility criterion is applied on the cracked element since the crack disrupts the horizon of the node.

### Appendix C: Linearized pairwise force function

The linearized pairwise force function as introduced in [Silling 2000] imposes an implicit assumption of small rigid body rotations. Specifically, consider Equation (12), which defines the stretch of a bond.

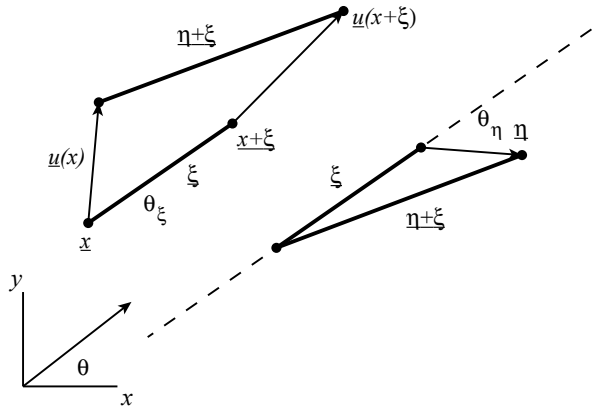


**Figure C.1.** One bond before and after deformation.

Carrying out the calculations yields

$$s = \left| 1 + \frac{\underline{\eta}}{\underline{\xi}} \right| - 1. \quad (\text{C.1})$$

Next, using complex notation for the vectors yields

$$\underline{\eta} = |\underline{\eta}|(\cos \theta_\eta + i \sin \theta_\eta), \quad \underline{\xi} = |\underline{\xi}|(\cos \theta_\xi + i \sin \theta_\xi), \quad (\text{C.2})$$

where  $\theta_\eta$  and  $\theta_\xi$  are the angles of the vectors with respect to the orthogonal reference system. Figure C.1 helps elucidate the concept. Next, combining both parts of (C.2) yields

$$\frac{\underline{\eta}}{\underline{\xi}} = \frac{|\underline{\eta}|}{|\underline{\xi}|} (\cos(\theta_\eta - \theta_\xi) + i \sin(\theta_\eta - \theta_\xi)). \quad (\text{C.3})$$

Obviously the angles of the vectors determine if the vector division yields a vector or a scalar. For the case of

$$\theta_\eta \simeq \theta_\xi, \quad (\text{C.4})$$

(C.3) yields

$$\frac{\underline{\eta}}{\underline{\xi}} \simeq \frac{|\underline{\eta}|}{|\underline{\xi}|}, \quad (\text{C.5})$$

and (C.1) becomes

$$s \simeq \frac{|\underline{\eta}|}{|\underline{\xi}|}. \quad (\text{C.6})$$

Equation (C.6) implicitly assumes that the deformation of the bond is collinear with the bond's initial orientation or that the bond exhibits small rotation which can be neglected.

## References

- [Belytschko et al. 1994] T. Belytschko, L. Gu, and Y. Y. Lu, "Fracture and crack growth by element free Galerkin methods", *Model. Simul. Mater. Sci. Eng.* **2**:3A (1994), 519–534.
- [Belytschko et al. 1995] T. Belytschko, Y. Y. Lu, and L. Gu, "Crack propagation by element-free Galerkin methods", *Eng. Fract. Mech.* **51**:2 (1995), 295–315.

- [Bobaru 2007] F. Bobaru, "Influence of van der Waals forces on increasing the strength and toughness in dynamic fracture of nanofibre networks: a peridynamic approach", *Model. Simul. Mater. Eng.* **15**:5 (2007), 397–417.
- [Bobaru et al. 2009] F. Bobaru, M. Yang, L. F. Alves, S. A. Silling, E. Askari, and J. Xu, "Convergence, adaptive refinement, and scaling in 1D peridynamics", *Int. J. Numer. Methods Eng.* **77**:6 (2009), 852–877.
- [Emmrich and Weckner 2007a] E. Emmrich and O. Weckner, "On the well-posedness of the linear peridynamic model and its convergence towards the Navier equation of linear elasticity", *Commun. Math. Sci.* **5**:4 (2007), 851–864.
- [Emmrich and Weckner 2007b] E. Emmrich and O. Weckner, "The peridynamic equation and its spatial discretisation", *Math. Model. Anal.* **12**:1 (2007), 17–27.
- [Eringen et al. 1977] A. C. Eringen, C. G. Speziale, and B. S. Kim, "Crack-tip problem in non-local elasticity", *J. Mech. Phys. Solids* **25**:5 (1977), 339–355.
- [Fleming et al. 1997] M. Fleming, Y. A. Chu, B. Moran, and T. Belytschko, "Enriched element-free Galerkin methods for crack tip fields", *Int. J. Numer. Methods Eng.* **40**:8 (1997), 1483–1504.
- [Gdoutos 1990] E. E. Gdoutos, *Fracture mechanics: criteria and applications*, edited by G. C. Sih, Engineering Application of Fracture Mechanics **10**, Kluwer Academic, Dordrecht, 1990.
- [Ghanem and Spanos 1991] R. G. Ghanem and P. D. Spanos, *Stochastic finite elements: a spectral approach*, Springer, New York, 1991.
- [Kansa 1990a] E. J. Kansa, "Multiquadratics—a scattered data approximation scheme with applications to computational fluid-dynamics, I: Surface approximations and partial derivative estimates", *Comput. Math. Appl.* **19**:8-9 (1990), 127–145.
- [Kansa 1990b] E. J. Kansa, "Multiquadratics—a scattered data approximation scheme with applications to computational fluid-dynamics, II: Solutions to parabolic, hyperbolic and elliptic partial differential equations", *Comput. Math. Appl.* **19**:8-9 (1990), 147–161.
- [Kröner 1967] E. Kröner, "Elasticity theory of materials with long range cohesive forces", *Int. J. Solids Struct.* **3**:5 (1967), 731–742.
- [Macek and Silling 2007] R. W. Macek and S. A. Silling, "Peridynamics via finite element analysis", *Finite Elem. Anal. Des.* **43**:15 (2007), 1169–1178.
- [Silling 2000] S. A. Silling, "Reformulation of elasticity theory for discontinuities and long-range forces", *J. Mech. Phys. Solids* **48**:1 (2000), 175–209.
- [Silling and Askari 2005] S. A. Silling and E. Askari, "A meshfree method based on the peridynamic model of solid mechanics", *Comput. Struct.* **83**:17-18 (2005), 1526–1535.
- [Silling et al. 2003] S. A. Silling, M. Zimmermann, and R. Abeyaratne, "Deformation of a peridynamic bar", *J. Elasticity* **73**:1-3 (2003), 173–190.
- [Silling et al. 2007] S. A. Silling, M. Epton, O. Weckner, J. Xu, and E. Askari, "Peridynamic states and constitutive modeling", *J. Elasticity* **88**:2 (2007), 151–184.
- [Warren et al. 2009] T. L. Warren, S. A. Silling, A. Askari, O. Weckner, M. A. Epton, and J. Xu, "A non-ordinary state-based peridynamic method to model solid material deformation and fracture", *Int. J. Solids Struct.* **46**:5 (2009), 1186–1195.
- [Zhou and Du 2010] K. Zhou and Q. Du, "Mathematical and numerical analysis of linear peridynamic models with nonlocal boundary conditions", *SIAM J. Numer. Anal.* **48**:5 (2010), 1759–1780.
- [Zi and Belytschko 2003] G. Zi and T. Belytschko, "New crack-tip elements for XFEM and applications to cohesive cracks", *Int. J. Numer. Methods Eng.* **57**:15 (2003), 2221–2240.

Received 27 Aug 2010. Revised 28 Feb 2011. Accepted 10 Apr 2011.

GEORGIOS I. EVANGELATOS: [Georgios.Evangelatos@bp.com](mailto:Georgios.Evangelatos@bp.com)

*Department of Civil and Environmental Engineering, Rice University, 6100 Main Street, Mail Stop 318,  
Houston, TX 77005-1892, United States*

POL D. SPANOS: [spanos@rice.edu](mailto:spanos@rice.edu)

*Departments of Civil and Mechanical Engineering, Rice University, 6100 Main Street, Mail Stop 321,  
Houston, TX 77005-1892, United States*



## SUBMISSION GUIDELINES

### ORIGINALITY

Authors may submit manuscripts in PDF format online at the Submissions page. Submission of a manuscript acknowledges that the manuscript is original and has neither previously, nor simultaneously, in whole or in part, been submitted elsewhere. Information regarding the preparation of manuscripts is provided below. Correspondence by email is requested for convenience and speed. For further information, write to one of the Chief Editors:

Davide Bigoni      bigoni@ing.unitn.it  
Iwona Jasiuk      ijasiek@me.concordia.ca  
Yasuhide Shindo    shindo@material.tohoku.ac.jp

### LANGUAGE

Manuscripts must be in English. A brief abstract of about 150 words or less must be included. The abstract should be self-contained and not make any reference to the bibliography. Also required are keywords and subject classification for the article, and, for each author, postal address, affiliation (if appropriate), and email address if available. A home-page URL is optional.

### FORMAT

Authors can use their preferred manuscript-preparation software, including for example Microsoft Word or any variant of TeX. The journal itself is produced in L<sup>A</sup>T<sub>E</sub>X, so accepted articles prepared using other software will be converted to L<sup>A</sup>T<sub>E</sub>X at production time. Authors wishing to prepare their document in L<sup>A</sup>T<sub>E</sub>X can follow the example file at [www.jomms.org](http://www.jomms.org) (but the use of other class files is acceptable). At submission time only a PDF file is required. After acceptance, authors must submit all source material (see especially Figures below).

### REFERENCES

Bibliographical references should be complete, including article titles and page ranges. All references in the bibliography should be cited in the text. The use of BibTeX is preferred but not required. Tags will be converted to the house format (see a current issue for examples); however, for submission you may use the format of your choice. Links will be provided to all literature with known web locations; authors can supply their own links in addition to those provided by the editorial process.

### FIGURES

Figures must be of publication quality. After acceptance, you will need to submit the original source files in vector format for all diagrams and graphs in your manuscript: vector EPS or vector PDF files are the most useful. (EPS stands for Encapsulated PostScript.)

Most drawing and graphing packages—Mathematica, Adobe Illustrator, Corel Draw, MATLAB, etc.—allow the user to save files in one of these formats. Make sure that what you're saving is vector graphics and not a bitmap. If you need help, please write to [graphics@mathscipub.org](mailto:graphics@mathscipub.org) with as many details as you can about how your graphics were generated.

Please also include the original data for any plots. This is particularly important if you are unable to save Excel-generated plots in vector format. Saving them as bitmaps is not useful; please send the Excel (.xls) spreadsheets instead. Bundle your figure files into a single archive (using zip, tar, rar or other format of your choice) and upload on the link you been given at acceptance time.

Each figure should be captioned and numbered so that it can float. Small figures occupying no more than three lines of vertical space can be kept in the text (“the curve looks like this:”). It is acceptable to submit a manuscript with all figures at the end, if their placement is specified in the text by means of comments such as “Place Figure 1 here”. The same considerations apply to tables.

### WHITE SPACE

Forced line breaks or page breaks should not be inserted in the document. There is no point in your trying to optimize line and page breaks in the original manuscript. The manuscript will be reformatted to use the journal's preferred fonts and layout.

### PROOFS

Page proofs will be made available to authors (or to the designated corresponding author) at a Web site in PDF format. Failure to acknowledge the receipt of proofs or to return corrections within the requested deadline may cause publication to be postponed.

# Journal of Mechanics of Materials and Structures

Volume 6, No. 7-8

September–October 2011

## Special issue

### Eleventh Pan-American Congress of Applied Mechanics (PACAM XI)

Preface	ADAIR R. AGUIAR	949
Influence of specimen geometry on the Portevin–Le Châtelier effect due to dynamic strain aging for the AA5083-H116 aluminum alloy	RODRIGO NOGUEIRA DE CODES and AHMED BENALLAL	951
Dispersion relations for SH waves on a magnetoelectroelastic heterostructure with imperfect interfaces	J. A. OTERO, H. CALAS, R. RODRÍGUEZ, J. BRAVO, A. R. AGUIAR and G. MONSIVAI	969
Numerical linear stability analysis of a thermocapillary-driven liquid bridge with magnetic stabilization	YUE HUANG and BRENT C. HOUCHENS	995
Numerical investigation of director orientation and flow of nematic liquid crystals in a planar 1:4 expansion	PEDRO A. CRUZ, MURILO F. TOMÉ, IAIN W. STEWART and SEAN MCKEE	1017
Critical threshold and underlying dynamical phenomena in pedestrian-induced lateral vibrations of footbridges	STEFANO LENCI and LAURA MARCHEGGIANI	1031
Free vibration of a simulation CANDU nuclear fuel bundle structure inside a tube	XUAN ZHANG and SHUDONG YU	1053
Nonlinear dynamics and sensitivity to imperfections in Augusti's model	D. ORLANDO, P. B. GONÇALVES, G. REGA and S. LENCI	1065
Active control of vortex-induced vibrations in offshore catenary risers: A nonlinear normal mode approach	CARLOS E. N. MAZZILLI and CÉSAR T. SANCHES	1079
Nonlinear electromechanical fields and localized polarization switching of piezoelectric macrofiber composites	YASUHIDE SHINDO, FUMIO NARITA, KOJI SATO and TOMO TAKEDA	1089
Three-dimensional BEM analysis to assess delamination cracks between two transversely isotropic materials	NICOLÁS O. LARROSA, JHONNY E. ORTIZ and ADRIÁN P. CISILINO	1103
Porcine dermis in uniaxial cyclic loading: Sample preparation, experimental results and modeling	A. E. EHRET, M. HOLLOWSTEIN, E. MAZZA and M. ITSKOV	1125
Analysis of nonstationary random processes using smooth decomposition	RUBENS SAMPAIO and SERGIO BELLIZZI	1137
Perturbation stochastic finite element-based homogenization of polycrystalline materials	S. LEPAGE, F. V. STUMP, I. H. KIM and P. H. GEUBELLE	1153
A collocation approach for spatial discretization of stochastic peridynamic modeling of fracture	GEORGIOS I. EVANGELATOS and POL D. SPANOS	1171



1559-3959(2011)6:7;1-9